I. R. IRAN

ISSN: 1728-1431
e-ISSN: 1735-9244

International Journal of Engineering

Journal Homepage: www.ije.ir

MERC

TRANSACTIONS A: BASICS

Volume 37, Number 01, January 2024

Materials and Energy Research Center

In the Name of God

INTERNATIONAL JOURNAL OF ENGINEERING
Transactions A: Basics

DISCLAIMER
The publication of papers in International Journal of Engineering does not imply that the editorial board, reviewers or publisher accept, approve or endorse the data and conclusions of authors.

International **J**ournal of **E**ngineering *Transactions A: Basics* (ISSN 1728-1431) (EISSN 1735-9244)
International **J**ournal of **E**ngineering *Transactions B: Applications* (ISSN 1728-144X) (EISSN 1735-9244)
International **J**ournal of **E**ngineering *Transactions C: Aspects* (ISSN 2423-7167) (EISSN 1735-9244)
Web Sites: www.ije.ir & www.ijeir.info E-mails: ije.editor8@gmail.com, Tel: (+9821) 88771578, Fax: (+9821) 88773352
Materials and Energy Research Center (MERC)

ISSN: 1728-1431, e-ISSN: 1735-9244

International Journal of Engineering, Volume 37, Number 01, January 2024

CONTENTS

Transactions A: Basics

ISSN: 1728-1431, e-ISSN: 1735-9244

International Journal of Engineering, Volume 37, Number 01, January 2024

IJE TRANSACTIONS A: Basics Vol. 37 No. 01, (January 2024) 1-13

International Journal of Engineering

Journal Homepage: www.ije.ir

A New Comprehensive Model for Integrating Environmental, Economic, and Social Performance of Deep and Large-scale Open-Pit Copper Mines

M. Heydari, M. Osanloo*

Amirkabir University of Technology, Mining Engineering Department, Tehran, Iran

PAPER INFO

Paper history:
Received 05 August 2023
Received in revised form 12 September 2023
Accepted 13 September 2023

Keywords:
Sustainability Assessment
Deep and Large-scale
Open-Pit Copper Mine
Environmental Impact
Economic Impact
Social Impact
Scenarios

ABSTRACT

Deep and large-scale (D&LS) open-pit mines pose various environmental, social, and economic impacts on the mining projects' stakeholders and local, regional, national, and international communities. Identifying these impacts and having a comprehensive model to assess these impacts altogether is critical to achieving sustainable development (SD) goals. This study develops a robust sustainability assessment model for D&LS open-pit mining projects. The model comprehensively considers 99 impact factors across environmental, social, and economic dimensions. The sustainability score is calculated using the Z-FDAHP technique to reduce the bias and uncertainty of experts' judgments. Then, the scenario-based technique is used to apply the stakeholders' perspective to the model. The model is applied to Sungun Copper Mine (SCM) in northwest Iran for verification. Results show SCM's sustainability performance is highly sensitive to index weightings. The highest score was achieved with sole social prioritization (scenario 8 with a sustainability score of 6.364 out of 10), highlighting the critical role of community impacts. Environmental or economic focus alone (scenarios 2 and 5) was not very sustainable, with scores of 3.326 and 5.298 respectively. Scores of 5.543, 5.330, and 5.117 for sustainability can be achieved by optimizing all three SD aspects with a long-term, stakeholder-centered approach (scenarios 9, 4, and 6). The proposed sustainability assessment model exhibits robustness through its comprehensive set of 99 environmental, social, and economic indicators; its ability to customize indicator weights under different stakeholder-perspective scenarios; and validation of the quantitative scoring approach through an empirical case study, while continuous improvement would further reinforce its robustness over time.

doi: *10.5829/ije.2024.37.01a.01*

Graphical Abstract

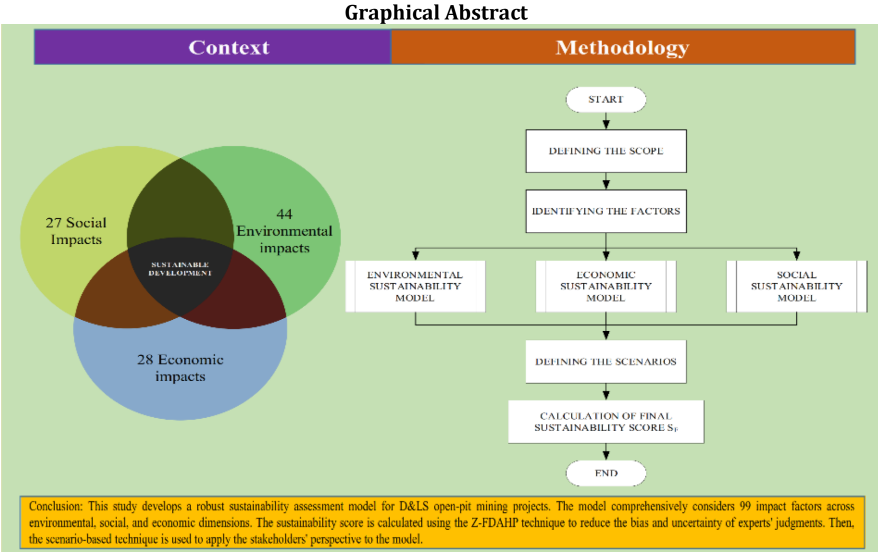

*Corresponding author email: *morteza.osanloo@gmail.com* (M. Osanloo)

Please cite this article as: Heydari M, Osanloo M. A New Comprehensive Model for Integrating Environmental, Economic, and Social Performance of Deep and Large-scale Open-Pit Copper Mines. International Journal of Engineering, Transactions A: Basics, 2024;37(01): 1-13.

1. INTRODUCTION

Copper mining provides a resource that is important for many industrial uses. Reasons for rising copper demand include a growing world population, greater economic activity, and increased manufacturing of copper-containing products like power cables, electronics, plumbing, and building materials. Along with the depletion of high-quality, easily accessible copper sources, large-scale mining of lower-grade and deeper copper deposits has become necessary due to this increased demand. However, copper mining, like many other metals and minerals mining, impacts environmental, economic, and social aspects requiring management for sustainable development. Deep and Large-Scale (D&LS) open-pit mines present unique sustainability challenges due to their large scale, high resource throughput, emissions, water usage, land use impacts, and potential effects on communities and ecosystems. These complex projects require thorough, sophisticated analyses to balance mining needs with environmental and social responsibility. However, with careful planning and stakeholder involvement, such operations can help meet increasing copper demand in an environmentally and socially responsible manner while minimizing negative impacts. Numerous scholars have researched the environmental, economic, and social impacts of mining activities.

Vizayakumar and Mohapatra (1) addressed the environmental impacts of coal mining activity. Coal is the primary source of energy in India, but environmental pollution in agricultural areas is very severe. Rybicka (2) examined the environmental impacts of mines in Poland and noted an increasing concentration of pollutants, especially heavy metals, in natural soils and water systems from industrial sources poses a serious threat. Work on defining key parts of Environmental Impact Assessments (EIAs) started with Sadler's 1996 report [3]. He described effectiveness as how well an assessment achieves its intended objectives. Three main types of effectiveness were identified: procedural, material, and financial. Procedural focuses on process structure and policy continuity. The material examines the impact on decision-making and reducing negative environmental impacts. Financial concerns costs and time of EIA (3). Jarvis and Younger (4) studied the EIA of mine water, with pollution from mines being a major water problem in the UK (United Kingdom) and internationally. Kuma et al. (5) researched EIAs in Ghana, proposing an approach for pre-mining groundwater economic and technical impact identification, though neglecting other environmental impacts. Folchi (6) proposed a widely used model to investigate the environmental impacts of open-pit mines, considering only 8 impact factors. The Folchi model has been used by many scholars ever since, but it has a narrow scope and does not account for all impacts (7-9). In 2006, Kitula (10) examined the socioeconomic impacts of mining activities in the Geita district in Ghana. The findings showed that approximately 66% of mining community households' income was derived from the mining industry. Additionally, it was found that less than 5% of Ghana's Gross Domestic Product (GDP) originated from mineral extraction. The small amount added to GDP compared to mining's large local importance means Ghana's mining industry needs more investment. Pandey et al. (11) studied the environmental impacts of the Malanjkhand copper mine in India. They investigated various factors such as acid mine drainage (AMD), impacts on flora and fauna, general environmental pollution, water quality, and impacts on aquatic organisms. Rashed (12) assessed and monitored pollution from the tailings of the Allaqi Wadi Aswan gold mine in southeast Egypt. Aryafar et al. (13) employed a modified Folchi method to assess the environmental implications of the East-Alborz coal-washing plant in northeastern Iran. The researchers used an adapted Folchi approach to analyze the environmental impacts of a coal facility in Iran. Similarly, Northey et al. (14) assessed impacts of copper mining through sustainability report data. By using corporate sustainability reports, they could evaluate the environmental consequences of copper mining operations. Minaei Mobtaker and Osanloo (15) conducted a study examining the potential positive outcomes of mining operations. The research showed mining can provide various economic, social, and environmental benefits based on the evaluation of impacts. Northey et al. (16) evaluated the environmental impacts of copper mining using data from sustainable development reports. They focused on factors like greenhouse gas emissions, fossil fuel consumption, and water consumption. Taušová et al. [17] investigated the socioeconomic impacts of mining over time in Slovakia. Research has found around 4,000 employees work in the Prievidza region directly involved in mining. Additionally, approximately 6,000 more jobs are indirectly supported by or connected to mining activities in the area (17). Amirshenava and Osanloo (18) developed a framework to assess the impact of mining activities on sustainable development indicators. Their model included 14 criteria: 8 environmental criteria, 3 social criteria, and 3 economic criteria. Yankson and Gough (19) studied the influence of gold mining on livelihoods and transformations in the mining scale. The research found that between 2001 and 2011, gold mining contributions to household income increased up to five-fold in certain localities. This suggests mining, particularly artisanal and small-scale gold extraction, played a dramatically heightened economic role for communities over that decade-long period according to the income data analyzed. Von der Goltz and Barnwal (20) conducted an extensive analysis of 800 mines across 44 developing nations, finding mining operations provide considerable long-term economic gains but these are also spatially constrained. They discovered that asset levels were higher for those within 20 km of mines, showing mining wealth mainly stays within close local communities. But for people living farther than 20 km, there was no correlation between mining activity and increased household assets or prosperity. So, while mining boosts local economies, these economic impacts do not spread much past the tight sphere of direct influence around 20 km from mine sites, with the gains mostly confined to nearby local communities close to the mining operations. Argimbaev et al. (21) examined iron-bearing tailings from waste dumps at ore processing facilities in the Kursk Magnetic Anomaly region of Russia. Microscope examination from 90-600x magnification revealed varied particle sizes and shapes indicating potential construction uses for tailings after further processing. Tabasi and Kakha (22) evaluate the environmental impacts of granite quarrying activities near Boog, Iran. By quantifying the impacts of factors on designated environmental components with a systematic fuzzy approach, this research assisted in environmental impact assessments for mining projects. Atienza et al. (23) examined the impacts of mining on urban growth in Chile. Through standard econometric analysis, they discovered that real estate investment expansion primarily correlated with mining activity, copper exports, national monetary fluidity, and regional wages. Consequently, mining income in urban areas appears predominantly influenced by household earnings from mining and the subsequent redistribution of this income into property and asset investments. Hosseinpour et al. (24) proposed a framework of 29 positive and negative impacts; but it is not specific to D&LS mines. Cacciuttolo and Cano (25) analyzed the environmental impacts of gold and copper extraction in Chile and Peru, which considered metallurgical processing. Kumar et al. (26) analyzed the geotechnical properties and remediation of contaminated soil from gold mines in Karnataka, India. The research sought to characterize the contaminated mine soil geotechnically and identify a soil-washing method to prevent surrounding environmental pollution. Sanjuan-Delmás et al. (27) evaluated the life cycle environmental impacts of European copper production using SimaPro and GaBi software. Gümüşsoy et al. (28) investigated the economic potential and environmental consequences of extracting metals from copper flotation slag. Song et al. (29) assessed the environmental conditions in mineral-rich areas of China using remote sensing techniques. The impacts of noise and noise control strategies at the large-scale Zijin copper mine in Serbia was evaluated by Pantelic et al. (30). Dust levels in a Chinese coal mine was estimated by Luan et al. (31) applying machine learning models. Jafarzadeh et al. (32) used numerical modelling to analyze different cover system designs for mine tailing dams in arid regions. The research found that a capillary barrier cover system was most effective at maintaining around 80% saturation in the storage layer, immediately cutting off oxygen diffusion compared to other designs. By optimizing the cover system and controlling oxygen entry parameters, mine waste sites can better reduce AMD. Alsaleh et al. (33) analyzed the effect of geothermal energy output on carbon dioxide emissions across European nations from 1990 to 2021. Heydari et al. (34) proposed a 37-factor social impact assessment model for mining. However, it focuses only on social impacts, not environmental and economic impacts. Heydari and Osanloo (35) proposed a 44-factor environmental impact assessment model for D&LS open-pit mines. In another study, they developed a 28-factor economic impact assessment model (36). The existing studies on the environmental impacts of mining have limitations. None of the research looks at the effects of D&LS open-pit mines comprehensively. The models also do not address all three indexes of sustainable development - environmental, economic, and social - in their assessment. A sustainability model is needed that considers all three dimensions to identify sustainability issues. This type of mine requires a customized sustainability assessment model. The current studies do not fully examine the impacts of D&LS open-pit mines or provide a solution for assessing sustainability in this context by looking at all SD indexes together.

This study aims to (1) combine three separate models for environmental, economic, and social assessment to make a single inclusive sustainability model under different scenarios, (2) calculate a sustainability score for D&LS copper mines from different stakeholders' point of view, and (3) give mine managers and stakeholders a unified tool to inform decisions for more sustainable mining. The model will be verified using the Sungun Copper Mine in Iran.

2. METHODOLOGY

Previous studies proposed individual models for assessing the social, environmental, and economic aspects of copper mine sustainability (34-36). This study combines those three models into one comprehensive sustainability model for D&LS open-pit copper mines. It includes all three sustainable development areas. This helps work towards the Sustainable Development Goals (SDGs). The proposed model involves defining the model scope, collecting data, and getting final results from the three component models, which were developed by the authors. Then it calculates importance weights, scores, and the overall sustainability score. This provides a unified assessment approach. to calculate the sustainability score for each sustainable development (SD) index. Scenarios are then defined to capture various stakeholders' points of view. Finally, the sustainability score for D&LS copper open-pit mines can be determined (see Figure 1).

2. 1. The Scope When modeling the sustainability score of a D&LS open-pit copper mine, the following items should be considered as part of the model scope:

1. Environmental sustainability: This aspect of the model scope should consider the impact of mining activities on the environment, including air and water quality, land use, and biodiversity.
2. Economic sustainability: This aspect should consider the mine's ability to generate economic benefits, such as employment opportunities and contributions to local and national economies. The model should also evaluate the costs associated with D&LS open-pit mining, such as waste disposal and remediation.
3. Social sustainability: This aspect of the model scope should consider the mine's impact on the health, safety, and well-being of workers and local communities, as well as its contribution to the development of local infrastructure and social programs. The model should evaluate the mine's performance in terms of labor standards, community engagement, and social responsibility.

By considering these items in the model scope, a comprehensive assessment of the sustainability performance of a D&LS open-pit copper mine can be obtained.

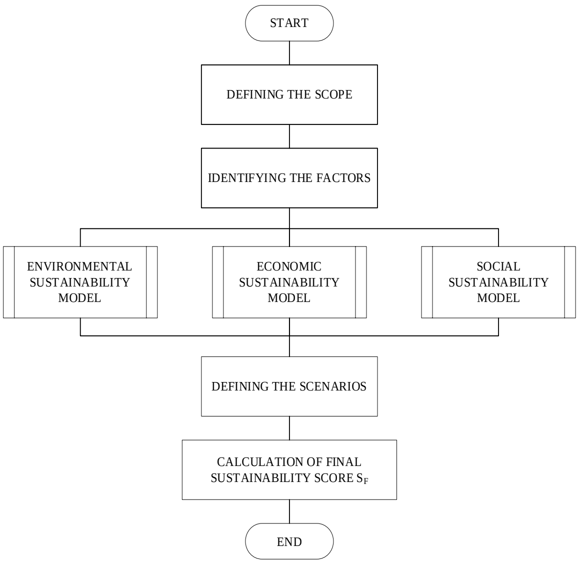

Figure 1. Schematic overview of the proposed model

2. 2. Factors Identification Identifying factors for a sustainability model of a D&LS open-pit copper mine requires a multidisciplinary approach and the collection of data from various sources. The following are some steps that can be taken to identify the factors for the model:

1. Identify the requirements: Based on the items considered in the model scope, identify the requirements for each of the models that need to be considered. The requirements include possible environmental, economic, and social factors.
2. Create a list: Create a list by conducting site visits, surveys, and interviews with stakeholders such as mine workers, local communities, and various sources such as company reports, academic papers, government reports, and industry databases.
3. Ensure completeness of the list: It is important to ensure the list collected is complete by using reliable sources and validated methods.

TABLE 1. Environmental Factors for a Comprehensive Model

No.	Affecting factor	Definition
1	Overburden	Volume of overburden rock removed to access orebody at depths near 1000m
2	Waste rock	Volume of waste rock from low-grade orebodies at depths near 1000m
3	Tailing	Volume of tailings from processing low-grade orebodies mined at depths near 1000m
4	Waste Management	Reusing mine tailings and managing waste materials
5	Acid Mine Drainage	Acid mine drainage potential from pyrite in orebody
6	Ecosystem	Impacts on local biodiversity from habitat loss or fragmentation affecting species
7	Deforestation	Removing forest canopy to access orebody underneath
8	Life Below Water	Impacts on aquatic life from polluting nearby water
9	Ecotoxicity	Toxic impacts and contaminants harming terrestrial and aquatic organisms
10	Ecosystems amend due to reclamation	Improving ecosystem health through habitat, water, and biodiversity restoration

11	Topsoil quality	Topsoil removal eliminates organic matter, nutrients, and microbes. Heavy equipment compacts soil reducing porosity and aeration. Waste rock piles degrade soils.
12	Deep soil quality	Soil properties at depth differ from topsoil due to compaction, depletion, and changes from mining.
13	Terrestrial ecotoxicity	Potential soil contamination varies by project scale and waste volumes.
14	Eutrophication	Mining could affect nutrient-rich surface water through mineral and nutrient inputs.
15	Freshwater ecotoxicity	Freshwater ecotoxicity metrics like heavy metals, pH, and sensitive organisms.
16	Surface water quality	Mining introduces pollutants into waterways affecting surface water quality.
17	Underground water quality	Groundwater contamination potential from leaching chemicals and metals from waste/tailings with long-term impacts.
18	Water Table change	Upward water pressure in open pits presents slope stability and safety issues and impedes mining due to poor drainage.
19	Water consumption	Water demand/consumption depends on project technical aspects and site conditions.
20	Water management	Appropriate water management depends on project/site characteristics.
21	Photochemical ozone formation	Ground-level ozone degrades local air quality and risks respiratory health in communities near mining due to emissions from equipment and machinery.
22	Ozone depletion	Stratospheric ozone depletion from mining operations may occur through emissions of chlorofluorocarbons from equipment, machinery, and explosives used.
23	Atmosphere heat	Alterations to local atmospheric heating and terrestrial radiation levels in open-pit mines can vary depending on pit depth, regional geology, and climate.
24	Temperature inversion	Temperature inversions risk trapped air pollution between mine surface and bottom temperatures.
25	Particulate matter	Particulate emissions from diverse sources like drilling, blasting, crushing, and transport operations.
26	Dust	Dust is pervasive due to heavy equipment, blasting, and in-pit crushing common in D&LS mining.
NO	Affecting factor	Definition
27	Air quality	Air quality impacts from mining dust, diesel exhaust, and blasting emissions.
28	Energy demand/consumption	D&LS open-pits require significant energy prompting efficiency improvements and renewable integration to reduce footprints.
29	Clean/Renewable energy generation	Incorporating renewables like solar, wind, geothermal, and hydro aims to lower emissions and fossil fuel dependence in energy-intensive mining.
30	Fossil fuel depletion/ consumption	Heavy trucks rely mostly on fossil fuels to support open-pit operations.
31	Greenhouse Gas Emissions (GHG)	Mechanization and changes to land use, deforestation, and erosion alter carbon cycles and local climates.
32	Carbon Sinks	Destroying carbon sinks exacerbates carbon dioxide increases contributing to climate change.
33	Surface ground's stability/subsidence	Extensive pre-mining disturbance is required, involving vegetation clearing, topsoil and overburden stripping, excavation works, road and infrastructure development, and waste deposition.
34	Slope Stability	At the regional scale, D&LS open-pit mining usually demands sizeable tracts of land undergo alterations through surface clearing and terrestrial excerption practices
35	Land disturbance	Extensive pre-mining disturbance through clearing, soil/overburden removal, excavation, infrastructure development, and waste deposition.
36	Land use	D&LS open-pits usually demand sizeable, altered tracts of land.
37	Reclamation	Extensive clearing, overburden removal, mining, and infrastructure impact landscapes needing reclamation.
38	Landscape & topography	Operations significantly alter topography through excavations and waste piles visible from afar.
39	Fly rock	Fly rock incidents stem from overcharging, poor fragmentation, blasting issues, and timing.
40	Ground Vibration	Ground vibrations impact stability and safety from blasting, machinery, and seismicity.
41	Transport and access roads	Road development benefits and impacts must be weighed at 1000m depths.
42	Geothermal effect	Deeper exposures result in greater subsurface temperatures from natural gradients.
43	Noise	Drilling, blasting, machinery, and crushing generate noise health concerns.
44	Air overpressure	Explosive shockwaves require control and management.

TABLE 2. Economic Factors for a Comprehensive Model

No.	Affecting factor	Definition
1	Production capacity	Mine scale and production capacity are directly tied.
2	Net present value	As capacity rises with scale, mining income will rise.
3	Net profit	As capacity rises with scale, mining profits will rise.
4	Income	As capacity rises with scale, mining income will rise.
5	Mining & plant equipment	IPCC systems need greater capital than trucks and out-of-pit crushers for D&LS open-pit mines.
6	Infrastructures development	D&LS open-pits require considerable capital for automation, mechanization, robotic equipment, and related infrastructure.
7	Construction	D&LS open-pit mines require considerable capital for construction.
8	Recapitalize	D&LS open-pit mines require considerable capital for depreciation costs.
9	Rate of Return	The larger the investment, the longer to return on investment.
10	Drilling and blasting costs	Drilling and blasting costs are directly tied to production capacity, which reflects the mining scale.
11	Loading costs	Loading costs are directly tied to production capacity, which reflects the mining scale.
12	Haulage costs	Haulage costs are significantly dependent on open-pit depth.
13	Primary Crushing costs.	Primary crushing costs are significantly dependent on open-pit depth.
14	Reclamation costs	Rehabilitation costs are directly related to mine depth and scale.
15	Income tax	Large-scale mines pay greater taxes as production capacity is closely associated with income tax.
16	Royalty	Royalty levels are established by legal frameworks and agreements between mines and authorities.
17	Fixed and indirect costs	Fixed and indirect costs are not affected by depth or scale but do affect regional development.
18	Processing, Smelting, refining	Depth or scale does not directly influence processing costs but affects regional development.
19	Gross domestic product	Higher production from a larger scale means a greater contribution to the country's GDP.
NO	Affecting factor	Definition
20	Export	Increased production from a greater scale also increases contribution to national exports.
21	Business opportunities in other sectors	D&LS open-pits require advanced technology and infrastructure leading to other business opportunities.
22	Foreign exchange	
23	Inflation	Exchange rates, inflation, and metal prices are outside miner's control, so depth has no direct impact.
24	Metal/mineral price	
25	Employment rate & duration	Employment rates and durations in D&LS mines lead to varied economic impacts.
26	Poverty generation or reduction	Income generation will affect poverty reduction/generation.
27	Crime generation or prohibition	Economic crimes may increase or decrease.
28	Regional development	Socioeconomic development occurs due to mining activities in a region.

TABLE 3. Social Factors for a Comprehensive Model

No.	Affecting factor	Definition
1	Job Satisfaction	Job security and salaries are affected by increased depth and scale.
2	Social Relationship	Mining projects affect family life and community communication.
3	Freedom & Justice	D&LS mines influence freedom and justice in nearby communities.
4	Livability	D&LS mines affect food security, living costs, and communication services.

5	Social Infra & Amenity	D&LS mines develop education, health centers, public services, and leisure activities.
6	Political Stability	Political stability affects investment with a direct relation to social impacts.
7	People's Safety	Communication tools and training for safety assurance are vital in D&LS mines.
8	Equipment Safety	Some equipment used in D&LS open-pit mines are partly different in size, type, and usage and their safety assessment is vital.
9	Material Safety	Materials used in D&LS open-pit mines can be different and their safety assessment is important.
10	Employment	D&LS open-pit mines affect employment/unemployment rates (direct, indirect, local, and national employment).
11	Business Opportunity	D&LS open-pit mines create business opportunities above and underhand.
12	Stakeholders Inclusion	Vital to include stakeholders, especially for D&LS open-pit mine lifetimes.
13	Future Generation Rights	It is important to emphasize the efficient depletion of resources for future generations' rights.
14	Land Ownership & Regin Importance	Land ownership is affected by D&LS open-pit mines, which impacts the region's value.
15	Education	D&LS mines can boost local training and education through new technologies.
16	Equipment & Materials Availability	New technologies and unknown environmental conditions in deep open-pit mines will impact the employment of skilled labor.
17	Human Capital	The availability of skilled, trained, and educated human resources is essential in D&LS open-pit mines.
18	Child/Forced Labor	The inclusion of child labor or forced labor in the mining project has a negative social impact.
19	Health and Safety	Community exposure to physical and mental health issues, fatalities, work-related accidents (failure of structures such as dams), and diseases caused by environmental impacts of the mine.
20	Crimes	Crime in the local community (corruption, bribery, robbery, alcoholism, drugs, domestic, and sexual violence).
21	Demographic Changes	Demographic changes due to mining such as the migration of indigenous people to other regions or the migration of professionals to the mining region.
22	Income Generation & Poverty	Income generation in D&LS open-pit mines can impact poverty (poverty prohibition or generation).
23	Wealth Distribution	The distribution of wealth in mining regions should be fair, to include all stakeholders.
24	Tourism Attraction	Mining projects, specifically D&LS projects, can be a positive tourism attraction if managed in line with SDGs, or reduce tourism attraction if not.
25	Culture	Growing tangible culture (buildings, monuments, landscapes, books, works of art, and artifacts) and intangible culture (folklore, traditions, language, and knowledge) due to the mining project.
26	Legislative Frameworks	The mining project needs to apply the legislative frameworks in the regions.
27	Mining Image	Conflict between indigenous people and mining.

The outcome of this step reveals 44 environmental factors, 28 economic factors, and 27 social factors identified for developing a comprehensive sustainability assessment model, respectively (Tables 1 to 3).

2. 3. SD Indexes Models Distinct models for three sustainable development (SD) indices were proposed (34-36). The Fuzzy Delphi Analytic Hierarchy Process (FDAHP) technique was used to calculate the importance weight of each factor. To reduce uncertainty in expert judgments and increase the reliability of their responses, Z-numbers were also used along with FDAHP (formula summarized in Table 4). First, the importance weight for each factor group was calculated. Then their scores were found through scenario-based analysis. This process was repeated for each sustainable development index separately. It resulted in scores for the three distinct SD indexes.

2. 4. Defining Scenarios Scenarios can test how sensitive the assessment is to different stakeholders' points of view, by varied weightings given to each index. To capture the complexity of sustainable development in D&LS copper mines, 10 scenarios were created. Each gave a unique set of weights to the environmental, social, and economic dimensions.

The purpose was to thoroughly look at different trade-offs and priorities of stakeholders. By varying the weights in each scenario, different stakeholder views could be considered. For example, one scenario might emphasize the environment more to minimize ecological harm. Another could weigh social factors higher to focus on community rights and job opportunities. Another could prioritize economics to look at profit, income, and national growth. The defined scenarios capture these varied priorities (Table 5).

Under Equation 12, the final sustainability score for a specific mining site can be determined by multiplying the sustainability score (as shown in Equation 11 in Table 4) of each index by its corresponding weight.

$$S_F = \sum_{n=1}^{3} W_n S_n = \sum_{n=1}^{3} W_n * (\sum_{k=1}^{k} W_k * \frac{\sum_1^j S_{Fj}^*}{j}) \quad (12)$$

$$S_F = \sum_{n=1}^{3} W_n S_n = S_{En}W_{En} + S_{Ec}W_{Ec} + S_{So}W_{So} \quad (13)$$

where

S_n is the final sustainability score for the n^{th} pillar of SD, calculated by the Z-FDAHP technique,

W_n is the assigned weight of the n^{th} pillar of SD, defined in scenarios,

S_{Fj}* is the affecting factor score the j^{th} factor,

W_k is the importance weight of the K^{th} category, and

S_{En}, S_{Ec}, and S_{So} are the environmental, economic, and social sustainability scores calculated by the Z-FDAHP technique, respectively.

TABLE 4. Summary of formulas for Z-Fuzzy Delphi AHP (34)

No.	Equation	Variables definition	Explanation
(1)	$\alpha = \frac{\int x\mu_{\tilde{R}}(x)dx}{\int \mu_{\tilde{R}}(x)dx}$	$\mu_{\tilde{R}}(x)$ a triangular membership function	Transforming linguistic Z-numbers to fuzzy triangular numbers
(2)	$A_{ij} = (a_{ij}, \delta_{ij}, \gamma_{ij}) * \sqrt{\alpha}$	$\widetilde{A_{ij}}$ the fuzzy representation of the value assigned by experts	Reducing uncertainty of experts' judgments
(3)	$a_{ij} = Min(\beta_{ijk}), k = 1,2,\dots,n$	a_{ij} The minimum value of the questionnaires	The 1^{st} component of the fuzzy number $\widetilde{A_{ij}}$
(4)	$\delta_{ij} = (\prod_{k=1}^{n} \beta_{ijk})^{\frac{1}{n}}, k = 1,2,\dots,n$	β_{ijk} The relative importance of factor i on factor j from the expert's viewpoint k	The second component of the fuzzy number $\widetilde{A_{ij}}$
(5)	$\gamma_{ij} = Max(\beta_{ijk}), k = 1,2,\dots,n$	γ_{ij} The maximum value of the questionnaires	The third component of the fuzzy number $\widetilde{A_{ij}}$
(6)	$\tilde{A} = [\tilde{a}_{ij}]$ $\widetilde{a_{ij}} \times \widetilde{a_{ij}} \approx 1, \forall i,j = 1,2,\dots,n$	$\tilde{A}$ The fuzzy positive reciprocal matrix between the various factors	The different factors' fuzzy positive reciprocal matrix
(7)	$\tilde{Z}_i = [\tilde{a}_{ij} \otimes \dots \otimes \tilde{a}_{in}]^{\frac{1}{n}}$	$\tilde{Z}_i$ The relative fuzzy weight of the factors	The relative fuzzy weight of the factors
(8)	$\widetilde{W}_i = \tilde{Z}_i \otimes [\tilde{Z}_i \oplus \dots \oplus \tilde{Z}_n]^{-1}$	$\widetilde{W}_i$ Fuzzy weight of the ith factor.	$\widetilde{W_i}$ is a row vector that contains a fuzzy weight for the i^{th} factor
(9)	$W_i = (\prod_{i=1}^{3} w_{ij})^{\frac{1}{3}}$	W_i Weight of factor i.	The defuzzification formula
(10)	$S_k = \frac{\sum_1^j S_{Fj}^*}{j}$	S_k is the final score of the K^{th} category S_{Fj}* is the affecting factor score the j^{th} factor	Scoring the affecting factors
(11)	$S_n = \sum_{k=1}^{k} W_k S_k$	W_k is the importance weight of the K^{th} category S_n the sustainability score for each SD index	Sustainability Score (S_n)

TABLE 5. Different scenarios for SD index weights

Scenario No	$W_{Environment}$	$W_{Economic}$	W_{Social}
Base Model (Scenario 1)	0.33	0.33	0.33
Scenario 2	1	0	0
Scenario 3	0.6	0.2	0.2
Scenario 4	0.2	0.4	0.4
Scenario 5	0	1	0
Scenario 6	0.2	0.6	0.2
Scenario 7	0.4	0.2	0.4
Scenario 8	0	0	1
Scenario 9	0.2	0.2	0.6
Scenario 10	0.4	0.4	0.2

The final sustainability score ranges from 0 to 10. This shows how well a mine meets its environmental, economic, and social duties to stakeholders.

A score of 10 means full sustainability - the mine handles all three SD indexes very well.

A score of 0 means unsustainability in all three parts. It shows the mine is not managing the environmental, economic, or social aspects properly.

3. VERIFICATION

The Sungun Copper Mine (SCM) in northwest Iran is the second largest copper mine in the region, with the Sarcheshmeh copper mine in the southeast being the largest. It is globally renowned for its large copper deposits, with a total ore reserve of approximately 1.2 billion tons and an average copper grade of 0.67% (see Figure 2). The mine design specifies that the final pit top will have a maximum width of 1.7 km and a minimum width of 1.2 km. The Ultimate Pit Limit (UPL) is anticipated to be at an altitude of 1,400 meters above sea level, resulting in an ultimate pit depth of approximately 900 meters (36).

To evaluate and benchmark the sustainability performance of SCM, a sustainability assessment model has been applied. Previous studies conducted by the authors have determined "the environmental, economic, and social sustainability scores of SCM to be 3.326, 5.298, and 6.364, respectively. By applying 10 different scenarios defined in Table 5, the sustainability score of the SCM mine can be determined under each scenario, using Equation 12.

4. RESULTS

The model applied the 10 scenarios in Table 5 using Equation 12 to determine SCM's final sustainability score. The highest score was achieved under scenario 8, where social factors received the highest weight of 1. This suggests social indicators strongly influence SCM's sustainability performance. Aspects like community impacts and worker conditions are important considerations for long-term sustainable operations. Focusing only on the economic viability of a mining project may overlook these dimensions.

The lowest score was under scenario 2, relying solely on environmental indicators. This implies SCM is not paying enough attention to the environmental impacts of the mining activity.

The highest and lowest scoring scenarios likely show how sensitive the overall results are to how sustainability dimensions are weighted. Valid perspectives exist beyond any single weighting approach.

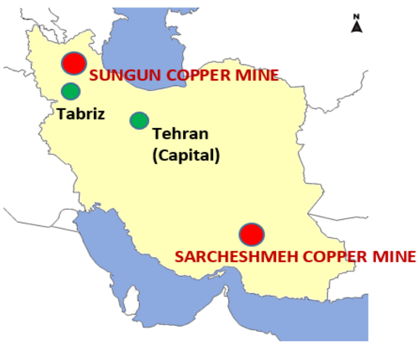

Figure 2. SCM’s geographical location (34)

Table 6 shows the score calculations for each scenario. Tables 7 and Figure 3 present the final scores for all ten scenarios.

TABLE 6. Calculations for each scenario (On a scale of 0-10)

Scenario	Calculation	Final Score
Base Model (Scenario 1)	$S_F = \sum_{n=1}^{3} W_n S_n = S_{En}W_{En} + S_{Ec}W_{Ec} + S_{So}W_{So} = 3.326 * 0.33 + 2.111 * 0.33 + 6.364 * 0.33 = 3.894$	3.894
Scenario 2	$S_F = 3.326 * 1 + 2.111 * 0 + 6.364 * 0 = 3.326$	3.326
Scenario 3	$S_F = 3.326 * 0.6 + 2.111 * 0.2 + 6.364 * 0.2 = 3.691$	3.691
Scenario 4	$S_F = 3.326 * 0.2 + 2.111 * 0.4 + 6.364 * 0.4 = 4.055$	4.055
Scenario 5	$S_F = 3.326 * 0 + 2.111 * 1 + 6.364 * 0 = 2.111$	2.111
Scenario 6	$S_F = 3.326 * 0.2 + 2.111 * 0.6 + 6.364 * 0.2 = 3.205$	3.205
Scenario 7	$S_F = 3.326 * 0.4 + 2.111 * 0.2 + 6.364 * 0.4 = 4.298$	4.298
Scenario 8	$S_F = 3.326 * 0 + 2.111 * 0 + 6.364 * 1 = 6.364$	6.364
Scenario 9	$S_F = 3.326 * 0.2 + 2.111 * 0.2 + 6.364 * 0.6 = 4.906$	4.906
Scenario 10	$S_F = 3.326 * 0.4 + 2.111 * 0.4 + 6.364 * 0.2 = 3.448$	3.448

TABLE 7. Final sustainability score for each scenario (On a scale of 0-10)

Sustainability Indexes’ scores		Environment	Economic	Social	Final Sustainability Score
		3.326	5.298	6.364	
Sustainability Indexes’ Weights	Base Model (Scenario 1)	0.33	0.33	0.33	4.946
	Scenario 2	1	0	0	3.326
	Scenario 3	0.6	0.2	0.2	4.328
	Scenario 4	0.2	0.4	0"4	5.330
	Scenario 5	0	1	0	5.298
	Scenario 6	0.2	0.6	0.2	5.117
	Scenario 7	0.4	0.2	0.4	4.936
	Scenario 8	0	0	1	6.364
	Scenario 9	0.2	0.2	0.6	5.543
	Scenario 10	0.4	0.4	0.2	4.722

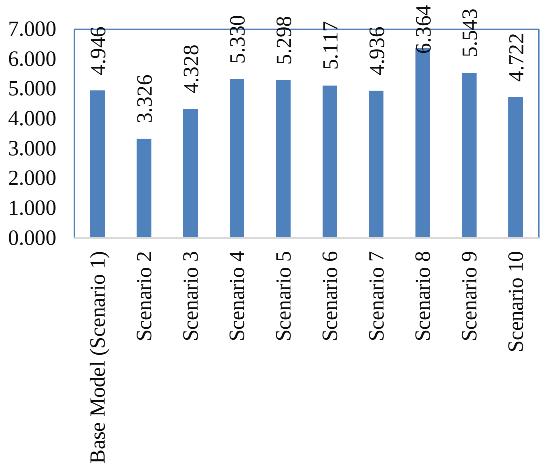

Figure 3. Final sustainability score for each scenario

5. DISCUSSION

The sustainability assessment model was applied to determine the Sungun Copper Mine's (SCM) final sustainability score. SCM is a D&LS open-pit mine in northwest Iran. The results show SCM's sustainability depends on the weights given to environmental, social, and economic factors, from different stakeholders' perspectives.

D&LS open-pit mines can generate long-lasting environmental impacts by stripping away large areas of land and disposing of huge amounts of waste rock and tailings. Surface and groundwater quality may be greatly lowered from acid mine drainage. Greenhouse gas emissions are also high due to energy-intensive mining and materials movement. Irreparable damage to ecosystems and biodiversity may occur without mitigation measures.

At SCM specifically, deforestation of the Arasbaran region could be a concern. Mitigation plans should minimize the project's footprint in forest areas as much as possible to limit habitat loss. Creating new habitats may be needed. Rehabilitation of disturbed forest zones could help accelerate the recovery of this ecosystem since revegetation timelines exceed the mine's lifespan. Priority rehabilitation could help speed up forest recovery.

Economic viability is also important for sustainability. D&LS open-pit mines require massive upfront costs and finances to justify expenses. Financial stability ensures ongoing local jobs and benefits as mining progresses deeper. Neglecting economics risks project cancellation due to a lack of profits, disputes, or funding access.

Prioritizing only social factors also threatens to undermine trust in companies over time. Communities and markets increasingly demand responsibility across all aspects of sustainability.

The mine scored lowest under scenario 2 where only the environment mattered. But exclusively focusing on environmental protection is problematic for major open-pit mines too. It could make projects uneconomical or impose constraints making the core business unviable, without considering economic and social trade-offs. Ignoring economics risks financial instability. Uncontrolled rising costs from unrealistic environmental demands could force early closure. Similarly, dismissing social issues ignores communities near major environmental disruptions. Failing to address social impacts could weaken acceptance over time. This implies that to gain SDG in D&LS open-pit mines, a balanced approach is needed. Rather than favor any single sustainability factor, sustainable development at SCM requires adaptive, integrated strategies that find the right balance between environmental, economic, and social impacts over the long run through close collaboration with stakeholders. This balance can be achieved through scenarios 9, 4, and 6 with scores of 5.543, 5.330, and 5.117 out of 10, respectively.

Deep and Large-scale open-pit mines like SCM present unique difficulties due to their extensive excavation, potential harm to the environment, and social consequences. The proposed model offers an effective way to address these challenges. By including economic, environmental, and social aspects, the final sustainability model in this study understands the complexity of these mining operations and encourages balanced decision-making.

The model examines a wide range of 99 indicators as sustainability measures. This broad examination gives a comprehensive look at how the mine is doing across multiple areas, including issues specific to D&LS open-pit mines.

The Z-FDAHP technique used to calculate importance weights for the sustainability indicators deals with the natural uncertainties and biases involved in assessing sustainability, especially for complex mines. It allows expert input and consensus building, leading to more reliable weights.

The model also analyzes scenarios to assess sustainability performance from different stakeholders' perspectives, under various weightings assigned to each sustainability index. This recognizes sustainability frequently changes as priorities and stakeholder views differ. Looking at different scenarios provides a greater understanding of the relative significance of environmental, social, and economic aspects for sustainable development at these mines. It is important to consider the intended audience of the sustainability report and their particular priorities. The recipient may place more emphasis on some factors over others. Evaluating scenarios allows for a more nuanced analysis that accounts for the end user's perspective. This consideration of the target audience is an important but often overlooked part of environmental impact assessments and sustainability evaluations in previous related studies. Considering who will receive the findings and what matters most to them enhances the relevance and usefulness of the analysis.

The results of this study provide a valuable understanding of prioritizing environmental, social, and economic aspects in D&LS open-pit mines to identify the most sustainable practices under different conditions. This can encourage sustainable practices in mining and help meet sustainable development goals.

6. CONCLUSION

This study developed a comprehensive sustainability assessment model and validated it through application to the Sungun Copper Mine case study. The model takes a holistic, multi-dimensional approach to evaluate mining projects across a wide range of 99 environmental, social, and economic indicators. Its scenario-based structure allows customization based on project contexts and stakeholder perspectives.

Application of the model to Sungun Copper Mine demonstrated its functionality and provided valuable insights into priority issues. Examining varied scenarios highlighted the importance of tailoring assessments based on audience. The results also showed the need for balanced consideration of all sustainability factors. Engaging stakeholders in the application process helps ensure assessments remain grounded in operational realities. Integration of outputs into sustainability strategies and programs supports focused action.

The model incorporates the 99 factors using Z-FDAHP and offers a formula to calculate sustainability scores under scenarios. This tool allows stakeholders to assess adherence to responsible practices. Quantifying performance provides a transparent and measurable representation aligned with sustainability goals. This enhances stakeholder involvement and decision-making.

Considering diverse aspects of sustainable development across multiple scenarios strengthens the model's usefulness across mining contexts. The model fills gaps in knowledge by taking a comprehensive approach tailored to this context.

7. REFERENCES

1. Vizayakumar K, Mohapatra PKJ. Environmental impact analysis of a coalfield. Journal of Environmental Management. 1992;34(2):79-103. https://doi.org/10.1016/S0301-4797(06)80016-2
2. Rybicka HE. Environmental Impact of The Mining Industry in Poland. Heavy Metals. Berlin, Heidelberg: Springer; 1995. p. 271-85.
3. Sadler B. International Study of the Effectiveness of Environmental Assessment. Canadian Environmental Assessment Agency; 1996.
4. Jarvis A, Younger P. Broadening the scope of mine water environmental impact assessment: a UK perspective. Environmnetal Impact Assessment Review. 2000;20(1):85-96. https://doi.org/10.1016/S0195-9255(99)00032-3
5. Kuma JS, Younger PL, Bowell RJ. Expanding the hydrogeological base in mining EIA studies: A focus on Ghana. Environmental Impact Assessment Review. 2002;22(4):273-87. https://doi.org/10.1016/S0195-9255(02)00006-9
6. Folchi R, editor Environmental impact statement for mining explosives: a quantitative method. ISEE 29th Annual Conference Explosives and Blasting Technique; 2003; Northville, Tennessee, U.S.A.
7. Saffari A, Ataei M, Sereshki F, Naderi M. Environmental impact assessment (EIA) by using the Fuzzy Delphi Folchi (FDF) method (case study: Shahrood cement plant, Iran). Environment, Development and Sustainability. 2019;21(2):817-60. https://doi.org/10.1007/s10668-017-0063-1
8. Mwakesi IW, Wahome RG, Ichang'i DW. Impact of mining on environment: A case study of Taita Taveta County, Kenya. African Journal of Environmental Science and Technology. 2021;15(5):202-13. https://doi.org/10.5897/AJEST2020.2926
9. Zhang Y, Lu W-x, Yang Q-c. The impacts of mining exploitation on the environment in the Changchun–Jilin–Tumen economic area, Northeast China. Natural Hazards. 2015;76:1019-38. https://doi.org/10.1007/s11069-014-1533-5
10. Kitula A. The environmental and socio-economic impacts of mining on local livelihoods in Tanzania: A case study of Geita District. Journal of Cleaner Production. 2006;14(3-4):405-14. https://doi.org/10.1016/j.jclepro.2004.01.012
11. Pandey PK, Sharma R, Roy M, Pandey M. Toxic mine drainage from Asia's biggest copper mine at Malanjkhand, India. Environmental Geochemistry and Health. 2007;29:237-48. https://doi.org/10.1007/s10653-006-9079-4
12. Rashed M. Monitoring of contaminated toxic and heavy metals, from mine tailings through age accumulation, in soil and some wild plants at Southeast Egypt. Journal of Hazardous Materials. 2010;178(1-3):739-46. https://doi.org/10.1016/j.jhazmat.2010.01.147
13. Aryafar A, Yousefi S, Doulati Ardejani F. The weight of interaction of mining activities: groundwater in environmental impact assessment using fuzzy analytical hierarchy process (FAHP). Environmental Earth Sciences. 2013;68:2313-24. https://doi.org/10.1007/s12665-012-1910-x
14. Northey S, Haque N, Mudd G. Using sustainability reporting to assess the environmental footprint of copper mining. Journal of Cleaner Production. 2013;40:118-28. https://doi.org/10.1016/j.jclepro.2012.09.027
15. Minaei Mobtaker M, Osanloo M, editors. Positive impacts of mining activities on environment. Conference: Beijing International Symposium on Land Reclamation and Ecological Restoration (LRER 2014); 2014; Beijing, China.
16. Northey SA, Mudd GM, Saarivuori E, Wessman-Jääskeläinen H, Haque N. Water footprinting and mining: Where are the limitations and opportunities? Journal of Cleaner Production. 2016;135:1098-116. https://doi.org/10.1016/j.jclepro.2016.07.024
17. Taušová M, Čulková K, Domaracká L, Drebenstedt C, Muchová MS, Koščo J, et al. The importance of mining for socio-economic growth of the country. Acta Montanistica Slovaca. 2017;22(4).
18. Amirshenava S, Osanloo M. A hybrid semi-quantitative approach for impact assessment of mining activities on sustainable

development indexes. Journal of Cleaner Production. 2019;218:823-34. https://doi.org/10.1016/j.jclepro.2019.02.026

19. Yankson PW, Gough KV. Gold in Ghana: The effects of changes in large-scale mining on artisanal and small-scale mining (ASM). The Extractive Industries and Society. 2019;6(1):120-8. https://doi.org/10.1016/j.exis.2018.09.009
20. Von der Goltz J, Barnwal P. Mines: The local wealth and health effects of mineral mining in developing countries. Journal of Development Economics. 2019;139:1-16. https://doi.org/10.1016/j.jdeveco.2018.05.005
21. Argimbaev K, Ligotsky D, Mironova K, Loginov E. Investigations on material composition of iron-containing tails of enrichment of combined mining and processing in kursk magnetic anomaly of Russia. International Journal of Engineering, Transactions A: Basics. 2020;33(7):1431-9. https://doi.org/10.5829/ije.2020.33.07a.31
22. Tabasi S, Kakha GH. An Application of Fuzzy-VIKOR Method in Environmental Impact Assessment of the Boog Mine Southeast of Iran. International Journal of Engineering, Transactions C: Aspects. 2021;34(6):1545-56. 10.5829/ije.2021.34.06c.19 https://doi.org/10.5829/ije.2021.34.06c.19
23. Atienza M, Fleming-Muñoz D, Aroca P. Territorial development and mining. Insights and challenges from the Chilean case. Resources Policy. 2021;70:101812. https://doi.org/10.1016/j.resourpol.2020.101812
24. Hosseinpour M, Osanloo M, Azimi Y. Evaluation of positive and negative impacts of mining on sustainable development by a semi-quantitative method. Journal of Cleaner Production. 2022;366:132955. https://doi.org/10.1016/j.jclepro.2022.132955
25. Cacciuttolo C, Cano D. Environmental Impact Assessment of Mine Tailings Spill Considering Metallurgical Processes of Gold and Copper Mining: Case Studies in the Andean Countries of Chile and Peru. Water. 2022;14(19):3057. https://doi.org/10.3390/w14193057
26. Kumar CL M, KG S, Sunagar P, Noroozinejad Farsangi E. Studies on Contaminated Mine Soil and Its Remediation Using Soil Washing Technique-A Case Study on Soil at Kolar Gold Fields. International Journal of Engineering, Transactions A: Basics. 2022;35(1):201-12. https://doi.org/10.5829/ije.2022.35.01A.19
27. Sanjuan-Delmás D, Alvarenga R, Lindblom M, Kampmann TC, van Oers L, Guinée JB, et al. Environmental assessment of copper production in Europe: an LCA case study from Sweden conducted using two conventional software-database setups. The International Journal of Life Cycle Assessment. 2022;27(2):255-66. https://doi.org/10.1007/s11367-021-02018-5
28. Gümüşsoy A, Başyiğit M, Kart EU. Economic potential and environmental impact of metal recovery from copper slag flotation tailings. Resources Policy. 2023;80:103232. https://doi.org/10.1016/j.resourpol.2022.103232
29. Song W, Gu H-H, Song W, Li F-P, Cheng S-P, Zhang Y-X, et al. Environmental assessments in dense mining areas using remote sensing information over Qian'an and Qianxi regions China. Ecological Indicators. 2023;146:109814. https://doi.org/10.1016/j.ecolind.2022.109814
30. Pantelic U, Lilic P, Cvjetic A, Lilic N. Environmental Noise Impact Assessment for Large-Scale Surface Mining Operations in Serbia. Sustainability. 2023;15(3):1798. https://doi.org/10.3390/su15031798
31. Luan B, Zhou W, Jiskani IM, Wang Z. An Improved Machine Learning Approach for Optimizing Dust Concentration Estimation in Open-Pit Mines. International Journal of Environmental Research and Public Health. 2023;20(2):1353. https://doi.org/10.3390/ijerph20021353
32. Jafarzadeh Marandi M, Ghiasi V, Badv K. Numerical Evaluation of Two-dimensional Multi-layer Cover System to Regulate Acid Mine Drainage of Tailing Dams. International Journal of Engineering, Transactions A: Basics. 2023;36(10):1839-56. https://doi.org/10.5829/ije.2023.36.10a.10
33. Alsaleh M, Yang Z, Chen T, Wang X, Abdul-Rahim AS, Mahmood H. Moving toward environmental sustainability: Assessing the influence of geothermal power on carbon dioxide emissions. Renewable Energy. 2023;202:880-93. https://doi.org/10.1016/j.renene.2022.11.060
34. Heydari M, Osanloo M, Başçetin A. Developing a new social impact assessment model for deep open-pit mines. Resources Policy. 2023;82:103485. https://doi.org/10.1016/j.resourpol.2023.103485
35. Heydari M, Osanloo M. Developing a New Comprehensive Environmental Impact Assessment Model for Sustainability Practice in Deep and Large-Scale Open-Pit Mines. International Journal of Cleaner Production. 2023;under review.
36. Heydari M, Osanloo M. A new model for the economic impact assessment of large-scale and deep open-pit mines. International Journal of Mining, Reclamation and Environment. 2023:1-26. https://doi.org/10.1080/17480930.2023.2243175

Persian Abstract

چکیده

معادن روباز عمیق و بزرگ مقیاس (D&LS) می‌توانند اثرات مختلف محیط‌زیستی، اجتماعی و اقتصادی بر ذینفعان و جوامع محلی، منطقه‌ای، ملی و بین‌المللی داشته باشند. شناسایی این اثرات و داشتن مدل جامعی برای ارزیابی همزمان آنها برای دستیابی به اهداف توسعه پایدار (SD) حیاتی است. در این مطالعه یک مدل ارزیابی پایداری ارائه شده است که شامل ۹۹ عامل تأثیر در بعدهای محیط‌زیستی، اجتماعی و اقتصادی است. امتیاز پایداری با استفاده از تکنیک Z-FDAHP محاسبه شد تا قضاوت شخصی و عدم قطعیت در نظرات متخصصان کاهش یابد. سپس از تکنیک مبتنی بر سناریو برای لحاظ کردن دیدگاه‌های ذی‌نفعان مختلف در مدل استفاده شد. این مدل در معدن مس سونگون در شمال‌غربی ایران پیاده شد. نتایج نشان داد که عملکرد پایداری معدن مس سونگون حساسیت بسیار بالایی نسبت به وزن‌دهی شاخص‌ها دارد. بالاترین امتیاز پایداری با تاکید بر شاخص اجتماعی (امتیاز پایداری ٦/٣٦٤ از ١٠) بدست آمد که نقش حیاتی تاثیرات پروژه معدنی در جوامع اطراف را روشن می‌سازد. تاکید انحصاری بر شاخص‌های زیست محیطی یا اقتصادی، امتیاز پایداری کمتری داشته و نتایج آن به ترتیب ۳/۳۲٦ و ٥/٢٩٨ بود. رویکرد مبتنی بر در نظرگرفتن همزمان سه شاخص توسعه پایدار با همکاری ذینفعان به معنای اجرای همزمان سه شاخص توسعه پایدار است که توسط امتیازات پایداری ٥/٣٤٥، ٥/٣٣٠ و ٥/١١٧ در سناریوهای ٨، ٣ و ٥ به ترتیب نشان داده شده است. مدل ارزیابی پایداری ارائه شده، اطلاعات باارزشی را برای شرکت‌های معدنی و ذی‌نفعان فراهم می‌کند تا بهتر بتوانند تاثیرات پروژه‌های معدنی، بالاخص معادن روباز عمیق و بزرگ مقیاس را بر ابعاد مختلف توسعه پایدار ارزیابی کنند. مدل پایداری ارزیابی ارائه شده به دلیل به کارگیری مجموعه جامع ۹۹ عامل محیط‌زیستی، اجتماعی و اقتصادی؛ توانایی در نظرگرفتن اوزان متفاوت برای شاخص‌ها در سناریوهای مختلف بر اساس دیدگاه ذی‌نفعان؛ و اعتبارسنجی با استفاده از مطالعه موردی، رویکردی جدید و نوآورانه ارائه داده است.

IJE TRANSACTIONS A: Basics Vol. 37 No. 01, (January 2024) 14-24

International Journal of Engineering

Journal Homepage: www.ije.ir

Development of a Novel Super-active Ziegler-Natta Polyethylene Catalyst: Study on Structure, Performance and Application

M. A. Nikoohemmat[a], H. Mazaheri*[a], A. H. Joshaghani[a], E. Joudaki[b]

[a] *Department of Chemical Engineering, Arak Branch, Islamic Azad University, Arak, Iran*
[b] *Department of Chemical Engineering, Faculty of Engineering, Arak University, Arak, Iran*

P A P E R I N F O

Paper history:
Received 11 July 2023
Received in revised form 28 August 2023
Accepted 16 September 2023

Keywords:
Polyethylene Pipes
Malvern
Super-active Catalyst-510
Ziegler-Natta Catalysts

A B S T R A C T

In this research, the synthesis process of a novel super-active catalyst, named *SAC-510* is investigated at experimental scale. The authors compared the analyzed data against those derived from a popular catalyst, *Finix-112*, and several other available alternatives. The data indicated that *SAC-510* catalyst derived the optimal activity from its spherical particles. Titanium and other chemical elements were less uniformly distributed in *SAC-510* than in *Finix-112* samples, with the mean particle size being slightly larger than that found in *Finix-112*. The pores' dispersion and sizes in *SAC-510* were not as uniformly distributed as those in *Finix-112* catalyst. Lastly, both *SAC-510* and *Finix-112* catalysts were equally adaptable for use in high-density polyethylene pipes (grade 100). Compared to other commercially available catalysts, the major advantages of *SAC-510* are the economical use of hydrogen and monomers, and low purging of its valuable gases during the polymerization process. The results obtained are as follows: the increase in oxidative induction time efficiency with SAC catalyst compared to Finix catalyst by 5.8%, activity by 35.7%, hydrogen responsibility by 24.39%, 1-butene consumption by 8.38% and triethylaluminium consumption by 27.27%.

doi: *10.5829/ije.2024.37.01a.02*

NOMENCLATURE

SAC-510	Super active catalyst	*d*	Diameter
PSD	Particle size distribution	*DSC*	Differential Scanning Calorimeter
OIT	Oxidation Induction Time	V_p	Pore volume
GPC	Gel permeation chromatography	r_p	Pore peak radius
HDPE	High density polyethylene	a_p	Specific pore area
PE100	Polyethylene pipe grade of 100	**Greek Symbols**	
SEM	Scanning electron microscopy	µ	Micron

1. INTRODUCTION

Society, in general, and the industry, in particular, have significantly included plastics for changing different materials. High density polyethylene (HDPE) is a semi-crystalline polymer widely used for the transport of drinking water supplies (1, 2). These are often exposed to different weathering conditions, for example in outdoor applications or when the freshly extruded pipes are stored in the open before their installation (3). Polyethylene (PE) is known as one of the most commonly-employed thermoplastic polymer, which have demonstrated its brilliant advantages in different industrial-based activities like wires/cables insulation, agricultural mulch, membrane-based gas separation and medical engineering due to its ease of installation, absence of corrosion-related problems, low cost and projected 50 to 100-year service life (4-6). Ziegler-Natta catalyst is a commonly-used catalyst in a bimodal slurry system for HDPE production. This promising catalyst is made based on the mixture of different chemical components that are prominently applied in the synthesis process of 1-alkenes

*Corresponding Author Email: Hossein.Mazaheri@iau.ac.ir (H. Mazaheri)

Please cite this article as: Nikoohemmat MMA, Mazaheri H, Joshaghani AH, Joudaki E. Development of a Novel Super-Active Ziegler-Natta Polyethylene Catalyst: Study of Structure, Performance and Application. International Journal of Engineering, Transactions A: Basics, 2024;37(01): 14-24.

polymers (i.e., alpha-olefins) (7, 8). Titanium, and to a lesser extent, chrome and vanadium are regarded as important metallic elements in Ziegler-Natta catalysts (9). They have enabled scientists to polymerize many organic compounds, such as alkenes and dienes with superior activity and selectivity, under a wide variety of experimental conditions. Since their advent, these catalysts have also played a significant role in the development of valuable products, highly needed in petrochemical and plastic industries (9). In this context, the role of titanium and magnesium is particularly well known in the production and use of polyethylene products (10). Currently, scientists are conducting much research with a focus on the activity, particle morphology and distribution, hydrogen response, and performance of catalysts and co-catalysts (11-13).

Among the commonly-applied polymerization processes, ethylene slurry has attracted much scientific attention. In addition to improving the activity of catalysts, controlling the particle size and its distribution in polyethylene products are of significant importance (14-17). In the recent published research articles, various aspects of catalysts and their interactions with co-catalysts and intermediate metals have been investigated. These include, ***a)*** controlling titanium oxidation; ***b)*** effect of external and internal donors (18, 19); ***c)*** the role of co-catalysts (20); ***d)*** effect of newly developed catalysts (21, 22); and, ***e)*** synthetic and modelling studies in the polymerization field (23-26). In addition to the molecular structures of catalysts, the polymerization and industrial process have an essential role in the production of polymers with a variety of properties, and promoting scientific research on these products (27-30). During 1980’s and 1990’s, a series of patented methods on the preparation of new Ziegler-Natta catalysts has been introduced (31, 32). Later studies proposed and examined the role of titanium alkoxide to replace the use of Titanium tetrachloride ($TiCl_4$). In these products at least one alkoxide ligand connects Ti $(OR)_4$ to tetra-titanium alkoxide. A good example of this subject is the polymerization of olefin compounds (33-35).

To introduce a wide range of molecular weights in manufacturing resins, Ziegler-Natta catalysts require different reactors that operate under specific conditions of temperature, monomers, and hydrogen concentration, used in series or singly, which involve high costs (17, 36-38). In this context, there exists an urgent need for new catalysts with better performance to produce bimodal resins with added market value. For this purpose, two methods are popular for the preparation of the main components of the catalyst. The first method involves a solid carrier, consisting of a magnesium dihalide reaction with titanium or vanadium in a suspended hexane environment. This method provides the components of the catalyst, although it is difficult to control the polyethylene product, the particle size, and its distribution (39). In the second method, a magnesium compound, such as magnesium dichloride, is dissolved in a solvent, so that homogeneous solid particles of magnesium or titanium precipitate after adding a titanium compound. This process can provide the main component of the catalyst upon its solid processing with another liquid titanium compound and a co-catalyst (40).

This study aims to synthesize and manufacture a novel and efficient super-active Ziegler-Natta catalyst, named *SAC-510* toward the production of a new generation of high-density polyethylene pipes. Subsequently, the authors analyzed the particle morphology and its performance, compared to a popular catalyst, *Finix-112*, and several other commercially available alternatives. We have obtained some promising results, which are presented and discussed in the present article.

2. MATERIALS AND METHODS

2. 1. Materials All of the materials for the polymerization processes of both the support catalyst, and the final super-active catalyst (SAC-510) were obtained from the Shazand Petrochemical Technology Company (Arak, Iran) and Pooyesh Co. (Tehran, Iran). Hexane (C6H14) was utilized as the solvent and copolymerization agent. Ethylene was used as the main feed for the polymerization process. Lastly, 1- butylene and hydrogen were used as the components required for the polymerization. Triethylaluminium (97%) was purchased from Fluka Chemie GmbH (Buchs, Switzerland). Oxygen 4.5 (purity 99.995%) and nitrogen 5.0 (99.999% purity) were obtained from the Shazand Petrochemical company.

2. 2. Equipment

2. 2 .1. Glove Box To store and preserve the catalysts and co-catalysts in this study, we used a glove box unit (Cleatech; Orange, CA, USA). This unit prevented the active sites in catalysts and sensitive chemicals from getting contaminated and oxidized, under a nitrogen atmosphere.

2. 2. 2. Scanning Electron Microscopy/ Energy Dispersive X-ray Analysis (SEM/EDX) The surface morphology of the catalyst was examined by Scanning Electron Microscope (SEM) (model JSM-5910, JEOL Inc., Peabody, MA, USA) under high vacuum microprobe. This microscope provided scanned images, analyzed the X-ray emitted from the particles, and determined the accurate weight and percentage of the elements contained in the samples [40].

2. 2. 3. Malvern Analyzer In addition to the SEM analysis, the particle sizes and molecules contained in the samples were also measured on a Malvern analyzer (Entegris; Dresden, Germany). The images obtained from this analyzer were based on the principle of dynamic light scattering.

2. 2. 4 Buchi Reactor Made of stainless steel with a volume of 1 liter is used for slurry polymerization. The volume of the reactor jacket is 300ml. Addition of catalyst and co-catalyst is by injection under pressure**.**

2. 2. 5. Gel Permeation Chromatography (GPC) To analyze the different particle species of large molecular sizes, such as polymers, we measured the particle's molecular weights on a gel permeation chromatography unit (GPC-150-II+IR5; Cambridge Polymer Group, Inc.; Woburn, MA, USA) (41).

2. 2. 6. Differential Scanning Calorimeter (DSC) The objective of the test is to represent the duration in time of the heat stabilizer until its deterioration through oxygen and heat. The period of time from the switching over to oxygen until the onset of the oxidation reaction (point of intersection of the basis line with the tangent) is referred to as the induction period (Oxidation Induction Time, OIT). A long induction period shows good stabilization and vice versa. The described test method is carried out in dependence on DIN EN728 and we used Differential Scanning Calorimeter unit (Mettler-Toledo DSC 822e.) (42).

2. 2. 7. Huber Circulator We utilized a Huber circulating bath (Ministat CC3 Huber UK; Derbyshire, UK) to control the temperature within the reactor's jacket, ranging from -50 ˚C to +350 ˚C .

2. 3. Methods

2. 3. 1. Preparation and Polymerization The methods for the polymerization processes, as established by earlier studies (39, 40, 43).

2. 3. 1. 1. Magnesium Ethoxide Powder This material was necessary to make the base product. The construction of super active Ziegler-Natta catalysts for ethylene polymerization requires substrates for the stability of the active centers of the catalyst. Metal halides and oxides have been proposed as suitable bases for catalysts, and in the meantime, magnesium ethoxide is very suitable for making the super active Ziegler-Natta catalyst. To prepare the super active catalyst base, commercial magnesium ethoxide ($Mg(OC_2H_5)$) is first prepared in pure form with the conditions presented in Table 1. The average particle diameter of the primary magnesium ethoxide powder is 500 microns, so that more than 90% of the particles have a diameter in the range of 200 microns to 1200 microns. Titanium sits better on the substrate when the size of the primary powder particles is reduced and their distribution is uniform. Magnesium ethoxide with a diameter of about 500 microns forms a suspension in an inert saturated hydrocarbon after mechanical crushing by a jet mill to a size of about 8 microns using a Jet pulverizer (Jet Mills; Moorestown, NJ, USA). Table 1 presents aims to present different features of the magnesium ethoxide for the catalyst bed.

2. 3. 1. 2. Magnesium Ethoxide Suspension Gel The magnesium ethoxide powder was then suspended in a neutral, aliphatic hydrocarbon until the mixture was ready to convert into gel. Ideal hydrocarbons for this purpose are butane, hexane, cyclohexane, heptane, isooctane, and several others including toluene and xylene. Also, hydrogenated oils devoid of oxygen and sulphur would be appropriate. About 200 grams of the sample is taken under N_2 atmosphere and injected into a 5-liter reactor containing two liters of hexane. Then carbon tetrachloride is added and after mixing(100rpm), the temperature of the reactor is increased to about 60 degrees, and this process is allowed to continue for 24 hours. In this case, the solvent penetrates into the crystal layers and causes the particles to take a gel-like shape. If the gelling process has progressed correctly, after stopping the mixer, it takes about 30 minutes for the particles to settle.

Injecting 7 ml of titanium tetrachloride into the gel produced at 80 degrees Celsius to place titanium on the gel bed.

2. 3. 1. 3. Catalyst Assisted Preactivation The choice of co-catalyst has a great influence on the performance of titanium-based Ziegler Nata catalysts. Catalyst assistance affects activity, molecular weight and molecular weight distribution. By increasing the amount of catalyst aid, the activity of all active centers decreases to almost one level. In order to produce active sites, which Mr. Kissin divided into five types by fluorescent distribution, the catalyst must be placed in the vicinity of triethyl aluminum (TEA) for a certain period of time.

2. 3. 1. 4. Determination Of The Catalyst Content A 10ml aliquot of the catalyst was removed from its container, using a syringe, and poured in a small glass dish with known weight. After the sample was cooled

TABLE 1. Strouhal number for different geometric cases

Magnesium Species	Percentage of Total Weight
Total magnesium content	21-22%
Total Mg $(OH)_2$ & $MgCO_3$ contents	<1%
Total C_2H_5OH content	<0.3%

down, the weight of the empty dish is deducted from the total weight of the dish containing the catalyst 10ml aliquot. The net weight of the catalyst sample varies depending on the solvents, such as hexane, used for the polymerization processes.

2. 3. 1. 5. Polymerization Prior to this step, the reactor was purged by running nitrogen (≤0.1 bar) through it at 100°C for 60 minutes. Subsequently, the oil circulator pump of the reactor was set at 4500 rpm, and the temperature reset to 60°C. At this temperature, the reactor was cleared with ethylene gas three times at 3-bar pressure. Then, 500 ml hexane at 0.1 bar, and 400 mg/ml triethylaluminium (TEAL) were injected into the reactor and the agitator turned on at 200 rpm. The TEAL was mainly used for the purpose of removing contaminations from the solvent and activation of sites in the catalyst. After 30 minutes from the injection of TEAL, 1-butylene was injected to the reactor at a set amount, and allowed to mix with TEAL and the solvent for 15 minutes with the agitator set at 200rpm. During a 30-min pre-activation time, the concentration of catalyst diluted in hexane reached 2mg/ml.

After determining the reactor's pressure at optimal temperature, the catalyst was injected in the reactor under pressure. Next, the reactor's software program was set to reaction mode and the polymerization synthesis plots being printed. During this process, the reaction temperature was closely monitored at 83°C (±1°C) while ethylene was being injected into the reactor at 8 bar. The estimated time for the polymerization of ethylene with 1-butylene in the presence of the catalyst SAC-510 was approximately 180 minutes. At the completion of this final step, the reactor's software program was set to "*Reaction Off*". This terminated the ethylene entry into the reactor and the circulator's temperature was set at 60°C. After the reactor cooled down, the lid was opened, the chamber was cleaned thoroughly with nitrogen, and the catalyst and solvents residues were wiped out.

2. 3. 2. Surface Area Analysis (SSA) The surface area and pore size analysis of the catalyst were carried out by Surface Area Analyzer (Quanta chrome Nova Station A), using nitrogen adsorption method. The sample was initially degassed at 200 ºC for 4 h. Surface area of the catalysts was calculated from the nitrogen adsorption isotherm data, using Brunauer, Emmett and Teller (BET) equation. The pore size and pore volume of the catalysts were calculated from N_2 adsorption isotherm data with the help of Barrett, Joyner, Halenda (BJH) model (44).

3. RESULTS AND DISCUSSION

3. 1. Particles Morphology Understanding the morphology of micro particles can assist us predict their mass transfer and heat as they go through polymerization processes (45). Initially, monomers penetrate into the catalyst's pores and start numerous active reaction sites, forming the basic polymer particles and clumps as they combine with the catalyst and continue to grow. Later, layers of the polymer are deposited on the catalyst's spherical macro particles, leading to the final polymerized product. Thus, examining the particles reflects the true physical nature of the combined polymer and catalyst (46). Results from this study's tests and experiments are presented below followed by the pertinent discussion under each subsection.

3. 2. Energy Distribution Analyses of the Catalysts' Powders Table 2 represents the results of energy distribution in the two powdered catalysts, *Finix-112* and *SAC-510*, under scanning X-ray analysis (SEM-EDXA). As shown in Table 2, four and three zones were examined, respectively, under SEM-EDXA using the powdered samples of *Finix-112* and *SAC-510* catalysts. The results indicated that there were relatively uniform percentages of the chemical elements, especially titanium, in the *Finix-112* samples. However, much less uniformity was observed in the *SAC-510* samples. Figure 1 shows the electron microscopic images of powdered *Finix-112* and *SAC-510* catalysts, and the differences in the distribution of the particles for both samples.

Evidently, the differences in the percentage and uniformity of the elemental distributions in both catalysts' samples arise from their chemical nature and formulation. Based on the images illustrated in Figure 1, it is perceived that the presence of smaller catalyst particles makes the mobility of larger particles easier, thereby facilitates the polymerization reaction. A major advantage of SEM-EDXA is its better capability of determining the compositional elements in powdered catalysts than that achieved by either XRF or ICP method. The SEM-EDXA method is able to recognize such elements as oxygen, carbon and halogen. Also, it

TABLE 2. Scanning electron microscopic features of the Finix-112 and SAC-510 powders

Finix-112	Ti	Mg	Cl	Al	O	Cu	Si
EDAX-1	4.94	20.98	35.85	0.49	37.32	0.42	-
EDAX-2	3.37	14.17	36.06	0.34	45.72	0.38	-
EDAX-3	3.79	15.7	39.28	0.36	40.60	0.28	-
EDAX-4	4.36	13.3	44.70	0.09	36.77	0.51	-
SAC-510	Ti	Mg	Cl	Al	O	Cu	Si
EDAX-1	8.01	14.45	42.36	1.82	30.99	1.47	0.89
EDAX-2	5.48	17.44	28.01	3.29	42.79	0.73	2.25
EDAX-3	6.25	18.51	32.21	3.4	35.64	0.76	2.24

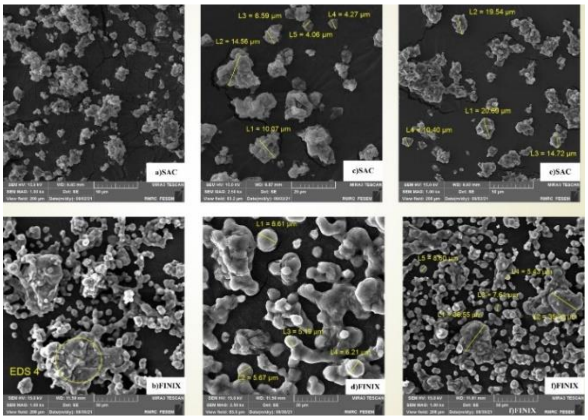

Figure 1. Scanning electron microscopic images of the catalysts Sac-510 and Finix-112 powders.a,b) SEM MAG=1 kx, 50µm; c,d) MAG=2.5kx, 20µm; e,f) SEM=1kx,50µm

provides the distribution patterns and variations in the concentration of elements in different areas of various samples at large magnification.

3. 2. Particle Size Distribution – Malvern's Method

Figure 2 represents the particles' volume of distribution and their sizes in the micron scale for both catalysts, based on Malvern's method. As seen in Figure 2, the particles in both catalysts occurred similarly in one uniform population each (range: 2-11 µm vs 3-30 µm). The single peak (50%) for Finix-112 catalyst occurred approximately at 6.8µ while that of SAC-510 was about 8.6 µm. The data for the particle size distribution in both groups of catalysts are summarized in listed in Tables 3 and 4.

The data in Tables 3 and 4 indicate that the average particle size for SAC-510 catalyst was slightly larger than that of Finix-112. In this context, 10% of the SAC-510

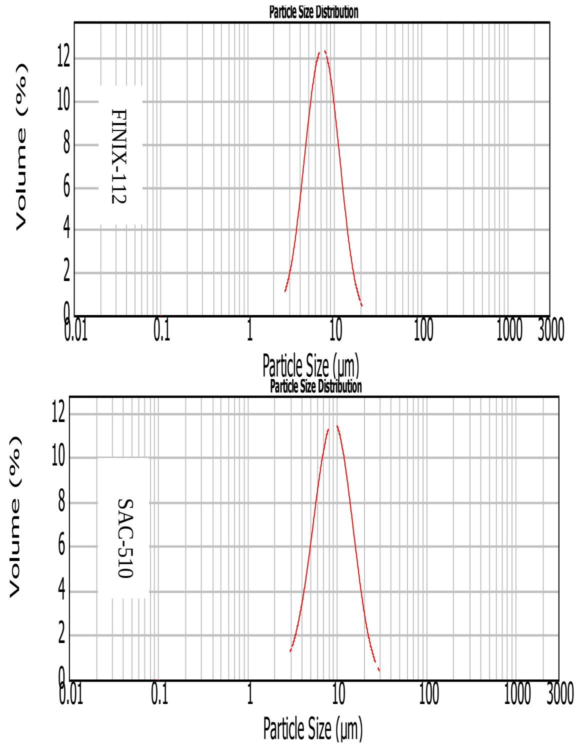

Figure 2. Particle size distribution of SAC-510 (super active) and Finix-112 catalysts

TABLE 3. Particle size distribution in Finix-112 and SAC-510 catalysts

	Size (µm)	Vol Under %	Size (µm)	Vol Under %	Size (µm)	Vol Under %	Size (µm)	Vol Under %	Size (µm)	Vol Under %	Size (µm)	Vol Under %
FINIX-112	2	8.97	16	97.77	45	100	128	100	345	100	850	100
	3	11.39	17	98.55	50	100	132	100	370	100	898	100
	4	17.81	18	99.09	52	100	142	100	385	100	950	100
	5	28.31	19	99.45	54.3	100	160	100	400	100	1000	100
	6	40.66	20.5	99.77	58.5	100	168	100	450	100	1125	100
	7	52.83	22.3	99.91	63	100	177	100	500	100	1250	100
	8	63.66	24	99.98	68	100	190	100	525	100	1325	100
	9	72.69	26	100	73	100	205	100	550	100	1400	100
	10	79.9	28	100	76.5	100	227	100	575	100	1500	100
	11	85.46	30.2	100	80	100	250	100	600	100	1600	100
	12	89.66	32	100	89	100	262	100	634	100	1740	100
	13	92.76	34.8	100	98.2	100	275	100	668	100	1880	100
	14	95.02	37	100	111	100	297	100	735	100		
	15	96.63	40.5	100	125	100	320	100	800	100		

	Size (μm)	Vol Under %	Size (μm)	Vol Under %	Size (μm)	Vol Under %	Size (μm)	Vol Under %	Size (μm)	Vol Under %	Size (μm)	Vol Under %
SAC-510	2	4	16	89.6	45	100	128	100	345	100	850	100
	3	6.25	17	91.8	50	100	132	100	370	100	898	100
	4	10.42	18	93.56	52	100	142	100	385	100	950	100
	5	17.19	19	94.97	54.3	100	160	100	400	100	1000	100
	6	25.86	20.5	96.56	58.5	100	168	100	450	100	1125	100
	7	35.38	22.3	97.86	63	100	177	100	500	100	1250	100
	8	44.87	24	98.66	68	100	190	100	525	100	1325	100
	9	53.76	26	99.26	73	100	205	100	550	100	1400	100
	10	61.72	28	99.6	76.5	100	227	100	575	100	1500	100
	11	68.64	30.2	99.82	80	100	250	100	600	100	1600	100
	12	74.53	32	99.91	89	100	262	100	634	100	1740	100
	13	79.46	34.8	99.97	98.2	100	275	100	668	100	1880	100
	14	83.54	37	99.99	111	100	297	100	735	100		
	15	86.89	40.5	100	125	100	320	100	800	100		

TABLE 4. Particle distribution in the catalysts based on Malvern method

Catalyst	SAC-510	Finix-112
D (0.1)	3.9μm	2.5μm
D (0.5)	8.6μm	6.8μm
D (0.9)	16.2μm	12.1μm

particles fell within 3.9 μm in size while the same percentage of Finix-112 particles had a 2.5 μm size. Further, about 90% of the particles in SAC-510 group had a size of 16.2 μm while those in Finix-112 group were about 12.1 μm in size.

The mechanical measurement of catalysts' particle size and their distribution are performed broadly in industries, which is a critical parameter for manufacturing numerous products. In this respect, Malvern is a highly accurate method for measuring particle sizes ranging from low nanometer to several millimeters.

3. 3. BET Test

Using the popular (BET) test (23), we analyzed the features and dimensions of the pores in both Finix-112 and SAC-510 catalysts. The data from this analysis are presented in Table 5.

TABLE 5. Results of the SAC-510 and Finix-112 powders based on BET test

Property	SAC-510	Finix-112
Specific area (m^2/g)	22.492	24.759
Total Pore volume (cm^3/g)	0.1746	0.1213
Average pore dimension (nm)	31.051	19.592

The overall results obtained from BET test revealed that the specific area for the pores in SAC-510 was 9% less than that of Finix-112. Also, the mean dimension and volume of the pores in SAC-510 catalyst were greater than those determined for Finix-112 catalyst.

Considering the above data, it can be argued that the dimensional features of the porosity in SAC-510, compared to those in Finix-112, decreases the ability of this catalyst to respond to physical forces. Also, it is likely that larger pores may be deeper in SAC-510 with smaller lateral surfaces, which further contribute to its lower tolerance against shocks, vibrations and other destructive forces.

3. 4. Barrett-Joyner-Halenda Test

Also, we used another popular test, Barrett-Joyner-Halenda (BJH), to determine the volume and distribution of pores in the catalysts (23). The data from our BJH test on both catalysts are presented in Table 6. Specifically, Table 6 reflects accurate information about three important variables for each of the two catalysts: a), the pore volume (Vp); b) the pore peak radius (rp); and c) specific pore area (ap). Figure 3 schematically presents the scatter diagram of pores and dimensions of super active SAC-510 and Finix-112 catalysts.

TABLE 6. Results of the SAC-510 and Finix-112 powders based on BJH test

Variable	Unit	Finix-112	SAC-510
Pore Volume (V_p)	Cm^3/g	0.1231	0.1762
Pore Peak Radius (R_p)	Nm	5.29	10.65
Specific Pore Area (A_p)	m^2/g	31.951	28.827

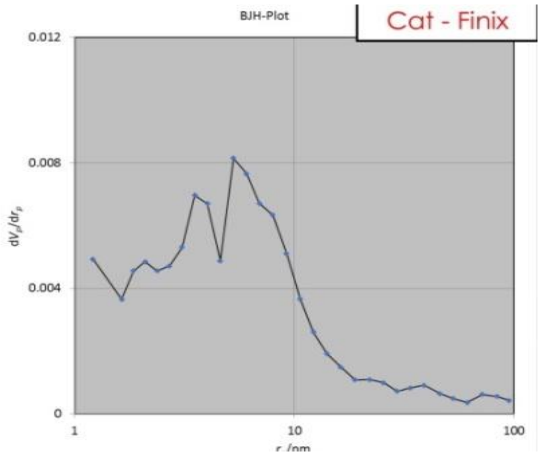

(a)

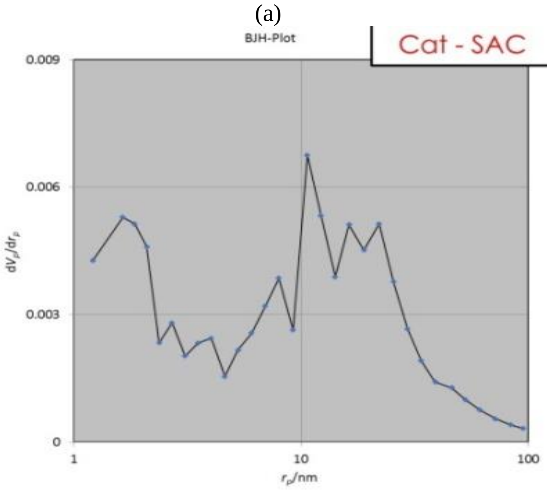

(b)

Figure 3. Scatter diagram of pores and dimensions of a) super active Finix-112 and b) SAC-510 catalysts. *Key:* V_p = Pore volume; R_p = Pore peak radius; a_p = Specific pore area

As seen in Table 6, the pore volume in catalyst SAC-510 was greater than that of Finix-112. This had an opposite effect on the specific surface and reduced this variable. Also as shown in Figure 3, the dVp/dRp ratios for SAC-510 indicate that the dispersion of the pores and sizes did not occur as uniformly as those found for Finix-112.

To assess the validity of the findings obtained through the BET analysis, we used BJH test (33). The advantage of BJH test is that it measures the volume and distribution of the pores while BET test provides a reliable measure of the areas associated with the solid material in the catalysts. Also, BJH test assists in obtaining approximate data regarding the absorption and release of isotherms, the pores' dimension, and their distribution within the catalysts.

3. 5. Gel Permeation Chromatography GPC-IR has been used to characterize the copolymer and the consequences are given in Figure 4 it is observed that the

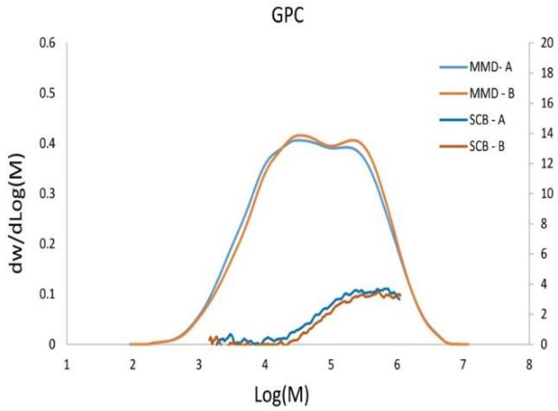

Figure 4. GPC analysis diagram of product HDPE-100 with novel and commercial catalyst A) HDPE-100 obtained from commercial catalyst (Finix112): B) HDPE-100 obtained from novel catalyst (SAC-510)

bimodal molecular weight has been formatted. The copolymer received from the novel catalyst has a high branch degree in the high molecular weight fraction and lower branch degree in the low molecular weight fraction, that's favorable to enhance the resin mechanical properties.

The polymer properties are determined by the characteristics of the polymer including molecular weight, its distribution, and degree of branching. The breath of the molecular weight distribution, Mw/Mn, additionally affects the process ability of the polymer. The degree of short chain branching strongly influences a few variables together with crystallinity and density, which in flip determines the last properties of the material. The slurry polymerization processes give resins, which have great mechanical properties preserving wonderful process ability. It can be found out via bimodal high molecular weight HDPE. The low molecular weight component product in a single reactor offers suitable process ability, even as the high molecular weight component created with inside the different reactor offers exceptional mechanical strength.

3. 6. Comparison of both SAC-510 and Finix-112 with Industrial Catalysts and Efficiency Table 7 represents major important factors and performance about some currently used catalysts in chemical engineering science, as well as in industries, compared with the novel, super-active catalyst, SAC-510. All of the currently available catalysts have been used for the manufacturing of polyethylene pipes grade 100.

Hydrogen is the most broadly used chain-transfer agent for molecular weight control with Ziegler-Natta structures in industry. Hydrogen is the simplest commercially relevant chain-transfer agent in the low-pressure olefin polymerization process over the Ziegler-Natta catalysts.

Valuable and important points aspects that are suggested from the data analysis, as shown in Table 7 in support of the super-active SAC-510 catalyst application toward the manufacturing of grade 100 polyethylene pipes are as follows: a) superior performance and durability; b) little consumption of triethylaluminum, 1-Butylene and hydrogen; c) better hydrogen response; and, d) ideal strength of the polyethylene pipes made of HDPE-100 product compared to other currently available industrial catalysts.

As can be seen in Table 8, the efficiency with the Sack catalyst has a considerable advantage over other catalysts in almost all parameters, such as reducing 1-butene consumption, reducing hydrogen consumption, reducing triethylaluminum consumption and increasing activity, and using this Catalyst is recommended in the production of polyethylene 100 product.

3. 7. Oxidation Induction Time In Table 9, some characteristics of super catalyst product are listed with the products of other catalyst. The comparison of OIT in the product of the novel catalyst with the product of other catalyst shows an acceptable OIT and indicates the successful performance of the SAC-510 catalyst.

Oxidative induction time (OIT) is widely used for the determination of the thermal oxidative resistance of polyethylene materials The OIT testing only provides a relative measure of the level of antioxidants remaining in the pipe material but is a suitable analytical technique to monitor the degree of depletion of antioxidants from the pipe surface. Oxygen induction times (OIT) indicate the stabilities of the products (47). The concentration of effective antioxidant was assessed by determining the oxidation induction time (OIT) at 210 ºC. The data presented on the deterioration of polyolefin pipes exposed to water containing chlorine dioxide have been mostly concerned with lifetime issues. Choosing a constant testing temperature which delivers OIT times of around 60 min for the unaged reference samples can be too high for the aged samples. On the other hand, a much lower temperature for OIT tests could result in high differences between the unaged and aged samples (48).

4. LIMITATIONS OF THE STUDY

This study faced several challenges due to limited or lack of laboratory equipment and organic chemicals when it was being conducted as follows:

1. Lack of nuclear magnetic resonance facility to quantify the extent that butylene-1 was incorporated into the copolymer chains at 125°C.
2. Difficulty with separating 1- butylene from the solvent due to their close boiling points.

TABLE 7. Results of the SAC-510 performance versus other industrial catalysts at our site (32)

Catalyst	Unit	PE100/article	PE100/THS	PE100/BCE7	PE100/Finix-112	PE100-/SAC510
1-Butene Consumption	Kg/ton PE	18.51	21.21	15.6	16.8	15.5
H_2 Consumption	g/ton PE	1129.6	387	426	406	319
TEAL Consumption	Liter/ton PE	-	1.38	1.82	1.4	1.1
$Q_{RA}H_2/C_2H_4$	-	8	3.5	7.5	4.1	3.3
$Q_{RB}H_2/C_2H_4$	-	0	0.02	0.06-0.07	0.03	0.01
R_B Pressure	Bar gauge	2.5	3.5-4	2.5-3	2.6	2.8
Activity	Kg PE/g Catalyst	8.82	20.6	20.75	27	28
R_A Pressure	Bar gauge	-	-	-	-8.4	6.4

TABLE 8. Results of the SAC-510 efficiency versus other industrial catalysts at our site (32)

Catalyst	Unit	SAC/article	SAC /THS	SAC /BCE7	SAC /Finix-112
1-Butene Consumption	%	19.42%	36.83%	0.6%	8.38%
H_2 Consumption	%	254.1%	21.31	33.54%	27.27%
TEAL Consumption	%	-	25.45%	67.27%	27.27%
$Q_{RA}H_2/C_2H_4$	%	142.4%	6%	127.3%	24.39%
$Q_{RB}H_2/C_2H_4$	%	0	100%	600%	200%
R_B Pressure	%	-10.7%	33.9%	-1.78%	-7.14%
Activity	%	68.5%	26.42%	25.89%	3.57%
R_A Pressure	%	-	-	-	31.25%

TABLE 9. Material properties of the reference samples (Mw: molecular weight, OIT: oxidation induction time at 210 ˚C, X: degree of crystallinity)

HDPE pipe	$PE_1(48)$	$PE_2(48)$	$PE_{SAC-510}$	$PE_{Finix-112}$
Molecular weight (M_w)	115561	131344	241203	233372
OIT (min)	66	67	69	65
Crystallinity (%)	52	45	51.22	49.92

3. Inability to conduct mechanical strength and strain tests on the PE-100 pipe made of the novel catalyst. Ideal tests would include burst, hydro, and slow-crack-growth tests.

5. RECOMMENDATIONS FOR FUTURE STUDIES

We recommend the conduction of future researches with a focus on the following points:
1. Adjusting the use of hydrogen to improve control over the catalyst's molecular mass.
2. Testing other co-catalysts and investigating their effects on the morphology and activity of the resultant catalyst.
3. Applying different organic solvents with higher boiling points to facilitate their removal from 1-butylene.
4. Rheological and viscosity experiments on the polymer's long chains at zero shear rate.

6. CONCLUSION

The prominent purpose of this research paper is the experimental production of a novel, cost-effective and efficient super-active catalyst (SAC-510) (patent pending), which is potentially ideal for manufacturing a wide range of high-density polyethylene pipes used in various industrial applications. The generation process of SAC-510 heterogeneous catalyst took place on a bed of magnesium ethoxide (as the co-catalyst), and halocarbon in the presence of titanium tetrachloride. The co-polymerization of ethylene and 1-butylene slurry was implemented in a Buchi's reactor under optimal conditions of temperature and barometric pressure.

Based on the SEM results, it was corroborated that the SAC-510 catalyst derives its active property from its spherical particles, in the presence of triethylaluminium in Buchi's reactor. Analysis of the obtained results from BET test demonstrated that the specific area for the pores in SAC-510 was 9% less than that of Finix-112. Also, the particle distribution of SAC-510 catalyst was about 60% greater than that of determined for Finix-112 catalyst, which demonstrates the superior efficiency of SAC-510. Compared to other catalysts, the major advantages of SAC-510 are: a) the economical use of hydrogen and co-monomers, b) better crystalizing capacity, and, c) low purge of valuable gases during the polymerization process. Further improvements on this subject await future research.

7. ACKNOWLEDGEMENTS

The authors are thankful to the professors and staff of the Department of Chemical Engineering, Arak Branch, Islamic Azad University, Arak, Iran.

8. SUPPLEMENTAL DATA AVAILABILITY

The detailed datasets generated and analyzed during the current study are available for review from the Corresponding Author upon request.

9. REFERENCES

1. Devilliers C, Fayolle B, Laiarinandrasana L, Oberti S, Gaudichet-Maurin E. Kinetics of chlorine-induced polyethylene degradation in water pipes. Polymer Degradation and Stability. 2011;96(7):1361-8.
2. Abeysinghe S, Gunasekara C, Bandara C, Nguyen K, Dissanayake R, Mendis P. Engineering performance of concrete incorporated with recycled high-density polyethylene (HDPE)—A systematic review. Polymers. 2021;13(11):1885.
3. Maria R, Rode K, Brüll R, Dorbath F, Baudrit B, Bastian M, et al. Monitoring the influence of different weathering conditions on polyethylene pipes by IR-microscopy. Polymer Degradation and Stability. 2011;96(10):1901-10. 10.3233/JIFS-201201
4. Whelton AJ, Dietrich AM. Critical considerations for the accelerated ageing of high-density polyethylene potable water materials. Polymer Degradation and Stability. 2009;94(7):1163-75. https://doi.org/10.1016/j.polymdegradstab.2009.03.013
5. Ronca S. Polyethylene. Brydson's plastics materials: Elsevier; 2017. p. 247-78.
6. Zha S, Lan H-q, Huang H. Review on lifetime predictions of polyethylene pipes: Limitations and trends. International Journal of Pressure Vessels and Piping. 2022;198:104663. 10.1016/j.ijpvp.2022.104663
7. Soga K, Shiono T. Ziegler-Natta catalysts for olefin polymerizations. Progress in Polymer Science. 1997;22(7):1503-46. https://doi.org/10.1016/S0079-6700(97)00003-8
8. Zarupski J, Piovano A, Signorile M, Amodio A, Olivi L, Hendriksen C, et al. Silica-magnesium-titanium Ziegler-Natta catalysts. Part 1: Structure of the pre-catalyst at a molecular level. Journal of Catalysis. 2023;424:236-45. https://doi.org/10.1016/j.jcat.2023.05.024
9. Zifang G, Wei C, Junling Z, Hongxu Y. Novel high performance Ziegler-Natta catalyst for ethylene slurry polymerization. Chinese Journal of Chemical Engineering. 2009;17(3):530-4. 10.5829/IJE.2022.35.11B.15
10. Galli P, Luciani L, Cecchin G. Advances in the polymerization of polyolefins with coordination catalysts. Die Angewandte

Makromolekulare Chemie: Applied Macromolecular Chemistry and Physics. 1981;94(1):63-89.

11. Böhm LL, editor High mileage Ziegler-catalysts: excellent tools for polyethylene production. Macromolecular Symposia; 2001: Wiley Online Library.
12. Klaue A, Kruck M, Friederichs N, Bertola F, Wu H, Morbidelli M. Insight into the synthesis process of an industrial Ziegler–Natta catalyst. Industrial & Engineering Chemistry Research. 2018;58(2):886-96. 10.1021/acs.iecr.8b05296
13. Qian A, Han X, Liu Q, Ye L, Pu X, Chen Y, et al. Ultrathin Pd metallenes as novel co-catalysts for efficient photocatalytic hydrogen production. Applied Surface Science. 2023;618:156597.
14. Klaue A, Kruck M, Binel P, Friederichs N, Bertola F, Wu H, et al. Ziegler–Natta catalyst sonofragmentation for controlling size and size distribution of the produced polymer particles. AIChE Journal. 2019;65(9):e16676. https://doi.org/10.1002/aic.16676
15. Ikeda T, Wada T, Bando Y, Chammingkwan P, Taniike T. Bottom-Up Synthesis of Multi-Grained Ziegler–Natta Catalyst Based on MgO/MgCl2/TiCl4 Core–Shell Catalyst. Catalysts. 2021;11(9):1092.
16. Yashiki T, Minami S. Solid titanium catalyst component, ethylene polymerization catalyst containing the same, and ethylene polymerization process. Google Patents; 2004.
17. Zeynali M, Ranjbarbaranlo H, Olad A. Study of Titanium/Vanadium Ziegler–Natta hybrid catalysts performance in slurry-phase ethylene polymerization for producing polyethylene with broad/bimodal molecular weight distribution. Journal of Polymer Research. 2023;30(3):100.
18. Vyas PB, Kaur S, Patil HR, Gupta VK. Synthesis of polypropylene with varied microstructure and molecular weights characteristics using supported titanium catalyst system. Journal of polymer research. 2011;18(2):235-9. 10.1007/s10965-010-9411-7
19. Gao F, Xia X, Mao B. MgCl2-supported catalyst containing mixed internal donors for propylene polymerization. Journal of Applied Polymer Science. 2011;120(1):36-42. 10.1002/app.31363
20. Zhang HX, Lee YJ, Park JR, Lee DH, Yoon KB. Control of molecular weight distribution for polypropylene obtained by a commercial Ziegler–Natta catalyst: effect of a cocatalyst and hydrogen. Journal of Applied Polymer Science. 2011;120(1):101-8. 10.1007/s00289-011-0472-5
21. Marchetti F, Pampaloni G, Patil Y, Galletti AMR, Renili F, Zacchini S. Ethylene polymerization by niobium (V) N, N-dialkylcarbamates activated with aluminum co-catalysts. Organometallics. 2011;30(6):1682-8. https://doi.org/10.1021/ja00823a064
22. Thorne JE, Zhao Y, He D, Fan S, Vanka S, Mi Z, et al. Understanding the role of co-catalysts on silicon photocathodes using intensity modulated photocurrent spectroscopy. Physical Chemistry Chemical Physics. 2017;19(43):29653-9. https://doi.org/10.1021/acsenergylett.9b02555
23. Machado F, Lima EL, Pinto JC, McKenna TF. An experimental study on the early stages of gas-phase olefin polymerizations using supported Ziegler–Natta and metallocene catalysts. Polymer Engineering & Science. 2011;51(2):302-10. https://doi.org/10.1002/pen.21830
24. Alshaiban A, Soares JB. Mathematical Modeling of the Microstructure of Poly (propylene) Made with Ziegler-Natta Catalysts in the Presence of Electron Donors. Macromolecular Reaction Engineering. 2011;5(2):96-116. https://doi.org/10.1002/mren.201000036
25. Yan W-C, Dong T, Zhou Y-N, Luo Z-H. Computational modeling toward full chain of polypropylene production: From molecular to industrial scale. Chemical Engineering Science. 2023;269:118448. https://doi.org/10.1016/j.ces.2023.118448
26. Jung K, Corrigan N, Wong EH, Boyer C. Bioactive synthetic polymers. Advanced Materials. 2022;34(2):2105063. https://doi.org/10.1002/adma.202105063
27. Cho HS, Choi YH, Lee WY. Characteristics of ethylene polymerization over Ziegler–Natta/metallocene catalysts: Comparison between hybrid and mixed catalysts. Catalysis today. 2000;63(2-4):523-30. https://doi.org/10.1016/S0920-5861(00)00499-5
28. Liu B, Fukuda K, Nakatani H, Nishiyama I, Yamahiro M, Terano M. 27Al MAS solid state NMR study on coordinative nature of alkyl-Al cocatalysts on a novel SiO2-supported Ziegler–Natta catalyst for controlled multiplicity of molecular weight distribution. Journal of Molecular Catalysis A: Chemical. 2004;219(2):363-70. https://doi.org/10.1021/ja01510a019
29. Alizadeh M, Mostoufi N, Pourmahdian S, Sotudeh-Gharebagh R. Modeling of fluidized bed reactor of ethylene polymerization. Chemical Engineering Journal. 2004;97(1):27-35. 10.1016/S1385-8947(03)00133-5
30. Fukuda K, Liu B, Nakatani H, Nishiyama I, Yamahiro M, Terano M. Significant variation of molecular weight distribution (MWD) of polyethylene induced by different alkyl-Al co-catalysts using a novel surface functionalized SiO2-supported Ziegler-Natta catalyst. Catalysis Communications. 2003;4(12):657-62. https://doi.org/10.1016/j.catcom.2003.10.001
31. Berthold J, Diedrich B, Franke R, Hartlapp J, Schafer W, Strobel W. Process for the preparation of a polyolefin, and a catalyst for this process. Google Patents; 1984.
32. J.C Bailly, S. Sandis, inventors; BP Chemicals Ltd. Ziegler-Natta catalyst. United States patent US 4,960,741,1990.
33. Mao B, Yang A, Zheng Y, Yang J, Li Z. Catalyst system for use in olefinic polymerization. Google Patents; 1988.
34. Razavi-Nouri M. Studies of comonomer distributions and molecular segregations in metallocene-prepared polyethylenes by DSC. Polymer testing. 2006;25(8):1052-8. https://doi.org/10.1016/j.polymertesting.2006.07.004
35. Vadlamudi M, Subramanian G, Shanbhag S, Alamo R, Varma-Nair M, Fiscus D, et al., editors. Molecular Weight and Branching Distribution of a High Performance Metallocene Ethylene 1-Hexene Copolymer Film-Grade Resin. Macromolecular symposia; 2009: Wiley Online Library.
36. Fazeli N, Arabi H, Bolandi S. Effect of branching characteristics of ethylene/1-butene copolymers on melt flow index. Polymer testing. 2006;25(1):28-33. 10.1016/j.polymertesting.2005.09.008
37. Keating M, Lee I-H, Wong CS. Thermal fractionation of ethylene polymers in packaging applications. Thermochimica acta. 1996;284(1):47-56. https://doi.org/10.1021/acs.macromol.2c00773
38. Mohammadi Z, Moradi G, Teimoury H. Ziegler Natta catalyst by precipitation of soluble precursor in different synthesis conditions. Journal of Organometallic Chemistry. 2023;991:122675. 10.1016/j.jorganchem.2023.122675
39. Monji M, Pourmahdian S, Vatankhah M, Taromi FA. Synthesis of highly improved Ziegler-Natta catalyst. Journal of applied polymer science. 2009;112(6):3663-8. https://doi.org/10.1002/app.29786
40. Nowlin TE, Mink RI, Kissin YV. Supported Magnesium/Titanium-Based Ziegler Catalysts for Production of Polyethylene. Handbook of Transition Metal Polymerization Catalysts. 2010;131. 10.5829/IJE.2023.36.04A.02
41. Nikoohemmat MA, Mazaheri H, Joshaghani A, Joudaki E. Investigation on Physical and Mechanical Properties of High Density Polyethylene (PE100) Using Novel Catalyst. International Journal of Engineering, Transactions B:

Applications. 2022;35(11):2205-12. 10.5829/IJE.2022.35.11B.15

42. Shariatzadeh S, Salimi M, Fathinejad H, Hassani Joshaghani A. Nanostructured α-Fe_2O_3: Solvothermal synthesis, characterization, and effect of synthesis parameters on structural properties. International Journal of Engineering, Transactions C: Aspects. 2022;35(6):1186-92. 10.5829/IJE.2022.35.06C.10

43. ASTM D. 1505-10-Standard Test Method for Density of Plastics by the Density-Gradient Technique. Current Edition Approved Jul. 2010;1:7.

44. Karevan M. Investigation of Carbon Black/Polyester Micro-composites: An Insight into Nano-size Interfacial Interactions. International Journal of Engineering, Transactions C: Aspects 2022;35(6):1135-43. 10.5829/IJE.2022.35.06C.05

45. Kissin YV, Mink R, Nowlin T. Ethylene polymerization reactions with Ziegler–Natta catalysts. I. Ethylene polymerization kinetics and kinetic mechanism. Journal of Polymer Science Part A: Polymer Chemistry. 1999;37(23):4255-72.

46. McKenna T, Dupuy J, Spitz R. Modeling of transfer phenomena on heterogeneous Ziegler catalysts. III. Modeling of intraparticle mass transfer resistance. Journal of applied polymer science. 1997;63(3):315-22. https://doi.org/10.1002/(SICI)10974628(19970118)63:3<315::AID-APP6>3.0.CO;2-Q

47. Yu W, Azhdar B, Andersson D, Reitberger T, Hassinen J, Hjertberg T, et al. Deterioration of polyethylene pipes exposed to water containing chlorine dioxide. Polymer degradation and stability. 2011;96(5):790-7. https://doi.org/10.1016/j.polymdegradstab.2011.02.009

48. Bredács M, Frank A, Bastero A, Stolarz A, Pinter G. Accelerated aging of polyethylene pipe grades in aqueous chlorine dioxide at constant concentration. Polymer Degradation and Stability. 2018;157:80-9. https://doi.org/10.1016/j.polymdegradstab.2018.09.019

Persian Abstract

چکیده

در این تحقیق، فرآیند سنتز یک کاتالیزور فوق فعال جدید به نام SAC-510 در مقیاس تجربی بررسی شده است. نویسندگان داده های تجزیه و تحلیل شده را با داده های به دست آمده از یک کاتالیزور پرکاربرد، Finix-112، و چندین جایگزین موجود دیگر مقایسه کردند. داده ها نشان داد که کاتالیزور SAC-510 فعالیت بهینه را از ذرات کروی خود به دست آورده است. تیتانیوم و سایر عناصر شیمیایی در SAC-510 با یکنواختی کمتری نسبت به نمونه های Finix-112 توزیع شده بودند، و اندازه متوسط ذرات در آن ها کمی بزرگتر از اندازه موجود در Finix-112 بود .پراکندگی و اندازه منافذ در SAC-510 به اندازه موارد موجود در کاتالیزور Finix-112 به طور یکنواخت توزیع نشده است. در نهایت، هر دو کاتالیزور SAC-510 و Finix-112 به یک اندازه برای استفاده در لوله های پلی اتیلن با چگالی بالا (درجه ۱۰۰) سازگار بودند. در مقایسه با سایر کاتالیزورهای تجاری موجود، مزایای عمده SAC-510 استفاده اقتصادی از هیدروژن و مونومرها و پاکسازی کم گازهای ارزشمند آن در طول فرآیند پلیمریزاسیون است. نتایج به‌دست‌آمده به شرح زیر است: افزایش راندمان زمان القای اکسیداتیو با کاتالیزور SAC-510 نسبت به کاتالیزور Finix-112 به میزان ۵.۸ درصد، افزایش فعالیت به میزان ۳۵.۷ درصد، پاسخ دهی هیدروژن به میزان ۲٤.۳۹ درصد، کاهش مصرف ۱-بوتن به میزان ۸.۳۸ درصد و نیز کاهش مصرف تری اتیل آلومینیوم به میزان ۲۷.۲۷ درصد.

IJE TRANSACTIONS A: Basics Vol. 37 No. 01, (January 2024) 25-36

International Journal of Engineering

Journal Homepage: www.ije.ir

Smart City Surveillance: Edge Technology Face Recognition Robot Deep Learning Based

A. Medjdoubi*, M. Meddeber, K. Yahyaoui

Faculty of Exact Science, Department of Computer Science, University of Mustapha Stambouli, Mascara, Algeria

PAPER INFO

Paper history:
Received 20 July 2023
Received in revised form 10 September 2023
Accepted 16 September 2023

Keywords:
Convolutional Neural Network
Deep Learning
Edge Technology
Face Recognition
Smart City
Security System

ABSTRACT

In the contemporary context, the imperative to strengthen security and safety measures has become increasingly evident. Given the rapid pace of technological advancement, the development of intelligent and efficient surveillance solutions has garnered significant interest, particularly within the realm of smart city (SC). Surveillance systems have been transformed with the emergence of edge technology (ET), the Internet of Things (IoT), and deep learning (DL) to become key components of SC, notably the domain of face recognition (FR). This work introduces a smart surveillance car robot based on the ESP32-CAM micro-controller, coupled with a FR model that combines DL models and traditional algorithms. The Haar-Cascade (HC) algorithm is employed for face detection, while feature extraction relies on a proposed convolutional neural network (CNN) and predifined DL models, VGG and ResNet. While the classification is made by two distinct algorithms: Naive Bayes (NB) and K-nearest neighbors (KNN). Validation experiments demonstrate the superiority of a composite model comprising HC, VGG, and KNN, achieving accuracy rates of 92.00%, 94.00%, and 96.00% on the LFW, AR, and ORL databases, respectively. Additionally, the surveillance car robot exhibits real-time responsiveness, including email alert notifications, and boasts an exceptional recognition accuracy rate of 99.00% on a custom database. This ET surveillance solution offers advantages of energy efficiency, portability, remote accessibility, and economic affordability.

doi: *10.5829/ije.2024.37.01a.03*

Graphical Abstract

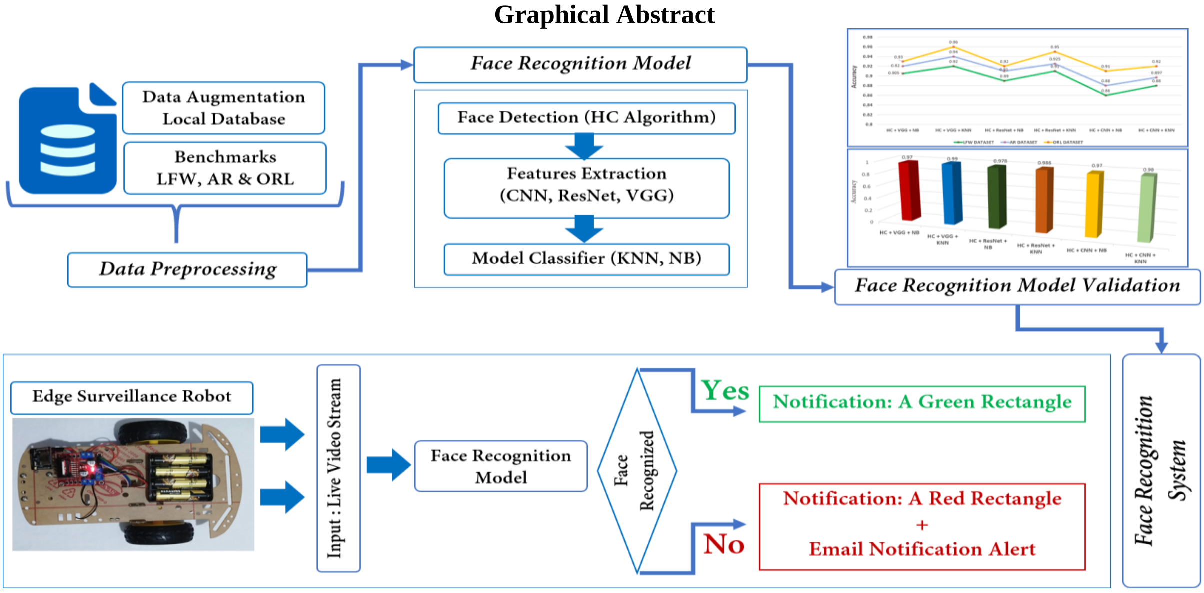

*Corresponding Author Email: *abdelkader.medjdoubi@univ-mascara.dz* (A. Medjdoubi)

Please cite this article as: Medjdoubi A, Meddeber M, Yahyaoui K. Smart City Surveillance: Edge Technology Face Recognition Robot Deep Learning Based. International Journal of Engineering, Transactions A: Basics, 2024;37(01): 25-36.

1. INTRODUCTION

Technology is undergoing rapid and continuous transformation, exerting a profound impact on our daily lives. Our society is increasingly shaped by innovation, scientific progress, and the pervasive deployment of artificial intelligence (AI) in practical applications, including smart automobiles, robotic systems, and wearable devices like smartwatches and smartphones. In this context, ensuring security and safeguarding individuals have assumed unparalleled significance, given the extensive exchange and generation of data by this technological wave (1). The imperative of ensuring the safety and well-being of individuals has become an essential facet of modern life, particularly in the context of SCs. The overarching objective of SCs is to enhance the overall quality of life for their inhabitants, with a particular emphasis on security. This goal is achievable through the integration of advanced technologies, such as intelligent surveillance systems that incorporate cutting-edge components like smart video cameras, sensors, and data analytics techniques (2). The demand for surveillance systems is expanding, given their integral role in safeguarding individuals, preserving public safety, and facilitating efficient urban governance. As SCs continue to expand, the adoption of edge technology (ET) presents new opportunities and advantages. ET enables data processing and analysis in proximity to the data source, as opposed to relying solely on centralized systems. It is the convergence of ET and IoT that has reshaped the lives of millions, simplifying and fortifying virtually every aspect of their daily routines (3). ET, also referred to as edge computing, represents a paradigm where certain services are delivered in close proximity to, or directly on, the devices that initiate the requests (4, 5). This paradigm has contributed significantly to the transformative impact of technology on contemporary society. It provides a variety of advantages; we listed below some main points among them :

- Real-Time Response and Decision Making: ET enables immediate data analysis at the data source, enhancing public safety through rapid processing and response (6, 7).
- Scalability and Flexibility: Distributed architecture accommodates data growth, expands surveillance coverage, and supports real-time video analytics (8).
- Resilience and Reliability: ET's decentralization ensures uninterrupted surveillance, even during network disruptions or emergencies (6, 8).
- Cost Efficiency: ET reduces reliance on expensive cloud resources, optimizing resource use and lowering operational expenses (8).

Many and various industrial security solutions are based on these IoT, ET, and DL advanced technologies. Taking the example from literature (9), a DL-based blockchain-driven scheme for SC security. I this work, the blockchain aspect is employed in a distributed manner at the fog layer to secure the integrity, decentralization, and security of manufacturing data. DL is applied at the cloud layer to boost productivity, automate data processing, and increase the communication bandwidth of smart factory and smart manufacturing applications. They give a case study of vehicle production with the newest service scenarios for the proposed scheme and a comparison to previous research studies utilizing critical characteristics such as security and privacy tools. The solution comprises five layers: a device layer for data collection using physical IoT devices; an edge layer that contains industrial gateways for data communications; a cyber-layer blockchain-based to verify and validate the data; a data analytics layer for data processing and analysis using DL to extract knowledge; and an application layer that employs the knowledge and the results to realize self-management, self-automation, scalable production, and rapid development in smart manufacturing.

Providing solutions that incorporate IoT and ET into the surveillance aspect is the need of the hour and what the researchers and scientists are striving to do, since it’s characterized by various advantages but mainly high efficiency and a reasonable cost (2). For that, video surveillance is one of the most crucial and fundamental parts of ensuring security for SC. Providing new tools and methods that enable people to monitor, control, and increase the stability of the city with fewer human errors (2). This paradigm shift centers around real-time video streaming and data generation through intelligent ET and IoT devices, increasing image processing, collecting more vision data to analyze every day, and information extraction. Consequently, the visual component emerges as an essential element for smart biometric security applications (10). In particular, the FR systems, that play a significant role in enabling the identification of individuals based on their physiological, physical, and behavioral attributes (11). The human face, in this context, stands as a prominent element in biometric identification and verification. This method boasts several advantages, including user friendliness, contactless operation, remote applicability, and real-time decision-making (11, 12). The evolution of FR systems has witnessed substantial progress, transitioning from controlled environments to the processing of faces captured in uncontrolled settings and extending from traditional feature extraction techniques to the adoption of DL methods (8).

Various works and studies have been put out by researchers as for FR IoT and DL-based solutions. DL-based intelligent FR in an IoT-cloud environment is proposed by Masud et al. (12). This research suggests a tree-based DL for automatic FR in a cloud setting. As mentioned in the paper, the proposed deep model is computationally less expensive without affecting accuracy. In the model, an input volume is split into numerous volumes, and a tree is produced for each volume. A tree is described by its branching factor and height. Each branch is represented by a residual function, which is made of a convolutional layer, a batch normalization, and a non-linear function. The proposed model is examined in standard databases. A comparison of performance is also done with state-of-the-art deep models for FR. The results of the experiments reveal accuracies of 98.65%, 99.19%, and 95.84% on the FEI, ORL, and LFW databases, respectively. Kumar et al. (13) suggested a framework using visual recognition for IoT-based SC surveillance. In this manuscript, a quick subspace decomposition over Chi Square transformation is proposed. This technique extracts the characteristics of visual data using a local binary pattern histogram (LBPH). The redundant features are removed by using rapid subspace decomposition over the Gaussian-distributed Local Binary Pattern (LBP) features. As mentioned in the paper, the redundancy removal is a major contribution to memory and time consumption for battery-powered surveillance systems, which makes the methodology suitable for all image recognition applications and deployment into IoT-based surveillance devices due to improved dimension reduction. The technique was implemented on the Raspberry Pi and validated over well-known databases. The least error rate is attained by the suggested technique with maximal feature reduction in minimum time, with 0.28%, 1.30%, 9.00%, and 2.5% rates over AR, O2FN, LFW, and Dyn Tex++ databases, respectively. Other FR-DL-based solution is presented by Charoqdouz and Hassanpour (14). The goal of this study is to estimate the feature vector of a full-face image when there are numerous angular facial images of the same individual. This method extracts the essential elements of a facial image using the non-negative matrix factorization (NMF) method. Then, the feature vectors are merged using a generative adversarial network (GAN) to estimate the feature vector associated with the frontal image. The experiments were made on the FERET dataset, which contains angular pose images with an angle of up to 40 degrees. As concluded by the research, the proposed strategy can greatly increase the accuracy of FR technology. Shahbakhsh and Hassanpour (15) provided a solution to increase the image resolution at the feature level and improve the accuracy of FR methods. The methodology is based on extracting the edges of the face image using LBP and unsharp masking techniques and then adding them to the input image as a preprocessing that can help the used GAN model extract the high-frequency information of the low-resolution data images. The GAN examines picture edges and reconstructs high-frequency information to preserve the facial structure. The experiments were made on the FERET database along with images from other datasets such as MUCT, FEI, and Face94. The results demonstrated a considerable influence on the accuracy of FR in low-resolution photos compared to other state-of-the-art FR technologies.

DL, as a transformative facet of AI, has demonstrated remarkable performance not only in FR systems but also in various signal processing applications such as speech recognition, image recognition, and video recognition (16). Leveraging the inherent advantages of DL, IoT, and ET to construct intelligent FR security applications is not merely a contemporary pursuit but a pressing necessity. The fusion of these technologies offers the promise of delivering high-performance efficiency, aligning with the evolving needs of modern urban security (16).

The major contributions in the paper are: first, implementing a complex DL-FR system capable of making real-time decisions and predictions close to the IoT origin data source. Secondly, presenting a smart surveillance solution with a real-world ET robot application. Finally, we propose a SC surveillance solution that offers several advantages: low economic cost, less power consumption, portability, and remote utility.

The paper is divided into four sections. The first section described above highlights and discusses the research problem and presents the literature survey. The second section explains what the FR system is, what its essential phases are, and how it is functioning. The third section illustrates the suggested methodology based on approaches, techniques, and the materials used. The fourth section of the paper presents the experimental setup, results, and discussion. The last section concludes the paper.

2. FACE RECOGNITION SYSTEM

Over the course of the previous three decades, FR has garnered significant attention as an efficient image analysis and pattern recognition tool (17, 18). This heightened interest is largely attributable to the advancements in relevant technologies, which have facilitated a diverse range of commercial applications across various domains. These domains encompass transportation, where FR is employed for person identification and passport verification; law enforcement, where it aids in tracking suspicious individuals and identifying criminals; smart homes, which utilize FR for intelligent access control; healthcare, with the implementation of patient tracking systems; and marketing, where FR facilitates smart payment and personalized advertising (14, 18, 19).

The functionality of the FR system entails the creation of additional subtasks in a pipeline that are essential for its proper execution; an illustration of these subtasks is presented in Figure 1.

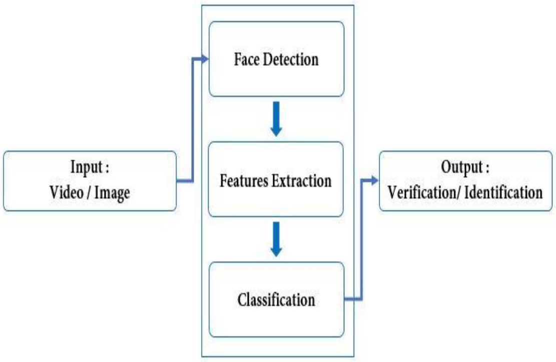

Figure 1. Face recognition system

- Face detection: It's the initial phase in the system; it shows if the image contains a face(s) or not by determining human facial location and dimensions. A lot of methods and algorithms are proposed for this task; some of them, among others, are the HC method by Viola and Jones (20) to identify facial characteristics with Haar-like features. Dlib HOG (21), which employs support vector machines (SVM) in conjunction with histograms of oriented gradients. Dlib CNN (21) combines a maxi-mum-margin object detector with a CNN to extract facial features. Another method is FaceNet (22), which is also based on CNN.
- Features Extraction: A key step that follows the detection phase consists of extracting the features, also called the signatures, which must be sufficient to represent a human face in the form of a vector, as we can call it, encoding the face. It is necessary to examine the uniqueness and individuality of the human profile (23). It should be mentioned that this process can be completed in the face detection step (17). Many different techniques can do this operation, such as deep neural nets like ResNet (23), FaceNet, and OpenFace (24). A novel technique was introduced by Firouzi et al. (25). An optimized hexagonal canny edge detection method. Images were first transformed to a hexagonal grid, followed by hexagonal image filtering using a Gaussian filter. Then, the magnitude and direction of gradients are estimated on the three axes x, y, and z. In the next stage, non-maximum suppression is applied to the amplitude and direction of gradients. Finally, threshold selection, double thresholding, untrue edge tracking, and edge removal are done successively to reach edges in the hexagonal domain.
- Classification: The encoders or the face vectors from the previous phase are classified into one of the classes offered during the training to make the general decision of either a known or unknown person. So, at this final stage, we have the process of finding an image label with a level of confidence. It is based on using supervised learning algorithms, which are frequently employed to do this type of operation. At this point in the system outcome, we will be doing either identification by comparison to other faces in order to determine the person's identity or verification of the person, which entails matching one face to another for accomplishing tasks like guaranteeing access, for example.

3. METHODOLOGY

The suggested ET surveillance robot works via a web-based application applying a FR model based on DL. This section will describe all the aspects, including the main steps, methods, and tools used to build our system.

3. 1. Face Recognition Study Proposal

The proposed FR models in this work were developed using multiple processes, as depicted in Figure 2. Each stage will be illustrated and discussed. Starting with data preparation and preprocessing, moving on to face detection, feature extraction, and classification. Each FR model will be a combination of several algorithms and DL models.

3. 1. 1. Data Preprocessing

As we can see in Figure 2, the data section is divided into two parts: one for benchmarks and the other for a local dataset. Benchmarks are a common database used for FR problems; in this work, we chose three of them: the LFW, the ORL, and the AR database. Such databases are for validating our FR-proposed models. The first one is the LFW[1] database, which has 13233 images of 5749 people. The second is the AR[2] database, which contains over 4,000 images corresponding to 126 people's faces. The third is the ORL[3] database, which comprises 400 images, represented by 40 subjects that have 10 photos per subject.

Moving to the second part of data preparation, in order to acquire a successful, correct outcome, a substantial amount of training data is required, but on the other hand, it is difficult and challenging work to do in a real-time context. Therefore, we create our own database using the data augmentation approach. It is utilized to generate more and new samples by modifying the existing data images. This database is used for testing our proposed FR models to be deployed with surveillance car robot. Therefore, we combine three different human face pictures together; two of them were chosen randomly from the AR database, and the third was from the author

[1] https://www.ece.ohio-state.edu/~aleix/ARdatabase.html
[2] https://cam-orl.co.uk/facedatabase.html
[3] http://vis-www.cs.umass.edu/lfw/

itself. Each image will be labeled with a class name, "Class_0", Class_1," and Class_2," as shown in Figure 3.

The augmentation process is made by applying different operations as described and listed in Table 1. Using this strategy, we built a local database containing 2430 face images with 810 data images per class.

Reshaping all the images to 64 by 64 grayscale photos is another preprocessing step to guarantee that all the data have the same shape. Next, a normalization strategy will be employed to verify that all data are in the same range.

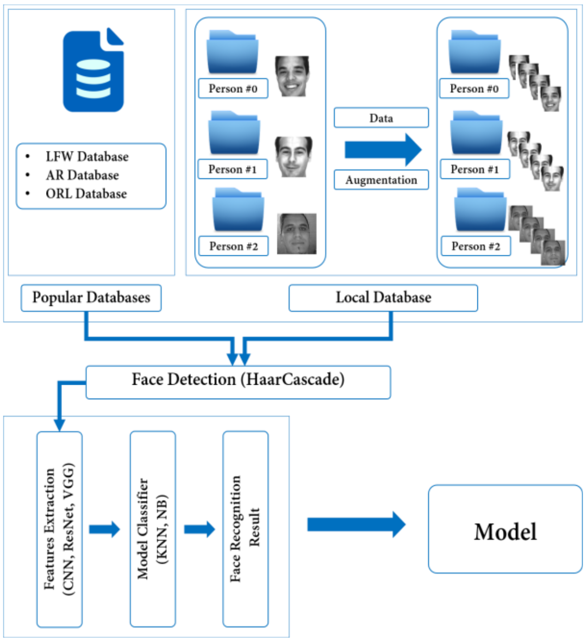

Figure 2. The proposed face recognition models

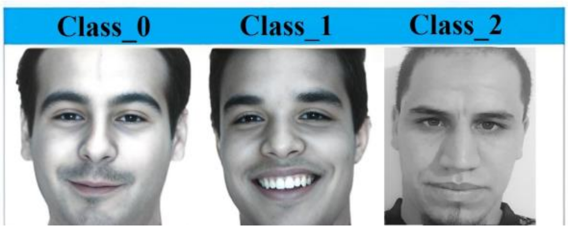

Figure 3. Local database classes labelling

TABLE 1. Data augmentation operations

Parameter	Interval or Value
Zoom	[-5, 5]
Shear	0.5
Height shift	0.3
Width shift	0.3
Rotation	[0, 15]

[1] https://github.com/fchollet/keras

3. 1. 2. Face Detection After preparing four distinct databases, a second step of face detection took place using HC. This algorithm uses a collection of predetermined features based on the foundation of Haar-like features, including edges, lines, and corners, as illustrated in Figure 4, to identify facial features like the eyes, nose, and mouth. It takes the frontal face as an input that will be exposed to a cascade application of the classifier. The image is divided into portions before the classifier is applied to each area. If a region is recognized as a face, the cascade continues to the next phase; otherwise, it is discarded, and the next region is processed. Figure 5 represents an example of this process.

3. 1. 3. Features Extraction CNNs have changed the domain of computer vision (CV) by imitating the human visual system's hierarchical processing. CNNs learn and extract internal representations or features straight from raw picture data, making them highly effective for tasks like FR, image categorization, object detection, and more. In this part, we will discuss the training process of our DL models. Three different DL models will be applied; two of them are predefined: the VGG (26) and the ResNet model. The third one is a proposed CNN built using the TensorFlow (27) and Keras[1] frameworks. Our suggested CNN is composed of 13 layers and has an architecture as explained in Table 2.

Following normalization, feature extraction and redundancy reduction take place in a pair of

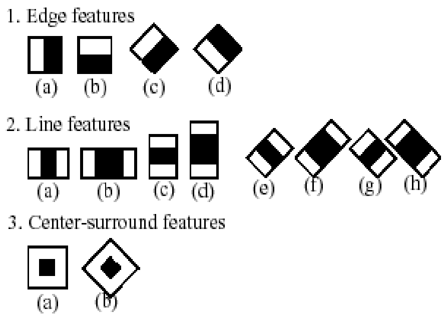

Figure 4. The Haar features used in the HC algorithm

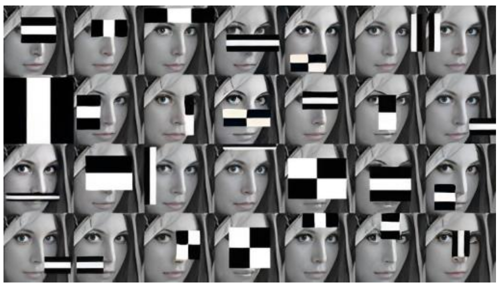

Figure 5. Haar features application over an image

TABLE 2. Proposed CNN model architecture

Layer Type	**Number of Layer**
Two-Dimensional Convolutional Layer (Conv2D)	04 layers
Batch Normalization Layer	02 layers
Max Pooling Layer	02 layers
Dense Layer	03 layers

convolutional layers coupled with pooling layers. Simple features come together efficiently over time. The features are then partially blended, with each resulting feature accounting for a portion of the configuration of the designated class. Finally, the fully connected layer receives these top attributes and delivers an estimation of the classification. To understand in more detail the process of feature extraction by the CNN, we have to illustrate each layer functionally. Figure 6 (28) shows a graphical representation of a CNN model where each layer is responsible for a specific operation.

Convolutional layers play the role of feature extractors. To generate feature maps, inputs are convolved with learned weights, and the results are then sent through a nonlinear activation function. Equation 1 specifies the output of the kth feature map, denoted by Y_{k}.

$$Y_{\mathrm{k}} = W_{\mathrm{k}} © M \tag{1}$$

where:

- W_k is the convolution filter.
- The sign "©" refer to the 2D convolution operation.
- M refer to the input data image.

The batch normalization layer has the role of normalizing the input and tackling the vanishing gradient problems (16). It uses a normalization approach that takes place between the layers of the network instead of in the input data, in the form of mini-batches. By including additional layers, the learning process can be faster and more reliable. When a layer's input comes from a prior layer, the new layer standardizes and normalizes it.

For the pooling layer, as the name suggests, the operation of pooling or named subsampling also works as a bridge between several convolutional layers. The most popular pooling approaches in CNNs are max-pooling and average-pooling. It minimizes the spatial dimensions of the feature map, thereby lowering the computing process and aiding in translational invariance. In our study, we utilized the max pooling operation. It involves dividing the input feature map into regions called pooling windows and selecting the maximum value from each region. Equation 2 shows the process of this operation, where the output of this layer is denoted by Y_{kij} representing the kth maximum element of a region from an image.

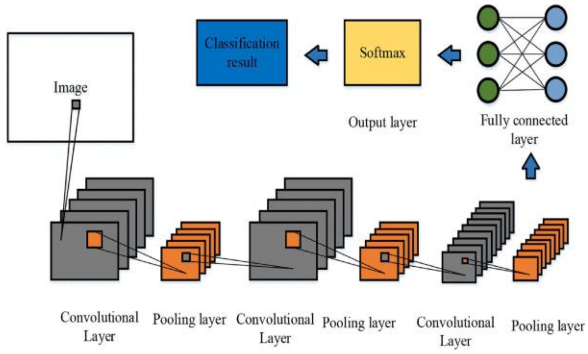

Figure 6. CNN model graphical representation

$$Y_{\mathrm{kij}} = maximum_{(\mathrm{p},\ \mathrm{q}) \in R_{\mathrm{ij}}} (M_{\mathrm{kpq}}) \tag{2}$$

where:

- M_{kpq} denotes kth element at location (p, q) from input data image M contained by the $maximum$ of region R_{ij}.

Figure 7 demonstrates even more this operation. A convolution layer's inputs are converted to the pooling layer's inputs. The greatest value in each 2x2 sub-area is mapped using a 4x4 mask.

After the feature extraction, the classification phase takes over, utilizing dense layers, which are completely connected layers employed to map the learned features to specific classes. These layers are critical for accurate classification and comprehending complicated relationships between features.

The training process for our DL models involved employing several parameters discussed as follows:

- Learning Rate: The learning rate controls how much the model's weights are changed during training. In our study, we fixed it to 0.001.
- Batch Size: Batch size defines the number of training samples utilized in each iteration of gradient descent, which in our case was 32.
- Number of Epochs: The number of epochs denotes the number of times the full training dataset is transmitted forward and backward through the network. We adjust it to 150.
- Optimizer: The optimizer governs the weight adjustments during training. Our DL models were trained using the RMSprop optimizer (29).

During the neural network training, a common challenge frequently addressed is the phenomenon known as overfitting. It occurs when the model learns to perform very well on the training data but fails to generalize to new, unknown input. As a solution to our work, three strategies are being applied, as given below:

- Regularization: One of the main methods employed is the integration of regularization techniques, such as L1 and L2 regularization. These methods contain penalty terms in the loss function, deterring the

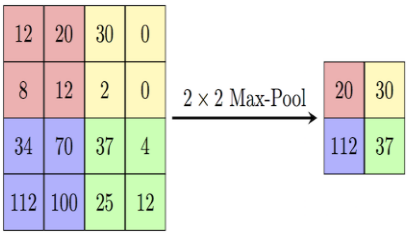

Figure 7. Illustrative example of max pooling operation

model from allocating excessive value to certain features or parameters. This, in turn, promotes a more balanced model. In our case, we use the L2 method.

- Dropout: We add some dropout regularization that entails the random deactivation of a fraction of neurons during training, effectively introducing an element of unpredictability and preventing co-adaptation among neurons. This enhances the network's ability to generalize by reducing reliance on specific neurons.
- Early Stopping: Monitor the validation accuracy during training and stop when it starts to drop. In order to apply it to our models, we use call-backs, an object that can perform actions at various stages of training. We fixed the monitoring operation for 30 consecutive epochs.

3. 1. 4. Model Classifier In this stage, we will use two supervised algorithms, the NB and the KNN, each at a time, to finish each FR model combination. The method is to classify the features encoded previously. The classification will be into one of the classes labeled with an amount of confidence, like a supervised classification strategy. It is about identifying and recognizing the face, and the result will be either a recognized person with a known label or an unknown person. After each training and classification phase, a model combination will be saved and exported for deployment purposes and to test our surveillance car robot. The best model of the six-model combination will be picked based on the accuracy results in the created database.

3. 2. Edge Surveillance System Proposal The suggested system in this study is predicated on the three parts detailed in the subsections below. The first one is the edge system, the second is the recognition system, and the third is the monitoring system, as indicated in Figure 8, where the functionality is as follows:

- Step 1: The edge surveillance robot captures the area with the camera module.
- Step 02: The recognition system captures the video transmitted by the robot, processes it, and extracts the images in real time.
- Step 03: If a face is detected, the FR model will take place and apply all the necessary steps to recognize it.
- Step 04: Presenting the outcomes on the live streaming web application, and also a notification email alert will be provided in case of unrecognized faces.

3. 2. 1. Edge Surveillance System Our proposed edge system is a surveillance car robot developed using several components, including:

- ESP32-CAM module.
- L298N Motor Driver
- Car robot that comes with 1 car chassis, 2 DC gear motors, 2 car tires, 1 universal wheel, 1 battery holder, and jumper wires.

Starting with the main module, the ESP32-CAM, which is a compact microcontroller and a low-cost ESP32-based development board featuring an inbuilt camera that works independently, powered by its own Wi-Fi and Bluetooth connectivity, among other specifications, as follows:

- Built in 520 KB of SRAM plus 4 MB of PSRAM.
- An SD card slot is supported.
- Built-in flash LED.
- The camera supports, which in our case, an OV5640 camera with a 5-megapixel image sensor.

The final result of the assembled car robot is represented in Figure 9.

After putting all the parts together and in order to make the system functioning, both for live streaming via the ESP32-CAM and for car robot control via the L298N motor drive, we have to program the ESP32-CAM board. Using the Arduino integrated development environment, we upload the main code written in C++ to synchronize the tasks between the components. The key functions are presented in Figure 10. Managing and using the robot will be done via a web application using a web browser.

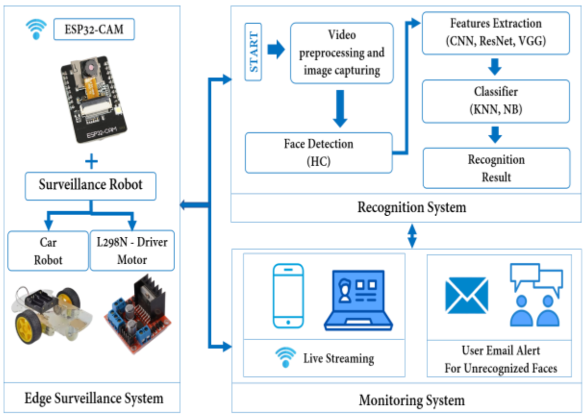

Figure 8. The proposed face recognition surveillance system

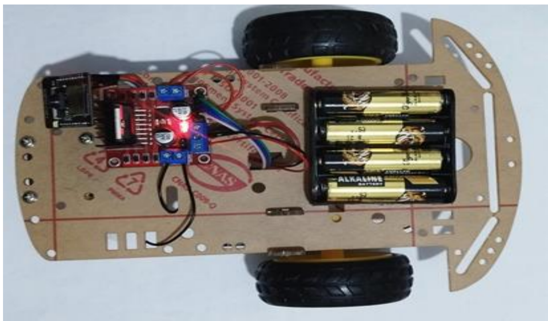

Figure 9. Edge surveillance car robot

3. 2. 2. Recognition System We applied a preprocessing step to the live streaming video provided through the ESP32-CAM module to extract the facial photos. Each video frame is turned into an image in order to identify the face inside it, after which features are extracted using DL models in order to classify them using the classification methods based on the confidence threshold.

3. 2. 3. Monitoring System The ability to drive the car and view the live streaming video using the same web application has been included as a final element in the proposed edge surveillance system, as shown in Figure 11. The buttons allow us to steer it in whatever direction we like while also managing the speed and lights. Our system has an email notification feature to alert users to unfamiliar faces as a security response.

```
void Car_Movement_control(int inputValue)
{
  Serial.printf("Got value as %d\n", inputValue);
  switch(inputValue)
  {

    case UP:
      rotateMotor(RIGHT_MOTOR, FORWARD);
      rotateMotor(LEFT_MOTOR, FORWARD);
      break;

    case DOWN:
      rotateMotor(RIGHT_MOTOR, BACKWARD);
      rotateMotor(LEFT_MOTOR, BACKWARD);
      break;

    case LEFT:
      rotateMotor(RIGHT_MOTOR, FORWARD);
      rotateMotor(LEFT_MOTOR, BACKWARD);
      break;

    case RIGHT:
      rotateMotor(RIGHT_MOTOR, BACKWARD);
      rotateMotor(LEFT_MOTOR, FORWARD);
      break;

    case STOP:
      rotateMotor(RIGHT_MOTOR, STOP);
      rotateMotor(LEFT_MOTOR, STOP);
      break;

    default:
      rotateMotor(RIGHT_MOTOR, STOP);
      rotateMotor(LEFT_MOTOR, STOP);
      break;
  }
}
```

```
void setup(void)
{
  setUpPinModes();
  Serial.begin(115200);

  WiFi.softAP(ssid, password);
  IPAddress IP = WiFi.softAPIP();
  Serial.print("AP IP address: ");
  Serial.println(IP);

  server.on("/", HTTP_GET, handleRoot);
  server.onNotFound(handleNotFound);

  wsCamera.onEvent(onCameraWebSocketEvent);
  server.addHandler(&wsCamera);

  wsCarInput.onEvent(onCarInputWebSocketEvent);
  server.addHandler(&wsCarInput);

  server.begin();
  Serial.println("HTTP server started");

  setupCamera();
}
```

```
void rotateMotor(int motorNumber, int motorDirection)
{
  if (motorDirection == FORWARD)
  {
    digitalWrite(motorPins[motorNumber].pinIN1, HIGH);
    digitalWrite(motorPins[motorNumber].pinIN2, LOW);
  }
  else if (motorDirection == BACKWARD)
  {
    digitalWrite(motorPins[motorNumber].pinIN1, LOW);
    digitalWrite(motorPins[motorNumber].pinIN2, HIGH);
  }
  else
  {
    digitalWrite(motorPins[motorNumber].pinIN1, LOW);
    digitalWrite(motorPins[motorNumber].pinIN2, LOW);
  }
}
```

Figure 10. Edge surveillance car robot main functions

Figure 11. Surveillance system web application

4. RESULTS AND DISCUSSION

The first part of our analysis will focus on the results of model validation toward benchmarks, while the second part will deal with the local data set that was developed to represent the results of the deployed model and the performance of the edge surveillance robot. The experiments made in this work, from training, testing, and validating the models, were using Google Colab [33], the free tier of the platform that delivers the needs with a system configuration as shown in Table 3.

TABLE 3. Google Colab platform free tier configuration

Hardwar	Specifications
GPU	Nvidia Tesla K80
CPU	2x Intel Xeon @ 2.20GHz
RAM	13 GB
HARD DISK	78 GB

The model's performance evaluation was based on the accuracy metric as described in Equation 3.

$$Accuracy = \frac{TN + TP}{TN + TP + FN + FP} \quad (3)$$

where: TN (true negative) are the examples correctly classified as negative class; TP (true positive) are the examples correctly classified as positive class; FP (false positive) are the examples incorrectly classified as positive class; and FN (false negative) are the examples incorrectly classified as negative class.

4. 1. Face Recognition Model Validation Results

As demonstrated in Figure 12, evaluating the models over the LFW, AR, and ORL databases provides different outcomes in terms of accuracy.

4. 1. 1. LFW Database The training set was 90% from this database, while the rest was for the testing set with 1330 samples using the train-test cross-validation. Each one of the model's combinations has its own accuracy. We can observe from Figure 12 that the best model with the highest accuracy over this database is HC + VGG + KNN, with a value of 92.00%.

4. 1. 2. AR Database As the first database, we apply cross-validation to get 10% of the data for testing with 400 samples. Analyzing the results of each combination represented in Figure 12 it is noticed that the HC + VGG + KNN model combination fit the best, with a 94.00% accuracy rate.

4. 1. 3. ORL Database The results demonstrate the accuracy of each combination in this database with a testing set of 40 samples with the same percentage of 10% from the whole database. Also, we notice that the HC + VGG + KNN model combination is the best, with 96.00% accuracy.

4. 1. 4. Validation Results Summary As a sum up of the model's validation process, we conclude that the HC + VGG + KNN combination provides the highest accuracy, as presented in Table 4. Observing that our models are affected directly by the number of classes, we notice that when the number of classes decreases, the accuracy of the models will increase.

4. 2. Surveillance System Results

In order to detail the suggested surveillance system results, we first represent the best model that was chosen for deployment into the system, where the combination was extracted after analyzing the model's accuracy results over the created database. Secondly, we represent the results of testing our surveillance car robot.

4. 2. 1. Face Recognition Model Testing Results The testing set had 10% of the database and 243 data

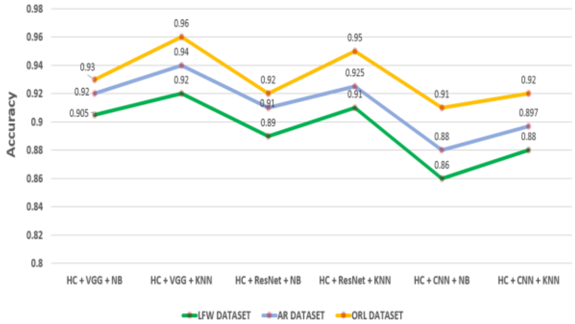

Figure 12. Model's performance over the benchmarks Model's performance over the benchmarks

TABLE 4. Comparison of the model's validation accuracy

Models \ Databases	LFW with 5749 classes	AR with 126 classes	ORL with 40 classes
HC + VGG + NB	90.50%	92.00%	93.00%
HC + VGG + KNN	**92.00%**	**94.00%**	**96.00%**
HC + ResNet + NB	89.00%	91.00%	92.00%
HC + ResNet + KNN	91.00%	92.50%	95.00%
HC + CNN + NB	86.00%	88.00%	91.00%
HC + CNN + KNN	88.00%	89.70%	92.00%

samples. By observing the model performance, we found the best model, which consists of HC + VGG + KNN, has the highest accuracy rate of 99.00%. Starting with the confusion matrix represented in Table 5, the samples labeled "Class_0" and "Class_1", were all correctly classified, while the class labeled "Class_2" had two miss-classified examples.

We can observe in Figure 13 the performance of the other models in terms of accuracy results. Noting that the HC + ResNet + KNN model also gives a high accuracy of 98.76% with a small deference to the chosen model.

4. 2. 2. Face Recognition Deep Learning Model Testing Results To do comparison analysis, we apply another training phase with the same parameters as mentioned earlier on the same local database using the CNN, VGG, and ResNet models, without the NB and

TABLE 5. Confusion matrix of the HC+VGG+ KNN model on local database

Actual Class \ Predicted Class	Class_0	Class_1	Class_2
Class_0	78	0	0
Class_1	0	83	0
Class_2	0	2	80

KNN classifiers. Aiming to observe the performance of these DL models since they can accomplish the classification task on their own. Figure 14 displays the test performance in terms of accuracy results. It indicates that this strategy of using the DL model for classification is superior to the approach of adding a traditional classification algorithm to the FR model. In terms of accuracy, the VGG outperforms the other models with a 99.15% rate, where we note 99.04% and 98.70% rates for the ResNet and the CNN, respectively.

To ascertain the robustness and effectiveness of each network architecture in terms of their performance, we added even more experiments based on accuracy and standard deviation for a series of experiments that were conducted repeatedly five times. The mean and standard deviation of the diagnostic accuracy are shown in Table 6. It can be concluded that the FR model based on HC and VGG outperforms all the other methods.

4. 2. 3. Surveillance Robot System Testing Results

The surveillance car robot created throughout the research has been examined in a real-world setting to test its efficiency. The system's reaction was in real time, with an average of 0.30 seconds. The live video streaming provided by the robot will be analyzed and processed by the HC + VGG + KNN model, where it has successfully predictions over the captured face images. Figure 15 shows a system response inside a house environment to a known case where the face was successfully recognized.

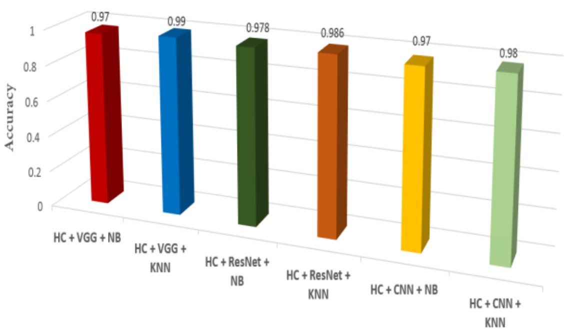

Figure 13. Model's performance over local database

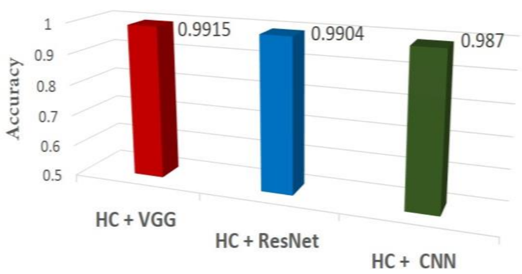

Figure 14. Deep learning model's performance over local database

TABLE 6. The mean and Standard deviation of accuracy results

Metrics / FR Models	Accuracy	Standard deviation
HC + VGG	99.22%	0.10
HC + ResNet	99.004%	0.12
HC + CNN	98.71%	0.17

To do more evaluations for the surveillance robot, we made some changes to the face positioning. The model was unable to recognize the features since it was not in frontal positioning, as represented in Figure 16a. We put our edge robot in another situation by changing the environment outside the house in cloudy weather, where it works as it should in terms of movements, video streaming, and image capturing, but the illumination affected the processing operations and the model was unable to recognize the face. The case scenario is illustrated in Figure 16b.

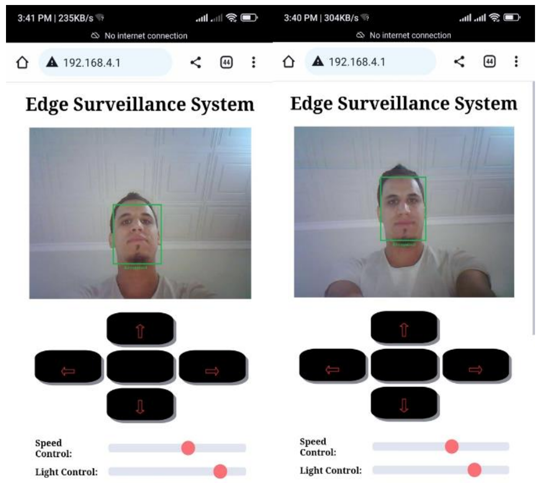

Figure 15. Edge system response for normal case scenario

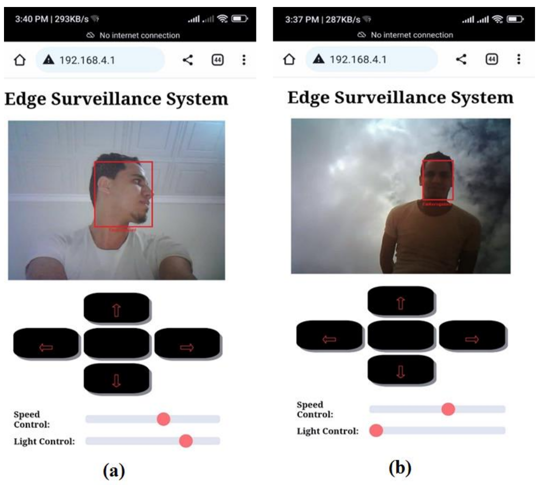

Figure 16. (a) Edge robot response for non-frontal face scenario. (b) Edge robot response with bad lighting scenario

5. CONCLUSION

In this study, we developed a FR system based on DL and ET. We have successfully built an edge car robot that works with an implemented system that consists of various algorithms and a DL approach for SC surveillance. A notification feature is included in the system to alert the user about intruders or unidentified people nearby via email address. Our suggested solution has several advantages, including being a low-cost, affordable solution, less power-consuming, lightweight, supporting remote usage, and accomplishing the task of recognition in real time with high efficiency. This paper also demonstrates how edge devices with specific computational capabilities may now run complicated AI models while maintaining effectiveness and efficiency in terms of results. Further work and more aspects need to be covered, such as lightning changes since they affect the prediction results, face positioning, and face expressions, to give the model the best performance possible.

6. REFERENCES

1. Bellavista P, Chatzimisios P, Foschini L, Paradisioti M, Scotece D, editors. A support infrastructure for machine learning at the edge in smart city surveillance. 2019 IEEE Symposium on Computers and Communications (ISCC); 2019: IEEE. 10.1109/iscc47284.2019.8969779
2. Ezzat MA, Abd El Ghany MA, Almotairi S, Salem MA-M. Horizontal review on video surveillance for smart cities: Edge devices, applications, datasets, and future trends. Sensors. 2021;21(9):3222. 10.3390/s21093222
3. Nauman A, Qadri YA, Amjad M, Zikria YB, Afzal MK, Kim SW. Multimedia Internet of Things: A comprehensive survey. Ieee Access. 2020;8:8202-50. 10.1109/access.2020.2964280
4. Jiménez-Bravo DM, Lozano Murciego Á, Sales A, Augusto Silva L, De La Iglesia DH. Edge Face Recognition System Based on One-Shot Augmented Learning. 2022. 10.9781/ijimai.2022.09.001
5. Shi W, Pallis G, Xu Z. Edge computing [scanning the issue]. Proceedings of the IEEE. 2019;107(8):1474-81.
6. Silva BN, Khan M, Han K. Towards sustainable smart cities: A review of trends, architectures, components, and open challenges in smart cities. Sustainable cities and society. 2018;38:697-713. 10.1016/j.scs.2018.01.053
7. Lai CS, Jia Y, Dong Z, Wang D, Tao Y, Lai QH, et al. A review of technical standards for smart cities. Clean Technologies. 2020;2(3):290-310. 10.3390/cleantechnol2030019
8. Al-Turjman F, Zahmatkesh H, Shahroze R. An overview of security and privacy in smart cities' IoT communications. Transactions on Emerging Telecommunications Technologies. 2022;33(3):e3677. 10.1002/ett.3677
9. Singh SK, Azzaoui A, Kim TW, Pan Y, Park JH. DeepBlockScheme: A deep learning-based blockchain driven scheme for secure smart city. Human-centric Computing and Information Sciences. 2021;11(12):1-13. 10.22967/HCIS.2021.11.012
10. Khan PW, Byun Y-C, Park N. A data verification system for CCTV surveillance cameras using blockchain technology in smart cities. Electronics. 2020;9(3):484. 10.3390/electronics9030484
11. Kortli Y, Jridi M, Al Falou A, Atri M. Face recognition systems: A survey. Sensors. 2020;20(2):342. 10.3390/s20020342
12. Masud M, Muhammad G, Alhumyani H, Alshamrani SS, Cheikhrouhou O, Ibrahim S, et al. Deep learning-based intelligent face recognition in IoT-cloud environment. Computer Communications. 2020;152:215-22. 10.1016/j.comcom.2020.01.050
13. Kumar M, Raju KS, Kumar D, Goyal N, Verma S, Singh A. An efficient framework using visual recognition for IoT based smart city surveillance. Multimedia Tools and Applications. 2021:1-19. 10.1007/s11042-020-10471-x
14. Charoqdouz E, Hassanpour H. Feature extraction from several angular faces using a deep learning based fusion technique for face recognition. International Journal of Engineering, Transactions B: Applications. 2023;36(8):1548-55. 10.5829/ije.2023.36.08b.14
15. Shahbakhsh MB, Hassanpour H. Empowering face recognition methods using a gan-based single image super-resolution network. International Journal of Engineering, Transactions A: Basics. 2022;35(10):1858-66. 10.5829/ije.2022.35.10a.05
16. Faisal F, Hossain SA, editors. Smart security system using face recognition on raspberry Pi. 2019 13th International Conference on Software, Knowledge, Information Management and Applications (SKIMA); 2019: IEEE. 10.1109/skima47702.2019.8982466
17. Adjabi I, Ouahabi A, Benzaoui A, Taleb-Ahmed A. Past, present, and future of face recognition: A review. Electronics. 2020;9(8):1188. 10.20944/preprints202007. 0479.v1
18. Hassanpour H, Ghasemi M. A three-stage filtering approach for face recognition. International Journal of Engineering. 2021;34(8):1856-64. 10.5829/ije.2021.34.08b.061
19. Kakarla S, Gangula P, Rahul MS, Singh CSC, Sarma TH, editors. Smart attendance management system based on face recognition using CNN. 2020 IEEE-HYDCON; 2020: IEEE. 10.1109/hydcon48903.2020.9242847
20. Viola P, Jones MJ. Robust real-time face detection. International journal of computer vision. 2004;57:137-54. 10.1023/B:VISI.0000013087.49260.fb
21. King DE. Dlib-ml: A machine learning toolkit. The Journal of Machine Learning Research. 2009;10:1755-8. 10.1145/1577069.1755843
22. Schroff F, Kalenichenko D, Philbin J, editors. Facenet: A unified embedding for face recognition and clustering. Proceedings of the IEEE conference on computer vision and pattern recognition; 2015. 10.48550/ARXIV.1503.03832
23. Kaur P, Krishan K, Sharma SK, Kanchan T. Facial-recognition algorithms: A literature review. Medicine, Science and the Law. 2020;60(2):131-9. 10.1177/0025802419893168
24. Baltrusaitis T, Zadeh A, Lim YC, Morency L-P, editors. Openface 2.0: Facial behavior analysis toolkit. 2018 13th IEEE international conference on automatic face & gesture recognition (FG 2018); 2018: IEEE. 10.1109/fg.2018.00019
25. Firouzi M, Fadaei S, Rashno A. A new framework for canny edge detector in hexagonal lattice. International Journal of Engineering. 2022;35(8):1588-98. 10.5829/ije.2022.35.08b.15
26. Simonyan K, Zisserman A. Very deep convolutional networks for large-scale image recognition. arXiv preprint arXiv:14091556. 2014. 10.48550/ARXIV.1409.1556
27. Developers T. TensorFlow (Zenodo, 2021). DOI.
28. Liu J. Convolutional neural network-based human movement recognition algorithm in sports analysis. Frontiers in psychology. 2021;12:663359. 10.3389/fpsyg.2021.663359
29. Tieleman T, Hinton G. Divide the gradient by a running average of its recent magnitude. coursera: Neural networks for machine learning. Technical report. 2017. https://www.cs.toronto.edu/~tijmen/csc321/slides/lecture_slides_lec6.pdf

Persian Abstract

چکیده

در زمینه معاصر ، ضرورت تقویت اقدامات امنیتی و ایمنی به طور فزاینده ای آشکار شده است. با توجه به سرعت سریع پیشرفت تکنولوژیکی ، توسعه راه حل های نظارت هوشمند و کارآمد علاقه قابل توجهی را به خود جلب کرده است ، به ویژه در قلمرو شهر هوشمند (SC). سیستم های نظارتی با ظهور فناوری edge (ET) ، اینترنت اشیاء (IoT) و یادگیری عمیق (DL) به اجزای کلیدی SC تبدیل شده اند ، به ویژه حوزه تشخیص چهره (FR). این کار یک ربات ماشین نظارت هوشمند را بر اساس میکروکنترلر ESP32-CAM معرفی می کند ، همراه با یک مدل FR که مدل های DL و الگوریتم های سنتی را ترکیب می کند. الگوریتم Haar-Cascade (HC) برای تشخیص چهره استفاده می شود ، در حالی که استخراج ویژگی به یک شبکه عصبی کانولوشن پیشنهادی (CNN) و مدل های dl پیش تعریف شده ، VGG و ResNet متکی است. در حالی که طبقه بندی توسط دو الگوریتم متمایز ساخته شده است: ساده لوح Bayes (NB) و k-نزدیکترین همسایگان (KNN). آزمایشات اعتبارسنجی برتری یک مدل ترکیبی شامل HC، VGG و KNN را نشان می دهد و به ترتیب میزان دقت ۹۲.۰۰ ٪ ، ۹٤.۰۰ ٪ و ۹٦.۰۰ ٪ را در پایگاه داده های LFW، ar و ORL به دست می آورد. علاوه بر این ، ربات ماشین نظارتی پاسخگویی در زمان واقعی را نشان می دهد ، از جمله اطلاعیه های هشدار ایمیل ، و دارای نرخ دقت تشخیص استثنایی ۹۹.۰۰ ٪ در یک پایگاه داده سفارشی است. این راه حل نظارت ET مزایای بهره وری انرژی ، قابلیت حمل ، دسترسی از راه دور و مقرون به صرفه بودن اقتصادی را ارائه می دهد.

IJE TRANSACTIONS A: Basics Vol. 37 No. 01, (January 2024) 37-47

International Journal of Engineering

Journal Homepage: www.ije.ir

Probabilistic Reactive Power Flow Optimization of Distribution System in Presence of Distributed Units Uncertainty Using Combination of Improved Taguchi Method and Dandelion Algorithm

M. Najjarpour, B. Tousi*

Electrical Engineering Department, Faculty of Electrical and Computer Engineering, Urmia University, Urmia, Iran

PAPER INFO

Paper history:
Received 31 July 2023
Received in revised form 28 September 2023
Accepted 30 September 2023

Keywords:
Renewable Energy
Improved Taguchi Method
Orthogonal Arrays
Optimal Reactive Power Distribution
Dandelion Optimizer
Uncertainty

ABSTRACT

Nowadays, due to the growing population, rising global warming, environmental pollution, and the reduction of fuel sources, the use of Distributed Generation Sources (DGs) has grown, and because of their random nature, the conventional performance of power systems is being changed. Reactive power has a considerable role in power systems management and control indexes such as loss, stability, reliability, and security, among which the loss index usually can be easily minimized and controlled. Thus the modeling and optimizing of reactive power must be done accurately and correctly. This paper uses a novel metaheuristic algorithm which is called Dandelion, to solve the constrained non-linear optimal reactive power dispatch problem, and the Improved Taguchi method based on orthogonal arrays has been applied in order to the uncertainty of DG units modeling. The applied optimal reactive power dispatch algorithm is tested and validated using standard IEEE 30-bus test power systems. These results show that the Computational time of the applied algorithm in comparison with other used algorithms is the least value and reduces the reactive power from 22.244 to 2.366 Mvar; also, the losses of the power system significantly will be decreased with the tested and introduced algorithm. Genetic Algorithm(GA), Particle swarm optimization algorithm (PSO), and Prairie dog optimization algorithm (PDO) have been utilized to solve the problem.

doi: *10.5829/ije.2024.37.01a.04*

Graphical Abstract

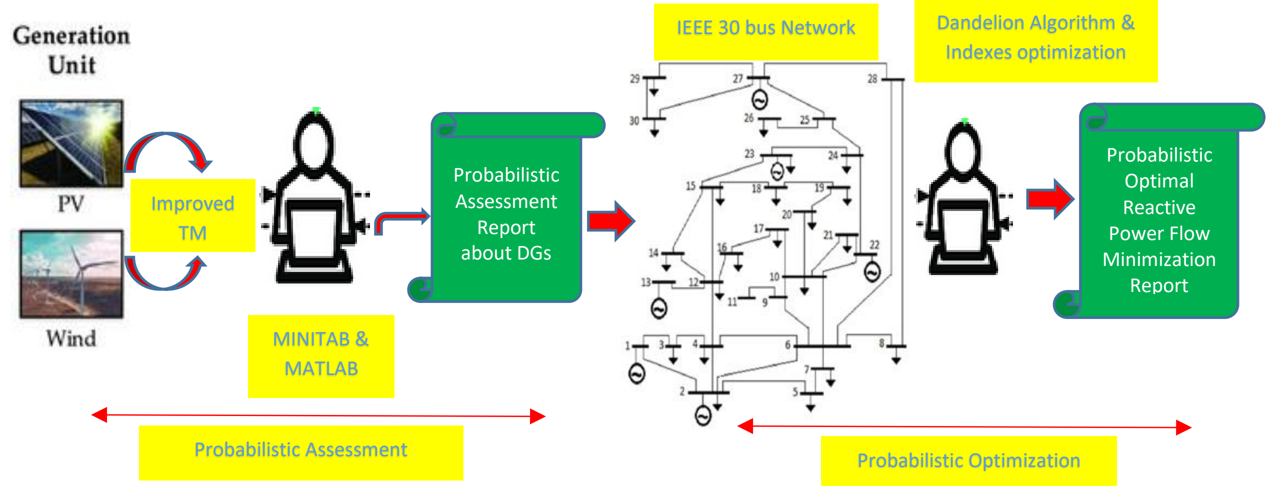

*Corresponding Author Email: b.tousi@urmia.ac.ir (B. Tousi)

Please cite this article as: Najjarpour M, Tous B. Probabilistic Reactive Power Flow Optimization of Distribution System in Presence of Distributed Units Uncertainty Using Combination of Improved Taguchi Method and Dandelion Algorithm. International Journal of Engineering, Transactions A: Basics, 2024;37(01):37-47.

NOMECLATURE

V_i^{min} , V_i^{max}	The minimum and maximum voltage in the bus i, respectively.	N_{exp}, n_g, N_C, N_T, N, N_B, N_L	Number of experiments, generator, compensators, transformers,modules, buses, and lines, respectively.
P_i^{min} , P_i^{max}	The minimum and maximum active power in the bus i, respectively.	GA, nb-1	Genetic algorithm, All basses except Slack bus, respectively.
Q_i^{min} , Q_i^{max}	The minimum and maximum reactive power in the bus i, respectively.	OA, FF, WT, PV	Orthogonal Arrays, Full factor, Wind turbine, and Photovoltaics, respectively.
s_{ij}^{max}	Maximum apparent transmission power.	${V_{out}}^{cut}$, ${V_{in}}^{cut}$, V_{rated}	The minimum, maximum, and nominal speed of the turbine.
${T_i}^{max}$, ${T_i}^{min}$	The maximum, and minimum taps number of transformers, respectively.	Voc, I_{SC}	Module open circuit/ short circuit voltage/ current , respectively.
$f_{j\psi}$, f^*_{ψ}	The power and the nominal power passing through the ψ transmission line and experiment j and , respectively.	T_C ,T_a, N_{OT}	Photovoltaics, Ambiance, and Nominal operating temperatures, respectively.
σ , μ, Y_j	Standard deviation, Mean, and Test performance index, respectively.	Kv ,K_I	Voltage and current temperature coefficient $(\frac{A}{°C})$ $(\frac{V}{°C})$, respectively.
$\overline{A}_j$, P_d	Average effects levels factor, Active demand power, respectively.	V_{MPP} , I_{MPP}	Maximum power point voltage and current flow, respectively.
Level	The value of a random variable is based on an orthogonal array.	$V_{i,j}$	The voltage of bus i, and j respectively.
Delta	The main effect of random variables on performance indicators.	$G_{i,j}$, B_{ij}	Line i – j conductance, and suspension respectively.
Rank, TM	Random variable class, and Taguchi method, respectively.	$Q_{ci,min}$, $Q_{ci,max}$	The minimum and maximum allowable reactive power generation, respectively.

1. INTRODUCTION

Optimal reactive power dispatch (ORPD) is a major condition for the secure and economic operation of power systems, which will be reachable by suitable coordination of the system equipment used to manage the reactive power flow in order to reduce the active power losses.

The active power losses have been set as an objective in the ORPD problem. In order to achieve the desired objective, the generator bus voltages, and settings of passive devices such as transformers and shunt VAR compensators are adjusted to reduce the active power losses (1). The issue of reactive power control is vital in the distribution networks because if the consumption of reactive power in the distribution part has increased the power plants will not be able to produce more reactive power due to their technical limitations, so the losses will increase and thus the stability of distribution networks will change (2). Due to the reactive power consumption by the loads, the power factor of the distribution network will change, which will affect the network losses; according to technical concepts, the power factor must be near to one; of course, the unit power factor is an ideal state that will not be reachable (3). In distribution networks, capacitors have been used in order to loss reduction and also power factor correction, when the power factor has been decreased the reactive power will be injected into the network (4, 5). According to the above-mentioned statements explains, due to many consumed loads and transformers and generators, and other equipment, it is required to apply the optimal power flow (OPF) to control the reactive power because (6). Similar to OPF, the OPRD includes some continuous and discrete variables every one of them at least has one limitation, to solve the nonlinear problem, and optimization of reactive power, using classic mathematics methods such as Gradient (7), Newton-Raphson (8), the interior point (9), linear programming (LP) (10), non-linear programming (11), and Quadratic programming (QP) (12). Enormous mathematical calculations and operations, getting stuck in local answers, are disadvantages of the mentioned classical methods (13). Using the metaheuristic method in order to solve the ORPD problem is strongly recommended because the mentioned disadvantages of the classical method will be eliminated. These algorithms are such as Whale Optimization Algorithm (WOA) (14), Particle Swarm Optimization (PSO) (15), Ant Lion Optimizer (ALO) (16), Improved Social Spider Optimization Algorithm (ISSO) (17), Improved Antlion Optimization Algorithm (IALO) (18), Genetic Algorithm (GA) (19), Ant Colony Optimizer (ACO) (20), Opposition-Based Gravitational Search Algorithm (OGSA) (21), Wind Driven Optimization Algorithm (WDO) (22), modified differential evolution algorithm (MDEA) (23), Specialized Genetic Algorithm (SGA) (24), evolutionary programming (19), comprehensive learning particle swarm optimization (25), fuzzy adaptive PSO (FAPSO) (26), seeker optimization algorithm (SOA) (27), cuckoo search algorithm (CA) (28), Hybrid Evolutionary Programming (HEP) (29), harmony search algorithm (30), Teaching Learning-Based Optimization (31), biogeography-based optimization (32), modified sine cosine algorithm (1), water cycle algorithm (33), hybrid Fuzzy- Jaya optimizer (34). With population and global warming increasing, the sources of fossil fuels are being decreased, so traditional power plants will have a problem in order to produce electrical power. These traditional power plants pollute the air and cause other environmental problems and have low efficiency (35). In recent years the use of DGs has increased. The produced electrical power of DGs depends on the intensity of sunlight, the angle of sunlight, wind speed, and the altitude of the turbine tower respectively in photovoltaic cells and wind turbines (36). These DG units, due to their random and probabilistic natures thus in OPF or OPRD should be used in probabilistic modeling methods. These DGs do not have the traditional power plants problems, even having high efficiency (37-39). According to the random nature of DG units, in order to convert uncertainties of their inputs the probabilistic modeling methods such as the Latin hypercube [26], point estimate method [27], scenario-based method [28] , and Monte Carlo method, the Monte Carlo method is the basic method for any probabilistic assessment method [29] , must be used. An optimization algorithm which is named improved social spider optimization algorithm (ISSO) has been used for optimizing the active and active power distribution, which is compared to the standard SSO, passes each process with two equations, using only one modified equation of the first and the second generations, creates the solution and has good and fast performance, less computation, less simulation time, and higher quality results in the ORPD problem than the standard SSO [31]. In order to solve the problem of ORPD, the water wave optimization algorithm (WWO) was used by Bhattacharya and Chattopadhyay [32]. The improved antlion optimization algorithm (IALO) has been used to solve OPRD and OPF for different constrained IEEE distribution networks, the good and accurate results in networks with bus voltage limitations and limitations of all capacitor banks prove that this algorithm is a powerful and accurate algorithm [33]. A new adaptive multi-objective optimization artificial safety algorithm has been used for OPRD, which is based on the Pareto coefficient, a method that is provided by Gafar et al. [34] for the classification of antibodies. Using the integration of three algorithms, particle swarm optimization (PSO), genetic algorithm (GA), and search for symbiotic organisms (SOS) (HGPSOS) to OPRD, which (SOS) has been based on the interactions between two various organisms which in the ecosystem - mutualism, hybridism, and parasitism are used. The HGPSOS algorithm has high computational speed and accuracy due to the presence of three precise and powerful algorithms, and it also has a high convergence rate, because it is combined with the GA, it shows that it is a stable and accurate algorithm [30]. Combining the heat transfer optimization algorithm (HTO) and the simulated coronary circulation system optimization algorithm (SCCS) was used by Zhang et al. [36] to reduce the losses and OPRD, each factor in the HTO algorithm is considered such as a cooling entity that is surrounded by other factors, like heat transfer, the thermodynamic law is used in the HTO algorithm. A candidate solution algorithm, which has been built and has been designed from the mechanisms of the human body and capillaries, and is being used to optimize the OPRD and loss reduction, in this algorithm, the Coronary Development Factor (CDF) is responsible for the evaluation, and the initial population space has been selected freely, then in the whole population, the best solution is considered as the stem and the minimum value of the coronary will be expansion coefficient, then the crown production of the stem has been called the divergence phase, and the growth of other capillaries has been called the clip phase. According to the coronary artery growth factor (CDF), there will be superior capillary growth (BCL), With and without the L index (voltage stability). The (ORPD) problem, as a sub-problem of OPF, has significant effects on providing reliability and economical performance [37]. A new optimization algorithm which has been named Turbulent Flow Water Based Optimization Algorithm (CTFWO) is used to solve the OPRD which is a complex mixed integer nonlinear optimization problem that includes discrete and continuous control variables (40). The Benchmark table was utilized by Kumar et al. (41), which could be an enormous table with awfully expansive numbers that need much time and calculations to run for OPRD while the improved TM, employs OAs that have lower numbers and need lower time and calculations to run for the ORPD problem. The TM is a statistical and quality-control-based strategy (42) that is utilized to show the vulnerabilities of DGs, and OPF calculations using the relationship and correlation concepts of RVs while the improved TM is being utilized in the MINITAB and MATLAB computer software that the relationship and correlation concepts of RVs run automatically in the computer programs. The improved TM is accurate and has lower computational levels than TM, the time, and speed of converge are quick. to assess the capability of the Dandelion calculations and improved TM to solve the ORPD, the simulation results of the Dandelion algorithm calculation are compared with varied algorithms, including PSO, GA, HGPSOS, HTO, PDO, ISSO, WWO, and IALO. The calculations and the results of PSO, PDO, DO, and GA are compared and discussed in thr presentation of results. Furthermore, the results of the improved TM are compared with the results of the assessed execution of different POPF methods in Tables 3 and 4. The results show that the Dandelion algorithm calculation has the finest response, and is excellent in comparison to other algorithms in terms of arrangement precision, joining rate, and solidness. The improved TM is accurate in comparison to the TM and employs data amid the optimization process in other words, utilizing the POPF results amid optimization and the correlation of RVs, the discharge variable is required for more examination and optimization with more precision afterward in arrange to assess the productivity of the displayed strategy.

The notable contributions of this study can be categorized as follows:
1) Solving ORPD problem considering uncertainties of DG units and Time-varying load.
2) Applying the Improved Taguchi method for modeling load, solar irradiance, and wind speed uncertainties.
3) Using a new optimizing algorithm for solving the ORPD problem with and without DGs presence.
4) Comparing the performance of the Dandelion algorithm with the GA, PSO, and PDO for solving the ORPD problem.

2. FORMULATION OF THE PROBLEM

In this section, the objective function of the OPRD problem is equal to loss minimization of the distribution network using reactive power optimization which has been expressed as Equation (1).

$$P_{Loss} = \sum_{l=1}^{nl} G_{ij}(V_i{}^2 + V_j{}^2 - 2V_iV_j \cos\delta_{ij}) \quad (1)$$

The minimization of the objective function is being limited by various constraints, such as Equations 2 and 3 which show equal limits in the network,indexes G, and D have been applied to represent generation, and demand respectively. Equations 4 and 5 express unequal constraints which include the voltage constraints of generators, tap transformers, and the reactive power of compensating equipment. The taps of the transformers are also limited in their minimum and maximum range according to Equtaion 6. The constraints of parallel compensators are also according to Equtaion 7. In addition to these restrictions, according to Equtaion 8. The three main parameters in this function are: V_{rated}, V_{in}, and V_{out}. When the wind speed reaches V_{in}, the WTs start generating power; when the wind speed reaches V_{rated}, the output power reaches the nominal P_{rated}. If the wind speed exceeds V_{out}, power generation will be stopped [25]. From a probabilistic aspect, the outputs can no longer be called definitive. In other words, all the outputs of the problem will be presented as mathematical expected values. This means that in this case, the outputs of losses and voltages are the mathematical expected values of voltages and losses.

$$PG_i - PD_i = V_i \sum_{j=1}^{nb} V_j \left(G_{ij}\cos\delta_{ij} + B_{ij}\sin\delta_{ij}\right) \quad (2)$$

$$QG_i - QD_i = -V_i \sum_{j=1}^{nb} V_j \left(G_{ij}\sin\delta_{ij} - B_{ij}\cos\delta_{ij}\right) \quad (3)$$

$$QG_i{}^{min} \leq QG_i \leq QG_i{}^{max} \quad (4)$$

$$VG_i{}^{min} \leq VG_i \leq VG_i{}^{max} \quad (5)$$

$$T_i{}^{min} \leq T_i \leq T_i{}^{max} \quad (6)$$

$$QC_i{}^{min} \leq QC_i \leq QC_i{}^{max} \quad (7)$$

$$V_i{}^{min} \leq V_i \leq V_i{}^{max} \quad (8)$$

2. 1. Uncertainties Modelling In probabilistic planning, it is important to state an appropriate statistical model for RnVr s, and it is being used in some models of uncertainty sources such as PV, WT, and electrical vehicle (EV) which the EV can charge at parking in smart distribution networks and can control the network indexes such as losses, voltage drop (43, 44).

2. 2. Load Modelling Using normal distribution, the density function of the corresponding probability distribution has been expressed in Equtaion 9:

$$f(P_d) = \frac{1}{\sqrt{2\pi\sigma}} \exp\left(-\frac{(P_d-\mu)^2}{2\sigma^2}\right) \quad (9)$$

2. 3. Wind Turbine Modeling The modeling of wind has consisted includes two steps, as follows:
I) **Wind speed modeling:** Due to the wind speed having random behavior, the wind speed must be modelled using a proper statistical distribution, and usually, to do so the continuous Weibull probability distribution is utilized according to Equtaion 10.

$$f(v) = \frac{h}{c}\left(\frac{v}{c}\right)^{h-1} \exp\left(-\left(\frac{v}{c}\right)^h\right) \quad (10)$$

in the above-mentioned equation, v, c, and h represent the wind speed, the shape factor, and the scale factor respectively.
II) **Turbine output power modeling:** depends on the wind speed and other parameters of the wind turbine, which has been explained in Equtaion 11.

$$p = \begin{cases} 0 & V_{out}{}^{cut} \leq V \text{ or } V \leq V_{in}{}^{cut} \\ K_1V + K_2 & 0 \leq V \leq V_{in}{}^{cut} \\ P_{rated} & V_{rated} \leq V \leq V_{out}{}^{cut} \end{cases} \quad (11)$$

$K_1 = \frac{P_{rated}}{V_{rated} - V_{in}{}^{cut}}$, $K_2 = -K_1V_{in}{}^{cut}$, V is the wind speed.

The details of power generation using wind turbines are shown in Figure 1.

2. 4. Photovoltaics Modelling Due to the sunlight radiation having random behavior, the radiation should be modeled using an appropriate statistical distribution, and usually, to do so the continuous Beta probability distribution is used according to Equtaion 12-a, using Equtaions 12-16 the active power can be calculated.

$$F(G) = \frac{1}{G\sigma\sqrt{2\pi}} exp\left[-\frac{\ln(G-\mu)^2}{2\sigma^2}\right] \quad (12\text{-a})$$

$$P_{pv}(s) = N * FF * V(s) * I(s) \quad (12)$$

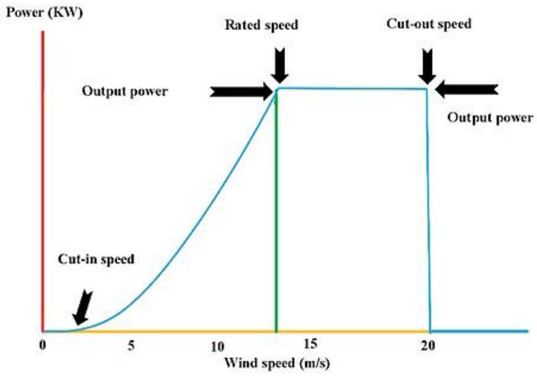

Figure 1. Wind turbine production capacity

$$V(s) = V_{oc} - K_V * T_C \quad (13)$$

$$I(s) = s * (I_{SC} + K_I * (T_C - 25)) \quad (14)$$

$$T_C = T_a + s * (\frac{N_{OT} - 20}{0.8}) \quad (15)$$

$$FF = \frac{V_{MPP} * I_{MPP}}{V_{OC} * I_{OC}} \quad (16)$$

TABLE 1. Orthogonal array $OA_{N_{exp}}\ (N_L)^N$

Experiment number	Levels			
	RnVr1	RnVr 2	…	RnVr N
1	L_{11}	L_{12}	…	L_{1N}
2	L_{21}	L_{22}	…	L_{2N}
….	….	….	…	….
N_{exp}	LN_{exp1}	LN_{exp2}	…	LN_{expN}

TABLE 2. Orthogonal array $OA_8 2^7$

Experiment	Level of each variable						
1	1	1	1	1	1	1	1
2	1	1	1	2	2	2	2
3	1	2	2	1	1	2	2
4	1	2	2	2	2	1	1
5	2	1	2	1	2	2	2
6	2	1	2	2	1	1	1
7	2	2	1	1	2	2	1
8	2	2	1	2	1	1	2

3. ORTHOGONAL ARRAYS

An OA is a fractional factorial matrix whose rows represent factor levels in each run and its columns represent a specific factor whose levels change in each experiment. All traditional factorial designs and fraction arrays are orthogonal. In the past, OA was known as magic squares. Perhaps the effect of OA in experiments has led to such naming. Because a fraction of the experiments is chosen in it, each combination is repeated in equal numbers, the reason they are named orthogonal is that all the columns are examined independently. The OAs are denoted by the letter L, which comes from the Latin word because the use of OA in experimental designs is related to Latin square designs. An OA is basically a table whose rows are used for experiments and whose columns are used for an RnVr (Table 1). Each of the numbers in the table describes the modes of a RnVr. OAs are sorted with the symbol $OA_{N_{exp}}\ (N_L)^{N}$.

For example, Table 2 is used for a problem with seven random variables and eight experiments; each random variable has two levels. Generally, must be done 128 processes, but by using the OA just eight experiments are needed. So, the calculation steps will be decreased to 6.25% of the total steps; this shows the ability and Advantage of OA (45, 46).

4. IMPROVED TAGUCHI METHOD

The improved Taguchi method is to increase the accuracy of the Taguchi method and the flowchart of this method is discussed as illustrated in this section. In this method, steps 1 to 5 of the Taguchi method, and the Improved Taguchi method are exactly repeated, but in the following, other steps are also performed. By comparing sets 1 and 2, probably some of the same variables will have the same levels. These variables are called certain variables and other variables are called uncertain variables. The reason for this naming is that are being obtained the same levels for these variables from two different paths, one of the experiments and the other of averaging the values obtained from the experiments. Certain variables are excluded from the optimization process. In the next section, the sixth step, the placement process is explained.

4. 1. Placement of Uncertain Variables in the Experiment with the Best Value

The experiment that has the best result among the experiments performed is one of the possible experiments to examine all combinations of different variables. Therefore, there may be another combination of variables that has a better outcome compared to the current best available test. One of these more suitable combinations may be the combination corresponding to the best experiment, while its uncertain variables are placed according to set 2. Because the averaging of the obtained results was the basis for choosing set 2, the statistical nature of this process increases the probability of choosing the optimal values for the variables. The certain variables determined by the task are removed from the process and only the uncertain variables are re-examined. In order to prevent the interaction of variables, the process of placing uncertain variables from the second set in the best experiment is done individually. If the inserted variable causes a better result than the previous variable, we call this variable definite and fix it in the best test. Other uncertain variables will be placed in the same way.

4. 2. Choosing the Orthogonal Array for the Remaining Uncertain Variables In this stage, uncertain variables are optimized by using another Taguchi table that is selected for them. If the number of remaining variables is small, we test all possible combinations. The optimization process continues until the optimization completion condition is met.

4. 3. The Differences between the TM and the Improved TM In the TM, finally, the levels of the RVs in sets 1 and 2 are placed in the best experiment, and each of the two sets that bring a better result is considered as the set containing the optimal values. In the improved TM, the RVs are divided into two groups of certain and uncertain variables. Certain variables are determined and removed from the optimization process. While the uncertain variables are checked more carefully, this is the difference between the improved TM and the TM. Since the presented method uses the TM, there is no need to prove the convergence towards the optimal point. To prevent the interaction of variables, the improved TM suggests the placement of individual variables. In this paper, the aim is to show the effect of the high precision of the simulation results of the Improved TM utilizing the Dandelion algorithm.

5.DANDELION ALGORITHM

A new swarm intelligence bioinspired optimization algorithm that has low computational time and high convergence speed has been called the Dandelion algorithm (DA) which has been introduced recently (47). Dandelion algorithm flowchart is shown in Figure 2. It includes three stages,

1. Growth stage: In this stage, the seeds spiral down from a high height due to eddies, or they are driven locally due to different climatic conditions.
2. Descending stage: In this stage, the flying seeds decrease their height by continuously adjusting their direction.
3. Landing or sitting stage: In this stage, the seeds descend to grow and grow in places they have chosen randomly. Using Brownian motions and Levy's random walk, the movement path of grains is determined in the stages of decline and settlement, respectively.

6.OPRD USING IMPROVED TM

In Improved TM every uncertainty is named as a random variable (RnVr). In general, the relationship between

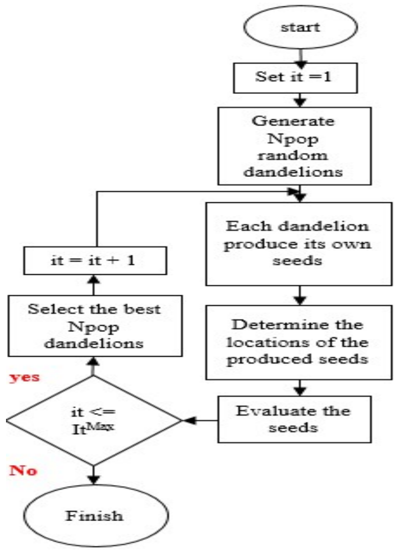

Figure 2. Dandelion algorithm flowchart

input and output RnVr s in a distribution network is expressed according to Equation 18:

$$Y_{in} = f\ (X_{out}) \tag{18}$$

The f is a nonlinear relation that establishes the relationship between Xout and Yin. In OPRD, the factors are the same as RnVr s. In OPRD, the number of factors is expressed in m and the number of levels in n, and then the next mn test must be performed. In this paper, an OPRD of a distribution system that includes PV and WT DGs is investigated and analyzed using Improved TM based on OA.

In order to solve the OPRD problem:

(i) The structure and information of the power system equipment are important and practical.

(ii) The input RnVrs are shown by the vector Y_{in} according to Equation 18.

(iii) "Level" means the value below the curve is a function of the probability density of incoming RnVr s.

(iv) Every experiment refers to a load flow, if there are several RnVr s, thus the number of load flows will be increased, thus the final answer will be obtained after a long computational time and several mathematics operations. As the above- mentioned advantage of OA, thus should be used. The first step in deploying Improved TM is to determine the levels of each RnVr. Selecting two levels and three levels for each factor requires the least and most time and calculations, respectively. In Improved TM, levels 1 and 2 are being selected, respectively μ - σ and $\mu + \sigma$. In the TM, the final optimal answer is being reached using an optimal experiment based on the optimal levels of RnVr s instead of all experiments based on OAs. To use this optimal experiment, one must first express an index according to Equation 19.

$$Y_j = \sum_{\psi}^{NL} \left| f_{j\psi} - f^*{}_{\psi} \right| \quad j = 1،2،3، \dots \tag{19}$$

The second step is to determine the average effect of the factors based on Equations 19 to 25.

The third step is to define the main effect of each factor on Y_j. These main effects of the factors are being calculated according to Equations 26 to 29:

$$\bar{A}_1 = (Y_1 - Y_2)/2 \tag{20}$$

$$\bar{A}_2 = (Y_3 - Y_4)/2 \tag{21}$$

$$\bar{B}_1 = (Y_1 - Y_3)/2 \tag{22}$$

$$\bar{B}_2 = (Y_2 - Y_4)/2 \tag{23}$$

$$\bar{C}_1 = (Y_1 - Y_4)/2 \tag{24}$$

$$\bar{C}_2 = (Y_2 - Y_3)/2 \tag{25}$$

$$\Delta A = (\bar{A}_2 - \bar{A}_1) \tag{26}$$

$$\Delta B = (\bar{B}_2 - \bar{B}_1) \tag{27}$$

$$\Delta C = (\bar{C}_2 - \bar{C}_1) \tag{28}$$

If the major effect is positive in RnVr or the same factor, the second level is considered otherwise.

It is now shown how to apply the OAs to the OPRD by performing the following main steps:

a) Determining the input RnVr s.
b) Determine the number and values of the levels of variables.
c) Determine the OA.
d) Execute OPRD.
e) Analysis of results.

$$\mu_j = \frac{1}{Nexp} \sum_{i=1}^{Nexp} x_{ji} \quad , \sigma_j = \left[\frac{(\sum_{i=1}^{Nexp} x_{ji} - \mu_i)^2}{Nexp} \right] \tag{29}$$

x_{ji} is the value of the jth output RV for the ith experiment.

7. SIMULATION RESULTS

In this study, the 30-bus IEEE standard system has been used in order to solve ORPD. This system includes 6 generators and 80 transmission lines, of which 17 lines have a tap changer. Also, three reactive power compensating equipment, which are installed in buses 15, 25, and 53, have been used for compensating. The initial active, and reactive power loss of the network without the presence of DGs are 22.244 Mvar and 17.59 MW respectively. The performance range of the variables is given in Table 3 and other network information has been obtained from (48). The Improved TM is tested in MATLAB and MINITAB software. In this study, there are two wind farms in bus 38, 39 and a PV cell in bus 16, which has a nominal capacity of 100 MW. To simulate this wind farm and PV cell, data has been received from the North Dekta site and the Watford area (49). Figure 3 shows IEEE 30-bus test system. The results are illustrated in Figures 4 and 5 show the converged plot of GA, PDO, DO, and PSO algorithms. Any of the optimizations have been run in 100 Iteration and more information about any optimization algorithms is explained below:

TABLE 3. Values of μ and σ using other methods

Entire losses	TM	Scenario	LHS	2PEM
μ [MW]	30.5	40.8	52.42	36.3
σ	11.15	26.1	36.22	12.2

7. 1. Genetic Algorithm

This optimization has been run in 26 populations and 100 iterations and in 44.076 (s). The number of the control variables is 13 and the percent of crossover is 0.1 and the best value for OPRD with GA is 3.891 MVar.

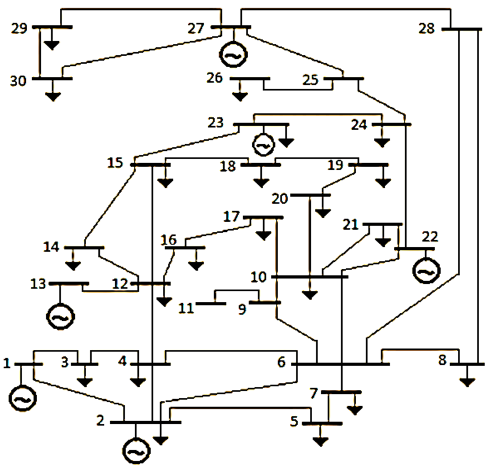

Figure 3. IEEE 30-bus Test system

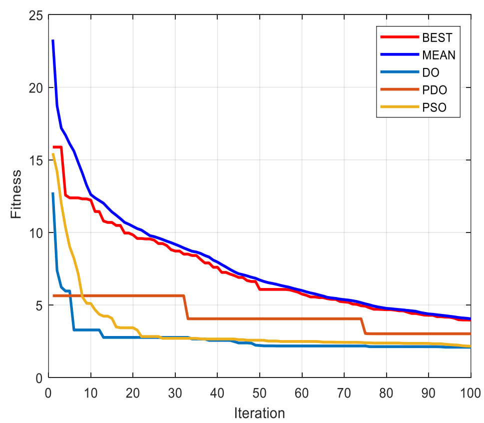

Figure 4. Reactive power optimization with algorithms

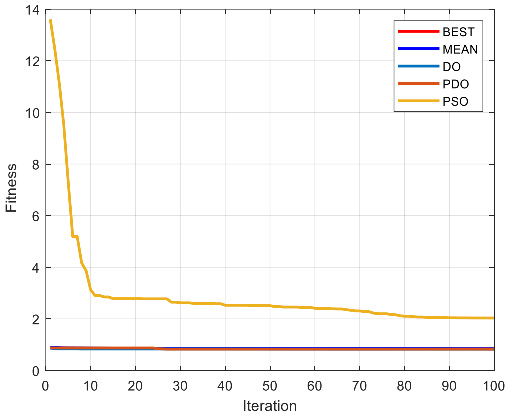

Figure 5. GA, DO, PDO, PSO Buses Voltage

7. 2. Particle Swarm Optimization Algorithm This optimization has been run in 26 populations and 100 iterations and in 21.940 (s). The number of the control variable is 13 and the inertia weight is 1 and inertia weight damping ratio is 0.99 and personal learning coefficient is 1.5 and global learning coefficient is 2 and the best value for OPRD with PSO is 2.038 Mvar.

7. 3. Prairie Dog Optimization Algorithm This optimization has been run in 26 populations and 100 iterations and in 82.830 (s). The number of the control variables is 13 and the best value for OPRD with PDO is 3.584 MVar.

7. 4. Dandelion Algorithm This optimization has been run in 26 populations and 100 iterations and in 19.996 (s), and the number of the control variables is 13 and the best value for OPRD with DA is 2.366 MVar according to Figure 6. Table 4 shows in terms of optimal value the PSO has a minimum value for OPRD and in terms of time the DA has a minimum value for OPRD so an algorithm that gives the best value in terms of time and optimal value for OPRD must be used and must be selected, according to Table 4 the PSO has a minimum value and maximum time even that time is equal to quadruple of DA time, but with pay attention to Table 4, the DA has closet value to PSO just with 0.3 MVar difference also has minimum time for solving of OPRD so the DA should be in OPRD problems. Before the use of the algorithms, the reactive power of 30 bus IEEE standard network was solved in 0.083(s) was equal to 22.244, and with paying attention to Table 4, it is concluded that the DA has closet time and much difference with the reactive power before using the optimization algorithms. using DA 20.2 MVar reductions will be had in reactive power which will be effective in terms of power losses and power transfer for power systems. Table 3 shows other probabilistic assessment methods such as point estimation, Taguchi, Scenario-based, and Latin hypercube sampling and their results.

Flowchart of improved Taguchi method is illustraed in Figure 6.

TABLE 4. Results of OPRD before and after using the algorithms

Algorithms	GA	PDO	DO	PSO	OPF
Time (s)	28.7	99.002	22.119	19.493	0.083
Reactive (MVar)	**3.9611**	**3.0206**	**2.0917**	**2.2106**	**22.244**
Buses Voltages (v)	**0.8429**	**0.8298**	**0.8301**	**2.0410**	
Time(sec)	**19.207**	**82.022**	**18.827**	**21.940**	

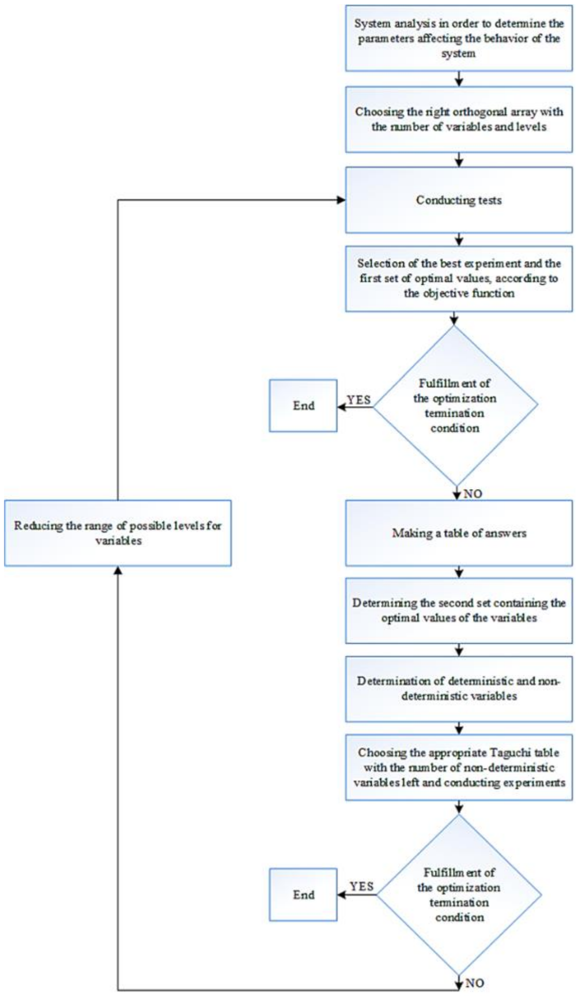

Figure 6. Flowchart of improved Taguchi method

8. CONCLUSIONS

The loss is an important index for power systems that can be controlled by reactive power, thus it is necessary to optimize the reactive power by increasing the DGs in power systems. In this paper, the dandelion optimization algorithm, and the improved Taguchi method which is based on orthogonal arrays have been utilized to solve complicated optimal reactive power dispatch problems and the modulation uncertainties of DG units, respectively. The use of portable systems such as wind turbines and photovoltaics as the most used technologies has been considered. Moreover, the load and uncertainties of wind turbines and photovoltaics have been investigated. The results show that the Dandelion algorithm has solved the OPRD in minimum time and has decreased the reactive power by about 20.2 Mvar which will be very good for the power system in terms of power losses and other aspects. Thus it is concluded that the Dandelion optimization algorithm and the Improved Taguchi method are effective, and accurate in solving the probabilistic ORPD problem compared with algorithms (GA, PDO, and PSO) applied for the ORPD problem.

9. REFERENCES

1. Abdel-Fatah S, Ebeed M, Kamel S, Yu J, editors. Reactive power dispatch solution with optimal installation of renewable energy resources considering uncertainties. 2019 IEEE Conference on power electronics and renewable energy (CPERE); 2019: IEEE. 10.1109/CPERE45374.2019.8980056
2. Lee K, Han Y. Reactive-power-based robust MTPA control for v/f scalar-controlled induction motor drives. IEEE Transactions on Industrial Electronics. 2021;69(1):169-78. 10.1109/TIE.2021.3055183
3. Saodah S, Kastawan IMW, Yusuf E, Manunggal BP, Maryanti M, editors. Simulation of effects of using capacitor for reactive power (VAR) compensation on electrical power supply quality. 5th FIRST T1 T2 2021 International Conference (FIRST-T1-T2 2021); 2022: Atlantis Press. 10.2991/ahe.k.220205.029
4. Fernando M, Gamini D, Naveendra J. Reduction of Reactive Power Waste of Inductive Electrical Appliances using Power Factor Correction. Vidyodaya Journal of Science. 2021;24(01). 10.31357/vjs.v24i01.4960
5. Nazarpour D, Sattarpour T. Assessing the impact of size and site of dgs and sms in active distribution networks for energy losses cost. International Journal of Engineering, Transactions A: Basics. 2015;28(7):1002-10. 10.5829/idosi.ije.2015.28.07a.06
6. Verma R, Padhy NP. Optimal Power Flow Based DR in Active Distribution Network With Reactive Power Control. IEEE Systems Journal. 2021.
7. Polprasert J, Ongsakul W, Dieu VN. Optimal reactive power dispatch using improved pseudo-gradient search particle swarm optimization. Electric Power Components and Systems. 2016;44(5):518-32. 10.1080/15325008.2015.1112449
8. Jan R-M, Chen N. Application of the fast Newton-Raphson economic dispatch and reactive power/voltage dispatch by sensitivity factors to optimal power flow. IEEE transactions on energy conversion. 1995;10(2):293-301. 10.1109/60.391895
9. Granville S. Optimal reactive dispatch through interior point methods. IEEE Transactions on power systems. 1994;9(1):136-46. 10.1109/59.317548
10. Terra L, Short M. Security-constrained reactive power dispatch. IEEE transactions on power systems. 1991;6(1):109-17. 10.1109/59.131053
11. Lee K, Park Y, Ortiz J. A united approach to optimal real and reactive power dispatch. IEEE Transactions on power Apparatus and systems. 1985(5):1147-53. 10.1109/TPAS.1985.323466
12. Quintana V, Santos-Nieto M. Reactive-power dispatch by successive quadratic programming. IEEE transactions on energy conversion. 1989;4(3):425-35. 10.1109/60.43245
13. Ebeed M, Kamel S, Jurado F. Optimal power flow using recent optimization techniques. Classical and recent aspects of power system optimization: Elsevier; 2018. p. 157-83.
14. ben oualid Medani K, Sayah S, Bekrar A. Whale optimization algorithm based optimal reactive power dispatch: A case study of the Algerian power system. Electric Power Systems Research. 2018;163:696-705. 10.1016/j.epsr.2017.09.001
15. Zhao B, Guo C, Cao Y. A multiagent-based particle swarm optimization approach for optimal reactive power dispatch. IEEE transactions on power systems. 2005;20(2):1070-8. 10.1109/TPWRS.2005.846064
16. Mouassa S, Bouktir T, Salhi A. Ant lion optimizer for solving optimal reactive power dispatch problem in power systems. Engineering science and technology, an international journal. 2017;20(3):885-95. 10.1016/j.jestch.2017.03.006
17. Nguyen TT, Vo DN. Improved social spider optimization algorithm for optimal reactive power dispatch problem with different objectives. Neural Computing and Applications. 2020;32(10):5919-50. 10.1007/s00521-019-04073-4
18. Li Z, Cao Y, Dai LV, Yang X, Nguyen TT. Finding solutions for optimal reactive power dispatch problem by a novel improved antlion optimization algorithm. Energies. 2019;12(15):2968. 10.3390/en12152968
19. Wu QH, Ma J. Power system optimal reactive power dispatch using evolutionary programming. IEEE Transactions on power systems. 1995;10(3):1243-9. 10.1109/59.466531
20. Abou El-Ela A, Kinawy A, El-Sehiemy R, Mouwafi M. Optimal reactive power dispatch using ant colony optimization algorithm. Electrical Engineering. 2011;93:103-16. 10.1007/s00202-011-0196-4
21. Shaw B, Mukherjee V, Ghoshal S. Solution of reactive power dispatch of power systems by an opposition-based gravitational search algorithm. International Journal of Electrical Power & Energy Systems. 2014;55:29-40. 10.1016/j.ijepes.2013.08.010
22. Shaheen AM, El-Sehiemy RA, Farrag SM, editors. A novel framework for power loss minimization by modified wind driven optimization algorithm. 2018 International Conference on Innovative Trends in Computer Engineering (ITCE); 2018: IEEE. 10.1109/ITCE.2018.8316648
23. Sakr WS, El-Sehiemy RA, Azmy AM. Adaptive differential evolution algorithm for efficient reactive power management. Applied Soft Computing. 2017;53:336-51. 10.1016/j.asoc.2017.01.004
24. Villa-Acevedo WM, López-Lezama JM, Valencia-Velásquez JA. A novel constraint handling approach for the optimal reactive power dispatch problem. Energies. 2018;11(9):2352. 10.3390/en11092352
25. Mahadevan K, Kannan P. Comprehensive learning particle swarm optimization for reactive power dispatch. Applied soft computing. 2010;10(2):641-52. 10.1016/j.asoc.2009.08.038
26. Zhang W, Liu Y. Multi-objective reactive power and voltage control based on fuzzy optimization strategy and fuzzy adaptive particle swarm. International Journal of Electrical Power & Energy Systems. 2008;30(9):525-32. 10.1016/j.ijepes.2008.04.005
27. Dai C, Chen W, Zhu Y, Zhang X. Seeker optimization algorithm for optimal reactive power dispatch. IEEE Transactions on power systems. 2009;24(3):1218-31. 10.1109/TPWRS.2009.2021226

28. Sulaiman M, Rashid MM, Aliman O, Mohamed M, Ahmad A, Bakar M. Loss minimisation by optimal reactive power dispatch using cuckoo search algorithm. 2014. 10.1049/cp.2014.1479
29. Yan W, Lu S, Yu DC. A novel optimal reactive power dispatch method based on an improved hybrid evolutionary programming technique. IEEE transactions on Power systems. 2004;19(2):913-8. 10.1109/TPWRS.2004.826716
30. Khazali A, Kalantar M. Optimal reactive power dispatch based on harmony search algorithm. International Journal of Electrical Power & Energy Systems. 2011;33(3):684-92. 10.1016/j.ijepes.2010.11.018
31. Mandal B, Roy PK. Optimal reactive power dispatch using quasi-oppositional teaching learning based optimization. International Journal of Electrical Power & Energy Systems. 2013;53:123-34. 10.1016/j.ijepes.2013.04.011
32. Bhattacharya A, Chattopadhyay PK. Solution of optimal reactive power flow using biogeography-based optimization. International Journal of Electrical and Computer Engineering. 2010;4(3):621-9. 10.5281/zenodo.1057965
33. Heidari AA, Abbaspour RA, Jordehi AR. Gaussian bare-bones water cycle algorithm for optimal reactive power dispatch in electrical power systems. Applied soft computing. 2017;57:657-71. 10.1016/j.asoc.2017.04.048
34. Gafar MG, El-Sehiemy RA, Hasanien HM. A novel hybrid fuzzy-JAYA optimization algorithm for efficient ORPD solution. IEEE Access. 2019;7:182078-88. 10.1109/ACCESS.2019.2955683
35. Jahangir MH, Eslamnezhad S, Mousavi SA, Askari M. Multi-year sensitivity evaluation to supply prime and deferrable loads for hospital application using hybrid renewable energy systems. Journal of Building Engineering. 2021;40:102733. 10.1016/j.jobe.2021.102733
36. Zhang Y, Wang L, Ding H, Zhu Y, Hu Q, Lv Z, editors. An overview of virtual power plant prospects from the perspective of optimal scheduling, market bidding and transient analysis. 2021 IEEE Sustainable Power and Energy Conference (iSPEC); 2021: IEEE. 10.1109/iSPEC53008.2021.9735631
37. Shi Y, Tuan HD, Savkin AV, Lin C-T, Zhu JG, Poor HV. Distributed model predictive control for joint coordination of demand response and optimal power flow with renewables in smart grid. Applied Energy. 2021;290:116701. 10.1016/j.apenergy.2021.116701
38. Ranjbar A, Vig S, Sharma K. Performance Analysis of Grid Connected Distributed Generation Sources (DGS) Using ETAP. Cognitive Informatics and Soft Computing: Springer; 2022. p. 105-14.
39. Hosseini Mola J, Barforoshi T, Adabi Firouzjaee J. Distributed generation expansion planning considering load growth uncertainty: A novel multi-period stochastic model. International Journal of Engineering, Transactions C: Aspects. 2018;31(3):405-14. 10.5829/ije.2018.31.03c.02
40. Abd-El Wahab AM, Kamel S, Hassan MH, Mosaad MI, AbdulFattah TA. Optimal Reactive Power Dispatch Using a Chaotic Turbulent Flow of Water-Based Optimization Algorithm. Mathematics. 2022;10(3):346. 10.3390/math10030346
41. Kumar L, Kar MK, Kumar S. Statistical analysis based reactive power optimization using improved differential evolutionary algorithm. Expert Systems. 2023;40(1):e13091. 10.1111/exsy.13091
42. Ali MH, Soliman AMA, Adel AH. Optimization of Reactive Power Dispatch Considering DG Units Uncertainty By Dandelion Optimizer Algorithm. International Journal of Renewable Energy Research (IJRER). 2022;12(4):1805-18. 10.20508/ijrer.v12i4.13573.g8606
43. Gholami M, Sanjari MJ. Optimal Operation of Multi-Microgrid System Considering Uncertainty of Electric Vehicles. International Journal of Engineering, Transactions B: Applications. 2023;36(8). 10.5829/ije.2023.36.08b.01
44. Peiravi M, Domiri Ganji D. Generating electrical power using movement of various vehicles in new lighting base. International Journal of Engineering, Transactions B: Applications. 2022;35(2):387-96. 10.5829/ije.2022.35.02b.15
45. Najjarpour M, Tousi B, Jamali S. Loss Reduction in Distribution Networks With DG Units by Correlating Taguchi Method and Genetic Algorithm. Iranian Journal of Electrical and Electronic Engineering. 2022;18(4):1.
46. Najjarpour M, Tousi B, editors. Loss Reduction of Distribution Network by Optimal Reconfiguration and Capacitor Placement Using Cuckoo and Cultural Algorithms. 2023 8th International Conference on Technology and Energy Management (ICTEM); 2023: IEEE. 10.1109/ICTEM56862.2023.10083643
47. Zhao S, Zhang T, Ma S, Chen M. Dandelion Optimizer: A nature-inspired metaheuristic algorithm for engineering applications. Engineering Applications of Artificial Intelligence. 2022;114:105075. 10.1016/j.engappai.2022.105075
48. Eberhart R, Kennedy J, editors. A new optimizer using particle swarm theory. MHS'95 Proceedings of the sixth international symposium on micro machine and human science; 1995: Ieee. 10.1109/MHS.1995.494215
49. Solc J, Botnen BW. JV Task 99-Integrated Risk Analysis and Contaminant Reduction, Watford City, North Dakota. Univ. of North Dakota, Grand Forks, ND (United States); 2007.

Persian Abstract

چکیده

امروزه با توجه به رشد روزافزون جمعیت، افزایش گرمایش زمین، آلودگی محیط زیست و کاهش منابع سوخت فسیلی، استفاده از DG ها رشد کرده و به دلیل ماهیت تصادفی آن ها، عملکرد متعارف سیستم های قدرت در حال تغییر است. توان راکتیو نقش قابل توجّهی در شاخص های مدیریت و کنترل سیستم های قدرت مانند تلفات، پایداری، قابلیت اطمینان و امنیت دارد که در این میان معمولاً شاخص تلفات را می توان به راحتی به حداقل رساند و کنترل کرد. بنابراین مدل سازی و بهینه سازی توان راکتیو باید به طور دقیق و صحیح انجام شود. در این مقاله از یک الگوریتم فراابتکاری جدید به نام قاصدک برای حل مسئله توزیع توان راکتیو بهینه غیرخطی محدود شده استفاده می‌شود و همچنین از روش تاگوچی بهبود یافته مبتنی بر آرایه‌های متعامد برای مدل‌سازی عدم قطعیت واحدهای DG استفاده شده است. الگوریتم توزیع توان راکتیو بهینه اعمال شده با استفاده از سیستم های قدرت تست استاندارد 30 باسه IEEE آزمایش و تایید می شود. این نتایج نشان می دهد که زمان محاسباتی الگوریتم اعمال شده در مقایسه با سایر الگوریتم های مورد استفاده کمترین مقدار را دارد و توان راکتیو را از ۲۲.۲٤٤ به ۲.۳٦٦ Mvar کاهش می دهد. همچنین تلفات سیستم قدرت با الگوریتم تست شده و معرفی شده به میزان قابل توجهی کاهش می یابد. الگوریتم ژنتیک (GA) ، الگوریتم بهینه‌سازی ازدحام ذرات (PSO) و الگوریتم بهینه‌سازی سگ دشتی (PDO) برای حل این مشکل استفاده شده‌اند.

IJE TRANSACTIONS A: Basics Vol. 37 No. 01, (January 2024) 48-55

International Journal of Engineering

Journal Homepage: www.ije.ir

Effect of $Al_{59}Cu_{25.5}Fe_{12.5}B_3$ Quasi-crystals on Microstructure and Flexural Strength of Aluminum Matrix Composites Prepared by Spark Plasma Sintering Method

A. Faraji[a], V. Aghaali[b], M. Rahimipour*[a]

[a] *Ceramic Department, Materials and Energy Research center, Karaj, Iran*
[b] *School of Metallurgy and Materials Engineering, Iran University of Science and Technology (IUST), Tehran, Iran*

PAPER INFO

Paper history:
Received 05 January 2023
Received in revised form 25 September 2023
Accepted 26 September 2023

Keywords:
Quasi-crystals
Al Matrix
Spark Plasma Sintering
Mechanical Properties

ABSTRACT

In this study, Al-based composites reinforced with $Al_{59}Cu_{25.5}Fe_{12.5}B_3$ quasicrystal (QC) were prepared by spark plasma sintering (SPS) method. Microstructural and mechanical properties were examined. It is observed that with addition of quasi-crystalline reinforcement the intensity of the quasi-crystalline peak has increased. Also, it is observed that by performing spark plasma sintering, the quasi-crystalline particles maintain their stability. Due to low temperature of the process and the short time of spark plasma sintering, the occurrence of destructive phases within the quasi-crystal has been prevented. based on field emission scanning electron microscopy (FESEM) images, the distribution of quasi-crystalline particles at the sample level has increased. In addition, the mechanical properties are improved by increasing the quasi-crystalline particles. Therefore, the sample with 15 vol.% of quasi-crystal has better results than other samples in improving microstructural and mechanical properties and it can be considered as an optimal sample with suitable practical properties.

***doi**: 10.5829/ije.2024.37.01a.05*

Graphical Abstract

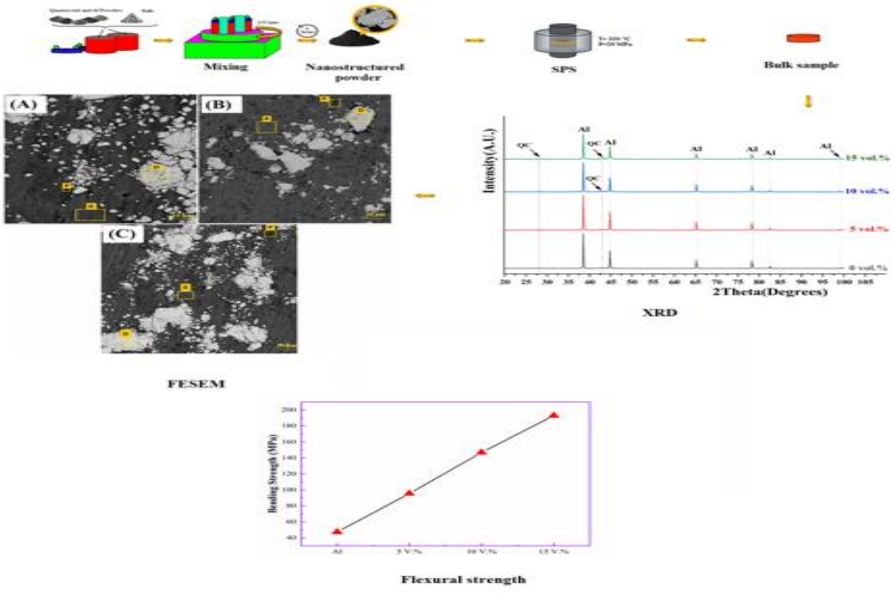

*Corresponding Author Email: m.rahimipour@merc.ac.ir (M. Rahimipour)

Please cite this article as: Faraji A, Aghaali V, Rahimipour M. Effect of $Al_{59}Cu_{25.5}Fe_{12.5}B_3$ Quasi-crystals on Microstructure and Flexural Strength of Aluminum Matrix Composites Prepared by Spark Plasma Sintering Method. International Journal of Engineering, Transactions A: Basics, 2024;37(01): 48-55.

1. INTRODUCTION

After classifying solids into two categories of crystalline materials and amorphous materials, quasi-crystals were introduced as the third type of solids by Avar et al. [1] and Shechtman et al.(1, 2). The quasi-crystals are among the new materials that have a non-periodic long-range order (3, 4). There is a repetitive periodicity in the arrangement of atoms with a forbidden rotational symmetry for the crystals in the quasi-crystalline material. Symmetries in quasi-crystals have been observed. Icosahedral, octagonal, decagonal and dodecagonal structural are among the most important quasi-crystals (2, 4, 5). There are several methods for the synthesis of the quasi-crystalline materials, these methods are: melt spinning, casting, mechanical alloying, gas atomization, physical vapour deposition (PVD), sol-gel, electrodeposition, gas evaporation, plasma spray and laser- or electron-beam superficial fusion and electron irradiation (4). One of the most widely used methods for the synthesis of quasi-crystals is mechanical alloying (MA) (3, 6). This method is a powder method that produces homogeneous materials from a mixture of pure powders. Mechanical alloying method has been used over the years as an acceptable fabrication method for the development of a variety of advanced materials such as nanomaterials, quasi-crystals, amorphous materials and nanocomposites (7, 8). The most important mechanisms of this method are repeated welding, fracturing, and re-welding of particles (9). Metal matrix composites (MMCs) consist of two main components including the matrix phase and reinforcement phase. The purpose of placing a high-performance secondary phase in these materials is to create a combination of aspects that would not be possible by the components alone. The reinforcement phase is continuous or discontinuous in the matrix. The reinforcement phases are continuous or discontinuous in the matrix, which may make up about 10 to 60 volume percentage of composite. The purpose of creating reinforcement phase in these materials is to achieve the desired properties that these properties will not be possible by the components alone (10). One of the most important and widely used metal matrix composites are aluminum matrix composites (AMCs) (10). Aluminum matrix composites are advanced engineering materials that have superior properties compared to conventional aluminum alloys (11). Due to high hardness, high thermal conductivity, low thermal expansion coefficient, wear resistance, impact resistance, corrosion resistance, low density, strength to weight ratio, relatively reasonable price and isotropic properties, these composites have many applications in various industries (11, 12). Reinforcements can be particles, layers, fibers or interpenetrating type. Also, according to the type of reinforcement, the composite can be classified into laminar composite, flake composite, fiber-reinforced composites, filled composite and particle-reinforced composite (10). Particle-reinforced composites are divided into two categories. In the first category, the heat treatment process leads to chemical reactions between the reinforcement phase and the matrix phase, which results in a homogeneous distribution of the stable reinforcement phase in the matrix. In the second category, reinforcement particles are embedded in a metal matrix, and the best way to make this type of composite is to use powder metallurgy (13, 14). Recently, the use of quasi-crystalline materials as reinforcement particles in aluminum-based composites has received much attention (15, 16), because quasi-crystalline alloys and composites containing quasi-crystalline phase improve some properties due to their complex atomic structure, unique mechanical and tribological properties, and special thermal behavior (17, 18) .These properties make them suitable for applications such as surface coatings, reinforcement particles in composites and catalytic applications (4, 19, 20). Conventional sintering methods such as hot press, high temperature extrusion, hot isostatic press lead to grain growth which affects the properties of the final product. Spark plasma sintering (SPS) method is one of the techniques using powder metallurgy (21, 22). Compared to conventional sintering techniques, the SPS method can be very effective due to its unique sintering mechanisms. In this method, pressure and pulsed current simultaneously are used to achieve high density components (21, 23, 24). In the SPS method, momentary melting and evaporation on the particle surfaces leads to the formation of necks between the particles (22). When particles are in contact with each other, a high-density electric current passes through these particles, causing a bond between the particles. Uniaxial pressure also causes plastic deformation, which ultimately increases the density (25). Using this method, high density samples can be obtained at very low temperatures and times (26). Excessive interfacial diffusion can be avoided by using this method because the quasi-crystals exist only in a small composite range (27). Amini et al. (3) synthesized $Al_{67}Cu_{20}Fe_{10}B_3$ quasi-crystalline alloys using mechanical alloying method. They studied the microstructural and structural evolutions of these materials at different times of the mechanical alloying process. Their results showed that the stable AlCuFeB single quasi-crystalline phase can be synthesized using high energy planetary ball milling in a short time from mechanical alloying process (around ~ 4 hours). Yong et al. (28) achieved the quasi-crystalline phase using the method of mechanical alloying and heat treatment. Asahi et al. (29) and Tsai et al. (30) also synthesized the quasi-crystalline phase by mechanical alloying method. According to the findings of other researchers, the compositional range from 10 to 14 atomic percent of iron and 20 to 28 atomic percent of copper is a very suitable range for the formation of icosahedral phase (4, 31, 32). In this compositional range, the peritectic reaction between λ2-Al3Fe and β-AlFe(Cu) phases with the remaining molten liquid is reported to be the main reason for the creation of this quasi-crystalline icosahedral phase (4). The quasi-crystalline icosahedral phase in aluminum-copper-iron system has high hardness and low fracture toughness (33, 34). It is also reported that adding boron to this alloy system can significantly change the brittleness, hardness and toughness of these alloys (35, 36). In addition to these properties, boron causes more stability of the quasi-crystalline icosahedral phase and reduces the coefficient of friction and electrical resistance compared to alloys without boron (35, 37). Due to the special crystal structure and special properties, quasi-crystals have a wide variety of applications. One of the most important potentials of quasi-crystals is as a catalyst for steam-reforming of methanol (4). Also, quasi-crystals can be used in thermometry and heat flow detection due to their temperature-dependent electrical conductivity (4, 38). Another application of quasi-crystals is light absorption. Thin layers of these materials are suitable as selective absorbers in solar thermal applications. These materials can also be used in glass and window applications, thermal insulation plates, and electrical insulation (4). In another research by Amini et al. [42] the effect of quasi-crystal on solar properties was investigated. In this research, they obtained a quick method for the synthesis of the quasi-crystalline phase, based on which there was no need for annealing operations and complex methods for the synthesis of the quasi-crystalline phase. Also, their results showed that the quasi-crystalline phase increased the amount of sunlight in solar. Addition of quasi-crystals to aluminum alloys leads to new properties in these materials. Lityńska-Dobrzyńska et al. (39) prepared aluminum matrix composites with $Al_{65}Cu_{20}Fe_{15}$ quasi-crystalline reinforcement phase with different percentages of the quasi-crystalline phase (20, 40 and 60 wt%). In order to prepare these composites, they used the hot vacuum pressing method. Their results showed that with increasing amount of quasi-crystalline phase, hardness and compressive strength of the composite increased (173 $HV_{0.5}$ and 370 MPa, respectively). They also reported that the friction coefficient of these composites depends on the composition (in the range 0.5-0.7). Sainfort and Dubost (40) used icosahedral Al-Li-Cu as reinforcement particles in the aluminium based MMCs. Tsai et al. (41) created composite material that contained quasi-crystals as reinforcement particles using powder metallurgy. It has also been shown that the hardness of this type of composite increased by increasing the quasi-crystalline reinforcement particles up to 5 times compared to pure aluminum. Therefore, the use of quasi-crystalline reinforcement particles in aluminum base composites has been proposed in order to overcome the low surface hardness of aluminum and increase the wear resistance of these materials (27). In this research, our goal was to synthesize Al59Cu25.5Fe12.5B3 quasi-crystalline compound using a new method without annealing and then to obtain Al/Al59Cu25.5Fe12.5B3 composite for the first time using SPS method. Also, according to the research of others, we realize that others use higher percentages of quasi-crystals as reinforcement, but considering that this project is a field for the industrial and practical use of quasi-crystals in the industry, from the volumetric percentages The bottom is used as reinforcement (5, 10, and 15) to investigate the effect on microstructure and mechanical properties.

2. MATERIALS AND METHOD

The raw materials of this research included Aluminum (purity percentage 99% < , particle size = 3 to 5 µm), Copper (purity percentage 99.8% < , particle size = 14 µm), Iron (purity percentage 99% < , particle size = 45 µm >) and Boron (purity percentage 99% < , particle size = 5 µm) powders supplied by Aldrich company. Also, the $Al_{59}Cu_{25.5}Fe_{12.5}B_3$ quasicrystal composition used in this study was prepared using the optimal research process by mechanical alloying method (42). Therefore, before the SPS process, first 4 samples were prepared according to the specifications of TABLE 1 and then the powders of quasicrystal and aluminum are mixed using ball-milling at 210 rpm for 4 hours. Composite samples of aluminum matrix were obtained by SPS method at a synthesis temperature of 320 °C and pressure of 20 MPa. Also, Figure shows a schematic of the process of sintering a bulk sample.

Phase analysis was carried out by a Philips MPD 1880 X-ray diffractometer (XRD) system with Cu-Kα radiation at 40 mA and 40 kV. The composition and microstructure of the sintered pellets were investigated by a JEOL JSM-5600LV field emission scanning electron microscope (FESEM), and Oxford energy dispersive spectroscopy (EDX) attachments with them. To evaluate the mechanical properties of the prepared samples, three-point flexural strength (Santam-STm 20) test was performed. It should be noted that three samples were used to reduce the measurement error for each test.

TABLE 1. Specifications of samples

Number	Combination
1	Al
2	Al + 5 vol. % $Al_{59}Cu_{25.5}Fe_{12.5}B_3$
3	Al + 10 vol. % $Al_{59}Cu_{25.5}Fe_{12.5}B_3$
4	Al + 15 vol. % $Al_{59}Cu_{25.5}Fe_{12.5}B_3$

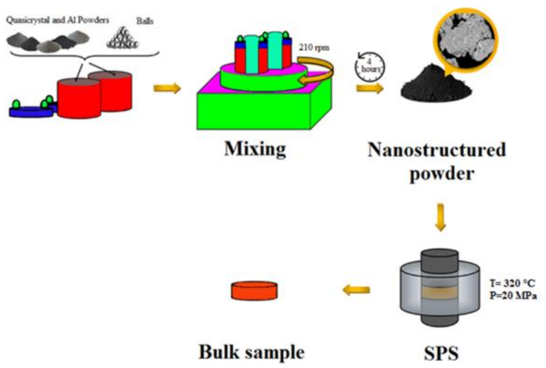

Figure 1. Schematic of the process of sintering a bulk sample

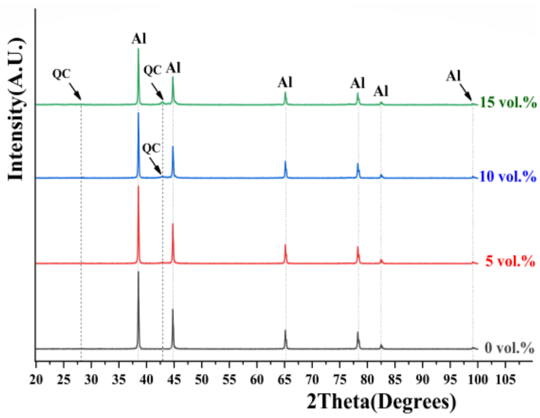

Figure 2. X-ray diffraction patterns for samples with different volume percentages of the quasi-crystalline phase in the aluminum matrix

3. RESULTS

Figure 2 shows for samples with different percentages of quasi-crystalline phase, there are only peaks related to the aluminum phase (cubic structure) as well as the quasi-crystalline phase. Therefore, by performing the sintering process by SPS method, the peaks related to the quasi-crystalline phase have not been eliminated and this phase has maintained its stability during the SPS process. In other words, in the SPS process, there is no interfacial reaction for this type of composite. It has been reported that in Al/Al-Cu-Fe composites, the ω-tetragonal phase is also formed due to the reaction between the quasi-crystalline particles and the aluminum phase (43). However, as can be seen, the sintering process using SPS method has prevented the formation of ω phase due to lower temperature and shorter sintering time. These results are consistent with the other researchers (27). Al/QC composites are stable in a large temperature regime and phase transformations occur at high sintering temperatures (43). With the occurrence of these phase transformations, the amount of quasi-crystalline phases also decreases. Kenzari et al. (44) concluded that the quasi-crystalline phase transformations to the ω phase occur at approximately 450℃. It has also been reported that the reaction between aluminum and the quasi-crystalline phase occurs at approximately 482 ℃ (43).

Figure 3 shows electron microscopy images for composites with different percentages of quasi-crystalline phase. Also, Table 2 summarized the results of EDX elemental analysis from different regions (as shown in Figure 3). As can be seen for the sample with 5 vol% of the quasi-crystalline phase (region D in Figure 3 A), the amount of aluminum is equal to 68.03 at%, and the amounts of copper and iron are equal to 18.55 and13.42 at%, respectively. Also, for samples with 10 and 15 vol% of quasi-crystalline phase, the amount of elements in regions D are very similar to samples with 5 vol% of quasi-crystalline phase. Therefore, the white areas (regions D in Figure 3) are related to quasi-crystalline reinforcement particles. In region E, for sample with 5 vol% of the quasi-crystalline phase (region E in Figure 3 A), the amounts of aluminum, copper and iron are 96.90, 1.98 and 1.12 at%, respectively. In regions E, the amount of the elements for samples with 10 and 15 at% of the quasi-crystalline phase are almost similar to samples with 5 vol% of the quasi-crystalline phase. Therefore, the dark gray areas (regions E in Figure 3) are related to the aluminum matrix phase. In region F, for the sample with 15 vol.% Of the quasi-crystalline phase (region F in Figure 3 C), the amounts of aluminum, copper and iron are 52.34, 0.33 and 0.31at%, respectively. As can be seen, reinforcement particles are scattered in the aluminum matrix. It can also be seen that the quasi-crystalline particles are agglomerated together. In addition to these elements, the elemental EDX analysis for this region also indicates the presence of the oxygen. For samples with 5, 10 and 15 vol% of the quasi-crystalline phase, the amount of oxygen in the F regions are 39.61, 37.77 and 46.97at%, respectively. As shown in Figure 3, the F regions are mostly formed at the interface between the quasi-crystalline phase and aluminum. It is reported that at the interface between the quasi-crystalline particles and aluminum, an amorphous oxide layer is formed in these composites, which acts as a strong bond between the quasi-crystalline particles and the aluminum matrix (27, 45). According to Figure 3, it is also observed that agglomerates of quasi-crystalline particles have formed in some areas. In addition, pores are observed in some areas, which can be due to the time of the mechanical alloying process and the temperature and sintering time.

The Flexural strength results of the pure Al sample and the samples with different percentages of the quasi-crystalline phase are shown in Figure 4. Due to the fact that aluminum is a soft and ductile material, during the bending test, brittle fracture does not occur in this sample.

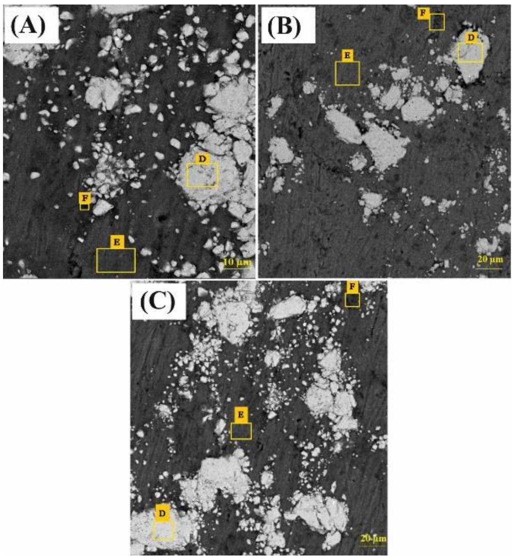

Figure 3. Scanning Electron microscopy images of composites with different percentages of quasi-crystalline phase A) 5vol.% of the quasi-crystalline phase B) 10vol.% of the quasi-crystalline phase and C) 15vol.% of the quasi-crystalline phase

TABLE 2. Results of EDX elemental analysis for samples with different percentages of quasi-crystalline phase

Samples	Phase areas	Al (at%)	Cu (at%)	Fe (at%)	O (at%)
	D	68.03	18.55	13.42	
5vol.%	E	96.90	1.98	1.12	
	F	59.42	0.53	0.44	39.61
	D	68.46	18.02	13.52	
10vol.%	E	97.59	1.39	1.02	
	F	49.57	0.54	0.39	37.77
	D	69.03	17.61	13.36	
15vol.%	E	98.69	0.73	0.58	
	F	52.34	0.33	0.31	46.97

However, in composite samples with different percentages of quasi-crystalline materials, it is observed that by performing the flexural strength test, the samples break brittle. And the fracture in these samples is of the brittle fracture type. Based on this, it is observed that composite samples do not have a plastic region, Accordingly, for the Al sample, the elastic region is examined and compared with other samples. It is observed that in the elastic region, the flexural strength for Al sample is about 47.30 MPa and for composite samples reinforced with 5, 10 and 15% of the quasi-crystalline phase are 95.51, 146.83 and 192.92 MPa, respectively. Therefore, with increasing amounts of reinforcing quasi-crystalline materials improve the mechanical properties (46). One of the factors affecting the final properties of composites is the interface between the reinforcing phase particles and the matrix phase. In such a way that a joint with strong adhesion leads to the distribution and transfer of force from the matrix to the reinforcing particles, which leads to an increase in modulus and strength. A suitable joint is created by the wetting of the particles by the liquid phase during the sintering process. Other factors affecting the final properties of the composite are the surface reaction at the interface of the reinforcing particles with the matrix phase. This reaction due to its products and factors such as the adhesion of reactive products to the matrix and reinforcing phase, thermal expansion coefficient and strength of reactive products, etc. can have a positive or negative effect on the mechanical properties of the composite (47). Also, the final mechanical properties of the composite are affected by the joint quality season of the reinforcing particles with the matrix phase, which depends on factors such as the adhesion of the phases in the composite, the thickness and amount of reaction products in the joint season, and so on (48).

The level below the applied load diagram in terms of displacement in the 3-point flexural strength test indicates the fracture energy, which is also a measure of toughness for the samples (48-50). Figure 5 shows the changes in applied load in terms of displacement in the flexural strength test of composite samples. Also, Table 3 presents the results related to the flexural strength of the samples. Therefore, it is observed that fracture energy, elastic modulus and stress increase with increasing amount of reinforcement in composite samples (51). But the percentage of elongation in the sample with 10% by volume is higher than other samples. In addition, it is observed that the amount of toughness in samples 10 and 15 is almost equal, while in the sample 15% of fracture energy, elastic modulus and stress is more than 10% of the sample.

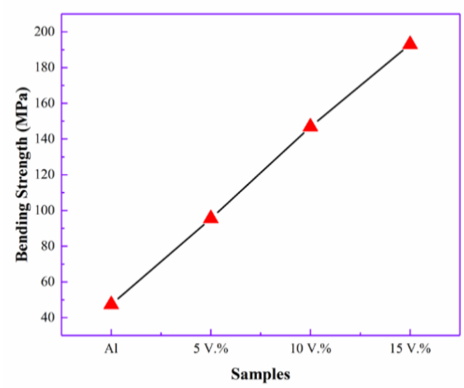

Figure 4. Flexural strength changes in the elastic region for pure aluminum sample and samples with different percentages of quasi-crystalline materials

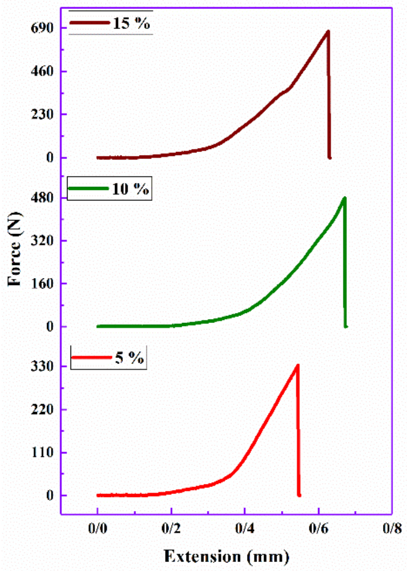

Figure 5. Load changes in terms of displacement in flexural strength test of samples with aluminum reinforcement reinforced with 5, 10 and 15 vol% quasi-crystalline

TABLE 3. Results related to flexural strength for samples with different percentages of quasi-crystalline phase

Sample	Stress (MPa)	Elongation (%)	Module (MPa)	Energy (J)	Elastic Module (MPa)
2	14.74	2.72	541.91	90.63	144.71
3	22.02	3.35	656.47	160.94	171.61
4	29.90	3.31	953.39	210.92	296.70

4. CONCLUSIONS

In this research, the microstructural and mechanical properties of $Al_{59}Cu_{25.5}Fe_{12.5}B_3$ composite samples synthesized by SPS method were investigated and the following results were obtained:

1. According to the XRD results, the quasi-crystalline particles maintain their stability due to the use of the SPS method and prevent the formation of the destructive ω phase in the composite sample.
2. According to the FESEM images, with the increase of quasi-crystalline particles in the sample, in addition to the increase in dispersion, the accumulation of quasi-crystalline particles is observed in some areas, which may be due to short mixing or sintering temperature and time.
3. According to the Flexural strength results, due to the high hardness and excellent properties of the quasi-crystalline particles, it is observed that by adding their amounts in the composite samples, it increases the fracture energy, stress and toughness.

According to the obtained results, it is possible to investigate the practical use cases in the industry and their properties in the future research of quasi-crystals with volume percentages in this research. In addition, other properties such as corrosion and wear can be investigated for this research.

5. REFERENCES

1. Avar. B, Gogebakan. M, Yilmaz. F. Characterization of the icosahedral quasicrystalline phase in rapidly solidified Al-Cu-Fe alloys. 2008:731–4. 10.1524
2. Shechtman D, Blech I, Gratias, D. and Cahn, J. W. Metallic Phase with Long-range Orientational Order and No Translational Symmetry. 1984;53:1951-3.
3. Amini M, Rahimipour M, Tayebi A, Palizdar Y. Effect of milling time on XRD phases and microstructure of a novel Al67Cu20Fe10B3 quasicrystalline alloy. Materials Research Express. 2020;7. 10.1088/2053-1591/ab9b37
4. Huttunen-Saarivirta E. Microstructure, fabrication and properties of quasicrystalline Al–Cu–Fe alloys: a review. Journal of Alloys and Compounds. 2004;363(1):154-78. https://doi.org/10.1016/S0925-8388(03)00445-6 http://www.sciencedirect.com/science/article/pii/S0925838803004456
5. D.J. Sordelet, J.M. Dubois. Quasicrystals: perspectives and potential applications. Mater Res Soc Bull. 1997:34–7.
6. Aghaali V, Ebadzadeh T, Karimi Z, Kazemzadeh A, Marzbanrad E. Effect of mechanical alloying and preheating treatment on the phase transformation of the Al-Cu-Fe compacts annealed by microwave radiation. Journal of Materials Research and Technology. 2021. https://doi.org/10.1016/j.jmrt.2021.02.089 https://www.sciencedirect.com/science/article/pii/S2238785421002155
7. Ghanbariha M, Farvizi M, Ebadzadeh T. Microstructural development in nanostructured AlCoCrFeNi–ZrO2 high-entropy alloy composite prepared with mechanical alloying and spark plasma sintering methods. Materials Research Express. 2019;6:1265b5. 10.1088/2053-1591/ab5fc9
8. Liaw P, Yeh J-W, Zhang Y. High-entropy alloys: Fundamentals and applications2016. 1-516 p.
9. Shamah AM, Ibrahim S, Hanna FF. Formation of nano quasicrystalline and crystalline phases by mechanical alloying. Journal of Alloys and Compounds. 2011;509(5):2198-202. https://doi.org/10.1016/j.jallcom.2010.11.001 https://www.sciencedirect.com/science/article/pii/S0925838810027180
10. Ramanathan A, Krishnan PK, Muraliraja R. A review on the production of metal matrix composites through stir casting – Furnace design, properties, challenges, and research opportunities. Journal of Manufacturing Processes. 2019;42:213-45. https://doi.org/10.1016/j.jmapro.2019.04.017 https://www.sciencedirect.com/science/article/pii/S1526612518312489
11. Dev Srivyas P, S. Charoo M. Aluminum metal matrix composites a review of reinforcement; mechanical and tribological behavior. 2018. 2018;7(2.4):6. 10.14419/ijet.v7i2.4.13020 https://www.sciencepubco.com/index.php/ijet/article/view/13020
12. Rajan T, Pillai RM, Pai B. Reinforcement coatings and interfaces in aluminium metal matrix composites. Journal of Materials Science. 1998;33:3491-503.

13. Aikin RM. The mechanical properties of in-situ composites. JOM. 1997;49(8):35. 10.1007/BF02914400 https://doi.org/10.1007/BF02914400
14. Singh M, Lewis D, Committee TAJCM, editors. In situ composites : science and technology : proceedings of a symposium sponsored by the Joint SMD and MSD Composite Materials Committee held during Materials Week '93, October 17-21, 1993 in Pittsburgh, Pennsylvania1994; Warrendale, Pa.: Minerals, Metals & Materials Society.
15. Laplanche G, Joulain A, Bonneville J, Gauthier-Brunet V, Dubois S, Kabir TE. Microstructural and mechanical study of an Al matrix composite reinforced by Al-Cu-Fe icosahedral particles. Journal of Materials Research. 2011;25(5):957-65. 10.1557/JMR.2010.0118 https://www.cambridge.org/core/article/microstructural-and-mechanical-study-of-an-al-matrix-composite-reinforced-by-alcufe-icosahedral-particles/F12E87BE83E7E266EE1571CDB1616764
16. Kang N, El Mansori M, Lin X, Guittonneau F, Liao HL, Huang WD, et al. In-situ synthesis of aluminum/nano-quasicrystalline Al-Fe-Cr composite by using selective laser melting. Composites Part B: Engineering. 2018;155:382-90. https://doi.org/10.1016/j.compositesb.2018.08.108 https://www.sciencedirect.com/science/article/pii/S1359836818316135
17. Dubois J. Properties- and applications of quasicrystals and complex metallic alloys. Chemical Society reviews. 2012;41 20:6760-77.
18. Wolf W, Bolfarini C, Kiminami CS, Botta WJ. Recent developments on fabrication of Al-matrix composites reinforced with quasicrystals: From metastable to conventional processing. Journal of Materials Research. 2020:1-17. 10.1557/jmr.2020.292 https://www.cambridge.org/core/article/recent-developments-on-fabrication-of-almatrix-composites-reinforced-with-quasicrystals-from-metastable-to-conventional-processing/7F4D09E42BA3C28731AB053C43856631
19. Koch CC, Whittenberger JD. Mechanical milling/alloying of intermetallics. Intermetallics. 1996;4(5):339-55. https://doi.org/10.1016/0966-9795(96)00001-5 https://www.sciencedirect.com/science/article/pii/0966979596000015
20. Ohtsuki M, Koshikawa N, Yoda S, Tamura R, Edagawa K, Takeuchi S. Icosahedral quasicrystal in the Al–Rh–Si ternary system. Journal of Alloys and Compounds. 2002;342(1):42-4. https://doi.org/10.1016/S0925-8388(02)00130-5 https://www.sciencedirect.com/science/article/pii/S0925838802001305
21. Deng S, Li R, Yuan T, Xie S, Zhang M, Zhou K, et al. Direct current-enhanced densification kinetics during spark plasma sintering of tungsten powder. Scripta Materialia. 2018;143:25-9. 10.1016/j.scriptamat.2017.09.009
22. Shinohara T, Fujii T, Tohgo K, Shimamura Y. Densification process in fabrication of PSZ-Ti composites by spark plasma sintering technique. Materials Characterization. 2017;132:230-8. https://doi.org/10.1016/j.matchar.2017.08.016 https://www.sciencedirect.com/science/article/pii/S1044580317315231
23. Guillon O, Gonzalez-Julian J, Dargatz B, Kessel T, Schierning G, Räthel J, et al. Field-Assisted Sintering Technology/Spark Plasma Sintering: Mechanisms, Materials, and Technology Developments. Advanced Engineering Materials. 2014;16. 10.1002/adem.201300409
24. Kubota M. Properties of nano-structured pure Al produced by mechanical grinding and spark plasma sintering. Journal of Alloys and Compounds. 2007;434-435:294-7. https://doi.org/10.1016/j.jallcom.2006.08.329 https://www.sciencedirect.com/science/article/pii/S0925838806012369
25. Trzaska Z, Couret A, Monchoux J-P. Spark plasma sintering mechanisms at the necks between TiAl powder particles. Acta Materialia. 2016;118:100-8. 10.1016/j.actamat.2016.07.043
26. Saheb N, Iqbal Z, Khalil A, Hakeem AS, Al Aqeeli N, Laoui T, et al. Spark Plasma Sintering of Metals and Metal Matrix Nanocomposites: A Review. Journal of Nanomaterials. 2012;2012:983470. 10.1155/2012/983470 https://doi.org/10.1155/2012/983470
27. Li FZ, Tian LH, Li RT, Wang Y, Liu ZQ. Microstructure and wear resistance properties of Al/Al–Cu–Cr–Fe composites consolidated using spark plasma sintering. Composite Interfaces. 2020;27(5):515-27. 10.1080/09276440.2019.1655317 https://doi.org/10.1080/09276440.2019.1655317
28. Yong X, Chang IT, Jones IP. Formation of a quasicrystalline phase in mechanically alloyed Al65Cu25Fe15. Journal of Alloys and Compounds. 2005;387(1):128-33. https://doi.org/10.1016/j.jallcom.2004.06.082 http://www.sciencedirect.com/science/article/pii/S0925838804008941
29. Asahi N, Maki T, Matsumoto S, Sawai T. Quasicrystallization characteristics of mechanically alloyed Al65Cu20Fe15 powder. Materials Science and Engineering: A. 1994;181-182:841-4. https://doi.org/10.1016/0921-5093(94)90752-8 http://www.sciencedirect.com/science/article/pii/0921509394907528
30. Tsai A-P, Inoue A, Masumoto T. A Stable Quasicrystal in Al-Cu-Fe System. Japanese Journal of Applied Physics. 1987;26(Part 2, No. 9):L1505-L7. 10.1143/jjap.26.l1505 http://dx.doi.org/10.1143/JJAP.26.L1505
31. F. Faudot, A. Quivy, Y. Calvayrac, D. Gratias, M. Harmelin. About the Al–Cu–Fe icosahedral phase formation. Materials Science and Engineering. 1991:383–7.
32. Kim B-H, Kim D, Kim W. Quasicrystalline phase formation in Al62Cu22.5Fe12.5 and Al55Cu22.5Fe12.5Be7 alloys. Journal of Materials Research - J MATER RES. 2001;16:1535-40. 10.1557/JMR.2001.0213
33. Köster U, Liebertz H, Liu W. Plastic deformation of quasi-crystalline and crystalline phases in Al□Cu□Fe alloys. Materials Science and Engineering: A. 1994;181-182:777-80. https://doi.org/10.1016/0921-5093(94)90737-4 http://www.sciencedirect.com/science/article/pii/0921509394907374
34. Giacometti E, Baluc N, Bonneville J, Rabier J. Microindentation of Al-Cu-Fe icosahedral quasicrystal. Scripta Materialia. 1999;41(9):989-94. https://doi.org/10.1016/S1359-6462(99)00242-0 https://www.sciencedirect.com/science/article/pii/S1359646299002420
35. Ramond L, Bernard-Granger G, Addad A, Guizard C. Sintering of a quasi-crystalline powder using spark plasma sintering and hot-pressing. Acta Materialia. 2010;58(15):5120-8. https://doi.org/10.1016/j.actamat.2010.05.047 https://www.sciencedirect.com/science/article/pii/S1359645410003320
36. Lu D, Celis JP, Kenzari S, Fournée V, Zhou DB. Tribological behavior of aluminum matrix composites containing complex metallic alloys AlCuFeB or AlCuFeCr particles. Wear. 2011;270(7):528-34. https://doi.org/10.1016/j.wear.2011.01.007 https://www.sciencedirect.com/science/article/pii/S0043164811000081
37. Brien V, Khare V, Herbst F, P W, Ledeuil J-B, Weerd M-C, et al. Influence of boron content on the microstructure of sintered Al62.5-xCU25.3Fe12.2Bx alloys (x=0, 3, 5). Journal of Materials Research. 2004;19:2974-80. 10.1557/JMR.2004.0366

38. Bilušić A, Pavuna D, Smontara A. Figure of merit of quasicrystals: the case of Al–Cu–Fe. Vacuum. 2001;61(2):345-8. https://doi.org/10.1016/S0042-207X(01)00290-1 http://www.sciencedirect.com/science/article/pii/S0042207X01002901
39. Lityńska-Dobrzyńska L, Dutkiewicz J, Stan-Głowińska K, Wajda W, Dembinski L, Langlade C, et al. Characterization of aluminium matrix composites reinforced by Al–Cu–Fe quasicrystalline particles. Journal of Alloys and Compounds. 2015;643:S114-S8. https://doi.org/10.1016/j.jallcom.2014.11.125 https://www.sciencedirect.com/science/article/pii/S092583881402773X
40. Sainfort P, Dubost B. COPRECIPITATION HARDENING IN Al-Li-Cu-Mg ALLOYS. Journal de Physique Colloques. 1987;48(C3):C3-407-C3-13. 10.1051/jphyscol:1987346 https://hal.archives-ouvertes.fr/jpa-00226577
41. Tsai AP, Aoki K, Inoue A, Masumoto T. Synthesis of stable quasicrystalline particle-dispersed Al base composite alloys. Journal of Materials Research. 1993;8(1):5-7. 10.1557/JMR.1993.0005 https://doi.org/10.1557/JMR.1993.0005
42. Amini M, Reza Rahimipour M, Ali Tayebifard S, Palizdar Y. Ultrafast synthesis of the nanostructured Al59Cu25.5Fe12.5B3 quasicrystalline and crystalline phases by high-energy ball milling: Microhardness, electrical resistivity, and solar cell absorptance studies. Advanced Powder Technology. 2020;31(10):4319-35. https://doi.org/10.1016/j.apt.2020.09.013 https://www.sciencedirect.com/science/article/pii/S0921883120304325
43. Ali F, Scudino S, Anwar MS, Shahid RN, Srivastava VC, Uhlenwinkel V, et al. Al-based metal matrix composites reinforced with Al–Cu–Fe quasicrystalline particles: Strengthening by interfacial reaction. Journal of Alloys and Compounds. 2014;607:274-9. https://doi.org/10.1016/j.jallcom.2014.04.086 https://www.sciencedirect.com/science/article/pii/S0925838814008998
44. Kenzari S, P W, Curulla M, Geandier G, Fournée V, Dubois J-M. Formation and properties of Al composites reinforced by quasicrystalline AlCuFeB particles. Philosophical Magazine. 2008;88:755-66. 10.1080/14786430801955253
45. Saiz E, Tomsia AP, Suganuma K. Wetting and strength issues at Al/α–alumina interfaces. Journal of the European Ceramic Society. 2003;23(15):2787-96. https://doi.org/10.1016/S0955-2219(03)00290-5 https://www.sciencedirect.com/science/article/pii/S0955221903002905
46. Li RT, Wang ZY, Sun W, Hu HL, Khor KA, Wang Y, et al. Microstructure and strengthening mechanisms in the Al/Al–Cu–Cr–Fe composites consolidated using spark plasma sintering. Materials Characterization. 2019;157:109917. https://doi.org/10.1016/j.matchar.2019.109917 https://www.sciencedirect.com/science/article/pii/S1044580319315177
47. Borgonovo C, Apelian D, Makhlouf MM. Aluminum nanocomposites for elevated temperature applications. JOM. 2011;63(2):57-64. 10.1007/s11837-011-0030-5 https://doi.org/10.1007/s11837-011-0030-5
48. Karimzadeh F, Rastar V, Enayati MH. Thermal Stability and Mechanical Properties of Al-Al2O3 Nanocomposites Produced by Mechanical Milling and Hot-Pressing. Proceedings of the International Conference Nanomaterials: Applications and Properties. 2012;1:1-4.
49. Peng LM, Li Z, Li H, Wang JH, Gong M. Microstructural characterization and mechanical properties of TiAl–Al2Ti4C2–Al2O3–TiC in situ composites by hot-press-aided reaction synthesis. Journal of Alloys and Compounds. 2006;414(1):100-6. https://doi.org/10.1016/j.jallcom.2005.07.024 https://www.sciencedirect.com/science/article/pii/S0925838805012302
50. Suzuki T, Nagumo M. Synthesis of TiAl-Al2Ti4C2 Composite by Reaction Milling. Materials Science Forum. 1995;179-181:189-94. 10.4028/www.scientific.net/MSF.179-181.189 https://www.scientific.net/MSF.179-181.189
51. Lee SM, Jung JH, Fleury E, Kim WT, Kim DH. Metal matrix composites reinforced by gas-atomised Al-Cu-Fe powders. Materials Science and Engineering: A. 2000;294-296:99-103. https://doi.org/10.1016/S0921-5093(00)01223-5 http://www.sciencedirect.com/science/article/pii/S0921509300012235

Persian Abstract

چکیده

در این مطالعه، کامپوزیت‌های زمینه Al تقویت‌شده با ساختار شبه بلور $Al_{59}Cu_{25.5}Fe_{12.5}B_3$ به روش تف جوشی پلاسمای جرقه‌ای (SPS) تهیه شدند و خواص ریزساختاری و مکانیکی آن ها مورد بررسی قرار گرفت. مشاهده شد که با افزودن مقدار تقویت کننده شبه بلور، شدت پیک فاز شبه بلور افزایش یافت. همچنین با انجام SPS ذرات شبه بلور پایداری خود را حفظ کردند و به دلیل دمای پایین فرآیند و زمان کوتاه SPS فازهای مخرب در شبه بلور به وجود نیامد. علاوه بر این، با توجه به تصاویر میکروسکوپ الکترونی روبشی (FESEM)، توزیع ذرات شبه بلور در سطح نمونه افزایش یافت. خواص مکانیکی نیز با افزایش درصد حجمی شبه بلور بهبود یافت و نمونه با ۱۵ درصد حجمی شبه بلور به دلیل خواص مکانیکی و ریزساختاری بهتر نسبت به سایر نمونه ها، به عنوان نمونه بهینه با خواص کاربردی مناسب انتخاب شد.

IJE TRANSACTIONS A: Basics Vol. 37 No. 01, (January 2024) 56-66

International Journal of Engineering

Journal Homepage: www.ije.ir

Experimental Study of Thermal Ageing and Hydrogen Embrittlement Effect on the Equipments of a Rocket Engine

A. Rezala*, A. Jabbar Hassan

Mechanical and Process Engineering Faculty, University of Science and Technology Houari Boumediene (USTHB), B.P. 32, El-Alia, 16111, Bab-Ezzouar, Algiers, Algeria

P A P E R   I N F O

Paper history:
Received 17 January 2023
Received in revised form 22 August 2023
Accepted 23 August 2023

Keywords:
Disc Pressure Tests
Thermal Embrittlement
Hydrogen Embrittlement
Rocket Engine
Fatigue Cycle

A B S T R A C T

In the present study employed disc pressure tests to assess the effects of hydrogen embrittlement and thermal ageing on the fatigue life of a thin-wall circular part within a rocket engine. The technique compared the pressure resistance of membranes tested under helium and hydrogen, offering a simple, sensitive, and reliable method. Disc tests were selected to mimic natural operating conditions, as they align with those of a thin-wall circular part within a rocket engine. The originality of these tests appears to lie in their enhanced performance in terms of sensitivity and reproducibility. To achieve this, tests were conducted across various conditions, including sample thicknesses of 0.75 mm, a broad range of strain rates from 10^{-6} s^{-1} to 10^{0} s^{-1}, temperatures spanning from 20°C to 900°C, and pressure rates from 10^{-2} to 2.10^{4} MPa/min. Furthermore, a variety of materials were investigated, including copper, nickel alloy, and stainless steel. The results demonstrated that thermal aging leads to precipitation, particularly intergranular precipitation. These precipitates diminish the material's ductility, particularly when they are nearly continuous. Additionally, the material's sensitivity to hydrogen becomes significant when hydrogen, supersaturated due to rapid cooling, becomes trapped on precipitates formed at high temperatures. Furthermore, the results indicated that thermal and hydrogen-induced damage mutually reinforces each other, resulting in reduced fatigue life under high deformation.

***doi**: 10.5829/ije.2024.37.01a.06*

1. INTRODUCTION

Hydrogen embrittlement (HE) is a common and significant issue for various metallic materials. The challenges posed by hydrogen embrittlement are diverse, stemming from its introduction during material development, part manufacturing, and service stages. This occurs when the equipment comes into contact with hydrogen-containing gases or is exposed to hydrogen generated through corrosion, electrochemical processes, and water dissociation. The actual service environment constitutes an external factor influencing HE behavior, while the internal factor involves the accumulation of hydrogen atoms due to interactions with shallow hydrogen traps. Potential sites for these traps in martensitic materials include grain boundaries (1) and dislocations (2). Several studies have highlighted the pivotal role of hydrogen-dislocation interaction in local hydrogen accumulation and plasticity (3, 4). This phenomenon can be accelerated through the hydrogen-enhanced localized plasticity (HELP) mechanism, suggesting that trapped hydrogen in dislocations facilitates dislocation emission and movement (5).

For many metal alloys, mechanical strength, ductility, and fatigue life can be substantially reduced when exposed to hydrogen. Hydrogen-related brittle fracture becomes more intricate due to the interaction between hydrogen and stress under various loads. Wang et al.'s findings (6) demonstrated that the fracture strength of SSRT (slow strain rate tensile) at a rate of 1×10^{-7} s^{-1} surpassed the threshold strength for CLT (constant loading tensile). Introducing nanoparticles into the matrix significantly enhanced the strength of DSHS (Dual-Phase Steel) without compromising its toughness and plasticity, as these nanoparticles served as effective irreversible hydrogen traps, mitigating HE risk (7).

*Corresponding Author Email: aicha.rezala@usthb.edu.dz (A. Rezala)

Please cite this article as: Rezala A, Jabbar Hassan A. Experimental Study of Thermal Ageing and Hydrogen Embrittlement Effect on the Equipments of a Rocket Engine. International Journal of Engineering, Transactions A: Basics, 2024;37(01): 56-66.

Qianqian et al. (8) studied the influence of adding Mo to Ti which was investigated concerning hydrogen-induced cracking behavior. They concluded that Mo addition affected the interaction between hydrogen, defects, and cracking behavior, offering insights into enhancing the hydrogen-cracking resistance of titanium alloys in structural materials. Additionally, Momotani et al. (9) revealed hydrogen accumulation at the prior austenite grain boundaries, particularly at lower strain rates (8.3×10^{-6} s^{-1}). However, the impact of temperature on hydrogen accumulation and hydrogen-induced fracture remains unclear. Literature indicates increased hydrogen diffusion rates with rising temperatures (10), while hydrogen susceptibility initially increases and then decreases (11, 12).

Extensive research into metals' sensitivity to hydrogen has led to established solutions for specific contexts. However, evolving contexts and demands for enhanced material performance necessitate further exploration without compromising hydrogen resistance. Theoretical and bibliographical approaches aid in pre-selecting materials based on numerous embrittlement parameters, though accurate qualification through tests reflecting service conditions remains essential. To mimic these conditions, Shenguang et al. (13) systematically studied hydrogen embrittlement in 15Cr martensitic stainless steel used for steam turbine blades. Slow strain rate tensile (SSRT) and constant loading tensile (CLT) tests were conducted at room temperature and 80°C.

Notably, despite lower hydrogen concentration during SSRT, the hydrogen-induced fracture strength of 15Cr steel in SSRT was lower than the threshold for CLT due to enhanced local hydrogen concentration from mobile dislocation transport during SSRT. Moreover, even with higher hydrogen concentration absorbed during SSRT at 80°C, the hydrogen embrittlement susceptibility was lower due to reduced local hydrogen accumulation at higher temperatures.

Standard techniques for characterizing metals under hydrogen conditions fall short in simulating combustion chamber behavior subjected to on-off cycles. Rocket engines, for example, experience detrimental cycles where hydrogen content increases during high-temperature usage, remains trapped during rapid cooling upon shutdown, and leads to super-saturation-induced damage during low-temperature restart. This super-saturation can shorten material fatigue life.

Additionally, thermal ageing following medium to high-temperature usage leads to uneven growth of initial precipitates, especially near grain boundaries, resulting in metallurgical embrittlement. Such embrittlement amplifies when materials are employed in hydrogen-rich atmospheres. To effectively understand hydrogen embrittlement and thermal aging effects on rocket engine fatigue life, practical service conditions must be simulated in the lab. Monotonic biaxial tests, such as gas disc pressure tests on membranes loaded by internal gas pressure, offer advantages over traditional tensile tests by providing wider temperature and strain rate ranges. The interplay of load conditions and service temperature, alongside varying materials' susceptibility to HE, is pivotal during rocket engine service.

This article introduces a specific technique for characterizing metals under hydrogen conditions using disc testing. The aim is to uncover the impacts of thermal aging and hydrogen on rocket engine service life during on-off cycles while considering multiple parameters. Moreover, numerical results are presented to enhance awareness of hydrogen-related issues among designers and analysts. This technique surpasses conventional approaches to hydrogen embrittlement, especially for equipment under severe stress like rocket engines. Materials for such engines must demonstrate low hydrogen embrittlement across broad temperature ranges. Current research primarily focuses on studying hydrogen embrittlement degradation mechanisms and thermal aging to address long-term performance demands of rocket engines.

2. MATERIALS AND METHODS

2. 1. Material Three materials have been used in the present study:

2. 1. 1. Low-alloy Copper (CuCrZr) DLR provided a copper alloy (Cu-0.65%Cr-0.05%Zr), which is a material with structural hardening properties. It as-delivered state, the alloy underwent a solution treatment, followed by over-aging and precipitation tempering at 450°C. The alloy, after undergoing this treatment, offers a favorable balance between high thermal conductivity and improved mechanical characteristics.

2. 1. 2. Nickel Alloy (Inconel 600) Imphy provided Inconel 600, a nickel-based superalloy containing (14 to 17%) chromium and (6 to 10%) iron. The melting range of this alloy falls between 1350-1410°C. This alloy exhibits good high-temperature strength up to 1150°C and resists chemical corrosion at elevated temperatures. In terms of high-temperature engineering, the alloy demonstrates strong resistance to oxidation and carburization. Due to its versatility, Inconel 600 finds applications across various fields with demanding thermo-mechanical and chemical conditions, including the chemical industry, aeronautics, space, and nuclear reactors. The cold-rolled sheet is pickled and annealed at 970°C in a continuous furnace.

2. 1. 3. Stainless Steel: AISI 321 Steel (14) AISI 321 steel is also known as austenitic stainless steel due to its titanium content, which prevents corrosion. Type 321 cannot be hardened through thermal treatment, but its strength and hardness can be significantly increased by cold working, despite a reduction in ductility. Annealing: Heat it to 1750 - 2050°F (954 - 1121°C), then water quench or air cool.

The chemical composition, mechanical and thermal properties of the materials used are provided in Tables 1 and 2, respectively. It should be noted that for the copper alloy, chromium (Cr) and zirconium (Zr) contents adhere to the specifications, while other elements are present only in trace amounts.

2. 2. Presentation of the Disc Testing

2. 2. 1. Experimental Procedure

The setup for the disc testing cell is illustrated in Figure 1. The disc testing employs a flat piece with a consistent thickness, closely resembling the thickness of the combustion chamber wall. The disc, embedded at its periphery, is subjected to increasing gas pressure on its bottom face, and the deflection at the midpoint of the upper face is measured. The pressurization rate remains constant throughout the usual rupture tests. The evolution of the gas pressure during the test exhibits three main steps, as illustrated in Figure 2:

- The transient loading period: This results from gradually opening the adjusting valve to achieve the desired gas flow.
- The steady increase in gas pressure: The curve's slope corresponds to the intended loading rate.
- The abrupt drop in gas pressure: This corresponds to the failure of the disc.

The influence of hydrogen on material properties can be measured by comparing results obtained with interstitial helium and deleterious hydrogen. Additionally, this disc testing method offers a wide range of strain rates (from 10^{-6} s^{-1} to 10^{0} s^{-1}) and temperatures (from 300K to 1200K); the prior heating duration is relatively short (about 1.5 hours).

The choice of material components for the disc testing cell depends on the testing temperature and the gas used (inert or harmful). An elastomeric O-ring (see Figure 3) is used for testing the material under inert gas at room temperature; at higher testing temperatures, a metallic O-ring (see Figure 4) must be employed. Because the loading gas should not be contaminated by gases occluded in the O-ring or permeating through the elastomer, the O-ring is also metallic during any environmental testing. The metallic O-ring is not

TABLE 1. Chemical composition of the materials studied (spectrum, wt, %)

Materials studied	C	Cu	Cr	Zr	P	S	Ni	Al	Fe	Si	Ti	Mo	Mn
CuCrZr alloy	-	99	0.69	0.056	0.006	0.0013	0.006	<0.002	0.007	<0.005	-	-	-
Inconel 600	0.044	0.22	15.26	-	-	0.003	75.5	-	8.27	0.5	-	-	0.18
AISI 321 steel	0.08	-	19.00	-	0.04	0.03	12.00	-	remain	0.75	0.70	0.50	2.00

TABLE 2. Mechanical and thermal properties of the materials studied (as it is)

Materials studied	Young's modulus E [GPa]	Elastic limit σel [MPa]	Fracture limit σf [MPa]	Elongation A [%]	Thermal conductivity λ [Wm-1K-1]	Coefficient of thermal expansion, α
CuCrZr alloy	120	255	370	18	320	18.10^{-6}/K
Inconel 600	207	352	693	36	14.9	$13.3x10^{-6}$/°C
AISI 321 steel	180	276	612	45	16.2	17.2 µm/m/°C

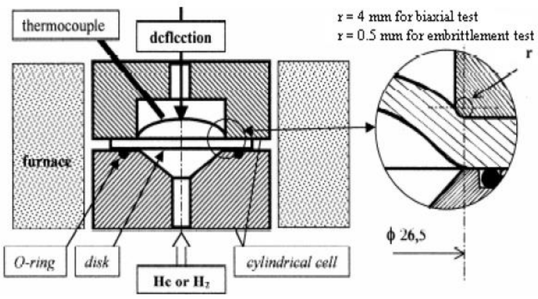

Figure 1. Schematic of the used disc testing cell

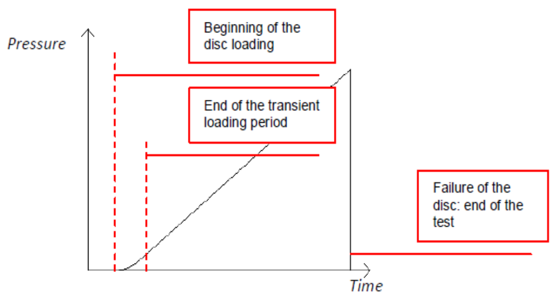

Figure 2. Typical evolution of the gas pressure during the disc testing

Figure 3. Standardized Elastomeric O-ring

Figure 4. Metal O-ring provided by Advanced Products

reusable. The sample and the cell can be heated by an annular resistor furnace. Both the cell and the furnace are insulated with ceramic fiber-based panels and stainless steel sheets (see Figure 7).

2. 2. 2. Samples The samples of disc testing are flat discs with constant thickness; the disc thickness is similar to the thickness of the combustion chamber wall to be close to the real material service conditions.

- The disc diameter is 58 mm (see Figure 5).
- The disc thickness is 0.75 mm (see Figure 6).

2. 2. 2. Disc Testing Equipment As shown in Figure 7, the disc testing equipment consists of three main subsystems: the tightening system, the gas supply system, and data acquisition. The tightening pressure applied to the periphery of the bottom disc face is provided by a high-pressure hydraulic jack. The pressure amplifier ENERPAC AHB-46, shown in Figure 8, is the core device in the tightening system. This device amplifies the low air pressure (0.4 MPa) up to the high oil pressure (20 MPa), as illustrated in Figure 9. The relative air elasticity is crucial to ensure a nearly constant load on the disc periphery during thermal cycles and subsequent thermal differential deformations.

The gas supply system provides mechanical loading through gaseous pressure and the ambient atmosphere around the disc. Since hydrogen damage can be partially or fully masked if the hydrogen used is not sufficiently pure, adsorbed gases (particularly oxygen and water vapor from the initial ambient atmosphere) must be purged from the supply pipes and downstream volumes. Prior equipment rinsing is achieved through three cycles of alternating filling with pure gas at low pressure (0.1 MPa) and vacuum pumping of the contaminated gas. The loading gas is sourced from a gas cylinder at very high pressure (up to 150 MPa), as shown in Figure 10.

Figure 5. Disc sample with a diameter of 58 mm

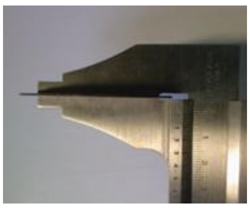

Figure 6. Flat disc with constant thickness of 0.75 mm

Gas supply is regulated using opening and throttle valves depicted in Figure 11. Gas pressure is measured by a digital pressure sensor with a precision of ±0.1 MPa. The deflection of the disc pole is measured using a Low Voltage Differential Transformer (LVDT) displacement transducer with a precision of ±10 μm. Sample temperature is measured with a thermocouple on the upper disc face. All experimental data are monitored and recorded using a digital plotter (see Figure 12). The sampling period is short enough to capture data at a high rate.

2. 3. Mathematical modelling of the disc mechanical properties To calculate the plastic strain and stress at the pole of the disc from the measured deflection and pressure (15, 16), an analytical calculation similar to Hill's method (17) is employed. The calculation of plastic strains and stresses is based on the following assumptions: the stresses are biaxial because the

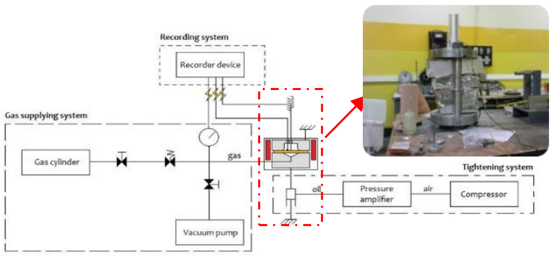

Figure 7. Schematic of the disc testing equipment

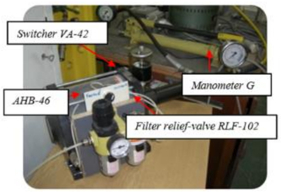

Figure 8. Air-oil pressure amplifier ENERPAC AHB-46

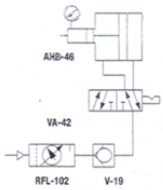

Figure 9. Hydraulic diagram of the pressure amplifier

Figure 10. Gas storage at high pressure

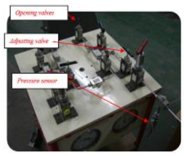

Figure 11. Gas supplying

Figure 12. Data acquisition Digital plotter SEFRAM 8400

maximum axial stress is the gas pressure, which is negligible in comparison to planar stresses; the material is homogeneous and isotropic, and the volume of a metallic material remains constant during plastic deformation; the thin disc is deformed as a membrane, meaning flexion is neglected at the pole.

The most general mechanical loading involves 6 independent parameters: 3 principal stresses and 3 principal strains. For the disc loading, the axial stress is nullified; the Von Mises stress and strain are calculated from the remaining 5 parameters to facilitate the comparison of results between disc testing and tensile testing. While the Von Mises stress and strain are limiting factors due to the reduction of the disc behavior description from 5 initial parameters to 2, they have consistently enabled coherent comparisons of different mechanical loadings in various applications (18-21). The Von Mises stress and strain are determined from Equations 1 and 2.

Note: The Equations 1 and 2 are referenced in the text, but the actual equations themselves are not provided. Please make sure to include the equations if they are relevant to the context.

$$\bar{\sigma} = \frac{P.\rho}{2.t} \tag{1}$$

$$\bar{\varepsilon} = \ln\left(t_0 / t\right) \tag{2}$$

where : P is the gas pressure, ρ is the cupola radius at the disc pole, t is the pole thickness of the deformed disc and t_0 is the initial thickness of the disc.

If the deformed disk is assumed to be a spherical cupola, the pole radius ρ becomes the radius of the sphere. This radius is determined from the deflection W using the geometrical Equation 3 formulated for the outer fiber of the disc (refer to Figure 13). We have confirmed through dimensional measurements that the disc indeed deforms into the assumed spherical cupola.

$$\rho = \left(W^2 + A^2\right) / \left(2.W\right) - r \tag{3}$$

where : W is the deflection at the disc pole, A is the internal radius of the disc embedding and r is the die radius at the disc embedding.

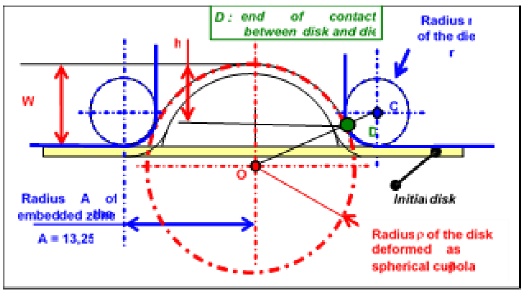

Figure 13. Disc deformation-geometrical parameters

The strains at the disc pole are calculated from the deflection W by the analytic Equation 4 based on the above mentioned assumptions; this formula has been validated by measurements of the pole thickness obtained after the deformation of discs made of various materials,

$$\bar{\varepsilon}_i = 2.\int_0^{W_i} \frac{\left[1 - \frac{2.r}{A}.\left(\frac{1}{1+W^2/A^2}\right).\sin\left(2.Arctg\left(\frac{W}{A}\right)\right)\right]}{\rho} dW \tag{4}$$

where : W is the deflection at the disc pole, A is the internal radius of the disc embedding, r is the die radius at the disc embedding and ρ the radius of the disc deformed as a spherical cupola; the radius ρ is calculated from the deflection with the Equation 3.

Testing disc associated to the previous calculation method provides coherent mechanical properties, similar to the usual tensile mechanical properties.

The biaxial tests can be performed at temperatures between 20°C-900°C and at strain rates between 10^{-6}-10^{0} s^{-1}; for instance, the tests can be performed at 900°C at high strain rate (22), which is difficult with another experimental technique.

2. 4. Flowchart of Rocket Engine Damage

Figure 14 depicts the flowchart of the rocket engine damage procedure, where the combustion chamber undergoes several 'Start-Stop' cycles, rapid cooling, rapid heating, and high temperature gradients, resulting in low cycle fatigue. Similarly, exposure to medium and high temperatures leads to thermal aging and subsequent low cycle fatigue. Furthermore, hydrogen embrittlement and its effects on low cycle fatigue occur. Additionally, the presence of trapped hydrogen contributes to embrittlement and super-saturation, reducing the material's lifespan. When the engine operates at high temperatures in a hydrogen environment, the material absorbs more hydrogen. During engine shutdown, rapid cooling prevents the hydrogen from escaping. Upon restarting, the material experiences plastic deformation at low temperatures and damage due to hydrogen supersaturation. Hydrogen supersaturation significantly reduces the material's lifespan. Another damaging factor

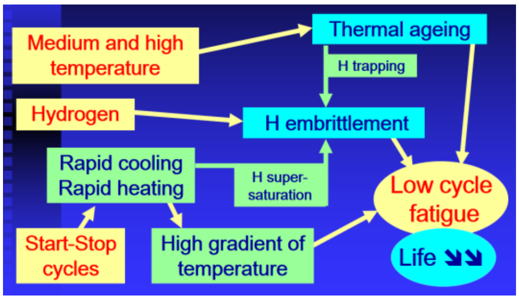

Figure 14. Flowchart of rocket engine damage

for the combustion chamber is the thermal aging of alloys resulting from frequent use at medium or high temperatures. These actions are taken to understand and clarify the impacts of hydrogen embrittlement and thermal aging on the fatigue life of a thin-walled circular part, which is a component of a rocket engine.

3. RESULTS AND DISCUSSIONS

The results of disc testing are presented in order to reveal the influence of thermal ageing and hydrogen embrittlement on the fatigue life of rocket engines subject to on-off cycles.

3. 1. Thermal Embrittlement

Thermal ageing is in two types, called stable and unstable thermal of alloys.

3. 1. 1. Stable Thermal Alloys

For stable stainless steel, ductility increases at the highest temperatures when the rupture deflection increases (see Figure 15). For this alloy, the main phenomenon is the deflection drop at the intermediate temperatures (normalized T = 0.3 - 0.5); this light embrittlement is created by thermal ageing related to atom diffusion and consecutive precipitation; thermal ageing is relatively rapid during mechanical testing due to plastic deformation improves atom mobility; at intermediate temperatures, precipitation appears especially around the grain boundaries.

For the nickel alloy, Figure 15 shows that the fracture elongation changes minimally with temperature, as recrystallization and precipitation occur simultaneously, offsetting their effects. Micrographs confirm that holding at a sufficiently high temperature (T = 0.75 T melting) enhances intergranular precipitation, making it nearly continuous (see Figure 16). The heat treatment of the nickel alloy strengthens intergranular precipitation, rendering it almost continuous.

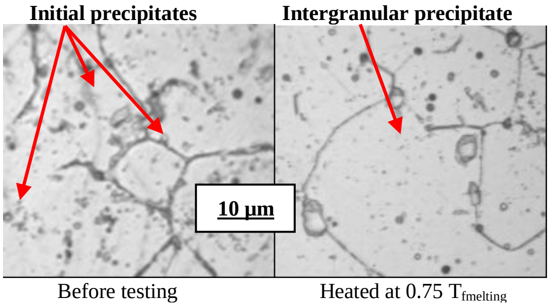

Figure 16. Micrographs of the nickel alloy before and after testing at high temperature (results of Figure 15)

3. 1. 2. Unstable Thermal Alloys

The tested copper alloy (see Figure 17) is initially treated by artificial ageing; this heat treatment at medium temperature gives fine, coherent and well-distributed precipitates, which increases mechanical resistance and decreases ductility. When the material is tested at temperatures higher than the ageing temperature (normalized T $\geq$ 0.3), the initial precipitates become coarser and less coherent with the matrix; this evolution is more important around the grain boundaries especially at the lowest temperatures; consecutive embrittlement may becomes very significant if the heating duration is long enough. Additionally, the precipitation modification increases the material ductility at normalized temperatures up to 0.35 and decreases the ductility for higher temperatures. The embrittlement increases if the heating duration increases.

For the nickel alloy as shown in Figure 17 is also unstable although it has not been treated by artificial ageing: for this material, the heating duration is great enough to obtain quasi continuous precipitates around the

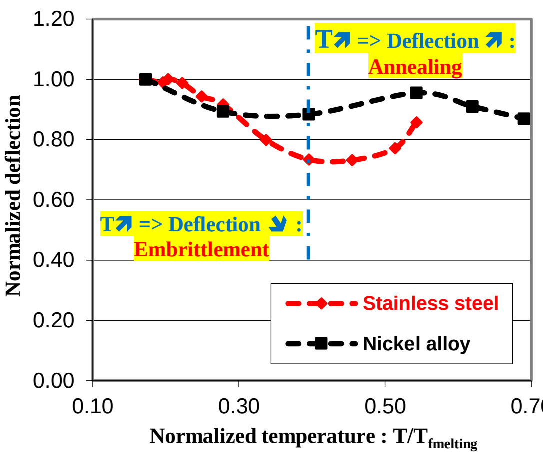

Figure 15. Disc testing at different temperatures of stable thermal of alloys

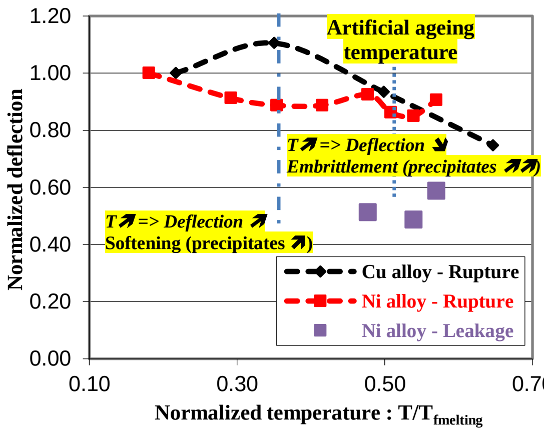

Figure 17. Disc testing at different temperatures of unstable thermal of alloys

grain boundaries; under mechanical loading, these precipitates initiate inter-granular cracks and ruptures (see Figure 18). From grain to grain, the cracks propagate along the whole disc thickness and fine gas leakages appear; the leakages are detected by the mass spectrometer, while as they are very fine, the disc can be pressurized until rupture. The leakages are detected at relatively low deflection (see Figure 17); they characterize initiation of metal damage; obviously, tensile testing is not sensitive enough to detect such fine cracking and associate the initiation of damage.

3. 2. Hydrogen Embrittlement Hydrogen embrittlement includes two types: Gaseous and internal hydrogen embrittlement.

3. 2. 1. Gaseous Hydrogen Embrittlement The two presented cases are influenced on testing temperature and precipitation duration.

3. 2. 1. 1. Influence of Testing Temperature The different effects of testing temperature as shown in Figure 19 illustrate:

- At lower temperatures, the copper alloy is hardly sensitive to hydrogen due to fine and coherent precipitates do not trap significant quantities of hydrogen,
- At medium temperatures, the precipitates become coarse and incoherent enough to trap hydrogen with the result that cracks are more easily initiated on the precipitates (23),
- At higher temperatures, the hydrogen embrittlement disappears because it cannot be trapped by the precipitates as it is very mobile.

Concerning the comparison with and without hydrogen, Figure 19 shows that at low temperatures the case without hydrogen is similar to that with hydrogen. However, at medium and higher temperatures the phenomenon observed without hydrogen is less intense than in the presence of this element, as shown by the relative arrow. Finally, in current study observes that this relative arrow decreases at higher temperatures in the case without hydrogen, conversely to the case with hydrogen.

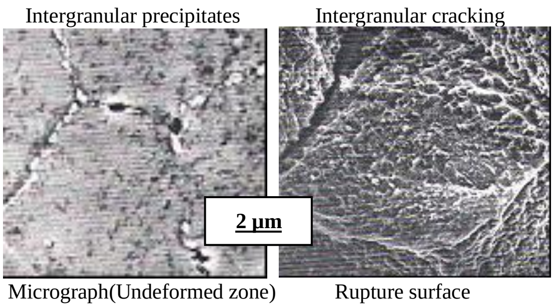

Figure 18. Observations of tested discs (results of Figure 5); Nickel alloy tested at T > 0.5T$_{fmelting}$

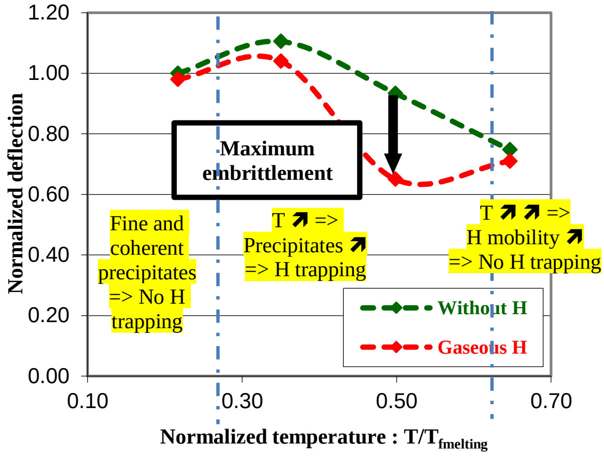

Figure 19. Disc testing at different temperatures of stable thermal of copper alloy

Concerning high temperatures, the value of the hydrogen content C_H in the engine wall reaches the hydrogen solubility S_H when steady state of diffusion has been reached. On this subject, Fick's equations give the theoretical time t_∞ to obtain the steady state when a thin wall is subjected to hydrogen on a single face (24):

$$t_\infty = 0.5e^2/D_H \tag{5}$$

where: e is wall thickness (e = 0.75 mm) and D_H is hydrogen diffusivity.

In the case of copper alloy, and to quote an order of magnitude, the steady state is obtained in about 40 s at the temperature of 900 K; however, at this example at high temperature a rocket engine is used during longer periods. During the steady state, hydrogen solubility S_H depends on the absolute temperature T (Arrhenius's law) and on the hydrogen partial pressure P_H (Sieverts's law),

$$S_H = S_0 P_H^{1/2} \exp(-Q/R/T) \tag{6}$$

where: S_0 is frequency factor; P_H is hydrogen partial pressure; T is absolute temperature; Q is activation energy and R = 8.31 Jmole^{-1}K^{-1}.

However, the hydrogen solubility in copper alloy is identical at 900 K under partial pressure P_{H900} at 600 K under hydrogen pressure $P_{H600} \approx 450\ P_{H900}$ (25).

At 300 K, the hydrogen pressure P_{H300} would have to be much higher than that at 600 K to achieve the same hydrogen solubility. These calculations seem during service at high temperatures, a large amount of hydrogen is introduced into the engine walls; disc testing at room temperature must be performed under high gas pressure to introduce hydrogen into the material with content as high as during service at high temperature.

In addition, when the engine is stopped, it is rapid cooling kept hydrogen trapped on the precipitates that created at high temperatures. When the engine is restarted, high thermal gradients appear in the thin walls; these gradients create thermal strains in the material while it is super-saturated with hydrogen.

3. 2. 2. 1. Influence of Precipitation Duration The thermal embrittlement of the nickel alloy strongly increases for the shortest ageing time (normalized t < 0.2) and its variation is less important for the longest ageing time (see Figure 20). Hydrogen embrittlement is almost identical at any ageing time and the hydrogen effect is added to thermal embritt1ement.

3. 2. 2. Internal Hydrogen Embrittlement Figure 21 shows the stable thermal of stainless steel where the hydrogen sensitivity determined at room temperature is almost identical without treatment (normalized T=0.18) or after heat treatment at medium normalized temperature (T = 0.4 - 0.5); the internal hydrogen embrittlement is identical to the gaseous hydrogen embrittlement.

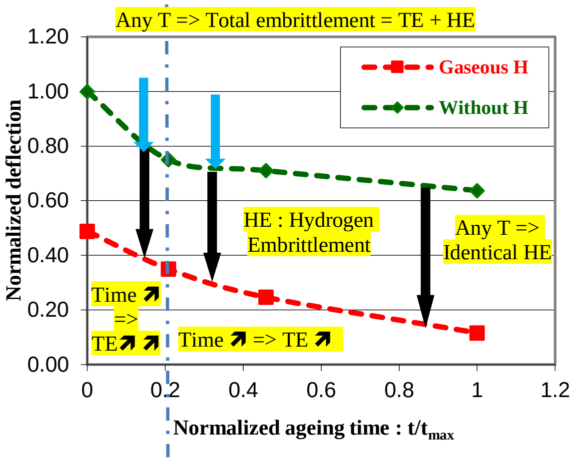

Figure 20. Disc testing at 20°C after ageing treatments of Nickel alloy aged at T(K) > 0.5 melting temperature during t < tmax

For unstable thermal of stainless steel (see Figure 22), the internal hydrogen embrittlement is more important than for the stable alloy (Figure 21); at medium temperature, the precipitates of the unstable alloy have been modified and they become more efficient to trap hydrogen. For this unstable alloy, the internal hydrogen embrittlement seems more important than the gaseous hydrogen embrittlement; the precipitates trap more hydrogen during charging at medium temperature than during gaseous hydrogen testing at room temperature.

Precipitation evolution during thermal ageing is an important factor of hydrogen embrittlement. Discs tests under gaseous hydrogen may be slightly over-optimistic when they are used to characterize internal hydrogen embrittlement, consecutive to super-saturation during rapid cooling; this super-saturation may be simulated by internal hydrogen charging before mechanical testing.

Comparing Figures 9 and 10, we can say that Internal H embrittlement Unstable stainless steel > Internal H embrittlement Stable stainless steel => H trapping by precipitates (Int H ≈ Gas H in the case of Stable stainless steel et Int H > Gas H in the case of Unstable stainless steel.

The disc testing method, used in conjunction with the previously mentioned calculation approach, yields consistent mechanical properties comparable to those obtained through conventional tensile testing. Both the ultimate strength and proof strength are identical, whether determined through disc testing or tensile testing. The mean values of uniform elongation are also the same for both methods, although there is relatively more significant scattering compared to strength scattering. This elongation scattering is influenced by local deformations initiated by material heterogeneities, such as surface defects (e.g., machining defects) and

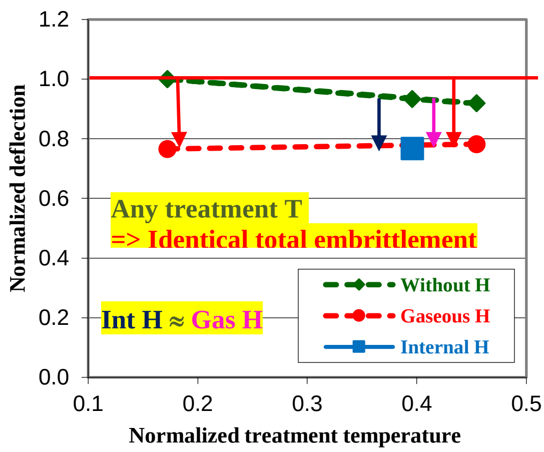

Figure 21. Disc testing at 20°C after heat treatment of stable thermal of stainless steel

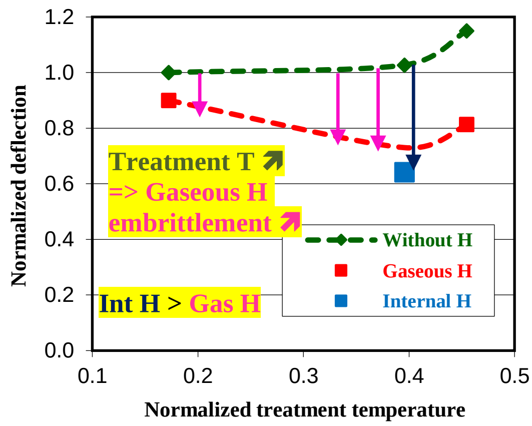

Figure 22. Disc testing at 20°C after heat treatment of unstable thermal of stainless steel

metallurgical flaws (e.g., coarse inclusions). These heterogeneities induce area reductions that are detected with differing sensitivities in thick tensile specimens and thin discs. Furthermore, the outer periphery of the disc is not subjected to stress, preventing area reduction from edge defects, as observed in tensile specimens.

The mechanical properties are appropriately correlated with temperature and loading rate-dependent phenomena. At elevated temperatures, the strength of low-alloyed steel diminishes due to dynamic recrystallization during high-temperature deformation. At intermediate temperatures, the material experiences hardening attributed to solute atoms. Notably, hardening is more pronounced in disc testing compared to tensile testing due to distinct strain rates, a crucial hardening factor, in both specimen types.

Biaxial tests can be conducted within a temperature range of 20°C to 900°C and at strain rates from 10^{-6} to 10^{0} s^{-1}. For instance, high-temperature, high-strain-rate tests can be performed at 900°C [26], a task that proves challenging with other experimental techniques. The aforementioned results underscore consistent comparisons between disc testing and tensile testing. As observed in other applications, the Von Mises stress and strain are sufficient for achieving coherent comparisons, even though they reduce the initial set of 6 stresses and strains to only 2 parameters.

3. 3. Low Cycle Fatigue

Figures 23, 24 and 25 show the influence of themal ageing, influence of gaseous hydrgen and influence of ageing and hydrogen of unstable Ni alloy respectely.

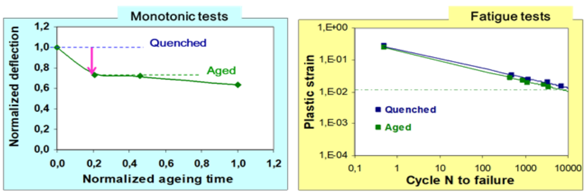

Thermal embrittlement

Strain ≈ 1 % Fatigue life
Quenched : 10000
Aged : 10000

Figure 23. Low cycle fatigue : Influence of thermal ageing of unstable Ni alloy

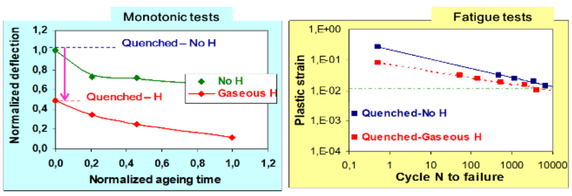

Gaseous H embrittlement

Strain ≈ 1 % Fatigue life
Quenched : 10000
Quenched + H : 8000

Figure 24. Low cycle fatigue: Influence of gaseous hydrogen of unstable Ni alloy

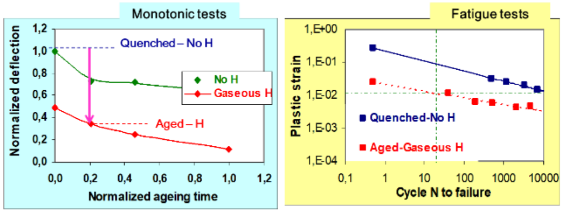

Total embrittlement: Synergy of thermal and hydrogen thermal + gaseous H embrittlement

Strain ≈ 1 % Fatigue life
Quenched : 10000
Aged : 10000
Quenched + H : 8000
Aged + H : 20

Figure 25. Low cycle fatigue : Influence of ageing and hydrogen of unstable Ni alloy

Monotonic disc tests showed that the thermally unstable nickel alloy was weakened by thermal ageing and hydrogen. Disc fatigue tests revealed the same phenomena: service life was reduced by thermal ageing and hydrogen gas.

Service life is reduced more by hydrogen than by ageing; this result is logical since hydrogen embrittlement is higher than that obtained by ageing.

Disc fatigue shows the significant synergy between ageing and hydrogen embrittlement ; for a maximum fatigue strain of around 10^{-2}, the life of a hydrogen-aged material is only 20 cycles, whereas it is around 10000 cycles if the material is damaged only by ageing or only by hydrogen.

When several on-off cycles are applied to the engine, its material subjected to low cycle fatigue; fatigue life may be reduced by the thermal embrittlement and by the hydrogen embrittlement; thus, the life reduction may be mutually amplified by both embrittlements. Fatigue results are not as detrimental for the alloys of rocket engines as for the prior nickel alloy but the phenomena may be similar; consequently, the phenomena must be identified and their influence on the fatigue life must be correctly characterized.

4. CONCLUSION

The various results obtained in the present study have led to the following conclusions:

- The fatigue life of rocket engines can be estimated through numerical calculations of damage; before conducting these calculations, both thermal and hydrogen damage must be correctly identified, characterized, and their mutual influence must be verified.
- There is significant synergy between degradation due to thermal aging and embrittlement caused by gaseous hydrogen, as the fatigue life is reduced from 10000 to 20 cycles in alternate fatigue tests at a deformation equal to 10^{-2}.

- Thermal ageing primarily leads to precipitations around grain boundaries; intergranular precipitates reduce material ductility, particularly if they are nearly continuous.
- While hydrogen damage is minimal under usual service conditions, it might become unacceptable when hydrogen is supersaturated due to rapid cooling, remaining trapped on precipitates formed at elevated temperatures.
- Thermal and hydrogen damage mutually reinforce each other, significantly reducing fatigue life under relatively high deformation.
- In the nickel alloy, leaks occur at higher temperatures ($T(K) > 0.5T_{melting}$) with deflections significantly lower than those obtained at rupture on the same sample.
- For thermally unstable stainless steel, embrittlement induced by hydrogen introduced before mechanical testing is more significant than that obtained under gaseous hydrogen.
- For reduced temperatures from 0.3 to 0.5, intergranular precipitation causes a loss of stainless steel ductility.
- Hydrogen sensitivity is sufficiently low when alloys are hardened by precipitates if they are fine, well distributed and coherent with matrix,
- The precipitate properties depend on chemical composition and thermal exposure consecutive to prior heat treatments or consecutive to services at medium and high temperature,
- The detection of very small leaks through the disc is useful to detect metallurgical evolutions of the material that create relatively short cracks while not changing the macroscopic mechanical properties.

5. REFERENCES

1. Zhao N, Zhao Q, He Y, Liu R, Zheng W, Liu W, et al. Investigation on hydrogen embrittlement susceptibility in martensitic steels with 1000 MPa yield strength. Journal of Materials Research and Technology. 2021;15:6883-900. https://doi.org/10.1016/j.jmrt.2021.11.130
2. Moshtaghi M, Loder B, Safyari M, Willidal T, Hojo T, Mori G. Hydrogen trapping and desorption affected by ferrite grain boundary types in shielded metal and flux-cored arc weldments with Ni addition. International Journal of Hydrogen Energy. 2022;47(47):20676-83. https://doi.org/10.1016/j.ijhydene.2022.04.260
3. Chen W, Zhao W, Gao P, Li F, Kuang S, Zou Y, et al. Interaction between dislocations, precipitates and hydrogen atoms in a 2000 MPa grade hot-stamped steel. Journal of Materials Research and Technology. 2022;18:4353-66. https://doi.org/10.1016/j.jmrt.2022.04.094
4. Zheng Z, Liang S, Huang M, Zhao L, Zhu Y, Li Z. Studying the effects of hydrogen on dislocation mobility and multiplication in nickel by phase-field method. Mechanics of Materials. 2022;173:104443. https://doi.org/10.1016/j.mechmat.2022.104443
5. Yu H, Cocks A, Tarleton E. Discrete dislocation plasticity HELPs understand hydrogen effects in bcc materials. Journal of the Mechanics and Physics of Solids. 2019;123:41-60. https://doi.org/10.1016/j.jmps.2018.08.020
6. Wang S, Xu D, Zhang Z, Ma Y, Qiao Y. Effect of electrochemical hydrogen charging on the mechanical behavior of a dual-phase Ti–4Al–2V–1Mo–1Fe (in wt.%) alloy. Materials Science and Engineering: A. 2021;802:140448. https://doi.org/10.1016/j.msea.2020.140448
7. Li P, Wang J, Du M, Qiao L. Hydrogen embrittlement sensitivity of dispersion-strengthened-high-strength steel welded joint under alternating wet-dry marine environment. International Journal of Hydrogen Energy. 2023. https://doi.org/10.1016/j.ijhydene.2023.05.276
8. Wang Q, Liu X, Zhu T, Ye F, Wan M, Zhang P, et al. Mechanism of hydrogen-induced defects and cracking in Ti and Ti–Mo alloy. International Journal of Hydrogen Energy. 2023;48(15):5801-9. https://doi.org/10.1016/j.ijhydene.2022.11.119
9. Momotani Y, Shibata A, Tsuji N. Hydrogen embrittlement behaviors at different deformation temperatures in as-quenched low-carbon martensitic steel. International Journal of Hydrogen Energy. 2022;47(5):3131-40. https://doi.org/10.1016/j.ijhydene.2021.10.169
10. Xu J, Yu C, Lu H, Wang Y, Luo C, Xu G, et al. Effects of alloying elements and heat treatment on hydrogen diffusion in SCRAM steels. Journal of Nuclear Materials. 2019;516:135-43. https://doi.org/10.1016/j.jnucmat.2019.01.019
11. Safyari M, Moshtaghi M, Kuramoto S. Effect of strain rate on environmental hydrogen embrittlement susceptibility of a severely cold-rolled Al–Cu alloy. Vacuum. 2020;172:109057. https://doi.org/10.1016/j.vacuum.2019.109057
12. Metalnikov P, Eliezer D, Ben-Hamu G. Hydrogen trapping in additive manufactured Ti–6Al–4V alloy. Materials Science and Engineering: A. 2021;811:141050. https://doi.org/10.1016/j.msea.2021.141050
13. Liu S, Wu W, Fu H, Li J. Effect of the loading mode and temperature on hydrogen embrittlement behavior of 15Cr for steam turbine last stage blade steel. International Journal of Hydrogen Energy. 2023;48(23):8668-84. https://doi.org/10.1016/j.ijhydene.2022.10.061
14. Lamani E, Jouinot P, editors. Embrittlement phenomena in an austenitic stainless steel: influence of hydrogen and temperature. AIP Conference Proceedings; 2007: American Institute of Physics. 10.1063/1.2733230
15. Genevois-Stasi J. Etude de l'évolution des propriétés mécaniques et métallurgiques de l'inconel 625 au cours du vieillissement, utilisation de l'essai de disques sous pression de gaz. These, Paris. 1998;6.
16. Jouinot P, Gantchenko V, Inglebert G, Riccius J, editors. Material damage induced by environment and temperature and identification process. European Congress on Computational Methods in Applied Sciences and Engineering ECCOMAS 2004; 2004.
17. Hill R. C. A theory of the plastic bulging of a metal diaphragm by lateral pressure. The London, Edinburgh, and Dublin Philosophical Magazine and Journal of Science. 1950;41(322):1133-42. https://doi.org/10.1080/14786445008561154
18. Duncan J. The hydrostatic bulge test as a laboratory experiment. Bulletin of Mechanical Engineering Education. 1965;4:29-37.
19. Aubin V, Quauaegebeur P, Degallaix S, editors. Yield surface behaviour under biaxial fatigue. Proceedings of 8th international fatigue congress, Stockhom, Sweden; 2002.

20. Mesrar R. Comportement plastique des tôles sous sollicitation biaxiale et analyse numérique de la mise en forme par gonflement hydraulique: Metz; 1991.

21. Boulila A, Ayadi M, Zghal A, Jendoubi Ke. Validation expérimentale du modèle de calcul en calotte sphérique des plaques circulaires minces sous l'effet d'un gonflement hydraulique. Mécanique & industries. 2002;3(6):627-38.

22. Jouinot P, Gantchenko V. Lois de comportement mécanique et endommagement de membranes sous pression de gaz. Actes de ITCT, Paris, France. 2006.

23. Örnek C, Mansoor M, Larsson A, Zhang F, Harlow GS, Kroll R, et al. The causation of hydrogen embrittlement of duplex stainless steel: Phase instability of the austenite phase and ductile-to-brittle transition of the ferrite phase–Synergy between experiments and modelling. Corrosion Science. 2023;217:111140. https://doi.org/10.1016/j.corsci.2023.111140

24. McAllester D. On the Mathematics of Diffusion Models. arXiv preprint arXiv:230111108. 2023. https://doi.org/10.48550/arXiv.2301.11108

25. Gale WF, Totemeier TC. Smithells metals reference book: Elsevier; 2003.

Persian Abstract

چکیده

در مطالعه حاضر از آزمایش‌های فشار دیسک برای ارزیابی اثرات شکنندگی هیدروژن و پیری حرارتی بر عمر خستگی یک بخش دایره‌ای دیواره نازک در موتور موشک استفاده شد. این تکنیک مقاومت فشار غشاهای آزمایش شده تحت هلیوم و هیدروژن را مقایسه کرد و روشی ساده، حساس و قابل اعتماد ارائه کرد. آزمایش‌های دیسک برای تقلید از شرایط عملیاتی طبیعی انتخاب شدند، زیرا آنها با بخش دایره‌ای با دیواره نازک در موتور موشک هماهنگ هستند. به نظر می رسد اصالت این تست ها در عملکرد بهبود یافته آنها از نظر حساسیت و تکرارپذیری باشد. برای دستیابی به این هدف، آزمایش‌هایی در شرایط مختلف از جمله ضخامت نمونه ۰.۷۵ میلی‌متر، طیف وسیعی از نرخ کرنش از ۱۰–٦ s-1 تا ۱۰۰ s-1، دماهای بین ۲۰ تا ۹۰۰ درجه سانتیگراد و فشار انجام شد. نرخ از ۱۰–۲ تا ۲.۱۰٤ مگاپاسکال در دقیقه. علاوه بر این، مواد مختلفی از جمله مس، آلیاژ نیکل و فولاد ضد زنگ مورد بررسی قرار گرفت. نتایج نشان داد که پیری حرارتی منجر به بارش، به ویژه بارش بین دانه‌ای می‌شود. این رسوبات شکل پذیری مواد را کاهش می دهند، به ویژه زمانی که تقریباً پیوسته باشند. علاوه بر این، حساسیت ماده به هیدروژن زمانی قابل توجه می شود که هیدروژن، فوق اشباع شده به دلیل سرد شدن سریع، روی رسوبات تشکیل شده در دماهای بالا به دام می افتد. علاوه بر این، نتایج نشان داد که آسیب های حرارتی و ناشی از هیدروژن به طور متقابل یکدیگر را تقویت می کنند و در نتیجه باعث کاهش عمر خستگی تحت تغییر شکل زیاد می شود.

IJE TRANSACTIONS A: Basics Vol. 37 No. 01, (January 2024) 67-82

International Journal of Engineering

Journal Homepage: www.ije.ir

Optimal Prediction of Shear Properties in Beam-Column Joints Using Machine Learning Approach

S. Ramavath*, S. R. Suryawanshi

Department of Civil Engineering, Sardar Vallabhbhai National Institute of Technology (SVNIT), Surat, India

P A P E R I N F O

Paper history:
Received 01 June 2023
Received in revised form 05 July 2023
Accepted 08 July 2023

Keywords:
Joint Shear Strength
Beam-Column Joint
Reinforced Concrete
Artificial Neural Network
Shallow Feed Forward Model
MATLAB

A B S T R A C T

The failure of shear-type beam-column joints in reinforced concrete (RC) frames during severe earthquake attacks is a critical concern. Traditional methods for determining joint shear capacity often lack accuracy due to improper consideration of governing parameters, impacting the behaviour of these joints. This study assesses the capabilities of machine learning techniques in predicting joint shear capacity and failure modes for exterior beam-column joints, considering their complex structural behaviour. An artificial neural network (ANN) model is proposed for predicting the shear strength of reinforced exterior beam-column joints. ANN, a component of artificial intelligence that learns from past experiences, is gaining popularity in civil engineering. The ANN model is developed using a dataset comprising material properties, specimen dimensions, and seismic loading conditions from previous experimental investigations. The model considers twelve input parameters to predict shear strength in exterior beam-column joints. Training and testing of the ANN model are conducted using established design codes, empirical formulas, and a specific algorithm. The results demonstrate the superiority of the proposed Shallow Feed Forward Artificial Neural Network (SFF-ANN) compared to previous approaches. The effectiveness of an Artificial Neural Network (ANN) model was quantitatively assessed in this study, with a focus on its performance in comparison to various design codes commonly used in structural engineering. The model was assessed using the coefficient of determination (R^2) and achieved R-squared values of 99%, 94%, and 98% during the training, testing, and validation stages, respectively. The study highlights the significance of beam reinforcement as a key element in estimating shear capacity for exterior RC beam-column connections. Although the proposed models exhibit a high degree of precision, future research should focus on developing improved models using expanded datasets and advanced algorithms for enhanced pattern recognition and performance.

doi: *10.5829/ije.2024.37.01a.07*

Graphical Abstract

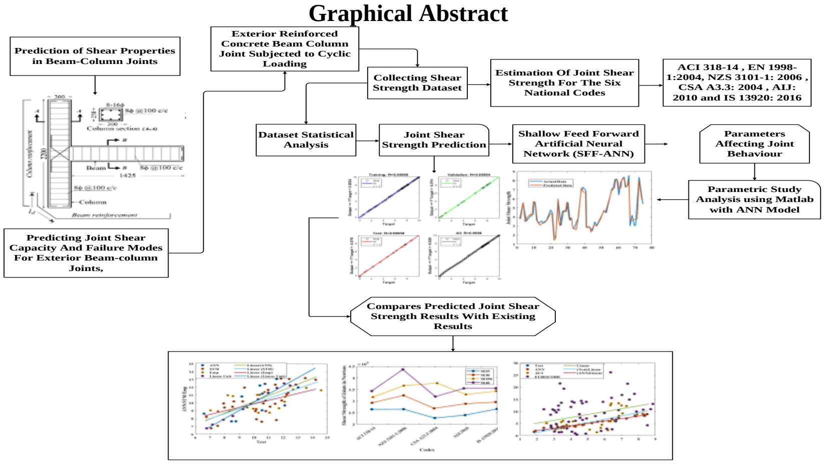

*Corresponding Author Email: *d19am002@amd.svnit.ac.in* (S. Ramavath)

Please cite this article as: Ramavath S, Suryawanshi S. R. Optimal Prediction of Shear Properties in Beam-Column Joints Using Machine Learning Approach. International Journal of Engineering, Transactions A: Basics, 2024;37(01):67-82.

1. INTRODUCTION

Beam-column joints are vital components of reinforced concrete moment resisting frames (RCMRF), and they are particularly susceptible to seismic loads as failure in these joints can result in the collapse of the entire structure (1). Extensive investigations following earthquakes have emphasized the significance of beam-column joints as they significantly influence the overall seismic performance of reinforced concrete (RC) frames (2). Beam-column joints play a crucial role in maintaining the structural integrity of the system. However, during strong seismic events, these joints may experience large deformations, leading to a reduction in their capacity to carry lateral and gravity loads. This can result in partial damage or even the complete collapse of the structure (3). In modern building design, joint shear failure is a common type of failure observed in beam-column joints.

This failure mode often occurs because the joints were not designed to withstand the anticipated loads based on the capacity design principles recommended in contemporary seismic codes. Shear failure in beam-column joints, even at relatively low deformations, is a

brittle failure mode that can potentially trigger a building's collapse (4). Given the critical role of beam-column joints and their vulnerability to seismic forces, it is imperative to properly design and reinforce these joints to ensure the overall safety and integrity of structures in seismically active regions.

Determining the dimensions of the strut and cut-point regions, which are crucial for predicting the shear strength of beam-column joints, presents a significant challenge when using the Strut and Tie Model (STM) (5). The shear strength of the joint plays a vital role as the beam-column joint can become a weak link if it is not adequately considered. Previous research has employed various individual-type machine learning (ML) algorithms, such as ANN-PSO, SVM, XGBoost, and decision trees, for predicting the shear strength of reinforced concrete joints (6). Among these techniques, ANN, GEP, and fuzzy logic-based evaluations of cement strength have shown promise as efficient ML-based prediction techniques for engineering structures (7).

The resisting mechanisms provided by the beam-column joint are fundamental in enabling RC-framed buildings to withstand seismic excitations (8). In predicting the shear strength of RC joints, the deformation of Type 2 joints indirectly informs the prediction of member shear strength and follows the conservative approach recommended by ACI 352-R02 (9). Before the adoption of "earthquake-resistant" structural design in the late 1970s and early 1980s, many buildings were primarily designed to carry gravity loads, lacking sufficient shear strength, flexural capacity, and flexibility to resist strong seismic ground motions (10). In the design and seismic analysis of tall structures, lateral load-resisting systems like RC shear walls are commonly utilized. Accurately predicting the capacity of these systems is a critical aspect of the design process (11). Predicting the capacity becomes complex due to the reinforcement characteristics of concrete and the interactions between flexure and shear. Furthermore, the response of the structure during seismic activity can influence the behaviour of the joint (12).

The limited lateral force-carrying capacity of beam-column joints is influenced by the material properties used during the structure's construction, which in turn impact the overall response of the structure (13). To ensure structural safety and prevent shear failure, it is crucial to accurately forecast the shear strength of RC beam-column joints in the design process (14). With the advancement of Artificial Intelligence in recent years, there has been a paradigm shift towards applying machine learning (ML) methods for predicting the shear strength of beam-column joints (6). As part of this trend, the present research aims to analyze the shear strength prediction of beam-column joints using a neural network tool in MATLAB.

2. LITERATURE SURVEY

For the forecast of outer beam-column joint shear capacity, Alagundi and Palanisamy (2) proposed using an artificial neural network. The simulations show that the suggested model of the neural network can predict the Exterior Beam-Column joint’s shear strength. There are three effective artificial neural network methods, radial basis function neural network (RBFNN), back-propagation neural network (BPNN) and generalized regression neural network (GRNN) Zhang et al. (15) suggested identifying the failure modes and shear strengths. With the results, the testing and training phases are compared, which prove that both GRNN, BPNN and RBFNN models are powerful approaches for predicting the mode of failure and shear strength. By using ANN, Gene Expression Programming (GEP) and Network-Based Group Method of Data Handling (GMDH-NN) Naderpour et al. (16) predicted shear strength. The simulation confirms the ability of the patterns expected by, GMDH-NN, GEP and ANN which are appropriate for use as a tool in forecasting the concrete shear walls with high accuracy and shear strength. For the forecast of shear strength an artificial neural network model was proposed by Alagundi and Palanisamy (17) in the Joint of reinforced concrete exterior BC joints are themed to seismic loading; thus, the proposed ANN model can be used. For estimating the reinforced concrete shear strength, the beam-column is subordinated to regular load Marie et al. (6) proposed a framework. The simulation also reveals that the shear strength of the joint was predicted by using the Kernel regression, where the experimental values are closer than the joint shear strength which is predicted by using the parametric equation. Detailed methodologies and discussions of the two disciplines were presented by Marcos and Silva (3). Powerful digital technologies and computer systems showed dominance by presenting the regression and performance analysis through different trained neural network models.

To determine the RC beam-column joints stochastic shear strength Yu et al. (18) employed, the GPR algorithm. The simulations show that the kernel can efficiently enhance the generalization performance and prediction accuracy of the GPR Truong et al. (19) presented the Bayesian optimization (BO), BO-XGBoost hybrid model and extreme gradient boosting (XGBoost) algorithms was made and its hyperparameters were improved based on a collection of data of 320 test specimens. The suggested model exposed that the beam width, effective depth, tension reinforcement ratio, shear span-to-depth ratio and concrete compressive strength are crucial to the deep beams' shear strength. Zayan et al. (20) presented the ANN model offered a more accurate tool to compute R and capture the impacts of five primary parameters: steel reinforcement ratio, concrete compressive strength steel yield strength, steel fibre aspect ratio fibre and volumetric ratio given from trial data. The gathered results show that the first significant argument is the compressed power of the concrete. Al-Bayati (21) introduced a numerical pattern for the calculations of shear strength in the exterior and interior reinforced concrete beam-column joints that are subordinated to seismic loads. The results of 110 exteriors and 105 interiors of beam-column joints gathered from the literature, the fresh pattern is gauged. This research study contributes to the shear strength of the beam-column joint and its prediction using artificial neural networks.

Mabrouk et al. (22) evaluate the effect of using different shear reinforcement details on the punching shear behaviour of interior slab column connections. A comprehensive experimental program is conducted on sixteen specimens having the same concrete dimensions of 1100×1100×160 mm where the slab depth is chosen to be less than that stipulated by different design codes. The parameters under examination were the type of shear reinforcement arranged in a cross shape perpendicular to the column edges (single leg, multi-leg, and closed stirrups), the spacing between stirrups (25 and 50 mm), and the extended length covered by the stirrups (300 and 425 mm). Experimental results showed that slabs reinforced with multi-leg or closed stirrups, even for slabs with a thickness of 160 mm, had an increase in the shear capacity by up to 40% depending on the stirrup amount. A noticeable enhancement in ductility was also observed.

Singh and Sangle (23) presented a nonlinear static response of a vertically oriented coupled wall subjected to horizontal loading. The 3-storey vertically oriented coupled wall interconnected with coupling beams is modelled as solid elements in a finite element (FE) software named Abaqus CAE and the steel reinforcement is modelled as a wire element. For the simulation of concrete models, a concrete damaged plasticity constitutive model is taken into consideration in this research. Moreover, with the help of concrete damage plasticity parameters, the validation of two rectangular planar walls was executed with an error of less than 10%. Finally, these parameters are used for modelling and analyzed the static behaviour of coupled walls connected with coupling beams. Furthermore, the maximum unidirectional horizontal loading helped in obtaining the compression and tensile damage as well as scalar stiffness degradation.

Sfaksi et al. (24) concern a numerical study of the behaviour of reinforced masonry (RM) structures under seismic loading. These structures are made of small hollow elements with reinforcements embedded in the horizontal joints. They were dimensioned according to the rules and codes commonly used. They are subject to vertical loads due to their weight and to horizontal loads due to seismic forces introduced by the accelerograms. The software used is the non-linear analysis program Drain2D, based on the finite element method, where the shear panel element was introduced. A series of calculations were performed on several structures at different levels, excited by three major accelerograms (El Centro, Cherchell, and Kobe). Throughout the study, our main interest was to evaluate the behaviour factor, ductility, and failure mode of these structures while increasing the intensity of earthquakes introduced. The results of this present study indicate that the average values of the behaviour factor and the global ductility were of the order of $q \approx \mu \approx 3.00$. The reinforced masonry structures studied have been broken by interstage displacement.

The literature review provides valuable insights into the use of various techniques for predicting shear strength in beam-column joints. Several authors have proposed the application of artificial neural networks (ANN) to forecast the shear strength of exterior beam-column joints (2, 17). Different types of ANN models, including radial basis function neural network (RBFNN), back-propagation neural network (BPNN), and generalized regression neural network (GRNN), have shown promising results in predicting failure modes and shear strengths. Furthermore, other researchers have explored the effectiveness of machine learning algorithms such as gene expression programming (GEP) and network-based group method of data handling (GMDH-NN) in predicting shear strength (16). The application of these techniques, along with ANN, has demonstrated high accuracy in forecasting concrete shear walls and their shear strength.

Additionally, studies have utilized techniques like kernel regression, Bayesian optimization (BO), and extreme gradient boosting (XGBoost) to determine the stochastic shear strength of RC beam-column joints (3, 6, 18, 19). These techniques have shown improvements in prediction accuracy and generalization performance. Moreover, the use of artificial neural networks (ANN) has proven to be an accurate tool for computing shear strength, considering various parameters such as steel reinforcement ratio, concrete compressive strength, steel yield strength, steel fibre aspect ratio, and volumetric ratio.

Furthermore, studies have examined the behaviour of vertically oriented coupled walls under horizontal loading (23). Nonlinear static response analysis, incorporating concrete damaged plasticity constitutive models, has been conducted to assess the behaviour of these structures. The analysis includes the evaluation of compression and tensile damage, as well as scalar stiffness degradation. Lastly, a numerical study explores the behaviour of reinforced masonry structures under seismic loading (24). The study investigates the effects of vertical and horizontal loads on these structures, with a focus on behaviour factors, ductility, and failure modes. Results indicate that the average values of the behaviour factor and global ductility are approximately 3.00, and the reinforced masonry structures exhibit failure due to interstage displacement.

In conclusion, the literature review presents a diverse range of approaches and techniques employed to predict shear strength in beam-column joints and analyzed the behaviour of related structural elements. These studies contribute to the advancement of knowledge in this field and provide valuable insights for designing safer and more resilient structures.

3. RESEARCH PROBLEM DEFINITION AND MOTIVATION

Flexural strengthening garnered the majority of attention than shear strengthening in RC beams and it has received very little research. Particularly dangerous are structures exhibiting brittle failure to shear force. Shear, a sudden, unexpected structural collapse mechanism is mostly caused by this. Deep beams are subject to shear force, which has a shear span to effective depth proportion (a/d) smaller than two. The behaviours of a deep beam exposed to vertical static stress differ significantly from those of a narrow beam in both the analytical approach and design. Because of the fast and brittle fracture of RC beams caused by shear action and the absence of logical design formulas in building regulations, the behaviour and design of RC beams under shear remain a source of worry for structural engineers.

The deformations that beam-column connections experience under earthquake loading have a substantial impact on the seismic behaviour of reinforced concrete structures. Some locations fail before they should under powerful earthquakes if they are not properly planned. The researchers show several variables, such as column and beam dimensions, joint transverse reinforcement yield strength, concrete compressive strength, volumetric joint reinforcement ratio, beam longitudinal reinforcement ratios, beam eccentricity, and column axial load, affect joint shear strength. The shear strength of joint elements makes it challenging to forecast the connection between beams and columns. Machine learning (ML) approaches are being used to forecast the beam-column joint’s shear strength of connections as a result of the recent advancements in AI. Shear strength is crucial while applying ML to forecast joints. Based on the outcomes of earlier experiments, the most crucial variables that impact shear strength joint were selected to develop a parametric equation to predict joint shear strength.

The Objective of the Study

- To study how different parameters impact beam-column joints' shear strength.
- To prepare data from pre-existing literature to model a neural network in MATLAB.
- Using prepared data Neural Network Model was trained and tested in MATLAB.
- To compare the analytical results extracted from MATLAB with experimental results from Pre-Existing Literature.

4. PROPOSED RESEARCH METHODOLOGY

Failure in shear is a sort of brittle failure with no warning signs, hence numerous studies have been conducted in the literature. To reduce shear failure in design techniques and preserve structural safety, it is crucial to properly forecast the strength of the RC beam-column connections. This problem can be resolved by using ML techniques, such as ANNs, as reliable modelling tools for calculating the shear strength of the joint and its connections in the beam-column. ANNs give patterns for a variety of artificial and natural phenomena, many of which are difficult to model using conventional parametric techniques. Consequently, the article proposed using Artificial Neural Network (ANN) with Shallow Feed-Forward (SFF) architecture for estimating the strength of exterior RC beam-column connections was subsequently proposed in the article. The block diagram of the proposed method is shown in Figure 1.

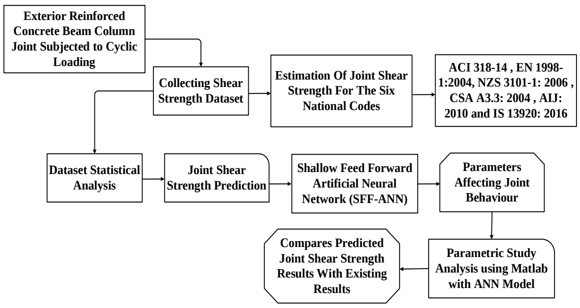

Figure 1. Block Diagram of the Proposed Work

A better understanding of the variables influencing the shear strength joint of connections in beam-column can be achieved by using machine learning analysis to look into the significance of input variables. This could result in the recommendation of useful potential methods for exploratory studies and the facilitation of lab experiments. The provisions for estimating joint shear strength for the six national codes viz., EN 1998-1:2004 (European Code EC-8), CSA A3.3:2004 (Canadian Code), IS 13920:2016 (Indian Code), NZS 3101-1:2006 (New Zealand Code), ACI 318-14 (American Code), and AIJ:2010 (Japanese Code) have been compared and evaluated in the current study using 13 experimental findings gathered from the literature. The aforementioned codes recommend different limitations on the parameters viz. confinement of joint by the effective joint depth, eccentricity between beam and column, beams, concrete compressive strength, and effective joint width. An investigation of the parameters' effects on joint shear strength revealed significant discrepancies between the code projections. The methodology equates forecast joint shear strength values with known experimental results to provide a credible design strategy.

4. 1. Experimental Program The primary objective of this study is to examine the periodic behaviour of exterior beam-column joints in reinforced concrete structures. To train, test, and validate the neural network, data sets have been prepared using experimental studies conducted by various researchers. The shear strength of these external beam-column joints is influenced by multiple factors, and a suggested approach involves utilizing an artificial neural network to predict this strength. Key inputs for the ANN model include the compressive strength of the concrete, the supports at the bottom and top of the beam, the beam-to-column depth ratio, the beam bar index, the depth and width of the joint, the yield strength of the linear support in the beam, the column load index, the joint shear reinforcement index, and the length of the beam. To assess the performance of the neural network, statistical measures such as the coefficient of correlation, root mean square error, and scatter index are employed.

In Figure 2, a typical exterior beam-column connection in an RC frame is illustrated. This region of the frame, where the beam and columns intersect, is subjected to both gravitational and lateral loads, resulting in significant shear forces, axial forces, and bending moments. The analysis considered the coupling between the beam and column in this joint region, taking into account these various forces. The beam's flexural capacity within the reference joint subassembly, as determined by geometry, reinforcing details, and material parameters, was estimated to be approximately 75 kN at the point of yielding for the longitudinal reinforcement. The dimensions of the concrete beam and column were assumed to be 230mm×230 mm, with a concrete grade of M25, while the axial load applied to the column was considered to be 1000kN. All other relevant factors were obtained from the respective codes and standards.

4. 2. Parameters Affecting Joint Behaviour Previous experimental findings have highlighted the substantial influence of material strength, both in steel and concrete, on the shear capacity of beam-column joints. Additionally, the level of confinement plays a crucial role in determining the behaviour of these joint systems. Confinement can be provided through cross supports within the joint or by incorporating the framing of cross beams and slabs into the linking area. The adequate constraint of the joint core is necessary to effectively transfer shear forces, anchor the beam reinforcement, and transmit the axial load of the column. To assess the degree of confinement, the volume of cross support in the connection region is calculated and then divided by the core volume, gross volume, or the effective volume for a single layer of transverse reinforcement. This computation yields the volumetric confinement ratio. The ratio that exhibits the strongest correlation with the results is identified as a significant contributing factor in determining the joint's strength.

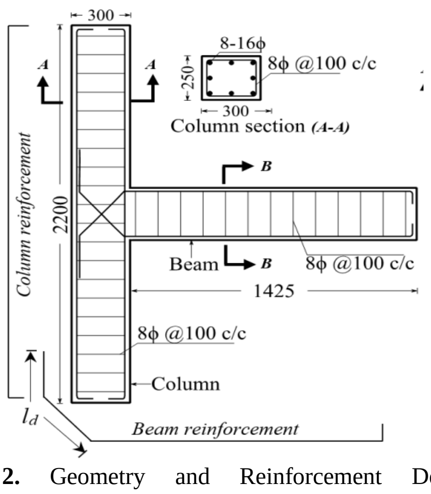

Figure 2. Geometry and Reinforcement Details (Dimensions in mm)

Furthermore, several additional parameters have been identified as influential factors impacting the shear strength of the joint. These include the eccentricity between the longitudinal beam and column center lines, the sizes of the column and beam, and the magnitude of the axial load applied to the column. Consideration of these parameters is essential for a comprehensive understanding of the joint behaviour and shear strength.

To evaluate the influence of different parameters on joint shear strength, a correlation coefficient is employed as defined in Equation 5. In this statistical approach, the independent variable x represents various parameters, while the dependent variable y represents the joint shear strength. Establishing a direct comparison between shear strength and each variable, this gain insights into their relationship. It is important to note that these correlation values provide approximate estimations of the parameters' impact on shear strength, as the correlations are expected to exhibit nonlinearity. While there may be correlations among the individual parameters, this analysis does not consider cross-correlations. The primary objective at this stage is to understand the degree of association between the parameters and joint shear strength. Interestingly, the results indicate that the joint geometry has a relatively minor influence compared to the reinforcement ratio and axial load, which exhibit high correlation coefficients. This finding highlights the significance of the reinforcement ratio and axial load in determining joint shear strength.

$$Correlation(x,y) = \frac{\sum(x-\bar{x})\cdot(y-\bar{y})}{\sqrt{\sum(x-\bar{x})^2 \cdot \sum(y-\bar{y})^2}} \quad (1)$$

The important variables that might be taken into account in the joint strength prediction are chosen when the correlation coefficients are achieved. Concrete compressive strength and volumetric joint reinforcement ratio, which shows the confinement given by the transverse reinforcement, are the two most important criteria, as was previously mentioned. As a result, values for the spacing, joint core, gross area, number of transverse reinforcing layers, and stirrup area are obtained. According to the following equations, the volumetric transverse reinforcement ratio can be calculated in three different ways by using the joint core volume, the effective confined amount as the gross bond volume and the efficient volume contains one covering of joint transverse reinforcement.

4. 2. 1. RC Beam-Column Joint Modelling The shear and compression acting forces for a typical external RC beam-column junction under seismic load are depicted in Figure 2. In the joint coreV_{jh}, the flat joint shear force can be calculated as follows:

$$V_{jh} = T_b - V_{c1} \quad (2)$$

where:

$$T_b = A_{sb} \cdot f_b \quad (3)$$

where, A_{sb} and f_b represent the area and stress of the longitudinal reinforcement of the beam, respectively, V_{c1} represents the horizontal shear of the column above the joint, and T_b illustrates the tensile force in the beam longitudinal reinforcement. The following formulas are used to compute the column shear above the joint, the beam shearV_b, and the beam flexural moment M_b.

$$V_b = \frac{A_{sb} f_b j_{bd}}{L} \quad (4)$$

$$M_b = V_b \cdot L \quad (5)$$

$$V_{c1} = \frac{L + h_c/2}{H} V_b \quad (6)$$

where, H is the height of the column, which is equal to the height between the upper and lower column inflexion points, L is the length from the beam's inflexion point to the column's face, h_c is the total height of the column cross-section, and j_{bd} is the internal moment arm of the beam cross-section, which can be calculated as follows:

$$j_{bd} = h_b - \frac{x_b}{3} - \delta_{sb} \quad (7)$$

In Equation 7, h_b is denoted as the breadth of the beam, x_b for the intensity of the contraction zone in the beam cross-section, and δ_{sb} for the distance between the closest edge of the beam cross-section and the centroid of the tensile beam reinforcement. By imposing the equilibrium of the internal forces on the beam after confirming that the concrete in compression remains within the elastic range, the value of x_b can be derived, which leads to:

$$\frac{b_b x_b^2}{2} + (A_{sb} + A'_{sb}) n_{h,b} x_b - (A_{sb} d_b + A'_{sb} \delta'_{sb}) n_{h,b} - A'_{sb} \delta'_{sb} = 0 \quad (8)$$

where, δ'_{sb} is the distance from the centroid of compressive beam reinforcement to the closest edge of the beam cross-section, b_b is the thickness of the beam cross-section at the face of the column, A'_{sb} is the area of longitudinal compressive reinforcement, d_b is the efficient breadth of the beam cross-section, and $n_{h,b}$ is the modular ratio given by:

$$n_{h,b} = \frac{E_{sb}}{E_c} \quad (9)$$

where, E_c is the concrete elastic modulus, which can be assumed to be 4700 MPa if its value is not specified, and E_{sb} is the reinforced elastic modulus of the beam reinforcement. The following method is used to compute the joint shear.

$$M_b = P(L + d^1) \quad (10)$$

where, P is the failure load (N), L is the distance from the load's application point to the column's face (mm), and d^1 is the cover (mm). The strain in the tensile support of the beam is given a value. The process is terminated, if the moment produced by the force in the beam tensile reinforcement equals the moment computed in Equation 10. If not, the assumed strain is raised gradually until the moment equals the moment specified in Equation 11. The elastic modulus of the reinforcement was estimated to be 200 GPa. The formula for shear strength joint is represented as follows:

$$V_j = T_b - V_{col} \tag{11}$$

where, T_b is the tensile force in the beam longitudinal reinforcement (N), V_{col} is the force of the shear in the upper column (N), and V_j is the joint shear force (N).

4. 3. Artificial Neural Network (ANN) Model for Shear Strength Prediction Artificial Neural Networks (ANN) is a computational framework inspired by the learning process of the human brain. In the human brain, information is received and stored in the connections between neurons, forming a complex network. Similarly, an ANN consists of interconnected artificial neurons that can process and store information. The main goal of an ANN is to establish a relationship between input data and corresponding output, similar to how the human brain recalls information from its network of neurons. Through training, an ANN modifies its internal components to learn from the input-output patterns presented during the training process.

Once trained, an ANN can be used as a prediction model for new inputs that were not part of the training dataset. It uses the learned information from the training phase to make predictions for the missing data. However, the accuracy of these predictions is a crucial concern. To address this issue, the available data is divided into two parts: a training set and a testing set. The ANN is trained using the training set, and the predictions made by the model are compared with the known output values from the testing set. High performance in the testing phase indicates a reliable prediction model that generalizes well beyond the training data, avoiding overfitting. However, optimizing the weights in ANNs with multiple hidden layers can be challenging due to issues like vanishing gradients and convergence to local minima. Even with large datasets, these problems can limit the performance of ANNs with deep architectures, posing a bottleneck in their optimization process.

4. 3. 1. Shallow Feed Forward Neural Network Neural network fitting occurs when a series of neurons, connected through activation functions, are accumulated. During the training of a neural network, the coefficients of the activation functions in each neuron are gradually optimized. The adjustment of biases and weights is performed to establish a relationship between the input and output values provided in the training dataset. The performance of the network is evaluated using an error function, such as mean squared error, which compares the neural network's response to the training objective. To facilitate learning during the training process, back-propagation algorithms are commonly employed. These algorithms update the weights (w) and biases (b) of each neuron in a way that minimizes the performance function (error). This minimization process involves propagating the output error backwards from the output layer to the hidden and input layers, adjusting the weights and biases accordingly.

For this work, an SNN pattern with an easy form and ideal performance containing a hidden layer and an output layer was used. Among these, the hidden layer has several neurons, whereas the output layer just has one. Figure 3 depicts the topology of the SNN model. Each output of the neuron in an SNN model's hidden layer can be described as Equation 12.

$$y_i = \sum_{i=1}^{N} w_i x_i + b_i \quad (i = 1,2,\cdots,i \leq N) \tag{12}$$

where, y_i denotes the neuron's output, N is denoted as the whole value of the hidden layer's neurons, w_i and b_i stand for the i_{th} neuron's weight and bias, respectively; and x_i stands for the input data, which is made up of $x_1, x_2, \cdots,$ and x_n. The hidden layer's neurons perform a nonlinear transformation on the input signal x_i to create the output signaly_i. The activation function within the secret covering is the Sigmond nonlinear function$\sigma(x)$, which is not readily divergent and is simple to derive during the transfer process. It can be expressed as follows:

$$\sigma(x) = \frac{1}{1+e^{-x}} \tag{13}$$

The system can obtain the creation of the SNN model as shown in the equation according to the topology of the SNN model.

$$Y = W\sum_{i=1}^{N} \sigma\left(\sum_{i=1}^{N} w_i x_i + b_i\right) + B = W\sum_{i=1}^{N} y_i + B \tag{14}$$

where, W and B represent the output layer's weight and bias, respectively. The output value Y of the SNN pattern can be produced after linear transformation from the output signal y_i of each hidden layer in the neuron, which is transferred to the output layer. The output layer's activation function is the linear function. The Mean

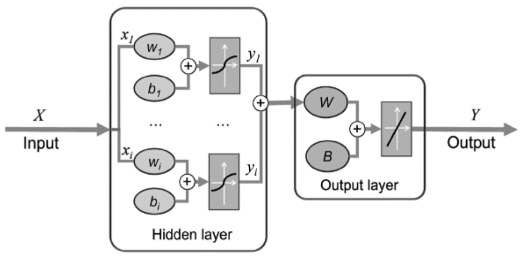

Figure 3. Shallow Neural Network Topology

Squared Error (MSE), whose minimal value denotes the best curve fit for the dataset, is used to determine when the function ends during training. To compare the MSE of the output value of the SNN pattern Y with the test data $\hat{Y}$, the weights and biases of the neurons inside the hidden and output layers are changed. Iterative training learning using the error descent along the gradient direction method is used to determine the model parameters corresponding to the minimum root of the MSE.

4. 4. Database Collection The effectiveness and validity of the proposed model in the training process rely significantly on the quantity and quality of the data available. To ensure reliable results, a comprehensive database of reinforced concrete joint tests has been meticulously compiled. The database includes detailed information on geometric dimensions, material properties, specific configurations, and the stress-strain history of the specimens.

The data collection process focuses on gathering testing results from various references, specifically targeting specimens with plain reinforced concrete. These specimens cover a wide range of parameters, such as different amounts of joint, beam, and column reinforcement, diverse material characteristics, varying column axial loads, eccentricities, and transversely framed beams. It is important to note that retrofitted specimens have been excluded from the database to maintain consistency and relevance.

Table 1 in this section summarized the results of 120 specimens tested by Hanson et al. (25), Karayannis et al. (26) and Salim et al. (27). In all of these experimental studies where joints in beam-column are subordinated to monotonic or cyclic load until one of the collapse types of failure in the joint or beam yielding followed by joint failure is presented.

TABLE 1. Dataset Collection 1

Investigator		fc′, ksi	fyc, ksi	fyb, ksi	Lb, in.	hb, in.	bb, in.	ρ	ρ′	Lc, in.	hc, in.	bc, in.	ρc	P/fc′ Ag	γj TEST
Hanson et al. (25)	Specimen ID	3.3	64.8	51	120	20	12	0.02	0.01	137	15	15	0.05	0.86	11.6
Pantelides et al. (28)	Unit 3	4.9	68.1	66.5	63	16	16	0.02	0.02	166	16	16	0.02	0.1	10.8
	Unit 4	4.9	68.1	66.5	63	16	16	0.02	0.02	166	16	16	0.02	0.25	12.4
	Unit 6	4.9	68.1	66.5	63	16	16	0.02	0.02	166	16	16	0.02	0.25	11.7
	Unit 5	4.6	68.1	66.5	63	16	16	0.02	0.02	166	16	16	0.02	0.1	10.4
Wong et al. (29)	BS-L	4.48	75.6	75.4	52	17.7	10.2	0.01	0.01	98.1	11.8	11.8	0.02	0.15	8.13
	BS-U	4.5	75.6	75.4	52	17.7	10.2	0.01	0.01	98.1	11.8	11.8	0.02	0.15	8.78
	BS-LL	6.12	75.6	75.4	52	17.7	10.2	0.01	0.01	98.1	11.8	11.8	0.02	0.15	8.8
	BS-L-LS	4.58	75.6	75.4	52	17.7	10.2	0.01	0.01	98.1	11.8	11.8	0.02	0.15	8.79
	BS-L-V2T10	4.73	75.6	75.4	52	17.7	10.2	0.01	0.01	98.1	11.8	11.8	0.02	0.15	10
	BS-L-V4T10	4.1	75.6	75.4	52	17.7	10.2	0.01	0.01	98.1	11.8	11.8	0.02	0.15	10.8
	BS-L-600	5.28	0	75.4	52	23.6	10.2	0.01	0.01	98.1	11.8	11.8	0.02	0.15	6.74
Ghobarah et al. (30)	T1	4.48	61.7	61.6	65.8	15.8	9.84	0.01	0.01	108	15.7	9.84	0.02	0.19	12.1
	T2	4.48	61.7	61.6	65.8	15.8	9.84	0.01	0.01	112	15.7	9.84	0.02	0.1	12.2
Karayannis et al. (26)	B0	4.59	84.3	84.3	39.4	11.8	7.87	0.01	0.01	59	11.8	7.87	0.01	0.05	8.18
	C0	4.59	84.3	84.3	39.4	11.8	7.87	0.01	0.01	59	11.8	7.87	0.01	0.05	8.6
Tsonos et al. (31)	L1	2.61	66.8	70.5	35.4	11.8	7.88	0.01	0.01	55.1	7.87	7.87	0.02	0.21	10.2
	L2	2.61	66.8	70.5	35.4	11.8	7.88	0.01	0.01	55.1	7.87	7.87	0.02	0.21	11.6
	O1	2.61	66.8	70.5	35.4	11.8	7.88	0.01	0.01	55.1	7.87	7.87	0.02	0.21	10.2
Antonopoulos et al. (32)	C1	2.82	66.8	84.8	39.4	11.8	7.87	0.01	0.01	50.9	7.87	7.87	0.02	0.06	7.04
	C2	3.44	66.8	84.8	39.4	11.8	7.87	0.01	0.01	50.9	7.87	7.87	0.02	0.05	7.31
Sarsam et al. (33)	EX2	7.5	61.6	80	56	12	5.98	0.01	0.01	60	8.03	6.18	0.03	0.19	9.15

Filiatrault et al. (34)	S1	4.93	69	69	78.8	17.7	13.8	0.01	0.01	118	13.8	13.7	0.03	0.08	12
Hoffschild et al. (35)	—	3.82	65.4	83.2	32.2	7.9	6.5	0.01	0.01	99.8	7.48	7.48	0.01	0.13	10.5
Park et al. (36)	UJ2-EW	3.96	68.1	72.2	96	30	16	0.01	0.01	145	18	18	0.03	0.17	8.76
	UJ2-NS	3.96	68.1	72.2	96	30	16	0.01	0.01	145	18	18	0.03	0.15	8.37
	UJ1-EW	4.3	70	68	96	18	16	0.02	0.02	145	18	18	0.03	0.31	14.4
	UJ1-NS	4.3	70	68	96	18	16	0.02	0.02	145	18	18	0.03	0.31	13.1
Hassan et al. (37)	UJ2-EW	4.43	70	77	96	30	16	0.01	0.01	145	18	18	0.03	0.45	9.97
	UJ2-NS	4.43	70	77	96	30	16	0.01	0.01	145	18	18	0.03	0.45	9.47
	BJ1-EW	4.41	70	77	96	18	16	0.02	0.02	145	18	18	0.03	0.45	11.4
	BJ1-NS	4.41	70	77	96	18	16	0.02	0.02	145	18	18	0.03	0.45	10.8
Salim et al. (27)	S1	4.39	68.1	66.8	35.8	11.8	5.91	0.02	0.01	74.8	7.09	7.09	0.02	0.09	8.59

The following factors are taken into consideration for the neural network's inputs in the current study: Joint width (b_j), Joint depth (h_c), Compressive strength of concrete (f_c), Beam Reinforcement at the Top (T_{Ast}), Beam Reinforcement at the Bottom (B_{Ast}), Beam length (L), Yield strength of beam bars (f_{yb}), Joint Shear Reinforcement Index (φ_s), Column Axial Load Level (P_y), Beam Bar Index (x_b), Beam-Column depth ratio (h_b/h_c) and τ. Table 2 displays the experiment analysis of the 53 data that were obtained for this investigation. The MATLAB scripting language is used to construct an object-oriented framework to collect certain joint specimen properties. A gathering of sample assets and measured outcomes, such as concrete strength, joint type, joint reinforcement ratio, etc., constitute an instance of the experiment class.

TABLE 2. Dataset Collection 2

S. no.	b_j	h_c	f_c	T_{Ast}	B_{Ast}	L	f_{yb}	φ_s	P_y	x_b	h_b/h_c	τ
1	280	300	31	0.806	0.806	1500	520	0	0	0.1538	1.5	3.75
2	280	300	33	0.806	0.806	1500	520	0.0819	0	0.1538	1.5	4.631
3	280	300	42	0.806	0.806	1500	520	0.1442	0	0.1538	1.5	5.7024
4	280	300	36	0.6045	0.6045	1500	520	0	0	0.1154	2	3.381
5	280	300	42	0.6045	0.6045	1500	520	0.0928	0	0.1154	2	4.2857
6	280	300	30	0.6045	0.6045	1500	520	0.2184	0	0.1154	2	4.0714
7	200	200	35	0.5234	0.5234	900	510	0.6602	0.1429	0.1333	1.5	4.3
8	200	200	35	0.5134	0.5134	900	495	1.0322	0.1429	0.0933	1.5	4.1
9	200	200	22	0.77	0.77	900	495	1.2184	0.2273	0.14	1.5	5.8
10	200	200	22	0.77	0.77	900	495	0.9767	0.2273	0.14	1.5	5.55
11	200	300	34	0.755	0.755	1000	580	0.2603	0.05	0.24	1	3.6333
12	200	300	34	0.755	0.755	1000	580	0.6764	0.05	0.24	1	3.45
13	200	300	32	0.785	0.785	1000	580	0	0.05	0.3	1	3.35
14	200	300	32	0.785	0.785	1000	580	0.0854	0.05	0.3	1	3.65
15	100	200	21	0.785	0.785	1000	470	0	0.1	0.2	1	3.3
16	100	200	21	0.785	0.785	1000	470	0.2564	0.1	0.2	1	3.6
17	100	200	21	0.785	0.785	1000	470	0.5179	0.1	0.2	1	3.6
18	100	200	23	1.18	1.18	1000	470	0	0.1	0.3	1	4.2

19	100	200	23	1.18	1.18	1000	470	0.245	0.1	0.3	1	4.85
20	100	200	23	1.18	1.18	1000	470	0.4949	0.1	0.3	1	4.4
21	200	200	36	0.2617	0.2617	1000	574	0	0.0486	0.0667	1.5	1.8
22	200	200	36	0.2617	0.2617	1000	574	1.0212	0.0486	0.0667	1.5	1.9
23	280	300	34	1.209	1.209	1500	520	0	0.1607	0.2308	1	6.0119
24	280	300	31	0.806	0.806	1500	520	0	0.1605	0.1538	1.5	3.75
25	280	300	36	0.6045	0.6045	1500	520	0	0.1607	0.1154	2	3.381
26	280	300	33	0.806	0.806	1500	520	0.1692	0.1605	0.1538	1.5	4.75
27	280	300	28	0.806	0.806	1500	520	0.3673	0.1607	0.1538	1.5	4.7976
28	280	300	33	0.806	0.806	1500	520	0.0819	0.1605	0.1538	1.5	4.631
29	280	300	42	0.806	0.806	1500	520	0.1442	0.1607	0.1538	1.5	5.7024
30	280	300	31	0.806	0.806	1500	520	0	0.1502	0.1538	1.5	3.7619
31	280	300	31	0.806	0.806	1500	520	0	0.1502	0.1538	1.5	4.0595
32	215	230	19	0.7137	0.7137	1375	300	0.2185	0.0798	0.2091	1.4348	2.8311
33	250	250	26	0.5491	0.5491	1375	300	0.7136	0.0615	0.1455	1.32	2.832
34	350	350	24	0.7272	0.7272	1780	417	1.5629	0	0.18	1.1429	3.4612
35	350	350	20	0.7272	0.7272	1780	417	1.7121	0	0.18	1.1429	3.6816
36	370	420	67	1.3639	1.3639	1900	430	1.0651	0.0188	0.2917	1.0714	6.4157
37	370	420	69	1.3639	1.3639	1900	430	1.3075	0.0183	0.2917	1.0714	7.2844
38	370	420	71	1.3639	1.3639	1900	430	1.1358	0.0178	0.2917	1.0714	6.9498
39	370	420	73	1.3639	1.3639	1900	430	1.1202	0.0173	0.2917	1.0714	6.686
40	200	200	16	0.77	0.77	1100	585	0	0.0719	0.14	1.5	2.925
41	200	200	19	0.77	0.77	1100	585	0	0.0605	0.14	1.5	2.875
42	200	200	15	0.77	0.77	1100	585	0.0839	0.0767	0.14	1.5	3.1
44	275	300	39	0.7856	0.7856	850	570	0	0	0.12	1.6667	2.3273
45	275	300	39	0.7856	0.7856	850	570	0	0.0932	0.12	1.6667	2.7152
46	275	300	37	0.7856	0.7856	850	570	0	0.1867	0.12	1.6667	3.3455
47	275	300	39	0.7856	0.7856	850	570	0	0	0.12	1.6667	2.9576
48	275	300	40	0.7856	0.7856	850	570	0	0.0909	0.12	1.6667	3.1515
49	275	300	38	0.7856	0.7856	850	570	0	0.1914	0.12	1.6667	3.6
50	275	300	43	0.7856	0.7856	850	485	0.2005	0	0.12	1.6667	4.1939
51	275	300	43	0.7856	0.7856	850	485	0.2005	0.0846	0.12	1.6667	4.6545
52	275	300	43	0.7856	0.7856	850	485	0.2005	0.1691	0.12	1.6667	4.7636
53	275	300	43	1.2872	1.2872	850	515	0.2005	0	0.1536	1.6667	4.4485

5. EXPERIMENTATION AND RESULTS DISCUSSION

The suggested ANN model is created via MATLAB code and operates in MATLAB. The codes are developed in MATLAB with its toolbox. The dataset (input and output) used in this section is the same as the regression models' dataset. A popular training algorithm (so-called "Trainlm" (34)) that updates weight and bias values according to Levenberg-Marquardt optimization is used. Activation functions for the hidden and output layers are hyperbolic tangent sigmoid (Tansig) and linear transfer function (Purelin), respectively. To achieve the best-performing model, a single ANN architecture is built with the hidden layer neurons set through experimentation (trial and error). Gradient descent is utilized to minimize error in the current study's backpropagation-type training procedure, which is used in shallow feed-forward with a single hidden layer. Using the Levenberg-Marquardt algorithm, the network is trained. The achievement of the ANN model is quantified using statistical metrics.

In Figure 4, the analysis focuses on the shear strength of beam-column joints according to various concrete grades. Specifically, this study employs grade M25 concrete and compares it with other grades such as M35, M40, and M30 across six different codes. The analysis aims to determine the shear strength of beam-column joints for each concrete grade within these codes. The results of this analysis reveal that the shear strength of M25 grade concrete in the beam-column joint is calculated as 2.6. This value indicates improved ductility and stiffness in the anchorage system, which can be attributed to reduced crack width and the formation of multiple cracks in the joint. Based on the findings, it can be concluded that the ACI 318-14 code provides a more suitable prediction for shear strength in the beam-column joint.

5. 1. Models Evaluation Measures To evaluate the constructed prediction models, a mathematical technique commonly employed in research to study machine learning models was utilized in this study. Several mathematical measures were employed to assess the accuracy of the models, including measures that aimed to minimize the discrepancy between the observed and predicted shear strength and others that aimed to identify the best-fit model. Eight evaluation measures were employed to accurately assess the anticipated accuracy of the models. These measures included the determination coefficient, Mean Square Error (MSE), Root Mean Square Error (RMSE), and Mean Absolute Error (MAE). In evaluating the models, better performance is indicated by lower values of MSE and higher values of the determination coefficient (R^2), which should be closer to 1. By employing these evaluation measures, the study aimed to provide a comprehensive and accurate assessment of the predictive accuracy of the models.

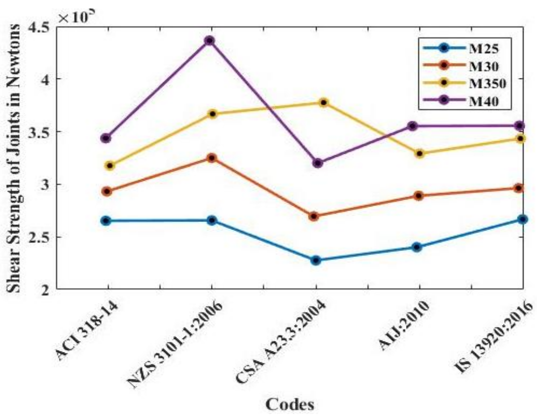

Figure 4. Shear Strength of Joint with Several Codes

Figure 5 illustrates the Mean Squared Error (MSE) curve, which provides valuable insights into the training process. Initially, the error exhibits a rapid decline, indicating effective learning. As the training progresses, the rate of error reduction slows down. Notably, the MSEs of the validation data and test data follow a similar pattern to that of the training data, indicating the model's consistency and reliability. The minimum MSE value for the validation performance, reaching 0.00010534, is achieved after 13 training iterations. Importantly, no significant overfitting is observed up to this point, which is evident from the similar characteristics of the error in the test set and validation set. Consequently, the training results of this model can be considered reasonable and promising. The performance analysis for prediction accuracy is illustrated in Figure 6.

To evaluate the influence of different parameters on joint shear strength, a correlation coefficient is employed as defined in Equation 5. In this statistical approach, the

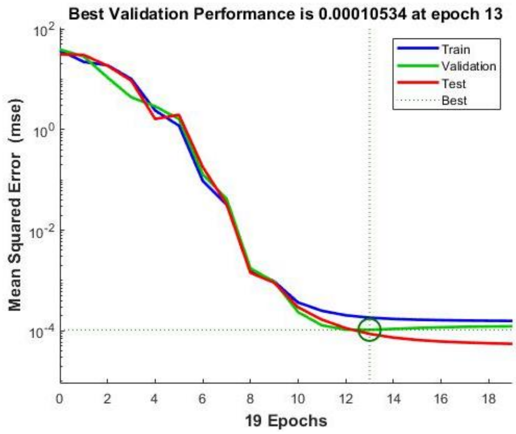

Figure 5. Mean Square Error Performance Analysis

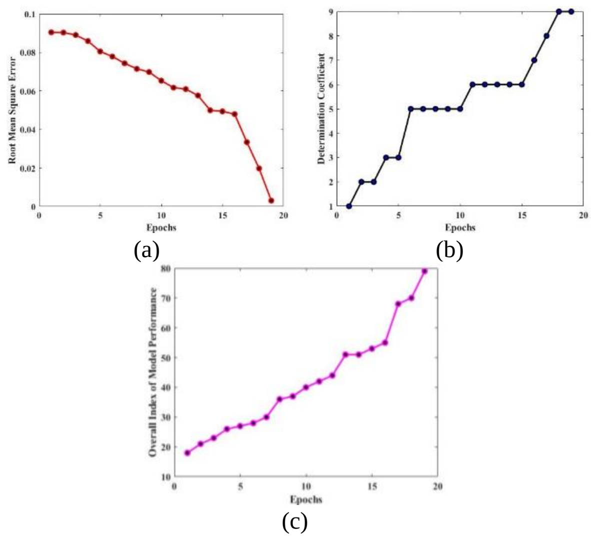

(a) (b)

(c)

Figure 6. Performance Analysis for Prediction Accuracy

independent variable x represents various parameters, while the dependent variable y represents the joint shear strength. Establishing a direct comparison between shear strength and each variable, this gain insights into their relationship. It is important to note that these correlation values provide approximate estimations of the parameters' impact on shear strength, as the correlations are expected to exhibit nonlinearity. While there may be correlations among the individual parameters, this analysis does not consider cross-correlations. The primary objective at this stage is to understand the degree of association between the parameters and joint shear strength.

Interestingly, the results indicate that the joint geometry has a relatively minor influence compared to the reinforcement ratio and axial load, which exhibit high correlation coefficients. This finding highlights the significance of the reinforcement ratio and axial load in determining joint shear strength.

The Levenberg-Marquardt method was used to train an optimised feed-forward neural network for each response parameter. Table 3 illustrates this neural network training and testing procedure with different initial, stooped, and target value parameters. To prevent overfitting, where the network perfectly matches the training data but performs poorly on the testing set, the number of epochs is kept to a minimum during the development of the optimal topology of the networks. Seven trained neural networks were used as experimental data and the findings of the FE study.

In Figure 7, the comparison between predicted and actual responses is displayed for different parameters of the response curves. The data points forming clusters along the diagonal line indicate the accuracy of the trained neural networks. The validation set was utilized to assess the generalizability of the model and to prevent overfitting by halting the training process. The R-squared (R^2) value measures the proportion of variance in the response variable that can be predicted by the trained artificial neural network. In this study, the R^2 values range from 0.92 to 0.99, indicating a high level of prediction accuracy. The ANN model achieves R-squared values of 99%, 94%, and 98% for the training,

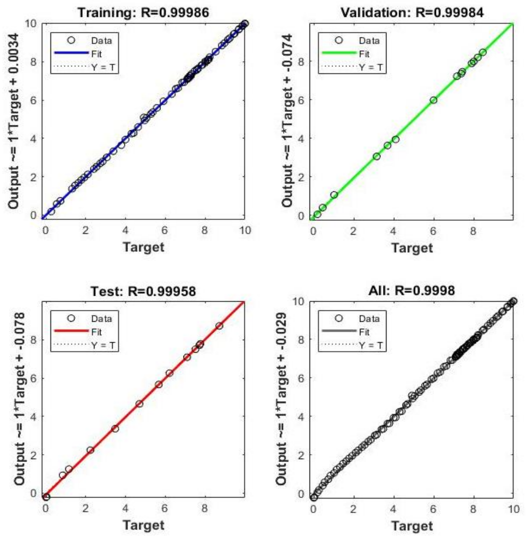

Figure 7. Target Data versus Predicted Response in the Training, Validation, and Test Sets

testing, and validation sets, respectively, across all the data. These results demonstrate the robust performance of the ANN model in accurately predicting the responses, providing a reliable tool for estimating the desired parameters.

To ensure the superior robustness of the neural network model compared to traditional fitting methods, a random sampling method was employed for data set segmentation. Moreover, the Levenberg-Marquardt method was utilized for training the Self-Organizing Neural Network (SNN). The results, as presented in Table 4, highlight the overall superiority of ANN training and testing compared to other algorithms. This demonstrates that the proposed ANN model exhibits excellent alignment with experimental test results when compared to alternative models. Furthermore, the empirical model demonstrates improved performance compared to the results obtained from existing codes, emphasizing its effectiveness and accuracy.

TABLE 3. Testing and Training of Neural network model

Unit	Initial Value	Stopped Value	Target Value
Epoch	0	14	1000
Elapsed Time	-	00:00:00	-
Performance	22.8	0.0323	0
Gradient	65.6	0.0182	1e-07
Mu	0.001	0.001	1e+10
Validation Checks	0	6	6

TABLE 4. Results for Test Dataset with Existing Techniques

Test	ANN	STM	Emp
11.6	13.16	10.1	11.4
10.8	12.46	11.5	11
12.4	12.69	12.8	11.6
11.7	12.69	12.4	11.6
10.4	12.33	11.1	11
8.13	9.13	9.16	8.98
8.78	9.14	9.17	8.98
8.8	9.44	10.4	8.98
8.79	9.15	9.25	8.98

10	9.19	9.37	8.98
10.8	9.04	8.83	8.98
6.74	8.55	8.11	7.78
12.1	11.44	12	11.3
12.2	11.32	10.7	11
8.18	7.83	9.79	11
8.6	7.83	9.62	11
10.2	10.20	7.99	9.21
11.6	10.20	7.79	9.21
10.2	10.20	7.79	9.21
7.04	7.13	6.79	8.98
7.31	7.36	7.27	8.98
9.15	10.72	11.9	9.15
12	9.88	10.4	9.7
10.5	8.96	10.8	10.7
8.76	7.77	8.81	8.57
8.37	7.66	8.79	8.52
14.4	11.82	13.2	12
13.1	11.82	13.2	12
9.97	9.48	10.2	9.55
9.47	9.48	10.4	9.55
11.4	11.66	10.1	9.06
10.8	11.66	10.2	9.06
8.59	9.31	9.34	8.52

In Figure 8, several plots depict the analysis of the full data set, including the correlation coefficient (CC) plot comparing actual values with predicted values, the error histogram, and the graph illustrating predicted versus accurate shear strength values. Figure 8a presents the CC plot, where a correlation coefficient of 98.24% demonstrates a strong correlation between the predicted values and the actual values. This indicates that the ANN model's predictions align well with the true values. Figure 8b displays an error histogram, showcasing the distribution of errors between the predicted and actual shear strength values. Approximately 85% of the predictions made by the ANN model fall within a 9% margin of error. This suggests that the model performs well in accurately estimating the shear strength values, with a relatively small margin of error for the majority of predictions. These visualizations highlight the effectiveness of the ANN model in capturing the correlation between predicted and actual shear strength values and demonstrate its ability to generate accurate predictions for the full data set.

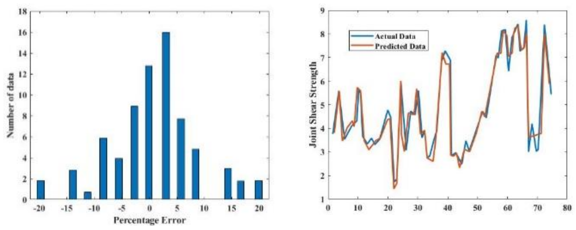

(a) (b)

Figure 8. CC Plot for Actual and Predicted Values

In Figure 9, a performance analysis graph is presented, comparing precision and recall for concrete cracking, spalling, rebar exposure, and rebar buckling. The objective was to evaluate the network's performance as the percentage of modules varied and to analyse its impact on the model's effectiveness. The curve precision-recall (PR) was employed for this assessment, as shown in Figure 9.

For the cracking model, the obtained values range from 0.764 to 0.831. Notably, the proposed SFF-ANN network achieves an accuracy that is 8.8% higher compared to other models, indicating its improved performance in predicting concrete cracking. The PR curve provides insights into the precision and recall achieved by the model, offering a comprehensive evaluation of its performance across different scenarios. The results demonstrate the superiority of the SFF-ANN network in accurately predicting concrete cracking, leading to enhanced accuracy and improved performance compared to alternative models.

In Figure 10, a comparison analysis is presented, comparing the performance of the Artificial Neural

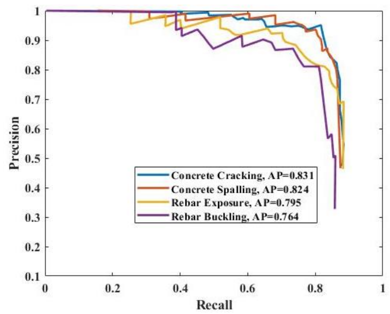

Figure 9. Precision Vs Recall Performance Graph

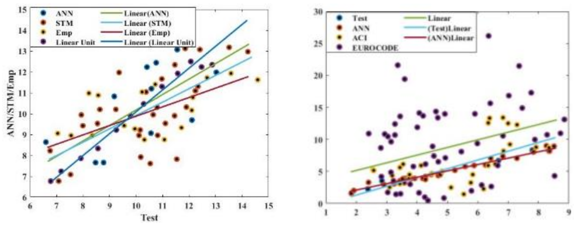

(a) (b)

Figure 10. Comparison Analysis of ANN with Two Datasets

Network (ANN) with the Strut and Tie Model (STM) and Empirical Model (Emp). Figure 10(a) focuses on the analysis of the ANN test data using dataset 1. The plot showcases the regression lines for the three models, representing the line of best fit that minimizes the total error of the model. It is important for the relationship between variables to be linear, and this can be visually assessed through a scatter plot. In this case, the data points exhibit a distribution implying a linear relationship. In Figure 10(b), a comparative analysis is conducted using dataset 2, and the regression plot is determined for the ANN, ACI, and Eurocode models. The scatter plot in this case does not align in a straight line but appears more scattered. This indicates that in the comparative study of ANN, the collected dataset performs better when compared to dataset 2. These visualizations in Figure 10 provide insights into the comparative performance of the ANN model against the Strut and Tie Model (STM) and Empirical Model (Emp.). The results suggest that the ANN model shows promising performance, particularly when compared to the specific datasets analyzed in this study.

6. RESEARCH CONCLUSION

The article successfully developed an artificial neural network (ANN) model using artificial intelligence technology to assess the reinforced concrete shear ability of external beam-column (BC) joints. Experimental data from various literature works were gathered and assembled to create an input and output data set for the ANN model. The proposed ANN model outperformed other models and empirical formulas provided in design codes in terms of precision and accuracy.

- The ANN-based model, implemented in MATLAB, can effectively predict the shear strength of external BC joints made of reinforced concrete.
- Five main parameters, namely joint aspect ratio, joint transverse reinforcement, concrete compressive strength, beam reinforcement ratio, and joint width, were used to develop the ANN model.
- The ANN model's effectiveness was quantitatively assessed using the coefficient of determination (R^2), with R-squared values of 99%, 94%, and 98% obtained during the training, testing, and validation stages, respectively.
- Comparison of the ANN model results with experimental data showed strong agreement and better alignment compared to results calculated using various design codes such as ACI 318-14, EN 1998-1:2004, NZS 3101-1:2006, CSA A3.3:2004, AIJ:2010, and IS 13920:2016.
- The proposed SFF-ANN model, which combines the ANN model with experimental data, is considered an efficient tool for predicting the shear strength of interior joints exposed to cyclic loading.

In conclusion, this research contributes to the scientific field by introducing an ANN model that outperforms existing empirical formulas and design codes in accurately predicting the shear strength of reinforced concrete external BC joints. The study's findings have significant practical implications, as the developed model can be applied to real-world projects, providing engineers with a reliable tool for assessing the performance and structural integrity of external BC joints. This joint shear strength prediction model can be readily implemented into joint response models for the evaluation of earthquake performance and inelastic responses of building frames.

Consequently, the proposed model holds tremendous potential as a valuable resource for researchers and reinforced concrete engineers, enabling them to make precise estimations of the joint shear strength of beam-column connections. This model proves particularly advantageous in two key aspects: it operates within the input data ranges established in this study, ensuring accuracy, and it significantly reduces both time and cost compared to the construction of alternative numerical schemes. As such, this model emerges as an efficient and cost-effective tool for professionals in the field, streamlining the estimation process while maintaining reliability. Further research should focus on gathering field data and conducting comparative studies to validate the model's predictions and explore its applicability in diverse structural configurations.

7. REFERENCES

1. Mashhadi R, Dastan Diznab MA, Tehrani FM. Strut-and-tie model for predicting the shear strength of exterior beam-column joints without transverse reinforcement. Journal of Structural Engineering. 2022;148(2):04021256. https://doi.org/10.1061/(ASCE)ST.1943-541X.0003223
2. Alagundi S, Palanisamy T, editors. Neural network prediction of joint shear strength of exterior beam-column joint. Structures; 2022: Elsevier.
3. Marcos CJL, Silva DL, editors. Shear Strength Prediction of Unusual Interior Reinforced Concrete Beam-Column Joint Using Multi-Layer Neural Network: a Data Collection by Digital 3D Finite Element Simulation. 2022 XXV International Conference on Soft Computing and Measurements (SCM); 2022: IEEE.
4. Park SH, Yoon D, Kim S, Geem ZW, editors. Deep neural network applied to joint shear strength for exterior RC beam-column joints affected by cyclic loadings. Structures; 2021: Elsevier.
5. Murad YZ, Hunifat R, Wassel A-B. Interior reinforced concrete beam-to-column joints subjected to cyclic loading: Shear strength prediction using gene expression programming. Case Studies in Construction Materials. 2020;13:e00432. https://doi.org/10.1016/j.cscm.2020.e00432
6. Marie HS, Abu El-hassan K, Almetwally EM, El-Mandouh MA. Joint shear strength prediction of beam-column connections using machine learning via experimental results. Case Studies in Construction Materials. 2022;17:e01463. https://doi.org/10.1016/j.cscm.2022.e01463

7. Barbagallo F, Bosco M, Ghersi A, Marino EM, Sciacca F. A simple but effective capacity model for check and design of beam-column joints in RC seismic buildings. Procedia Structural Integrity. 2023;44:363-70. https://doi.org/10.1016/j.prostr.2023.01.048

8. Velasco MAP, Dela Cruz OG, Guades EJ, editors. Reinforced Concrete Beam–Column Joint: A Review of Its Cyclic Behavior. Advances in Civil Engineering Materials: Selected Articles from the 6th International Conference on Architecture and Civil Engineering (ICACE 2022), August 2022, Kuala Lumpur, Malaysia; 2023: Springer.

9. Hung C-C, Hsiao H-J, Shao Y, Yen C-H. A comparative study on the seismic performance of RC beam-column joints retrofitted by ECC, FRP, and concrete jacketing methods. Journal of Building Engineering. 2023;64:105691. https://doi.org/10.1016/j.jobe.2022.105691

10. Suhail R, Amato G, Alam MS, Broderick B, Grimes M, McCrum D. Seismic retrofitting of nonseismically detailed exterior reinforced concrete beam-column joint by active confinement using shape memory alloy wires. Journal of Structural Engineering. 2023;149(3):04023003. https://doi.org/10.1061/JSENDH.STENG-11843

11. Farzinpour A, Dehcheshmeh EM, Broujerdian V, Esfahani SN, Gandomi AH. Efficient boosting-based algorithms for shear strength prediction of squat RC walls. Case Studies in Construction Materials. 2023;18:e01928. https://doi.org/10.1016/j.cscm.2023.e01928

12. Sim H-J, Chun S-C, Kim I-H. Side-Face Blowout Strength of Large-Diameter High-Strength Headed Bars in a Single Layer or Two Layers Terminated within Exterior Beam–Column Joints. Journal of Structural Engineering. 2023;149(2):04022233. https://doi.org/10.1061/JSENDH.STENG-11450

13. Patel MK, Joshi S. A Review "Cyclic Performance of Beam-Column Joint under lateral loading".

14. Feng D-C, Fu B. Shear strength of internal reinforced concrete beam-column joints: intelligent modeling approach and sensitivity analysis. Advances in Civil Engineering. 2020;2020:1-19. https://doi.org/10.1155/2020/8850417

15. Zhang J, Zhao X, Gao Y, Guo W, Zhai Y. Shear Strength Prediction and Failure Mode Identification of Beam–Column Joints Using BPNN, RBFNN, and GRNN. Arabian Journal for Science and Engineering. 2023;48(4):4421-37. 10.1007/s13369-022-07001-2

16. Naderpour H, Sharei M, Fakharian P, Heravi MA. Shear strength prediction of reinforced concrete shear wall using ANN, GMDH-NN and GEP. Journal of Soft Computing in Civil Engineering. 2022;6(1):66-87. https://doi.org/10.22115/SCCE.2022.283486.1308

17. Alagundi S, Palanisamy T. Prediction of joint shear strength of RC beam-column joint subjected to seismic loading using artificial neural network. Sustainability, Agri, Food and Environmental Research. 2022;10. https://doi.org/10.7770/safer-V10N1-art2490

18. Yu Z, Xie W, Yu B, Cheng H. Probabilistic prediction of joint shear strength using Gaussian process regression with anisotropic compound kernel. Engineering Structures. 2023;277:115413. https://doi.org/10.1016/j.engstruct.2022.115413

19. Truong GT, Choi K-K, Nguyen T-H, Kim C-S. Prediction of shear strength of RC deep beams using XGBoost regression with Bayesian optimization. European Journal of Environmental and Civil Engineering. 2023:1-21. https://doi.org/10.1080/19648189.2023.2169357

20. Zayan HS, Mahmoud AS, Hamdullah DN. Shear transfer strength estimation of concrete elements using generalized artificial neural network models. Journal of the Mechanical Behavior of Materials. 2023;32(1):20220219. https://doi.org/10.1515/jmbm-2022-0219

21. Al-Bayati AF. Shear strength of reinforced concrete beam–column joints. Asian Journal of Civil Engineering. 2023;24(1):319-51. https://doi.org/10.1007/s42107-022-00505-0

22. Mabrouk R, Younis G, Ramadan O. Experimental Evaluation of the Punching Shear Strength of Interior Slab-Column Connection with Different Shear Reinforcement Details. Civil Engineering Journal, CEJ. 2022;8(09). http://dx.doi.org/10.28991/CEJ-2022-08-09-015

23. Singh V, Sangle K. Analysis of vertically oriented coupled shear wall interconnected with coupling beams. HighTech and Innovation Journal. 2022;3(2):230-42. https://doi.org/10.28991/HIJ-2022-03-02-010

24. Sfaksi OH, Bouheraoua A, Aider HA, Mechiche MO. Seismic Behavior of Reinforced Masonry Structure: Relation between the Behavior Factor and the Ductility. Civil Engineering Journal. 2022;8(10):2205-19. https://doi.org/10.28991/CEJ-2022-08-10-012

25. Hanson NW, Connor HW. Seismic resistance of reinforced concrete beam-column joints. Journal of the structural Division. 1967;93(5):533-60.

26. Karayannis CG, Sirkelis GM. Strengthening and rehabilitation of RC beam–column joints using carbon-FRP jacketing and epoxy resin injection. Earthquake Engineering & Structural Dynamics. 2008;37(5):769-90. https://doi.org/10.1002/eqe.785

27. Salim I. The influence of concrete strengths on the behaviour of external beam-column joints: Universiti Teknologi Malaysia Skudai, Malaysia; 2007.

28. Pantelides CP, Clyde C, Reaveley LD. Performance-based evaluation of reinforced concrete building exterior joints for seismic excitation. Earthquake spectra. 2002;18(3):449-80. https://doi.org/10.1193/1.1510447

29. Wong HF. Shear strength and seismic performance of non-seismically designed reinforced concrete beam-column joints: Hong Kong University of Science and Technology (Hong Kong); 2005.

30. Ghobarah A, Said A. Seismic rehabilitation of beam-column joints using FRP laminates. Journal of earthquake engineering. 2001;5(01):113-29. https://doi.org/10.1142/S1363246901000297

31. Tsonos A, Stylianidis K. Seismic retrofit of Beam-to-Column joints with high-strenght fiber jackets. European Earthquake Engineering. 2002;16(2):56-72.

32. Antonopoulos CP, Triantafillou TC. Experimental investigation of FRP-strengthened RC beam-column joints. Journal of composites for construction. 2003;7(1):39-49. https://doi.org/10.1061/(ASCE)1090-0268(2003)7:1(39)

33. Sarsam K, Phipps M. The shear design of in situ reinforced concrete beam–column joints subjected to monotonic loading. Magazine of Concrete Research. 1985;37(130):16-28. https://doi.org/10.1680/macr.1985.37.130.16

34. Filiatrault A, Lebrun I. Seismic rehabilitation of reinforced concrete joints by epoxy pressure injection technique. Special Publication. 1996;160:73-92.

35. Hoffschild TE. Retrofitting beam-to-column joints for improved seismic performance microform: University of British Columbia; 1992.

36. Park S, Mosalam KM, editors. Analytical and experimental study of RC exterior beam–column joints without transverse reinforcement. Proceedings of the 7th international conference on urban earthquake engineering (7CUEE) & 5th international conference on earthquake engineering (5ICEE); 2010.

37. Hassan WM. Analytical and experimental assessment of seismic vulnerability of beam-column joints without transverse reinforcement in concrete buildings: University of California, Berkeley; 2011.

Persian Abstract

چکیده

شکست اتصالات تیر و ستون نوع برشی در قاب های بتن مسلح (RC) در هنگام حملات شدید زلزله یک نگرانی حیاتی است. روش های سنتی برای تعیین ظرفیت برشی اتصال اغلب به دلیل در نظر گرفتن نادرست پارامترهای حاکم بر رفتار این اتصالات، دقت کافی ندارند. این مطالعه قابلیت‌های تکنیک‌های یادگیری ماشین را در پیش‌بینی ظرفیت برشی مشترک و حالت‌های شکست برای اتصالات تیر-ستون خارجی، با توجه به رفتار ساختاری پیچیده آن‌ها ارزیابی می‌کند. یک مدل شبکه عصبی مصنوعی (ANN) برای پیش‌بینی مقاومت برشی اتصالات تیر-ستون خارجی تقویت‌شده پیشنهاد شده‌استANN ،. جزء هوش مصنوعی که از تجربیات گذشته درس می گیرد، در مهندسی عمران محبوبیت پیدا می کند. مدل ANN با استفاده از مجموعه داده ای شامل خواص مواد، ابعاد نمونه و شرایط بارگذاری لرزه ای از تحقیقات تجربی قبلی توسعه یافته است. این مدل دوازده پارامتر ورودی را برای پیش‌بینی مقاومت برشی در اتصالات تیر-ستون خارجی در نظر می‌گیرد. آموزش و آزمایش مدل ANN با استفاده از کدهای طراحی ایجاد شده، فرمول های تجربی و یک الگوریتم خاص انجام می شود. نتایج نشان‌دهنده برتری شبکه عصبی مصنوعی پیش‌روی کم عمق (SFF-ANN) در مقایسه با رویکردهای قبلی است. اثربخشی یک مدل شبکه عصبی مصنوعی(ANN) به صورت کمی در این مطالعه با تمرکز بر عملکرد آن در مقایسه با کدهای طراحی مختلف که معمولاً در مهندسی سازه استفاده می‌شوند، ارزیابی شد. مدل با استفاده از ضریب تعیین (R^2) ارزیابی شد و مقادیر R-squared به ترتیب ۹۹٪، ۹٤٪ و ۹۸٪ در طول مراحل آموزش، آزمایش و اعتبارسنجی به دست آمد. این مطالعه اهمیت تقویت تیر را به عنوان یک عنصر کلیدی در برآورد ظرفیت برشی برای اتصالات تیر-ستون RC خارجی برجسته می‌کند. اگرچه مدل‌های پیشنهادی درجه بالایی از دقت را نشان می‌دهند، تحقیقات آینده باید بر روی توسعه مدل‌های بهبودیافته با استفاده از مجموعه داده‌های توسعه‌یافته و الگوریتم‌های پیشرفته برای تشخیص و عملکرد بهتر الگو تمرکز کند

IJE TRANSACTIONS A: Basics Vol. 37 No. 01, (January 2024) 83-93

International Journal of Engineering

Journal Homepage: www.ije.ir

Predictive Modelling and Optimization of Double Ring Electrode Based Cold Plasma Using Artificial Neural Network

S. K. Bhat, G. D. Deepak*

Department of Mechanical and Industrial Engineering, Manipal Institute of Technology, Manipal Academy of Higher Education, Manipal, Karnataka, India

P A P E R I N F O

Paper history:
Received 11 July 2023
Received in revised form 14 August 2023
Accepted 26 August 2023

Keywords:
Artificial Neural Network
Cold Plasma
Machine Learning
Biomedical Devices
Desirability Function Analysis
Ring Electrode

A B S T R A C T

Cold Atmospheric Pressure Plasma (CAP) is very potent and impactful technology implemented for both technological and biomedical applications. This paper focuses on the implementation of artificial neural network (ANN) for a novel double ring electrode based cold atmospheric pressure plasma which is to operated only in the glow discharge region for its application in biomedical field. ANN inherently helps in visualizing the effective output parameters such as peak discharge current, power consumed, jet length (with sleeve) and jet length (without sleeve) for given set of input parameters of supply voltage and supply frequency using machine learning model. The capability of the ANN model is demonstrated by predicting the output parameters of the CAP beyond the experimental range. Finally, the optimized settings of supply voltage and supply frequency will be determined using the composite desirability function approach to simultaneously maximize the peak discharge current, jet length (with sleeve) and jet length (without sleeve), and minimize the power consumption.

***doi**: 10.5829/ije.2024.37.01a.08*

1. INTRODUCTION

Plasma is considered the fourth state of matter and is considered as ionized gas (1). Plasma is generated due to the association of strong electromagnetic field, gas and heat. Generally, reactive nitrogen and oxygen species (RONS) (2) have a main role in atmospheric pressure plasma formation (APP). As the key components of air are oxygen and nitrogen, reactive oxygen species (ROS) comprise of hydroxide and oxygen radicals, while nitrogen oxides are included as reactive nitrogen species (RNS) (3). The APP generates neutral reactive species, free electron, atom such as oxygen (O) and molecules, radicals and nitrogen oxide (NO) (4-6). Cold atmospheric pressure plasma (CAP) is applications in many fields such as: sterilization (6), surface modification (7), food safety (8), water purification (9), textiles (10), medical (11) and others. The effect of CAP is very unique and it is for specific application.

Amongst the various technologies implemented for generating atmospheric cold plasma, there are two major categories which are dominant in clinical and preclinical research in the field of plasma medicine which includes plasma jets (12-15) and dielectric barrier discharge (DBD) (16, 17). In DBD's the plasma is ignited in the gap between the powered and ground electrode. There are various types of DBD's such as volume DBD, Surface DBD used for various applications. The plasma jet experimental typically comprises of tube-like structure such as quartz tube, the plasma is generated using a working gas such as argon that would flow inside this tube. There are various electrode designs such as DBD-like jets, DBD jets and single electrode jets. The gas flow inside the quartz tube enables the resulting plasma to be carried out and is focused on the target material to be treated. Mostly noble gases are used as working gases for the generation of plasma jet.

ANN has been applied successfully in plasma medicine; Lin et al. (18) implemented ANN approach for predicting gas compositions and gas temperature using spontaneous emission spectroscopy, wherein the ANN output is used to control the power consumption of the

*Corresponding Author Email: divya.deepak@manipal.edu (G. D. Deepak)

Please cite this article as: Bhat SK, Deepak GD. A New Comprehensive Model for Integrating Environmental, Economic, and Social Performance of Deep and Large-scale Open-Pit Copper Mines. International Journal of Engineering, Transactions A: Basics. 2024;37(01): 83-93.

device and gas injection rate, thereby optimizing the plasma chemistry. Furthermore, Wan et al. (19) implemented an ANN model to predict NO conversion by DBD in the N_2/O_2/NO system. Their ANN model results indicated that the primary factor influencing the production of NO_2 is the concentration of NO at the inlet, responsible for 36.22% of the effect. The other factors that impacted NO_2 production were discharge power at 23.52% and residence time at 26.25 %.

The cold plasma technology involves various important operating parameters, viz., supply voltage (SV), supply frequency (SF), pulse discharge current (PDC), jet length and power consumption (P) (11). From the perspective of development of CAP devices, it is of vital importance to determine the optimum levels of input parameters of supply voltage and supply frequency to achieve the desired levels of pulse discharge current, jet length and power consumption. Furthermore, since experimental tests usually have certain limitations with respect to the range of parameters, an accurate and reliable predictive model can be useful to make performance predictions beyond the range of parameters considered in the experiments. Recently, one of the robust and popular machine learning techniques called artificial neural network (ANN) has been implemented to predict the efficiency of CAP-based technologies in terms of the input parameters towards applications such as plasma treatment and CO_2 splitting (20, 21). However, there is a paucity of research in the literature on development of predictive models for the fundamental performance characteristics such as PDC, jet length and power consumption. This paper aims to develop an ANN model for the novel double ring electrode based cold atmospheric pressure plasma using a benchmark experimental data (11) to train, test and validate the model. The robustness of the neural network to model the physics of the cold plasma device is demonstrated by making performance predictions beyond the range of the experimental data used for training the model. Finally, the well-established statistical method of desirability function analysis (DFA) will be used to perform the multi-response optimization to determine the optimum settings of the input parameters for the best performance.

2. GEOMETRY AND EXPERIMENTAL SETUP

The double ring electrode configuration (11)examined in this paper comprises of quartz tube with nozzle as shown in Figure 1. Ring electrodes are the two metal sleeves that are put on top the nozzle indicated as 3 in Figure 1. One of these electrodes is connected to supply and another electrode is grounded. The nozzle outlet diameter is 3 mm and has been indicated as 2 (see Figure 1). The working gas used Argon enters through the inlet of quartz tube indicated as 1 (see Figure 1). The outer diameter and length of quartz tube is 25 mm and 155 mm, respectively. The quartz tube thickness is 1.5 mm. The diameter and axial length of ring electrodes are 4 mm and 18 mm respectively. The ring electrodes are separated by distance of 3 mm as indicated -3 in Figure 1. A quartz sleeve of 4 mm diameter and 15 mm length was placed on the nozzle of the quartz tube (see Figure 2) to observe the length of plasma jet without the effect of surrounding air. To examine the plasma jet length without the effect of surrounding air, a quartz sleeve of 15 mm length and 4 mm diameter was placed on nozzle of quartz tube (Figure 2). Jet length was examined for both without and with quartz sleeve.

The double ring electrode implemented in this paper has been subjected to supply voltages upto 6 kV and supply frequencies upto 25 kHz. Working gas employed was Argon as shown in Figure 2. The V-I characteristic of the developed DBD-based cold plasma jet (Figure 2) has been studied and the consumption of power has been analyzed at various input combinations (supply voltage and frequency). The supply frequency and voltage have been varied from 10 to 25 kHz and 3.5 to 6 kV, respectively. The gas flow rate is fixed at 1 liter/min. The experimental results of pulse discharge current (PDC), jet length without and with sleeve (JLwoS and JLwS) and power (P), for the various supply voltage and supply frequencies is listed in Table 1.

In this paper, ANN is implemented for the experimental data as listed in Table 1 to analyze and

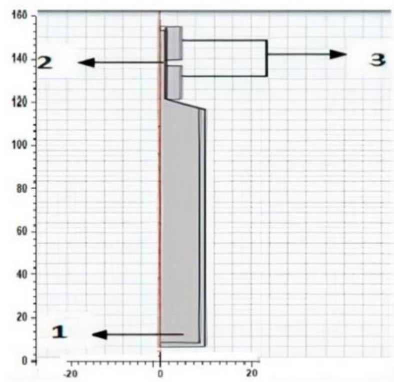

Figure 1. Geometry of double ring electrode based cold plasma jet using Argon

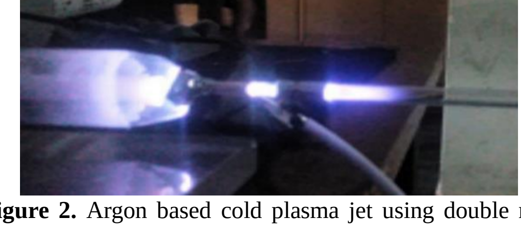

Figure 2. Argon based cold plasma jet using double ring electrode

TABLE 1. Experimental results [11]

Expt. No.	SV (kV)	SF (kHz)	PDC (mA)	JLwoS (mm)	JLwS (mm)	P (W)
1	3.5	10	152	2	5	0.28
2	4	10	160	4	7	0.33
3	4.5	10	176	7	9	0.46
4	5	10	144	12	15	0.46.
5	5.5	10	176	15	21	0.56
6	6	10	192	17	22	0.42
7	3.5	15	96	4	7	0.33
8	4	15	112	6	9	0.58
9	4.5	15	152	8	12	0.58
10	5	15	144	14	17	0.69
11	5.5	15	176	18	23	0.78
12	6	15	232	20	24	0.63
13	3.5	20	88	6	10	0.59
14	4	20	128	8	12	0.73
15	4.5	20	112	12	15	0.82
16	5	20	152	18	22	1.12
17	5.5	20	168	20	25	1.04
18	6	20	184	22	27	0.72
19	3.5	25	88	8	12	0.94
20	4	25	96	11	14	0.89
21	4.5	25	152	12	17	0.88
22	5	25	128	22	25	0.97
23	5.5	25	144	24	28	1.27
24	6	25	216	25	29	1.04

predict the output parameters (discharge current, jet length (with and without sleeve) and power consumption for higher values of supply voltage and supply current for the double ring electrode-based argon cold plasma jet.

3. ANN APPROACH

Artificial neural network (ANN) is a soft computing paradigm which derives its functionality through inspiration from the neurons in the biological nervous systems. ANN operates with a similar principle of that of biological neurons wherein the information processing takes place in the individual neurons starting with a feedforward training process, also involving a backpropagation feedback loop to estimate the errors in prediction, to derive a mathematical formulation to model the relationship between process parameters and the output responses (22).

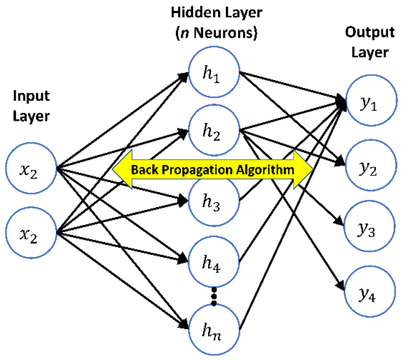

Figure 3. General architecture of a single hidden layer NN model with *n* neurons

In the simplest configuration, a neural network model consists of an input layer which consists of the input parameters, followed by a hidden layer which consists of an arbitrary number of neurons according to the requirements of the problem, and finally the output layer which is nothing but the list of the output parameters (Figure 3). In this study, a multi-layer perceptron ANN model was developed using the *fitnet* function in MATLAB (MathWorks, Natick, Massachusetts, USA). The multi-layer perception basically falls into the category of neural networks with more than one hidden layer. To ensure a good predictive accuracy of the model, the possibility of having one or more hidden layers was investigated. The Levenberg-Marquardt algorithm was employed for training the model (23). The inputs are the two control parameters, i.e., SV and SF; and the outputs are the four response parameters, PDC, JLwS, JLwoS, and P.

The input data was divided into three sets such that 70% of it was used for training and remaining 15% each were used for testing and validation of the network. Numerous trials were conducted with the number of hidden layers and the number of neurons in them to arrive at a model which provided a good descriptive performance (refer Appendix for details), which is then made use to make predictions beyond the experimental range of control parameters.

Each neuron in the artificial neural network consists of three components, weights ($w_{k,j}$), biases (b_k), and an activation function. The weights and biases are fed to individual neurons along with the inputs to obtain the mathematical operation in each neuron as Equation (1) (24):

$$U_k = b_k + \sum_{j=1}^{n} w_{k,j} \times I_j \qquad (1)$$

where, n is the number of inputs and k signifies the k^{th} neurons in the hidden layer. The same equation can be written in the matrix form as Equation 2 (22):

$$U_k = \begin{pmatrix} w_{11} & \cdots & w_{1n} \\ \vdots & \ddots & \vdots \\ w_{m1} & \cdots & w_{mn} \end{pmatrix}_{m\times n} \begin{bmatrix} I_1 \\ \vdots \\ I_n \end{bmatrix}_{n\times 1} + \begin{bmatrix} b_1 \\ \vdots \\ b_n \end{bmatrix}_{m\times 1} = \begin{bmatrix} U_1 \\ \vdots \\ U_n \end{bmatrix}_{m\times 1} \tag{2}$$

The inputs and outputs in each neural network are typically normalized between $[-1, +1]$. Finally, the overall mathematical relationship to predict the output 'Y' can be written as Equation 3 (22):

$$Y = b_{output-layer} + \sum_{k=1}^{m} LW_k \times f(U_k) \tag{3}$$

where, $b_{output-layer}$ is the output layer weight and LW_k is the layer weight matrix. The activation function $f(x)$ is a tan-sigmoid (*tansig*) or hyperbolic tangent function as shown by Equation 4 (23):

$$f(U_k) = \frac{2}{1-e^{-2U_k}} - 1 \tag{4}$$

In this study, the *tansig* function was used for the connections between the input and hidden layers and the hidden layers to output layers [20-22]. The descriptive accuracy of the model was evaluated based on the coefficient of determination (R^2), which is given by Nateghi- and Ahmadi (24):

$$R^2 = 1 - \frac{\sum_i^n \left(y_i - y_{\exp-i}\right)^2}{\sum_i^n \left(y_i - \bar{y}_{\exp-i}\right)^2} \tag{5}$$

where, y_i and y_{exp-i} are the model predictions and the corresponding experimental data, respectively, and $\bar{y}_{exp-i}$ indicates the mean of the experimental response, for a particular response parameter.

4. DESIRABILITY FUNCTION ANALYSIS

Desirability Function Analysis (DFA) is a statistical method used for multi-response optimization, particularly in the field of experimental design and quality improvement. It provides a way to simultaneously optimize multiple responses or variables in a process or system. The main idea behind DFA is to convert individual response variables into a single overall desirability value.

Firstly, the individual desirability function for each factor setting is calculated. This is called as the desirability index (DI). Next, the overall desirability for a particular combination of factor settings, termed as composite desirability index (CDI), is calculated as the geometric mean of the individual desirability values. This approach ensures that all responses contribute equally to the overall desirability assessment [25-27].

$$d_i = \begin{cases} 0 & y_i < y_{\min} \\ \left(\dfrac{y_i - y_{\max}}{y_{\max} - y_{\min}}\right)^s & y_{\min} \le y_i \le y_{\max}, s \ge 0 \\ 1 & y_i > y_{\max} \end{cases} \tag{6}$$

$$d_i = \begin{cases} 1 & y_i < y_{\min} \\ \left(\dfrac{y_i - y_{\max}}{y_{\min} - y_{\max}}\right)^r & y_{\min} \le y_i \le y_{\max}, r \ge 0 \\ 0 & y_i > y_{\max} \end{cases} \tag{7}$$

The goal of DFA is to find the factor settings that maximize the overall desirability (or CDI). This can be achieved using optimization techniques such as response surface methodology. By optimizing the overall desirability, DFA helps identify the factor settings that simultaneously optimize multiple responses and improve the quality or performance of a process or system.

The principle of DFA first propounded by Harrington in 1965 (25) was refined and brought to its presently used form by Derringer and Suich in 1980 (26). The method of DFA is enunciated as follows. Firstly, based on the criteria of whether a response variable needs to be maximized (larger-the-better) or minimized (smaller-the-better), the desirability index (DI) for each factor setting combination is calculated using the Equations 6 and 7, respectively (27).

Equations 6 and 7, y_{min} and y_{max} indicate the minimum and maximum of the response y_i. The exponents s and r are the weights assigned to each response variable. Here, we assign equal weightage to all the response, implying, $s = r = 0.25$. In this study, the PDC and P were subjected to the condition of smaller-the-better, whereas the larger-the-better condition was imposed on JLwS and JLwoS. Now, the composite desirability index (CDI) is computed as follows (27):

$$CDI_i = \left(d_{i,1}^{w_1} \times d_{i,2}^{w_2} \times d_{i,3}^{w_3} \times \ldots \times d_{i,k}^{w_k}\right)^{1/k} \tag{8}$$

where, k indicates the number of responses (here, $k = 4$), $d_{i,k}^{w_k}$ represents the desirability index of the k^{th} response and w_1, w_2, w_3,…, are the weightages assigned to individual responses, such that $\sum_i^k w_i = 1$. Here, we assign equal weightage, implying, $w_i = 0.25$. Now, the mean of factor effect at each level is analyzed to obtain the best combination of the control parameters to achieve the maximum possible CDI (27). The maximum possible CDI signifies the optimized control parameter setting combination at which the multiple responses are achieving their best possible combinatorial outcome.

5. RESULTS AND DISCUSSION

5. 1. Descriptive and Predictive Modeling using Artificial Neural Network The artificial neural network for modeling the performance of the double ring electrode based cold plasma jet was developed by a trial-and-error approach by varying the number of hidden layers and the number of neurons in them. The number of layers were varied from 1 to 3, and in each layer, the number of neurons were changed from 3 to 20. During these trials, the descriptive accuracy of the model was evaluated by means of the coefficient of determination (R^2) for each of the four performance parameters (PDC, JLwS, JLwoS and P). It was found that, a two-layered ANN with 8 and 12 neurons, in the first and second hidden layers, respectively (Figure 4), provided the best descriptive accuracy with $R^2 > 0.96$ for all the parameters. Figure 5 graphically depicts the descriptive accuracy of the ANN model for the parameters. Table 2 (Expt. No. 1 – 24) lists the numerical predictions of the ANN model for the experimental data shown in Table 1.

A robust model not only needs to accurately model the experimental data, but also make predictions for new set of data beyond the experimental range, while being consistent with the physics of the problem. After confirming the descriptive accuracy of the ANN model, its predictive capability is investigated by forecasting the performance parameters beyond the range of control parameters used in the experiments. Table 2 (Expt. No.25 – 56) shows the predictions of the ANN model for 6.5 kV $\leq$ SV $\leq$ 10 kV and 10 kHz $\leq$ SF $\leq$ 25 kHz.

The split of the datasets for training, testing and validation steps were chosen randomly in each trial using the MATLAB function dividerand, which splits the data based on random indices. For the optimum model (2-8-20-4) the expt no. 1, 3, 5, 7, 8, 9, 10, 11, 12, 13, 14, 15, 17, 18, 20, 21, 23 were used for training, expt no. 16, 29, 22, 24 were used for validation and remaining (2, 4, 6, 19) were used for testing purposes.

From Table 2, for (3 kV, 10 kHz) the power consumed in the plasma is 0.33 W with short plasma jet lengths (5.1 mm (JLwS), 2.1 mm (JLwoS)), as the energy is consumed by the seed electrons for plasma generation. Whereas, when supply voltage approaches 6 kV, 10 kHz then power consumption is 0.56 W with longer jet lengths (26.1 mm (JLwS), 20.3 mm (JLwoS)) indicating that power is utilized for plasma generation. It is also observed that plasma jet lengths with sleeve for most cases of supply voltages and frequency (3.5 kV – 10 kV,

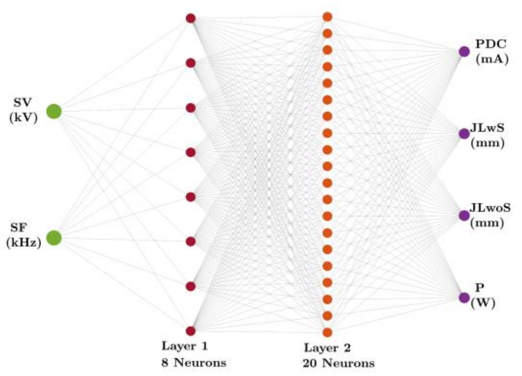

Figure 4. ANN architecture with '2-8-20-4' topology

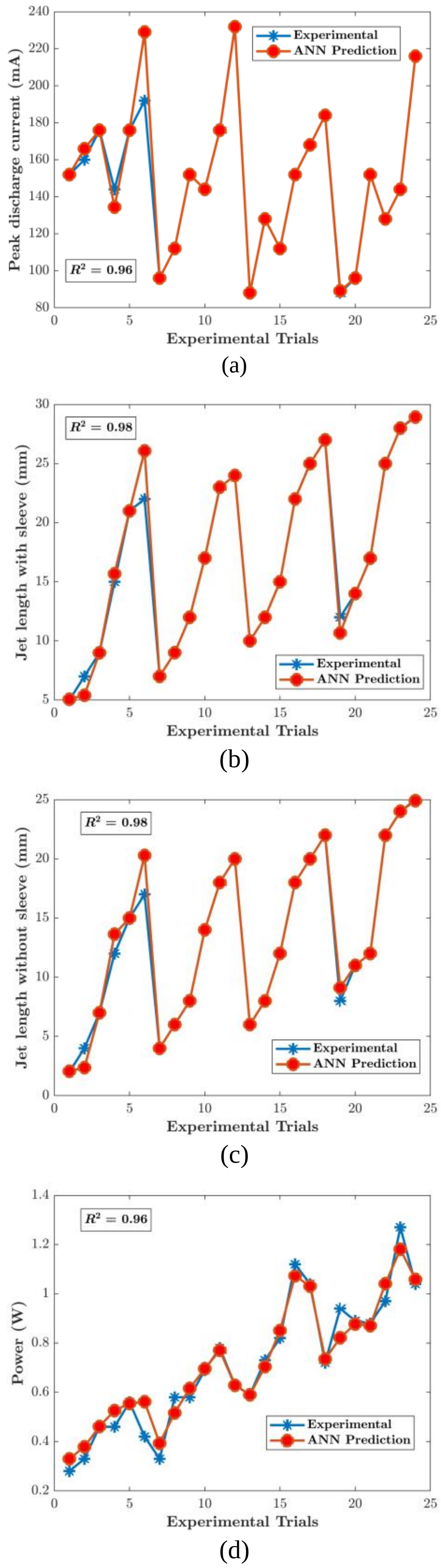

Figure 5. Comparison of ANN predictions for (a) PDC, (b) JLwS, (c) JLwoS, (d) P, with the corresponding experimental responses

TABLE 2. ANN predictions for within the range of experimental data provided in Table 1 and beyond the range of supply voltage (6 kV ≤ SV ≤ 10 kV and 10 kHz ≤ SF ≤ 25 kHz)

Expt. No.	SV (kV)	SF (kHz)	PDC (mA)	JLwoS (mm)	JLwS (mm)	P (W)
1	3.5	10	152.0	5.1	2.1	0.33
2	4	10	165.9	5.4	2.4	0.38
3	4.5	10	176.0	9.0	7.0	0.46
4	5	10	134.4	15.7	13.6	0.53
5	5.5	10	176.0	21.0	15.0	0.55
6	6	10	229.1	26.1	20.3	0.56
7	3.5	15	96.0	7.0	4.0	0.39
8	4	15	112.0	9.0	6.0	0.52
9	4.5	15	152.0	12.0	8.0	0.62
10	5	15	144.0	17.0	14.0	0.70
11	5.5	15	176.0	23.0	18.0	0.77
12	6	15	231.9	24.0	20.0	0.63
13	3.5	20	88.1	10.0	6.0	0.59
14	4	20	128.0	12.0	8.0	0.70
15	4.5	20	112.0	15.0	12.0	0.85
16	5	20	152.0	22.0	18.0	1.07
17	5.5	20	168.0	25.0	20.0	1.03
18	6	20	184.0	27.0	22.0	0.74
19	3.5	25	89.1	10.7	9.1	0.82
20	4	25	96.0	14.0	11.0	0.88
21	4.5	25	152.0	17.0	12.0	0.87
22	5	25	128.0	25.0	22.0	1.04
23	5.5	25	144.0	28.0	24.0	1.18
24	6	25	216.0	28.9	24.9	1.06
25	6.5	10	232.0	26.6	22.5	0.53
26	7	10	232.0	26.1	23.2	0.52
27	7.5	10	232.0	25.7	23.5	0.51
28	8	10	232.0	25.5	23.6	0.50
29	8.5	10	232.0	25.4	23.6	0.50
30	9	10	232.0	25.4	23.6	0.50
31	9.5	10	232.0	25.4	23.6	0.50
32	10	10	232.0	25.4	23.6	0.50
33	6.5	15	232.0	25.6	22.9	0.54
34	7	15	232.0	25.8	23.4	0.52
35	7.5	15	232.0	25.7	23.5	0.51
36	8	15	232.0	25.6	23.6	0.51
37	8.5	15	232.0	25.5	23.6	0.50
38	9	15	232.0	25.5	23.6	0.50
39	9.5	15	232.0	25.4	23.6	0.50
40	10	15	232.0	25.4	23.6	0.50
41	6.5	20	220.0	27.7	23.5	0.56
42	7	20	229.2	27.5	23.6	0.52
43	7.5	20	231.5	27.1	23.4	0.51
44	8	20	231.9	26.8	23.3	0.51
45	8.5	20	232.0	26.5	23.3	0.51
46	9	20	232.0	26.2	23.4	0.51
47	9.5	20	232.0	26.0	23.5	0.51
48	10	20	232.0	25.9	23.5	0.51
49	6.5	25	223.7	29.0	25.0	0.85
50	7	25	222.9	29.0	25.0	0.74
51	7.5	25	220.7	28.9	24.9	0.67
52	8	25	217.8	28.9	24.9	0.62
53	8.5	25	216.2	28.8	24.7	0.58
54	9	25	218.1	28.6	24.5	0.55
55	9.5	25	223.4	28.3	24.2	0.53
56	10	25	228.6	27.8	23.8	0.52

10 kHz – 25 kHz) is longer as compared to jet length without sleeve as seen in Table 2. This is because the sleeve shields the plasma jet coming out from electronegative gases such as water vapor that impede the propagation of the plasma jet. The power consumed by the plasma jet increases as the supply voltage and frequency reaches up to 6 kV, 25 kHz (1.06 W). Any higher supply voltage resulted in the power being lost in heating of dielectric tube and not utilized in the plasma generation which is clearly seen in Table 2 indicating the decrease in power consumed (0.85 W at 6.5 kV, 25 kHz).

It can be further seen from Table 2 that at higher voltages of (6.5 kV, 10 kHz – 25 kHz) there is only variation of power consumption (0.53 W – 0.85 W) by the plasma as most of the power supplied is not utilized in the plasma generation but lost in the dielectric material as thermal dissipation, leading to heating of the dielectric tube. However, at (6.5 kV, 10 kHz – 25 kHz) the plasma jet length both with and without sleeve increases (26.6 mm – 29 mm (JLwS), 22.5 mm – 25 mm (JLwoS)) with increase in supply frequency. This is due to the higher energy absorbed by the seed electrons at higher supply frequency (20 kHz – 25 kHz) resulting in longer jet lengths as seen in Table 2.

A similar result has been observed at (7.5 kV, 10 kHz – 25 kHz) where there is only slight variation in the power consumed (0.51 W – 0.67 W) due to supply power being lost in thermal dissipation of the material. Further higher voltages of 8.5 kV – 10 kV (10 kHz – 25 kHz) also show only a slight variation in the power consumption as the supply power is lost as thermal dissipation. However, at (7.5 kV, 10 kHz – 25 kHz) the plasma jet length both with and without sleeve increases (25.7 mm – 28.5 mm (JLwS), 22.5 mm – 25 mm (JLwoS)) with increase in supply frequency. This is due to the higher energy absorbed by the seed electrons at higher supply frequencies (20 kHz – 25 kHz) resulting in longer jet lengths as seen in Table 2.

But at supply voltage of (8.5 kV – 10 kV, 25 kHz) there is hardly any variation of power consumed as seen in Table 2; in fact, the power consumed reduces from 0.58 W (8.5 kV/25 kHz) to 0.52 W (10 kV/25 kHz) due to power supply lost in thermal dissipation of dielectric material and also as the plasma discharge approaches the arc discharge region which is not suitable for biomedical applications. Due to this thermal dissipation heat loss at (8.5 kV – 10 kV, 25 kHz) it must be observed that there is a decrease in plasma jet length (28.8 mm – 27.8 mm (JLwS), 24.7 mm – 23.8 mm (JLwoS)) which is evidently indicating that the power supply is not being utilized in the generation of plasma.

5. 2. Multi-Response Optimization using DFA and Optimum Level Prediction using ANN

For the multi-response optimization, firstly, the desirability indices (d_i) are calculated using Equations 6 and 7. The parameters JLwS and JLwoS were maximized using Equation 6, whereas PDC and P were minimized using Equation 7. Table 3 shows the d_i of the four response parameters (PDC, JLwS, JLwoS and P) for each experimental trial shown in Table 2 under the column of individual desirability (d_i). Subsequently, the composite desirability indices (CDI) are calculated to take simultaneously optimize the multiple response parameters (Table 3). Finally, the values of CDI are ranked in the descending order from highest to the lowest value to determine the best possible combination of the control parameter to achieve the best performance of the double ring electrode based cold plasma jet. It is observed that, Expt. No. 22 with SV = 5 kV and SF = 25 kHz provides the best performance (highlighted in boldface in Table 3).

To statistically evaluate the factor effects on CDI, its main effect plot is shown in Figure 6(a). It is found that the mean of means of CDI becomes maximum for the control parameter setting of SV = 5 kV and SF = 25 kHz, which is consistent with the results of DFA. Further, a contour plot of CDI is presented in Figure 6(b), wherein its variation is better visualized with respect to the interaction of SV and SF. Here, it is observed that SV < 6 kV results in CDI > 0.6 for almost the entire range of SF. However, for SV > 6 kV, the SF needs to be > 23 kHz to obtain a higher performance output. Also, it can be ascertained that SV = 5 kV and SF = 25 kHz yields the best output since it achieves the maximum CDI (> 0.8).

Regarding the fact that plasma processes require several factors, each of which may have a substantial effect on plasma production. An artificial neural network (ANN) can be used to analyze and predict the impact of such elements with different values operational parameters (supply voltage & supply frequency). For instance, in our study the pulsed power supply cannot be operated at higher voltages such as 7 kV- 10 kV due to physical constraints of the device. Hence, ANN served to be a potent predictive tool for estimating the performance of the device with higher level of accuracy at those operational range (7-10 kV). Also, ANN is highly impactful in analyzing the sensitivity of each of input variables with the performance output such as power consumption, jet length (with/without sleeve).

TABLE 3. Estimated desirability indices using DFA

Expt. No.	Individual desirability (d_i)				CDI	Rank
	PDC	JLwoS	JLwS	P		
1	0.8633	0.0000	0.0000	1.0000	0.0000	46
2	0.8409	0.5373	0.5430	0.9871	0.7015	31
3	0.7897	0.6389	0.6828	0.9511	0.7566	29
4	0.8842	0.8034	0.8120	0.9511	0.8606	7
5	0.7897	0.9036	0.8671	0.9202	0.8687	4
6	0.7260	0.9174	0.8987	0.9626	0.8712	3
7	0.9858	0.5373	0.5430	0.9871	0.7300	30
8	0.9554	0.6389	0.6458	0.9137	0.7747	26
9	0.8633	0.7349	0.7147	0.9137	0.8023	21
10	0.8842	0.8409	0.8499	0.8749	0.8623	6
11	0.7897	0.9306	0.9133	0.8388	0.8662	5
12	0.0000	0.9433	0.9406	0.8967	0.0000	46
13	1.0000	0.6756	0.6458	0.9104	0.7939	24
14	0.9219	0.7349	0.7147	0.8594	0.8031	20
15	0.9554	0.8034	0.8120	0.8211	0.8458	9
16	0.8633	0.9174	0.9133	0.6239	0.8196	18
17	0.8165	0.9554	0.9406	0.6943	0.8448	11
18	0.7598	0.9785	0.9657	0.8633	0.8873	2
19	1.0000	0.7349	0.7147	0.7598	0.7948	23
20	0.9858	0.7825	0.7909	0.7871	0.8325	13
21	0.8633	0.8409	0.8120	0.7922	0.8267	15
22*	**0.9219**	**0.9554**	**0.9657**	**0.7419**	**0.8913**	**1**
23	0.8842	0.9894	0.9889	0.0000	0.0000	46
24	0.5774	1.0000	1.0000	0.6943	0.7957	22
25	0.0913	0.9738	0.9713	0.9298	0.5323	35
26	0.0000	0.9684	0.9801	0.9329	0.0000	46
27	0.0000	0.9636	0.9832	0.9360	0.0000	46
28	0.0000	0.9612	0.9842	0.9391	0.0000	46
29	0.0000	0.9603	0.9845	0.9391	0.0000	46

30	0.0000	0.9601	0.9848	0.9391	0.0000	46
31	0.0000	0.9598	0.9848	0.9391	0.0000	46
32	0.0000	0.9598	0.9848	0.9391	0.0000	46
33	0.0000	0.9623	0.9762	0.9267	0.0000	46
34	0.0000	0.9646	0.9823	0.9329	0.0000	46
35	0.0000	0.9637	0.9837	0.9360	0.0000	46
36	0.0000	0.9625	0.9842	0.9360	0.0000	46
37	0.0000	0.9617	0.9844	0.9391	0.0000	46
38	0.0000	0.9611	0.9847	0.9391	0.0000	46
39	0.0000	0.9607	0.9847	0.9391	0.0000	46
40	0.0000	0.9603	0.9848	0.9391	0.0000	46
41	0.5374	0.9864	0.9834	0.9202	0.8322	14
42	0.3738	0.9842	0.9839	0.9329	0.7623	28
43	0.2475	0.9798	0.9821	0.9360	0.6871	32
44	0.1535	0.9757	0.9811	0.9360	0.6090	33
45	0.0913	0.9724	0.9812	0.9360	0.5344	34
46	0.0000	0.9698	0.9819	0.9360	0.0000	46
47	0.0000	0.9676	0.9828	0.9360	0.0000	46
48	0.0000	0.9657	0.9835	0.9360	0.0000	46
49	0.4894	0.9998	0.9996	0.8071	0.7926	25
50	0.5008	0.9997	0.9995	0.8554	0.8089	19
51	0.5297	0.9995	0.9991	0.8823	0.8266	16
52	0.5607	0.9989	0.9985	0.9002	0.8423	12
53	0.5758	0.9977	0.9971	0.9137	0.8506	8
54	0.5571	0.9956	0.9946	0.9235	0.8448	10
55	0.4941	0.9921	0.9911	0.9298	0.8198	17
56	0.3914	0.9876	0.9873	0.9329	0.7725	27

*The double ring electrode-based argon cold plasma jet operating conditions corresponding to the highest composite desirability.

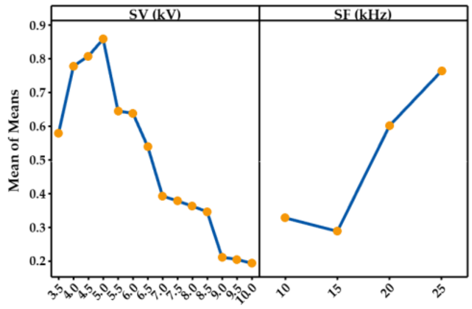

(a)

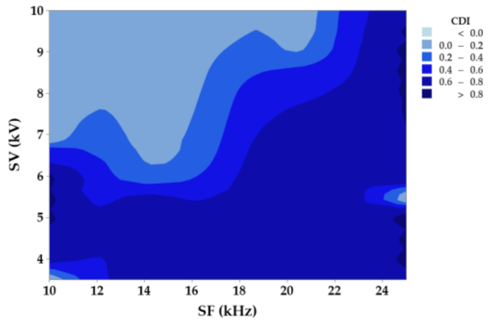

(b)

Figure 6. (a) Main effect plot and (b) contour plot of composite desirability with respect to SV and SF

5. 3. Combinatorial Effects of Supply Voltage and Supply Frequency on the Responses To visually analyze the effects of SV and SF on the output parameters, Figure 7 presents the 3D surface plots of the experimental responses, PDC, JLwS, JLwoS and P with respect to variations in SV and SF. From Figure 7(a), it is observed that, PDC increases from 100 mA to 200 mA with increase in SV from 3.5 kV to 6 kV. However, the effect of SF appears to be more nonlinear with peaks observed near 15 kHz and 25 kHz. The effects on JLwS and JLwoS are more straightforward (Figure 7(b) and (c)). Both JLwS and JLwoS are found to increase with rise in SV and SF, both as individual and interaction effects, yielding a maximum of ≥ 25 mm at the highest values of SV and SF. Another observation is that, SV has a greater influence than SF on both JLwS and JLwoS. The power consumption (P) reaches a minimum of around 0.3 W at the minimum values of both SV and SF (Figure 7(d)). Comparing the effects of the two control parameters, it is found that, SF induces a greater change in P compared to SV.

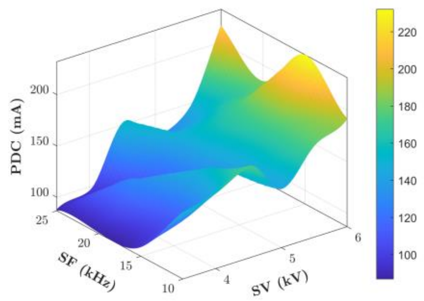

(a)

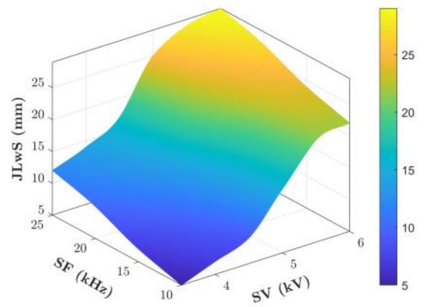

(b)

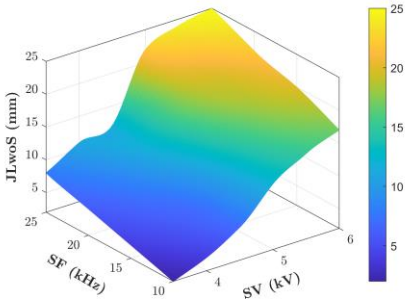

(c)

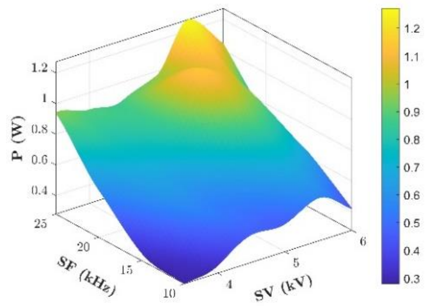

(d)

Figure 7. 3D surface plots showing the contours of responses: (a) PDC, (b) JLwS, (c) JLwoS, (d) P, with respect to the variations in the control parameters: SV and SF

6. CONCLUSIONS

This work presents a modeling and optimization methodology for the performance of the double ring electrode-based argon cold plasma jet using ANN and DFA techniques. The feedforward backpropagation ANN model with '2-8-20-4' topology using the Levenberg-Marquardt algorithm and *tansig* activation function accurately described the experimental responses of pulse discharge current, jet length with and without sleeve, and power consumption ($R^2 > 0.96$) throughout the experimental range: 3.5 kV ≤ SV ≤ 6 kV and 10 kHz ≤ SF ≤ 25 kHz. The optimization using DFA revealed that SV = 5 kV and SF = 25 kHz yielded the best multi-response performance of PDC = 128 mA, JLwS = 25 mm, JLwoS = 22 mm and P = 0.97 W. The interaction effect analysis of composite desirability index showed that SV < 6 kV is advisable for a good performance (CDI > 0.6) for the entire range of 10 kHz ≤ SF ≤ 25 kHz. The analysis of combinatorial effects of SV and SF showed that JLwS and JLwoS become maximum at SV = 6 kV and SF = 25 kHz. PDC becomes minimum near SV = 3.5 kV and 15 kHz ≤ SF ≤ 25 kHz, and P is minimized at SV = 3.5 kV and SF = 10 kHz. The findings of this study demonstrated that the proposed ANN model can be used to evaluate, obtain insights on, and predict the performance of the double ring electrode-based argon cold plasma jet. The results of this study would serve as a benchmark for development of such fundamental predictive models for various types of cold plasma technologies and their optimization.

7. REFERENCES

1. Laroussi M, Lu X. Room-temperature atmospheric pressure plasma plume for biomedical applications. Applied Physics Letters. 2005;87(11). https://doi.org/10.1063/1.2045549
2. Janda M, Martišovitš V, Hensel K, Machala Z. Generation of antimicrobial NO x by atmospheric air transient spark discharge. Plasma Chemistry and Plasma Processing. 2016;36:767-81. https://link.springer.com/article/10.1007/s11090-016-9694-5
3. Klämpfl TG, Isbary G, Shimizu T, Li Y-F, Zimmermann JL, Stolz W, et al. Cold atmospheric air plasma sterilization against spores and other microorganisms of clinical interest. Applied and environmental microbiology. 2012;78(15):5077-82. https://doi.org/10.1128%2FAEM.00583-12
4. Sands BL, Ganguly BN, Tachibana K. A streamer-like atmospheric pressure plasma jet. Applied Physics Letters. 2008;92(15). https://doi.org/10.1063/1.2909084
5. Girard-Lauriault PL, Mwale F, Iordanova M, Demers C, Desjardins P, Wertheimer MR. Atmospheric pressure deposition of micropatterned nitrogen-rich plasma-polymer films for tissue engineering. Plasma Processes and Polymers. 2005;2(3):263-70. http://dx.doi.org/10.1002/ppap.200400092
6. Laroussi M. Low-temperature plasmas for medicine? IEEE Transactions on plasma science. 2009;37(6):714-25. http://dx.doi.org/10.1109/TPS.2009.2017267
7. Kong MG, Kroesen G, Morfill G, Nosenko T, Shimizu T, Van Dijk J, et al. Plasma medicine: an introductory review. new Journal of Physics. 2009;11(11):115012. https://doi.org/10.1088/1367-2630/11/11/115012
8. Morrison KA, Asanbe O, Dong X, Weinstein AL, Toyoda Y, Guevara D, et al. Rapid sterilization of cell phones using a novel portable non-thermal plasma device. Plasma Medicine. 2015;5(1). http://dx.doi.org/10.1615/PlasmaMed.v5.i1.50
9. Mansouri J, Harrisson S, Chen V. Strategies for controlling biofouling in membrane filtration systems: challenges and opportunities. Journal of Materials Chemistry. 2010;20(22):4567-86. https://doi.org/10.1039/B926440J
10. Qi K, Daoud WA, Xin JH, Mak CL, Tang W, Cheung W. Self-cleaning cotton. Journal of Materials Chemistry. 2006;16(47):4567-74. https://doi.org/10.1039/B610861J
11. Deepak GD, Joshi N, Pal U, Prakash R. Electrical characterization of atmospheric pressure dielectric barrier discharge-based cold plasma jet using ring electrode configuration. Laser and Particle Beams. 2016;34(4):615-20. https://doi.org/10.1017/S0263034616000501
12. Weltmann KD, Kindel E, von Woedtke T, Hähnel M, Stieber M, Brandenburg R. Atmospheric-pressure plasma sources: Prospective tools for plasma medicine. Pure and Applied Chemistry. 2010;82(6):1223-37. https://doi.org/10.1351/PAC-CON-09-10-35
13. Von Woedtke T, Reuter S, Masur K, Weltmann K-D. Plasmas for medicine. Physics Reports. 2013;530(4):291-320. https://doi.org/10.1016/j.physrep.2013.05.005
14. Deepak GD, Joshi N, Prakash R. Model analysis and electrical characterization of atmospheric pressure cold plasma jet in pin electrode configuration. AIP Advances. 2018;8(5). https://doi.org/10.1063/1.5023072
15. Divya Deepak G, Joshi N, Pal DK, Prakash R. A low power miniaturized dielectric barrier discharge based atmospheric

pressure plasma jet. Review of Scientific Instruments. 2017;88(1). https://doi.org/10.1063/1.4974101

16. Deepak GD, Joshi NK, Prakash R, Pal U. Electrical characterization of argon and nitrogen based cold plasma jet. The European Physical Journal Applied Physics. 2018;83(2):20801. https://doi.org/10.1051/epjap/2018180057
17. Tanaka H, Ishikawa K, Mizuno M, Toyokuni S, Kajiyama H, Kikkawa F, et al. State of the art in medical applications using non-thermal atmospheric pressure plasma. Reviews of Modern Plasma Physics. 2017;1:1-89. http://dx.doi.org/10.1007/s41614-017-0004-3
18. Lin L, Yan D, Lee T, Keidar M. Self-Adaptive Plasma Chemistry and Intelligent Plasma Medicine. Advanced Intelligent Systems. 2022;4(3):2100112. https://doi.org/10.1063/5.0096789
19. Wan C, Bao H, Chen Z, Lin Q, Liu S, Wu W, et al. The prediction of nitric oxide conversion by dielectric barrier discharge using an artificial neural network model. Journal of the Energy Institute. 2022;101:96-110. https://doi.org/10.1016/j.fochms.2022.100132
20. Nazari RR, Hajizadeh K. Modeling the performance of cold plasma in CO2 splitting using artificial neural networks. AIP Advances. 2022;12(8). http://dx.doi.org/10.1016/j.conbuildmat.2015.07.074
21. Jaddu S, Abdullah S, Dwivedi M, Pradhan RC. Multipin cold plasma electric discharge on hydration properties of kodo millet flour: Modelling and optimization using response surface methodology and artificial neural network–Genetic algorithm. Food Chemistry: Molecular Sciences. 2022;5:100132. https://doi.org/10.1016/j.sciaf.2020.e00413
22. Gholami A, Bonakdari H, Fenjan SA, Akhtari AA. Flow variables prediction using experimental, computational fluid dynamic and artificial neural network models in a sharp bend. International Journal of Engineering, Transaction A: Basics, . 2016;29(1):14-22. 10.5829/idosi.ije.2016.29.01a.03
23. Rajeev D, Dinakaran D, Kanthavelkumaran N, Austin N. Predictions of tool wear in hard turning of AISI4140 steel through artificial neural network, fuzzy logic and regression models. International Journal of Engineering, Transaction A: Basics. 2018;31(1):32-7. 10.5829/ije.2018.31.01a.05
24. Nateghi-A F, Ahmadi MH. Prediction of engineered cementitious composite material properties using artificial neural network. International Journal of Engineering, Transaction B: Applications. 2019;32(11):1534-42. 10.5829/IJE.2019.32.11B.04
25. Harrington EC. The desirability function. Industrial quality control. 1965;21(10):494-8.
26. Derringer G, Suich R. Simultaneous optimization of several response variables. Journal of quality technology. 1980;12(4):214-9. https://doi.org/10.1080/00224065.1980.11980968
27. Devarajaiah D, Muthumari C. Evaluation of power consumption and MRR in WEDM of Ti–6Al–4V alloy and its simultaneous optimization for sustainable production. Journal of the Brazilian Society of Mechanical Sciences and Engineering. 2018;40:1-18. http://dx.doi.org/10.1007/s40430-018-1318-y

8. APPENDIX

The results of various trails conducted to obtain the best accuracy ANN structure (shown in bold) are shown in Table 4. For additional quantitative comparison, the error metrics mean square error (MSE) and mean absolute percentange error (MAPE) have been included:

$$MSE = \frac{1}{n}\sum\left(y - \bar{y}\right)^2 \tag{8}$$

$$MAPE = \frac{100\%}{n}\sum\left|\frac{y - \bar{y}}{y}\right| \tag{9}$$

where, n is the number of data points, y and $\bar{y}$ are the actual and predicted output value, respectively.

TABLE 4. Errors with different ANN structures

Neurons in Layer 1	Neurons in Layer 2	R^2	MSE	MAPE (%)
20	3	0.62	37.119	25.52
18	6	0.76	30.234	19.35
16	8	0.77	27.292	19.01
14	12	0.82	25.632	15.67
12	14	0.91	20.246	9.13
10	16	0.90	20.842	10.02
8	**20**	**0.97**	**16.062**	**3.62**
6	20	0.89	21.423	10.34
3	20	0.71	31.357	21.35

Persian Abstract

چکیده

پلاسمای فشار اتمسفر سرد (CAP) یک فناوری بسیار قوی و تاثیرگذار است که هم برای کاربردهای تکنولوژیکی و هم برای کاربردهای زیست پزشکی اجرا شده است. این مقاله بر اجرای شبکه عصبی مصنوعی (ANN) برای پلاسمای فشار اتمسفر سرد مبتنی بر الکترود دو حلقه جدید متمرکز است که برای کاربرد آن در زمینه زیست پزشکی فقط در منطقه تخلیه درخشش عمل می‌کند. ANN ذاتاً به تجسم پارامترهای خروجی مؤثر مانند جریان دبی اوج، توان مصرفی، طول جت (با آستین) و طول جت (بدون آستین) برای مجموعه پارامترهای ورودی ولتاژ و فرکانس منبع تغذیه با استفاده از مدل یادگیری ماشین کمک می‌کند. قابلیت مدل ANN با پیش‌بینی پارامترهای خروجی CAP فراتر از محدوده تجربی نشان داده می‌شود. در نهایت، تنظیمات بهینه ولتاژ تغذیه و فرکانس منبع تغذیه با استفاده از رویکرد تابع مطلوبیت ترکیبی تعیین می‌شود تا همزمان جریان تخلیه پیک، طول جت (با آستین) و طول جت (بدون آستین) را به حداکثر برساند و مصرف برق را به حداقل برساند.

IJE TRANSACTIONS A: Basics Vol. 37 No. 01, (January 2024) 94-103

International Journal of Engineering

Journal Homepage: www.ije.ir

Physical, Mechanical, and Thermal Properties of Polyvinyl Alcohol/Nanocrystalline Cellulose Bioplastic Film

F. Yudhanto*[a], V. Yudha[b], H. S. B. Rochardjo[c], C. Budiyantoro[d], A. Khan[e], A. M. Asiri[e,f], M. J. M. Ridzuan[g]

[a] *Department of Automotive Engineering Technology, Universitas Muhammadiyah Yogyakarta, Indonesia*
[b] *Department of Mechanical Engineering, Institut Sains and Teknologi Akprind, Yogyakarta, Indonesia*
[c] *Department of Mechanical and Industrial Engineering, Universitas Gadjah Mada, Indonesia*
[d] *Department of Mechanical Engineering, Universitas Muhammadiyah Yogyakarta, Indonesia*
[e] *Center of Excellence for Advanced Materials Research, King Abdulaziz University, Jeddah, Saudi Arabia*
[f] *Chemistry Department, Faculty of Science, King Abdulaziz University, Jeddah, Saudi Arabia*
[g] *Faculty of Mechanical Engineering & Technology, Universiti Malaysia Perlis, Malaysia*

P A P E R I N F O

Paper history:
Received 09 June 2023
Received in revised form 22 August 2023
Accepted 24 August 2023

Keywords:
Bioplastic Film
Nanocrystalline Cellulose
Polyvinyl Alcohol

A B S T R A C T

The bioplastic film based on Polyvinyl Alcohol (PVA) for food packaging has been widely developed because of its biodegradable properties and safety. Nanocrystalline cellulose (NCC) is used as filler to improve mechanical strength. This study investigated how adding NCC into PVA films affects the physical, mechanical, and thermal properties. Combine acid hydrolysis 46 wt.% and ultrasonication process success to isolate commercial microcrystalline cellulose (MCC) became nanocrystalline cellulose (NCC). It has been characterized by x-ray diffraction (XRD), Fourier Transform Infrared (FTIR), Transmission Electron Microscope (TEM), Differential Scanning Calorimetry (DSC), and Thermal Gravimetric Analysis (TGA). NCC with needle shape form with an aspect ratio (L/D) of 12.4 has been high crystallinity index (76.4%). Addition of 6 wt.% NCC into PVA film improves the tensile strength and elongation by 35.30 MPa and 65.54%, respectively. The bioplastic film gives a barrier on the UV rays by 75% and still has good transparency. The thermal stability improves, indicated by the glass transition temperature (T_g) increase from 109 to 114°C and maximum temperature (T_{max}) from 275 to 300 °C.

***doi**: 10.5829/ije.2024.37.01a.09*

1. INTRODUCTION

Chemical treatment is one of the methods to isolate the cellulose nanocrystal. The treatment was carried out using hydrolysis by adding a sulfuric acid solution (H_2SO_4). The purified fiber has been done to minimize the hemicellulose and lignin content before the acid hydrolysis process. The acid hydrolysis aims to fibrillate and open bundle micro cellulose to nanocellulose. Several previous research like Morais et al. (1) isolated cotton fibers by adding a sulfuric acid solution (60 wt.%) in a bath a stirred at 200 rpm at a temperature of 45°C for one hour. It is successfully producing the nanocrystalline cellulose (NCC) with 12 nm of diameter and 177 nm of length. The aspect ratio (L/D) of NCC cotton is 19. Ghasemi et al. (2) have purified linter pulp followed by ultrafine grinder results the 30-70 nm of nanocellulose fiber's (NCF) diameter. The crystallinity index of nanocellulose is lower than purified fiber, it decreases from 79.5% to 65%. This phenomenon causes the decreased stability thermal of NCF from 280 to 240°C. Tonoli et al. (3) isolated the eucalyptus pulp sheets with the same concentration at 45°C for 30 minutes to produce nanocrystalline cellulose with diameters and lengths of 30 and 200 nm, respectively. Jiang and Hsieh (4), isolated rice straw by adding a sulfuric acid solution (64 wt.%) at

*Corresponding Author Institutional Email: ferriawan@umy.ac.id
(F. Yudhanto)

Please cite this article as: Yudhanto F, Yudha V, Rochardjo HSB, Budiyantoro C, Khan A, Asiri AM, Ridzuan MJM. A New Physical, Mechanical, and Thermal Properties of Polyvinyl Alcohol/Nanocrystalline Cellulose Bioplastic Film. International Journal of Engineering, Transactions A: Basics. 2024;37(01):94-103.

preheat temperature 45ºC for 45 minutes to produce NCC with 6.4 ± 1.8 nm of diameter and 113 ± 70 nm of diameter. Johar and Ahmad (5), isolated rice husks using a sulfuric acid of 10 mol/L at a preheat temperature of 50 ˚C for 40 minutes to produce NCC with 20 nm of diameter and 300 nm of length. It has an aspect ratio of 15. The aspect ratio depends on fiber resource, purified method, and fibrillated method. It is important to determine the NCC mechanical properties as filler in the polymer (6-9). Terzioglu and Parin (10) investigated the effect of adding lemon peel from 1 to 8 wt.% in the PVA (polyvinyl Alcohol)-starch biocomposite film. The mechanical strength increases by adding 1 wt.% lemon peel, showing good dispersion. The tensile strength increases from 24 to 25 MPa, whereas elongation rises from 260 to 275%. It is adding 2-8 wt. % causes aggregation in high concentration and starting to appear some voids in the matrix PVA-starch, it generates decreases in mechanical strength. Li et al. (11) developed bioplastic film combined the PVA 5 wt.%, it added by cellulose nanowhisker (CNWs) by 1 wt.%, concentration. The tensile strength and elongation PVA/CNWs bioplastic film are rises from 80 to 175 MPa and 170 to 330%, respectively. NCC's filler is known for high moisture absorption which leads to hydrophilic properties. To overcome this problem adding the biocompatible polymer is necessary to remove the reactivity of hydroxyl groups in the nanocellulose. The hydrophilic synthetics polymer, such as PVA, is easily dissolved in water, biodegradable, resistant to chemical conditions, and is an attractive material used for advanced applications. Furthermore, PVA is non-toxic to the human body, drug delivery systems, barrier materials, membranes, and yarn for surgery (12). Polymers can be degraded in two ways that are photodegradable or biodegradable. One definition of biodegradable polymer requires that the primary degradation mechanism is the result of the action and metabolism of microorganisms. Biodegradation can occur in either an aerobic or anaerobic environment. PVA is widely used as a sustainable plastic in the food industry because it is biodegradation; on the other hand, it has many advantages like high strength, good elasticity, lightweight, transparent, heat stable, and antimicrobial (13, 14).

This research aims to investigate the effect of adding NCC into PVA bioplastic film on mechanical and physical properties. There are several parameters and characteristics of NCC biocompatible with PVA bioplastic composites like aspect ratio (L/D), volume fraction (%V_f), and homogenized suspension (15). This research investigates commercial microcrystalline cellulose (MCC) isolated by sulfuric acid hydrolysis. The physical tests were carried out in this study, including evaluation of TEM (transmission electron microscope), SEM (scanning electron microscope), XRD (x-ray diffraction), FTIR (Fourier transform infrared), and Transmittance UV-Vis (Ultraviolet and Visible). The mechanical properties were tested through the tensile strength and then finally, the thermal stability was evaluated through TGA (thermal gravimetry analysis).

2. MATERIAL AND METHODS

2. 1. Materials Nanocrystalline cellulose was isolated from commercial microcrystalline cellulose (MCC) MERCK serial number 1.02330.0500, polyvinyl alcohol (PVA) fully hydrolyzed with 89-98 molecular weight from Sigma-Aldrich, sulfuric acid (H_2SO_4) purity 96% from Sigma Aldrich, Sodium Hydroxide (NaOH) purity 98% and distilled water. The tools used are a burette tube, clamp burette, Bekker glass, magnetic stirrer, pH meter, centrifuge, and ultrasonic homogenizer 12 mm diameter and the power set is 240W.

2. 2. Acid Hydrolysis Acid hydrolysis of the commercial MCC is isolated by sulfuric acid 46 wt.% H_2SO_4 with burrete tube into Erlenmeyer tube. The ratio of MCC powder and solution in the Erlenmeyer tube is 1:100. It was agitated at 350 rpm and preheated at 60ºC for one hour by a magnetic stirrer. The acid hydrolysis process aims to break the cellulose chain into individual cellulose. The hydrolysis process starts by breaking the oxygen bonds in the β-1,4-Glycosidic chain, then the glycosidic ring bonds reacted with H_2O molecules. Cellulose increased surface area and rise the hydroxyl group content. Figure 1 shows intramolecular reaction the decomposition of substances in chemical reactions caused by H_2SO_4 and H_2O molecules.

The acid suspension in the ice bath could stop the ionized process. Then it is gently dropped the sodium hydroxide NaOH with the same concentration by 46 wt.% into the acid suspension. Furthermore, centrifugation helps rinse the suspension for five cycles until neutral (pH=7). The NCC suspension was ultrasonicated for 15 minutes with a power of 240 watts and set the temperature at 60ºC. It aims to get a homogenized suspension of NCC (16, 17).

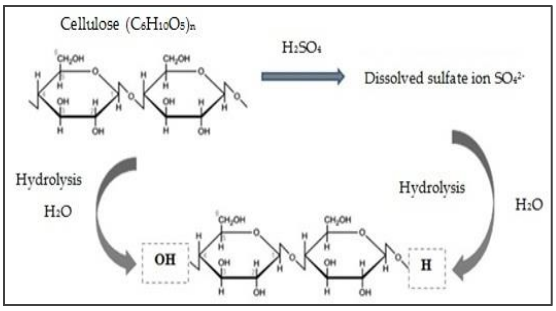

Figure 1. Scheme of chemical reaction of acid hydrolysis and nanocellulose

2. 3. Fabrication of PVA+NCC Bioplastic Film The fabrication of bioplastic films with different weight of NCC. Firstly, prepare the PVA powder with a 3 wt.% (density is 1.19 g/cm^3) and distilled water. It was mixed and heated constantly at 500 rpm at a temperature of 100^{o}C for one hour.

The PVA suspension was put into the desiccator with silica gel for one night until the bubble was gone. Secondly, the NCC gel has weight by 0, 3, and 6 wt.%, and it was mixed into the PVA solution. The PVA suspension is mixed with NCC gel at a temperature of 50^{o}C, stirred at 350 rpm for 30 minutes, followed by an ultrasonication of 240 watts for 15 seconds, 6 times. The last, it was poured into a hot Teflon plate at a temperature of 60°C for 4 hours to get a bioplastic composite film. The schematic process and production steps of the bioplastic composite are shown in Figure 2.

2. 4. Morphology Analysis The dimension of cellulose, nanocellulose, and surfaces of bioplastic composite have been identified by SEM (JSM-6510, LA-JEOL) and TEM (JEM-1400). The SEM photo can be detected surfaces solid material on the micro scale from 50 to 20,000 magnification. The voltage of SEM was set to 40 kV. The specimen has been coated with Au and used a sputtering method. The voltage of TEM is set at a range of 20 to 110 kV to get an excellent image contrast. NCC diameter (D) and length (L) were calculated by image-J software to results in the aspect ratio. The TEM photo can be detected nano scale material in the liquid suspension from 1000 to 300,000 magnification.

2. 5. XRD Analysis The XRD diffraction patterns for crystal structure are based on the scattering angle peaks and intensities of bioplastic composite. It was tested by using the Rigaku Miniflex-600 type which run at 40 kW, 15 mA, and CuKα radiation (λ=1.54060Å). The bioplastic film test sample was scanned in 2θ range from 2° to 40° with a scan speed by 4° min^{-1} and sampling pitch 0.02°. The solid structure of bioplastic film has a crystal and amorphous structure which is determined by crystallinity index according to Segal Equation 1.

$$CI = \frac{I_{110} - I_{am}}{I_{110}} \tag{1}$$

where I_{110} is a semi-crystalline structure plane at a scattering angle on the 2θ=19.8^o, and I_{am} is an amorphous structure at a scattering angle on the 2θ=16^o.

2. 6. FTIR Analysis FTIR is an analytical test method used to identify organic polymeric materials. The product composition analysis method with FTIR uses infrared light to scan the test sample and observe its chemical properties. It is used in the analysis to transmit infrared radiation from the sample test by absorbing and passing some of it through radiation. It measured wavenumber spectra from 4000-400 cm^{-1} with a Shimadzu 8400S Spectrometer. Thin pellet samples were prepared with the help of potassium bromide (KBr).

2. 7. UV-VIS Analysis The transparency and ultraviolet barrier bioplastic composites were identified by spectrophotometer with Ocean optics USB-4000 of UV-Vis (ultraviolet-visible) obtained by continuously changing the wavelength of light. It is which separately passes through the test sample.

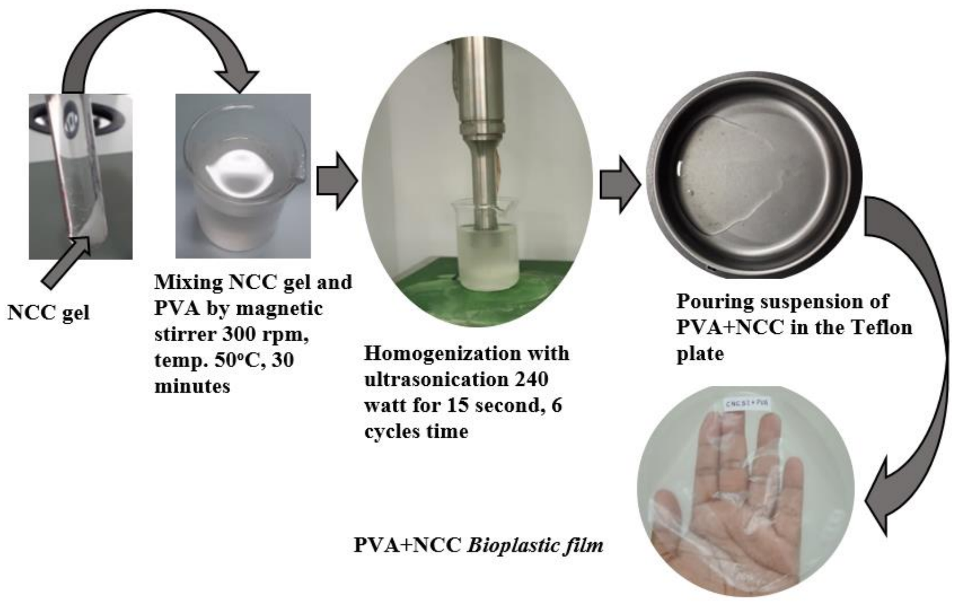

Figure 2. Scheme of fabrication of PVA+NCC bioplastic film

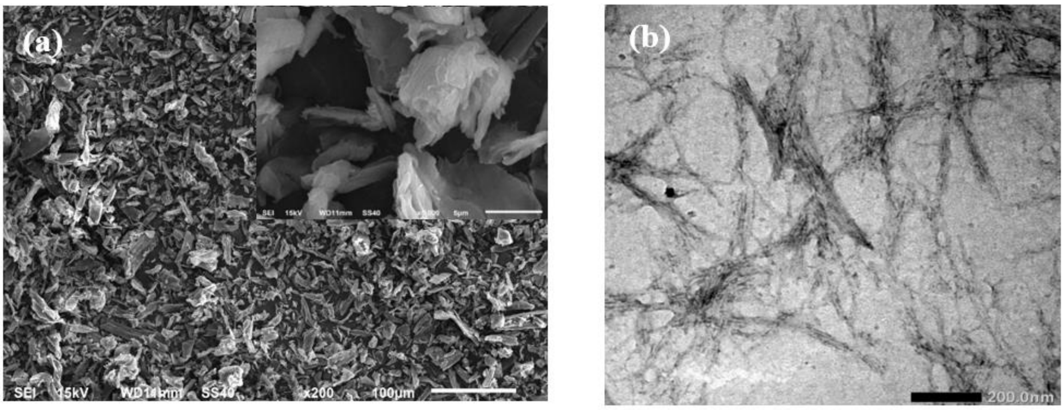

Figure 3. The photo of (a) MCC by SEM, (b) NCC by TEM

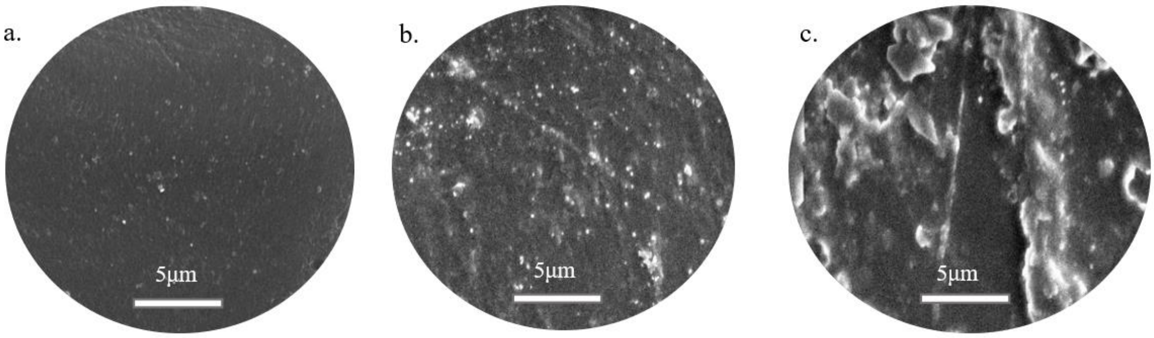

Figure 4. Surfaces morphology of bioplastic film: a) Neat PVA, b) PVA+NCC3%, and c) PVA+NCC6%

In an array spectrometer, light with a full wavelength that passes through the test sample is diffracted by a reflection and then received by the detector. As a result, it can provide a complete scan spectrum by 200–800 nm.

2. 8. Mechanical Analysis The mechanical analysis used the tensile test of ASTM D-882 for thin plastic sheets, including film less than 1 mm. The paper test specimen is 100 mm in overall length; the specimen test is 25 mm gage length and 5 mm in width. The UTM (universal testing machine) by Pearson Panke Equipment Ltd has a maximum load of 400 N and a set cross-head speed of 2 mm/minute.

2 .9. TGA Analysis The TGA (Thermogravimetric Analyzer) Mettler Toledo can run on a single temperature program (a constant heat rate at 10◦C/min from 30 to 600◦C with a nitrogen gas flow rate of 60 mL/minute). The bioplastic composite sample was tested in thin sheet film with a weight of 10 mg. Thermal degradation can be used to generate polymer degradation at different temperatures. Some examples of mass change processes are decompositions and oxidations. On the other hand, the TGA curve data are coupled with a derivative thermogram (DTG) curve to give the results better.

2. 10. DSC Analysis The Thermal degradability of bioplastic film can be calculated with DSC (Differential Scanning Calorimetry). DSC is one of the necessary tests to determine how much the energy a bioplastic film absorbs or release. This thermal analysis measures the heat energy absorbed and emitted by the test sample as a function of time and temperature. The glass temperature occurs when the material changes from the semi-liquid to the liquid phase (T_g). The final melting temperature occurs when most of the liquid has been burned (T_m). The gas used is nitrogen (N_2) with an average flow rate (flow rate) of 10 ml/minute at a temperature range of 30-300^oC.

3. RESULT AND DISCUSSIONS

3. 1. Morphology Analysis of NCC Figure 3a shows the morphology of MCC was investigated by SEM (Scanning Electron Microscope), and it found that the diameter of MCC is ±20 µm. Figure 3b shows NCC by acid hydrolysis process combined with ultrasonication. The NCC has a diameter and length of around 25 nm and 310 nm with aspect ratio 12.4. Furthermore, other similar research by Krishnadev et al. (18) has been isolated Agave americana fiber by chemical extracted by 4 wt.%

NaOH in hot water 80ºC for two hours followed by bleaching treatment using 2 wt.% $NaClO_2$ in hot water 80ºC for 4 hours and It's followed by acid hydrolysis with a nitric acid solution of 70% and acetic acid of 80% at a hot temperature 100ºC for 30 minutes. Its morphology results in that the NCC has a diameter of 18.2 ± 10 nm by TEM.

3. 2. Morphology Analysis of Bioplastics Film Figure 4a shows the morphology of PVA bioplastic composite products without addition of NCC. The surface morphology of bioplastic composites looks likes smooth and clear. Addition of NCC in the PVA bioplastic composite resulted in intermolecular cross-linked chemical bonds between NCC and PVA. It shows a little wrinkle spread on the surface structure (Figure 4b). Figure 4c shows big wrinkle spread well on the surfaces of the PVA matrix.

3. 3. XRD Analysis of Bioplastic Film Figure 5 shows the value of the crystallinity of bioplastic composites. The reference value in the crystallinity area with a value of 2θ=19.8º (plane 110) and the amorphous area at a value of 2θ=16º. Plane 110 of bioplastic film materials corresponding to d spacing 4.4801 Ȧ, and it indicates the semi-crystalline typical structure (19, 20). The NCC's crystallinity by 76.4% higher than commercial MCC (Sigma Aldrich) by 74.8% (16). Adding NCC in the PVA impacted the bioplastic film crystallinity raises fraom 48.7% to 65.1%.

The crystallinity index of Neat PVA, PVA+NCC 3%, and PVA+NCC 6% there are 48.7%, 62.0%, and 65.1%, respectively. The crystallinity and amorphous intensity summarized in Table 1. Ilyas et al. (21) isolated the palm fiber by chemical purification followed by hydrolysis of 60 wt.% sulfuric acids, 45ºC intermolecular for 45 minutes. The results of this treatment process increased the crystallinity index value from raw fiber to NCC from 55.8% to 85.9%.

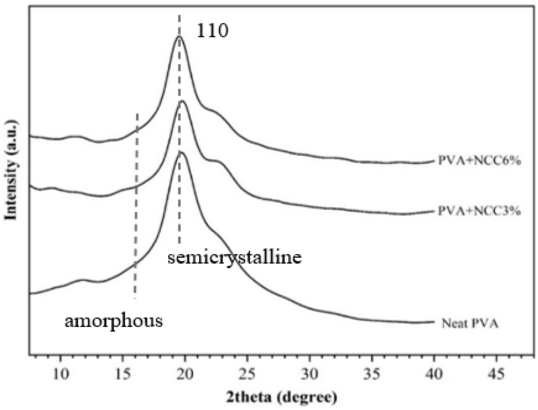

Figure 5. XRD diffraction of bioplastic film

The selection of concentration, time, and temperature parameters for acid hydrolysis determine the aspect ratio of NCC. Aspect ratio (L/D) and crystallinity indexed are important parameters to determine mechanical properties.

3. 4. FTIR Analysis Figure 6 shows the bioplastic films' wavenumber spectra region in four main areas. The relative content of functional groups or groups of atoms in the material was estimated by intensity ratio of optical density (22). The first wavenumber is 3490 cm^{-1}, it indicates O-H stretching (23). The NCC's hydroxyl make intermolecular cross-link bonded to PVA's hydroxyl (-OH) which is shown in Figure 7. It indicates by the peak

TABLE 1. Crystallinity index of bioplastic films

Samples	I_{110} (2θ=19.8º)	$I_{amorphous}$ (2θ=16º)	CI (%)
Neat PVA	158	81	48.7
PVA+NCC 3%	308	117	62.0
PVA+NCC 6%	395	138	65.1

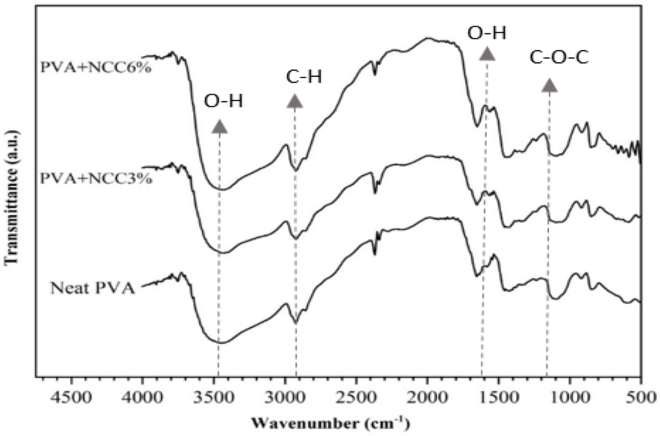

Figure 6. FTIR wavenumber spectra of bioplastic film

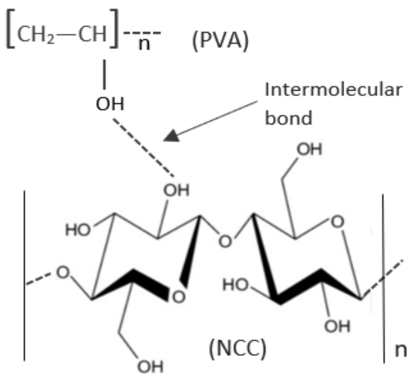

Figure 7. Schematic of intermolecular bond between PVA and NCC

of PVA+NCC sharper than neat PVA. The second area wavenumber region is 2931 cm^{-1}, meaning that the C-H stretching vibration. The third region is 1627 cm^{-1}, showing the O-H bending vibration means adsorbed of H_2O (water vapor) content. It indicates that NCC material is suitable for combination with the same hydrophilic properties as PVA (24). The four region is 1190 cm^{-1}, showing the asymmetric stretching vibration C-O-C indicates the glucose ring structure of cellulose (25).

Adding more NCC into PVA decreases the water vapor permeability of bioplastic film. Another study using hydrophilic polymers besides PVA like a Polylactic Acid (PLA) developed by Mirabolghasemi et al. (26). It was found that addition of NCC causes a decrease in the value of water vapor permeability (H_2O) content. The nano-scale of NCC homogeneous structure increases the crystallinity of bioplastic film material which inhibit the water vapor.

3. 5. The UV-Vis Absorbance Figure 8 shows that addition of NCC to the PVA matrix decreases the transparency of the bioplastic composite. Neat PVA has excellent transparency, which means the visible light transmission by 70% on the 650 nm wavelength. Adding NCC in PVA increases the absorbance of The UV rays at 300 nm wavelength. UV-A has a long wavelength of 400 nm, and UV-B has a short wavelength of 300 nm (27). Figure 9 shows that small transmittance on the wavelength range 300-400 nm, it indicates the material has good blocking of UV rays. Adding NCC 3 and 6 wt.% in the PVA could be reduced 70% and 75% of UV-A rays compared to without NCC. Therefore, the bioplastic composite could reduce UV rays to be applied as packaging. The average transmittance of visible light neat PVA is 70%. Addition of 3 and 6 wt.% CNF caused the decreases in the transmittance light to 45% and 37%, respectively.

3. 6. Mechanical Analysis Figure 10 shows the tensile properties and elongation at break of bioplastic films. The thickness of bioplastic film is 25-30 μm. Adding NCC as filler into the PVA could improve the performance of the bioplastic composite with more strength and elasticity than neat PVA. The interaction between NCC and PVA by intermolecular bonding of the hydroxyl functional group can raise the toughness of bioplastic composite. The tensile strength and elongation at break of neat PVA by 26.61 MPa and 46.95 %, respectively. Addition of 3 wt.% NCC slightly increases the effect by 35.30 MPa of tensile strength and 65.54% of elongation at break. Whereas adding 6 wt.% of NCC gives an excellent improvement in the tensile strength and elongation properties increase by 38.67 MPa and 84.06%. This condition shows that NCC provides a good stress distribution in the PVA bioplastic composite matrix. The other research by Fortunati et al. (28) has isolated the MCC (Sigma Aldrich) by hydrolysis by sulfuric acid 64 wt.% at a temperature of 45˚C for 30 minutes. It was produced at 10 nm in diameter and 200 nm in length. Adding NCC 5wt.% as filler in the PVA bio-nanocomposite film has increased tensile strength and elongation at the break by 44.3% and 300%, respectively. Previous research using PVA polymer as the matrix was conducted by Yudhanto et al. (29) extracted NCC from Agave cantala fiber with a combination process of sulfuric acid hydrolysis by 44 wt.% at temperature 60˚C for one hour followed by ultrasonication (240Watt, diameter probe is 12 mm, 30 minutes times). It produced 45 nm of diameter and 1975 nm (aspect ratio is 43.8) NCC. Adding 8 wt.% in PVA/NCC film results in the highest tensile strength of 76.7% and elongation at the break of 112%. Addition of NCC 10 wt.% results in agglomeration NCC, and it causes stress concentration and affects low tensile properties. Frone et al. (30) isolated MCC with ultrasonication (20 kHz, 19 mm diameter probe, 200 Watts) for 20 minutes. It produces the NCC 70-150 nm in diameter. Adding the NCC filler 5 wt.% in the PVA matrix increases the tensile strength by 39%.

3. 7. Thermal Degradability Analysis Thermogravimetric analysis (TGA) and corresponding derivative thermogravimetry (DTG) curves of the NCC is shown in Figure 11. It shows that the thermal stability of NCC is high. The weight mass loss could be divided into three stages.

The first stage is the evaporation of adsorbed water in the NCC and bioplastic composite before a temperature 100˚C. The second stage started at 230-300°C, the initial degradation temperature (T_{onset}). It degrades an amorphous material such as hemicellulose and lignin. It is similar to conducted research by Babu et al. (31), that lignin of *Phaseolus vulgaris* fiber (PVFs) content degrades in the same temperature range. The third stage is a maximum temperature (T_{max}) of NCC by 325°C, the cellulose degradation temperature range of 322-347°C. Figures 12 and 13 are shown the TGA and DTG curves of bioplastic film. Adding NCC into PVA causes the crystalline structure functional groups in the NCC to be able to inhibit heat flow. Furthermore, another research by Wang et al. (32), adding NCC into PVA and UPy (Ureido-Pyrimidinone) causes a rise the thermal stability. Table 2 shows an increase in thermal stability in each variation of bioplastic composites. The initial and maximum degradation of neat PVA is 253°C (T_{onset}) and 275°C (T_{max}) which are shown in Figures 12 and 13.

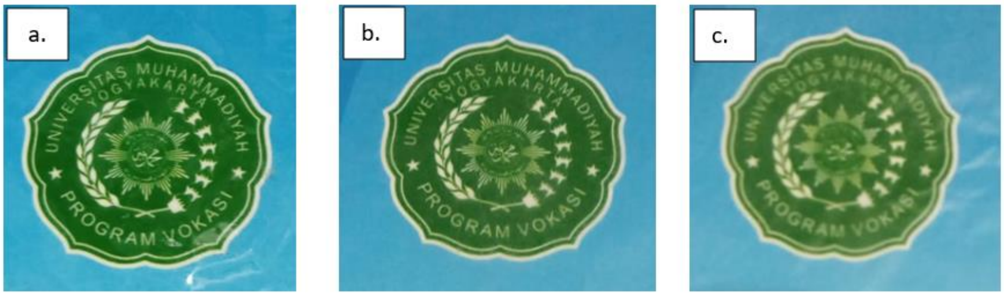

Figure 8. Transparency of bioplastic film (a) neat PVA, (b) PVA+NCC3%, (c) PVA+NCC6%

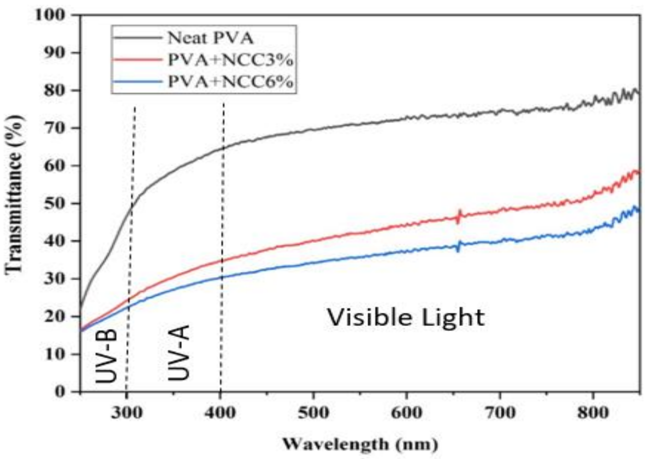

Figure 9. UV-Vis. transmittance spectra of bioplastic film

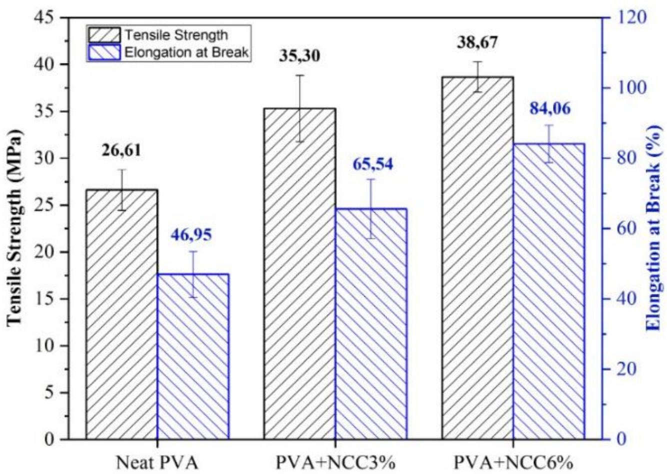

Figure 10. Tensile properties of bioplastic films

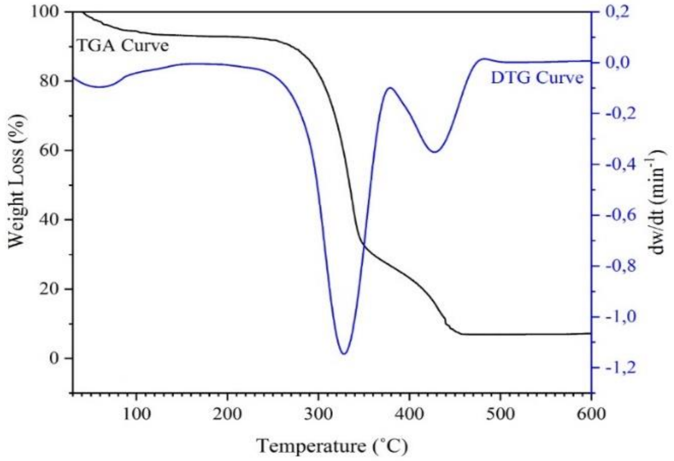

Figure 11. TGA/DTG curves of Nanocrystalline Cellulose (NCC)

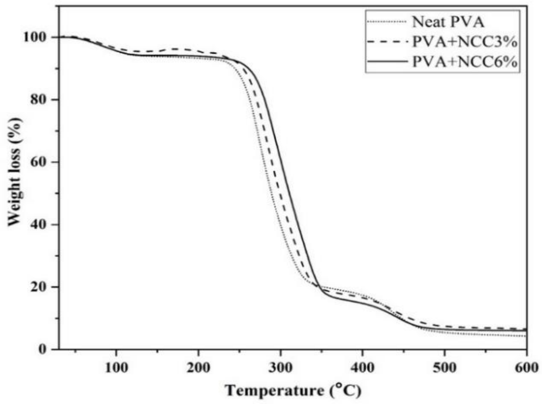

Figure 12. TGA curves of bioplastic film

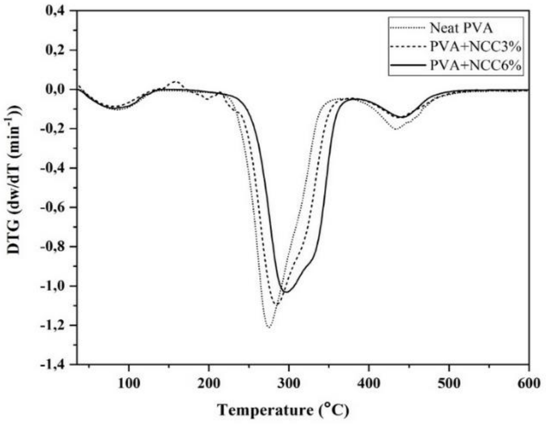

Figure 13. DTG curves of bioplastic film

According Gan et al. (33), addition of NCC into polymer as matrix give rise to intermolecular bonding between it, which rise the elongation at break and improvement the glass transition temperature (T_g), and T_{max}. The excellent bonding between hydrogen the filler

TABLE 2. Thermal stability of NCC on TGA and DTG test

Samples	T_{onset} (ºC)	T_{max} (ºC)
NCC	295	330
Neat PVA	253	275
PVA+NCC3%	270	290
PVA+NCC6%	280	300

(NCC) and the matrix can be improvement the stability thermal of bioplastic film.

The data obtained from the DSC (Differential Scanning Calorimetry) test include the glass transition temperature (T_g) and melting temperature (T_m). The glass transition is the initial transition temperature of the change in the material phase, which is rigid glass to rubbery (ductile stretching), meaning that the higher glass temperature shows the bioplastic film more rigid and elastic. In Figure 14 shows adding NCC into PVA film raises the glass temperature (T_g) from 109 to 114°C

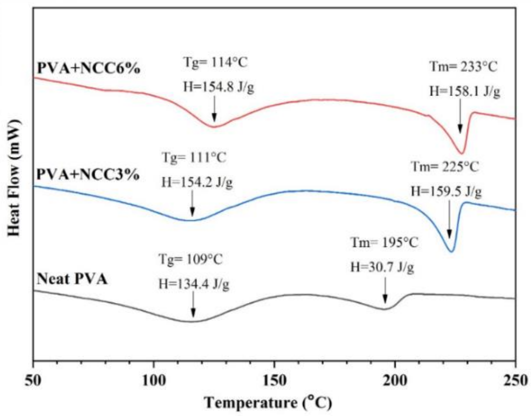

Figure 14. DSC curves of bioplastic film

and melting temperature (T_m) from 195 to 233°C. The enthalpy (H) on meting point shows that the high absorbs energy need to degrades the PVA+NCC 6 wt.% by 158.1 J/g. The neat PVA only absorbs energy by 30.7 J/g, it was caused the neat PVA film degrades earlier at the glass temperature (T_g).

4. CONCLUSION

NCC has been isolated from MCC was successful in combining acid hydrolysis and ultrasonication. The resulting NCC measures 25 nm in diameter and 310 nm in length with an aspect ratio of 12.4. The addition of 6 wt.% NCC into PVA increased the tensile strength and elongation at the break by 45.3% and 79.0%, respectively. The good mechanical strength correlated with the high crystallinity index by 65.1%. In addition, the TGA/DTG for maximum temperature (T_{max}) increases from 275 to 300°C. The DSC test shows rising the heat enthalpy and transition glass temperature (T_g), from 134.4 J/g (109 ˚C) to 154.8 J/g (114°C). It indicates adding NCC improving the thermal stability. The transparency properties are still good, and it was excellent barrier of UV rays by 75%. It's suitable to be applied to plastic packaging.

5. ACKNOWLEDGEMENT

This research was carried out under the Research Grants of Tri Dharma Improvement Program for Higher Education of LRI *(Lembaga Riset dan Inovasi), Universitas Muhammadiyah Yogyakarta*. Contract No. 01/RIS-LRI /I/2022, Batch 1.

6. REFERENCES

1. Morais JPS, de Freitas Rosa M, Nascimento LD, Do Nascimento DM, Cassales AR. Extraction and characterization of nanocellulose structures from raw cotton linter. Carbohydrate Polymers. 2013;91(1):229-35. https://doi.org/10.1016/j.carbpol.2012.08.010
2. Ghasemi S, Behrooz R, Ghasemi I. Extraction and characterization of nanocellulose structures from linter dissolving pulp using ultrafine grinder. Journal of Nanoscience and Nanotechnology. 2016;16(6):5791-7. https://doi.org/10.1166/jnn.2016.12416
3. Tonoli GHD, Savastano Jr H, Fuente E, Negro C, Blanco A, Lahr FR. Eucalyptus pulp fibres as alternative reinforcement to engineered cement-based composites. Industrial Crops and Products. 2010;31(2):225-32. https://doi.org/10.1016/j.indcrop.2009.10.009
4. Jiang F, Hsieh Y-L. Cellulose nanocrystal isolation from tomato peels and assembled nanofibers. Carbohydrate Polymers. 2015;122:60-8. https://doi.org/10.1016/j.carbpol.2014.12.064
5. Johar N, Ahmad I. Morphological, thermal, and mechanical properties of starch biocomposite films reinforced by cellulose nanocrystals from rice husks. BioResources. 2012;7(4). https://doi.org/10.15376/biores.7.4.5469-5477
6. Kargarzadeh H, Ioelovich M, Ahmad I, Thomas S, Dufresne A. Methods for extraction of nanocellulose from various sources. Handbook of nanocellulose and cellulose nanocomposites. 2017;1:1-49. https://doi.org/10.1002/9783527689972.ch1
7. Kassab Z, Aziz F, Hannache H, Youcef HB, El Achaby M. Improved mechanical properties of k-carrageenan-based nanocomposite films reinforced with cellulose nanocrystals. International Journal of Biological Macromolecules. 2019;123:1248-56. https://doi.org/10.1016/j.ijbiomac.2018.12.030
8. Maache M, Bezazi A, Amroune S, Scarpa F, Dufresne A. Characterization of a novel natural cellulosic fiber from Juncus effusus L. Carbohydrate Polymers. 2017;171:163-72. https://doi.org/10.1016/j.carbpol.2017.04.096
9. El Achaby M, Kassab Z, Barakat A, Aboulkas A. Alfa fibers as viable sustainable source for cellulose nanocrystals extraction: Application for improving the tensile properties of biopolymer nanocomposite films. Industrial Crops and Products. 2018;112:499-510. https://doi.org/10.1016/j.indcrop.2017.12.049
10. Terzioğlu P, PARIN FN. Polyvinyl alcohol-corn starch-lemon peel biocomposite films as potential food packaging. Celal Bayar University Journal of Science. 2020;16(4):373-8. https://doi.org/10.18466/cbayarfbe.761144
11. Li H-Z, Chen S-C, Wang Y-Z. Preparation and characterization of nanocomposites of polyvinyl alcohol/cellulose nanowhiskers/chitosan. Composites Science and Technology. 2015;115:60-5. http://dx.doi.org/10.1016/j.compscitech.2015.05.004
12. Zhang W, Yang X, Li C, Liang M, Lu C, Deng Y. Mechanochemical activation of cellulose and its thermoplastic polyvinyl alcohol ecocomposites with enhanced physicochemical properties. Carbohydrate Polymers. 2011;83(1):257-63. https://doi.org/10.1016/j.carbpol.2010.07.062
13. Perumal AB, Sellamuthu PS, Nambiar RB, Sadiku ER. Development of polyvinyl alcohol/chitosan bio-nanocomposite films reinforced with cellulose nanocrystals isolated from rice straw. Applied Surface Science. 2018;449:591-602. https://doi.org/10.1016/j.apsusc.2018.01.022
14. Darie-Niță RN, Râpă M. Processing of Commercially Available Bioplastics. Bioplastics for Sustainable Development. 2021:103-36. https://doi.org/10.1007/978-981-16-1823-9_4
15. Fatkhurrohman F, Rochardjo HSB, Kusumaatmaja A, Yudhanto F, editors. Extraction and effect of vibration duration in ultrasonic process of cellulose nanocrystal (CNC) from ramie fiber. AIP Conference Proceedings; 2020: AIP Publishing.
16. Yudhanto F, Jamasri J, Rochardjo HSB, editors. Physical and Mechanical Characterization of Polyvinyl Alcohol Nanocomposite Made from Cellulose Nanofibers. Materials Science Forum; 2020: Trans Tech Publ.
17. Frone AN, Panaitescu DM, Donescu D, Spataru CI, Radovici C, Trusca R, et al. Preparation and characterization of PVA composites with cellulose nanofibers obtained by ultrasonication. BioResources. 2011;6(1):487-512. https://doi.org/10.15376/biores.6.1.487-512
18. Krishnadev P, Subramanian KS, Janavi GJ, Ganapathy S, Lakshmanan A. Synthesis and characterization of nano-fibrillated cellulose derived from green Agave americana L. fiber. BioResources. 2020;15(2):2442-58. https://doi.org/10.15376/biores.15.2.2442-2458
19. Handoko F, Yusuf Y. Synthesis and physicochemical properties of poly (vinyl) alcohol nanocomposites reinforced with nanocrystalline Cellulose from Tea (Camellia sinensis) waste.

Materials. 2021;14(23):7154. https://doi.org/10.3390/ma14237154

20. Ibrahim NI, Shahar FS, Sultan MTH, Shah AUM, Safri SNA, Mat Yazik MH. Overview of bioplastic introduction and its applications in product packaging. Coatings. 2021;11(11):1423. https:/doi.org/10.3390/coatings11111423
21. Ilyas R, Sapuan S, Ishak M. Isolation and characterization of nanocrystalline cellulose from sugar palm fibres (Arenga Pinnata). Carbohydrate Polymers. 2018;181:1038-51. https://doi.org/10.1016/j.carbpol.2017.11.045
22. Stukhlyak P, Buketov A, Panin S, Maruschak P, Moroz K, Poltaranin M, et al. Structural fracture scales in shock-loaded epoxy composites. Physical Mesomechanics. 2015;18:58-74. https://doi.org/10.1134/S1029959915010075
23. Benchikh L, Merzouki A, Grohens Y, Guessoum M, Pillin I. Characterization of cellulose nanocrystals extracted from El Diss and El Retma local plants and their dispersion in poly (vinyl alcohol-co-ethylene) matrix in the presence of borax. Polymers and Polymer Composites. 2021;29(3):218-30. https://doi.org/10.1177/09673911209108
24. Vaezi K, Asadpour G, Sharifi SH. Bio nanocomposites based on cationic starch reinforced with montmorillonite and cellulose nanocrystals: Fundamental properties and biodegradability study. International Journal of Biological Macromolecules. 2020;146:374-86. https://doi.org/10.1016/j.ijbiomac.2020.01.007
25. Ali S, Khatri Z, Oh KW, Kim I-S, Kim SH. Preparation and characterization of hybrid polycaprolactone/cellulose ultrafine fibers via electrospinning. Macromolecular Research. 2014;22:562-8. https://doi.org/10.1007/s13233-014-2078-x
26. Mirabolghasemi SM, Najafi M, Azizi A, Haji Bagherian M. Physico-mechanical properties of polylactic acid bio-nanocomposites filled by hybrid nanoparticles. Polymers and Polymer Composites. 2021;29(9_suppl):S1510-S9. https://doi.org/10.1177/09673911211060132
27. Guzman-Puyol S, Hierrezuelo J, Benítez JJ, Tedeschi G, Porras-Vázquez JM, Heredia A, et al. Transparent, UV-blocking, and high barrier cellulose-based bioplastics with naringin as active food packaging materials. International Journal of Biological Macromolecules. 2022;209:1985-94. https://doi.org/10.1016/j.ijbiomac.2022.04.177
28. Fortunati E, Puglia D, Luzi F, Santulli C, Kenny JM, Torre L. Binary PVA bio-nanocomposites containing cellulose nanocrystals extracted from different natural sources: Part I. Carbohydrate Polymers. 2013;97(2):825-36. https://doi.org/10.1016/j.carbpol.2013.03.075
29. Yudhanto F, Jamasri J, Rochardjo H, Kusumaatmaja A. Experimental study of polyvinyl alcohol nanocomposite film reinforced by cellulose nanofibers from agave cantala. International Journal of Engineering, Transactions A: Basics,. 2021;34(4):987-98. https://doi.org/10.5829/IJE.2021.34.04A.25
30. Frone AN, Berlioz S, Chailan J-F, Panaitescu DM. Morphology and thermal properties of PLA–cellulose nanofibers composites. Carbohydrate Polymers. 2013;91(1):377-84. https://doi.org/10.1016/j.carbpol.2012.08.054
31. Babu BG, Princewinston D, Saravanakumar S, Khan A, Aravind Bhaskar P, Indran S, et al. Investigation on the physicochemical and mechanical properties of novel alkali-treated Phaseolus vulgaris fibers. Journal of Natural Fibers. 2022;19(2):770-81. https://doi.org/10.1080/15440478.2020.1761930
32. Wang Z, Ding Y, Wang J. Novel polyvinyl alcohol (PVA)/cellulose nanocrystal (CNC) supramolecular composite hydrogels: Preparation and application as soil conditioners. Nanomaterials. 2019;9(10):1397. https://doi.org/10.3390/nano9101397
33. Gan P, Sam S, Abdullah MFb, Omar MF. Thermal properties of nanocellulose-reinforced composites: A review. Journal of Applied Polymer Science. 2020;137(11):48544. https://doi.org/10.1002/app.48544

Persian Abstract

چکیده

فیلم بیوپلاستیک مبتنی بر پلی وینیل الکل (PVA) برای بسته بندی مواد غذایی به دلیل خواص زیست تخریب پذیر و ایمنی آن به طور گسترده توسعه یافته است. سلولز نانو کریستالی (NCC) به عنوان پرکننده برای بهبود استحکام مکانیکی استفاده می شود. این مطالعه بررسی کرد که چگونه افزودن NCC به فیلم‌های PVA بر خواص فیزیکی، مکانیکی و حرارتی تأثیر می‌گذارد. ترکیب هیدرولیز اسید ٤٦ درصد وزنی و موفقیت فرآیند فراصوت برای جداسازی سلولز میکروکریستالی تجاری (MCC) تبدیل به سلولز نانوبلور (NCC) شد. با پراش اشعه ایکس (XRD)، تبدیل فوریه فروسرخ (FTIR)، میکروسکوپ الکترونی عبوری (TEM)، کالریمتری اسکن تفاضلی (DSC)، و آنالیز وزنی حرارتی (TGA) مشخص شده است. NCC با فرم سوزنی شکل با نسبت ابعاد 4/12 (L/D) دارای شاخص کریستالینیتی بالا (٧٦/٤ درصد) بوده است. افزودن ٦ درصد وزنی NCC به فیلم PVA استحکام کششی و ازدیاد طول را به ترتیب ٣٥.٣٠ مگاپاسکال و ٦٥.٥٤ درصد بهبود می بخشد. فیلم بیوپلاستیک تا ٧٥ درصد مانعی بر روی اشعه ماوراء بنفش ایجاد می کند و همچنان شفافیت خوبی دارد. پایداری حرارتی بهبود می یابد که با افزایش دمای انتقال شیشه ای (Tg) از ١٠٩ به ١١٤ درجه سانتی گراد و حداکثر دما (Tmax) از ٢٧٥ به ٣٠٠ درجه سانتی گراد نشان داده می شود.

IJE TRANSACTIONS A: Basics Vol. 37 No. 01, (January 2024) 104-114

International Journal of Engineering

Journal Homepage: www.ije.ir

Seismic Vulnerability of Irregular Reinforced Concrete Buildings Considering the Soil-structure Interaction

S. El Janous*, A. El Ghoulbzouri

Laboratory of Applied Sciences, National School of Applied Sciences AL Hoceima, University AbdelmalekEssaadi, Tetouan, Morocco

P A P E R I N F O

Paper history:
Received 21 July 2023
Received in revised form 16 Augut 2023
Accepted 20 August 2023

Keywords:
Plastic Hinges
Seismic Response
Fragility Curves

A B S T R A C T

In this study, we present an investigation into the seismic vulnerability assessment of medium-rise reinforced concrete structures featuring vertical geometric irregularity (setback). We considered the effects of the percentage and location of the setback along the height of the building, as well as the impact of changing site classes. Additionally, we incorporated the effects of soil-structure interaction into the nonlinear response of the building. In the first part, we investigated the influence of the aforementioned parameters on the seismic response of a structure through nonlinear static analyses. We analyzed the capacity curves and the development of plastic hinges in the structural elements. In the second part, we analyzed the seismic fragility of building frames using a probabilistic study approach. We developed fragility curves to assess the vulnerability of the structures.In conclusion, the obtained results highlight the fundamental importance of considering structural irregularities as well as the impact of different site classes on the seismic vulnerability of buildings.

doi: *10.5829/ije.2024.37.01a.10*

NOMENCLATURE

μ_u	The ultimate ductility	$\overline{T}$	Period of the flexible-base structure
G	Shear modulus of the soil	ρ	Density
G_0	Initial shear modulus	D_y	Elastic displacement
L	Length of the foundation	V_y	Elastic shear velocity
B	Width of the foundation	I_f	Moment of inertial
υ	Poisson's ration	A_f	The area of foundation
$\tilde{\varepsilon}$	Total system damping	$r_u = \sqrt{A_f/\pi}$	The foundation radii of translation
ε_f	Damping of the foundation	$r_\theta = \sqrt[4]{4 \times I_F/\pi}$	The foundation radii of rotation
ε_i	Damping of the structure	$K_u = \frac{8}{2-\nu} \times G \times r_u$	The static stiffness of a disk on a half-space for translational deformation modes
T	Period of the fixed-base structure	$K_\theta = \frac{8}{3(1-\nu)} \times G \times r_\theta$	The static stiffness of a disk in a half-space for rotational deformation modes
D_u	The ultimate displacement		

1. INTRODUCTION

Research into vertical irregularities in buildings has been an active field of study since the 1970s. Several researchers have played a pioneering role in this field. Chopra and Kan (1) focused their study on the seismic response of eight-storey buildings, subjecting them to seismic ground motion data.

Similarly, Ruiz and Diederich (2) carried out analytical studies on models of five- and twelve-storey buildings with irregularities in resistance. The impact of building setback on the seismic response of multi-storey structures was assessed by Shahrooz and Moehle (3).

Valmundsson and Nau (4) undertook a parametric

*CorrespondingAuthorEmail: *soumaya.eljanous@etu.uae.ac.ma* (S. El Janous)

Please cite this article as: El Janous S, El Ghoulbzouri A. Seismic Vulnerability of Irregular Reinforced Concrete Buildings Considering the Soil-structure Interaction. International Journal of Engineering, Transactions A: Basics. 2024;37(01):104-114.

study of two-dimensional building structures with irregularities in mass, stiffness and strength. Their results indicate that strength irregularities have the most significant influence on response compared to mass and stiffness irregularities.

In another relevant study, Michalis et al. (5) examined the effect of vertical irregularities on the capacity of a 9-storey building using incremental dynamic analysis (IDA). They concluded that irregularities have a substantial impact on boundary states and depend on earthquake intensity.

As for Shaikh and Shinde (6), their interest focused on the seismic response of a reinforced concrete frame presenting a vertical irregularity associated with a mass irregularity.

Furthermore, Shah et al. (7) carried out a study on the seismic risk assessment of mid-rise steel buildings, highlighting different types of vertical irregularities, such as mass, stiffness and/or resistance irregularities.

In a recent study, Kyoung et al. (8) proposed a simplified modeling method to examine the behavior of buildings with irregularities. Their approach consists of transforming vertically irregular structures into geometrically regular ones using a floor stiffness equation.

Also Hait et al. (9) confirmed that the buildings with irregular configurations suffer greater damage than those with regular contours, mainly due to the increased influence of torsional effects.

On the other hand, Mouhine and Hilali (10) assessed the seismic vulnerability of twenty building structures with vertical geometric irregularities at different positions. They adopted a probabilistic approach based on non-linear static analysis to calculate damage probabilities. The results revealed that the percentage of shrinkage has a significant impact on the dynamic response of irregular structures and modifies building performance.

As part of our research, we focused on studying the seismic behavior of reinforced concrete buildings with vertical geometric irregularities, taking into account soil-structure interaction. We carried out three-dimensional simulations of medium-sized building structures, including shrinkage, using SAP 2000 finite element analysis software.

2. SOIL-STRUCTURE INTERACTION

2. 1. Non-linear Approach for Assessing the Seismic Performance of Strutures

We introduce a simplified model tailored to address the intricate challenges posed by nonlinear soil-structure interaction (SSI). The N2 method, originally formulated by Fajfar (11), is employed to assess the nonlinear behavior of the structure. In its initial version, this method assumes a fixed structure base, thereby excluding the influence of soil-structure interaction (SSI). Our proposed approach, named the N2-SSI method, extends the N2 method to incorporate soil effects into the nonlinear response (12).

2. 2. Foundation Impedances

The deformations of the structure during seismic shaking are affected by the interactions among the three interconnected systems: the structure, the foundation, and the geological media underlying and surrounding the foundations.

When a structure is built on soft soil, it is generally more susceptible to significant deformations compared to if it were erected on rock soil. As a result, various issues can arise, such as cracking due to differential settlements (13, 14).

The consideration of soil-structure interaction is accomplished by integrating a system of springs and dampers. The foundation and its interaction with the soil (spring-dampers) are modeled using impedance functions. The expression for these foundation impedances is cited in Table 1 according to the FEMA 356 (15) standard.

2. 3. Damping and the Effective Period of the Soil-structure System

Typically, a damping coefficient of 5% is employed in dynamic analyses for ordinary structures experiencing seismic forces. Nevertheless, this value holds limited significance for reinforced concrete buildings when considering Soil-Structure Interaction (SSI). Soil exhibits two forms of damping: internal damping caused by the soil's hysteresis (hysteretic damping), and damping resulting from the dispersion of seismic waves (radial damping).

To account for the increase in damping, Veletsos and Nair (16) propose the following similar Equation 1:

$$\tilde{\varepsilon} = \varepsilon_f + \frac{\varepsilon_i}{\left(\frac{\bar{T}^3}{T^3}\right)} \tag{1}$$

In the given equation, the total system damping is calculated by adding the damping of the foundation to a

TABLE 1. Foundation impedances and total damping for the cases studied

Degrees of Freedom	Foundation impedances
Translation along the x-axis	$K_x = \frac{GB}{2-\upsilon}[3.4\left(\frac{L}{B}\right)^{0.65} + 1.2]$
Translation along the y-axis	$K_y = \frac{GB}{2-\upsilon}[3.4\left(\frac{L}{B}\right)^{0.65} + 0.4\frac{L}{B} + 0.8]$
Translation along the z-axis	$K_z = \frac{GB}{1-\upsilon}[1.55\left(\frac{L}{B}\right)^{0.75} + 0.8]$
Rotation about the x-axis	$K_{xx} = \frac{GB^3}{1-\upsilon}[0.4\frac{L}{B} + 0.1]$
Rotation about the y-axis	$K_{yy} = \frac{GB^3}{1-\upsilon}[0.47\left(\frac{L}{B}\right)^{2.4} + 0.034]$
Rotation about the z-axis	$K_{zz} = GB^3[0.53\left(\frac{L}{B}\right)^{2.45} + 0.51]$

portion of the structure's damping, which is typically assumed to be 5% for conventional structures.

When determining the effective period, we can combine the two expressions for the period, using both the fixed T (rigid foundation) and $\overline{T}$ (flexible foundation) as bases (17), and it is easy to arrive at Equation 2:

$$\frac{\overline{T}}{T} = \sqrt{1 + \frac{K}{K_u} + \frac{K h_{eff}^2}{K_\theta}} \quad (2)$$

2. 4. The Results of Foundation Impedances and Total Damping for the Soil-structure System Used

Table 2 displays the values of spring stiffness corresponding to different directions, based on the shear wave velocity of the soil for each given site category. These values are specific to a foundation with a section of 18.47x3 m².

3. DEVELOPMENT OF FRAGILITY CURVES

Conducting a quantitative assessment of the likelihood of seismic damage under various seismic loads is crucial. In this context, seismic fragility analysis serves as a significant approach for evaluating the chances of structures or components surpassing a predefined damage threshold when exposed to progressively stronger seismic ground motions (18-22).

This method has been utilized to evaluate the susceptibility of diverse structures to seismic events.

Fragility curves represent the relationship between a specific seismic intensity parameter, such as peak acceleration, spectral intensity, or macroseismic intensity, and the estimated average damage value of a structure. These curves are utilized to evaluate the vulnerability of a particular building and estimate the potential damage it may experience in the event of an earthquake.

The fragility curve follows a logarithmic function in a normal distribution and can be described by the following Equation 4:

$$P(dsi/S_d) = \phi\left(\frac{1}{\beta_{dsi}} \times \ln\left(\frac{S_d}{\overline{S_{d,dsi}}}\right)\right) \quad (4)$$

where, β_{dsi} is the standard deviation of the logarithm of the spectral displacement of the damage state dsiand ϕ is the normal distribution function.

Threshold values $\overline{S_{d,dsi}}$ are given as a function of Dy and the ultimate displacement Du of the structure. For β_{dsi} is calculated directly as a function of μ_u (see Table 3):

4. THE GEOMETRIC CHARACTERISTICS OF THE STRUCTURES STUDIED

The following section focuses on quantifying the vulnerability of six reinforced concrete irregular

TABLE 2. The foundation impedances and total damping for the studied cases.

Total damping		Degrees of freedom	Foundation impedances (* 10^9 N/m)
Soil A	5%	translation along the x-axis 10^9 N/m	18445.92927
		translation along the y-axis 10^9 N/m	26978.8793
		translation along the z-axis 10^9 N/m	21565.30743
		rotation about the x-axis 10^9 N.m/rd	76129.92582
		rotation about the y-axis 10^9 N.m/rd	980618.9313
		rotation about the z-axis 10^9 N.m/rd	852367.2701
Soil B	5%	translation along the x-axis 10^9 N/m	88,86664316
		translation along the y-axis 10^9 N/m	129,975693
		translation along the z-axis 10^9 N/m	103,8948189
Soil B	5%	rotation about the x-axis 10^9 N.m/rd	366,769863
		rotation about the y-axis 10^9 N.m/rd	4724,31133
		rotation about the z-axis 10^9 N.m/rd	4106,435459
Soil C	6%	translation along the x-axis 10^9 N/m	12,9697263
		translation along the y-axis 10^9 N/m	18,96942546
		translation along the z-axis 10^9 N/m	15,16302762
		rotation about the x-axis 10^9 N.m/rd	53,5285746
		rotation about the y-axis 10^9 N.m/rd	689,4940859
		rotation about the z-axis 10^9 N.m/rd	599,3176075
Soil D	13%	translation along the x-axis 10^9 N/m	1,045263868
		translation along the y-axis 10^9 N/m	1,528795178
		translation along the z-axis 10^9 N/m	1,222027707
		rotation about the x-axis 10^9 N.m/rd	4,314006605
		rotation about the y-axis 10^9 N.m/rd	55,56811596
		rotation about the z-axis 10^9 N.m/rd	48,30055978

TABLE 3. Damage threshold values

Damage status thresholds	Definition	β_{dsi}	The state of damage
$\overline{Sd}_{ds1}$	0.7 D_y	$\beta_{ds1} = 0.25 + 0.07 \ln(\mu_u)$	Light
$\overline{Sd}_{ds2}$	D_y	$\beta_{ds2} = 0.2 + 0.18 \ln(\mu_u)$	Moderate
$\overline{Sd}_{ds3}$	$D_y + 0.25\,(D_u - D_y)$	$\beta_{ds3} = 0.1 + 0.4 \ln(\mu_u)$	Severe
$\overline{Sd}_{ds4}$	D_u	$\beta_{ds4} = 0.15 + 0.5 \ln(\mu_u)$	Complete

buildings, in accordance with FEMA 440 (23) standards. The column dimensions are 30x30 cm², and the beam dimensions are 25x30 cm², with a floor height of 3 meters, as shown in Table 4. The buildings are also depicted in Figure 1.

The structure is subjected to a live load of 2 kN/m^2 and a dead load of 7 kN/m^2.

Table 5 presents the properties of four different types of soil on which the studied structures are founded. The SAP2000 software was used to conduct numerical studies.

5. RESULTS AND DISCUSSION

5. 1. Capacity Curves and Plastic Hinge Development

Using nonlinear static analyses (24, 25), capacity curves have been constructed for structures

TABLE 4. Details of the structural elements

Type of structure	Type of section	Reinforcement	
Column	(30x30) cm^2	12T12	
Beam	(25x30) cm^2	Top	Upper
		3T10	6T10

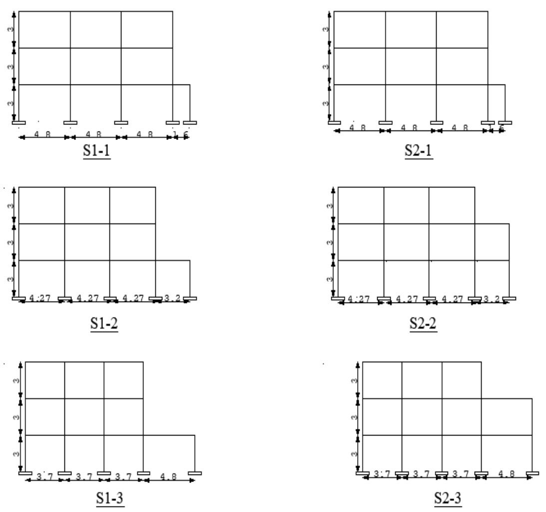

Figure 1. X-Z plan view of the studied construction models with vertical geometric irregularity

TABLE 5. The characteristics of the soils

Soil type	Description	G_0 (N/m) *10^6
Soil A	Rock soil	689475,6
Soil B	Hard soil	3321,675
Soil C	Soft soil	484,785
Soil D	Very soft soil	39,07008

S1-1, S1-2, and S1-3, as well as S2-1, S2-2, and S2-3, for each soil type, as illustrated in Figures 2-9. Subsequently, the development of plastic hinges in the structural elements of the six reinforced concrete buildings with irregularities has been examined.

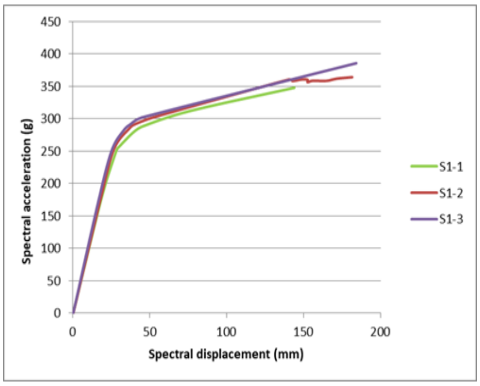

Figure 2. The capacity curves for the studied building models for soil type A (S1-1;S1-2;S1-3)

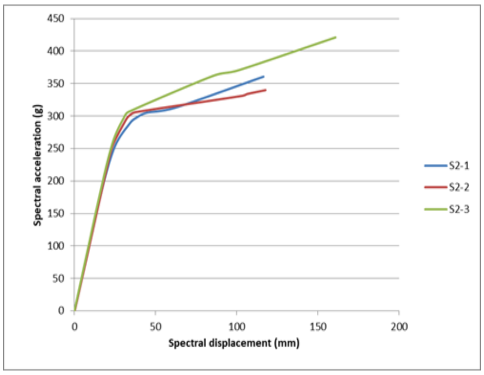

Figure 3. The capacity curves for the studied building models for soil type A (S2-1;S2-2;S2-3)

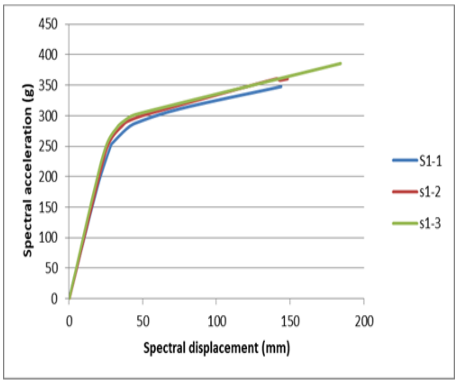

Figure 4. The capacity curves for the studied building models for soil type B (S1-1;S1-2;S1-3)

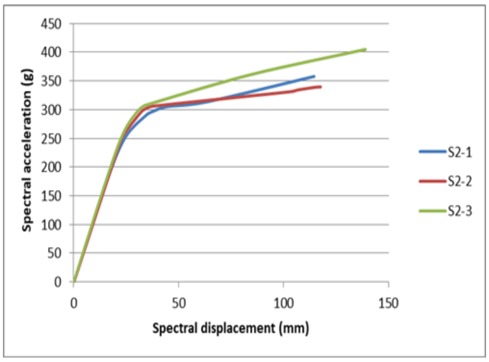

Figure 5. The capacity curves for the studied building models for soil type B (S2-1;S2-2;S2-3)

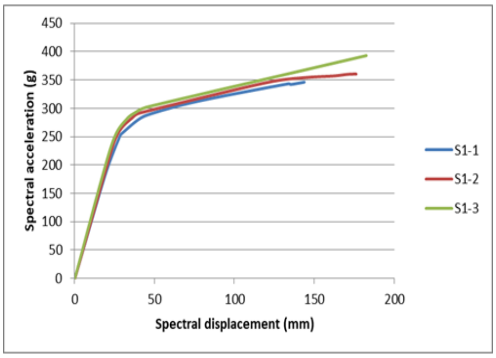

Figure 6. The capacity curves for the studied building models for soil type C (S1-1;S1-2;S1-3)

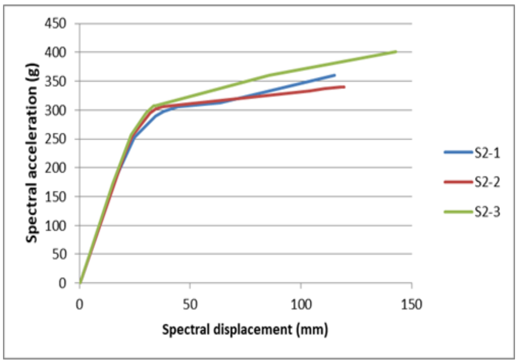

Figure 7. The capacity curves for the studied building models for soil type C (S2-1;S2-2;S2-3)

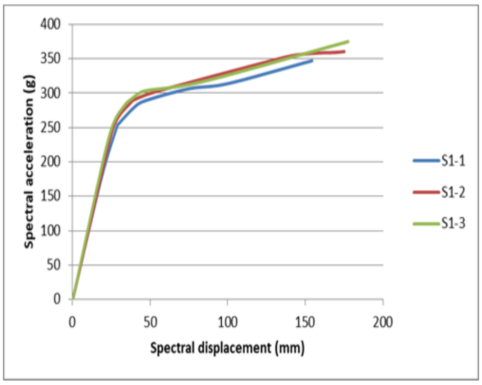

Figure 8. The capacity curves for the studied building models for soil type D (S1-1;S1-2;S1-3)

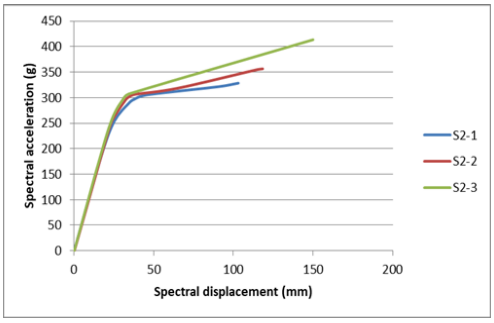

Figure 9. The capacity curves for the studied building models for soil type D (S2-1;S2-2;S2-3)

5. 1. 1. The Capacity Curves Based on the nonlinear static analysis PUSHOVER, capacity curves were established for each building and each soil type, as shown in Figures 2-9. Using these curves, capacity spectra were defined, and elastic capacity points for the modeled reinforced concrete buildings were identified, as indicated in Table 6. The results presented in Table 7 reveal that the setback value and soil type have an influence on the elastic capacity of the building. A significant reduction of 16% is observed for the S1 model with soil types A and B, and a reduction of approximately 11% for the S2 model.

For soil type C, a significant reduction of 16.41% is observed for the S1 model, and a reduction of approximately 11% is observed for the S2 model.

For soil type D, a notable reduction of 14% is observed for the S1 model, and a reduction of approximately 13.5% is observed for the S2 model.

Table 6 reveals that the displacement corresponding to the performance point decreases with an increase in the setback value, particularly for soil types C and D. This indicates that the setback has an influence on the inelastic deformation capacity of the structure during an earthquake, which explains the observed reduction in seismic performance. Consequently, the ductility of the structure will be diminished, potentially leading to significant energy release and damage to the structural elements of the buildings.

TABLE 6. Performance points for the studied buildings

Soil type	Type of structure	Performance point	
		V (kN)	D (mm)
Soil A	S1-1	17.143	1.95
	S1-2	16.486	1.93
	S1-3	15.859	1.696
	S2-1	18.804	1.825
	S2-2	18.512	1.936
	S2-3	18.274	1.676
Soil B	S1-1	21.429	2.397
	S1-2	20.607	2.345
	S1-3	19.823	2.072
	S2-1	23.51	2.249
	S2-2	23.129	2.355
	S2-3	22.828	2.079
Soil C	S1-1	20.293	2.273
	S1-2	19.514	2.236
	S1-3	18.771	1.976
	S2-1	22.262	2.124
	S2-2	21.902	2.243
	S2-3	21.616	1.978
Soil D	S1-1	14.773	1.626
	S1-2	14.201	1.7
	S1-3	13.66	1.527
	S2-1	16.19	1.43
	S2-2	15.936	1.685
	S2-3	15.727	1.512

TABLE 7. Elastic capacity of the studied buildings

Soil type	Type of structure	Elastic capacity	
		Vy (kN)	Dy (mm)
Soil A	S1-1	181.51	19.12
	S1-2	178.76	18.28
	S1-3	166.43	15.97
	S2-1	185.75	16.92
	S2-2	228.89	20.82
	S2-3	173.11	15.11
Soil B	S1-1	181.51	19.1
	S1-2	178.76	18.28
	S1-3	166.43	16
	S2-1	185.77	16.91
	S2-2	228.85	20.86
	S2-3	172.20	15.09
Soil C	S1-1	181.16	19.13
	S1-2	178.80	18.30
	S1-3	166.51	15.99
	S2-1	185.92	16.93
	S2-2	228.91	20.88
	S2-3	171.86	15.08
Soil D	S1-1	178.56	18.89
	S1-2	179.31	18.48
	S1-3	167.37	16.24
	S2-1	187.58	17.25
	S2-2	229.54	21.08
	S2-3	168.07	14.92

5. 1. 2.Distribution of Plastic Hinges The finite element software SAP2000 offers the capability to visualize the development of plastic hinges in structural elements. This allows for tracking and analyzing the behavior of the structure when subjected to loads, particularly in identifying areas where plastic deformations occur and plastic hinges form. This functionality is crucial for evaluating the ductility of the structure and understanding its response to extreme loads, such as those generated by an earthquake. Figures 10-15 provide an illustration of the distribution of plastic hinges for each building on each soil type. They highlight the presence of plastic hinges in most of the columns on the first and second floors, as well as in some columns on the third floor. These images allow for visualizing the areas of plastic deformation and identifying the structural elements that experience the most significant deformations during an earthquake.

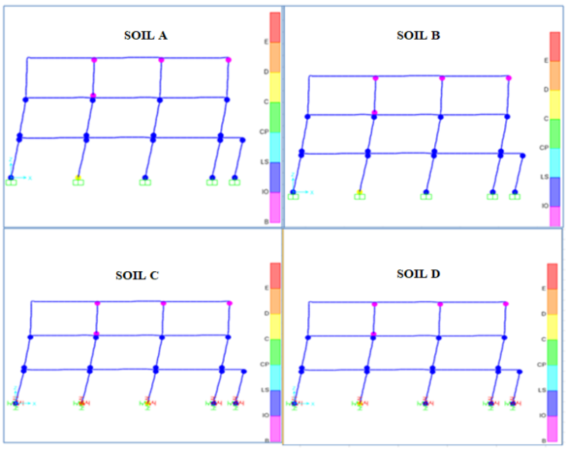

Figure 10. The development of plastic hinges in structural elements for the model S1-1

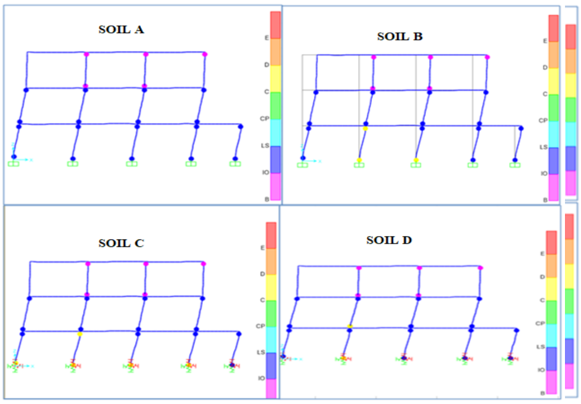

Figure 11. The development of plastic hinges in structural elements for the model S1-2

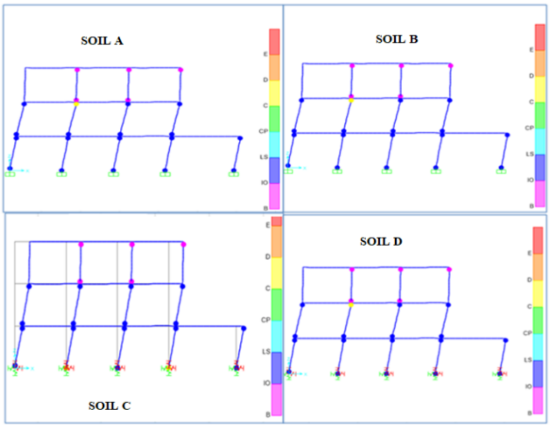

Figure 12. The development of plastic hinges in structural elements for the model S1-3

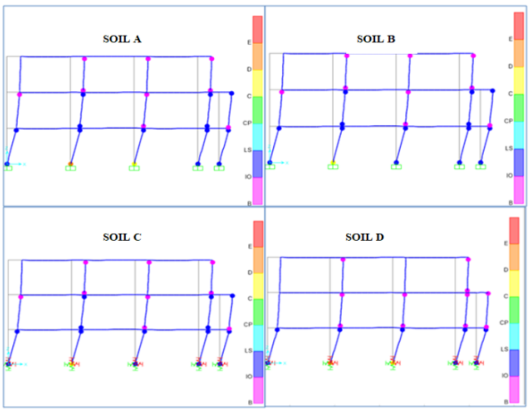

Figure 13. The development of plastic hinges in structural elements for the model S2-1

As the applied force and rotation of the plastic hinges increase, different types of hinges can be observed. For cases S1-1, S1-2, and S1-3 on soil types A and B, Type B, Type Intermediate Opening (IO), and Type C hinges are observed. This suggests the presence of damage in the

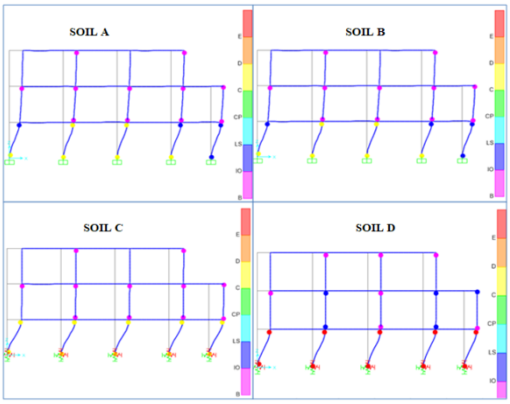

Figure 14. The development of plastic hinges in structural elements for the model S2-1

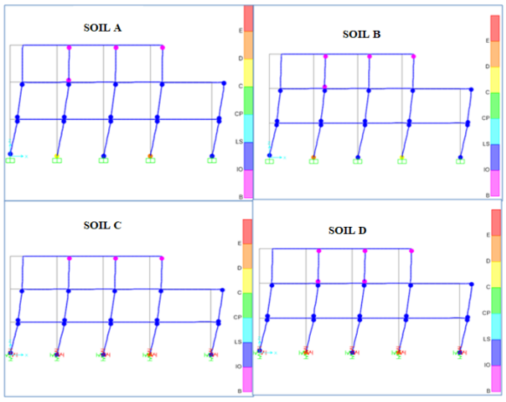

Figure 15. The development of plastic hinges in structural elements for the model S2-3

structure, but it is not yet considered to be very significant.

However, for soil types C and D, the appearance of Type D hinges is observed in addition to the other types mentioned earlier. This observation indicates the presence of more significant damage in the structure, requiring special attention.

These observations help in understanding the evolution of structural behavior and identifying the most vulnerable areas to damage during an earthquake.

By examining cases S2-1, S2-2, and S2-3, it is observed that for soil types A and B, Type B, Type IO, Type C, and Type D, hinges are formed. However, for soil types C and D, the appearance of Type E hinges is also observed, indicating a higher level of damage that could lead to structural failure.

These observations lead us to conclude that vertical geometric irregularities at different levels, as well as the soil type, have a negative influence on the behavior of the structure during an earthquake. Vertical geometric irregularities can result in stress concentration and an uneven redistribution of seismic forces, leading to zones that are more vulnerable to damage. Additionally, soil characteristics such as stiffness and the ability to dissipate seismic energy can also play a significant role in the overall behavior of the structure.

5. 2.Curves of Fragility The fragility curves are created through the compilation of seismic intensity values associated with a particular soil type until they align with a pre-established damage intensity threshold. These curves adeptly illustrate the propagation of seismic intensity influenced by variations in soil characteristics, highlighting a substantial likelihood of reaching or surpassing a notable level of seismic damage (26-28).

The vulnerability of a typical reinforced concrete structure will be analyzed using a seismic performance approach that integrates the effects of Soil-Structure Interaction (SSI) into the nonlinear response .

Fragility curves are constructed to assess the probability of exceeding different seismic intensities, as illustrated in Figures 16-19. The probability of exceeding is determined using Equation 4. The damages probabilities are shown in Figure 20; these are computed taking into account the performance points of each structure.

This approach allows for estimating the probability of experiencing different levels of damage based on the seismic intensity. It provides valuable insights to assess the vulnerability of the structure and make informed decisions regarding design and seismic strengthening.

Figure 20 displays the calculated damage probabilities for various construction models based on different site classes. The results emphasize the critical

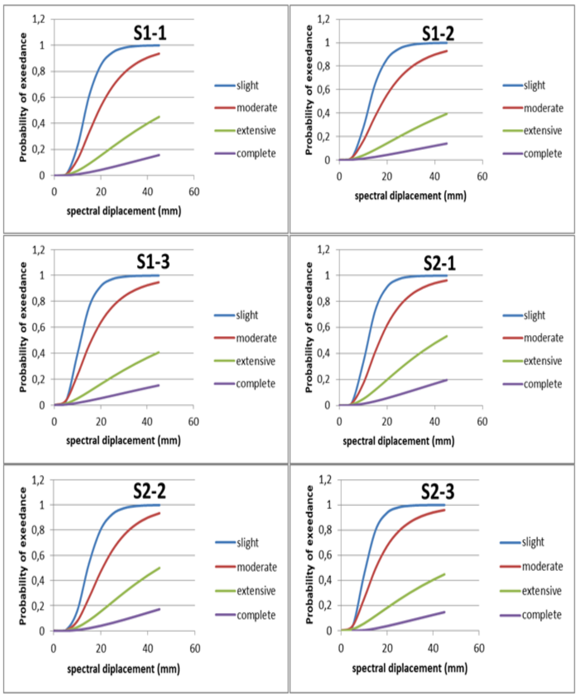

Figure 16. Fragility curves for Soil A

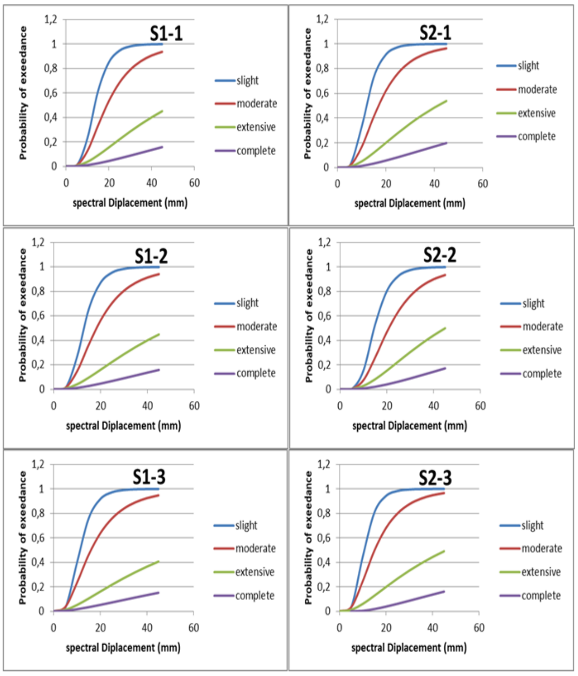

Figure 17. Fragility curves for Soil B

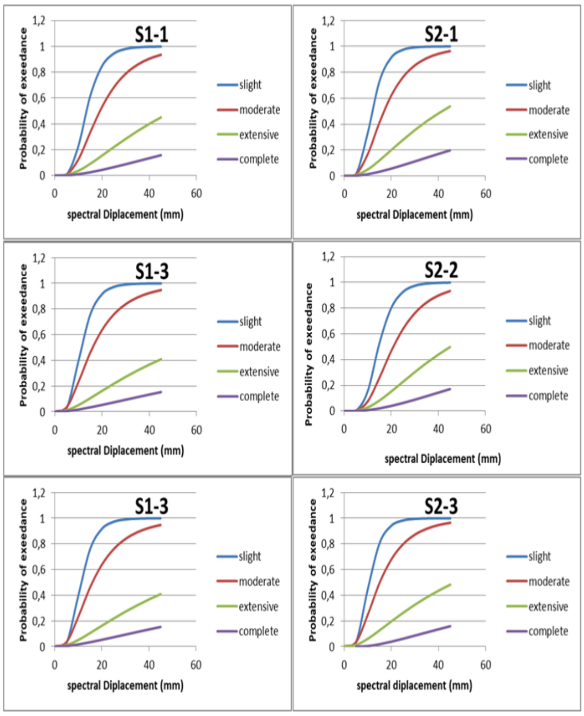

Figure 18. Fragility curves for Soil C

significance of site selection in seismic vulnerability analysis.

Structures constructed on soil types A and B exhibit low damage probabilities, regardless of the damage state under consideration. Conversely, structures built on soil types C and D demonstrate higher damage probabilities. This trend remains consistent regardless of the setback position along the building height.

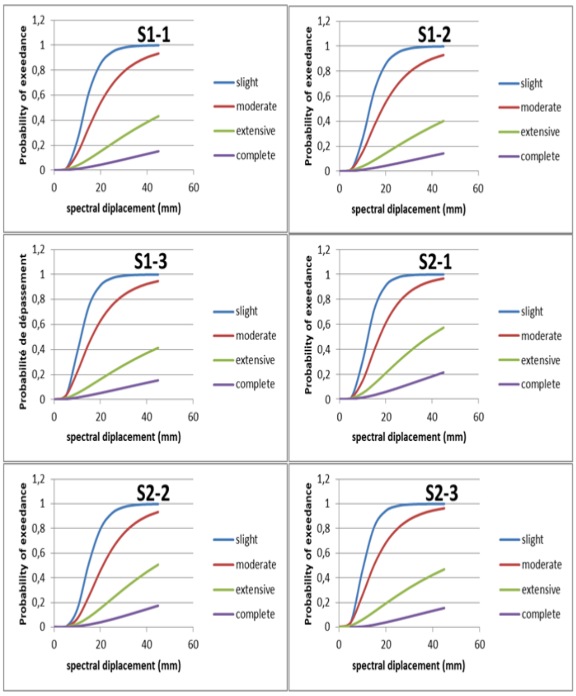

Figure 19. Fragility curves for Soil D

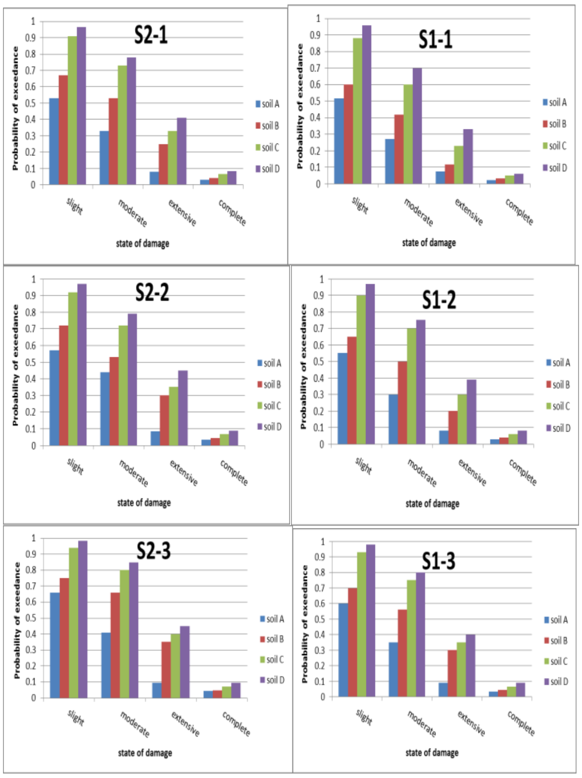

Figure 20. The effect of soil type on the seismic vulnerability of the studied models

It has been confirmed that the behavior of a structure is influenced not just by its motion characteristics and the specifics of the seismic forces it experiences, but also by the surrounding external conditions at its foundation. This encompasses the interplay between the structure, its base, and the underlying soil (29-31).

Furthermore, Figure 20 illustrates the considerable influence of shrinkage position on the probability of damage. As the building height increases, so does the likelihood of damage. In other words, the probability of damage rises as the shrinkage exceeds one storey.

These observations underscore the importance of considering both site selection and setback position when analyzing the seismic vulnerability of building structures (32). This comprehensive analysis provides a better understanding of the risks associated with different seismic scenarios and guides decisions on seismic design and strengthening. Incorporating these considerations is essential for enhancing the resilience of buildings against potential earthquakes.

6. CONCLUSIONS

The objective of this research was to investigate the impact of changing site class and incorporating Soil-Structure Interaction (SSI) effects on the structural vulnerability of irregular reinforced concrete buildings during earthquakes.

The main conclusions drawn from this study are as follows:

- Ultimate Capacity and Plastic Hinge Development:

The results of the study highlighted the influence of vertical geometric irregularity and changing soil class on the behavior of the structure. In the case of soft soil conditions, a significant decrease in the building's elastic capacity is evident. The S1 model displays a reduction of about 14%, while the S2 model shows an approximate reduction of 13.50%.

The development of plastic hinges in structural elements and the ultimate capacity of the building were notably affected. As the setback margin value increased, the structural fragility of reinforced concrete buildings also increased. Therefore, it can be concluded that the degree of vertical geometric irregularity has a significant impact on the performance of building structures. Higher irregularity values lead to a more pronounced reduction in inelastic deformation capacity.

- Damage Probabilities and Site Selection:

The calculated damage probabilities for different building models underscore the importance of site selection in seismic vulnerability analysis. Structures constructed on rocky soil exhibit low probabilities of damage, regardless of the considered damage state. In contrast, buildings erected on loose soil show higher probabilities of damage.

- Significance of Site Class and Geometric Irregularity:

The research highlights that both site class and geometric irregularity are crucial factors influencing the seismic vulnerability of these structures. During the structural analysis phase, it is vital to take these aspects into account to better understand the associated risks and implement appropriate design and reinforcement measures.

Considering these findings, it becomes evident that a comprehensive seismic risk assessment should consider both site selection and geometric irregularity to ensure the safety and resilience of irregular reinforced concrete buildings during earthquakes. Properly accounting for these factors in the design and strengthening processes will lead to more effective mitigation strategies and safer structures.

7. REFERENCES

1. Chopra AK, Kan C. Effects of stiffness degradation on ductility requirements for multistorey buildings. Earthquake Engineering & Structural Dynamics. 1973;2(1):35-45. 10.1002/eqe.4290020104
2. Ruiz S, Diederich R. The Mexico earthquake of September 19, 1985—the seismic performance of buildings with weak first storey. Earthquake Spectra. 1989;5(1):89-102. 10.1193/1.1585512
3. Shahrooz BM, Moehle JP. Seismic response and design of setback buildings. Journal of Structural Engineering. 1990;116(5):1423-39. 10.1061/(ASCE)0733-9445(1990)116:5(1423)
4. Valmundsson EV, Nau JM. Seismic response of building frames with vertical structural irregularities. Journal of Structural Engineering. 1997;123(1):30-41. 10.1061/(ASCE)0733-9445(1997)123:1(30)
5. Michalis F, Dimitrios V, Manolis P. Evaluation of the Influence of Vertical Irregularities on the Seismic Performance of a 9-storey steel frame. 10.1002/eqe.591
6. Sameer JS, Shinde S. Seismic response of vertically irregular RC frame with mass irregularity. International Journal of Civil Engineering and Technology. 2016;7(5):2016. IJCIET_07_05_028
7. Shah BM, Davis R, Nandakumar C, Sarkar P, editors. Review of Performance of Existing Vertical Irregularity Indicators for Steel Framed Buildings. Proceedings of SECON 2020: Structural Engineering and Construction Management 4; 2021: Springer.
8. Ro KM, Kim MS, Lee YH. A simplified approach to modeling vertically irregular structures for dynamic assessment. Journal of Asian Architecture and Building Engineering. 2022;21(6):2320-9. 10.1080/13467581.2021.1971682
9. Hait P, Sil A, Choudhury S. Damage assessment of reinforced concrete buildings considering irregularities (research note). International Journal of Engineering. 2019;32(10):1388-94. 10.5829/ije.2019.32.10a.08
10. Mouhine M, Hilali E. Seismic vulnerability assessment of RC buildings with setback irregularity. Ain Shams Engineering Journal. 2022;13(1):101486. 10.1016/j.asej.2021.05.001
11. Miranda E, Bertero VV. Evaluation of strength reduction factors for earthquake-resistant design. Earthquake Spectra. 1994;10(2):357-79.
12. Mekki M, Elachachi S, Breysse D, Zoutat M. Seismic behavior of RC structures including soil-structure interaction and soil variability effects. Engineering Structures. 2016;126:15-26. 10.1016/j.engstruct.2016.07.03428
13. Zhang X, Far H. Seismic Response of High-Rise Frame–Shear Wall Buildings under the Influence of Dynamic Soil–Structure Interaction. International Journal of Geomechanics. 2023;23(9):04023141. 10.1061/IJGNAI.GMENG-845
14. Aydin E, Ozturk B, Bogdanovic A, Farsangi EN, editors. Influence of soil-structure interaction (SSI) on optimal design of passive damping devices. Structures; 2020: Elsevier. 10.1016/j.istruc.2020.09.028
15. Safety IS. Recommended Provisions for Seismic Regulations for New Buildings and Other Structures (FEMA 450). FEMA: Washington, DC, USA. 2003.
16. Veletsos AS, Nair VD. Seismic interaction of structures on hysteretic foundations. Journal of the Structural Division. 1975;101(1):109-29. 10.1016/j.asej.2021.05.001
17. Veletsos AS, Verbič B. Vibration of viscoelastic foundations. Earthquake Engineering & Structural Dynamics. 1973;2(1):87-102. 10.1002/eqe.4290020108
18. Pan H, Li C, Tian L. Seismic fragility analysis of transmission towers considering effects of soil-structure interaction and depth-varying ground motion inputs. Bulletin of Earthquake Engineering. 2021;19(11):4311-37. 10.1007/s10518-021-01124-x
19. Kassem MM, Nazri FM, Farsangi EN, Ozturk B. Improved vulnerability index methodology to quantify seismic risk and loss assessment in reinforced concrete buildings. Journal of Earthquake Engineering. 2022;26(12):6172-207. 10.1080/13632469.2021.1911888
20. Kassem MM, Nazri FM, Farsangi EN, Ozturk B. Development of a uniform seismic vulnerability index framework for reinforced concrete building typology. Journal of Building Engineering. 2022;47:103838. https://doi.org/10.1016/j.jobe.2021.103838
21. Ozturk B, Sahin HE, Yildiz C, editors. Seismic performance assessment of industrial structures in turkey using the fragility curves. 15th World Conference on Earthquake Engineering, Lisbon, Portugal; 2012.
22. Nair S, Hemalatha G, Stephen E. Seismic vulnerability studies of a g+ 17 storey building in abu dhabi-uae using fragility curves. International Journal of Engineering, Transactions B: Applications. 2021;34(5):1167-75. 10.5829/IJE.2021.34.05B.10
23. Council AT. Improvement of nonlinear static seismic analysis procedures: FEMA Region II; 2005.
24. Chopra AK, Goel RK. A modal pushover analysis procedure for estimating seismic demands for buildings. Earthquake engineering & structural dynamics. 2002;31(3):561-82. 10.1002/eqe.144
25. Chintanapakdee C, Chopra AK. Evaluation of modal pushover analysis using generic frames. Earthquake engineering & structural dynamics. 2003;32(3):417-42. 10.1002/eqe.232
26. Porter K, Kennedy R, Bachman R. Creating fragility functions for performance-based earthquake engineering. Earthquake spectra. 2007;23(2):471-89. 10.1193/1.2720892
27. Park Y-J, Ang AH-S, Wen YK. Seismic damage analysis of reinforced concrete buildings. Journal of Structural Engineering. 1985;111(4):740-57. 10.1061/(ASCE)0733-9445(1985)111:4(740)
28. Taliakula P, Prasad DV. Seismic fragility analysis of regular and vertical setback R/C frame buildings. Int Journal of Engineering Research and Applications, ISSN. 2015:2248-9622.
29. Mekki M, Elachachi S, Breysse D, Nedjar D, Zoutat M. Soil-structure interaction effects on RC structures within a performance-based earthquake engineering framework. European

Journal of Environmental and Civil Engineering. 2014;18(8):945-62. 10.1080/19648189.2014.917056

30. Sharanya A, Heeralal M, Thyagaraj T. Soil shrinkage characterization of low plasticity soil using digital image analysis process. International Journal of Engineering, Transactions A: Basics. 2021;34(10):2206-12. 10.5829/ije.2021.34.10a.02

31. Shirzadi M, Behnamfar F, Asadi P. Effects of soil–structure interaction on inelastic response of torsionally-coupled structures. Bulletin of Earthquake Engineering. 2020;18:1213-43. 10.1007/s10518-019-00747-5

32. Mouhine M, Hilali E. Seismic vulnerability for irregular reinforced concrete buildings with consideration of site effects. Materials Today: Proceedings. 2022;58:1039-43. 10.1016/j.matpr.2022.01.038

Persian Abstract

چکیده

در این مطالعه، ما تحقیقی در مورد ارزیابی آسیب‌پذیری لرزه‌ای سازه‌های بتن مسلح با ارتفاع متوسط با بی‌نظمی هندسی عمودی (پسرفت) ارائه می‌کنیم. ما تأثیرات درصد و مکان عقب‌نشینی در طول ارتفاع ساختمان و همچنین تأثیر تغییر کلاس‌های سایت را در نظر گرفتیم. علاوه بر این، ما اثرات برهمکنش خاک-ساختار را در پاسخ غیرخطی ساختمان گنجانده ایم. در بخش اول، تأثیر پارامترهای فوق بر پاسخ لرزه‌ای یک سازه را از طریق تحلیل‌های استاتیکی غیرخطی بررسی کردیم. ما منحنی های ظرفیت و توسعه لولاهای پلاستیکی را در عناصر ساختاری تجزیه و تحلیل کردیم. در بخش دوم، شکنندگی لرزه‌ای قاب‌های ساختمان را با استفاده از رویکرد مطالعه احتمالی تحلیل کردیم. ما منحنی‌های شکنندگی را برای ارزیابی آسیب‌پذیری سازه‌ها ایجاد کردیم. در نتیجه، نتایج به‌دست‌آمده اهمیت اساسی در نظر گرفتن بی‌نظمی‌های سازه‌ای و همچنین تأثیر طبقات مختلف سایت بر آسیب‌پذیری لرزه‌ای ساختمان‌ها را برجسته می‌کند.

IJE TRANSACTIONS A: Basics Vol. 37 No. 01, (January 2024) 115-126

International Journal of Engineering

Journal Homepage: www.ije.ir

Formation Control and Obstacle Avoidance of a Multi-Quadrotor System Based on Model Predictive Control and Improved Artificial Potential Field

F. Ghaderi[a], A. Toloei*[a], R. Ghasemi[b]

[a] *Department of Aerospace Engineering, Shahid Beheshti University, Tehran, Iran*
[b] *Department of Engineering, University of Qom, Qom, Iran*

PAPER INFO

Paper history:
Paper history: Received 16 June 2023
Received in revised form 18 July 2023
Accepted 19 July 2023

Keywords:
Quadrotor
Formation Control
Model Predictive Control
Obstacle Avoidance
Improved Artificial Potential Field

ABSTRACT

The purpose of this article is to control the formation and pass static and dynamic obstacles for the quadrotor group, maintain the continuity and flight formation after crossing the obstacles, and track the moving target. Model Predictive Control (MPC) method has been used to control the status and position of quadrotors and formation control. Flight formation is based on the leader-follower method, in which the followers maintain a certain angle and distance from the leader using the formation controller. The improved Artificial Potential Field (APF) method has been used to pass obstacles, the main advantage of which compared to the traditional APF is to increase the range of the repulsive force of the obstacles, which solves the problem of getting stuck in the local minimum and not passing through the environments full of obstacles. The results of the design of the attitude and position controller showed that the quadrotors were stabilized and converged in less than 3 seconds. Formation control simulations in the spiral path showed that the followers, follow the leader. The results of the quadrotors passing through the obstacles were presented in four missions. In the first mission, 4 quadrotors crossed static obstacles. In the second mission, 4 quadrotors crossed dynamic obstacles. In these two missions, the quadrotors maintained a square flight formation after crossing the obstacles. In the third mission, the number of quadrotors increased to 6. The leader tracked the moving target and the quadrotors crossing the static obstacles. In the last mission, the quadrotors passed through the dynamic obstacles and the leader tracked the static target. In these missions, the quadrotors maintain the hexagonal formation after crossing the obstacles. The results simulations showed that the quadrotors crossed the fixed and moving obstacles and after crossing, they preserved the flight formation.

doi: *10.5829/ije.2024.37.01a.11*

1. INTRODUCTION

Robots have been widely used in military and civilian fields such as anti-terrorism operations, identification, agriculture, etc. (1, 2). In addition, instead of using a single robot, multiple robots in a group formation can complete some complex missions without incurring high costs (3, 4). Among the controllers used to control the formation is model predictive control (MPC). MPC is a controller where optimization is solved online. The vital advantage of this method is considering a performance criterion and constraints. For multi-agent systems, the time of optimization calculations increases with the number of agents. To solve this problem, decentralized MPC (5, 6) or distributed MPC (7) have been proposed. The formation control of multiple robots is generally classified into leaderless and leader-follower (8). In the leaderless formation control problem, the robots are driven to a prescribed pattern at a certain speed. In contrast in the leader-follower control problem, the follower robots agree on the reference information of a leader while maintaining the defined pattern. In the control of leader-follower formation, the problem of the availability of information about the leader can be solved by distributed technique. A distributed control approach was designed by Zou and Meng (8) by introducing

*Corresponding Author Institutional Email: toloei@sbu.ac.ir (A. Toloei)

Please cite this article as: Ghaderi F, Toloei A, Ghasemi R. Formation Control and Obstacle Avoidance of a Multi-Quadrotor System Based on Model Predictive Control and Improved Artificial Potential Field. International Journal of Engineering, Transactions A: Basics. 2024;37(01): 115-126.

distributed estimators to obtain reference information for leader-follower control. Another distributed control algorithm was proposed by Dong et al. (9) to track the flight formation of multiple robot leader-follower. In addition, a non-smooth distributed control algorithm was developed by Du et al. (10), so that the robot leader-follower control tracking was achieved. In addition, with the help of a sub-optimal H∞ strategy, a distributed leader-follower control algorithm is designed by Jasim et al. (11) that is robust to disturbances and parameter uncertainties. Although the control schemes proposed in the mentioned papers are convincing in hierarchical leader-follower formation control tracking, the control command extraction may cause singularities and chattering, which may cause implementation problems in practical applications. Also, in these articles, the flight group has a flight arrangement in a simple route, and the issue of moving target tracking has not been investigated. In this article, the MPC method is used for formation control in which there is no possibility of chattering, and the flight path is a spiral path, and the issue of moving target tracking is also investigated.

It is essential, to maintain the safety of the operations in the missions that the UAV group performs. One of the most important safety issues is avoiding obstacles. If a group of quadrotors encounters obstacles in an unknown environment, each drone must recognize the obstacle and pass through it. Crossing obstacles is necessary to avoid accidents and make the flight safe. This article focuses on the crossing of the quadrotor group through static and dynamic obstacles and maintaining the flight arrangement after crossing the obstacles. The methods of solving the collision avoidance problem are different for dynamic and static obstacles. A* (12), Genetic (13), Differential Evolution (14), Ant Colony Optimization (15), and Particle Swarm Optimization (16) methods are usually used to avoid static obstacles. Methods for dealing with dynamic obstacles include Fuzzy Logic Algorithm (17), Neural Network (18), Rapidly-exploring Random Trees (19), and APF (20). Shang et al. (21) used the terminal nonsingular sliding mode controller for the problem of control formation and obstacle avoidance. Quadrotors have maintained formation flight after crossing obstacles. In this paper, only static obstacles are considered.

One of the most widely used methods to identify and avoid obstacles is the APF method. Which is expressed by mathematical equations and has advantages such as high safety and simplicity of calculations. In this method, a positive potential field is considered for obstacles, and a negative potential field for the target. The drone is attracted to the target by avoiding obstacles. Pan et al. (22) introduced formation control which is based on the leader-follower method, in which the PD is used to control the position and attitude of the quadrotors, and the APF is used to pass the obstacles. To prove the effectiveness of the above method, several experiments have been performed. In this article, crossing dynamic obstacles is not investigated. Wang and Zhang (23) have presented a rapidly-exploring random trees algorithm for the formation control and crossing obstacles, in which the lack of vigilance and low speed of the APF method is compensated by the sampling method. In this article, crossing static obstacles is considered. Qiao et al. (24) have provided formation control based on distributed control. The potential function is used to avoid the collision. A virtual navigator determines the movement of agents. In this article, the obstacles are static, and the drones maintain the connection after crossing. Aljassani et al. (25) presented a new APF method for the UAV group to pass through obstacles, which solves the problem of getting stuck in a local minimum. The leader-follower method is used for group movement. The obstacles considered are two static obstacles. In these articles, the crossing of dynamic obstacles is not investigated. Huang et al. (26) have investigated dynamic obstacles avoidance and maintaining continuity and formation flight after crossing obstacles. The sliding mode method and the virtual potential field method are used for control formation and obstacle avoidance. Zhang et al. (27) proposed a distributed control method for quadrotor group flight formation. The disadvantages of this method are getting stuck in a local minimum and unreachable goals in environments full of obstacles (28). To solve these problems, some approaches have been proposed. Methods are also proposed for broader problems, such as dynamic obstacle avoidance or integration of UAV kinematic models to improve tracking accuracy (29, 30). In the mentioned articles, simultaneously crossing the dynamic and static obstacles and maintaining the flight formation after crossing the obstacles and tracking the mobility target simultaneously have not been discussed and, in a small number of these articles, the improvement of the potential field method has been investigated to solve its problems.

The necessity of doing this article is to improve the potential field method for the passage of the flight group through dynamic obstacles and maintain the connection between the agents.

The innovation of this paper is that it presented an improved potential field method for crossing static and dynamic obstacles and maintaining continuity after crossing obstacles. Where instead of considering a circular repulsion field for obstacles, an elliptical field is considered, which causes the repulsion range of obstacles to be greater and, as a result, solves the problem of getting stuck in the local minimum and not reaching the target in obstacle-filled environments to a great extent, and simultaneously, the leader tracks the moving target while maintaining the flight formation.

The article's structure is as follows: In the first section, the dynamic modeling of the quadrotor is presented. The following section deals with attitude and position controllers. In the third section, the control formation is given; in the fourth section, the crossing of obstacles is discussed; and in the last section, the results are presented.

2. DYNAMIC MODEL OF QUADROTOR

The six degrees of freedom model is obtained according to the Newton-Euler method. Total rotors velocity and the rotor velocity vector are as follows:

$$\Pi == +\varpi_4 + \varpi_2 - \varpi_1 - \varpi_3 \quad , \quad \Pi = \begin{bmatrix} \varpi_1 \\ \varpi_2 \\ \varpi_3 \\ \varpi_4 \end{bmatrix} \tag{1}$$

where $(\varpi_1, \varpi_2, \varpi_3, \varpi_4)$ show the speeds of the rotors. The effect of the motion vector on the quadrotor dynamics is given below:

$$U_B(\varpi) = E_B\varpi^2 = \begin{bmatrix} 0 \\ 0 \\ U_1 \\ U_2 \\ U_3 \\ U_4 \end{bmatrix} = \begin{bmatrix} 0 \\ 0 \\ b(\varpi_1^2 + \varpi_2^2 + \varpi_3^2 + \varpi_4^2) \\ bl(\varpi_4^2 - \varpi_2^2) \\ bl(\varpi_3^2 - \varpi_1^2) \\ c_d(\varpi_2^2 + \varpi_4^2 - \varpi_1^2 - \varpi_3^2) \end{bmatrix} \tag{2}$$

where, l is the length from the center of mass to each rotor, c_T is the thrust force coefficient, and c_d is the drag force coefficient. The E_B and $U_B(\varpi)$, which show the motion matrix and the motion vector, are as follows.

$$E_B = \begin{bmatrix} 0 & 0 & 0 & 0 \\ 0 & 0 & 0 & 0 \\ c_T & c_T & c_T & c_T \\ 0 & -c_T l & 0 & c_T l \\ -c_T l & 0 & c_T l & 0 \\ -c_d & c_d & -c_d & c_d \end{bmatrix} \tag{3}$$

The dynamical equations of the quadrotor are given below:

$$\dot{\vartheta}_1 = \dot{\phi} = \ddot{\phi} + \ddot{\theta} sin\phi tan\theta + \ddot{\psi} cos\,\phi tan\theta$$

$$\dot{\vartheta}_2 = \dot{\theta} = \ddot{\theta} cos\phi - \ddot{\psi} sin\,\phi$$

$$\dot{\vartheta}_3 = \dot{\psi} = \frac{sin\phi}{cos\theta}\ddot{\theta} + \frac{cos\phi}{cos\theta}\ddot{\psi}$$

$$\dot{\vartheta}_4 = \dot{x} = \vartheta$$

$$\dot{\vartheta}_5 = \dot{y} = \vartheta$$

$$\dot{\vartheta}_6 = \dot{z} = \vartheta$$

$$\dot{\vartheta}_7 = \dot{P} = \frac{I_{YY} - I_{ZZ}}{I_{XX}} RQ - \frac{J_{Tp}}{I_{XX}} Q\,\Omega + \frac{U_2}{I_{XX}}$$

$$\dot{\vartheta}_8 = \dot{Q} = \frac{I_{ZZ} - I_{XX}}{I_{YY}} RP + \frac{J_{Tp}}{I_{YY}} P\,\Omega + \frac{U_3}{I_{YY}}$$

$$\dot{\vartheta}_9 = \dot{R} = \frac{I_{XX} - I_{YY}}{I_{ZZ}} PQ + \frac{U_4}{I_{ZZ}}$$

$$\dot{\vartheta}_{10} = \dot{U} = (-WQ + VR) + gs_\theta$$

$$\dot{\vartheta}_{11} = \dot{V} = (-UR + WP) - gc_\theta s_\phi \tag{4}$$

$$\dot{\vartheta}_{12} = \dot{W} = (-UQ + VP) - gc_\theta s_\phi + \frac{U_1}{m}$$

where, J_{Tp} is the moment of total rotation of inertia about the rotor axis, (U, V, W) are the linear velocities, (P, Q, R) are roll, pitch, and yaw, and I_{XX}, I_{YY}, and I_{ZZ} are the moments of inertia in the x, y, and z-axis, whose values are given in Table 1. the rotors speed inputs U_1, U_2, U_3, and U_4 are as follows (21):

$$U_1 = c_T(\varpi_1^2 + \varpi_2^2 + \varpi_3^2 + \varpi_4^2)$$

$$U_2 = lc_T\,(-\varpi_2^2 + \varpi_4^2\,)$$

$$U_3 = l\,c_T\,(-\varpi_1^2 + \varpi_3^2\,) \tag{5}$$

$$U_4 = c_d(-\varpi_1^2 + \varpi_2^2 - \varpi_3^2 + \varpi_4^2)$$

$$\varpi = -\varpi_1 + \varpi_2 - \varpi_3 + \varpi_4$$

3. MPC CONTROLLER

The predictive controller is used in the industry because of its advantages, such as dealing with disturbances, limitations and uncertainties. In this article, a generalized predictive controller is used, which has features such as dealing with non-minimum phase systems and having additional control horizon parameters. In this controller, the control signal is obtained by minimizing the multi-step function in the prediction horizon. As a result, according to the integral behavior in the state space, it is possible to replace $u(k)$ with $\Delta u(k) = u(k) - u(k-1)$ in the equations. The state space equations are given below:

$$\begin{bmatrix} \Delta x_m(k+1) \\ y(k+1) \end{bmatrix} = \begin{bmatrix} A_m & 0_{q\times n}^T \\ C_m A_m & I_{q\times q} \end{bmatrix} \begin{bmatrix} \Delta x_m(k) \\ y(k) \end{bmatrix} + \begin{bmatrix} B_m \\ C_m B_m \end{bmatrix} \Delta u_m(k) + \begin{bmatrix} B_d \\ C_m B_m \end{bmatrix} \varepsilon(k) \tag{6}$$

$$y(k) = \begin{bmatrix} 0_{q\times n}^T & I_{q\times q} \end{bmatrix} \begin{bmatrix} \Delta x_m(k) \\ y(k) \end{bmatrix}$$

TABLE 1. Parameters of quadrotor dynamic

Parameter	Value
I_{XX}	$\mathbf{11 \times 10^{-2}\ kg\ m^2}$
I_{YY}	$\mathbf{19 \times 10^{-2}\ kg\ m^2}$
I_{ZZ}	$\mathbf{1.3 \times 10^{-2}\ kg\ m^2}$
J_{Tp}	$\mathbf{6 \times 10^{-5}\ kg\ m^2}$
m	$\mathbf{3.23\ \ kg}$
l	$\mathbf{0.23}$ **m**
c_d	$\mathbf{7.5 \times 10^{-7}\ N\ m\ s^2}$
c_T	$\mathbf{3.13 \times 10^{-5}\ N\ s^2}$

The output is defined as below:

$$Y = H'x(k) + H".\Delta U \tag{7}$$

where:

$$H' = \begin{bmatrix} CA \\ CA^2 \\ CA^3 \\ \vdots \\ CA^{N_p} \end{bmatrix}, H" = \begin{bmatrix} CB & 0 & 0 & \dots & 0 \\ CAB & CA & 0 & \dots & 0 \\ CA^2B & CAB & CB & \dots & 0 \\ \vdots & \vdots & \vdots & \ddots & \vdots \\ CA^{N_p-1}B & CA^{N_p-2}B & CA^{N_p-3}B & \cdots & CA^{N_p-N_c}B \end{bmatrix} \tag{8}$$

The cost function is considered as below:

$$J = (Y-w)^T W_y (Y-w) + \Delta U^T W_u \Delta U \tag{9}$$

where, Y is the vector of predicted outputs, w is the vector of reference signal values in future times, ΔU is the control signal, and W_u and W_y define the weight of inputs and outputs in the cost function.

The necessary condition for minimizing the cost function is given below:

$$\frac{\partial J}{\partial \Delta U} = 0$$

By satisfying the above condition, u is obtained as follows (31):

$$\Delta U = (H^{"T} W_y H^{"} + W_u)^{-1} H^{"T} W_y (w - H'x(k)) \tag{10}$$

4. FORMATION FLIGHT

Formation control patterns include virtual structure and behavior-based, and leader-follower. In the virtual structure method, each agent is considered an element of a larger structure. In this method, all the arrangement members act as a single rigid body and follow a determined path. This method is suggested to maintain formation while moving. As a result, this method is unsuitable for crossing a group of obstacles because it is necessary to change the formation to pass the obstacles. In addition to the group movement, searching and reaching the desired target is also investigated in the behavior-based structure. The weakness of this method is the difficulty of analyzing the overall behavior of the formation and its mathematical analysis and checking its stability.

In the leader-follower algorithm, one or more agents are designated as leaders, and other quadrotors are considered followers, so the followers must follow the leader with a fixed direction and position. The control of the formation of multi-agent systems using the leader-follower structure has received special attention due to its simplicity and scalability. Since the movement of other vehicles in the formation is completely determined by the leading position, the leading position creates coordination. Therefore, the followers follow the leader to maintain the formation. The advantage of this method is that it is easy to understand and more practical in implementation .This model is used in this article.

4. 1. Formation Control

In this article, quadrotor group control formation and obstacle avoidance are investigated. Formation flight is controlled by the MPC method. The pattern used is leader-follower. In the leader-follower method, the leader follows a determined path, and the followers maintain a certain angle and distance from the leader. Figure 1 illustrates this method. In this figure, λ is the distance from the center of the leader mass to the center of the follower mass, and φ is the angle between the x-axis and λ line.

$$\begin{cases} \lambda_x = -(x_L - x_F)\cos\psi_L - (y_L - y_F)\sin\psi_L \\ \lambda_y = -(x_L - x_F)\sin\psi_L - (y_L - y_F)\cos\psi_L \end{cases} \tag{11}$$

$$\begin{aligned} \lambda_x^d &= \lambda\cos\varphi \\ \lambda_y^d &= \lambda\sin\varphi \end{aligned} \tag{12}$$

The formation error is given below:

$$\begin{cases} e_x = \lambda_x^d - \lambda_x \\ e_y = \lambda_y^d - \lambda_y \\ e_\psi = \psi_F - \psi_L \end{cases} \quad \begin{cases} \dot{e}_x = \dot{\lambda}_x^d - \dot{\lambda}_x \\ \dot{e}_y = \dot{\lambda}_y^d - \dot{\lambda}_y \\ \dot{e}_\psi = \dot{\psi}_F - \dot{\psi}_L \end{cases} \tag{13}$$

λ^d and φ^d are constant parameters, therefore, λ_x^d and λ_y^d have constant values and, their derivatives $\dot{\lambda}_x^d$ and $\dot{\lambda}_y^d$ are zero. The transition dynamics on the x-y plane are present below:

$$\begin{cases} \dot{x}_i = v_{ix}\cos\psi_i - v_{iy}\sin\psi_i \\ \dot{y}_i = v_{ix}\sin\psi_i + v_{iy}\cos\psi_i \\ \dot{\psi}_L = \omega_L \end{cases} \tag{14}$$

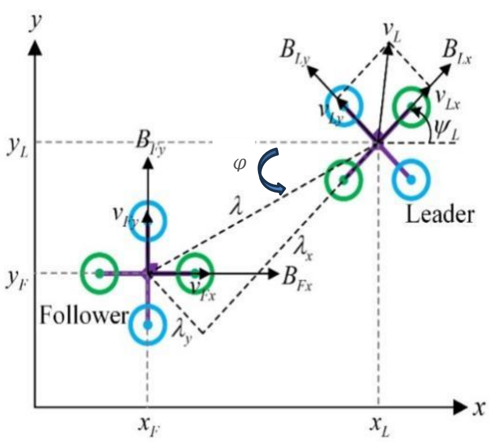

Figure 1. Quadrotor formation in x-y plane

i indicate leader (i = L) or follower (i = F). $\dot{x}_i$ and $\dot{y}_i$ are velocities in the ground coordinate system. ψ_i is the angle between the x-axis of the body and the ground coordinate system, and v_{ix} and v_{iy} are the velocities in the body coordinate system:

$$\begin{cases} v_{ix} = \dot{x}_i \cos\psi_i + \dot{y}_i \sin\psi_i \\ v_{iy} = -\dot{x}_i \sin\psi_i + \dot{y}_i \cos\psi_i \end{cases} \tag{15}$$

As a result, the following relations are obtained.

$$\begin{cases} \dot{e}_x = -\left(\lambda_y^d - e_y\right)\omega_L - v_{Fx}\cos e_\psi + v_{Fy}\sin e_\psi + v_{Lx} \\ \dot{e}_y = \left(\lambda_x^d - e_x\right)\omega_L - v_{Fx}\sin e_\psi - v_{Fy}\cos e_\psi + v_{Ly} \\ \dot{e}_\psi = \omega_F - \omega_L \end{cases} \tag{16}$$

The state space is as below.

$$\dot{x} = A(x) + B(x)\tau \tag{17}$$

where x is the state vector and τ is the control input, and M(x) and N(x) are defined as follows (32):

$$x = [e_x \quad e_y \quad e_\psi]^T \tag{18}$$

$$\tau = [\tau_{Fx} \quad \tau_{Fy} \quad \omega_F]^T \tag{19}$$

$$A(x) = \begin{bmatrix} e_y\omega_L + \tau_{Lx} - \omega_L\lambda_y^d \\ -e_x\omega_L + \tau_{Ly} + \omega_L\lambda_x^d \\ -\omega_L \end{bmatrix} \tag{20}$$

$$B(x) = \begin{bmatrix} -\cos e_\psi & \sin e_\psi & 0 \\ -\sin e_\psi & -\cos e_\psi & 0 \\ 0 & 0 & 1 \end{bmatrix} \tag{21}$$

The control law for the formation of the quadrotors based on MPC (33) is considered as follows:

$$\begin{gathered} M_i(k) = -\sum_{j=1}^{N+1} a_{ij}\left[\sum_{k=0}^{3}\beta_k\left(f_i^{(k)} - \hat{f}_j^{(k)}\right)\right], \\ i\epsilon\{1,2,\dots,N\}, \\ \hat{f}_j^{(k)} = f_j^{(k)} - d_{fj}^{(k)}, \quad j\epsilon\{1,2,\dots,N+1\}, \\ \begin{cases} \beta > 0 \ \forall k\epsilon\{0,1,2,3\} \\ \lambda_{min} > \frac{\beta_1^2}{\beta_1\beta_2\beta_3 - \beta_0\beta_3^2} \\ \beta_1\beta_2 > \beta_0\beta_3 \end{cases} \end{gathered} \tag{22}$$

where i and $N + 1$ represent quadrotor i and the leader. The control gains $\beta_k\epsilon\mathbb{R}, k\epsilon\{0,1,2,3\}$ must satisfy conditions (13). $d_{fj}^{(k)}\boldsymbol{\epsilon}\mathbb{R}^2$ is the desired state between $quadrotor\ j$ and the leader on the horizontal plane. The control law for the formation flight of $quadrotor\ i$ in the vertical direction (34) is as follows:

$$\begin{gathered} T_i(k) = -\sum_{j=1}^{N+1} a_{ij}\left[\sum_{k=0}^{3}\gamma_k\left(h_i^{(k)} - \hat{h}_j^{(k)}\right)\right], \\ i\epsilon\{1,2,\dots,N\}, \\ \hat{h}_j^{(k)} = h_j^{(k)} - d_{hj}^{(k)}, \quad j\epsilon\{1,2,\dots,N+1\}, \\ k\epsilon\{0,1\}, \\ \gamma_k > 0, \ k\epsilon\{0,1\}, \end{gathered} \tag{23}$$

where $\gamma_k\epsilon\mathbb{R}\ k\epsilon\{0,1\}$ is control gains and $d_{hj}^{(k)}\epsilon\mathbb{R}^2$ is the desired relative state between $quadrotor\ j$ and the leader in the vertical direction.

5. IMPROVED ARTIFICIAL POTENITIAL FIELD

In the APF, attractive potential is considered for the target, and repulsive potential is considered for the obstacles. The agent moves away from the obstacles by moving towards the target.

The control of the agent by the AFP is as below:

$$U_{ar}(x) = U_a(x) + U_r(x) \tag{24}$$

where, $U_{ar}, U_a, and\ U_r,$ represent the potential of attraction, the potential of repulsion, and the potential virtual field. Gradient functions are stated as follows:

$$\begin{gathered} F_{art} = F_a + F_r \\ F_a = -grad[U_a(x)] \\ F_r = -grad[U_r(x)] \end{gathered} \tag{25}$$

where $\boldsymbol{F_a}$ is the robot's attraction, and $\boldsymbol{F_r}$ is the force created by $\boldsymbol{U_r(x)}$. The attraction coefficient $\boldsymbol{k_a}$ and the potential attraction field $\boldsymbol{U_a(x)}$ are given below:

$$U_a = \frac{1}{2}k_a R_a^2 \tag{26}$$

The $\boldsymbol{U_r}$ (x) is as follows:

$$U_r(x) = \begin{cases} 0.5k_a\left(\frac{1}{R_r} - \frac{1}{X_0}\right)^2 & R_r \le X_0 \\ 0 & R_r > X \end{cases} \tag{27}$$

where $\boldsymbol{X_0}$ is the safe distance from the obstacles. $\boldsymbol{R_a} = \|\boldsymbol{X_d} - \boldsymbol{X}\| = \sqrt{(\boldsymbol{x}-\boldsymbol{x_d})^2 - (\boldsymbol{z}-\boldsymbol{z_d})^2 - (\boldsymbol{y}-\boldsymbol{y_d})^2}$ is the distance from the agent to the target, $\boldsymbol{R_r} = \|\boldsymbol{X_u} - \boldsymbol{X}\| = \sqrt{-(\boldsymbol{z}-\boldsymbol{z_u})^2 + (\boldsymbol{x}-\boldsymbol{x_u})^2 - (\boldsymbol{y}-\boldsymbol{y_u})^2}$ is the shortest distance from the agent, and the obstacles, where $\mathbf{X} = (\mathbf{x}, \mathbf{y}, \mathbf{z})$, $\boldsymbol{X_m} = (\boldsymbol{x_m}, \boldsymbol{y_m}, \boldsymbol{z_m})$, and $\boldsymbol{X_d} = (\boldsymbol{x_d}, \boldsymbol{y_d}, \boldsymbol{z_d})$ are the position of the agent, the position of obstacles and the position of the target. The functions of repulsion and attraction are present below:

$$\begin{gathered} F_a = -\nabla\left(\frac{1}{2}k_a R_a^2\right) k_a R_a \\ U_r(x) = \begin{cases} k_a\left(\frac{1}{R_r} - \frac{1}{{R_r}^2}\right)\frac{1}{{R_r}^2} & R_r \le X_0 \\ 0 & R_r > X_0 \end{cases} \end{gathered} \tag{28}$$

The traditional APF method works poorly in obstacle environments, and may get stuck in a local minimum. To solve this issue, the improved APF is used. The spherical repulsion field has been changed to an elliptic field in the APF. According to Figure 2, the agent is placed in the center of the ellipse and the locations of the obstacles are C and D. Around the agent, there is an ellipse repulsion field, and the obstacles are placed on the edges of the ellipse, which have different distances from the agent. As a result, the repulsive field created can repel obstacles more effectively (The range of repulsive increases). The advantage of this way is that it allows a greater safety distance for the agent to pass and makes it easier to pass obstacles in complex environments. The parameters of the ellipsoidal APF are proportional to the velocity of the agent. The magnitudes of its long semi-axis $\boldsymbol{\alpha}$ and middle semi-axis $\boldsymbol{b}$ are determined by the components of the agent's velocity. The focal length is $\boldsymbol{c_1} = \sqrt{\boldsymbol{\alpha^2 - \beta^2}}$, and combined with the agent's coordinates and the velocity direction can be derived from the coordinates of the two focal points of the ellipse, as follows:

$$
\begin{aligned}
&\boldsymbol{x_{c1} - x_m = -\varrho v_x}\\
&\boldsymbol{y_{c1} - y_m = -\varrho v_y}\\
&\boldsymbol{z_{c1} - z_m = -\varrho v_z}\\
&\boldsymbol{(x_{c1} - x_m)^2 + (y_{c1} - y_m)^2 + (z_{c1} - z_m)^2 = \alpha^2 - \beta^2}\\
&\boldsymbol{x_{c2} - x_m = -\varrho v_x}\\
&\boldsymbol{y_{c2} - y_m = -\varrho v_y}\\
&\boldsymbol{z_{c2} - z_m = -\varrho v_z}\\
&(x_{c2} - x_m)^2 + (y_{c2} - y_m)^2 + (z_{c2} - z_m)^2 = \alpha^2 - \beta^2
\end{aligned}
\tag{29}
$$

where $(\boldsymbol{x_m, y_m, z_m})$, $(\boldsymbol{x_{H1}, y_{H1}, z_{H1}})$, and $(\boldsymbol{x_{H2}, y_{H2}, z_{H2}})$ are the coordinates of the robot and focal $\boldsymbol{H_1}$, $\boldsymbol{H_2}$ of the ellipse. The condition for determining the presence of obstacles in the improved APF requires the geometric definition of an ellipse and the sum of the distances from the obstacles to the two focal points of the ellipse are:

$$
\begin{aligned}
&d^1, A, H_1, H_2 = \\
&\sqrt{(x - x_{H1})^2 + (y - y_{H1})^2 + (z - z_{H1})^2} + \\
&\sqrt{(x - x_{H2})^2 + (y - y_{H2})^2 + (z - z_{H2})^2}
\end{aligned}
\tag{30}
$$

The mentioned equation can be approximated as follows:

$$
d, A, H_1, H_2 = d^1, A, H_1, H_2 - 2X_0 \tag{31}
$$

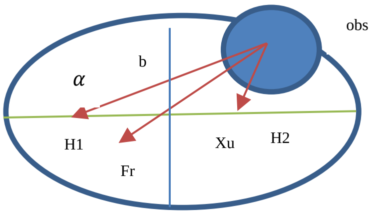

Figure 2. Diagram of the APF with elliptical cross-section

If $\boldsymbol{A, H_1, H_2 \leq 2\alpha}$ The obstacle will probably collide with the agent and needs a way to avoid the collision. If $\boldsymbol{A, H_1, H_2 > 2\alpha}$ there is no possibility of collision. For ease of calculations, the repulsive function of the improved APF is considered as below:

$$
U_r = \begin{cases} \frac{1}{2} k_a \left(\frac{1}{d,A,H_1,H_2 - 2\alpha} - \frac{1}{X_0} \right)^2, & A, H_1, H_2 \leq 2\alpha \\ 0, & A, H_1, H_2 > 2\alpha \end{cases} \tag{32}
$$

The repulsive force on the agent is given below:

$$
F_r = -\Delta U_r = \begin{cases} k_a \left(\frac{1}{d,A,H_1,H_2 - 2\alpha} - \frac{1}{X_0} \right) \frac{1}{d^2 A,H_1,H_2}, d & A, H_1, H_2 \leq 2\alpha \\ 0, & A, H_1, H_2 > 2\alpha \end{cases} \tag{33}
$$

where $\boldsymbol{d\ x, x_{H1}, x_{H1} \leq 2\alpha}$ indicates the repulsive force that acts within the ellipsoid. The total force on the agent is as below:

$$
F_{total}(x) = \sqrt{(F_{ax} + F_{rx})^2 + (F_{ay} + F_{ry})^2 + (F_{az} + F_{rz})^2} \tag{34}
$$

5. SIMULATIONS AND RESULTS

In this section, the results of obstacle avoidance using the improved APF for a group of quadrotors (Figure 3) in 4 missions are present. First, the simulation results of quadrotor attitude and position control are presented by the MPC method.

Figure 4 shows the attitude of the quadrotor controlled using the MPC method. Severe overshoot and undershoot are not seen in the responses. The convergence time of (ϕ, θ, ψ) are $(1,0.9,2)$ seconds.

Figure 5 shows the position of the robot. According to this figure, the responses track the reference well and converge in less than 1 second.

In the following, the simulation results of the control formation are presented.

Figure 6 indicates the position of robots in the S-shaped path in which five follower quadrotors follow the leader.

Figure 7 indicates the attitude of quadrotors in the S-shaped path in which five follower quadrotors follow the leader well. The maximum convergence time of the follower's attitude (ϕ, θ, ψ) is (6s,6s,9s).

Figure 8 presents the position of agents in 3D space, where followers follow the leader in the S-shaped path.

The results of the formation flight simulation are more than 90% consistent with the reported data in literature (32, 35).

The results of avoiding collision with obstacles using the improved APF are given in 3 missions. In the first mission, the quadrotors have a square formation that

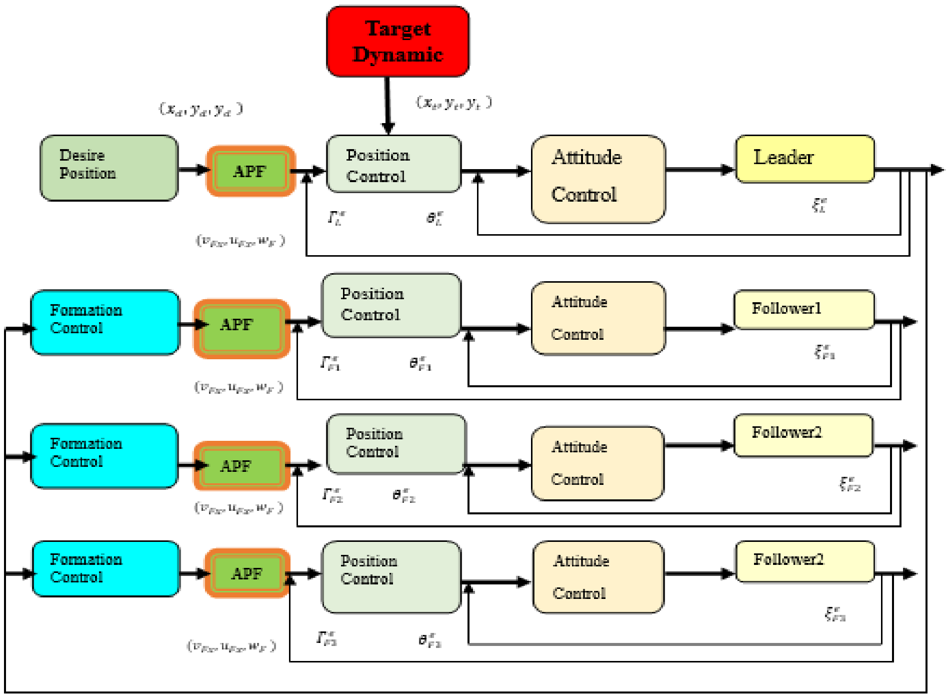

Figure 3. Formation control block diagram

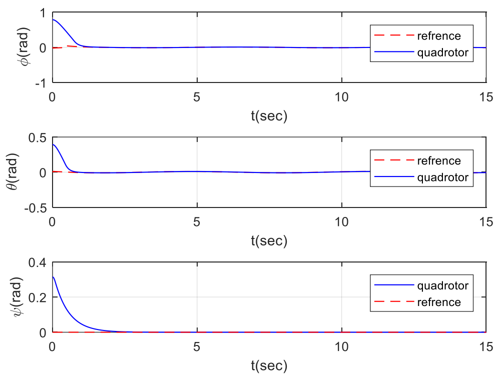

Figure 4. Response curves of attitude for quadrotor

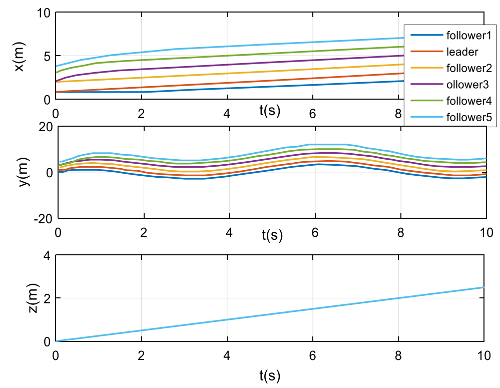

Figure 6. The position of the robots in the S-shaped path

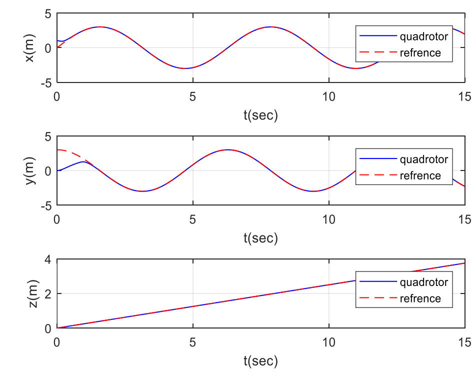

Figure 5. Response curves of position for quadrotor

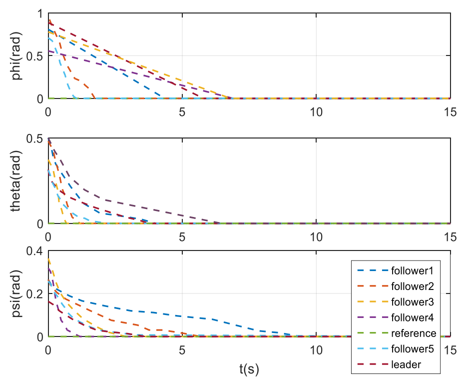

Figure 7. The attitude of the quadrotors in the s-shaped path

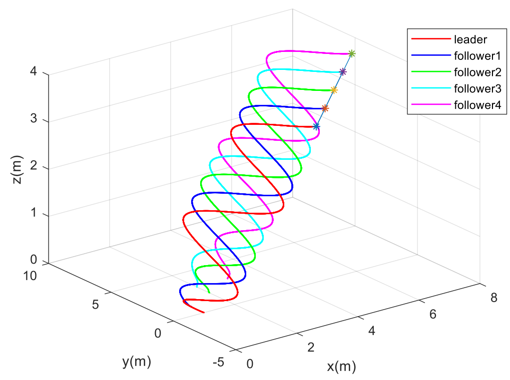

Figure 8. 3D diagram of quadrotors along the s-shaped path

passes through static obstacles. In the second mission, the quadrotors have a square arrangement, and the obstacles are dynamic. In the third mission, the quadrotors have a hexagonal arrangement, and the obstacles are fixed. In this mission, the target is dynamic. In the final mission, the quadrotors have a hexagonal arrangement, and the obstacles are dynamic.

The results of the first mission are given in Figure 9. The quadrotors have passed the static obstacles and have maintained a square formation, and the leader has reached the target. In this figure, the leader is at the point (-3, -43), and after passing the obstacles, she reaches the point (7, 20). Followers are also located at points (-10, 50), (-3, 50) and (-10, -43), and after passing the dynamic obstacles, they are placed in points (-3, 10), (7, 9.5), and (-3, 19.5), which maintain up to 95% accuracy of the square shape after passing the obstacles. The locations of obstacles are shown in Table 2.

In the second mission, four agents were considered. The obstacles are dynamic. The simulation results of this mission are given in Figures 10-12. The velocity of all obstacles is $V = [-3t(i), 9t(i), 12t(i)]$.

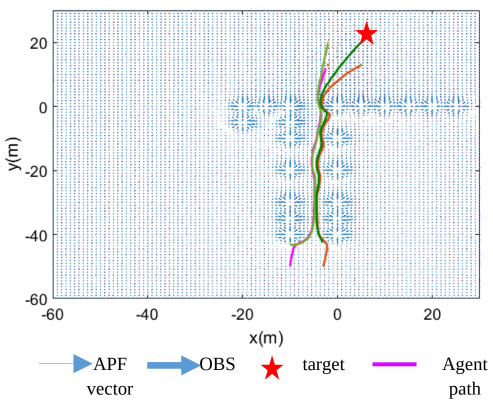

Figure 9. The flight path of the agents in the square arrangement

TABLE 2. Position of obstacles

Obstacle	X(m)	Y(m)	Z(m)
1	-10	-40	15
2	-10	-35	14
3	-10	-30	12
4	-10	-20	15
5	-10	-10	12
6	-10	-5	12
7	-10	0	15
8	-15	0	20
9	-20	0	20
10	-20	-5	18
11	0	-40	25
12	0	-35	15
13	0	-30	15
14	0	-20	20
15	0	-10	20
16	0	0	18
17	5	0	18
18	10	0	15
19	15	0	15
20	20	0	20

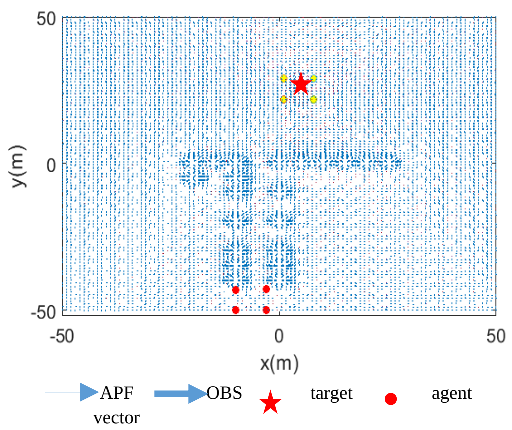

Figure 10. The positions of the agents at the beginning of the flight

Figure 10 indicates the position of the agents at the beginning of the flight, as well as the expected position of the agents after crossing the obstacles.

Figure 11 presents the position of agents while crossing the obstacles.

Figure 12 indicates the position of agents after crossing the obstacles. This figure shows the successful passing of the agents through the dynamic obstacles and maintaining the square arrangement after crossing. As it is clear from Figures 10, 11, and 12, the leader is at the point (-3, -43) at the beginning of the flight, and after passing the dynamic obstacles, it reaches the point (10, 30). Which is as expected. Followers, who were initially located at points (-10, -50), (-3,50), and (-10, -43), after passing the obstacles, reach points (3, 19.7), (10, 20) and (3, 29.6), which as expected should be at points (3, 20), (10, 20) and (3, 30), and therefore, the simulation with 95% accuracy has kept its square formation and is as expected.

In the third mission, the number of agents has increased to 6. Obstacles are fixed, and the target is moving. The simulations of this mission are presented in Figure 13. The results indicate that the quadrotors passed the obstacles, and the leader tracked the target. According to Figure 13, the leader is at point (40, 32) at the beginning of the flight, and after passing through the obstacles, it reaches point (129, 107), which is expected to reach point (130, 107). Also, the followers are located at points (40, 15), (30, 15), (22, 22), (30, 32), and (47, 22) at beginning of the flight, which reach points (130, 90), (120, 91), (112, 98), (120, 107) and (140, 98) after passing the static obstacles. Which, as expected, should be placed in points (130, 90), (120, 90), (112, 97), (120, 107), and (140, 97), respectively. Therefore, the simulations maintain the hexagonal formation with an accuracy of more than 95%. Also, in this mission, the target is moving and is first located at the point (90, 65) and reaches the point (120, 107), which the leader tracks. The location of the obstacles is shown in Table 3.

In the fourth mission, six robots are considered. Obstacles are dynamic, and the target is static. The simulations of this mission are present in Figures 14-16. Figure 14, shows the initial position of the quadrotors and target.

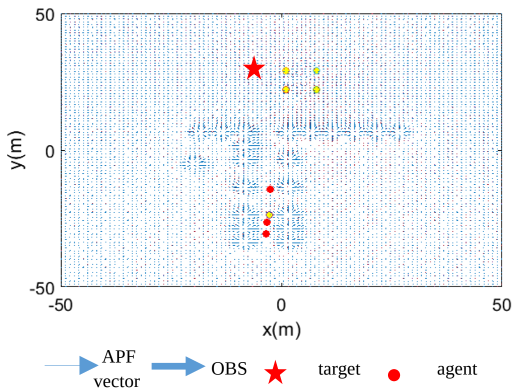

Figure 11. Agents crossing obstacles during flight

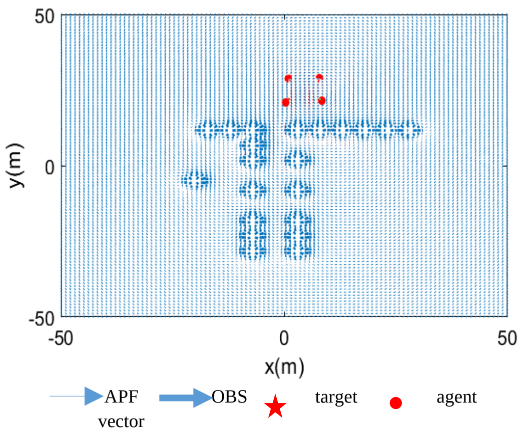

Figure 12. The position of the agents after crossing the obstacles

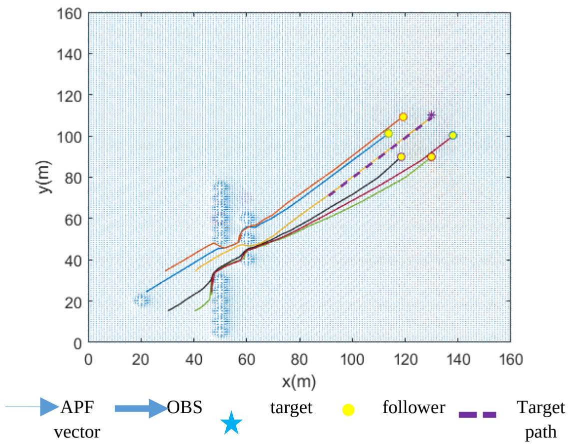

Figure 13. Quadrotors crossing static obstacles

TABLE 3. Obstacles position

Obstacle	X(m)	Y(m)	Z(m)
1	50	5	20
2	50	10	20
3	50	15	20
4	50	16	20
5	50	16	20
6	50	50	22.5
7	50	55	22.5
8	50	60	22.5
9	50	65	22.5
10	50	70	22.5
11	50	75	22.5
12	60	40	22.5
13	50	20	20
14	60	50	22.5
15	60	60	22.5

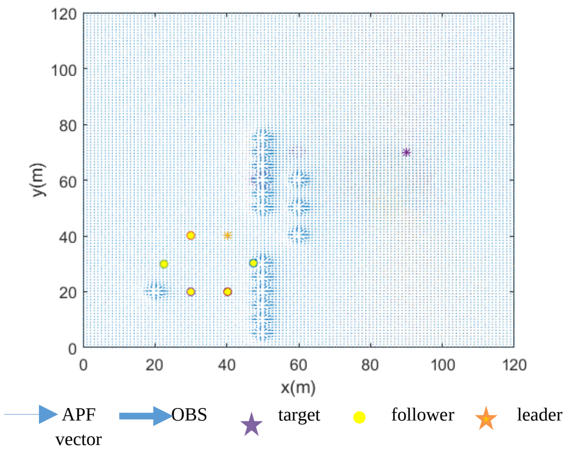

Figure 14. The initial position of quadrotors, obstacles, and targets

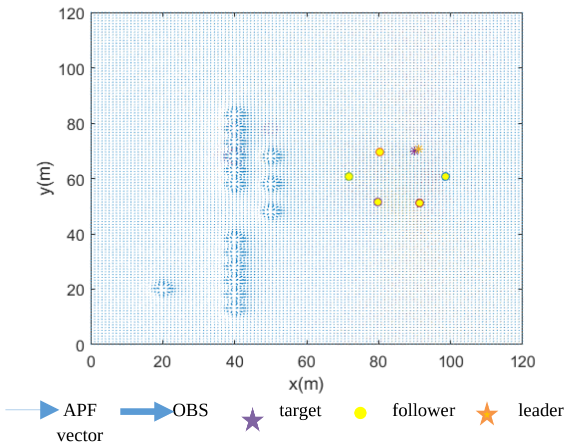

Figure 16. Preserving formation flight after crossing obstacles

Figure 15 indicates that the quadrotors are crossing obstacles, and the leader is moving towards the target.

Figure 16 indicates the quadrotors passing through the moving obstacles and the leader reaching the target. After passing through the obstacles, the quadrotors preserve the hexagonal flight arrangement.

In these figures, it is clear that the leader is initially located at point (40, 40) and reaches point (90, 71) after passing the obstacles. As expected, it should reach the point (90, 70). Other followers are located at the points (40, 20), (30, 20), (20, 30), (30, 40), and (47, 30) at the beginning of the flight, and after passing the dynamic obstacles, they have reached the points (90, 51), (80, 49), (70, 59), (80, 71) and (97, 60) according to Expectations should have reached the points (90, 50), (80, 50), (70, 60), (80, 70) and (97, 60). These results showed that the flight group maintained the hexagonal flight arrangement after crossing the obstacles with 95% accuracy. These results are consistent with crossing the obstacles of reported in literature (36), in which the APF method was used.

In this section, the simulation results are given. First, the results of controlling the position and condition of the quadrotor are shown. The quadrotors converged to the reference in less than two seconds, and there was no sharp fluctuation in the responses. The results of formation control show that five quadrotors have followed the leader. Finally, the results of avoiding collisions with obstacles on the improved artificial potential field in four missions were presented. In the first mission, four quadrotors were considered, and the obstacles were static. In the second mission, four agents crossed dynamic obstacles. In the third mission, six quadrotors crossed static obstacles, and the target was moving. In the last scenario, six quadrotors crossed dynamic obstacles. The results of these simulations showed that the quadrotors maintained their flight formation after crossing the obstacles with 95% accuracy.

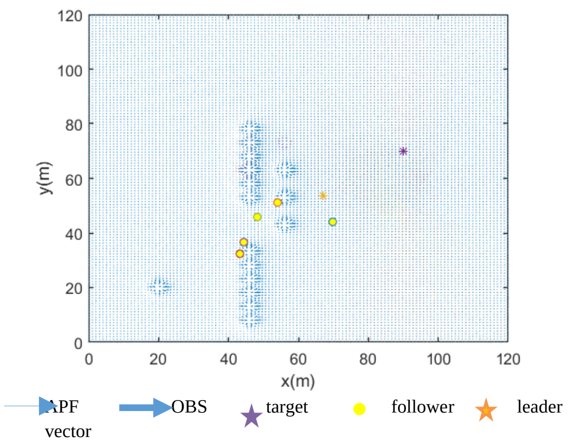

Figure 15. Agents passing through dynamic obstacles

6. CONCLUSION

In this article, quadrotor formation control and obstacle avoidance, and moving target tracking are investigated.

To achieve this goal, in the first step, the simulations of the position and attitude controller were presented, which showed that the convergence time of the responses is at most 3 seconds, which is an acceptable time, and severe overshoot and undershoot were not observed. The results of simulation of formation control by the MPC method in an S-shaped path and linear arrangement show that the followers follow the leader and maintain a certain distance and angle from the leader. Obstacle-crossing results using the improved APF were presented in 4 missions. In the first scenario, three quadrotors followed the leader and crossed static obstacles, and maintained a square formation. In the second scenario, four quadrotors passed dynamic obstacles and, after passing and preserved the square formation. In the third mission, six quadrotors crossed the static obstacles, and the leader tracked the moving target. In the last mission, six quadrotors crossed the dynamic obstacles. In these two missions, the flight group maintained a hexagonal formation after passing through the dynamic and static obstacles. The results of these simulations show the success of the method used to track the moving target and pass the quadrotors through fixed and moving obstacles, by increasing the agents and changing the flight formation. Also, the problem of getting stuck in the local minimum and not passing through environments with many obstacles has not occurred, which indicates the efficiency of the improved APF method.

7. REFERENCES

1. Procter S, Secco EL. Design of a biomimetic BLDC driven robotic arm for teleoperation & biomedical applications. J Hum Earth Future ISSN. 2022:2785-997. 10. 28991/HEF-2021-02-04-03
2. Arofiati F, Sekhar R, Rijalusalam DU. PID-based with Odometry for Trajectory Tracking Control on Four-wheel Omnidirectional Covid-19 Aromatherapy Robot. 2021. 10.28991/esj-2021-SPER-13
3. Doakhan M, Kabganian M, Azimi A. Cooperative payload transportation with real-time formation control of multi-quadrotors in the presence of uncertainty. Journal of the Franklin Institute. 2023;360(2):1284-307. 10.1016/j.jfranklin.2022.11.002
4. Andaluz GM, Leica P, Herrera M, Morales L, Camacho O. Hybrid Controller based on Null Space and Consensus Algorithms for Mobile Robot Formation. Emerging Science Journal. 2022;6(3):429-47. 10.28991/ESJ-2022-06-03-01
5. Chevet T, Vlad C, Maniu CS, Zhang Y. Decentralized MPC for UAVs formation deployment and reconfiguration with multiple outgoing agents. Journal of Intelligent & Robotic Systems. 2020;97:155-70. 10.1007/s10846-019-01025-x
6. Wang X, Xi L, Chen Y, Lai S, Lin F, Chen BM. Decentralized MPC-based trajectory generation for multiple quadrotors in cluttered environments. Guidance, Navigation and Control. 2021;1(02):2150007. 10.1142/S2737480721500072
7. Wang B, Han Y, Wang S, Tian D, Cai M, Liu M, et al. A Review of Intelligent Connected Vehicle Cooperative Driving Development. Mathematics. 2022;10(19):3635. 10.3390/math10193635
8. Zou Y, Meng Z. Coordinated trajectory tracking of multiple vertical take-off and landing UAVs. Automatica. 2019;99:33-40. 10.1016/j.automatica.2018.10.011
9. Dong X, Zhou Y, Ren Z, Zhong Y. Time-varying formation tracking for second-order multi-agent systems subjected to switching topologies with application to quadrotor formation flying. IEEE Transactions on Industrial Electronics. 2016;64(6):5014-24. 10.1109/TIE.2016.2593656
10. Du H, Zhu W, Wen G, Duan Z, Lü J. Distributed formation control of multiple quadrotor aircraft based on nonsmooth consensus algorithms. IEEE transactions on cybernetics. 2017;49(1):342-53. 10.1109/TCYB.2017.2777463
11. Jasim W, Gu D. Robust team formation control for quadrotors. IEEE Transactions on Control Systems Technology. 2017;26(4):1516-23. 10.1109/TCST.2017.2705072
12. Li M, Zhang H, editors. AUV 3D path planning based on A* algorithm. 2020 Chinese Automation Congress (CAC); 2020: IEEE. 10.1109/CAC51589.2020.9327873
13. Yan S, Pan F, editors. Research on route planning of AUV based on genetic algorithms. 2019 IEEE International Conference on Unmanned Systems and Artificial Intelligence (ICUSAI); 2019: IEEE. 10.1109/ICUSAI47366.2019.9124785
14. MahmoudZadeh S, Powers DM, Yazdani AM, Sammut K, Atyabi A. Efficient AUV path planning in time-variant underwater environment using differential evolution algorithm. Journal of Marine Science and Application. 2018;17:585-91. 10.1007/s11804-018-0034-4
15. Che G, Liu L, Yu Z. An improved ant colony optimization algorithm based on particle swarm optimization algorithm for path planning of autonomous underwater vehicle. Journal of Ambient Intelligence and Humanized Computing. 2020;11:3349-54. 10.1007/s12652-019-01531-8
16. Lim HS, Fan S, Chin C, Chai S, Bose N. Particle swarm optimization algorithms with selective differential evolution for AUV path planning. 2020. 10.11591/ijra.v9i2
17. Li X, Wang W, Song J, Liu D, editors. Path planning for autonomous underwater vehicle in presence of moving obstacle based on three inputs fuzzy logic. 2019 4th Asia-Pacific Conference on Intelligent Robot Systems (ACIRS); 2019: IEEE. 10.1109/ACIRS.2019.8936029
18. Sun B, Zhu D, Tian C, Luo C. Complete coverage autonomous underwater vehicles path planning based on glasius bio-inspired neural network algorithm for discrete and centralized programming. IEEE transactions on cognitive and developmental systems. 2018;11(1):73-84. 10.1109/TCDS.2018.2810235
19. Taheri E, Ferdowsi MH, Danesh M. Closed-loop randomized kinodynamic path planning for an autonomous underwater vehicle. Applied Ocean Research. 2019;83:48-64. 10.1016/j.apor.2018.12.008
20. Zhao Y, Hao L-Y, Wu Z-J. Obstacle Avoidance Control of Unmanned Aerial Vehicle with Motor Loss-of-Effectiveness Fault Based on Improved Artificial Potential Field. Sustainability. 2023;15(3):2368. 10.3390/su15032368
21. Shang W, Jing G, Zhang D, Chen T, Liang Q. Adaptive fixed time nonsingular terminal sliding-mode control for quadrotor formation with obstacle and inter-quadrotor avoidance. IEEE Access. 2021;9:60640-57. 10.1109/ACCESS.2021.3074316
22. Pan Z, Li D, Yang K, Deng H. Multi-robot obstacle avoidance based on the improved artificial potential field and PID adaptive tracking control algorithm. Robotica. 2019;37(11):1883-903. 10.1017/S026357471900033X
23. Wang X, Zhang J, editors. Path Planning of Load Transportation by Multi-Quadrotor Formation Based on RRT-APF Method. 2022 5th International Conference on Robotics, Control and Automation Engineering (RCAE); 2022: IEEE. : 10.1109/RCAE56054.2022.9995950
24. Qiao Y, Huang X, Yang B, Geng F, Wang B, Hao M, et al. Formation Tracking Control for Multi-Agent Systems with Collision Avoidance and Connectivity Maintenance. Drones. 2022;6(12):419. 10.3390/drones6120419
25. Aljassani AM, Ghani SN, Al-Hajjar AM. Enhanced multi-agent systems formation and obstacle avoidance (EMAFOA) control algorithm. Results in Engineering. 2023;18:101151. 10.1016/j.rineng.2023.101151
26. Huang Y, Liu W, Li B, Yang Y, Xiao B. Finite-time formation tracking control with collision avoidance for quadrotor UAVs.

Journal of the Franklin Institute. 2020;357(7):4034-58. 10.1016/j.jfranklin.2020.01.014

27. Zhang J, Xie F, Yin D, Qi Y, Luo D, editors. Formation Control and Obstacle Avoidance for UAV Group. International Conference on Autonomous Unmanned Systems; 2021: Springer. 10.1007/978-981-16-9492-9_77

28. Ge SS, Cui YJ. Dynamic motion planning for mobile robots using potential field method. Autonomous robots. 2002;13:207-22. 10.1023/A:1020564024509

29. Li Q, Wang L, Chen B, Zhou Z, editors. An improved artificial potential field method for solving local minimum problem. 2011 2nd International Conference on Intelligent Control and Information Processing; 2011: IEEE. 10.1109/ICICIP.2011.6008278

30. Abdellatif RA, El-Badawy AA, editors. Artificial potential field for dynamic obstacle avoidance with mpc-based trajectory tracking for multiple quadrotors. 2020 2nd novel intelligent and leading emerging sciences conference (NILES); 2020: IEEE. 10.1109/NILES50944.2020.9257973

31. Du Y, Zhang X, Nie Z. A real-time collision avoidance strategy in dynamic airspace based on dynamic artificial potential field algorithm. IEEE Access. 2019;7:169469-79. 10.1109/ACCESS.2019.2953946

32. Ghaderi F, Toloei A, Ghasemi R. Formation control of unmanned helicopters using the sliding mode controller method. Technology in Aerospace Engineering. 2023:1-11. 10.22034/jtae.2023.359555.1263

33. Kuriki Y, Namerikawa T. Formation control with collision avoidance for a multi-UAV system using decentralized MPC and consensus-based control. SICE Journal of Control, Measurement, and System Integration. 2015;8(4):285-94. 10.9746/jcmsi.8.285

34. Joelianto E, Maryami Sumarjono E, Budiyono A, Retnaning Penggalih D. Model predictive control for autonomous unmanned helicopters. Aircraft Engineering and Aerospace Technology. 2011;83(6):375-87. 10.1108/00022661111173252

35. Du H, Zhu W, Wen G, Wu D. Finite-time formation control for a group of quadrotor aircraft. Aerospace Science and Technology. 2017;69:609-16. 10.1016/j.ast.2017.07.012

36. Ma'Arif A, Rahmaniar W, Vera MAM, Nuryono AA, Majdoubi R, Çakan A, editors. Artificial potential field algorithm for obstacle avoidance in uav quadrotor for dynamic environment. 2021 IEEE International Conference on Communication, Networks and Satellite (COMNETSAT); 2021: IEEE. 10.1109/COMNETSAT53002.2021.9530803

Persian Abstract

چکیده

هدف از این مقاله کنترل شکل‌دهی و عبور از موانع ایستا و دینامیک برای گروه کوادروتور، حفظ تداوم و آرایش پرواز پس از عبور از موانع و ردیابی هدف متحرک است. برای کنترل وضعیت و موقعیت کوادروتورها و کنترل شکل‌دهی از روش MPC استفاده شده است. شکل گیری پرواز بر اساس روش پیرو-پیشرو است که در آن پیروان با استفاده از کنترل کننده شکل‌دهی، زاویه و فاصله مشخصی را از پیشرو حفظ می کنند. روش APF بهبود یافته برای عبور از موانع استفاده شده است که مزیت اصلی آن در مقایسه با APF سنتی افزایش برد نیروی دافعه موانع است که مشکل گیر افتادن در حداقل محلی و عدم عبور در محیط‌های پرمانع را حل می‌کند. نتایج طراحی کنترل کننده وضعیت و موقعیت نشان داد که کوادروتورها در کمتر از سه ثانیه همگرا شدند. شبیه سازی‌های کنترل شکل‌دهی در مسیر مارپیچی نشان داد که پیروان، از رهبر پیروی می‌کنند. نتایج عبور کوادروتورها از موانع در چهار ماموریت ارائه شد. در ماموریت اول چهار کوادروتور از موانع ساکن عبور کردند. در ماموریت دوم چهار کوادروتور از موانع دینامیکی عبور کردند. در این دو ماموریت، کوادروتورها پس از عبور از موانع، ساختار پروازی مربعی را حفظ کردند. در ماموریت سوم تعداد کوادروتورها به شش نفر افزایش یافت.لیدر هدف متحرک را ردیابی کرد و کوادروتورها از موانع ساکن عبور کردند. در آخرین ماموریت، کوادروتورها از موانع دینامیکی عبور کردند و لیدر هدف ثابت را ردیابی کرد. در این ماموریت ها، کوادروتورها پس از عبور از موانع، آرایش شش ضلعی را حفظ می کنند. شبیه سازی نتایج نشان داد که کوادروتورها از موانع ثابت و متحرک عبور کرده و پس از عبور، آرایش پرواز را حفظ کردند.

IJE TRANSACTIONS A: Basics Vol. 37 No. 01, (January 2024) 127-135

International Journal of Engineering

Journal Homepage: www.ije.ir

Corrosion Behavior Evaluation of Nanolayered CrN/CrAlN Coatings on Titanium and Ti6Al4V Substrates

N. Fereshteh-Saniee[a], H. Elmkhah*[a], M. Molaei[a], A. Zolriasatein[b]

[a] *Department of Materials Engineering, Bu-Ali Sina University, Hamedan, Iran*
[b] *Non-metallic Materials Research Group, Niroo Research Institute (NRI), Tehran, Iran*

PAPER INFO

Paper history:
Received 22 July 2023
Received in revised form 26 August 2023
Accepted 27 August 2023

Keywords:
CrN/CrAlN Coating
Titanium
Ti6Al4V
PVD
Ringer Solution
Corrosion Behavior

ABSTRACT

In recent years, implants are used as prostheses to replace and protect bone**.** Titanium, as an implantable material, needs to improve corrosion and wear properties for better performance. Therefore, in the current study nitride coatings were applied with the aim of improving corrosion and wear properties. Cathodic arc evaporation physical vapor deposition (CAE-PVD) technique was used to deposit nanolayered CrN/CrAlN coatings on commercially pure titanium and Ti6Al4V substrates for biomaterial applications. X-ray diffraction (XRD) was used to characterize the crystal structure of the coating, and scanning electron microscopy (SEM) and field emission scanning electron microscopy (FESEM) were utilized to observe the surface morphology and cross-section of the coating. The coating adhesion was measured according to VDI 3198 standard using a Rockwell-C indenter. The corrosion behavior was evaluated by potentiodynamic polarization and spectroscope electrochemical impedance in Ringer's solution. The results showed that the nanolayered coating changed the corrosion potential from -0.368 V to -0.054 V for the titanium sample and from -0.405 V to -0.028 V for the Ti6Al4V specimen. Additionally, the corrosion current density was reduced to about ***one-eighth*** and a third for the titanium and Ti6Al4V coated samples, respectively. The capacitator circle diameters increased due to the deposition of CrN/CrAlN coating, demonstrating enhanced corrosion behavior of the coated samples compared to uncoated specimens, as the coating acted as a barrier against corrosive liquids accessing the substrate.

doi: *10.5829/ije.2024.37.01a.12*

1. INTRODUCTION

As an implant material, titanium has been widely used in various medical applications due to its excellent biocompatibility properties, including the spontaneous formation of a stable and dense oxide layer on its surface. Additionally, titanium and its alloys have favorable mechanical, physical, and biological properties for implantation (1, 2). The desired characteristics of titanium and its alloys include a relatively suitable elastic modulus, good formability and machineability, excellent biocompatibility, and superior corrosion resistance compared to stainless steel and cobalt base-alloys (3). Therefore, damaged tissues can be replaced by titanium and its alloys in various situations (1).

However, pure titanium and Ti6Al4V alloy have some drawbacks such as low wear resistance, the possibility of passive layer interaction with H_2O (4), weak shear strength, and difficult production technique. Moreover, the surface oxide layer creates high friction and intensified wear rate for these materials. When the protective coating breaks down, the titanium substrate gets exposed to the surrounding environment, and if the protective layer is not repaired, the titanium is strongly exposed to shear stresses which can result in the formation of cold sores between it and the surrounding joints. Alternative separation and reformation of the oxide layer on the titanium surface consume the implant material. By continuing this phenomenon, the surface roughness increases, hard and coarse particles are created, causing abrasive wear at the implant surface (5). The worn particles can cause blood clots and swelling of the surrounding regions, leading to implant replacement and serious patient suffering (6, 7). Additionally, the

*Corresponding Author Email: *h.elmkhah@basu.ac.ir* (H. Elmkhah)

Please cite this article as: Fereshteh-Saniee N, Elmkhah H, Molaei M, Zolriasatein A. Corrosion Behavior Evaluation of Nanolayered CrN/CrAlN Coatings on Titanium and Ti6Al4V Substrates. International Journal of Engineering, Transactions A: Basics, 2024;37(01):127-135

higher elastic modulus of this material compared to that of bone can cause the stress shielding phenomenon (8). Moreover, using Ti6Al4V alloy as a long-term implant can create problems due to potential releases of vanadium and aluminum ions which may cause cellular toxicity and tissue noxious reactions (6, 7). Therefore, improving the corrosion resistance of titanium implants is essential to increase their biocompatibility and prolong their life (9, 10).

Surface modification is a method to enhance the chemical, mechanical, and biomedical properties of titanium composition. It can be achieved by chemical or mechanical methods (11, 12), such as shot penning (13, 14), sol gel (15), chemical vapor deposition (16), plasma-assisted chemical vapor deposition (17), thermal sputtering (18), electrochemical plating (19, 20), and physical vapor deposition (21-23). Among the above-mentioned techniques, cathodic arc evaporation, due to the creation of uniform properties such as continuous, dense, and homogeneous coating, high adhesion to the substrate, material structure protection, and the possibility of multilayer coating deposition, can be used to form nitride coatings. Nitride coatings have several desirable properties, including high chemical stability, favorite hardness and adhesion, excellent resistance to corrosion and wear, as well as good hammering (24).

Studies have shown that nitride coatings deposited on titanium and its alloys using cathodic arc evaporation can improve their corrosion resistance. Olia et al. (25) deposited CrN/CrAlN and TiN/TiAlN coatings on stainless steel using the cathodic arc evaporation method, and corrosion tests in 3.5% NaCl solution showed that Ecoor of coated samples shifted to more positive potential. Khan et al. (26) also coated stainless steel using TiN, CrN, AlTiN, and AlCrN and evaluated their electrochemical behaviors. The coated samples had better corrosion resistance, with the CrN coating showing the best corrosion resistance. Additionally, different nitride coatings were deposited on steel substrates using cathodic arc evaporation, and the corrosion behavior was evaluated in 0.1M Na_2SO_4 and 0.1M NaCl environments (27). The Ti-based coatings exhibited the best corrosion resistance and surface properties.

Several studies have been performed within the field of CrAlN coatings research (16, 28). The distinctive aspect of this study, in comparison to previous research, involves the utilization of two distinct substrates, including pure Ti and Ti6Al4V, and the subsequent evaluation of their respective corrosion characteristics in relation to one another. To enhance the performance of titanium as an implantable material, it is imperative to address the concerns regarding its corrosion and wear properties. Hence, in the present investigation, nitride coatings were employed with the objective of enhancing the corrosion resistance and wear characteristics. Therefore, the aim of this investigation is to study and assess the corrosion behavior of CrN/CrAlN coating deposited using cathodic arc evaporation on titanium and Ti6Al4V substrates in the Ringer solution.

2. MATERIALS AND METHODS

2. 1. Surface Preparation and Coating Parameters

To achieve a high-quality and desired surface for coating, pure commercial titanium and Ti6Al4V alloy samples were prepared in sheet form and polished using 120 to 3000 grit sandpapers. Following this, the samples were washed in an acetone solution using an ultrasound device for ten minutes. Finally, CrN/CrAlN nano-coatings were deposited on the titanium and Ti6Al4V substrate using the cathodic arc evaporation method. The coating parameters are briefly summarized in Table 1.

2. 2. Coating Characterization

The X-ray diffraction device (1730 PW Philips and PANalytical) was used to identify the structures and types of coating phases formed. The angle diffraction was selected in the range of 10-80 degrees with a step size of 0.05 degrees. To observe the cross-section of the coating, the titanium sample was first cut with a guillotine and then prepared for photography after the mount treatment, sanding, and polishing. A gold coating was applied to make the mount conductive. The surface morphology and cross-section of the coating were observed using scanning electron microscopy (840A-JSM, Jeol) and field emission scanning electron microscopy (Czech, TESCAN, MIRA3, FESEM), and the energy distribution spectrum was obtained by SAMX, France. The surface roughness was measured using a roughness meter (Roughness Tester PCE RT 2200). The adhesion test was carried out by applying 150 N force for 25 seconds using a Rockwell-C indenter and VDI3198 standard. The impression created by the indenter was observed via optical microscopy. According to the VDI3198 standard, coatings having adhesion conditions HF1 to HF3 are acceptable, whereas HF4 to HF6 states could be rejected. The classification of coating adhesion based on the VDI3198 standard is illustrated in Figure 1.

TABLE 1. The coating process parameters used in the present work

Working pressure (torr)	5×10^{-3}
Target electrical current (A)	100
Substrate-target distance (cm)	15
Deposition time (min)	90
Rotational speed of specimens (rpm)	5
Substrate bias voltage (V)	−100
Duty cycle (%)	50
Deposition temperature (ºC)	200

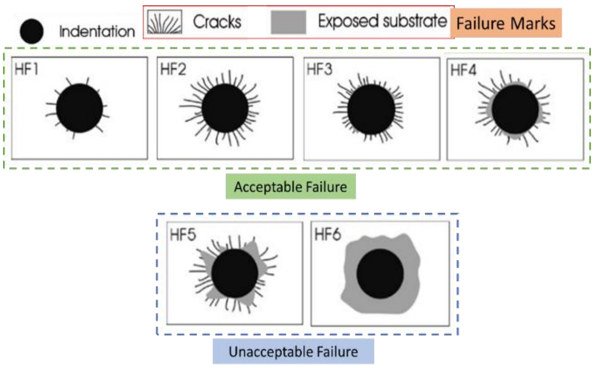

Figure 1. The classification of coating adhesion according to the VDI3198 standard

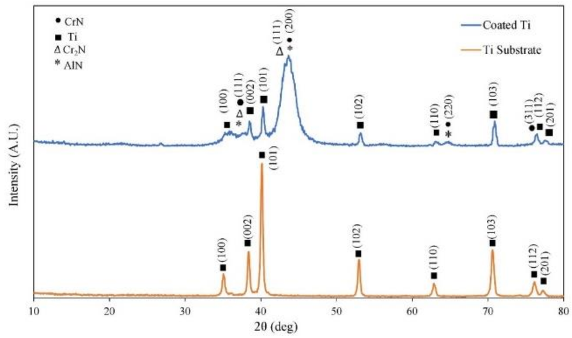

Figure 2. XRD pattern of CrN/CrAlN coating

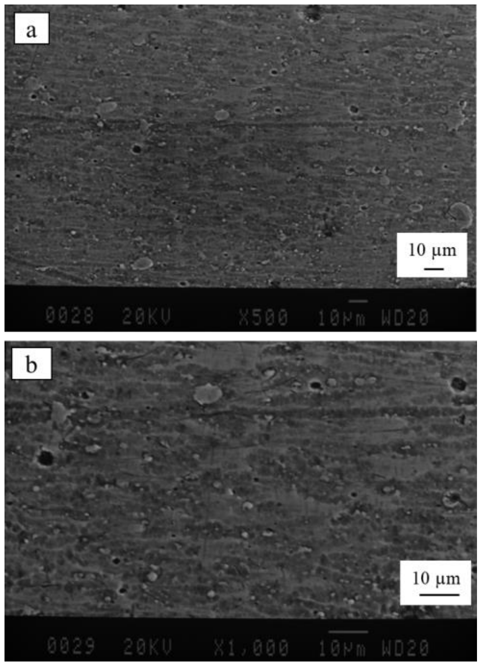

Figure 3. SEM images of CrN/CrAlN surface coating with different magnifications a) ×500, b) ×1000

2. 3. Corrosion Test The electrochemical impedance spectroscopy (EIS) and potentiodynamic polarization (PDP) tests using a potentiostat instrument (µAutolab, III/FRA2, made in the Netherlands) were conducted to evaluate the corrosion behavior of uncoated and CrN/CrAlN coated pure Ti and Ti6Al4V alloy substrates in a physiologic Ringer's solution (pH 7.4). The samples were set up according to the conventional three-electrode cell configuration. The EIS tests were operated with a signal amplitude of 10 mV and a frequency ranging from 100000 to 0.01 Hz when the open circuit potential (OCP) was stable, which occurred after 2 hours. The EIS test data were analyzed using NOVA software (version 2.1.3). The PDP test was performed at a scan rate of 1 mV/s, starting from −250 mV below the OCP. The PDP curves were analyzed using the Tafel extrapolation technique. The SEM was applied to study the corrosion surface morphologies characteristics of specimens.

3. RESULTS AND DISCUSSIONS

3. 1. Microstructure of the Coating Figure 2 displays the X-ray diffraction patterns of the Ti substrate and Ti coated with CrN/CrAlN. The latter pattern includes CrN and AlN with a face center cubic (FCC) structure, as well as the Cr2N and substrate with a hexagonal structure. For CrN and AlN phases of this coating, diffraction peaks associated with (111), (200), and (220) planes occur at 37.6, 43.7, and 63.5 angles. On the other hand, diffraction peaks of the titanium are at 35, 38.4, and 40.1 angles in relation to (100), (002), and (101) planes. According to the observed pattern, the coating's referred orientation is (200), consistent with previous researchers' reports (29, 30).

3. 2. Suface Morphology and Coating Thickness Figure 3 ehibits the SEM images of the CrN/CrAlN coating urface. Macroparticles can be observed on the surface. The presence of macroparticles is normal in the cathodic arc evaporation process and causes a partial increase in the roughness of the coated samples compared with the uncoated samples. The factors affecting the number and size of microparticles include the rate of evaporation of the target material, the deposition rate, and accumulation of the coating on the metal substrate (31). Figure 4 illustrates the FESEM images of the cross-section of the coating. The images display a continuous and dense coating microstructure. Additionally, the lack of a separation line between the substrate and coating reveals a high adhesion of the coating to the substrate. Moreover, the CrN and CrAlN nanolayers were compactly adhered together, without any visible cracks or holes in their interface resulting in improved corrosion resistance. The created coating possesses a nanostructure with a fully homogeneous, 2-micron thickness, and compact layers of CrN and CrAlN. Figure 5 shows the energy distribution spectroscopy (EDS) of the coated samples. The analysis was performed from the surface to the depth of the sample and includes Cr, Al, N, and Ti elements.

3. 3. Surface Roughness and Adhesion The coating adhesion was evaluated via Rockwell-C test in the present investigation. The condition of the coating surrounding the impression of the indenter was observed using an optical microscope. Figure 6 displays the images obtained from the adhesion tests for titanium and Ti6Al4V samples coated with CrN/CrAlN. No cracks or disintegration exist around the impression of the indenter, indicating a high level of coating adhesion in the HF1 group. Table 2 summarizes the surface roughness data for coated and uncoated samples. The coated samples have a higher roughness than the uncoated samples due to the nature of the cathodic arc evaporation process, explained in section 2.3.

3. 4. Electrochemical Behavior The corrosion behavior of the titanium and Ti6Al4V substrates before and after being coated with nanolayer CrN/CrAlN coatings was evaluated by EIS and PDP tests in the physiological Ringer's solution. Figure 7 illustrates the EIS test results in the form of Nyquist and Bode plots for uncoated and CrN/CrAlN coated titanium and Ti6Al4V substrates samples.

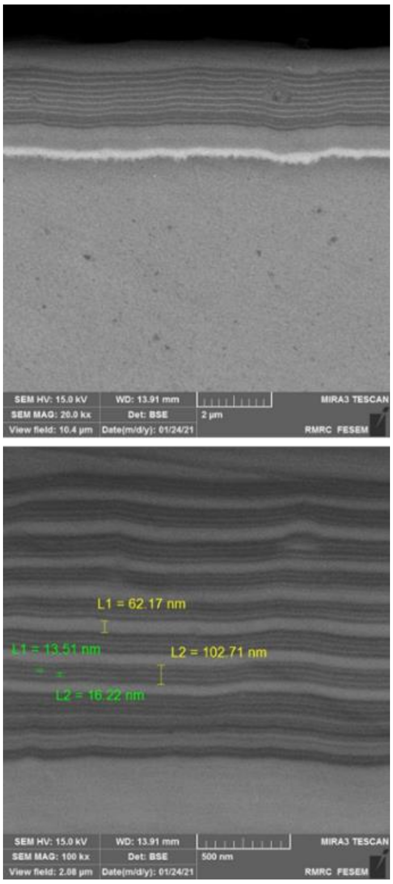

Figure 4. FESEM images of the cross section of CrN/CrAlN coating with different magnifications

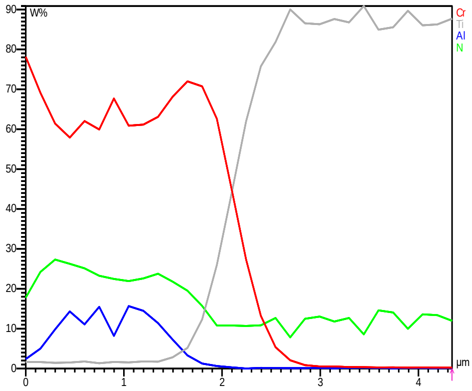

Figure 5. EDS line analysis of titanium sample with CrN/CrAlN coating

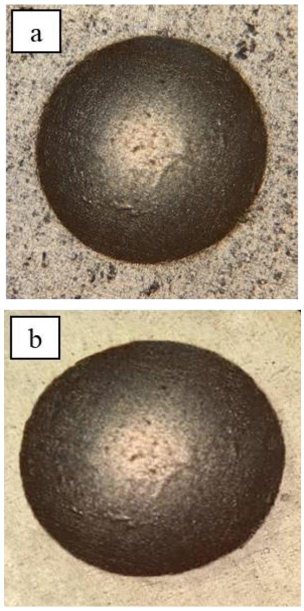

Figure 6. Optical microscope images of the indenter impression on coating ×100 magnification, (a) commercial pure titanium, and (b) Ti6Al4V

TABLE 2. Surface roughness values of uncoated and CrN/CrAlN coated titanium and Ti6Al4V samples

Sample	R_a (µm)	R_z (µm)	R_{max} (mm)
Titanium	0.169	0.893	0.02
CrN/CrAlN coated titanium	0.221	1.220	0.04
Ti6Al4V	0.125	1.186	0.03
CrN/CrAlN coated Ti6Al4V	0.158	1.374	0.04

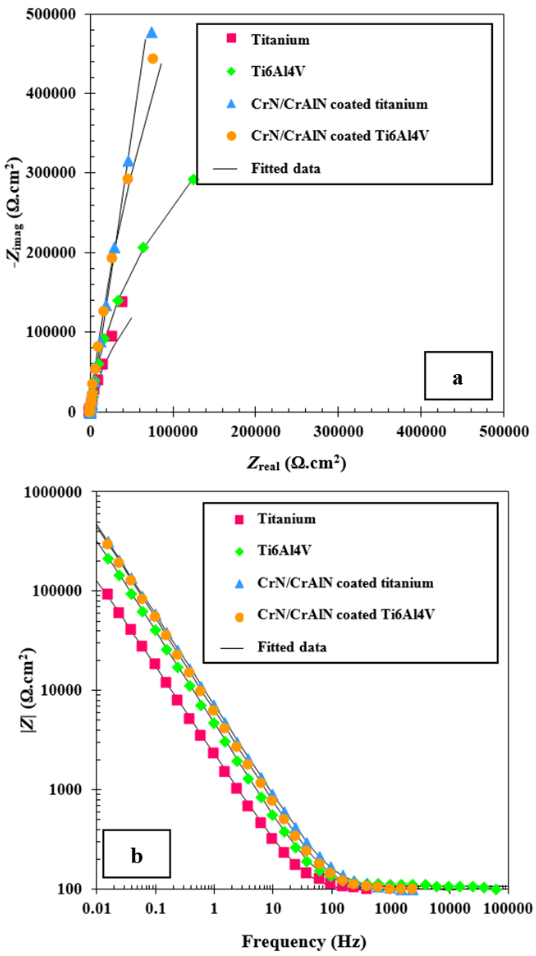

Figure 7. (a) Nyquist and (b) Bode plots of uncoated and CrN/CrAlN coated pure Ti and Ti6Al4V alloy substrates after 2 hours of exposure to physiological Ringer's solution

The Nyquist plots of all uncoated and coated substrates (Figure 7 (a)) showed an uncompleted semicircle-like shape, while those for CrN/CrAlN coatings were larger in diameter. As can be observed in Bode plots of specimens (Figure 7 (b)), the uncoated titanium and Ti6Al4V indicated only one time constant, which is related to the capacitive behavior of the electrical double layer (Cdl) and the charge transfer resistance (Rct) of the surface oxide layer. However, there were two-time constants in Bode plots of the CrN/CrAlN coated samples, representing the capacitive behavior of the coatings and the electrical double layers. Moreover, at high-frequency regions, the frequency independency of the absolute impedance values suggested pure resistance behavior of specimens. The experimental impedance data of the uncoated and CrN/CrAlN coated titanium and Ti6Al4V substrates were fitted utilizing the equivalent circuit models displayed in Figure 8 (a) and (b), respectively. In these models, Rs, Rct, and Rcoat are respectively ascribed to

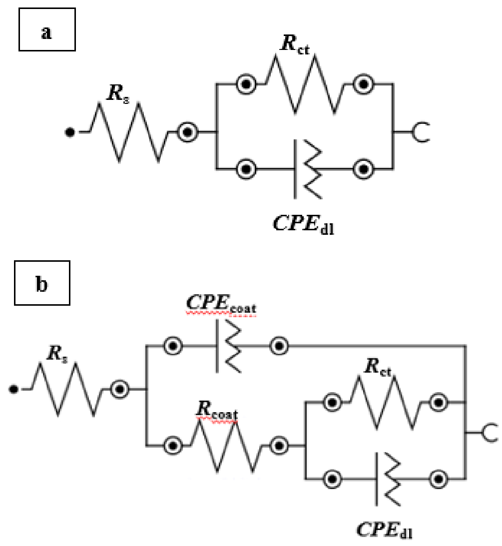

Figure 8. Equivalent circuits used to fit the EIS data of (a) uncoated and (b) CrN/CrAlN coated pure Ti and Ti6Al4V alloy substrates

Ringer's solution resistance, charge transfer resistance (at the interface of substrate/Ringer's solution), and coating resistance (at the interface of coating/Ringer's solution). Moreover, CPEdl and CPEcoat are assigned to the constant phase elements of the electrical double layer and the coating capacitance, respectively. Generally, the CPE is employed in the circuit to compensate for the deviation of Cdl and Ccoat from ideal capacitive behavior due to the surface inhomogeneity (32, 33). The equivalent circuits fitted parameters are reported in Table 3. According to Table 3, it was found that the Rct values of CrN/CrAlN coated titanium and Ti6Al4V substrates (2.27 and 2.09 MΩ.cm^2, respectively) were higher than that of the uncoated samples (0.20 and 0.66 MΩ.cm^2 for titanium and Ti6Al4V substrates, respectively) which indicated improved anticorrosion properties of titanium and Ti6Al4V after being modified with nanolayer CrN/CrAlN coatings. Furthermore, when comparing CrN/CrAlN coated titanium and Ti6Al4V specimens with each other, the former presented higher Rct and lower Rcoat values. The PDP curves of uncoated and CrN/CrAlN coated titanium and Ti6Al4V substrates are indicated in Figure 9. For both titanium and Ti6Al4V substrates specimens, because of the formation of a surface passive oxide layer, the passive behavior was observed. The Ecorr, corrosion current density (icorr), anodic and cathodic slopes (βa and βc, respectively), and polarisation resistance (Rp) values of specimens derived from the PDP curves utilizing the Tafel extrapolation technique are summarized in Table 4. The Rp values of specimens were calculated using the Stern-Geary equation (34). While the Ecorr reflects the tendency of

TABLE 3. Simulated EIS parameters for uncoated and CrN/CrAIN coated titanium and Ti6AI4V substartes in physicological Ringer's solution

Sample	R_s (Ω.cm²)	CPE_{dl} (μF/cm²)	n_{dl}	R_{ct} (MΩ.cm²)	CPE_{coat} (MΩ.cm²)	n_{coat}	R_{coat} (KΩ.cm²)
Titanium	100.08	85.42	0.88	0.20	-	-	-
CrN/CrAIN coated titanium	102.98	26.13	0.91	2.27	127.18	0.87	1.30
Ti6AI4V	111.78	38.34	0.93	0.66	-	-	-
CrN/CrAIN coated Ti6AI4V	102.87	28.44	0.92	2.09	105.02	0.81	2.03

TABLE 4. The E_{corr} and i_{corr} values of uncoated and CrN/CrAIN coated titanium and Ti6AI4V substartes

Sample	E_{corr} (mV)	i_{corr} (μA/cm²)	β_a	β_c	R_p (KΩ.cm²)
Titanium	100.08	85.42	0.88	0.20	-
CrN/CrAIN coated titanium	102.98	26.13	0.91	2.27	127.18
Ti6AI4V	111.78	38.34	0.93	0.66	-
CrN/CrAIN coated Ti6AI4V	102.87	28.44	0.92	2.09	105.02

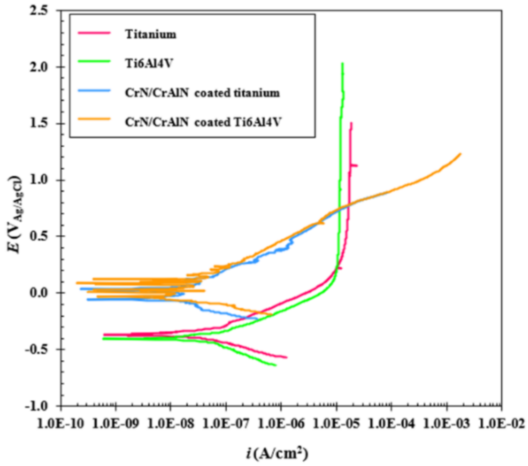

Figure 9. The classification of coating adhesion according to the VDI3198 standard

dissolution and stability, the icorr represents the corrosion rate. So, the lower the icorr and the more positive the Ecorr, the higher the corrosion resistance (29, 31, 35). The Ecorr and icorr values of CrN/CrAlN coated samples were respectively nobler and lower than those of uncoated ones, showing a remarkable enhancement in corrosion resistance of titanium and Ti6Al4V substrates after being coated with nanolayer CrN/CrAlN coatings. Titanium is corroded under the formation of soluble titanium oxychloride complexes and the consumption of the passive oxide layer by Cl− corrosive ions (36). According to Liang et al. (37), the following anodic and cathodic reactions happen during the corrosion of titanium and Ti6Al4V in Ringer's solution:

Anodic reactions:

$$Ti + 4Cl^- \rightarrow TiCl_4 + 4e^- \quad (1)$$

$$TiCl_4 + 2H_2O \rightarrow TiO_2 + 4Cl^- + 4H^+ \quad (2)$$

Cathodic reaction:

$$O_2+2H_2O+4e^-\rightarrow 4OH^- \quad (3)$$

The CrN/CrAlN coating can act as a barrier against corrosion, not allowing direct contact of the corrosive solution with the titanium substrate. The improved structural density due to the increased number of interfaces in multilayer coatings can significantly enhance the corrosion resistance of the substrate compared with single-layer ones (29, 38). Although the Ti6Al4V substrate possessed a more negative Ecorr value (−405 mV) than that of titanium (−368 mV), the icorr value of Ti6Al4V (0.0278 μA/cm²) was lower than the icorr value of titanium (0.0399 μA/cm²), suggesting better anticorrosion behavior of Ti6Al4V. The α + β two-phase structure of Ti6Al4V with additional Al and V promotes its anodic passivation and increases its corrosion resistance compared with titanium (37). However, after being coated with CrN/CrAlN coatings, titanium exhibited more negative Ecorr (−54 mV) and lower icorr (0.0046 μA/cm²) values than Ti6Al4V (with Ecorr and icorr values of −28 mV and 0.0086 μA/cm², respectively). Therefore, the corrosion resistance (Rp) of specimens was increased in the following order: uncoated titanium (64.842 KΩ.cm²) < uncoated Ti6Al4V (93.064 KΩ.cm²) < CrN/CrAlN coated Ti6Al4V (362.137 KΩ.cm²) < CrN/CrAlN coated titanium (581.472 KΩ.cm²).

Figure 10 shows the SEM surface morphologies of CrN/CrAlN coated titanium and Ti6Al4V substrates specimens after the corrosion test. Although some small

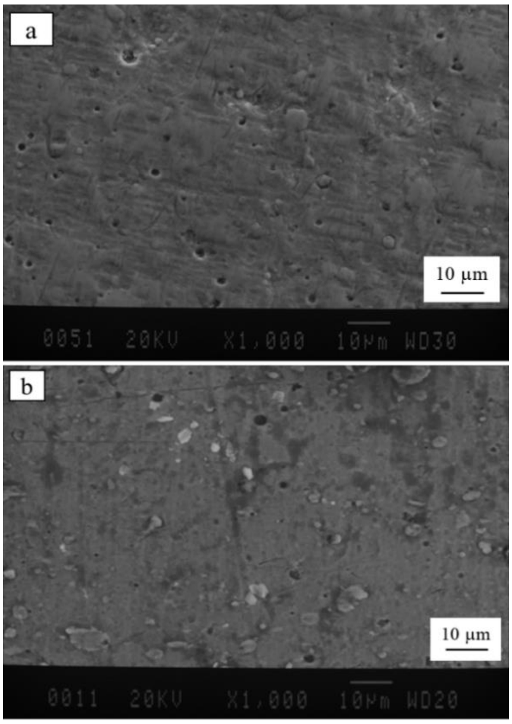

Figure 10. SEM surface morphologies of CrN/CrAlN coated specimens of (a) pure Ti and (b) Ti6Al4V alloy substrates after the corrosion test

corrosion pits were formed and no crack was seen on both coated surfaces, it seems that the CrN/CrAlN coated titanium underwent less damage compared to the coated Ti6Al4V. This showed the lower corrosion susceptibility of coated titanium in physiological Ringer's solution, as earlier discussed. Pits are formed because the coatings defects including cavities and macroparticles provide a direct path for corrosive ions to contact with the substrate (31-33). It can be concluded that pitting was the main corrosion mechanism of the specimens.

4. CONCLUSION

In this study, arc evaporation method was used to deposit CrN/CrAlN nanolayer coating on titanium and Ti6Al4V substrates. The results from the corrosion behavior evaluation of the coated and uncoated samples in Ringer's solution demonstrated that the deposited coating changed the corrosion potential from -0.386 V to -0.054 V for titanium and from -0.405 V to -0.0287 V for Ti6Al4V. In addition, the current density was reduced to about one-eighth and third for coated titanium and Ti6Al4V samples, respectively. Moreover, the increased capacitator circle diameters due to the deposition of CrN/CrAlN coating indicated improved corrosion behavior of the coated samples compared to the uncoated specimens.

5. REFERENCES

1. Renganathan G, Tanneru N, Madurai SL. Orthopedical and biomedical applications of titanium and zirconium metals. Fundamental biomaterials: metals: Elsevier; 2018. p. 211-41.
2. Kuphasuk C, Oshida Y, Andres CJ, Hovijitra ST, Barco MT, Brown DT. Electrochemical corrosion of titanium and titanium-based alloys. The Journal of prosthetic dentistry. 2001;85(2):195-202. 10.1067/mpr.2001.113029
3. Munsch M. Laser additive manufacturing of customized prosthetics and implants for biomedical applications. Laser additive manufacturing: Elsevier; 2017. p. 399-420.
4. Nematov D, Kholmurodov K, Husenzoda M, Lyubchyk A, Burhonzoda A. Molecular Adsorption of H2O on TiO2 and TiO2: Y Surfaces. Journal of Human, Earth, and Future. 2022;3(2):213-22.
5. Ramakrishna S, Ramalingam M, Kumar TS, Soboyejo WO. Biomaterials: a nano approach: CRC press; 2016.
6. Gomes CC, Moreira LM, Santos VJ, Ramos AS, Lyon JP, Soares CP, et al. Assessment of the genetic risks of a metallic alloy used in medical implants. Genetics and molecular biology. 2011;34:116-21. 10.1590/S1415-47572010005000118
7. Moghadasi K, Isa MSM, Ariffin MA, Raja S, Wu B, Yamani M, et al. A review on biomedical implant materials and the effect of friction stir based techniques on their mechanical and tribological properties. Journal of Materials Research and Technology. 2022;17:1054-121. 10.1016/J.JMRT.2022.01.050
8. Zhang L-C, Chen L-Y, Wang L. Surface modification of titanium and titanium alloys: technologies, developments, and future interests. Advanced Engineering Materials. 2020;22(5):1901258. 10.1002/adem.201901258
9. Prando D, Brenna A, Diamanti MV, Beretta S, Bolzoni F, Ormellese M, et al. Corrosion of titanium: Part 1: Aggressive environments and main forms of degradation. Journal of applied biomaterials & functional materials. 2017;15(4):e291-e302. 10.5301/jabfm.5000387
10. Mohammed MT, Khan ZA, Siddiquee AN. Surface modifications of titanium materials for developing corrosion behavior in human body environment: a review. Procedia Materials Science. 2014;6:1610-8. 10.1016/j.mspro.2014.07.144
11. Mozetič M. Surface modification to improve properties of materials. Mdpi; 2019. p. 441.
12. Xue T, Attarilar S, Liu S, Liu J, Song X, Li L, et al. Surface modification techniques of titanium and its alloys to functionally optimize their biomedical properties: thematic review. Frontiers in Bioengineering and Biotechnology. 2020;8:603072. 10.3389/fbioe.2020.603072
13. Li N-b, Sun S-j, Bai H-y, Xu W-h, Xiao G-y, Zhang Y-l, et al. Evolution of nano/submicro-scale oxide structures on Ti6Al4V achieved by an ultrasonic shot peening-induction heating approach for high-performance surface design of bone implants. Journal of Alloys and Compounds. 2020;831:154876. 10.1016/j.jallcom.2020.154876
14. Yang Q, Zhou W, Zheng X, Niu Z, Li Z, Zou B, et al. Investigation of shot peening combined with plasma-sprayed CuNiIn coating on the fretting fatigue behavior of Ti-6Al-4V dovetail joint specimens. Surface and Coatings Technology. 2019;358:833-42. 10.1016/j.surfcoat.2018.12.006
15. Jaafar A, Hecker C, Árki P, Joseph Y. Sol-gel derived hydroxyapatite coatings for titanium implants: A review. Bioengineering. 2020;7(4):127. 10.3390/bioengineering7040127
16. Din S, Shah M, Sheikh N. Tribological performance of titanium alloy Ti–6Al–4V via CVD–diamond coatings. Journal of Superhard Materials. 2018;40:26-39. 10.1016/j.ceramint.2022.09.286

17. Cho Y-S, Liao L-K, Hsu C-H, Hsu Y-H, Wu W-Y, Liao S-C, et al. Effect of substrate bias on biocompatibility of amorphous carbon coatings deposited on Ti6Al4V by PECVD. Surface and Coatings Technology. 2019;357:212-7. 10.1016/j.surfcoat.2019.07.011

18. Gan JA, Berndt CC. Thermal spray forming of titanium and its alloys. Titanium Powder Metallurgy. 2015:425-46. 10.1016/B978-0-12-800054-0.00023-X

19. Rao CR, Pushpavanam M. Electroless deposition of platinum on titanium substrates. Materials Chemistry and Physics. 2001;68(1-3):62-5. 10.1016/S0254-0584(00)00268-6

20. Mahmoud S. Electroless deposition of nickel and copper on titanium substrates: Characterization and application. Journal of alloys and Compounds. 2009;472(1-2):595-601. 10.1016/j.jallcom.2008.05.079

21. Bahi R, Nouveau C, Beliardouh NE, Ramoul CE, Meddah S, Ghelloudj O. Surface performances of Ti-6Al-4V substrates coated PVD multilayered films in biological environments. Surface and Coatings Technology. 2020;385:125412. 10.1016/j.surfcoat.2020.125412

22. Uddin GM, Jawad M, Ghufran M, Saleem MW, Raza MA, Rehman ZU, et al. Experimental investigation of tribo-mechanical and chemical properties of TiN PVD coating on titanium substrate for biomedical implants manufacturing. The International Journal of Advanced Manufacturing Technology. 2019;102:1391-404. 10.1007/s00170-018-03244-2

23. Ewald A, Glückermann SK, Thull R, Gbureck U. Antimicrobial titanium/silver PVD coatings on titanium. Biomedical engineering online. 2006;5(1):1-10. 10.1186/1475-925X-5-22

24. Jokar K, Elmkhah H, Fattah-alhosseini A, Babaei K, Zolriasatein A. Comparison of the wear and corrosion behavior between CrN and AlCrN coatings deposited by Arc-PVD method. Materials Research Express. 2019;6(11):116426. 10.1088/2053-1591/ab4645

25. Olia H, Ebrahimi-Kahrizsangi R, Ashrafizadeh F, Ebrahimzadeh I. Corrosion study of TiN, TiAlN and CrN multilayer coatings deposit on martensitic stainless steel by arc cathodic physical vapour deposition. Materials Research Express. 2019;6(4):046425. 10.1088/2053-1591/aaff11

26. Khan MF, Adesina AY, Gasem ZM. Electrochemical and electrical resistance behavior of cathodic arc PVD TiN, CrN, AlCrN, and AlTiN coatings in simulated proton exchange membrane fuel cell environment. Materials and Corrosion. 2019;70(2):281-92. 10.1002/maco.201810377

27. D'Avico L, Beltrami R, Lecis N, Trasatti SP. Corrosion behavior and surface properties of PVD coatings for mold technology applications. Coatings. 2018;9(1):7. 10.3390/coatings9010007

28. Vengesa Y, Fattah-alhosseini A, Elmkhah H, Imantalab O, Keshavarz MK. Investigation of corrosion and tribological characteristics of annealed CrN/CrAlN coatings deposited by CAE-PVD. Ceramics International. 2023;49(2):3016-29.

29. Mani SP, Agilan P, Kalaiarasan M, Ravichandran K, Rajendran N, Meng Y. Effect of multilayer CrN/CrAlN coating on the corrosion and contact resistance behavior of 316L SS bipolar plate for high temperature proton exchange membrane fuel cell. Journal of Materials Science & Technology. 2022;97:134-46. 10.1016/j.jmst.2021.04.043

30. Wang L, Zhang S, Chen Z, Li J, Li M. Influence of deposition parameters on hard Cr–Al–N coatings deposited by multi-arc ion plating. Applied Surface Science. 2012;258(8):3629-36.

31. Fazel ZA, Elmkhah H, Fattah-Alhosseini A, Babaei K, Meghdari M. Comparing electrochemical behavior of applied CrN/TiN nanoscale multilayer and TiN single-layer coatings deposited by CAE-PVD method. Journal of Asian Ceramic Societies. 2020;8(2):510-8.

32. Adesina AY, Gasem ZM, Madhan Kumar A. Corrosion resistance behavior of single-layer cathodic arc PVD nitride-base coatings in 1M HCl and 3.5 pct NaCl solutions. Metallurgical and Materials Transactions B. 2017;48:1321-32. 10.1007/s11663-016-0891-7

33. Kong J-Z, Hou T-J, Wang Q-Z, Yin L, Zhou F, Zhou Z-F, et al. Influence of titanium or aluminum doping on the electrochemical properties of CrN coatings in artificial seawater. Surface and Coatings Technology. 2016;307:118-24. https://doi.org/10.1016/j.surfcoat.2016.08.036

34. Ardila L, Moreno C, Sanchez J. Electrolytic removal of chromium rich PVD coatings from hardmetals substrates. International Journal of Refractory Metals and Hard Materials. 2010;28(2):155-62. https://doi.org/10.1016/j.ijrmhm.2009.07.008

35. Liao L, Gao R, Yang Z, Wu S, Wan Q. A study on the wear and corrosion resistance of high-entropy alloy treated with laser shock peening and PVD coating. Surface and Coatings Technology. 2022;437:128281. 10.1016/j.surfcoat.2022.128281

36. Oliveira V, Aguiar C, Vazquez A, Robin A, Barboza MJR. Improving corrosion resistance of Ti–6Al–4V alloy through plasma-assisted PVD deposited nitride coatings. Corrosion Science. 2014;88:317-27. https://doi.org/10.1016/j.corsci.2014.07.047

37. Chenghao L, Li'nan J, Chuanjun Y, Naibao H. Crevice corrosion behavior of CP Ti, Ti-6Al-4V alloy and Ti-Ni shape memory alloy in artificial body fluids. Rare Metal Materials and Engineering. 2015;44(4):781-5. https://doi.org/10.1016/S1875-5372(15)30046-1

38. Beliardouh NE, Bouzid K, Nouveau C, Tlili B, Walock MJ. Tribological and electrochemical performances of Cr/CrN and Cr/CrN/CrAlN multilayer coatings deposited by RF magnetron sputtering. Tribology International. 2015;82:443-52. 10.1016/j.triboint.2014.03.018

Persian Abstract

چکیده

در سال‌های اخیر از کاشتنی‌ها به عنوان پروتز برای جایگزینی و محافظت از استخوان استفاده می‌شود. تیتانیوم، به عنوان یک ماده کاشتنی، برای عملکرد بهتر نیاز به بهبود خواص خوردگی و سایش دارد. بنابراین، در مطالعه حاضر پوشش‌های نیترید با هدف بهبود خواص خوردگی و سایش بر زیرلایه تیتانیومی اعمال شدند. روش رسوب فیزیکی بخار تبخیر قوس کاتدی (CAE-PVD) برای رسوب پوشش های نانولایه CrN/CrAlN بر روی زیرلایه‌های تیتانیوم خالص تجاری و آلیاژ Ti6Al4V برای کاربردهای بیومواد استفاده شد. از پراش پرتو ایکس (XRD) برای مشخص کردن ساختار بلوری پوشش و از میکروسکوپ الکترونی روبشی (SEM) و میکروسکوپ الکترونی روبشی نشر میدانی (FESEM) برای مشاهده مورفولوژی سطح و سطح مقطع پوشش استفاده شد. چسبندگی پوشش طبق استاندارد VDI 3198 با استفاده از فرورونده Rockwell-C اندازه‌گیری شد. رفتار خوردگی توسط پلاریزاسیون پتانسیودینامیک و امپدانس الکتروشیمیایی طیف‌سنجی در محلول رینگر ارزیابی شد. نتایج نشان داد که پوشش نانولایه پتانسیل خوردگی را از 0/368 V- به 0/054 V- برای نمونه تیتانیوم و از 0/405 V- به 0/028 V- برای نمونه Ti6Al4V تغییر داد. علاوه‌براین، چگالی جریان خوردگی برای نمونه های پوشش داده شده تیتانیوم و Ti6Al4V به ترتیب به حدود یک هشتم و یک سوم کاهش یافت. قطر دایره خازن به دلیل رسوب پوشش CrN/CrAlN افزایش یافته است، که نشان دهنده رفتار خوردگی بهبود یافته نمونه‌های پوشش داده شده در مقایسه با نمونه های بدون پوشش است، زیرا پوشش به عنوان مانعی در برابر نفوذ محلول خورنده به زیرلایه عمل می کند.

IJE TRANSACTIONS A: Basics Vol. 37 No. 01, (January 2024) 136-150

International Journal of Engineering

Journal Homepage: www.ije.ir

Optimization of Operating Parameters of a Scroll Expander Based on Response Surface and NSGA II

L. Shi, B. Peng*

School of Mechanical & Electronical Engineering, Lanzhou University of Technology, Lanzhou, Gansu China

PAPER INFO

Paper history:
Received 29 July 2023
Received in revised form 28 August 2023
Accepted 30 August 2023

Keywords:
Output Power
Isentropic Efficiency
Response Surface Methodology
Multi-objective Optimization

ABSTRACT

Adjusting the operating parameters to optimize the performance of the scroll expander has been a hot research topic among scholars. This paper innovatively combines the response surface method and NSGA2 algorithm for parameter optimization. This novel method can accurately predict the optimal operating parameters of the scroll expander and improve the overall efficiency of the scroll expander. Initially, a three-dimensional transient simulation model of the scroll expander was established, and the effects of three key operating parameters (suction pressure, exhaust pressure, and rotational speed) on the output power and isentropic efficiency of the scroll expander were analyzed through numerical simulation. On this basis, the response surface model between the input parameters and the objective function was established by using the response surface methodology. Consequently, three different optimization algorithms were compared, and it was found that NSGA-II had a better performance both in terms of convergence and solution performance,. Threfore, the NSGA-II algorithm was used for the multi-objective optimization. Under the premise of considering the maximum output power and isentropic efficiency, based on the established response surface model, the Pareto optimal solution was used to determine the optimal combination of its operating parameters: suction pressure of 1.62 MPa, exhaust pressure of 0.45 MPa, and rotational speed of 2,099.58 rpm.Finally, the numerical model is verified by the laboratory-built test bed of the Organic Rankine cycle low-temperature waste heat oil-free power generation system. The experimental results match well with the numerical simulation results and verify the model accuracy. The results from this pioneering and thorough thr study will provide a solid benchmark for the development and refinement of upcoming scroll machines.

***doi**: 10.5829/ije.2024.37.01a.13*

1. INTRODUCTION

With the intensive research on scroll expanders, many scholars have attempted to improve the performance of scroll expanders by changing the geometry. Fanti et al. (1) investigated tooth side gap size on the features of vortex expanders. Alshammari et al. (2) used new mathematical models to improve the scroll expander's profile. Gao et al. (3) developed a new expander. It was shown that this design has better performance than conventional expanders.

As Computational Fluid Dynamics technology continues to evolve, the investigation into the internal flow field within the expander is garnering increasing interest among academic researchers. Feng et al. (4) used the custom way to solve the vortex motion problem. Emhardt et al. (5) constructed a Vortex Swellers with variable wall thickness. Emhardt et al. (6) used new way to analyze the effect of variable Vortex Swellers. Zheng et al. (7) investigated the effect of the resolution of the CO_2 property table on the numerical simulation. Song et al. (8) proposed a symmetric exhaust structure of Vortex Swellers. Singh et al. (9) proposed symmetric exhaust structure of a Vortex Swellers. Song et al. (10) performed three-dimensional numerical simulations of a Vortex Swellers with different suction port positions based on CFD. Du et al. (11) compared the performance differences between T-CO_2 and R123. CO_2 and R123 performance differences, T-CO_2 exhibited better performance with an average isentropic efficiency 14% higher than that of R123.

*Corresponding Author Email: pengb2000@163.com (B. Peng)

Please cite this article as: Shi L, Peng B. Optimization of Operating Parameters of a Scroll Expander Based on Response Surface and NSGA II. International Journal of Engineering, Transactions A: Basics, 2024;37(01):136-150.

With improvement of experimental conditions, more and more scholars also focus on the experimental study of vortex expanders. Zhang et al. (12) conducted an experimental study of vortex expanders at 65C-96°C and compared the effects of the work mass, Fatigati et al. (13) compared the difference in the performance of vortex expander and slide rotary expander on ORC respectively. Hsieh et al. (14) developed a new ORC using R123a as the work material and experimentally investigated the performanceof expander. Oh et al. (15) developed a new model of a Vortex Swellers, and through the coupling of the simulation model with the experimental vales, two key unknown parameters were identified. Jalili et al. (16) conducted research on the effect of carbon nanotube (CNT) particles on refrigeration cycle performance. They conducted specific and rigorous experiments. Vanaei et al. (17) conducted an evaluation and refinement of an altered incineration facility through the Organic Rankine Cycle.

Upon a thorough analysis of the research synopsis presented above, it can be inferred that output power and isentropic efficiency serve as pivotal metrics for assessing the operational efficacy of a scroll expander. These two key variables do not operate in a vacuum; instead, they are shaped by various factors, such as pressure, speed, and the distinct geometry of the scroll expander. Nevertheless, existing studies typically concentrate on examining the impact of a solitary factor on the performance of Vortex Swellers, leaving a noticeable gap in the comprehensive discussion on the adjustment of these operating parameters for performance optimization. Consequently, this study employs numerical simulation to conduct an all-encompassing investigation of the three operating parameters of Vortex Swellers, aiming to identify optimal parameters for real-world operation. Most notably, we introduce a novel optimization method, which combines the response surface methodology and the NSGA II algorithm to facilitate in-depth multi-objective optimization. This approach allows us to derive optimal operating parameters for the Vortex Swellers. The findings from this innovative and comprehensive study will offer a robust reference point for the design and enhancement of future scroll machines.

2. MODELING

2. 1. Geometric Modeling of a Vortex Expander

The design of the Vortex Swellers's profile is informed by circular involutes, with the tooth head correction relying on double arc correction. Figure 1 provides a visual representation of the Vortex Swellers's geometric model, while Table 1 lays out the specific geometric parameters in detail.

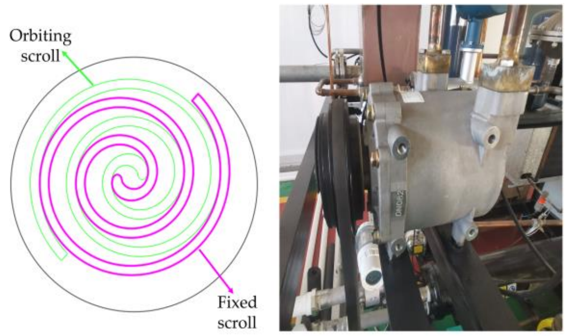

Figure 1. Geometric model of vortex expander

TABLE 1. Scroll expander geometric parameters

Definition	Parameters	Units	Value
Base circle radius	R	mm	4.647
Center distance	r	mm	9.6
Height of tooth	h	mm	42.5
Wall thickness	t	mm	5
Involute angle	a	°	30.767

2. 2. Turbulence Model

The continuity equation can be obtained by the following formulas (18).

$$\frac{\partial \rho}{\partial t}+\frac{\partial \rho u}{\partial x}+\frac{\partial \rho v}{\partial y}+\frac{\partial \rho w}{\partial z}-S_{\text{add}}=0 \tag{1}$$

where Ρ denotes mass per unit volume, t signifies temporal duration and u、v、w are speeds corresponding to the x、y、z axis, respectively. S_{add} embodies the accumulated mass in the continuous and any custom-defined origins. with a default value of 0.

The energy conservation equation can be obtained by the following formulas (19).

$$\frac{\partial}{\partial t}\left(\rho\left(U+\frac{v^2}{2}\right)\right)+\nabla\cdot\left(\rho v\left(h+\frac{v^2}{2}\right)\right)= \nabla\cdot\left(\lambda_{eff}\nabla T-\sum_j h_j\vec{J}_j+\tau_{eff}\cdot\vec{v}\right)+S_{\text{volume}} \tag{2}$$

$$U=h-\frac{p_{op}+p}{\rho},h=c_p dT+\frac{p}{\rho} \tag{3}$$

where λ_{eff} signifies the efficient transfer capacity, $\vec{J}_{\text{j}}$ alludes to the dispersion flow of the compound, U characterizes the intrinsic energy within the compound, h marks the perceptible heat content, τ_{eff} highlights the tension matrix, p_{op} pertains to the functional atmospheric force, P is the relative atmospheric force, and S_{volume} designates the bulk warmth origin.

2. 3. Vortex Expander Output Characteristics Equation for the output power of Vortex wellers (20):

$$\overline{M} = \int_t^{t+T} M_t(t)dt = \int_t^{t+T} F_t \cdot \mathrm{r}dt \tag{4}$$

$$W = \frac{2\pi n}{60}\overline{M} \tag{5}$$

where n signifies the spin frequency, $\overline{M}$ stands for the averaged momentum over time of the circulating scroll, F_t is the tangential force on the moving scroll disk, and r alludes to the foundational circle's diameter.

Equation for the isentropic efficiency of a vortex expander can be obtained by the following formulas (21):

$$\eta = \frac{H_1 - H_2}{H_1 - H_2{}'} = \frac{W}{\overline{m}\left(h_{\mathrm{in}} - h_{\mathrm{out}}\right)} \tag{6}$$

where $\overline{m}$ represents the weight flux of the operational liquids over a time interval, h_{in} designates the articular heat content at the entry point of these liquids, and h_{out} points to the particular heat content at the exit point of these operational liquids.

2. 3. Meshing The role of meshing is particularly important in computational fluid dynamics (CFD) analysis, which largely determines the accuracy and convergence of subsequent numerical simulations. ANSYS Fluent software will be used to perform numerical simulations. Taking the vortex expander as an example, a specific meshing strategy can effectively characterize the fluid region model of the vortex expander. Typically, a hybrid meshing strategy is used to model the fluid region of a vortex expander. This hybrid meshing approach is designed to maximize the reflection of the fluid flow characteristics inside the vortex expander. Figure 2 illustrates the mesh model.

2. 4. Grid Sensitivity Validation In order to select the appropriate grid scale and number of computational domain grids, the numerical calculation results of five different numbers of grid models for specific operating conditions were compared and the results are shown in Table 2. When comparing A3 grid to A1 grid and A2 grid , we found that their deviations in mass flow rate, driving moment and isentropic efficiency are less than 6%. While comparing the A3 grid to the A4 grid and A5 grid, we can observe that the deviations in mass flow rate, driving moment and isentropic efficiency are less than 8%. Considering the accuracy and efficiency together, A3 grid has met the requirements of grid independence and computational accuracy when performing the numerical simulation of the vortex expander.

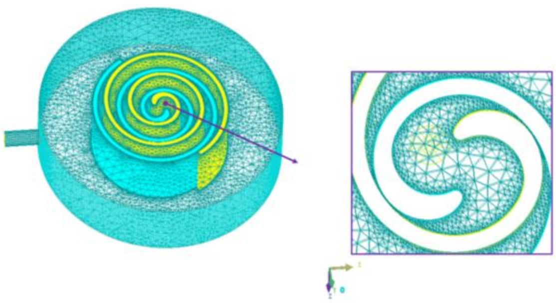

Figure 2. Meshing model

3. ANALYSIS OF RESULTS

3. 1. Effect of Different Exhaust Pressures on the Performance of Scroll Eexpanders We selected four distinct exhaust pressures for examination, with Table 3 detailing the specific working conditions associated with each other.

Figure 3 portrays the changes in isentropic efficiency and exported energy of the scroll expander under varying exhaust pressures. A close examination of Figure 3 reveals that an increase in exhaust pressure results in divergent trends for output power and isentropic efficiency. Specifically, exported energy decreases while isentropic efficiency increases. This is linked to the fact that the scroll expander's exported energy is influenced by the pressure differential between the inlet and outlet. An increase in exhaust pressure reduces this differential.

TABLE 2. Time-averaged performance of vortex expanders with different number of grids

Grid level	Total number of grids	Mass flow (kg/s)	Torques (N.m)	Isentropic efficiency (%)	Times (s)
A1	55E+4	0.11658	5.12	36.52	8h
A2	85E+4	0.12458	5.42	37.82	16h
A3	110E+4	0.12796	5.64	38.16	23h
A4	150E+4	0.13124	5.83	38.64	33h
A5	210E+4	0.13216	5.89	38.94	44h

TABLE 3. Different exhaust pressure parameters

Condition number	Suction pressure (MPa)	Inlet temperature (K)	Exhaust pressure (MPa)	Rotation speed (r/min)
S1	1.2	400	0.15	2000
S2	1.2	400	0.3	2000
S3	1.2	400	0.45	2000
S4	1.2	400	0.6	2000

Consequently, with a smaller pressure difference, the gas's capability to transform energy into mechanical work during expansion is restricted, leading to a reduction in the vortex expander's output power. On the other hand, a higher exhaust pressure decreases the pressure drop, which facilitates a more efficient conversion of pressure energy into kinetic energy. In addition, a moderate exhaust pressure helps to maintain a more stable flow velocity distribution and reduces the energy loss due to turbulence. In the actual expansion process, irreversible losses occur due to friction, turbulence, and non-uniform distribution of fluid pressure, leading to an increase in entropy (22). When the exhaust pressure is moderately increased, these irreversible losses are reduced; thus, increasing the isentropic efficiency.

The transient variation of the exported energy of the scroll expander at different exhaust pressures is given in Figure 4. Exported energy transient curve shows a downward flat trend Upon increasing the exhaust pressure as it goes from 0.15 MPa to 0.60 MPa. The exhaust pressure significantly affects the degree of gas expansion within the vortex expander, which in turn affects the output power. At lower exhaust pressures, the gas has to undergo a greater degree of expansion, releasing more energy and leading to an increase in output power. Conversely, at higher exhaust pressures, the gas expands less, releasing less energy and reducing the power output. Therefore, the magnitude of fluctuations in the output power transient plots and the average exported energy may vary under different exhaust pressure conditions.

3. 2. Effect of Different Suction Pressures on the Performance of Vortex Expanders

We maintained a constant inlet temperature for the Vortex Swellers's working mass, while varying the suction pressure. Table 4 presents the parameters pertaining to these simulated working conditions.

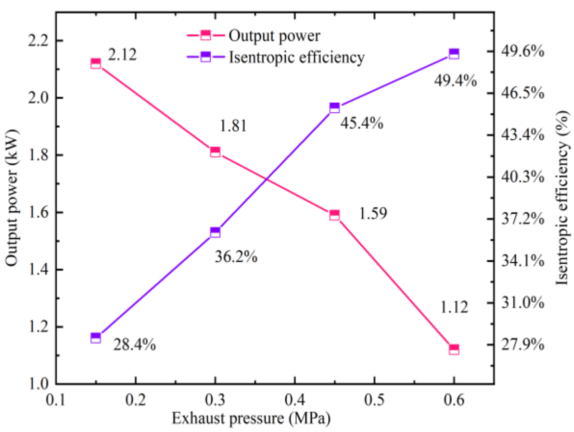

Figure 3. Isentropic efficiency and output power diagram for different exhaust pressure

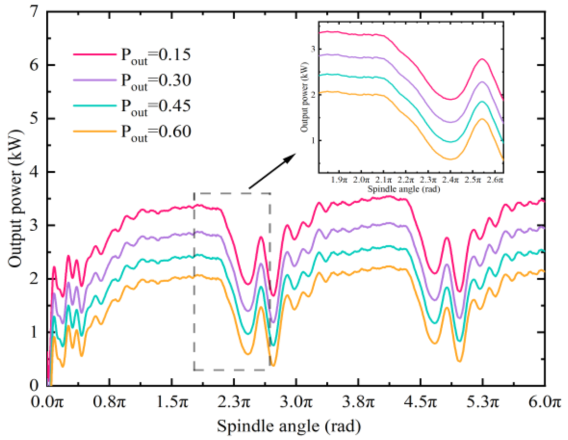

Figure 4. Variation of output power under different exhaust pressure

TABLE 4. Different suction pressure parameters

Condition number	Suction pressure (MPa)	Inlet temperature (K)	Exhaust pressure (MPa)	Rotation speed (r/min)
T1	0.8	400	0.25	2000
T2	1.1	400	0.25	2000
T3	1.4	400	0.25	2000
T4	1.7	400	0.25	2000

As latter escalates from 0.8 MPa to 1.7 MPa, the former sees a clear upward trend, moving from 1.074 kW to 3.056 kW. The underlying reason for this trend is the increased gas density with the rise in suction pressure. This enables Vortex Swellers to extract more energy from the gas, leading to an increment in output power. Figure 5 shows the isentropic efficiency and output power for different suction pressure. When assessing the isentropic efficiency in relation to suction pressure, a subtle increase is noticed as the suction pressure moves from 0.8MPa to1.1MPa. In contrast,

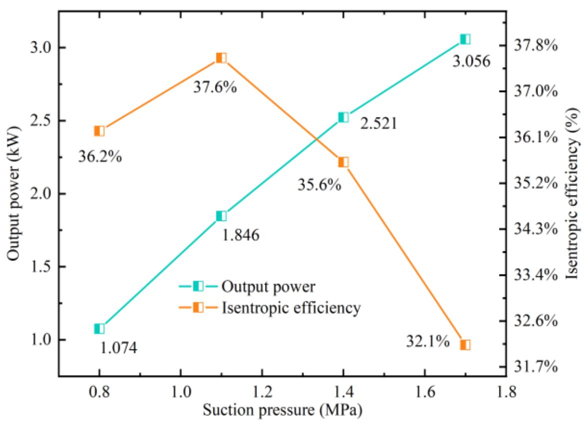

Figure 5. Isentropic efficiency and output power for different suction pressure

between 1.1MPa and 1.7MPa, the isentropic efficiency reveals a decline, falling from 37.6% to 32.1% - a total reduction of 5.5%.

Figure 6 illustrates the temporal changes in the Vortex Swellers 's output power at various suction pressures. It is evident from the figure that the output power increases in line with the rise in suction pressure. This allows more fluid to participate in the expansion process per time unit, leading to a greater conversion of pressure energy into rotational energy in the moving scroll disk, and thereby enhancing the scroll expander's output power.

3. 3. Effect of Different Rotational Speeds on the Behavior of Vortex Expanders

Specific parameters are shown in Table 5.

An inspection of Figure 7 reveals that within the speed range of 1200rpm-2100rpm. The output power escalates from 1.27kW to 2.07Kw, marking a growth rate of 62.9%, whereas the isentropic efficiency moves up from 25.5% to 37.7%, indicating a growth rate of 47.8%.

Figure 8 provides the transient diagrams of the scroll expander's energy output at varying speeds. A perusal of Figure 8 reveals that at lower speeds, the export of energy experiences less fluctuation in the range of 1.9π to 2.2π, maintaining an overall steady trajectory. However, at higher speeds, the output power exhibits t

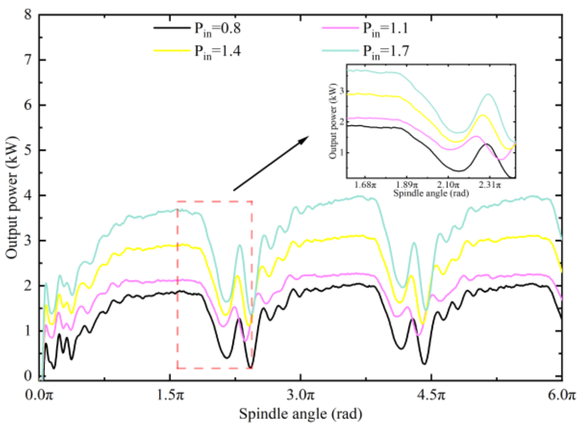

Figure 6. Transient curve of output power at different suction pressure

TABLE 5. Different exhaust pressure parameters

Condition number	Suction pressure (MPa)	Inlet temperature (K)	Exhaust pressure (MPa)	Rotation speed (r/min)
1	1.2	400	0.25	1200
2	1.2	400	0.25	1500
3	1.2	400	0.25	1800
4	1.2	400	0.25	2100

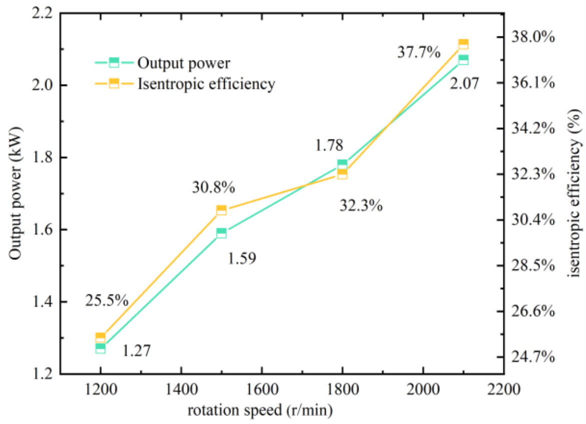

Figure 7. Graph of Isentropic efficiency and export of energy for different speeds

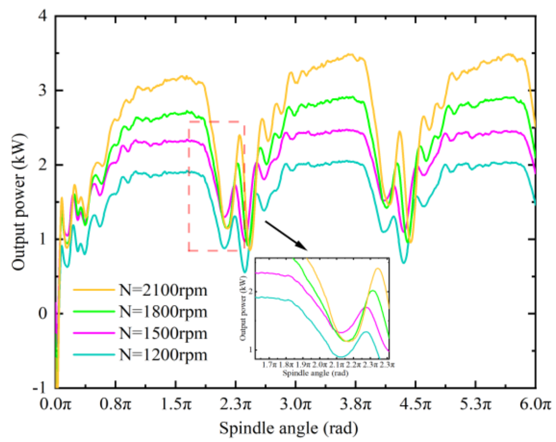

Figure 8. Transient diagram of output power at different speeds

more significan fluctuations, with a discernible downward trend. This can be attributed to the following reasons: In the scroll expander's low rotational speed phase, the gas expands slowly, resulting in a larger decrease in internal energy. This causes the export of energy to incrementally increase with the rise in rotational speed. As the Vortex Swellers moves into the mid-speed phase, the gas expansion speed picks up, the internal energy decreases, and the export of energy transient curve displays a slow growth, gradually stabilizing. However, in the high-speed phase, the gas expands too quickly, and the reduction in internal energy is limited. This results in the output power reaching a peak as the speed increases, after which an evident decline is observed.

4. MULTI-OBJECTIVE OPTIMIZATION

4. 1. Response Surface

Its main function is to form a response function that characterizes in detail the interrelationships between input and output variables. This objective function can usually be expressed as an equation of the following form:

$$Y_i = \beta + \sum_{i=1}^{k} \beta_i x_i + \sum_{i=1}^{k} \beta_{ii} x_{ii}^2 + \sum_{i=1}^{k} \sum_{j>1}^{k} \beta_{ij} x_i x_j \quad (7)$$

We chose to adopt BBD for the experimental design of this study. Table 6 lists the parameters of BBD design.

4. 1. ANOVA and Regression Models The magnitude of F-value is opposite to the magnitude of P-value. As shown in the Table 8, F of the model is 237.5 and P is less than 0.0001, these values indicate that the significance of our constructed model is very strong. In assessing the accuracy of the model, R² and R_{adj} important reference indicators. The closer the values of these two metrics are to 1 and the smaller the gap between them is, it means that the model is more accurate. In the table, R² is 0.9967 and R_{adj} is 0.9925, which are both very close to 1, and the difference between them is only 0.0042, these values fully indicate that our model has a very high accuracy. From Table 9 we can find that R² is 0.9913 and Radj is 0.9807, both which are close to 1, highlighting the model's ability to accurately reflect changes in isentropic efficiency. At the same time, the small difference of only 0.0106 strongly confirms the high accuracy of the model.

The fitted curves are expressed as Equations 8 and 9.

$$W = -0.5636 + 1.1353A - 0.3088B - 0.001C + 0.8449AB + 0.0009AC - 0.004BC - 0.3835A^2 - 2.9686B^2 + 1.0833\text{e-}8C^2 \quad (8)$$

$$\eta = -0.2366 - 0.3676A - 0.3938B + 0.0002C + 0.2769AB - 0.0024AC + 0.0006BC - 0.1135A^2 - 0.9037B^2 - -5.7451\text{e} - 8C^2 \quad (9)$$

4. 2. Response Surface Result Analysis In the response surface plot shown in Figure 9, we can find that the output power is at a low level at the combination of horizontal intervals of suction pressure taking the value range of 0.8-1.2 MPa and exhaust pressure taking the value range of 0.5-0.6 MPa. However, the output power is at a high level at the combination of horizontal intervals for the range of values of suction pressure 1.6-1.8 MPa and the range of values of exhaust pressure 0.15-0.3 MPa.

TABLE 6. Three-factor design table

Code	Variables	Level		
		-1	0	1
A	Suction pressure	0.8	1.3	1.8
B	Exhaust pressure	0.15	0.375	0.6
C	Rotation speed	1200	1600	2100

TABLE 7. Three-factor, three-level parameter design table

3	Suction pressure (MPa)	Exhaust pressure (MPa)	Rotation speed (r/min)	Output power (kW)	Isentropic efficiency (%)
	A	B	C		
S1	0.8	0.4	2000	0.683	40.5
S2	1.3	0.375	2000	2.312	33.4
S3	1.3	0.4	1600	1.599	37.9
S4	1.8	0.15	1600	2.736	26.1
S5	1.8	0.4	1300	2.033	30.3
S6	1.8	0.6	1600	1.999	38.6
S7	1.8	0.4	2000	2.982	40.6
S8	0.8	0.375	2000	1.074	36.2
S9	1.1	0.15	2000	1.843	37.6
S10	1.4	0.25	2000	2.504	35.6
S11	1.8	0.25	2000	3.053	32.1
S12	1.2	0.15	1600	2.123	28.4
S13	1.3	0.375	2000	1.811	36.4
S14	1.2	0.45	2000	1.591	45.5
S15	1.2	0.6	1200	1.095	49.4
S16	1.3	0.25	1200	1.276	25.5
S17	1.2	0.15	1600	1.598	30.8

TABLE 8. Output power analysis of variance table

Source	Sum of Squares	df	Mean Square	F-value	p-value
Model	7.27	9	0.8074	237.35	＜0.0001
A	0.6234	1	0.6234	183.26	＜0.0001
B	0.1297	1	0.1297	38.14	0.0005
C	0.1054	1	0.1054	30.99	0.0008
AB	0.0052	1	0.0052	1.52	0.2576
AC	0.0255	1	0.0255	7.49	0.0291
BC	0.0004	1	0.0004	0.1238	0.7353
A²	0.0152	1	0.0152	4.48	0.0720
B²	0.0331	1	0.0331	9.72	0.0169
C²	4.622E-06	1	4.622E-06	0.0014	0.9716
Residual	0.0238	7	0.0034		
Lack of Fit	0.114	10	0.0025		
Pure Error	0.001	1	0.0018	4.541	0.362
Cor Total	7.29	16			
R^2=0.9967		R_{adj}=0.9925		C.V%=3.07	

TABLE 9. Isentropic efficiencyanalysis of variance table

Source	Sum of Squares	df	Mean Square	F-value	p-value
Model	1474.36	9	147.43	91.43	< 0.0001
A-pin	16.28	1	16.28	1.11	0.3274
B-pout	216.86	1	216.86	13.19	0.0084
C-N	68.46	1	68.46	58.88	0.0001
AB	32.16	1	32.15	6.81	0.0349
AC	8.64	1	8.64	3.56	0.1013
BC	3.86	1	3.86	9.88	0.0163
A²	2.68	1	2.68	16.41	0.0049
B²	4.42	1	4.42	37.64	0.0005
C²	6.46	1	6.46	1.60	0.2468
Residual	122.24	7	7.86		
Lack of Fit	120.68	11	9.48		
Pure error	0.12	1	0.18		
Cor Total	1842.68	16			
R^2=0.9916		R_{adj}=0.9807		C.V%2.55	

As shown in Figure 10, it can be found that the fluctuation of the surface in the direction of suction pressure is large, while the fluctuation of the surface in the direction of speed is relatively small. This indicates that the effect of suction pressure on the output power is more significant compared to the effect of rotational speed. This finding is important for practical applications because the researcher can maximize the output power by adjusting the combination of suction pressure and rotational speed. The output power falls in the optimum range when the suction pressure is 1.6MPa-1.8MPa and the rotational speed lies in the range of 1850-2000rpm.

Figure 11 demonstrates the response surface plots of the output power as a function of exhaust pressure and rotational speed. Observing Figure 11, we can find that when the exhaust pressure is in the range of 0.15MPa-0.33MPa, the trend of output power reduction is more obvious as the exhaust pressure decreases. However,

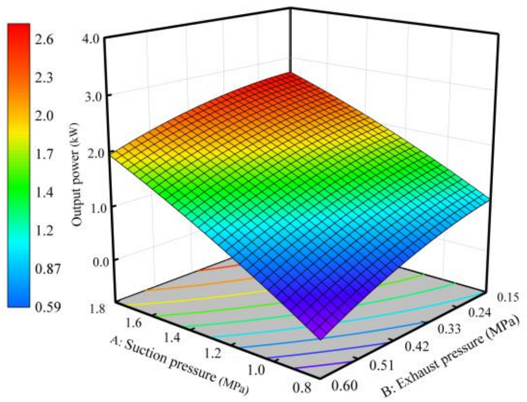

Figure 9. Response surface of output power under the interaction of suction pressure and exhaust pressure

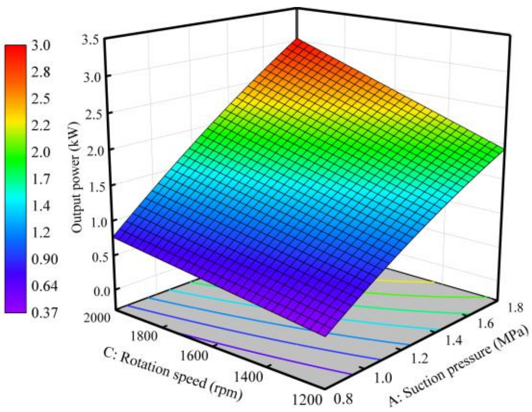

Figure 10. Response surface of output power under the interaction of suction pressure and rotational speed

when the exhaust pressure is at 0.33MPa-0.60MPa, the trend of output power reduction is relatively slower as the exhaust pressure decreases. This indicates that at different exhaust pressure intervals, the output power has different sensitivities to changes in exhaust pressure.

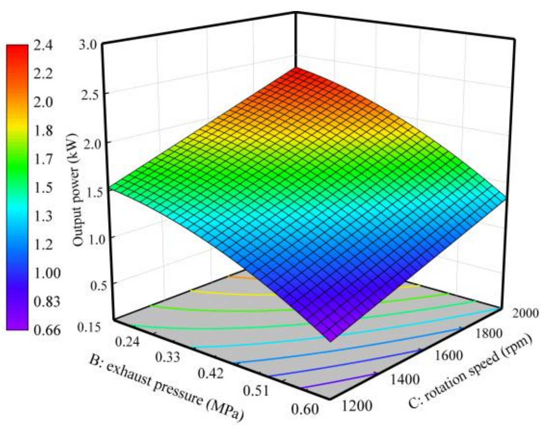

Figure 11. Response surface of output power under the interaction of exhaust pressure and rotational speed

The interaction between response surface and contour visuals, as depicted in Figure 12, demonstrates the trend of isentropic efficiency under varied inlet and exhaust pressure conditions. This analysis suggests that notable enhancement in isentropic efficiency can be achieved when the intake pressure is set between 1.6-1.8 MPa and the exhaust pressure falls within the 0.5-0.6 MPa range. This finding bears significant implications, serving as a valuable guide for optimizing the configuration of suction and exhaust pressures to boost the isentropic efficiency of the machinery in real-world applications.

The response surface as shown in Figure 13 reveals in detail the variation characteristics of isentropic efficiency under different conditions of intake pressure and rotational speed. Based on the data analysis in Figure 13, we can conclude that the optimal performance interval of isentropic efficiency is concentrated in the range of 1.1-1.3 MPa intake pressure and 1800-2000 rpm rotational speed under the consideration of only two influencing factors, namely, intake pressure and rotational speed.

The response surface shown in Figure 14 reflects the changing law of isentropic efficiency under different

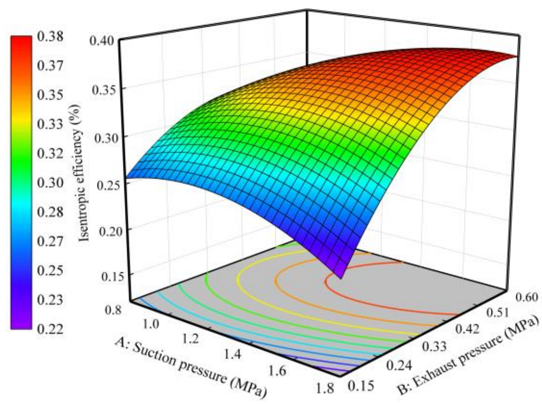

Figure 12. Isentropic efficiency response surface under the interaction of suction pressure and exhaust pressure

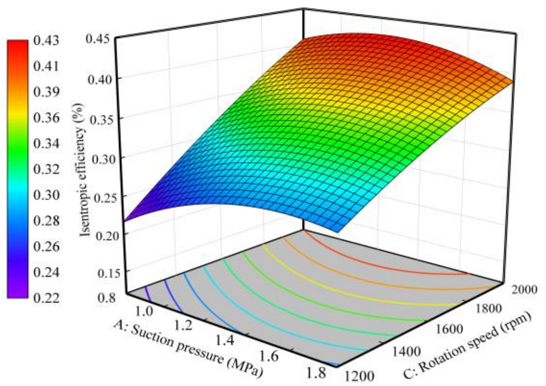

Figure 13. Isentropic efficiency response surface for the interaction of suction pressure and rotational speed

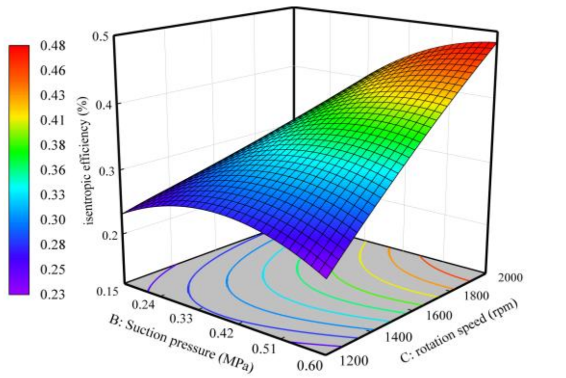

Figure 14. Isentropic efficiency response surface under the interaction of exhaust pressure and rotational speed

exhaust pressure and rotational speed conditions. We can conclude that the isentropic efficiency can reach the optimal parameter range when the exhaust pressure is about 0.51-0.6 MPa and the rotational speed is in the range of 1600-2000 rpm.

4. 3. Performance Comparison of Algorithms

To identify the best operational parameters, this research contrasts three frequently employed multi-objective optimization algorithms (MOPSO, NSGA-II, MOEA/D). Eventually, we settle on the NSGA-II algorithm as the most compatible with our model. Figure 15 provides the Pareto optimal solution set diagrams for the three optimization algorithms. The allocation of decision variables for these three optimization algorithms is depicted in Figure 16. From Figure 15, the NSGA-II algorithm has a more concentrated non-inferior solution set and a better diversity of solutions, and the solution set covers all regions of the solution space, which means that we can choose between solutions to satisfy different priorities and preferences. Algorithms with centralized and dense non-inferior solution sets tend to have better convergence. This means that the algorithms are able to find better solutions in a shorter time, which improves the efficiency of solving the optimization problem.

From Figure 16, the MOPSO algorithm as a whole has a more decentralized distribution of decision variables, which presents an unconcentrated character. This means that in the solution space, the MOPSO algorithm is not able to search better for excellent solutions in multiple regions, and the convergence and diversity performance is average (23). The NSGA-II has a fairly uniform distribution of decision variables on the whole, and exhibits better convergence. This indicates that the algorithm is able to effectively find a set of excellent solutions in the solution space with a strong search capability. Compared to the other two algorithms (NSGA II and MOPSO), the MOEA/D algorithm has a wider distribution of decision variables on exhaust pressure, which is mainly concentrated in the range of 0.1MPa-0.55MPa. This implies that the algorithm has a more comprehensive search capability in the exhaust pressure direction and is able to find more potentially excellent solutions. However, in the direction of suction pressure, the distribution of decision variables of the MOEA/D algorithm does not perform well.

In order to better and comprehensively evaluate the advantages and disadvantages of the three algorithms, we introduced HV, IGD, and computation time at the same time for comprehensive evaluation, and the values of the specific evaluation indexes are given in Table 10. Larger HV values and smaller IGD values indicate better performance of the algorithms, and we can see from the table that NSGA-II has obvious advantages over the other two algorithms in terms of HV, IGD, and computation time.

Equation 10 gives the range of values of the independent variables, and for subsequent optimization, the result of the NSGA-II algorithm are given Table 11.

$$\begin{cases} \textit{Maximize}: \text{output power}=f_1(P_{\text{in}}, P_{\text{out}}, n); \\ \textit{Maximize}: \text{Isentropic efficiency}=f_2(P_{\text{in}}, P_{\text{out}}, n). \\ 0.8\text{MPa} \le P_{\text{in}} \le 1.8\text{MPa}; \\ 0.15\text{MPa} \le P_{\text{out}} \le 0.6\text{MPa}; \\ 1200\text{rpm} \le n \le 2100\text{rpm}. \end{cases} \tag{10}$$

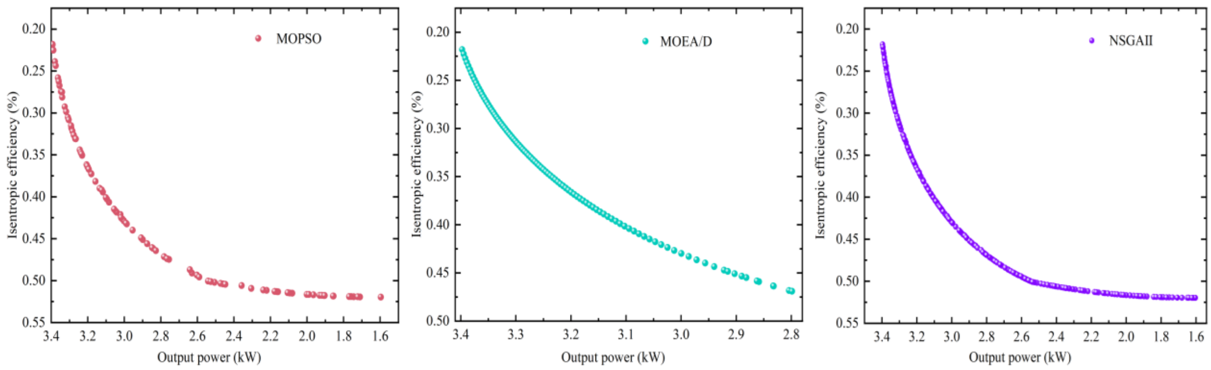

Figure 15. Non-inferiority solution set diagram of three multi-objective optimization algorithms

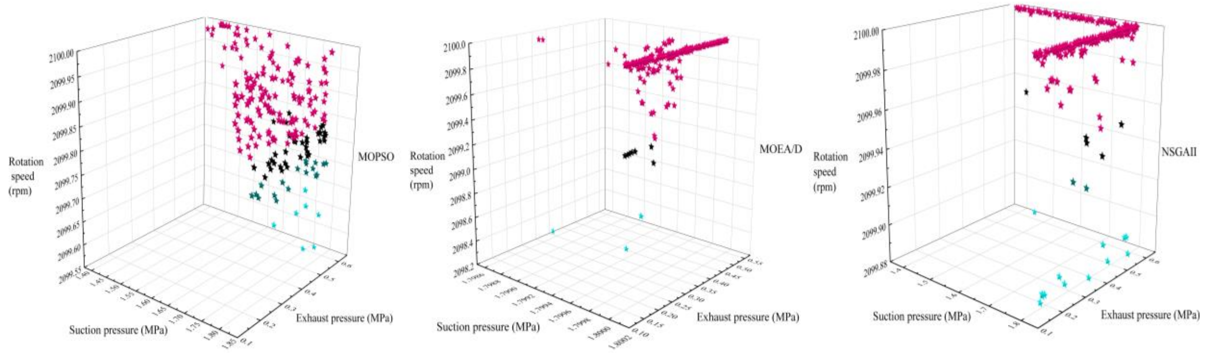

Figure 16. Distribution of decision variables for three multi-objective optimization algorithms

TABLE 10. Table of performance indicators of the three algorithms

Algorithms	HV	IGD	calculation time (s)
MOPSO	0.9168	1.7569	12.96
NSGA-II	0.9412	1.6686	8.59
MOEA/D	0.9356	2.4214	51.86

TABLE 11. Main parameters of NSGA-II algorithm

Parameters	Values
Population size	150
Crossover probability	0.9
Mutation probability	0.02
Maximum generation size	500

By running the NSGA-II algorithm, we obtained a set of Pareto solutions as shown in Figure 17. This set of solutions demonstrates the trade-offs between different objective functions, thus providing diversified choices for decision makers. Point C in Figure 17 is the desired ideal point, where the output power is 3.02 kW, the efficiency is 42.6%, and the optimal operating parameters are: suction pressure is 1.62 MPa, exhaust pressure is 0.45 MPa, and the rotational speed is 2099.58 rpm. The optimal operating parameters solved by the NSGA II algorithm are compared with the simulated values to determine the accuracy of the solution, and the results in Table 12. gives the comparison results. From Table 12, the predicted value of the output power solved by the NSGA II algorithm is 3.02 kW, and the simulated value calculated by numerical simulation is 3.16 kW, with a deviation of 4.4%, and the predicted value of the isentropic efficiency is 42.6%, and the simulated value is 45.4%, with a deviation of 6.2%. The deviation of both is less than 8%, which shows the high accuracy of the optimal solution

5. EXPERIMENTAL VALIDATION

To validate the reliability of the vortex expander's numerical simulation outcomes, we juxtaposed the predicted data with the findings from our experimental setup. Figure 18 provides an intricate depiction of the testing platform. At the heart of this setup is the scroll expander, adapted from an oil-free scroll compressor.

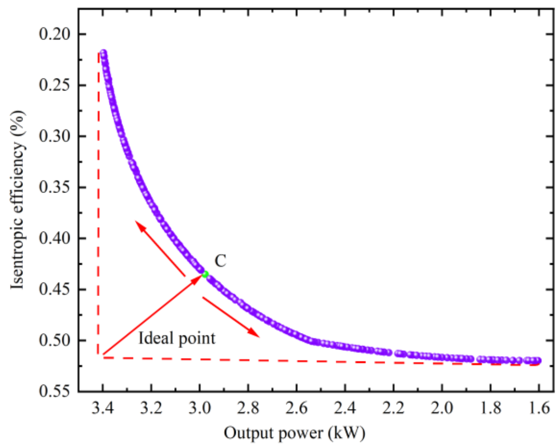

Figure 17. Pareto front plot of NSGA II algorithm

TABLE 12. Comparison of predicted values and simulations

Suction pressure (mpa)	Exhaust pressure (mpa)	Rotation speed (rpm)	Output power (kw)		Isentropic efficiency (%)	
			Predicted value	Simulated value	Predicted value	Simulated value
1.62	0.45	2099.58	3.02	3.16	42.6	45.4

Complementing this, the apparatus incorporates a specialized mass flow pump. It's further outfitted with an evaporator and condenser, each tasked with the vaporization and liquefaction of the working mass, respectively. For precise oversight, we have integrated a smart electromagnetic flow meter. This instrument continuously captures the mass flow rate, enabling meticulous oversight and precision throughout the experimentation phase.

To calibrate the measuring equipment, the following preparations are made:

(1) Make sure that the components of the ORC system are installed and well connected. Make sure the voltmeter is connected correctly and securely to avoid errors or accidents. Connect the ammeter in series with the generator output circuit. Typically, this means that the circuit needs to be disconnected and the two probes of the ammeter connected at each end of the disconnect. Make sure the ammeter is properly and securely installed during installation.

(2) System initialization and preheating: Start the work pump to circulate the work through the system. Start the heater and gradually increase the temperature of the evaporator to evaporate the work mass. During this process, pay attention to monitor the readings of each measuring instrument to ensure that the working parameters are within the safe range.

(3) Adjustment of suction pressure: Before starting the experiment, select the appropriate suction pressure according to the expected test range. The inlet pressure can be changed by adjusting the frequency of the work pump

(4) After adjusting the suction pressure, wait for the system to reach a stabilized condition. During this time, continuously monitor the readings of each measuring instrument to ensure that the operating parameters remain within the expected range. At the same time, record the suction pressure, temperature, and other parameters of scroll expander at this time.

Figure 19 depicts the schematic diagram of the experiment. The test implementation process strictly adheres to the provisions in the Organic Rankine Cycle Power Generation Unit (JB/T13305-2017)

All experimental data are averaged over several measurements to ensure the reliability of the data.

Firstly, we adjust the inlet pressure into the vortex expander by changing the operating frequency of the work pump.

Figure 18. Experimental platform diagram

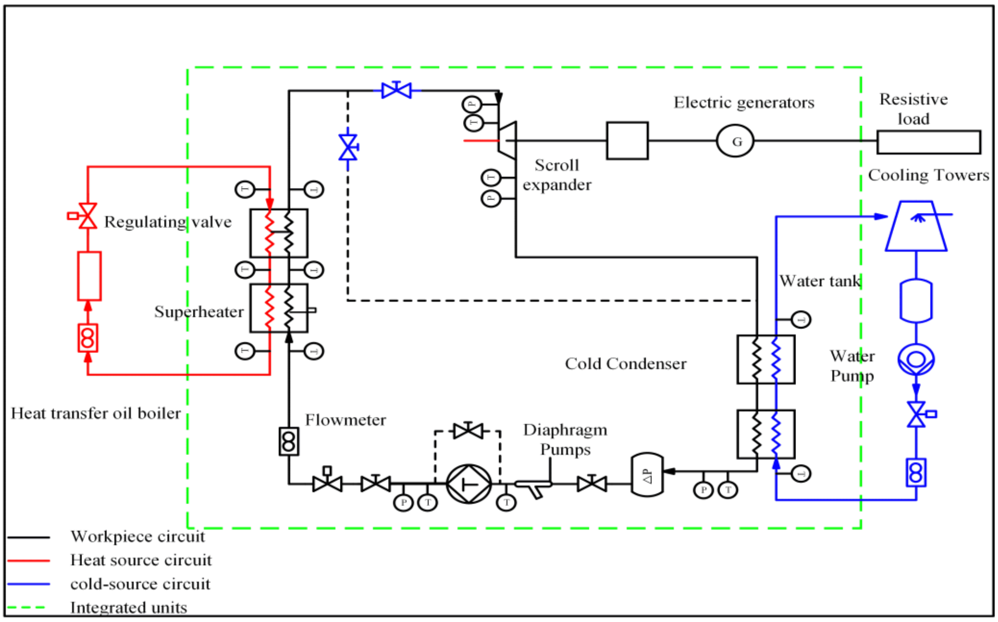

Figure 19. Experimental schematic

Secondary, we monitor in real time the voltage and current flowing through the scroll expander. Based on these parameters, we can calculate the export of energy of the scroll expander.

Finally, we compare experimental output power values at different inlet pressures with the simulated values.

Figure 20 shows the experimental values of voltage and current flowing through the scroll expander at different inlet pressures, as measured by our experimental platform. These data are an important basis for analyzing and understanding the operating conditions of the scroll expander.

Figure 21 shows the experimental and simulated output power values. The maximum deviation in output power is 10.86% at a suction pressure of 1.1 MPa. Overall, the deviation between the simulated and experimental results is between 3% and 11%, which constitutes a relatively small deviation. This indicates that model we established is relatively accurate and can effectively simulate the operating characteristics of the scroll expander under different operating conditions.

Meanwhile, we also measured the experimental and simulated values of isentropic efficiency. Figure 22 shows the experimental and simulated values of isentropic efficiency at different suction pressures. The maximum error occurs when the inspiratory pressure is 0.8 MPa, and the maximum error is 12.7%. The reasons for this deviation may be the existence of certain errors in the actual measurement process, the friction loss of the machine and other factors.

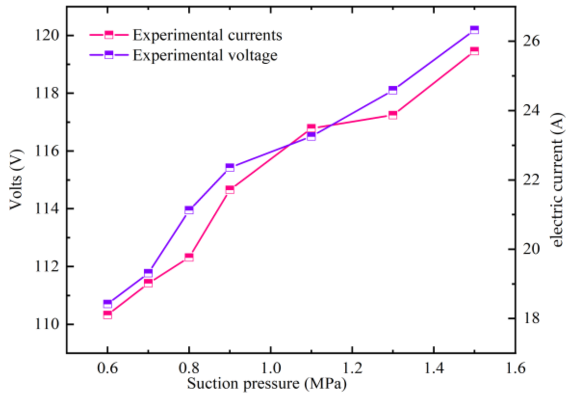

Figure 20. Experimental current-voltage diagram at different suction pressures

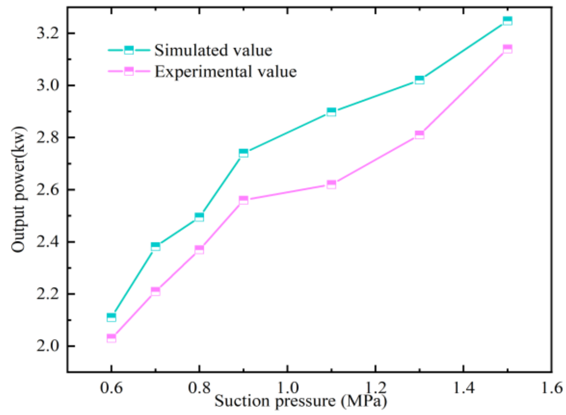

Figure 21. Simulated versus experimental values of output power

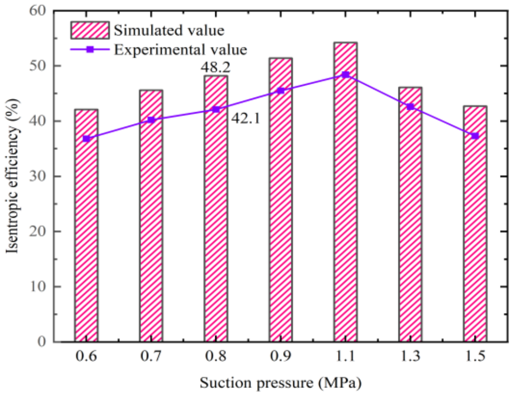

Figure 22. Experimental and simulated values of isentropic efficiency at different suction pressures

6. CONCLUSION

Distinct from the research undertakings of prior scholars regarding the operational parameters of the scroll expander, the majority have primarily focused on discerning the extent to which these parameters impact the generated energy and adiabatic effectiveness of the device. Significantly, some academics have deliberated on the optimal configuration of these parameters to ensure peak performance of the scroll expander. This study introduces a methodological fusion of the response surface technique and the NSGA-II algorithm, achieving the optimal operational parameters for the scroll expander. Under these parameters, the scroll expander's performance is comprehensively maximized. The accuracy of this innovative approach has been rigorously validated using a specially constructed experimental platform. Renowned for its high precision and rapid problem-solving capabilities, this novel methodology presents a fresh theoretical framework and perspective for the optimization of the scroll expander. The specific conclusions are as follows:

(1) As the exhaust pressure increases, the pressure difference at the inlet side of the scroll expander decreases, resulting in a lower mass flow rate at the inlet side. Due to the internal structure of the scroll expander, the mass flow rate at the outlet side remains essentially the same as the mass flow rate at the inlet side. A rise in exhaust pressure from 0.15 MPa to 0.60 MPa leads to contrasting trends in the generated energy and adiabatic effectiveness: there's a reduction in output power by 47.17%,while the isentropic efficiency surges by 73.94%. The output power shows a linear increase with the increase of suction pressure. An increase in suction pressure from 0.8 MPa to 1.7 MPa results in a rise in output power by 1.982 kW.the isentropic efficiency shows an initial increase and then a decrease due to factors such as friction and turbulence. When the speed is in the range of 1200 rpm to 2100 rpm, both the isentropic efficiency and the output power increase with the increase in speed.

(2) The NSGA-II algorithm is more suitable for the multi-objective optimization model both in terms of convergence and solution performance. The maximum export power and isotropy efficiency of the Vortex Expander are derived from solution to be 3.02 kW and 42.6%, respectively, with deviations of 4.4% and 6.2% from the simulated values. The optimum operating parameters: suction pressure, exhaust pressure and rotational speed were 1.62MPa, 0.45MPa and 2099.58rpm.

(3) The accuracy of our method is verified by the organic Rankine cool thermal waste energy production system built in laboratory. The maximum deviations of the experimental values of export power and isotropy efficiency from simulated values are 10.86% and 12.7%, respectively, and the errors are lower than 13%, indicating that the method has relatively better accuracy and can be applied to the actual manufacture. The reasons for this deviation may be the existence of certain errors in the actual measurement process, the friction loss of the machine and other factors.

7. REFERENCES

1. Fanti GR, Romo DA, Almeida RD, Mello PD. Influence of flank clearance on the performance of a scroll expander prototype. Energy. 2020;193.
2. Alshammari F, Pesyridis A, Elashmawy M. Turbine optimization potential to improve automotive Rankine cycle performance. Applied Thermal Engineering. 2021;186:116559. https://doi.org/10.1016/j.applthermaleng.2021.116559 https://www.sciencedirect.com/science/article/pii/S1359431121000168
3. Gao J, Ma C, Tian G, Xing S, Jenner P. Numerical investigations of an opposed rotary piston expander for the purpose of the applications to a small-scale Rankine cycle. Applied Thermal Engineering. 2021;182:116157.
4. Xiao GF, Liu GP, Wang JT, Song HG, University N, University J. Three-dimensional Numerical Simulation for Transient Flow in a Scroll Compressor Using Dynamic Mesh Technique. Fluid Machinery. 2014.
5. Emhardt S, Tian G, Song P, Chew J, Wei M. CFD modelling of small scale ORC scroll expanders using variable wall thicknesses. Energy. 2020;199:117399. https://doi.org/10.1016/j.energy.2020.117399 https://www.sciencedirect.com/science/article/pii/S0360544220305065
6. Emhardt S, Tian G, Song P, Chew J, Wei M. CFD analysis of the influence of variable wall thickness on the aerodynamic performance of small scale ORC scroll expanders. Energy. 2022;244. 10.1016/j.energy.2021.122586
7. Zheng S, Wei M, Song P, Hu C, Tian R. Thermodynamics and flow unsteadiness analysis of trans-critical CO2 in a scroll compressor for mobile heat pump air-conditioning system. Applied Thermal Engineering. 2020;175. 10.1016/j.applthermaleng.2020.115368
8. Song P, Wei M, Zhang Y, Sun L, Emhardt S, Zhuge W. The impact of a bilateral symmetric discharge structure on the

performance of a scroll expander for ORC power generation system. Energy. 2018;158:458-70. https://doi.org/10.1016/j.energy.2018.06.053 https://www.sciencedirect.com/science/article/pii/S0360544218311186

9. Singh S, Singh A, Dasgupta MS. CFD Modeling of a Scroll Work Recovery Expander for Trans-critical CO 2 Refrigeration System. Energy Procedia. 2017;109:146-52. 10.1016/j.egypro.2017.03.081

10. Song P, Wei M, Liu Z, Zhao B. Effects of suction port arrangements on a scroll expander for a small scale ORC system based on CFD approach. Applied Energy. 2015;150:274-85. 10.1016/j.apenergy.2015.04.046

11. Du Y, Tian G, Pekris M. Unsteady and three-dimensional computational fluid dynamics modelling of scroll expander for low-grade waste heat recovery transcritical carbon dioxide micro-scale power system. Energy Conversion and Management. 2023;282. 10.1016/j.enconman.2023.116857

12. Zhang H-H, Zhang Y-F, Feng Y-Q, Chang J-C, Chang C-W, Xi H, et al. The parametric analysis on the system behaviors with scroll expanders employed in the ORC system: An experimental comparison. Energy. 2023;268. 10.1016/j.energy.2023.126713

13. Fatigati F, Vittorini D, Coletta A, Cipollone R. Assessment of the differential impact of scroll and sliding vane rotary expander permeability on the energy performance of a small-scale solar-ORC unit. Energy Conversion and Management. 2022;269. 10.1016/j.enconman.2022.116169

14. Hsieh J-C, Chen Y-H, Hsieh Y-C. Experimental study of an organic Rankine cycle with a variable-rotational-speed scroll expander at various heat source temperatures. Energy. 2023;270. 10.1016/j.energy.2023.126956

15. Oh J, Jeong H, Kim J, Lee H. Numerical and experimental investigation on thermal-hydraulic characteristics of a scroll expander for organic Rankine cycle. Applied Energy. 2020;278. 10.1016/j.apenergy.2020.115672

16. Jalili B, Ghafoori H, Jalili P. Investigation of carbon nano-tube (CNT) particles effect on the performance of a refrigeration cycle. Int J Mater Sci Innov. 2014;2(1):8-17.

17. Vanaei P, Jalili B, Hosseinzadeh M, Jalili P. Efficiency Optimization Thermal Analysis and Power Output of a Modified Incinerator Plant Using Organic Rankine Cycle. International Journal of Engineering. 2023;36(7):1300-9.

18. Chang J-C, Chang C-W, Hung T-C, Lin J-R, Huang K-C. Experimental study and CFD approach for scroll type expander used in low-temperature organic Rankine cycle. Applied Thermal Engineering. 2014;73(2):1444-52. https://doi-org-s.lut.yitlink.com:443/10.1016/j.applthermaleng.2014.08.050 https://www-sciencedirect-com-s.lut.yitlink.com:443/science/article/pii/S1359431114007467

19. Feng Y-q, Xu J-w, He Z-x, Hung T-C, Shao M, Zhang F-y. Numerical simulation and optimal design of scroll expander applied in a small-scale organic rankine cycle. Energy. 2022;260:124981. https://doi-org-s.lut.yitlink.com:443/10.1016/j.energy.2022.124981 https://www-sciencedirect-com-s.lut.yitlink.com:443/science/article/pii/S0360544222018795

20. Feng Y-q, Liang H-j, Xu K, Wang Y, Lu Y, Lin C-H, et al. Experimental study on the performance of a great progress 10 kW organic Rankine cycle for low-grade heat source based on scroll-type expander. Energy. 2023;284:128627. https://doi-org-s.lut.yitlink.com:443/10.1016/j.energy.2023.128627 https://www-sciencedirect-com-s.lut.yitlink.com:443/science/article/pii/S0360544223020212

21. Narasimhan AK, Wickramaratne C, Kamal R, Goswami DY, Singh P. Mapping scroll expander performance for organic working fluids using dimensionless parameters in Ns-Ds diagram. Energy. 2019;182:739-52. https://doi.org/10.1016/j.energy.2019.06.054 https://www.sciencedirect.com/science/article/pii/S0360544219311831

22. Jalili B, Mousavi A, Jalili P, Shateri A, Domiri Ganji D. Thermal analysis of fluid flow with heat generation for different logarithmic surfaces. International Journal of Engineering. 2022;35(12):2291-6.

23. Shijing D, Hongru C, Xudong W, Deshi W, Yongyong Z. Modal Optimization Design of Supporting Structure Based on the Improved Particle Swarm Algorithm. International Journal of Engineering. 2022;35(4):740-9. 10.5829/ije.2022.35.04A.14 https://www.ije.ir/article_143223.html

Persian Abstract

چکیده

تنظیم پارامترهای عملیاتی برای بهینه‌سازی عملکرد گسترش‌دهنده اسکرول یک موضوع تحقیقاتی داغ در بین محققان بوده است. این مقاله به طور خلاقانه ای روش سطح پاسخ و الگوریتم NSGA2 را برای بهینه سازی پارامتر ترکیب می کند. این روش جدید می تواند پارامترهای عملیاتی بهینه گسترش دهنده اسکرول را با دقت پیش بینی کند و کارایی کلی گسترش دهنده اسکرول را بهبود بخشد. در ابتدا، یک مدل شبیه سازی گذرا سه بعدی از گسترش دهنده اسکرول ایجاد شد و اثرات سه پارامتر عملیاتی کلیدی (فشار مکش، فشار اگزوز و سرعت چرخش) بر توان خروجی و راندمان همسانتروپیک گسترش دهنده اسکرول از طریق عددی مورد تجزیه و تحلیل قرار گرفت. شبیه سازی. بر این اساس، مدل سطح پاسخ بین پارامترهای ورودی و تابع هدف با استفاده از روش سطح پاسخ ایجاد شد. در نتیجه، سه الگوریتم بهینه‌سازی مختلف با هم مقایسه شدند و مشخص شد که NSGA-II عملکرد بهتری هم از نظر هم‌گرایی و عملکرد حل دارد. بنابراین، الگوریتم NSGA-II برای بهینه‌سازی چند هدفه استفاده شد. با فرض در نظر گرفتن حداکثر توان خروجی و راندمان ایزنتروپیک، بر اساس مدل سطح پاسخ ایجاد شده، از راه حل بهینه پارتو برای تعیین ترکیب بهینه پارامترهای عملیاتی آن استفاده شد: فشار مکش 1.62 مگاپاسکال، فشار خروجی اگزوز 0.45 مگاپاسکال و سرعت چرخش 2,099.58 دور در دقیقه. در نهایت، مدل عددی توسط بستر آزمایشی ساخته‌شده در آزمایشگاه سیستم تولید برق بدون روغن حرارتی با دمای پایین چرخه ارگانیک رانکین تأیید می‌شود. نتایج تجربی به خوبی با نتایج شبیه‌سازی عددی مطابقت دارند و صحت مدل را تأیید می‌کنند. نتایج حاصل از این مطالعه پیشگامانه و کامل، یک معیار محکم برای توسعه و اصلاح ماشین‌های اسکرول آینده ارائه می‌کند.

IJE TRANSACTIONS A: Basics Vol. 37 No. 01, (January 2024) 151-166

International Journal of Engineering

Journal Homepage: www.ije.ir

Development of Temperature-strain Prediction Based on Deformation-induced Heating Mechanism in SCM440 Surface Cracked Shaft under Ultrasonic Excitation

P. Lap-Arparat, K. Tuchinda*

Material Manufacturing and Surface Engineering Research Center (MaSE), The Sirindhron International Thai-German Graduate School of Engineering (TGGS), King Mongkut's University of Technology North Bangkok (KMUTNB), Bangkok, Thailand

P A P E R I N F O

Paper history:
Received 13 August 2023
Received in revised form 07 September 2023
Accepted 09 September 2023

Keywords:
Cracked Shaft
Deformation-induced Heating
Elliptic Crack Parameter
SCM440
Temperature-Strain Analysis
Vibrothermography Inspection Method

A B S T R A C T

The mechanisms behind temperature and material deformation in vibrothermography remain questionable, presenting a gap in understanding. This study investigates the deformation-induced mechanism, focusing solely on the heat generation associated with strain development. Both experimental and simulation approaches are incorporated. The experimental segment explores the temperature-strain relationship of SCM440 material, commonly used for rotating shafts. This behavior is examined through the connection between temperature change and material deformation during a uniaxial tensile test. Results indicate that temperature change and distribution can be predicted based on plastic strain development. Finite Element Method (FEM) simulation is utilized to model the excitation of a shaft with and without an elliptic surface crack. Various cracked shaft configurations are investigated, revealing distinct strain generation and distribution patterns. High strain alteration is notably observed around the crack tips, enabling the detection of shaft discontinuity. Consequently, a temperature prediction technique is developed to estimate temperature based on strain alteration during deformation. Adequate excitation power and the use of a high-sensitivity IR camera are recommended for the effective application of the temperature prediction technique. Additionally, this study provides insights into understanding the utility and limitations of vibrothermography for inspecting engineering component damage based on experimental temperature-strain relationships and computational predictions of strain distribution in cracked shafts under excitation. These findings offer guidance for engineering applications and future research endeavors.

***doi**: 10.5829/ije.2024.37.01a.14*

Graphical Abstract

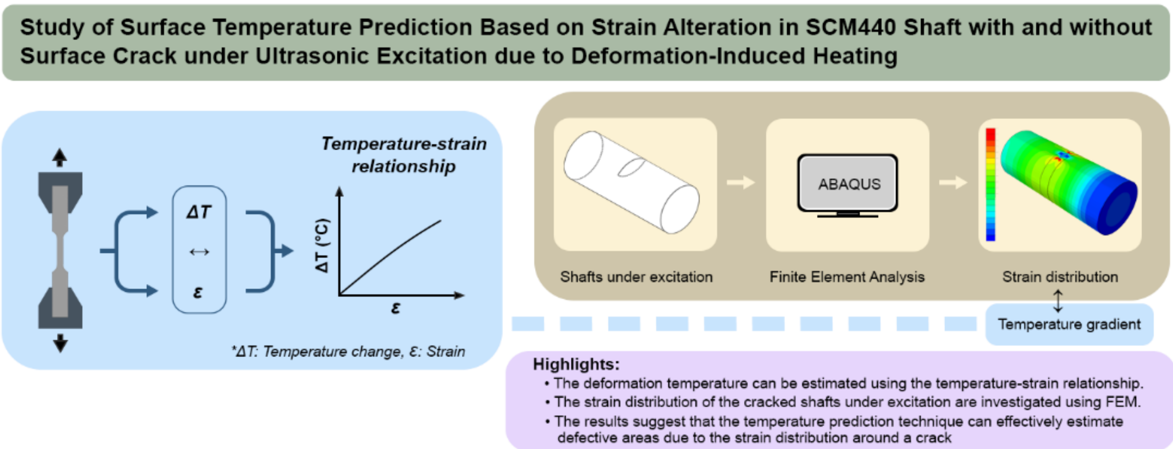

*Corresponding Author Email: karuna.t@tggs.kmutnb.ac.th (K. Tuchinda)

Please cite this article as: Fereshteh-Saniee N, Elmkhah H, Molaei M, Zolriasatein A. Development of Temperature-strain Prediction Based on Deformation-induced Heating Mechanism in SCM440 Surface Cracked Shaft under Ultrasonic Excitation. International Journal of Engineering, Transactions A: Basics, 2024;37(01):151-166.

1. INTRODUCTION

Vibrothermography (VT) is a technique to investigate the defect located on either the surface or near the surface via thermal energy release (1). This inspection technique requires an infrared (IR) camera to detect the diffused heat from vibrated defects. When the defects are vibrated, they rapidly generate heat that is diffused and radiated outward to the surface, which can be observed in a short time (2). Therefore, VT is less consumed in the inspection time compared with another nondestructive testing (NDT) technique, which is requisite for industrial interests. VT was first introduced in the late 80s by Reifsnider et al. (3). A series of experiments were conducted with noticeable heat generation in materials, and the thermographic pattern of heating depended on the material properties and structural geometry referred to by Reifsnider et al. (3) These indicated the unique characteristics of the thermal energy release on a specific material. Subsequently, VT became well-known after Favro et al. (4) placed an ultrasonic welder with a maximum power of 1 kW for the excitation source. Thereafter, an IR camera revealed the glow of a crack immediately after a sonic pulse was applied, which influenced more availability and reliability for industrial applications.

According to the industrial components, the metallic cylindrical-shaped component is a common part frequently involved in any system of the industry, i.e., axle, pin, shaft, etc. (5) Defects in these components are generally discovered as fatigue cracks, especially during the observation of shafts (6). In general, fatigue cracks are inevitable and normally appear in components that have operated repeatedly (7). A fatigue crack on a shaft can be initiated from a small discontinuity that occurs on the surface and transversely propagates to the center under cyclic loading conditions, which sequentially directs a large discontinuity and complete fracture (8-10). Recently, it has been observed that VT was applied for inspecting defects in industrial components, i.e. turbine disks, gas turbine blades, welded parts, etc. (11-14). The results revealed the good detectability of this inspection; VT could detect a known fatigue crack of 0.015 mm in length with a better possibility of detection (POD) than the traditional method (15). In addition, VT was capably performed on various materials such as concrete (16, 17), ceramics (18), polymers (19, 20), and metals (21-23). The aforementioned studies confirmed the usability, rapidity, and variety of this inspection method.

Vibroacoustic thermography (VT), also known as sonic IR and thermosonics, currently relies mainly on IR cameras and ultrasonic excitation. Ultrasonic excitation is typically selected at a predetermined frequency of 20, 40, or 60 kHz (24). However, the heating mechanism of VT remains questionable as it is not fully understood (14). It has been found that researchers attempted to investigate the source of heat generation. There are 2 major sources that have been discussed: (1) Frictional rubbing and (2) Deformation-induced heating (25). For instance, the severity of the closure crack rubbing during vibration can cause heat generation due to friction between the contracting faces of the crack. The evidence of frictional heating is shown in the following literature (26-28). Besides the closure crack, the asperity might be included, meaning no rubbing between crack faces. The heat can be induced beyond the crack tip due to the structural deformation under the vibration causing the stress concentration in the plastic zone, which is also known as plasticity-induced heating (29, 30). Nonetheless, deformation-induced heating in metal is rarely divulged due to the absence of demonstration. Therefore, the study of deformation-induced heating in metallic material is necessary for a better understanding of these heating mechanisms.

The understanding of material characteristics expedites the ability to estimate limitations or potential damage to engineering components within the system. In several instances, material characteristics have been employed to simulate their behavior under real working conditions or relevant scenarios in analytical models. The behavior of structures exhibits responses under assigned loading conditions, which aids in investigating structural deformations such as damage, elasticity, plasticity, and vibration (31-33). Analyzing these responses indicates the structural component usage experienced during operational conditions, allowing for the prediction of fatigue and service life (34-37). A similar approach is adopted to investigate temperature changes resulting from deformation-induced heating in this study. The developed temperature prediction technique demonstrates the object’s temperature based on the corresponding strain alteration during deformation. This study aims to establish a fundamental understanding of the deformation-induced heating mechanism and to enhance the comprehension of the VT inspection technique used in engineering components excluding the frictional heating from closure cracks, serving as a foundation for future developments in industrial applications.

In this study, the temperature prediction technique was examined based on deformation-induced heating from the perspective of the vibrothermography inspection method. The study focused on the inspection of engineering parts that are widely used in industrial systems. The circular SCM440 shaft was selected for the study as it is commonly used for shafts in many applications (38). The study included both experimental and computational research. The experimental-based research was performed on the investigation of the temperature-strain relationship of the selected material for developing the prediction technique. Meanwhile, the computational research observed the response of the shaft under virtual ultrasonic excitation to investigate the influence of the controlling parameters including crack shape, crack size, and excitation conditions. This study attempted to determine the strain characteristics of the shafts, either with a crack or without a crack. The developed temperature prediction technique was applied afterward to estimate the temperature of the shaft based on the computed strain under ultrasonic excitation. The research methodology flowchart is illustrated in Figure 1.

2. EXPERIMENTAL INVESTIGATION OF THE TEMPERATURE-STRAIN RELATIONSHIP ON SCM440 MATERIAL

As reported by Reifsnider et al. (3), thermal characteristics are individually dependent on the material. To understand the behavior of temperature induced during structural deformation based on deformation-induced heating, the thermal characteristics of SCM440 (AISI 4140) due to structural deformation were investigated. From observation of previous experimental work conducted by Kapoor and Nemat-Nasser (39), the temperature (T) of an object during deformation can be described as Equation 1:

$$T = T_0 + \Delta T \tag{1}$$

where T_0 is an initial temperature and ΔT is the temperature change due to the deformation. In this work, the temperature change (ΔT) was investigated via the experiment with the following details.

2. 1. Material Properties and Experimental Preparation SCM440 steel was machined into flat tensile specimens according to ASTM E8 standard for uniaxial tensile testing and chemical composition, as shown in Table 1. The inspection points on the specimen were selected to be in the gauge length and were marked as P1, P2, and P3. The P2 was in the middle of the specimen, while P1 and P3 were marked away from P2 with an equal spacing of 6 mm (see Figure 2). The influence of the surface preparation on the temperature-strain relationship was included in this investigation. During the surface preparation process, the specimens were ground in different directions, denoted as the axial direction (Y-axis) and transverse direction (X-axis), as illustrated in Figure 2. Furthermore, the Pulstec µ-X360s was applied for X-Ray Diffraction (XRD) analysis. The cosine technique was performed with an incident angle of 35° to investigate the residual stress at marked locations. Lastly, the specimens were sprayed in a sparkle pattern to be ready for strain analysis using the GOM Digital Image Correlation (DIC) system.

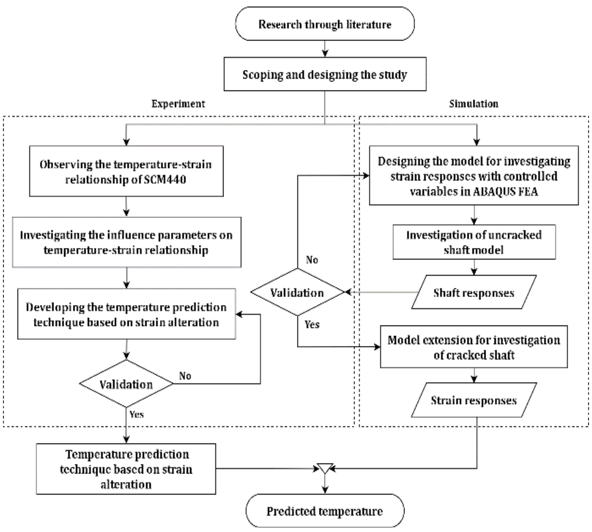

Figure 1. Research methodology flowchart

2. 2. Procedure A prepared specimen was attached with K-type thermocouples to the marked location and mounted on the universal testing machine. The thermocouples were connected to the NI-9213 temperature module for data logging. The sensitivity of the temperature-measuring module with K-type thermocouples was 0.02°C in resolution mode. An

TABLE 1. Chemical composition of SCM440 material

Element	C	Si	Mn	P	S	Cr	Cu	Ni	Mo
%Weight	0.41	0.23	0.78	0.16	0.13	1.06	0.02	0.01	0.17

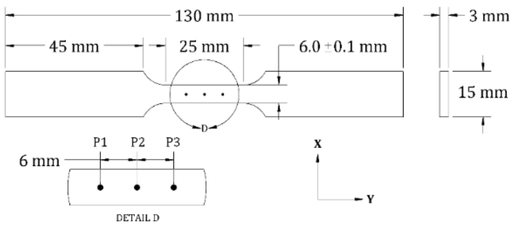

Figure 2. Dimensions of ASTM E8 specimen with marked point

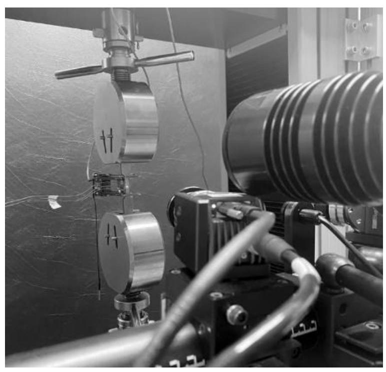

Figure 3. Experimental setup

extensometer and GOM ARAMIS adjustable camera were used for strain measurement where an extensometer griped across the specimen gauge and a GOM camera captured a deformation on the surface of the specimen, as shown in Figure 3. The tests were conducted at room temperature with 0.5 mm/min testing speed. A sampling rate was set at 1 Hz for all data logging. In the post-process step, GOM Correlate software was applied to analyze the local strain at the location of the thermocouple attachment that constructed the temperature-strain relationship.

This temperature-strain relationship exposed the temperature of the SCM440 object via strain alteration. Comprehension of the temperature-strain relationship was utilized to explain the behavior of the cracked shaft on the strain response under excitation, which was investigated in the computational study.

3. COMPUTATIONAL STUDY OF SURFACE CRACKED AND UNCRACKED SHAFT ON STRAIN RESPONSE UNDER EXCITATION

In this session, VT was applied to a shaft, which is a common part of the rotating machinery in industry. Surface cracked and uncracked shafts were subjected to excitation using a low-power ultrasonic cleaning transducer. The application of a low-power ultrasonic cleaning transducer as an excitation source for VT has been previously published (40-42). Cracks can propagate when applied force exceeds the resistance of the material, resulting in the release of stored energy (43). Before crack propagation, the quasistatic energy was stored in a small region beyond the crack tip, known as the plastic zone. Considering the early stage of loading, the fracture-characterizing parameter, i.e., the stress intensity factor (K), was used to define the stress fields. An example of the stress fields for the opening mode (Mode I) can be determined by Equation 2 (44):

$$\sigma^{(I)} = \frac{K_I}{\sqrt{2\pi r}} f^{(I)}(\theta) \tag{2}$$

where r denotes the distance from the tip and $f(\theta)$ is the angular function that depends on the crack geometry and fracture mode; the mode of fracture was also based on the loading condition (43). From Equation 2, crack geometry and the condition of load governed the behavior of the stress fields near the tip.

The stress and strain relationship could be described by the material model. For metal and alloy, the strain (ε) is usually directly proportional to stress (σ) under elastic deformation, which obeys Hooke's law and could be expressed as Equation 3:

$$\varepsilon = \frac{\sigma}{E} \tag{3}$$

where E was the elastic modulus of the material.

The elastic strain around the crack tip is related to the loading condition and crack geometry. The effect of loading conditions and crack geometry were considered and investigated in this study. The finite element method (FEM) is a preferred method used for such analysis in the field of fracture mechanics. Several studies have utilized FEM to analyze the elastic-plastic response in various ways (45-50). In this study, ABAQUS FEA software was employed for the investigation of influences of crack geometry and loading conditions on the strain responses of both surface cracked and uncracked shafts.

3. 1. Computational Model This study aimed to investigate the strain response of a shaft under excitation using a low-power ultrasonic cleaning transducer. The initial step involved experimental calibration of the 40 kHz ultrasonic cleaning transducer in the laboratory. A 100 W signal generator was used to determine the force exerted during the transducer's operation, resulting in a force of 0.35 N. This force was applied as the excitation load (P) in the subsequent computational model. The computational model was created in ABAQUS FEA and represented a 3D cylindrical shape resembling both cracked and uncracked shafts. The dimensions of the shaft were derived from a drive shaft in a water pump system with measurements of 24 mm in diameter and 60 mm in length. The material chosen for the shaft was SCM440, a commonly used material for shaft applications. The stress-strain behavior of SCM440 was obtained through uniaxial tensile testing in the laboratory. The computational model employed implicit-dynamic analysis to study the transient strain alteration under excitation. Note that, this study illustrated the methodology particularly on the adopted shaft geometry. The purposed methodology could later be extended without major difficulty to investigate other components with different geometry.

A simple cylindrical model was used to represent the uncracked shaft. For the cracked shaft, the contour integral technique, which is favored for studying the effect around the crack tip, was applied to create the crack. The elastic-plastic, power-law hardening material was adopted to control the strain singularity at the crack tips, which is commonly used for a stress-strain field analysis near the tips of elastoplastic materials (51-54). The cracks contained a crack front and crack faces, as illustrated in Figure 4. The crack tip that was located close to the angular displacement (θ) of 0 was denoted as CT1 and the far side was denoted as CT2. Interaction between crack faces was assigned as "Hard" in Abaqus nomenclature for normal behavior to prevent interferences. For tangential behavior, the coefficient of friction (COF) was selected arbitrarily at 0.8 according to the friction coefficient of steel on steel for dry contact conditions (COF = 0.5-0.8). However, the heat generated due to frictional rubbing and self-weight were not considered in this work. The shaft model was small and subjected to vibrate at high frequency thereby the self-weight was considered negligible as the previous research (55). The uncracked shaft model was globally meshed with the C3D8R elements of 0.5 mm of mesh seed for the entire model. The curvature control factor of the mesh seed was set at 0.005 to increase the mesh density of the model which directly affected the accuracy of the finite element analysis result (56). The cracked shaft was modeled with the spider-web technique being applied to the area surrounding the crack with C3D20R and C3D15, which were quadratic elements to provide a precise result. The size of the element around the crack tip was nearly 0.005 mm to acquire a converged result. However, the rest of the models were applied with C3D8R to optimize the computational time. Furthermore, both areas had a different type of element and were tied with surface-to-surface constraints. An example of model meshing on shafts is shown in Figure 5.

3. 2. Crack Characteristics and Loading Conditions

The transverse crack was one of the common cracks on a shaft that occurred frequently in a rotating shaft (57). In this study, the transverse crack was artificially created at the middle of the shaft length. The crack geometry was modeled based on a semi-elliptical crack shape with the crack length and shape factor serving as the controlled parameters. These parameters are illustrated in Figure 6.

Characteristic length of crack (α) ;

α = a/R = 0.05, 0.1, 0.25, 0.5, 0.75, 1

Shape factor of crack (β);

β = a/C = 0 (Straight crack front), 0.25, 0.5, 0.75, 1 (Circular crack front)

For the current study, the excitation directions and support conditions were varied to provide the different modes for the excited shaft. The modes of vibration depended on the direction of loading (58). The computational models consisted of two support conditions: cantilever support and fixed-end support. In the cantilever support configuration, the excitation load was applied on the free end of the shaft, referred to as axial excitation. In the fixed-end support configuration, the excitation load was applied transversely to the shaft at the middle, called transverse excitation, as shown in Figure 7. Furthermore, the diameter of the contact face for the ultrasonic transducer was measured at 45 mm.

4. TEMPERATURE-STRAIN RELATIONSHIP OF SCM440 AND TEMPERATURE PREDICTION

4. 1. Experimental Results of the Temperature-Strain Relationship

The residual stress of the

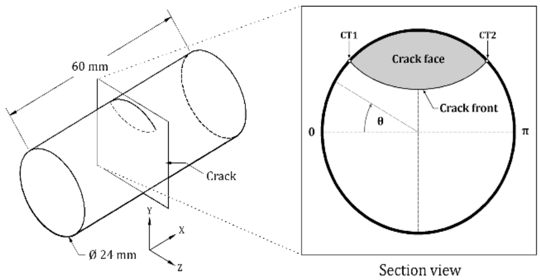

Figure 4. Isometric view of cracked shaft and cracked components

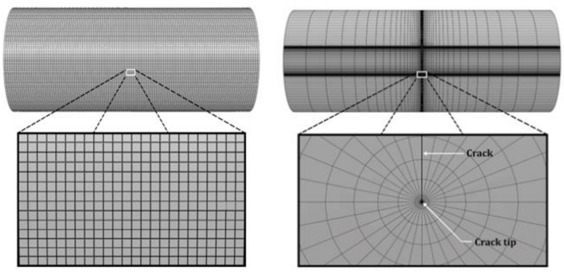

(a) Uncracked shaft (b) Cracked shaft

Figure 5. Model meshing

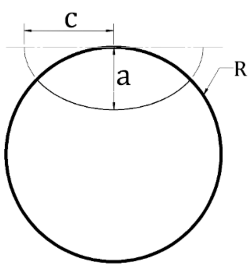

Figure 6. Controlled parameters of the semi-elliptical crack

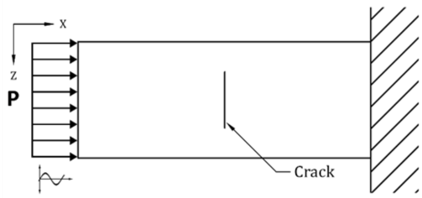

(a)

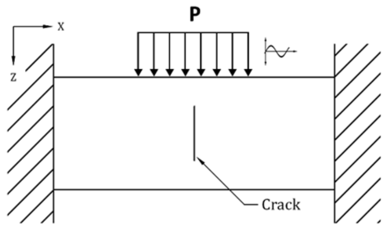

(b)

Figure 7. Excitation direction and boundary conditions on the cracked shaft; (a) Axial excitation with cantilever support, (b) Transverse excitation with fixed ends support

specimens is obtained as detailed in Table 2. The residual stress data provide a noticeable difference in the residual stress due to the different grinding directions under the surface preparation process. The larger compressive residual stress has been observed on the axis that is parallel to the direction of the grinding path. Under uniaxial tensile testing, the specimens that were ground similar to the loading direction are denoted as parallel ground and vice versa, denoted as perpendicular ground. The parallel ground specimens have slightly higher tensile stress than the perpendicular ground. The maximum difference of the ultimate tensile strength (UTS) between parallel ground and perpendicular ground specimens is approximately 40 MPa, which is less than 5%, indicating the negligible influence of the residual stress on the stress-strain curve. The average elastic modulus (E) and UTS of SCM440 steel are 201.4 GPa and 1080 MPa, respectively, as illustrated in Figure 8.

Temperatures have been observed under tensile testing, conveying the temperature increase during deformation. The temperatures increased corresponding to the strain of the tensile specimen. Considering the temperature before the necking, the temperature changes (ΔT) of the parallel ground and perpendicular ground specimens have been plotted against the true equivalent strains ($true\,\varepsilon_{eq}$) to investigate the influence of residual stress, as depicted in Figure 9. The average temperature changes were calculated individually for each case. The uncertainty of the temperature measurements on the parallel ground and perpendicular ground specimens was approximately ±0.2 °C, as shown in Figure 9a. The average temperature changes for both grinding specimens were compared to investigate the influence of residual stress, as shown in Figure 9b; the maximum difference of the temperature change between the parallel ground and perpendicular ground specimens was less than 0.07 °C. These results suggest that the residual stress had no significant influence on the temperature induced during deformation. Furthermore, the mean temperature change was calculated from the average temperature changes of both grinding conditions to describe the behavior of temperature during deformation.

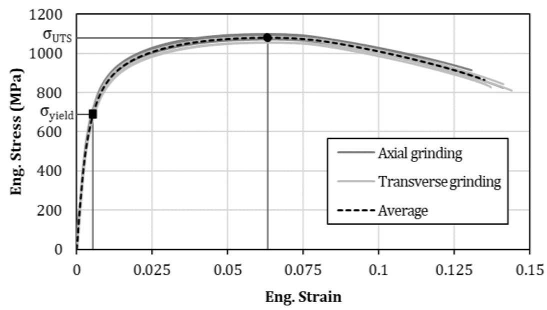

Figure 8. Engineering stress-strain curve of SCM440 specimens

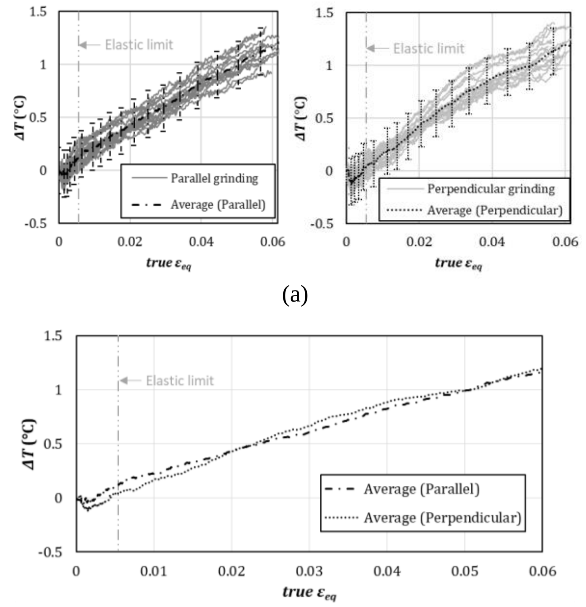

(a)

(b)

Figure 9. Temperature during deformation prior to necking, (a) Uncertainty of the temperature measurement, (b) Temperature variations under different grinding directions

TABLE 2. Residual stress at P1, P2, and P3

Grinding direction	No.	Y-axis P1	Y-axis P2	Y-axis P3	X-axis P1	X-axis P2	X-axis P3
Y-axis (Parallel)	1	-366.5	-364.5	-371	-134.5	-137.5	-132.5
	2	-362	-358	-364	-79	-88.5	-102.5
	3	-365	-356.5	-379.5	-134	-103.5	-116.5
	4	-384	-373.5	-357.5	-102.5	-103.5	-91
	5	-376	-370	-356.5	-126.5	-139.5	-139
X-axis (Perpendicular)	6	-58.5	-60	-44.5	-361	-372	-364
	7	-122	-112	-124.5	-352	-338	-347
	8	-56	-55	-44	-348	-383	-375
	9	-133	-106	-102	-349.5	-351	-351.5
	10	-49.5	-42.5	-59	-372.5	-365	-359

From the observation, the behavior of the mean temperature change exhibits a relatively low-temperature change with a fluctuation in the beginning of elastic region and the temperature increases noticeably along the strain-hardening region, indicating the temperature changes substantially during plastic deformation.

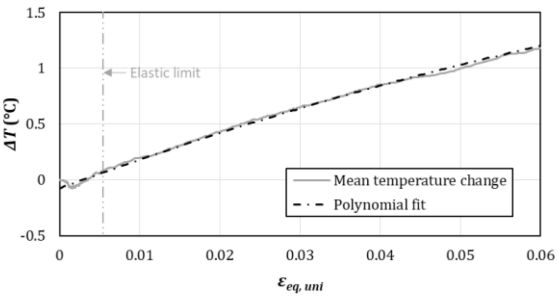

Figure 10. Temperature-strain relationship

Furthermore, the mean temperature change is plotted against true equivalent strain prior to the necking, denoted as uniform equivalent strain ($\varepsilon_{eq,uni}$), to construct the temperature-strain relationship, as demonstrated in Figure 10. The second degree of the polynomial curve fitting has good fit with the relationship curve, which has a confidence of R^2 = 0.9985. From curve fitting, the polynomial regression can be expressed as Equation 4:

$$\Delta T = -86.515\varepsilon_{eq,uni}^2 + 26.437\varepsilon_{eq,uni} - 0.0758 \quad (4)$$

4. 2. Prediction of Temperature Based on the Temperature-Strain Relationship The developed relationship was applied for the temperature prediction of the specimen under tensile testing. Similar material was machined into a standard tensile specimen with a circular cross-section of gauge diameter 6 mm and 25 mm long of gauge length, as shown in Figure 11a. These dog-bone specimens were painted in black to prevent reflection from ambient light. Moreover, an extensometer and FLIR A655sc infrared (IR) camera were also equipped in the test, as shown in Figure 11b. Non-Uniformity Correction (NUC) was set for the IR camera to automatically improve the temperature reading, which provided more accuracy during the record. The cross-head of the testing machine was set to 0.5 mm/min. The records were stopped after the specimen reached the necking stage to prevent accidental damage to the IR camera lens. Meanwhile, the computational model was additionally created to investigate the strain behavior during the test. The configurations were set accordingly to the constraints and boundary conditions of the experiment. As a result, the strain alteration of the tensile specimens obtained from the experiment and simulation are plotted to unveil the strain behavior during deformation, as observed in Figure 12. Under fixed-speed controlled deformation, the true strains of the tensile specimens have corresponding behavior, which barely changed under the elastic deformation and increased exponentially in the plastic deformation.

Regarding the temperature, the initial temperatures were measured prior to the test using an IR camera. The temperature behavior from the IR camera was investigated using ResearchIR software. The side-by-side view between the temperature gradient and the computational strain distribution is displayed simultaneously in Figure 13a, which reveals a comparable color contour. Hence, the strains were sequentially substituted into Equation 4 and Equation 1 for determining the predicted temperatures. The predicted temperatures were plotted to compare with Figure 13b demonstrates a significant correlation between the temperature predictions and the actual temperature during deformation. The accuracy of these predictions is detailed in Table 3. The maximum absolute error observed among the multiple tests was approximately 0.4 °C, which suggests a close agreement. These findings suggest the potential usability of the developed temperature-strain relationship for temperature prediction based on strain alteration with a disagreement of less than 1.5%. The results provide compelling evidence that the deformation temperature can be estimated effectively when the corresponding strain alteration is known. It is important to note that the developed relationship is specifically applicable to SCM440 material with a constant deformation speed of 0.5 mm/min.

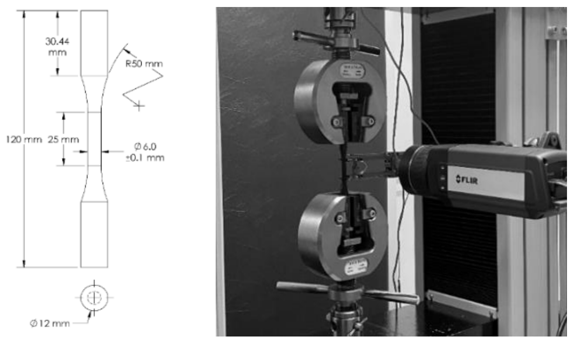

(a) (b)

Figure 11. Experimental temperature prediction setup

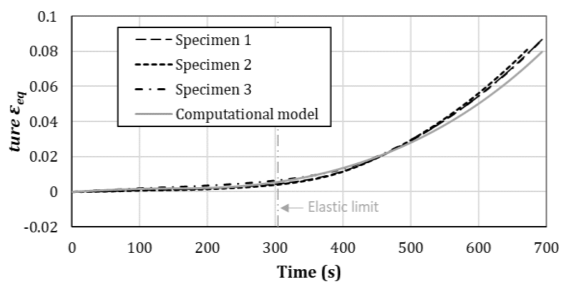

Figure 12. Strain alteration prior to necking the actual temperature within the gauge section, as presented in Figure 13b

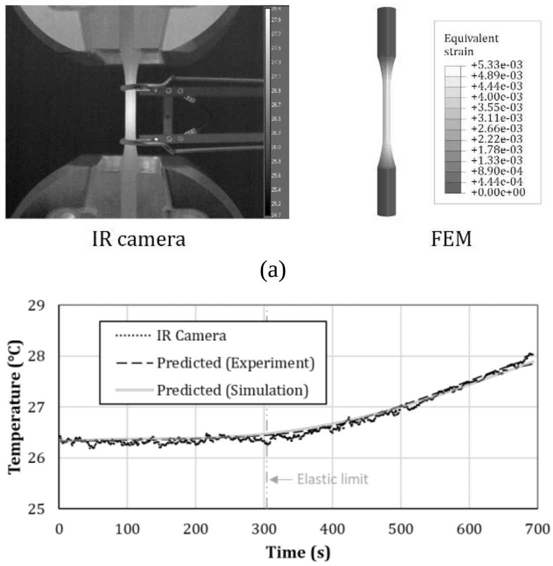

Figure 13. Temperature prediction, (a) Temperature and strain distribution at t= 630 s, (b) Comparison of temperature predictions

TABLE 3. Accuracy of temperature prediction under uniaxial tensile testing

No.	Initial temperature (°C)	Maximum error			
		Absolute (°C)		Percentage (%)	
		EXP.	FEM.	EXP.	FEM.
1	26.405	0.220	0.218	0.785	0.829
2	26.533	0.409	0.384	1.489	1.436
3	26.442	0.311	0.370	1.132	1.382

5. STRAIN RESPONSE OF THE CRACKED AND UNCRACKED SHAFT UNDER EXCITATION

5. 1. Computational Investigation of Uncracked Shaft

The computational results show the response of the stress field generated under excitation. Stress is generated following the deformation of the vibrated shaft. The shafts vibrate back and forth in different directions depending on the excitation direction. For example, axial vibration occurs under the axial excitation condition and transverse vibration occurs under the transverse excitation condition. Under the investigations, stresses were found within the yield limit, which could be directly converted into the corresponding strains using Hook's law (Equation 3). The behavior of stress distributions varies between the two excitation conditions due to the dissimilarity of the stress propagation. Under axial excitation, stress propagates along the length of the shaft, creating a longitudinal stress distribution. In contrast, stress is distributed from the top to the bottom of the shaft under transverse excitation, resulting in lateral stress distribution. These observations are displayed in Figure 14, which shows the distinct patterns of strain contour under each excitation condition. At the middle of the shaft where the stress is fluently distributed under both excitations, strain responses are observed, as shown in Figure 15a, which reveals the dynamic behavior of strain. The response between both excitations shows slight phase shifting and varying amplitudes. Examining the first peak of the responses that display close characteristics, the circumferential surface strains under both excitations are plotted to display the strain distribution, as depicted in Figure 15b. Under axial excitation, the strain distribution is uniform along the shaft circumference. On the contrary, the strain under transverse excitation exhibits a distinct pattern.

It is the highest at an angular displacement (θ) of 0, where excitation takes place and reaches its lowest at $\theta = \pi/2$. Then, the strain increases gradually as the angular displacement progresses towards $\theta = \pi$. This finding highlights the significant influence of the excitation source on strain generation in the excited shaft under transverse excitation, particularly in the vicinity of the excitation location. The excitation source plays a notable role in elevating strain levels, and it is crucial to recognize the influence of the excitation source on strain generation during analytic consideration. In this study, the strains at the opposite side of the excitation ($\theta = \pi$) for transverse excitation are considered to minimize the direct influence of the excitation source on the strain measurement. From the observation, the maximum strain generations due to the deformation under the excitations of uncracked shafts were found to be 3.89×10^{-9} and 4.72×10^{-9} for the axial and transverse excitation, respectively.

5. 2. Experimental Investigation of Uncracked Shaft

This section explains the experiments conducted to observe the deformation of the uncracked shaft under

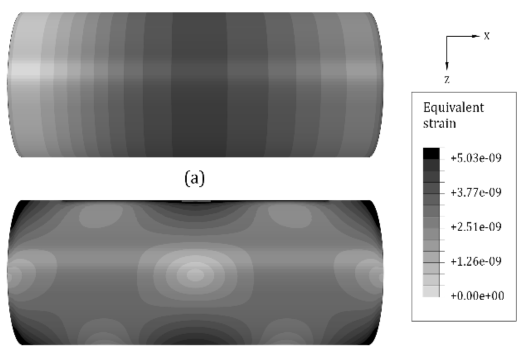

Figure 14. Top view of the strain distribution on the uncracked shaft under excitation, (a) Axial excitation, (b) Transverse excitation

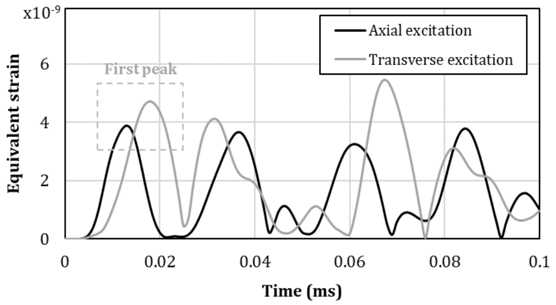

(a)

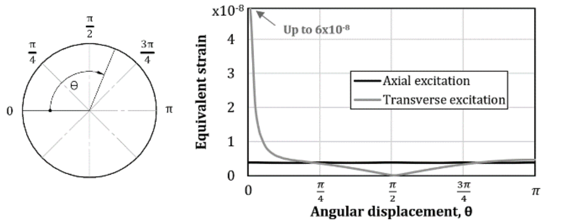

(b)

Figure 15. Strain responses of the uncracked shaft at the middle, (a) Example of the strain response at θ = π (b) Circumferential strain under excitations

excitation. For instance, in the case of the transverse excitation, the jig and fixture were designed to securely hold the uncracked shaft in fixed-ends support condition, as shown in Figure 16. An ultrasonic transducer was positioned on the slider body of the linear guide rail, which was utilized to minimize the influence of gravitational force and apply excitation to the side of the shaft. The slider body was connected to an adjustable pin, and a helical spring was incorporated to allow for the adjustment of contact pressure between the transducer and the shaft. The contact pressure can be calculated based on the compressive length and stiffness of the spring, which was determined to be 2.8 N/mm under the compression test. The designed jig and fixture were clamped securely onto a rigid table, with a rubber plate placed in between to isolate the system from the surrounding environment. To measure the deformation on the surface of the shaft during excitation, a 3D digital image correlation (DIC) system was utilized. The system was set to record real-time data at a maximum resolution of 40 frames per second. Before conducting the test, an SCM440 shaft with a diameter similar to the one used in the computational study was prepared by spraying a pattern for surface mapping and marking a reference point for precise analysis. Meanwhile, the computational model used in this section was modified to match the experimental setup. An initial load was applied to simulate the preloading caused by the contact pressure of the ultrasonic transducer. The load was offset by 19.7 N, corresponding to a 7 mm compression of the spring in the experimental setup. However, the other configurations remained the same as in the previous setups.

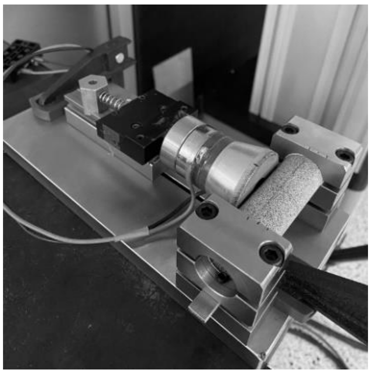

Figure 16. Experimental setup for validation of the computational results

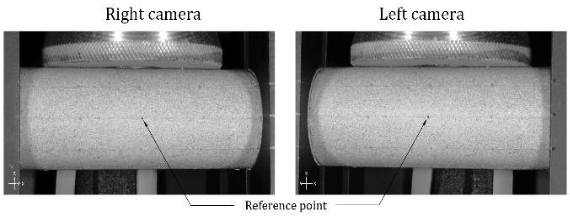

(a)

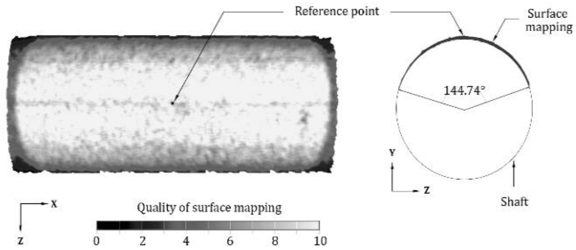

(b)

Figure 17. Digital image-processing using GOM correlation software, (a) Images captured by the GOM DIC system (b) Quality and angular displacement of the surface mapping

Under the investigation, the magnitudes of deformation on the shaft surface were observed in the response during excitation. For the experimental data, the different angles of the excited shaft were captured using the dual camera setup on the DIC system, as displayed in Figure 17a. Both images were used to construct a 3D surface model based on the prepared surface pattern, thus facilitating the measurement of surface changes. The shaft surface pattern was mapped using the GOM correction software for digital image processing. The surface mapping captured approximately 144° of angular displacement. The quality of the mapping was examined and rated on a scale from 0 to 10, with 10 indicating high quality and 0 indicating poor quality. The results indicated that the mapping exhibited high quality around the front part of the shaft, as illustrated in Figure 17(b). Furthermore, the magnitude of deformation was normalized with respect to the reference point located in the middle of the shaft.

When comparing the results, the steady state was considered where the response exhibited a consistent behavior. Figure 18 displays the contour of the magnitude of deformation from both experimental and computational investigations, revealing the similar behavior of the shaft. A significant deformation was observed in the middle region, which gradually decreased toward the fixed ends. The experimental investigation showed slightly higher deformation around the fixed-end supports compared to the computation, indicating a small translation motion of the designed fixture during excitation. Additionally, the magnitude of deformation along the circumference at the middle of the shaft was also investigated, as depicted in Figure 19. The experimental results showed a slight difference compared to the computational results, particularly in the vicinity of the excitation source. The magnitude of deformation observed in the experiment was higher than what was predicted by computation. The difference could be attributed to several factors, including potential issues with surface mapping quality at the edge of the shaft or the presence of a non-rigid fixture at the fixed ends. The percentage error prior to the angular displacement of π/4 was up to 10%. Nevertheless, the percentage error beyond the angular displacement of π/4 was less than 5%, indicating good agreement with the computational results beyond the angular displacement of π/4. Besides, both responses demonstrated similar behavior, exhibiting consistent patterns of deformation with high magnitudes of deformation near the excitation source and lower magnitudes on the opposite side. Based on the comparison of the shaft response in both investigations, the behaviors exhibited by the shaft under excitations are well-correlated, particularly in the middle region and the farther region of excitation. These findings strongly support the effectiveness of the current configurations of

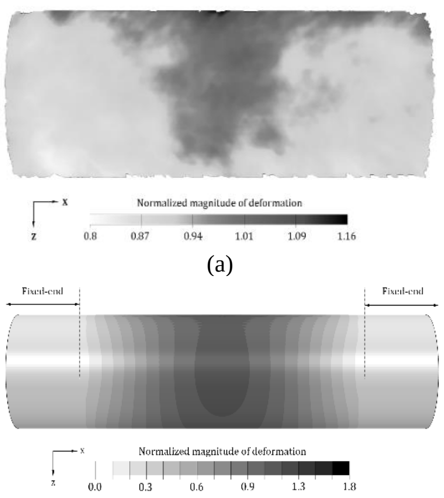

Figure 18. Deformation magnitude of the uncracked shaft under transverse excitation, (a) Experiment, (b) FEM

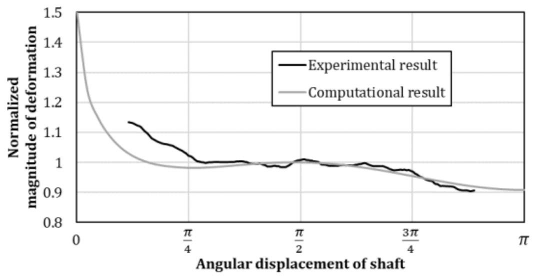

Figure 19. Comparison of deformation magnitude along the shaft circumference

the computational model for studying the shaft response under excitation.

Working under low-power excitation, especially for ultrasonic applications, is challenging because of the sensitivity and rapidity. Accurate measurement of alterations requires the use of highly responsive equipment with high sensitivity. In this experiment, the intention was to employ an infrared (IR) camera with a developed temperature prediction technique for temperature measurement.

However, the strain responses of the uncracked shaft under the excitations studied indicated that the technique was not yet fully applicable. The computational investigation revealed extremely low strain responses under excitations significantly below the yield point. Additionally, the DIC system could not accurately capture these low-strain alterations due to its limitations. The strain contour of the excited shaft under the computational investigation is displayed in Figure 20, including temperature prediction using the temperature-strain relationship, assuming a constant initial temperature of 25 °C. The predicted temperature was observed to be approximately 24.92°C ± 0.0001%. The maximum temperature difference was much less than the thermal sensitivity of the currently used IR camera (0.03 °C). Temperature changes were unnoticeable on the IR camera, as expected. The results indicated that the excitation power applied by the low-power ultrasonic cleaning transducer was insufficient, implying the need for the enhancement of excitation power to summarize the changes in practical measurement.

The temperature prediction technique based on strain alteration is likely to be applicable for deformation detection. However, the temperature of the uncracked shaft under excitation was well below the sensitivity threshold of the IR camera, resulting in undetectable changes. Nevertheless, the developed temperature prediction technique has the potential to be effective in estimating the temperature changes when utilized with a high-sensitivity IR camera and accurate predictions of the deformation are available. Hence, the study aims to investigate the strain response on the cracked shaft. The computational model of the uncracked shaft is extended, including a surface crack at the middle of the shaft.

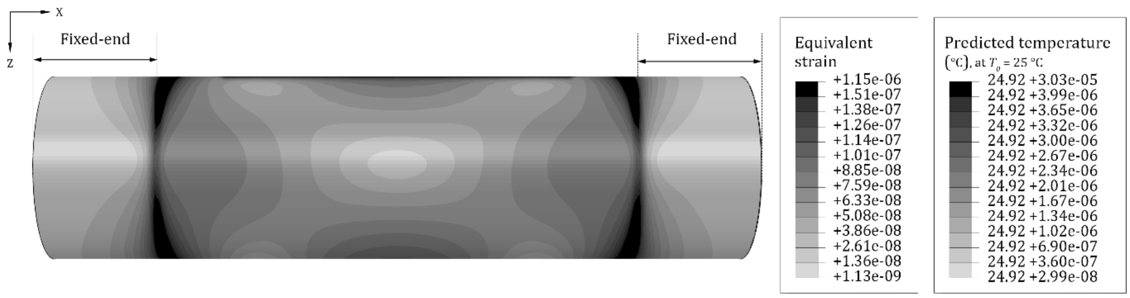

Figure 20. Temperature prediction of the uncracked shaft under the transverse excitation

5. 3. Extended Model for Investigation of Cracked Shaft During the investigation of the extended model for the cracked shaft, plasticity was not observed. The stresses under excitation remain within the yield limit of the material. Figure 21 displays the strain distribution under axial and transverse excitations, revealing a slightly different contour from the previous investigation of the uncracked shaft due to the meshing adjustment in the outside crack area to optimize computational time. For the vicinity of the middle region where the crack is located, the strain is mainly concentrated around the crack tips, where it is noticeably higher compared to the uncracked shaft. However, no crack propagation was observed. Considering the behavior of the strain around the crack tips under the stress flow due to excitation, the localized strains at both tips of the crack are simultaneously equivalent under the axial excitation. In contrast, strains under the transverse excitation exhibit time-dependent variations in strain generation at the crack tips. The strain generation at the crack tip oscillates over time showing periodic pattern, with higher strain observed initially at the tip closer to the excitation and then gradually reduced with higher strain being observed at the tip located farther away from the excitation. The crack tip at the far side of the excitation (CT2) is selected for the investigation of strain generation to minimize the influence of the excitation source, which was previously found in the investigation of the uncracked shaft under the excitation. The strain generation at the tip of the cracked shaft is significantly higher than the maximum strain generation of the uncracked shaft. The strains are normalized with the maximum strain observed in the uncracked shaft. Sequentially, the normalized strains are plotted against the characteristic parameters of the crack under various excitation conditions aiming to investigate the influence of the crack geometry on strain alteration at the crack tips. The results of the analysis are presented in Figure 22.

Figure 22 illustrates the influence of crack geometry on the strain alteration surrounding the crack tip. Larger cracks result in a higher strain, as demonstrated by a circular crack with a characteristic length of 0.75 ($\beta = 1$,

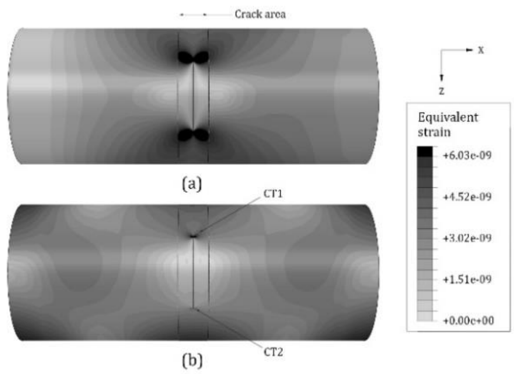

Figure 21. Example of the strain distribution on the cracked shaft under excitation, (a) Axial excitation on the circular cracked shaft ($\beta = 1$) with $\alpha = 0.5$ (b) Transverse excitation on the circular cracked shaft ($\beta = 1$) with $\alpha = 0.5$

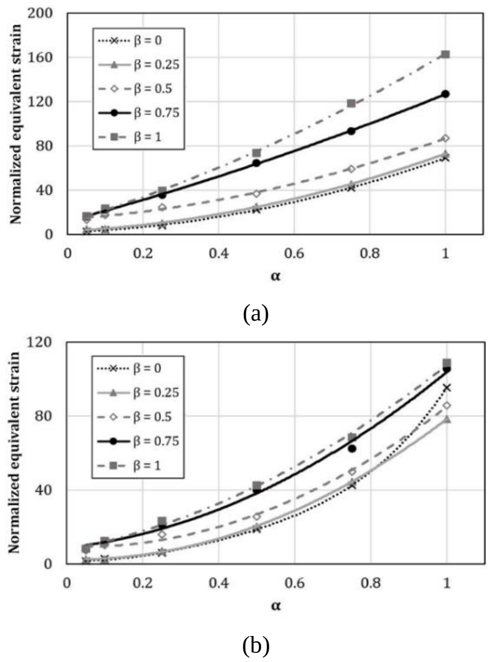

Figure 22. Influence of the crack geometry on strain alteration beyond the crack tip, (a) Axial excitation, (b) Transverse excitation

α = 0.75) exhibiting greater strain alteration compared to a circular crack with a characteristic length of 0.5 (β = 1, α = 0.5) under excitation. Besides, the circular crack front (β = 1) demonstrates the highest strain during excitation, while the straight front (β = 0) exhibits the lowest strain under observation. This behavior consistently shows a similar pattern, except for the straight front crack with α = 1 under transverse excitation. The strain of the straight front crack is noticeably higher than the crack with β = 0.5 at a similar characteristic length of α = 1. To understand the disparity, a comprehensive analysis was carried out by plotting the strain alteration over time for all examined crack geometries with α = 1 under the transverse excitation. Figure 23a reveals the extreme shift of phases on the straight front crack (β = 0), while the other crack fronts (β = 0.25 to 1) exhibit a slight shift of phases in the response. The reason for the massive phase shifting of the straight front crack (β = 0) shaft under the transverse excitation may arise from the alignment of the crack with the excitation direction. One of the tips of this crack configuration (β = 0, α = 1) locates directly under the excitation source, causing the load to transfer through the crack front to the other tip where the measurements are taken. Figure 23b illustrates the layout of the crack shaft, which contains a straight front with α = 1 under transverse excitation. The crack is aligned in line with the excitation direction, which could be the major cause of the phase shifting that leads to the difference in the strain behavior of the straight front crack (β = 0) with α = 1 under transverse excitation, highlighting the alignment of the excitation source must be considered in the analysis for estimation purpose. Overall, the crack geometry of the circular cracked shaft influenced the alteration in strain surrounding the crack tip, which increased with the shape factor (β) and the characteristic length (α). These findings align with prior research involving surface semi-elliptical cracked shafts. For instance, Carpinteri, A. unveiled the relationship between the geometry correction factor (FI) and the characteristic length of the stress intensity factor in the circular cracked shaft under cyclic axial loading (59). The geometry factor of the opening mode stress intensity factor for a surface crack in the solid cylinder can be expressed as Equation 5 (60):

$$F_I = \frac{K_I}{\sigma\sqrt{\pi \text{a}}}; F_I \propto \frac{1}{\sigma} \tag{5}$$

where the coefficient 'a' represented the crack depth. The relationship between the geometry factor and the characteristic length revealed a lower geometry factor with an increasing shape factor as depicted in Figure 24. Comparing this relationship with the strain alteration and characteristic length relationship found in the current study, it shows that the behavior of strain corresponds with Carpinteri's work. Since the lower geometry factor indicated the higher stress as it was inversely proportional according to Equation 5 and stress was directly proportional to strain within the elastic which was also found in the cracked shaft responses of this analysis. These findings indicate that strain alteration was higher with the increasing shape factor, similar to the findings of the current study as discussed. Other studies have shown similar results of the geometry factor and the characteristic length relationship as following literature (60-63).

In addition, the temperature prediction technique is applied to estimate the temperature from the strain of the excited cracked shaft to illustrate the surface temperature prediction. The technique is performed on the cracked shaft with a circular front and a characteristic length of 1 (β = 1, α = 1), which has been observed as the crack geometry generating the highest strain under both excitation conditions. Figure 25 displays the strain contour with the predicted corresponding temperature.

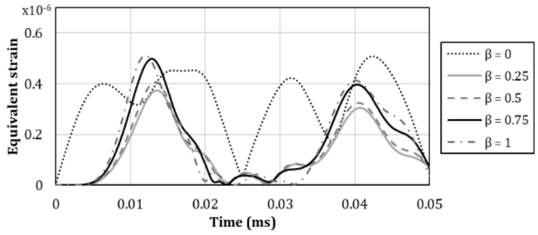

(a)

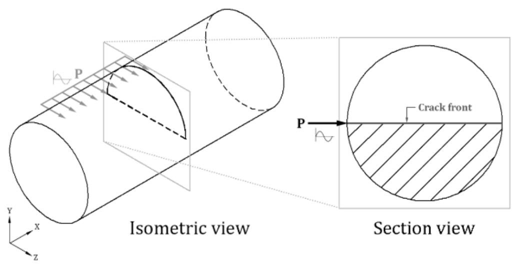

(b)

Figure 23. Responses of the cracks with α = 1 under transverse excitation, (a) Strain responses of the different crack front (b) Section view of the straight front crack under excitation

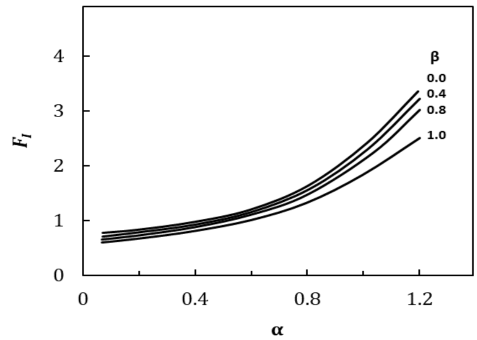

Figure 24. Geometry correction factor variation near crack tips along the crack characteristic

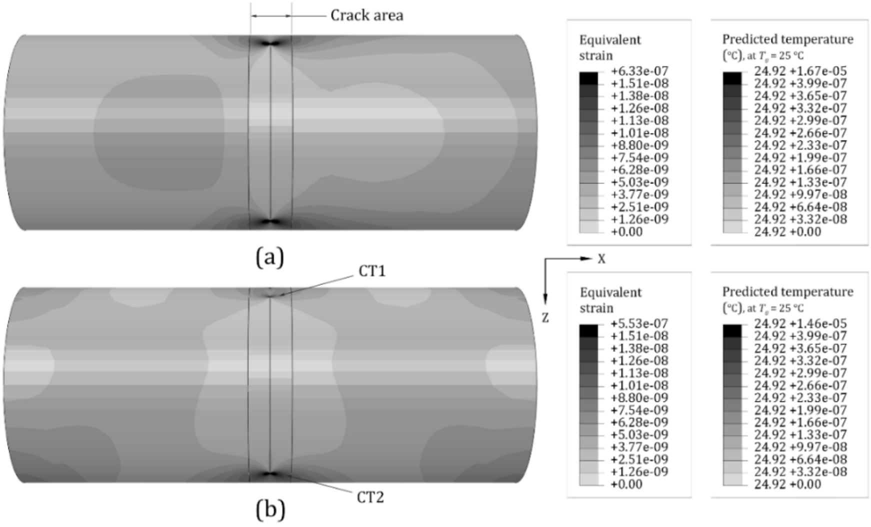

Figure 25. Strain contour and predicted corresponding temperature, (a) Axial excitation of the circular cracked shaft (β = 1) with α = 1, (b) Transverse excitation of the circular cracked shaft (β = 1) with α = 1

The maximum temperature differences are 1.67x10^{-5} °C and 1.46x10^{-5} °C for axial and transverse excitation, respectively. The temperature differences show a significant increase compared to the predicted temperatures of the maximum strain on the uncracked shaft (1.03x10^{-7} °C for axial excitation and 1.25x10^{-7} °C for transverse excitation), with percentage increments of 1.63x10^{4} % and 1.17x10^{4} %, respectively.

Despite the increment, the temperature changes in the cracked shaft are still hardly measurable in practice, emphasizing the insufficient excitation power from the currently used ultrasonic transducer.

The improvement of excitation power and the use of a high-sensitivity IR camera are strongly recommended to enhance the effectiveness of the temperature prediction technique in practical applications. Estimating the defective area is achievable by leveraging the strain distribution around the crack through the utilization of an IR camera to capture the corresponding temperature .

It's crucial to emphasize that the temperature prediction technique was developed within a controlled environment in a research laboratory. Temperature variations can potentially influence material stiffness and heat transfer (64). While conducting, the impact of the ambient conditions, especially the surrounding temperature, should be taken into account. Consequently, the technique may not be well-suited for use in hot-working conditions, where significant changes in material properties occur and are affected by thermal radiation from surrounding components. In such conditions, both of the temperature detectability and the prediction accuracy may be compromised.

In contrast, the technique appears more suitable for natural ambient conditions, where temperature fluctuations are relatively modest compared to the extreme conditions of the hot-working conditions. Nevertheless, it's essential to acknowledge that even in natural ambient conditions, the external variables like sunlight and wind can influence temperature-induced changes, affecting the accuracy of temperature predictions.

For a comprehensive understanding, further studies should be undertaken to improve this technique and observe its limitations in real-world inspection scenarios.

6. CONCLUSION

This study carried out observations on the deformation-induced heating mechanism of SCM440 material. The observations revealed a correlation between temperature and deformation strain, where the temperature increases along the strain alteration. The results of the study suggest that the temperature can be predicted from the strain using the temperature-strain relationship. The developed temperature prediction technique can be applied to estimate the temperature of tensile specimens, demonstrating good predictability with a maximum absolute error of approximately 0.4 °C among multiple tests. Moreover, computational-based studies were involved in this work. Both cracked and uncracked SCM440 shafts were investigated for strain responses under ultrasonic excitation. The computational model was tested under different control variables, including crack shapes, sizes, supports, and excitation conditions to investigate their influence on the strain responses. The experimental validation exhibited good agreement for the computational model with the shaft response under excitation. The results for the cracked shaft revealed significantly higher strain responses compared to the uncracked shaft, with the circular front crack exhibiting the greatest strain generation under any excitation conditions. The temperature prediction technique was also applied to estimate the temperature gradient from the strain distribution of shaft responses. However, the strain responses under the studies were very small with an excitation force of 0.35 N generated by the low-power ultrasonic cleaning transducer employed in this work, resulting in undetectable temperature changes in practice. To effectively utilize this prediction technique, improvements in the excitation power and the use of a high-sensitivity IR camera are required. Based on both investigations, the results strongly suggest that the temperature prediction technique can effectively estimate defective areas due to the strain distribution around a crack. Further studies should be conducted to optimize the temperature prediction based on the strain alteration technique for practical applications.

7. ACKNOWLEDGMENT

The research on Development of Temperature-Strain Prediction Based on Deformation-Induced Heating Mechanism in SCM440 Surface Cracked Shaft under Ultrasonic Excitation by King Mongkut's University of Technology North Bangkok (KMUTNB) received funding support from the National Science, Research and Innovation Fund (NSRF) (KMUTNB-FF-65-65).

8. REFERENCES

1. Morbidini M, Cawley P, Barden T, Almond D, Duffour P. Prediction of the thermosonic signal from fatigue cracks in metals using vibration damping measurements. Journal of Applied Physics. 2006;100(10). 10.1063/1.2361091
2. Mendioroz A, Martínez K, Celorrio R, Salazar A. Characterizing the shape and heat production of open vertical cracks in burst vibrothermography experiments. NDT & E International. 2019;102:234-43. 10.1016/j.ndteint.2018.12.006
3. Reifsnider K, Henneke EG, Stinchcomb W. The mechanics of vibrothermography. Mechanics of nondestructive testing. 1980:249-76. 10.1007/978-1-4684-3857-4_12
4. Favro L, Han X, Ouyang Z, Sun G, Sui H, Thomas R. Infrared imaging of defects heated by a sonic pulse. Review of scientific instruments. 2000;71(6):2418-21. 10.1063/1.1150630
5. Shih Y-S, Chen J-J. Analysis of fatigue crack growth on a cracked shaft. International Journal of Fatigue. 1997;6(19):477-85. https://api.semanticscholar.org/CorpusID:136058376
6. Chowdhury P, Sehitoglu H. Mechanisms of fatigue crack growth– a critical digest of theoretical developments. Fatigue & Fracture of Engineering Materials & Structures. 2016;39(6):652-74. 10.1111/ffe.12392
7. Stephens RI, Fatemi A, Stephens RR, Fuchs HO. Metal fatigue in engineering: John Wiley & Sons; 2000.
8. Zangeneh S, Ketabchi M, Kalaki A. Fracture failure analysis of AISI 304L stainless steel shaft. Engineering Failure Analysis. 2014;36:155-65. 10.1016/j.engfailanal.2013.09.013
9. Zhao L-H, Xing Q-K, Wang J-Y, Li S-L, Zheng S-L. Failure and root cause analysis of vehicle drive shaft. Engineering Failure Analysis. 2019;99:225-34. 10.1016/j.engfailanal.2019.02.025
10. Chatterton S, Pennacchi P, Vania A, Rubio P. Analysis of the periodic breathing of a transverse annular crack propagated in a real rotating machine. Engineering Failure Analysis. 2019;99:126-40. 10.1016/j.engfailanal.2019.02.029
11. Mayton D, Spencer F, Alvarez C, editors. Characterizing the effects of sonic IR variables on turbine disk inspection using a design of experiments approach. AIP Conference Proceedings; 2005: American Institute of Physics. 10.1063/1.1916736
12. Holland SD. Thermographic signal reconstruction for vibrothermography. Infrared Physics & Technology. 2011;54(6):503-11. 10.1016/j.infrared.2011.07.004
13. Gao C, Meeker WQ, Mayton D. Detecting cracks in aircraft engine fan blades using vibrothermography nondestructive evaluation. Reliability Engineering & System Safety. 2014;131:229-35. 10.1016/j.ress.2014.05.009
14. Szwedo M, Pieczonka L, Uhl T, editors. Application of vibrothermography in nondestructive testing of structures. 6th European Workshop on Structural Health Monitoring; 2012.
15. DiMambro J, Ashbaugh D, Nelson CL, Spencer FW, editors. Sonic infrared (IR) imaging and fluorescent penetrant inspection probability of detection (POD) comparison. AIP Conference Proceedings; 2007: American Institute of Physics. 10.1063/1.2718008
16. Jia Y, Tang L, Xu B, Zhang S. Crack detection in concrete parts using vibrothermography. Journal of Nondestructive Evaluation. 2019;38:1-11. 10.1007/s10921-019-0562-0
17. Luong MP. Infrared thermovision of damage processes in concrete and rock. Engineering Fracture Mechanics. 1990;35(1-3):291-301. 10.1016/0013-7944(90)90207-W
18. Tian G, Zhang W, Jin GF, Zhu L, Yang ZW. Detection of Ceramic Material Crack Defect Based on the Ultrasonic Infrared Thermal Wave Technique. Advanced Materials Research. 2013;791:949-53. 10.4028/www.scientific.net/AMR.791-793.949
19. Vaddi JS, Holland SD, Kessler MR. Loss modulus measurement of a viscoelastic polymer at acoustic and ultrasonic frequencies using vibrothermography. Measurement. 2021;168:108311. 10.1016/j.measurement.2020.108311
20. Katunin A, Wronkowicz-Katunin A, Wachla D. Impact damage assessment in polymer matrix composites using self-heating based vibrothermography. Composite Structures. 2019;214:214-26. 10.1016/j.compstruct.2019.02.003
21. Bolu G, Gachagan A, Pierce G, Harvey G. Reliable thermosonic inspection of aero engine turbine blades. Insight-Non-Destructive Testing and Condition Monitoring. 2010;52(9):488-93. 10.1784/insi.2010.52.9.488
22. Morbidini M, Cawley P. The detectability of cracks using sonic IR. Journal of Applied Physics. 2009;105(9). 10.1063/1.3125444
23. Ibarra-Castanedo C, Genest M, Guibert S, Piau J-M, Maldague XP, Bendada A, editors. Inspection of aerospace materials by pulsed thermography, lock-in thermography, and vibrothermography: a comparative study. Thermosense XXIX; 2007: SPIE. 10.1117/12.720097
24. Glass III SW. Guide to Nondestructive Evaluation Techniques. Nondestructive Evaluation of Materials: ASM International; 2018. p. 3-7.

25. Renshaw J, Chen JC, Holland SD, Thompson RB. The sources of heat generation in vibrothermography. Ndt & E International. 2011;44(8):736-9. 10.1016/j.ndteint.2011.07.012
26. Holland SD, Uhl C, Ouyang Z, Bantel T, Li M, Meeker WQ, et al. Quantifying the vibrothermographic effect. NDT & E International. 2011;44(8):775-82. 10.1016/j.ndteint.2011.07.006
27. Mabrouki F, Thomas M, Genest M, Fahr A. Frictional heating model for efficient use of vibrothermography. NDT & E International. 2009;42(5):345-52. 10.1016/j.ndteint.2009.01.012
28. Renshaw J, Holland SD, Thompson RB. Measurement of crack opening stresses and crack closure stress profiles from heat generation in vibrating cracks. Applied Physics Letters. 2008;93(8). 10.1063/1.2976310
29. Rizi AS, Hedayatrasa S, Maldague X, Vukhanh T. FEM modeling of ultrasonic vibrothermography of a damaged plate and qualitative study of heating mechanisms. Infrared Physics & Technology. 2013;61:101-10. 10.1016/j.infrared.2013.07.011
30. De Cazenove J, Rade D, De Lima A, Araújo C. A numerical and experimental investigation on self-heating effects in viscoelastic dampers. Mechanical Systems and Signal Processing. 2012;27:433-45. 10.1016/j.ymssp.2011.05.004
31. Singh V, Sangle K. Analysis of vertically oriented coupled shear wall interconnected with coupling beams. HighTech and Innovation Journal. 2022;3(2):230-42. 10.28991/HIJ-2022-03-02-010
32. El Yassari S, El Ghoulbzouri A. Numerical simulation of fiber-reinforced concrete under cyclic loading using extended finite element method and concrete damaged plasticity. International Journal of Engineering, Transactions A: Basics. 2023;36(10):1815-26. 10.5829/IJE.2023.36.10A.08
33. Talouti S, Benzerga D, Abdelkader H. Numerical Investigations of Damage Behaviour at the Weld/Base Metal Interface. International Journal of Engineering, Transactions C: Aspects. 2022;35(12):2337-43. 10.5829/IJE.2022.35.12C.09
34. Gholami P, Kouchakzadeh MA, Farsi M. A continuum damage mechanics-based piecewise fatigue damage model for fatigue life prediction of fiber-reinforced laminated composites. International Journal of Engineering, Transactions AC: Aspects. 2021;34(6):1512-22. 10.5829/IJE.2021.34.06C.15
35. Salarvand A, Poursaiedi E, Azizpour A. Probability Approach for Prediction of Pitting Corrosion Fatigue Life of Custom 450 Steel. International Journal of Engineering, Transactions A: Basics. 2018;31(10):1773-81. 10.5829/IJE.2018.31.10A.21
36. Boussalih F, Fedaoui K, Zarza T. Chaboche Model for Fatigue by Ratcheting Phenomena of Austenitic Stainless Steel under Biaxial Sinusoidal Loading. Civil Engineering Journal. 2022;8(3):505-18. 10.28991/CEJ-2022-08-03-07
37. Cuong DQ, Chinh VD. Estimation of Overall Fatigue Life of Jack-up Leg Structure. Civil Engineering Journal. 2022;8(03). 10.28991/CEJ-2022-08-03-06
38. Jeong J-I, Kim J-H, Choi S-G, Cho YT, Kim C-K, Lee H. Mechanical properties of white metal on scm440 alloy steel by laser cladding treatment. Applied Sciences. 2021;11(6):2836. 10.3390/app11062836
39. Kapoor R, Nemat-Nasser S. Determination of temperature rise during high strain rate deformation. Mechanics of materials. 1998;27(1):1-12. 10.1016/S0167-6636(97)00036-7
40. Lamboul B, Passilly F, Roche J-M, Balageas D, editors. Ultrasonic vibrothermography using low-power actuators: An impact damage detection case study. AIP Conference Proceedings; 2015: American Institute of Physics. 10.1063/1.4914626
41. Xu C, Xie J, Zhang W, Kong Q, Chen G, Song G. Experimental investigation on the detection of multiple surface cracks using vibrothermography with a low-power piezoceramic actuator. Sensors. 2017;17(12):2705. 10.3390/s17122705
42. Liu P, Xu C, Zhang Y, Qin Y, Xu Y, Xie J, et al. Low-power vibrothermography detection technique for surface cracks on composite sucker rod. Smart Materials and Structures. 2023;32(3):035034. 10.1088/1361-665X/acb979
43. Anderson TL. Fracture mechanics: fundamentals and applications: CRC press; 2017.
44. Tada H, Paris P, Irwin G. The stress analysis of cracks handbook, Del Research Corporation, St. Louis, Missouri. 1973.
45. Abbasnejad A, Moradi G. Frictional Strain Hardening-softening in Experimental and Numerical Investigation of Arching Effect. International Journal of Engineering, Transactions B: Applications. 2015;28(2):180-9. 10.5829/idosi.ije.2015.28.02b.03
46. Shahraini SI, Kadkhodayan M. Ratcheting Analysis of Steel Plate under Cycling Loading using Dynamic Relaxation Method Experimentally Validated. International Journal of Engineering, Transactions C: Aspects. 2021;34(6):1530-6. 10.5829/ije.2021.34.06c.17
47. McClung R, Sehitoglu H. On the finite element analysis of fatigue crack closure—1. Basic modeling issues. Engineering fracture mechanics. 1989;33(2):237-52. 10.1016/0013-7944(89)90027-1
48. De-Andrés A, Pérez J, Ortiz M. Elastoplastic finite element analysis of three-dimensional fatigue crack growth in aluminum shafts subjected to axial loading. International Journal of Solids and Structures. 1999;36(15):2231-58. 10.1016/S0020-7683(98)00059-6
49. Rigby S, Tyas A, Bennett T. Elastic–plastic response of plates subjected to cleared blast loads. International Journal of Impact Engineering. 2014;66:37-47. 10.1016/j.ijimpeng.2013.12.006
50. Shih Y-S, Chen J-J. The stress intensity factor study of an elliptical cracked shaft. Nuclear Engineering and design. 2002;214(1-2):137-45. 10.1016/S0029-5493(02)00022-5
51. Rice JR, Rosengren G. Plane strain deformation near a crack tip in a power-law hardening material. Journal of the Mechanics and Physics of Solids. 1968;16(1):1-12. 10.1016/0022-5096(68)90013-6
52. Dong P, Pan J. Elastic-plastic analysis of cracks in pressure-sensitive materials. International journal of solids and structures. 1991;28(9):1113-27. 10.1016/0020-7683(91)90106-P
53. Xia L, Wang T, Shih C. Higher-order analysis of crack tip fields in elastic power-law hardening materials. Journal of the Mechanics and Physics of Solids. 1993;41(4):665-87. 10.1016/0022-5096(93)90022-8
54. Nikishkov G, Matvienko YG. Elastic–plastic constraint parameter A for test specimens with thickness variation. Fatigue & Fracture of Engineering Materials & Structures. 2016;39(8):939-49. 10.1111/ffe.12390
55. El Arem S. On the mechanics of beams and shafts with cracks: A standard and generic approach. European Journal of Mechanics-A/Solids. 2021;85:104088. 10.1016/j.euromechsol.2020.104088
56. Liu Y, Glass G. Effects of mesh density on finite element analysis. SAE Technical Paper; 2013. Report No.: 0148-7191.
57. Bhalerao GN, Patil AA, Waghulde KB, Desai S. Dynamic analysis of rotor system with slant cracked shaft. Materials Today: Proceedings. 2021;44:4268-81. 10.1016/j.matpr.2020.10.544
58. Lap-Arparat P, Tuchinda K. Computational Study of Excitation Controlling Parameters Effect on Uniform Beam Deformation under Vibration. International Journal of Engineering, Transactions A: Basics. 2023;36(1):60-70. 10.5829/IJE.2023.36.01A.08
59. Carpinteri A. Shape change of surface cracks in round bars under cyclic axial loading. International Journal of Fatigue. 1993;15(1):21-6. 10.1016/0142-1123(93)90072-X
60. Miedlar PC, Berens AP, Gunderson A, Gallagher J. Analysis and support initiative for structural technology (ASIST) delivery

order 0016: USAF damage tolerant design handbook: guidelines for the analysis and design of damage tolerant aircraft structures. University of Dayton Research Institute: Dayton, OH, USA. 2002.

61. Shin C, Cai C. Experimental and finite element analyses on stress intensity factors of an elliptical surface crack in a circular shaft under tension and bending. International Journal of fracture. 2004;129:239-64. 10.1023/B:FRAC.0000047784.23236.7d

62. Astiz M. An incompatible singular elastic element for two-and three-dimensional crack problems. International Journal of Fracture. 1986;31:105-24. 10.1007/BF00018917

63. Couroneau N, Royer J. Simplified model for the fatigue growth analysis of surface cracks in round bars under mode I. International Journal of Fatigue. 1998;20(10):711-8. 10.1016/S0142-1123(98)00037-1

64. Wahrhaftig AdM, Magalhães KMM. Bifurcation Analysis of Columns of Composite Materials with Thermal Variation. Materials Research. 2021;24. 10.1590/1980-5373-MR-2021-0266

Persian Abstract

چکیده

مکانیسم‌های پشت تغییر شکل دما و مواد در ویبروترموگرافی همچنان مشکوک هستند و شکافی در درک ایجاد می‌کنند. این مطالعه مکانیسم ناشی از تغییر شکل را بررسی می‌کند و تنها بر تولید گرما مرتبط با توسعه کرنش تمرکز می‌کند. هر دو روش تجربی و شبیه سازی گنجانیده شده است. بخش تجربی رابطه دما–کرنش ماده SCM440 را که معمولاً برای شفت‌های چرخشی استفاده می‌شود، بررسی می‌کند. این رفتار از طریق ارتباط بین تغییر دما و تغییر شکل ماده در طول آزمایش کشش تک محوری بررسی می‌شود. نتایج نشان می دهد که تغییر دما و توزیع را می توان بر اساس توسعه کرنش پلاستیک پیش بینی کرد. شبیه‌سازی روش المان محدود (FEM) برای مدل‌سازی برانگیختگی شفت با و بدون ترک سطحی بیضوی استفاده می‌شود. پیکربندی‌های مختلف شفت ترک خورده بررسی می‌شوند و الگوهای تولید و توزیع کرنش متمایز را آشکار می‌کنند. تغییر کرنش بالا به طور قابل توجهی در اطراف نوک ترک مشاهده می شود که امکان تشخیص ناپیوستگی شفت را فراهم می کند. در نتیجه، یک تکنیک پیش‌بینی دما برای تخمین دما بر اساس تغییر کرنش در طول تغییر شکل توسعه داده می‌شود. قدرت تحریک کافی و استفاده از دوربین IR با حساسیت بالا برای کاربرد موثر تکنیک پیش‌بینی دما توصیه می‌شود. علاوه بر این، این مطالعه بینش‌هایی را در مورد درک کاربرد و محدودیت‌های لرزش‌گرموگرافی برای بازرسی آسیب اجزای مهندسی بر اساس روابط تجربی دما–کرنش و پیش‌بینی‌های محاسباتی توزیع کرنش در شفت‌های ترک خورده تحت تحریک ارائه می‌کند. این یافته‌ها راهنمایی برای کاربردهای مهندسی و تلاش‌های تحقیقاتی آینده ارائه می‌کنند.

IJE TRANSACTIONS A: Basics Vol. 37 No. 01, (January 2024) 167-177

International Journal of Engineering

Journal Homepage: www.ije.ir

Investigation of Antifouling Paints for Vessel in Tropical Seawater of North Jakarta in Indonesia

G. Priyotomo*[a], S. Prifiharni[a], A. Nikitasari[a], S. Musabikha[a], R. Kusumastuti[a], L. Nuraini[a], J. Triwardono[a], H. Nugraha[a], A. Budi Prasetyo[a], H. Julistiono[b]

[a] *Research Center for Metallurgy, National Research and Innovation Agency, Bld.720, Serpong, Tangerang Selatan, Banten, Indonesia*
[b] *Research Center for Applied Microbiology, National Research and Innovation Agency, Jakarta-Bogor No.KM 46, Pakansari, Cibinong, Bogor, Jawa Barat, Indonesia*

PAPER INFO

Paper history:
Received 28 July 2023
Received in revised form 12 September 2023
Accepted 15 September 2023

Keywords:
Antifouling Paint
Biofouling
Biocide
Tropical Seawater

ABSTRACT

The copper-based biocide is mostly used as primary additive of Antifouling (AF) paint in Indonesia especially on vessels. The evaluation for the efficacy of AF paint was conducted where anti corrosion (AC) paint was also as a reference. The panels with both paints were exposed to various sea depths of up to 3 meters until 12 months of exposures. The measurement of parameters of seawater consisting of water conductivity, pH, temperature, dissolved oxygen and salinity were carried out. There was no or less attached marine biofouling on AF-painted panels but not on AC-painted panels up to 12-months of field exposure in various sea depths. There was no difference between the properties of AF paints before and after exposure to various sea depths. The inhibitive performance of AF paint depends on the existence of AF layer containing Cu_2O biocide where the thickness of that layer decreases in increase of time exposure.

doi: *10.5829/ije.2024.37.01a.15*

1. INTRODUCTION

The existence of marine biofouling have potency of major issues for the physical and mechanical degradation of submerged offshore structures particularly metal and alloys (1). The growth and settlement of biofouling have a detrimental effect on submerged structure (2-4). The metabolism of biofouling organisms may cause a decrease in corrosion resistance, an increase in drag, and a reduction in the frequency of drydocking operations for ships (5-8). The presence of corrosion could induce mechanical properties and operational time on existing structures (9, 10). In addition, the safety issues have been taken an essential part of consideration when the decrease of structure stability due to the growth and settlement of marine biofouling (11, 12). The biological metabolism of marine biofouling is mainly affected by seawater factors such as salinity, pH, water flow, dissolved oxygen, water temperature and surface temperature (13, 14). Furthermore, the increased growth rate of biofouling organisms frequently occurs aggressively as a result of the warmer seawater temperature and higher salinity in tropical zones compared to those in temperate zones. Indonesia is one of several tropical countries with a hot and humid climate. Due to the warm surface water temperature and high salinity in the marine environment, the seasonal change is comparatively consistent every year. Additionally, Indonesia's ocean waters are home to a variety of marine species and ecosystems in both deep water and along the coast. Therefore, in Indonesia, marine biofouling continues to grow and settle without interruption, but not in subtropical countries. The usage of antifouling (AF) paint on marine submerged structures is a frequent mitigation strategy for the severity of associated marine biofouling. Biocide is typically the added chemical that makes up the majority of AF paints. The biocide of copper (Cu^{2+}) being released from the

*Corresponding Author Email: gadangp@gmail.com (G. Priyotomo)

Please cite this article as: Priyotomo G, Prifiharni S, Nikitasari A, Musabikha S, Kusumastuti R, Nuraini L, Triwardono J, Nugraha H, Budi Prasetyo A, Julistiono H. Investigation of Antifouling Paints for Vessel in Tropical Seawater of North Jakarta in Indonesia. International Journal of Engineering, Transactions A: Basics, 2024;37(01):167-177.

bulk of AF paint has the advantage of preventing biofouling from adhering to the structure (3).

Moreover, the poisonous property of copper compounds serves to inhibit the growth of some micro- and macroorganisms, including mollusks, algae, bacteria, and other organisms (15, 16). The usage of AF paint is the most proven method of mitigation up to now (17). Commonly AF paints comprise three types such as hard AF paint, ablative AF paint and self-polishing copolymer (SPC) AF paint. In Indonesia, SPC-AF paint is used at ship and boat due to the longer operational time service compared to other AF paints for the last 15 years. In addition, the other justification for using SPC-AF paint is the improved management of the discharge of copper compound or cuprous oxide (Cu_2O), which act as the primary biocides (12). Due to the negative impacts of tributyltin (TBT) compound as prior biocides, tin-free self-polishing copolymers (tin-free SPC) AF paint has now been used as AF paint incorporating copper biocide. Generally, generic SPC-AF paint comprises resin, solvent, pigment, biocide, co-biocide, anti-settling agent, extender and soon on.

In preceding investigation, few researchers had reported the efficacy of SPC-AF paint in North Jakarta and Madura strait, Indonesia within a month after field exposure (4, 18). However, there is no comprehensive investigation the efficacy of SPC-AF paint perfomance for a longer exposure in Indonesia in North Jakarta especially the relationship amongs the depth of seawater level, intrinsic properties of SPC-AF and seawater parameters againts tropical marine biofouling particulary a binder of silyl acrylate. Therefore, this research aims to clarify the effectiveness of performance on SPC-AF paint compared to anticorrosion paint as reference material for a longer exposure up to 12 months in North Coastal of Jakarta District, Indonesia.

2. MATERIALS AND METHODS

2. 1.The Preparation of Specimens A plate of low carbon steel was cut (length: 25 cm, width: 20 cm and thickness: 0.03 cm) for a coating metal substrate. By using a portable sandblaster, all metal substrates were sanded in accordance with ISO 8501-1 Sa 2.5. According to that ISO standard, stains, streaks, and rust should only cover 5% of the steel substrate's surface. In addition, SPC-AF paints is classified as a top coat which define as a final layer of multiple paint layers over intermediate layer and primer layer. SPC-AF paints are essentially a three-layer system made up of an epoxy primer base coat, an epoxy intermediate base coat, and an epoxy top coat. There were two commercial SPC-AF paints used in this current work (AFP-A and AFP-B). On other hand, as controlled paint, anticorrosion (AC) paint also was applied over epoxy primer coating. In addition, both AF paints were received from two distinct Indonesian companies that specialize in tin-free self-polishing copolymers (SPC). Those companies produced the generic type of AF paint using the certain chemical formulas as well as that in preceeding work (19).

In early September, during the tropical rainy season, each test rack of both samples of AF paint and AC paint was positioned on submerged piles of Muara Baru sea port in North Jakarta (6°05'46.0"S 106°48'01.0"E), as shown in Figure 1. In addition, Geographically, Jakarta is located in an alluvial plain that is low and flat, with an average elevation of 8 meters (26 feet) above sea level with historically large swampy areas. North Jakarta region is a suitable field area to represent the environmental parameters and the growth of tropical biological fouling. In this field work, the exposure time was carried out by 2, 3, 6 and 12 months. In addition, during operational times, the maximum lifespan of SPC-AF paints is approximately 36 months where the recent evaluation of those paints efficacy was conducted before that lifespan. The evaluation of potential damage to those paints before the maximum operational time is needed in this work, especially in tropical countries like Indonesia. Following a period of exposure, the specimen was retrieved from the water and kept in storage until further characterization and analytical steps, as shown in Figure 2.

Furthermore, the settlement of marine biofouling on structure is affected by the water parameters such as water conductivity, salinity, pH, water temperature and dissolved oxygen (1, 4, 18). Those water parameters could be considered to be carried out in this present work where were measured by using HACH HQ40d Advanced Portable meter during operational service.

2. 2. Evaluation of AF Paint Properties In this work, paint testing was conducted to evaluate physical and mechanical properties of paints before and after field test. Paint was tested for hardness using the Elcometer 501 pencil hardness tester in accordance with American Standard Testing and Material (ASTM) D-3363. The evaluation pencil hardness was valued through the ranges

Figure 1. Location of specimen placement in Muara Baru, Jakarta, Indonesia

Figure 2. An activity of paint specimen retrievement at certain time of exposure in Muara Baru Sea port, North Coastal of Jakarta

from 6B (softest) up to 9H (hardest). The adhesion strength of paint was carried out using Elcometer 510 Automatic Pull-Off Adhesion Gauge according to ASTM D-4541. Adhesive strength refers to the ability of a paint to stick to surface of metal subtract and bond two surfaces together. Horiba Gloss Checker IG-331 was also used to perform properties of glossy at a 60-degree angle (ASTM D-523). In order to maintain the accuracy of the results, the tests were also run five times. The specimens are visually examined to check for the presence and distribution of biofouling. A JEOL JSM-6390 series scanning electron microscope was used to observe the cross-sectional morphology of samples.

3.RESULTS AND DISCUSSION

3. 1. The Paint Properties and Seawater Parameters after Exposure

The gloss properties of AFP-A and AFP-B following field exposure in various depths of saltwater are shown in Figures 3, respectively. The value of AFP-A and AFP-B gloss are 7.0 and 3.0 in the field test before exposure, respectively. The cause of gloss values difference in both AF paints is due to the lesser solid content of Paint A compared to Paint B. On the basis of result, the magnitudes of AFP-A gloss were almost the same each exposure time as well as those of AFP-B gloss. Low gloss AF paint is defined as having values of less than 10 Gross Units (GU), which were achieved by both AF paints. On the basis of results, the magnitudes of gloss paint are almost the same in both certain exposure times and different sea depths. It was found that both AFP-A and AFP-B had nearly the same gloss properties both before and after exposure.

Furthermore, both AFP-A and AFP-B are classified as tin-free self-polishing copolymers that have self - polishing mechanism in paint matrix during service in marine environment. That mechanism can make surface of AF paint smooth until no more outer AF coating layer

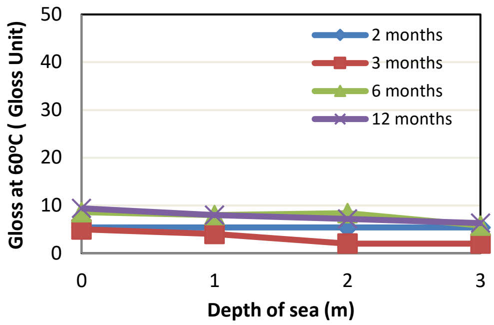

(a)

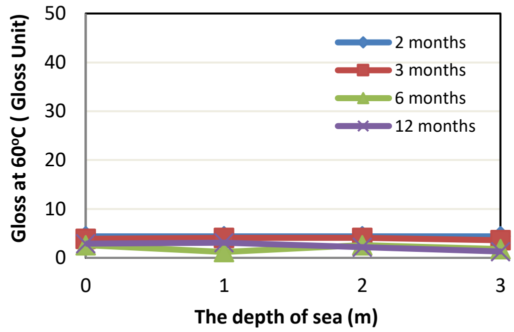

(b)

Figure 3. (a) Glossiness of the AFP-A as a function of sea depth and (b) Glossiness of the AFP-B as a function of sea depth

on primary coating during service (19). In addition, the roughness of paint surface is attributed with gloss degree of coating (20). Before and after field exposure, the pencil hardness values of both AFP-A and AFP-B were classified in B scale. In addition, during field exposure, the pencil hardness values of AFP-A and AFP-B are the same.

Figure 4 shows that adhesion strength for AFP-A and AFP-B as function of depth levels of the sea after exposure. In varying levels of sea depth, the adhesion strengths of the paints were almost the same. There is no significant alteration of adhesion strengths in both two type of antifouling paints in different sea depth. The category of coating failures refers to 100% cohesion pattern, where both AFP-A and AFP-B occurred failure in a layer of antifouling coating as shown in Figure 5. Cohesive failure is in the coating itself due to internal crack (21) where that crack caused by abrasion process and dissolving additive in coating matrix. Main factors include water temperature, salinity, pH, dissolved oxygen, and others cause biological fouling to settle (19, 22). Most marine biofouling organisms suitably grow and settle in the environment with pH 7.5-8.0 and temperature of more than 20oC (23). Furthermore, North Jakarta bay is distinguished by its shallow water, 13 rivers flowing into it, and connections to the Java Sea which has been impacted by tropical seawater parameters. On the basis of results, the temperatures and pH of seawater has the appropriate growth and settlement for marine organism where there are no or less shift alteration for those parameters in various depths of sea and different exposure times as shown in Table 1.

The dissolved salt concentration of bodily water is referred to as salinity, and the typical average saltwater salinity is around 35 ppt (24). The Muara Baru area of Jakarta Bay has salinity levels less than 35 ppt. North coastal of Jakarta has many estuaries near coastline which is lower salinity value in the range of 24-33.5 ppt (25) as well as the present results. Furthermore, the solubility of dissolved oxygen (DO) commonly increases in decreasing water temperature and vice versa (26) where DO concentration decreased with increasing seawater depth (27).

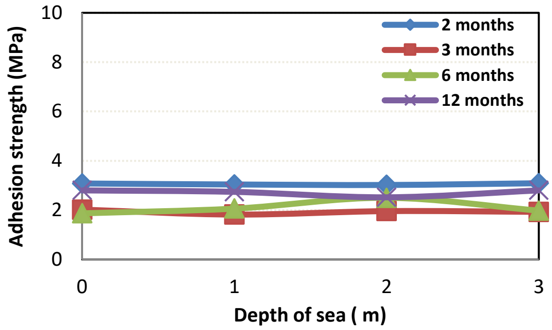

(a)

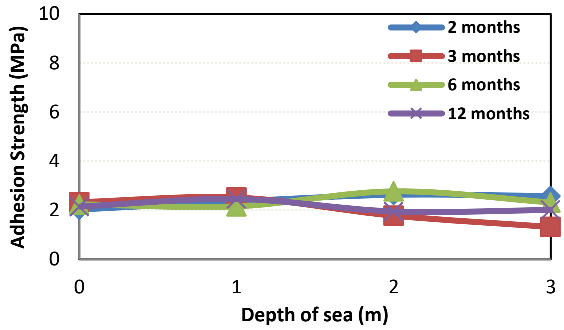

(b)

Figure 4. Adhesion strength for (a). AFP-A and (b). AFP-B as function of depth levels of the sea after exposure

Figure 5. An illustration of AF paint adhesion failure after exposure

TABLE 1. Seawater parameter during field exposure at Muara Baru, North Jakarta

Exposure time (months)	Depth (meter)	Temperature (°C)	pH	Salinity (ppt)	DO (mg/L)	Conductivity (mS/cm)
2	0	30.9	8.2	28.1	5.58	48.7
	1	30.7	8.3	28.2	5.44	48.7
	2	30.6	8.3	28.2	5.2	48.6
	3	30.6	8.3	28.1	5.25	48.5
3	0	30.45	8.35	28.15	5.06	48.45
	1	30.35	8.38	28.15	4.937	48.38
	2	30.25	8.41	28.15	4.814	48.31
	3	30.15	8.44	28.15	4.691	48.24
6	0	30.05	8.47	28.15	4.568	48.17
	1	29.95	8.5	28.15	4.445	48.1
	2	29.85	8.53	28.15	4.322	48.03
	3	29.75	8.56	28.15	4.199	47.96
12	0	30.7	7.79	29.9	1.89	51.4
	1	30.7	7.79	30.1	1.6	51.7
	2	30.7	7.8	30.5	1.05	52.4
	3	30.7	7.81	31.1	0.03	53.3

The level of DO is practically the same concentration at different depths below sea level up to a depth of three meters. The lowest magnitude of DO took place in 12 months of exposure. The authors presume that the significant decrease of DO concentration each depth of sea is caused by anthropogenic activity nearby Muara Baru, North Jakarta in 12 months of exposure. In addition, the euphotic zone is defined as the area with a maximum sea depth of 3 meters as well as this work. The penetration of the radiation of sunlight occurs intensively (27) where the active photosynthesis process supplies oxygen level in water (28). Moreover, Table 1 presents that water conductivity is nearly the same magnitude at different sea depths. Sea water commonly has average conductivity of approximately 55 mS/cm (29). However, in the present results, the values of conductivity each interval exposure is lower than 55 mS/cm.

When considering the effectiveness of antifouling paint, temperature, pH variations, DO and saltwater salinity are all essential factors. The solubility of biocides took place in small changes in the alkaline behavior of seawater, whether due to the production of hydrosulfide (pH decrease) or an increase in pH due to a decrease in CO_2 caused by the presence of algae. The effectiveness of antifouling paint is constrained by the rate of chemical and enzymatic reactions, which accelerate the slow stages of cell growth and the rate of polymeric coating crystallization in moderate temperatures. The higher salinity has impact to speed up the dissolution process of cuprous oxide (Cu_2O), a common binder in soluble antifouling paints where the performance of antifouling paints is more efficient in seawater compared to that in estuary water.

3. 2. Visual Examination of Exposed Specimens

The usage of anticorrosion and antifouling paints A and B as primary specimens in preceding research [19] is also utilized in the present research. All of the paints A and B specimens after being exposed to seawater are shown in images in Tables 2, 3, 4, and 5. The use of both AFP-A and AFP-B, compared to both AC paint A and AC paint B, could reduce the growth and settlement of marine biofouling organisms for up to 12 months.

Table 6 shows biofouling percentage on antifouling paint surface after certain field exposure. On the basis of results, the percentage of adherent biofouling increased gradually with the exposure time up to 12 months for both antifouling paints. The attachment of biofouling occurs at 6 months of exposure. The percentage of biofouling type A antifouling paint is less than type B antifouling paint.

TABLE 2. Visual observation of samples after two months of exposure

Depth of the sea (m)	AC paint A	AF paint A	Depth of the sea (m)	AC paint B	AF Paint B
0		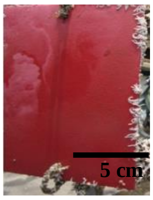	0	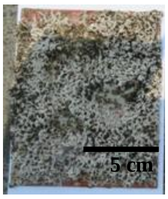	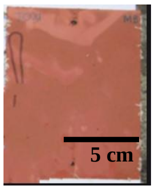
1	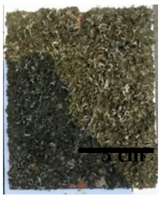	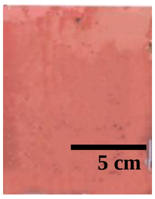	1	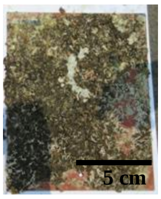	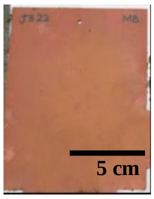
2		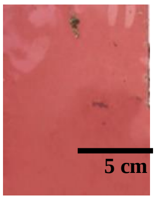	2	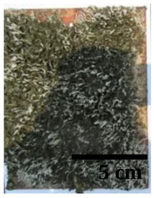	
3	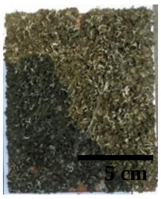	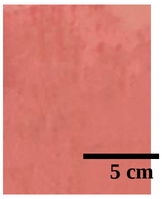	3	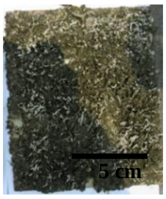	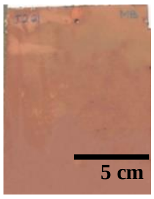

TABLE 3. Visual observation of samples after three months of exposure

Depth of the sea (m)	AC paint A	AF paint A	Depth of the sea (m)	AC paint B	AF Paint B
0		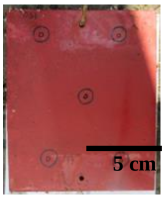	**0**	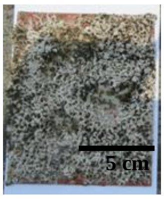	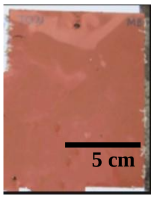
1	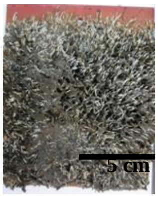	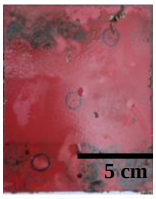	1	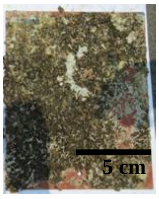	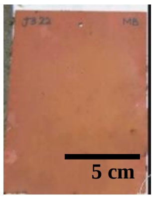
2		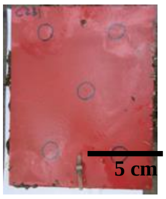	2		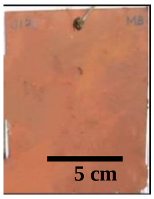
3	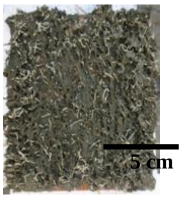	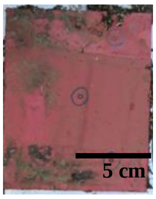	3	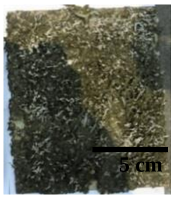	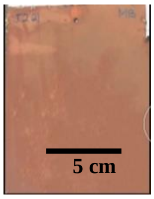

TABLE 4. After six months of exposure, the visual examination of representative specimens

Depth of the sea (m)	AC paint A	AF paint A	Depth of the sea (m)	AC paint B	AF Paint B
1	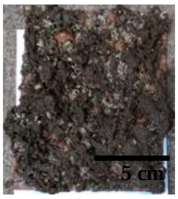	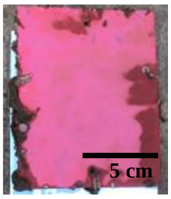	1	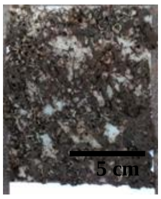	
2		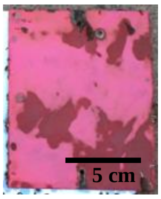	2		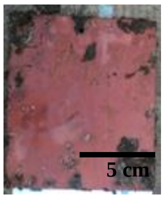

In the present research, tubeworms and barnacles are apparently some of the most significant and visible marine biofouling organisms on both AC paints during exposure. Mature barnacle species started appearing on both AC paints in 6 months of exposure. There is no or less different of marine biofouling growth distribution on both type of AC paints in different depth of the sea and various exposure times. The homogeneity of biofouling distribution on the samples of AC paint is caused by the installment of field test racks in euphotic zone where seawater quality parameters were almost the same in that zone. Furthermore, the existence of barnacles and tube worms as most attached biofouling organisms are categorized as calcareous macrofouling (30). Moreover,

TABLE 5. After twelve months of exposure, the visual examination of representative specimens

Depth of the sea (m)	AC paint A	AF paint A	Depth of the sea (m)	AC paint B	AF Paint B
0			**0**		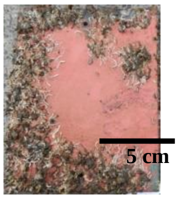
1			1	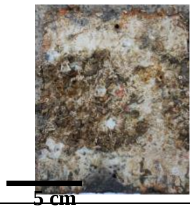	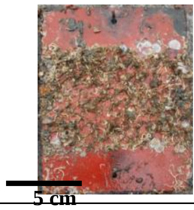

TABLE 6. Biofouling percentage on antifouling paint surface after certain field exposure

2 months of exposure					
Depth of the sea (m)	**AC Paint A (%)**	**AF Paint A (%)**	**Depth of the sea (m)**	**AC Paint B (%)**	**AF Paint B (%)**
0	100	0	0	100	0
1	100	0	1	100	0
2	100	0	2	100	0
3	100	0	3	100	0
3 months of exposure					
Depth of the sea (m)	**AC Paint A (%)**	**AF Paint A (%)**	**Depth of the sea (m)**	**AC Paint B (%)**	**AF Paint B (%)**
0	100	0	0	90	0
1	90	0	1	90	0
2	70	0	2	85	0
3	100	0	3	100	0
6 months of exposure					
Depth of the sea (m)	**AC Paint A (%)**	**AF Paint A (%)**	**Depth of the sea (m)**	**AC Paint B (%)**	**AF Paint B (%)**
1	100	5	1	100	35
2	100	5	2	100	10
12 months of exposure					
Depth of the sea (m)	**AC Paint A (%)**	**AF Paint A (%)**	**Depth of the sea (m)**	**AC Paint B (%)**	**AF Paint B (%)**
0	90	5	0	90	40
1	90	5	1	80	35

numerous different bacterial colonies are typically discovered on AC paints during the initial stages of biofouling growth, and these colonies serve as the principal nutrition for the growth of macroorganisms after few days to many weeks of exposure. Due to the ideal habitat of seawater, it can be assumed that marine biofouling will continue to grow and mature over month of exposure as well as the present results.

3. 3. The Inhibitive Mechanism of Antifouling Paint against Marine Biofouling

Figures 6 and 7 show cross sections of both AF paints, each of which has a three-layer coating consisting of a primer coating (the first layer), an intermediate coating (the second layer), and a top coating (AF layer). Before exposure, the average AF layer thickness of the two multiple systems of AFP-A and AFP-B was 226 μm and 116 μm, respectively. On the basis of the results, AF coating layer thickness decreased for both AFP-A and AFP-B during field exposure up to 12 months. In Figures 8 and 9, the AF coating layer thickness reduction on AFP-A is less than that on AFP-B after exposure. AF layer is not present in AFP-B after 12 months of exposure compared to AFP-A after 12 months of exposure. The difference in thickness loss of both AF paints after exposure is presumed due to the different initial thickness of AF coating layers. Moreover, the initial thickness of coating value prior to exposure is used to estimate the service life of AF paints (19, 31, 32) as well as recent study. It suggests that the initial thickness of the AF coating layer up to 12 months of field exposure determines the service life of the AF paint system.

In recent work, both of AFP-A and AFP-B is classified as tin-free-polishing copolymer (tin-free SPC) which based on silyl acrylate (SA) as primary binder according their technical data sheet. The efficacy of tin-free SPC AF paints is related to the ability of that paint which inhibit the growth and settlement of biofouling in controlled

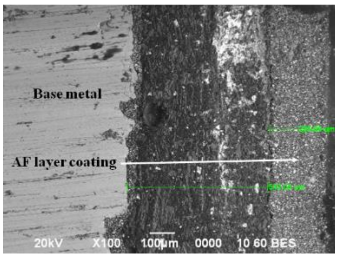

Figure 6. Prior to exposure, a cross-section picture of Paint A

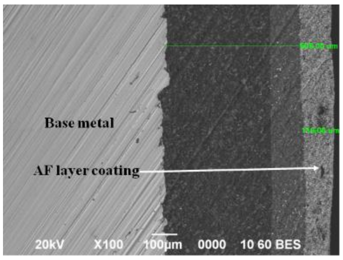

Figure 7. Prior to exposure, a cross-section picture of Paint B

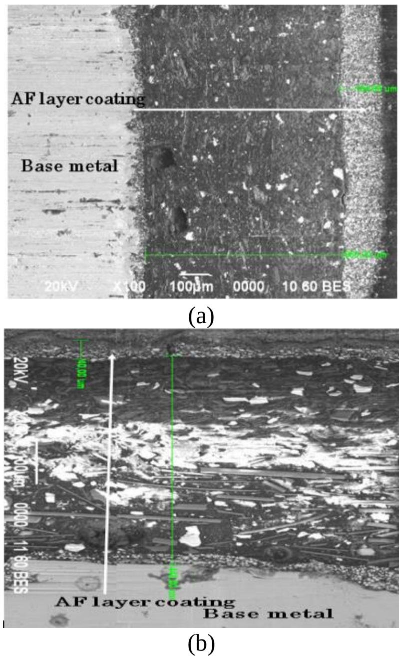

Figure 8. Cross-sectional pictures of Paint A that are representative after (a) 3 months of exposure, and (b) 12 months of exposure to seawater at a depth of 1 m

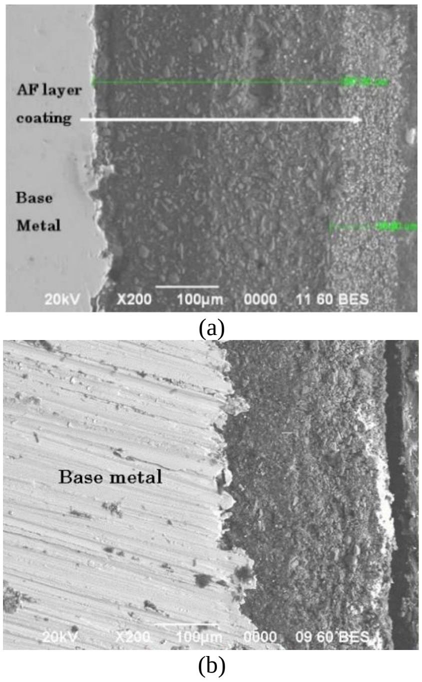

Figure 9. Cross-sectional pictures of Paint B that are representative after (a) 3 months of exposure, and (b) 12 months of exposure to seawater at a depth of 1 m

release rate of binder matrix. That ability could make to control the loss rate of AF paints thickness during field service compared to other type of AF paints such as hard AF paint and ablative paint. The inhibitive mechanism of SPC-AF paint against the settlement and growth of marine biofouling, the ingress of seawater takes place into the paint matrix, dissolve gradually all additives such as primary biocide, co-biocides and others to environment. That process takes place simultaneously and repeatedly which create a thin leached layer of AF coating without main dissolved additives such as Cu_2O and ZnO. The absence of soluble primary biocide, such as Cu_2O, results in pores being left in the matrix paint, which can be defined as a leached layer.

Furthermore, the leaching process of SPC AF paint comprises two sections such as initial leaching and steady-state leaching. When a freshly painted surface comes into touch with seawater environment and a biocide additive begins to dissolve at the top layer of AF paint, the leaching process for the painted structure begins immediately. The main ingredients used to formulate AF paints: solvent, binder, biocide, booster biocide, extenders, pigments, and miscellaneous additives (19). Generic Cu_2O is used as the primary inorganic biocide in both types of AF paints A and B, with co-biocides like ZnO additive also added to enhance the suppression of micro- and macro-algae growth and settlement. The presence of CuPt compound is necessary to boost the performance of primary biocide. Moreover, the following chemical Equation 1 is the proposed mechanism of the primary biocide of Cu_2O dissolving in seawater:

$$Cu_2O\,(s) + 2H^+\,(aq) + 4Cl\,(aq) \rightarrow 2CuCl^-\,(aq) + H_2O \qquad (1)$$

The presence of a high concentration of chloride ions, which increases the rate at which Cu_2O dissolves, is correlated with salinity levels of a high magnitude. In initial stage, when Cu_2O additive firstly contacts with sea water, that process yields soluble hydrated Cu(I) chloride complexes. That complexes compound is rapidly oxidized to Cu^{2+} ion as the main biocidal species against biofouling. The mechanisms of controlled release rate of biocides and co-biocides such as diffusion and chemical reactions where binder reaction, seawater water soluble pigments dissolution and polishing processes take place concurrently. In addition, those mechanisms could govern the magnitude of thin leached layer thickness for SPC AF paint. It is presumed that the disappearance of mostly biocide and co-biocide additives in silyl acrylate matrix creates many small pores in that matrix and enhances the magnitude of total wetted area on top surface of AF paint. During operational service, the wettability of the binder changes from hydrophobic to hydrophilic, causing the hydrolysis reaction to occur through the layer of AF coating that has been leached. Because partially reacted binder tends to be eroded by the motion of seawater and exposed at a less reacted AF layer surface, the AF coating has a self-polishing action. Biocides and co-biocides enriched matrix are present in the less-reacted AF coated surface or no leached layer zone, which inhibits the growth of marine biofouling. After completing the initial stage of leaching process, the steady-state leaching process starts simultaneously. In steady-state conditions, the rate of AF binder erosion caused by mechanical activity such as saltwater tide, current, and vessel movement is equal to the diffusion of ions from seawater bulk through the leached AF layer. The rate of biocide release from paint matrix is affected by seawater current, where leached AF layer can be eroded of polished easily. The role of seawater current rate is essential for the reduction of AF coating layer during service. The crucial function of the tidal current is its ability to easily wear or erode a leached layer of the AF layer, producing a fresh surface of the biocide-enriched layer. The simultaneous AF layer leaching process continues until there is no AF layer present during service. Therefore. It is pressumed that the thickness factor of SPC-AF paint can increase its lifespan during operational services at coastal aquifers of North Jakarta

4. CONCLUSIONS

The performance of both self-polishing copolymer (SPC) antifouling paints A and B showed remarkable efficacy compared to anticorrosion paints A and B in North Sea of Jakarta, Indonesia against the settlement of marine biofouling especially tubeworm and barnacle species. During operational service, the physical and mechanical properties of the AF paints are not significantly affected by variations in sea level up to 3 meters of depth and certain period of exposure such as pencil hardness, gloss and adhesion strength. In both AF paints A and B, the presence of a primary biocide like Cu_2O may minimize the growth and establishment of marine biofouling at coastal aquifers of North Jakarta. The seawater parameter such as salinity, water temperature, sea current and pH has a greater impact on the gradual lossed thickness for AF paints due to the dissolution of Cu_2O and other additives to seawater. The dissolution of Cu_2O took place in both initial and steady-state leachings of SPC-AF paint during service.

5. ACKNOWLEDGEMENTS

The National Research and Innovation Agency's Research Center for Metallurgy provided financial assistance for this work, which the authors gratefully recognize. The Research Center and Development of Roads and Bridge, Indonesia's Ministry of Public Works and Housing, provided the authors with really valuable assistance when they were performing their research, which they are grateful for.

6. REFERENCES

1. Priyotomo G, Nuraini L, Prifiharni S. A short review of antifouling paint perfomance in tropical seawater of Indonesia. Research & Development in Material Science. 2018;8(4). https://doi.org/10.31031/rdms.2018.08.000695
2. Peres RS, Armelin E, Moreno-Martinez JA, Aleman C, Ferreira CA. Transport and antifouling properties of papain-based antifouling coatings. Applied Surface Science. 2015;341:75-85. https://doi.org/10.1016/j.apsusc.2015.03.004
3. Ytreberg E, Bighiu MA, Lundgren L, Eklund B. XRF measurements of tin, copper and zinc in antifouling paints coated on leisure boats. Environmental Pollution. 2016;213:594-9. https://doi.org/10.1016/j.envpol.2016.03.029
4. Nuraini L, Prifiharni S, Priyotomo G, Sundjono S, Gunawan H, editors. Evaluation of anticorrosion and antifouling paint performance after exposure under seawater Surabaya–Madura (Suramadu) bridge. AIP Conference Proceedings; 2017: AIP Publishing.
5. Schwindt E, Gappa JL, Raffo MP, Tatián M, Bortolus A, Orensanz JM, et al. Marine fouling invasions in ports of Patagonia (Argentina) with implications for legislation and monitoring programs. Marine Environmental Research. 2014;99:60-8. https://doi.org/10.1016/j.marenvres.2014.06.006
6. Lord JP, Calini JM, Whitlatch RB. Influence of seawater temperature and shipping on the spread and establishment of marine fouling species. Marine Biology. 2015;162:2481-92. https://doi.org/10.1007/s00227-015-2737-2
7. Ferry M, Wan Nik W, Mohd Noor CW. The influence of seawater velocity to the corrosion rate and paint degradation at mild steel plate immersed in sea water. Applied Mechanics and Materials. 2014;554:218-21. https://doi.org/10.4028/www.scientific.net/AMM.554.218
8. Little BJ, Lee JS, Ray RI. The influence of marine biofilms on corrosion: a concise review. Electrochimica Acta. 2008;54(1):2-7. https://doi.org/10.1016/j.electacta.2008.02.071

9. Li L, Mahmoodian M, Li CQ. Effect of corrosion on mechanical properties of steel bridge elements. Maintenance, Safety, Risk, Management and Life-Cycle Performance of Bridges. 2018:1783-90. https://doi.org/10.1201/9781315189390-243
10. Li S, Dong H, Shi L, Li P, Ye F. Corrosion behavior and mechanical properties of Al-Zn-Mg aluminum alloy weld. Corrosion Science. 2017;123:243-55. https://doi.org/10.1016/j.corsci.2017.05.007
11. Almeida E, Diamantino TC, de Sousa O. Marine paints: the particular case of antifouling paints. Progress in organic coatings. 2007;59(1):2-20. https://doi.org/10.1016/j.porgcoat.2007.01.017
12. Turner A. Marine pollution from antifouling paint particles. Marine pollution bulletin. 2010;60(2):159-71. https://doi.org/10.1016/j.marpolbul.2009.12.004
13. Azemar F, Faÿ F, Réhel K, Linossier I. Development of hybrid antifouling paints. Progress in Organic Coatings. 2015;87:10-9. https://doi.org/10.1016/j.porgcoat.2015.04.007
14. Yebra DM, Kiil S, Dam-Johansen K. Antifouling technology—past, present and future steps towards efficient and environmentally friendly antifouling coatings. Progress in organic coatings. 2004;50(2):75-104. https://doi.org/10.1016/j.porgcoat.2003.06.001
15. Amal M, Wibowo J, Nuraini L, Senopati G, Hasbi M, Priyotomo G, editors. Antibacterial activity of copper oxide nanoparticles prepared by mechanical milling. IOP Conference Series: Materials Science and Engineering; 2019: IOP Publishing.
16. Carteau D, Vallée-Réhel K, Linossier I, Quiniou F, Davy R, Compère C, et al. Development of environmentally friendly antifouling paints using biodegradable polymer and lower toxic substances. Progress in Organic Coatings. 2014;77(2):485-93. https://doi.org/10.1016/j.porgcoat.2013.11.012
17. Liu C. Development of anti-fouling coating using in marine environment. Int J Environ Monit Anal. 2015;3:373. https://doi.org/10.11648/j.ijema.20150305.30
18. Nuraini L, Prifiharni S, Priyotomo G, editors. The corrosivity and performance evaluation of antifouling paint exposed in seawater Muara Baru Port, Jakarta. Journal of Physics: Conference Series; 2017: IOP Publishing.
19. Priyotomo G, Nuraini L, Gunawan H, Triwardono J, Sundjono S, Prifiharni S. A Preliminary field study of antifouling paint perfomance after short exposure in Mandara Bali, Indonesia. International Journal of Engineering, Transactions A: Basics,. 2021;34(4):976-86. https://doi.org/10.5829/ije.2021.34.04a.24
20. Jaić M, Palija T. High gloss finish: The impact of surface roughness on gloss. Zaštita materijala. 2015;56(4):457-62. https://doi.org/10.5937/zasmat1504457j
21. Fukumasu NK, Souza RM. Numerical evaluation of cohesive and adhesive failure modes during the indentation of coated systems with compliant substrates. Surface and Coatings Technology. 2014;260:266-71. https://doi.org/10.1016/j.surfcoat.2014.07.093
22. Amara I, Miled W, Slama RB, Ladhari N. Antifouling processes and toxicity effects of antifouling paints on marine environment. A review. Environmental toxicology and pharmacology. 2018;57:115-30. https://doi.org/10.1016/j.etap.2017.12.001
23. Rodriguez SGS, Sithole N, Dhakal N, Olive M, Schippers JC, Kennedy MD. Monitoring particulate fouling of North Sea water with SDI and new ASTM MFI0. 45 test. Desalination. 2019;454:10-9. https://doi.org/10.1016/j.desal.2018.12.006
24. Le Menn M, Albo PAG, Lago S, Romeo R, Sparasci F. The absolute salinity of seawater and its measurands. Metrologia. 2018;56(1):015005. https://doi.org/10.1088/1681-7575/aaea92
25. Wouthuyzen S, Tarigan S, Kusmanto E, Supriyadi HI, Sediadi A. Measuring sea surface salinity of the Jakarta bay using remotely sensed of ocean color data acquired by modis sensor. Marine Research in Indonesia. 2011;36(2):51-70. https://doi.org/10.14203/mri.v36i2.41
26. Kale VS. Consequence of temperature, pH, turbidity and dissolved oxygen water quality parameters. International Advanced Research Journal in Science, Engineering and Technology. 2016;3(8):186-90.
27. Leidonald R, Muhtadi A, Lesmana I, Harahap Z, Rahmadya A, editors. Profiles of temperature, salinity, dissolved oxygen, and pH in Tidal Lakes. IOP Conference Series: Earth and Environmental Science; 2019: IOP Publishing.
28. Jaud T, Dragon A-C, Garcia JV, Guinet C. Relationship between chlorophyll a concentration, light attenuation and diving depth of the southern elephant seal Mirounga leonina. 2012. https://doi.org/10.1371/journal.pone.0047444
29. Assiry A, Gaily M, Alsamee M, Sarifudin A. Electrical conductivity of seawater during ohmic heating. Desalination. 2010;260(1-3):9-17. https://doi.org/10.1016/j.desal.2010.05.015
30. Holm ER, Kavanagh CJ, Meyer AE, Wiebe D, Nedved BT, Wendt D, et al. Interspecific variation in patterns of adhesion of marine fouling to silicone surfaces. Biofouling. 2006;22(4):233-43. https://doi.org/10.1080/08927010600826129
31. Swain GW, Kovach B, Touzot A, Casse F, Kavanagh CJ. Measuring the performance of today's antifouling coatings. Journal of Ship Production. 2007;23(03):164-70. https://doi.org/10.5957/jsp.2007.23.3.164
32. Takahashi K. Release rate of biocides from antifouling paints. Ecotoxicology of antifouling biocides. 2009:3-22. https://doi.org/10.1007/978-4-431-85709-9_1

Persian Abstract

چکیده

بیوساید مبتنی بر مس بیشتر به عنوان افزودنی اولیه رنگ ضد رسوب (AF) در اندونزی به ویژه در مخازن استفاده می شود. ارزیابی کارایی رنگ AF در جایی انجام شد که رنگ ضد خوردگی (AC) نیز به عنوان مرجع بود. پانل ها با هر دو رنگ تا دوازده ماه در معرض اعماق دریاهای مختلف تا سه متر قرار گرفتند. اندازه گیری پارامترهای آب دریا شامل هدایت آب، pH، دما، اکسیژن محلول و شوری انجام شد. بر روی پانل های رنگ آمیزی شده با AF، رسوب زیستی دریایی چسبیده یا کمتری وجود نداشت، اما در پانل های رنگ شده با AC تا دوازده ماه قرار گرفتن در معرض میدان در اعماق مختلف دریا وجود نداشت. هیچ تفاوتی بین خواص رنگ های AF قبل و بعد از قرار گرفتن در اعماق مختلف دریا وجود نداشت. عملکرد بازدارنده رنگ AF به وجود لایه AF حاوی بیوسید Cu_2O بستگی دارد که در آن ضخامت آن لایه با افزایش زمان قرار گرفتن در معرض کاهش می یابد.

IJE TRANSACTIONS A: Basics Vol. 37 No. 01, (January 2024) 178-186

International Journal of Engineering

Journal Homepage: www.ije.ir

Laser Scanning Speed Influences on Assessment of Laser Remelted Commercially Pure Titanium Grade 2

T. Mohammed Naji, M. A. Ali Bash, A. M. Resen*

Department of Production Engineering and Metallurgy, University of Technology, Baghdad, Iraq

P A P E R I N F O

Paper history:
Received 29 July 2023
Received in revised form 15 September 2023
Accepted 16 September

Keywords:
Commercially Pure Titanium
Laser Re-melting
Microhardness
AFM Analysis
Pitting Corrosion

A B S T R A C T

In this research, the influences of laser surface remelting using different scanning speeds on the microstructure, roughness, and hardness of Commercial pure Titanium (Grade 2) were investigated. High power Nd: YAG pulsed laser was used. The laser scanning speeds used in this study were 4, 6, 8, and 10 mm/s and the other laser parameters (power, pulse frequency, beam diameter) were constant. The corrosion performance of the laser surface remelted and Cp titanium was then evaluated by potential dynamic measurements in a 3.5% NaCl solution. The results revealed that due to the diffusionless transformation after laser surface treatment and the formation of the martensite phase, the surface post-laser treatment was significantly different from those before the treatment. The results were indicated using an optical microscope, FE-SEM, XRD, AFM, and microhardness analysis. It was found the lowest scanning speed, 4 mm/s, had the slightest roughness and the smallest average grain size (26.06 nm) due to the high input energy and slow cooling rate, while the highest scanning speed (10 mm/s) had the greatest microhardness (291.5 Hv) due to the short interaction time between the substrate surface and laser beam and the higher cooling rate. The results also demonstrated the obvious improvement in the pitting resistance of Cp Ti in harsh environments as a result of the influence of laser remelting.

***doi**: 10.5829/ije.2024.37.01a.16*

Graphical Abstract

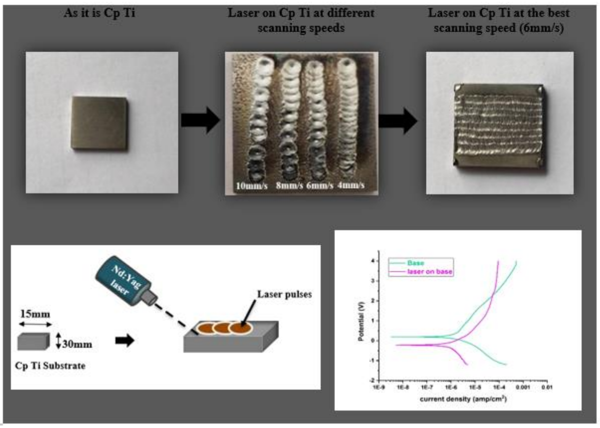

1. INTRODUCTION

In recent years, titanium as a metal and its alloys have attracted interest as a material in the marine, spacecraft, automotive, petrochemical, biomedical, and energy industries as well as steam condensers in the power generation industry (1, 2). Titanium alloy has great properties due to its high strength-to-weight ratio, low

*Corresponding Author Email: *Ali.M.Resen@uotechnology.edu.iq* (A. M. Resen)

Please cite this article as: Mohammed Naji T, Ali Bash MA, Resen AM. Laser Scanning Speed Influences on Assessment of Laser Remelted Commercially Pure Titanium Grade 2. International Journal of Engineering, Transactions A: Basics, 2024;37(01):178-186.

density, and high corrosion resistance (3, 4). Despite these excellent properties and high affinity for oxygen reaction to form spontaneous beneficial surface oxide film. However, any breakdown of the passivity film can lead to a localized attack such as pitting corrosion (5, 6). Furthermore, the absence of an oxygen source condition may result in the disability of regenerating this protective film (7). Surface engineering is a field of science that includes design, modification, and technique to enhance the performance of the bulk surface for different chemical, physical, and mechanical properties (8, 9). Surface engineering is crucial to providing high-quality services and preventing failure for an extended time (10). Surface modification of Cp Ti is considered an effective method to improve pitting corrosion (11). Modifying the microstructure of the base metal plays an important role in the improvement of performance (9). Laser surface remelting (LSR) is an emerging processing technology that involves rapid melting and cooling when a laser beam passes through a small localized region on a sample surface (12). LSR can remarkably provide metastable crystalline phase and grain refinement on the Ti alloy surface without compromising its bulk mechanical properties (13). The best results can be obtained from the laser beam interacting with the surface by controlling the process-independent parameters such as power, speed, pulse energy, etc. This enables highly accurate control of the depth, extension, and temperature change of the region subjected to the radiation of a laser, which may also be observed. Due to its outstanding adaptability and chemically clean processing methods, materials surface processing procedures can be provided with high added value and with respect for the environment. Laser treatment of materials produces no chemicals or significant waste. These characteristics lead to high processing speeds and inexpensive costs, which have an impact on applications involving the processing of materials (14). The primary laser parameters that can be influenced during processing are laser power, beam radius, specimen or work-piece velocity, and beam mode, which can be stationary, rotating, top hat, or Gaussian. In addition, the alloy's composition and concentration, as well as the concentration and flow rate of any processing-related gases, like nitrogen in the case of alloying. Further important factors include the dimensions, particularly the workpiece's thickness and its capacity to absorb laser energy (14). Furthermore, with increasing scanning speed, the remelting depth decreased (15). As the laser power rises, the roughness parameters increase too (16). There are few attempts in the literature to explain the detailed information of titanium alloys using laser treatment. Sun et al. (15) investigated the influence of laser remelting on the corrosion behavior of Cp Ti (Grade 2) in 3% NaCl. It was discovered that laser surface remelting significantly increased pitting potential. Bahloul et al. (16) used a short pulse Nd: YAG laser treatment to increase the surface corrosion resistance and fretting wear of Ti plates (Grade 4) by raising the surface hardness. The objective of this paper is to study the influence of laser remelting scanning speed on the general surface properties assessment of Cp Ti (Grade 2). However, the microstructure, phase, morphology, microhardness, and corrosion resistance have been reported. We leveraged the versatile cooling rate capabilities of laser surface remelting to vary critical microstructure attributes within the melted zone. This is done by altering the laser scanning speed of the Laser surface remelting.

2. MATERIALS AND METHODS

2. 1. Materials Characterization A square-shaped commercially pure titanium Cp Ti (grade 2) specimen of dimensions 15 mm*15 mm* 3 mm was chosen as the substrate material. Table 1 shows the chemical composition of the Cp Ti substrate as received from the supplier was agreed with ASTM B265 (17).

2. 2. Laser Treatment A PMT4297 model (Nd: YAG) pulsed laser has been utilized as the laser surface treatment (LST) platform. It emits radiation on a single wavelength of 1064 nm. The laser beam was focused on the specimen surface placed with suitable clamped onto a CNC table and scanned over the surface of specimens to generate a controlled overlap. The laser was operated with a typical repetition rate of 2 Hz. The overlapped tracks of approximately 25% were carried out to cover all the surface of the specimens. To select the best laser parameters for overlapping, it's essential to make a careful analysis of laser processing parameters. As indicated in Table 2, several experiments were conducted with various scanning speeds and constant values for other parameters (power, pulse frequency, and beam diameter). The shrouding gas for the laser-generated melt pool was argon gas.

2. 3. Characterization Techniques Various analytical techniques were used for the characterization of the Cp titanium before and after laser treatment. The

TABLE 1. Chemical composition of CP Ti grade according to ASTM B 265

C, max.	Element	H, max.	N, max.	O_2 max.	Fe max.	Other Elements max. each	Other Elements, max. total
0.08	Standard	0.015	0.03	0.18	0.2	0.1	0.4

surface microstructure was monitored by optical and Field emission scanning electron microscope (FESEM). X-ray diffraction test (XRD) was used to present the phases of Cp Ti before and after laser treatment. Topography, nano roughness, and grain size were determined using an Atomic Force Microscope (AFM). Vickers microhardness (Hv) measurements were evaluated using a (TH714) tester under 300g load for 15s. The corrosion rate in (mm/y) was determined using the polarization method after immersion in 3.5% NaCl by using a CHI 604e electrochemical system.

3. RESULTS

3. 1. Microstructure Results To study the effect of laser parameters on the general properties of Cp Ti, it's important to the microstructure's alterations from a top surface. As illustrated in Figure 1 (a, b), optical and FESEM images revealed that the Cp Ti is composed of a single alpha (α) phase that has been transformed to an acicular martensite phase (α') as a result of the high cooling rate and diffusionless transition. Figure 1(a) shows that the α phase grains are intermingled with small yet noticeable pockets of beta (β) grains, these beta pockets formed as a result of the presence of minor impurities (O_2, H, N, C, Fe) that revealed in Table 1. About 98 % or more alpha phase (α), the remaining being iron stabilized beta phase (18). While Figure 2 reveals the plate-like microstructure of martensite (α') that has a hexagonally packed crystal structure (HCP). As the laser intensity is highest in the middle of the pulses and decreases as one moves toward the sides of the pulse, the alpha prime martensite plates (α') were oriented toward the heat transfer direction (16). This is the reason for the beach marks on the edges of the pulse revealed in Figure 1(b).

Figure 3 displays the optical microscope images of the laser tracks on the (Cp Ti G2) substrate at various scan speeds. On the surface of Cp Ti, it can be noticed that as the laser speed decreased, the number of pulses per unit area increased (1.4 for the 10mm/s speed and 1.5 for the 4mm/s speed). Lower laser scanning speeds give the laser beam more time to alter the surface and more opportunities to produce more pulses on the Cp Ti surface (19).

The relationship between the number of laser pulses per unit area and laser speed is revealed in Figure 4. With increasing the laser speeds (4,6,8,10 mm/s) the heat input was deceased (200, 133.33, 100, 80J/mm, respectively) because as speed increased the interaction time decreased between the laser and substrate.

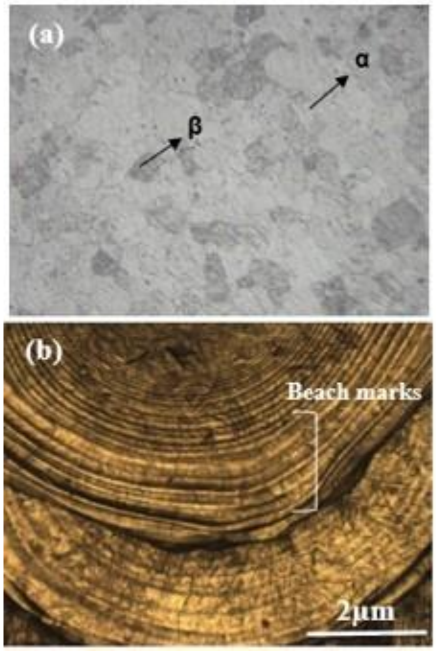

Figure 1. Optical micrographs showing the key micro-constituents for the Cp Ti substrate (a) As it is at magnification 125x (b) After laser treatment at magnification 10x

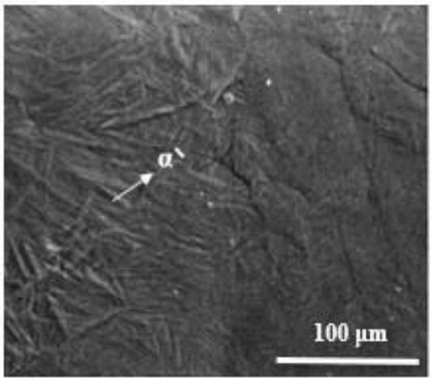

Figure 2. FESEM image of Cp Ti after laser treatment showing the plates-like structure of martensite phase (α`)

TABLE 2. The laser processing parameters used in laser surface treatment of Cp Ti in this investigation

Laser parameters	Track No.1	Track No.2	Track No.3	Track No.4
Power (W)	800	800	800	800
Pulse frequency (Hz)	2	2	2	2
Traverse speed (mm/s)	10	8	6	4
Interaction time (s)	0.08	0.1	0.133	0.2
Beam diameter (mm)	0.8	0.8	0.8	0.8
Heat input (J/mm)	80	100	133.33	200

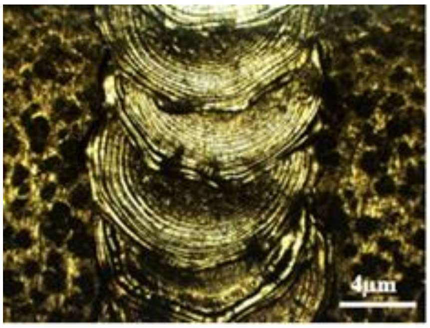

(a)

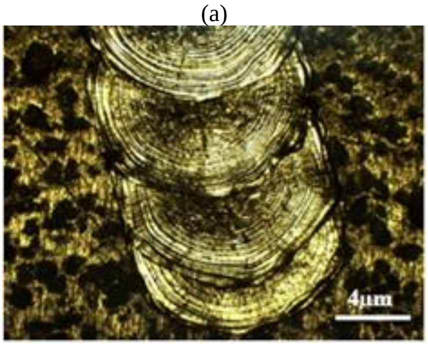

(b)

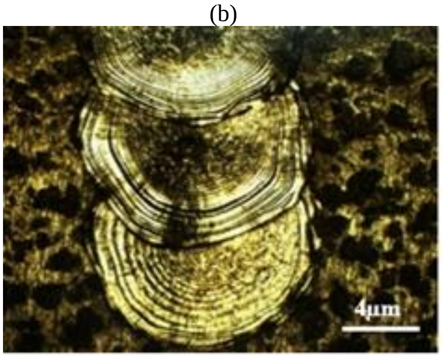

(c)

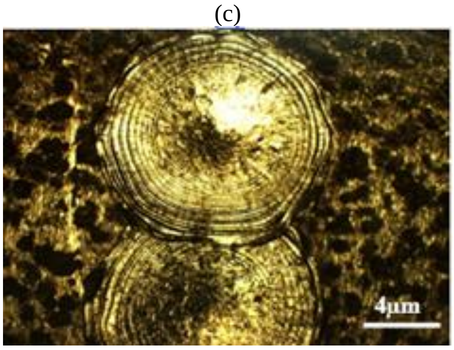

(d)

Figure 3. Shows the effect of laser scanning speed on the number of pulses per unit area. (a) Track No.1at V= 10mm/s (b) Track No.2 at V=8mm/s (c) Track No.3 at V=6mm/s (d) Track No.4 at V=4mm/s

3. 2. AFM Results

The topography and roughness of the Cp Ti surface were observed using AFM as shown in Table 3, and Figure 5. The results show that as the laser scanning speed increased, the surface roughness increased. Since the size of grains depends on the rate of cooling, the higher the cooling rate and higher thermal gradient (at the lowest laser speed of 4 mm/s) the smaller the size of grains (26.06nm) which agrees with reported data by Mahamood et al. (20). The relation between roughness and laser scanning speed can be revealed in Figure 6. It's important to note the AFM roughness values were taken from the middle of the pulse. The track with a laser speed of 4mm/s had minimal roughness (1.499nm), while the track with the highest laser scanning speed of 10mm/s in the investigated study had a higher roughness (8.948nm). Because the pulse edges were rougher than the middle due to the gradient of heat distribution. The track at 6 mm/s has a lower range of grain diameter (homogenous distribution) along the surface Figure 5g after laser remelting if compared with the rest tracks. The effect of heat input on the resultant grain diameter of different laser scanning speeds on Cp Ti can be clearly observed in Figure 7.

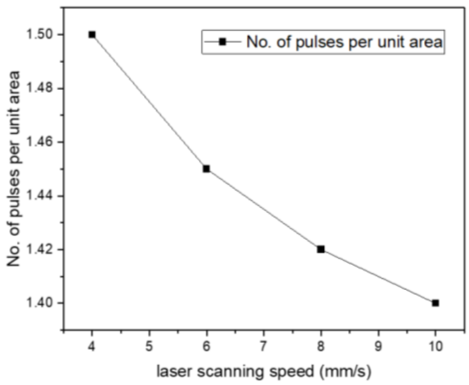

Figure 4. Shows the relationship between No. of laser pulses per unit area and laser speed

TABLE 3. surface topography and roughness for the laser tracks analyzed by AFM

No. of Track	Laser Speed (mm/s)	Sa (nm)	Sq (nm)	Grain dia. (nm)
1	10	6.180	8.948	61.05
2	8	5.454	7.849	57.93
3	6	1.637	2.208	39.39
4	4	1.177	1.499	26.06

3. 3. XRD Results

Phase identification of the Cp Ti before and after the laser surface treatment was established from an X-ray diffraction pattern. As illustrated in Figure 8 the Cp Ti before laser treatment had alpha (α) microstructure Figure 8a and it would transform to martensite structure (α') Figure 8b after the surface laser treatment due to the diffusion-less transformation and high cooling rate (15).

After laser remelting to the surface, the peaks become sharper as a result of the crystallinity.

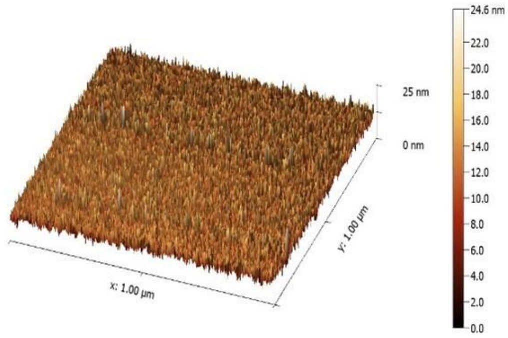

(a)

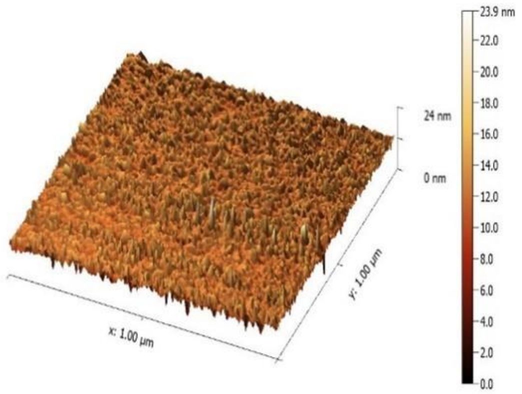

(b)

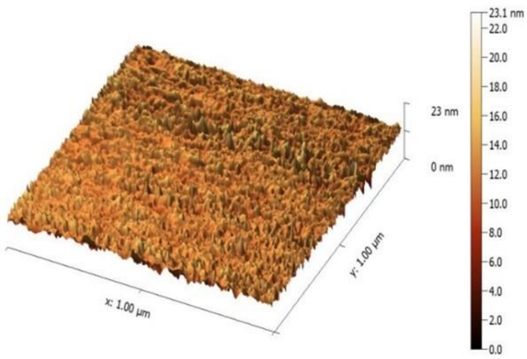

(c)

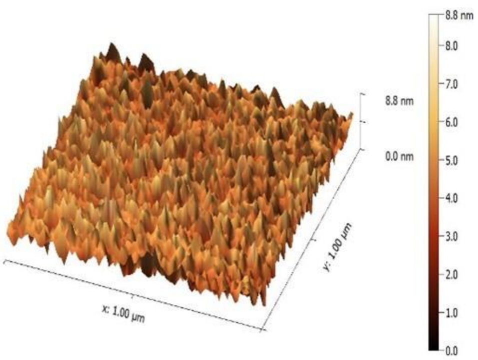

(d)

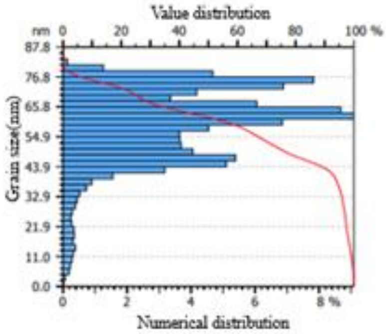

(e)

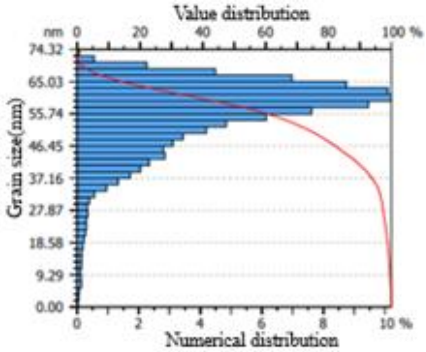

(f)

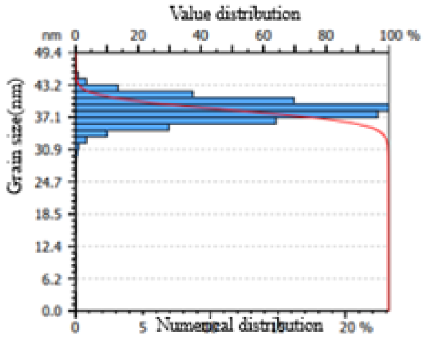

(g)

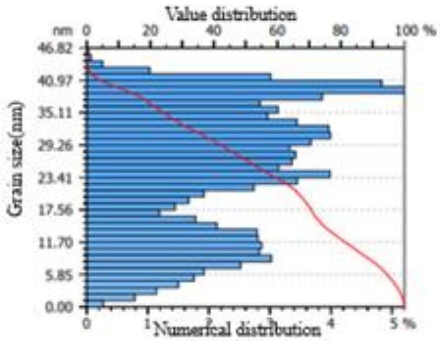

(h)

Figure 5. AFM 3D height surface topography of laser tracks on Cp Ti G2 at (a) 10 mm/s scanning speed (b) 8 mm/s scanning speed (C) 6 mm/s scanning speed (d) 4 mm/s scanning speed (e), (f), (g), (h) reveals the grains agglomeration at 10 mm/s, 8 mm/s, 6 mm/s, and 4 mm/s respectively

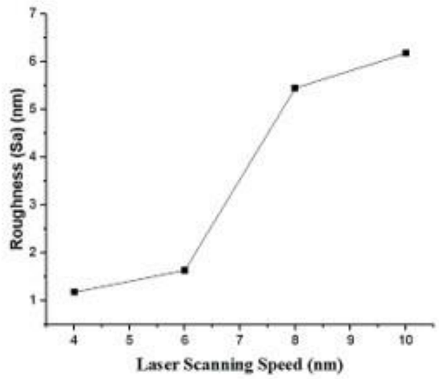

Figure 6. Shows the relationship between roughness and laser scanning speed

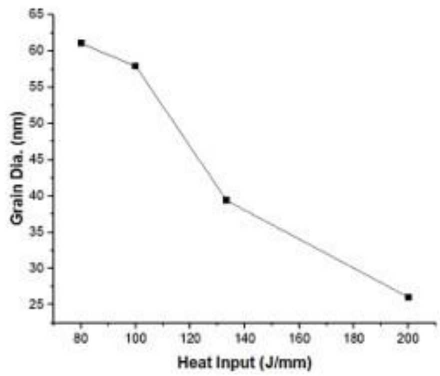

Figure 7. Shows the variation of heat input and grain diameter resulting from AFM analysis with laser scanning speed used in this investigation

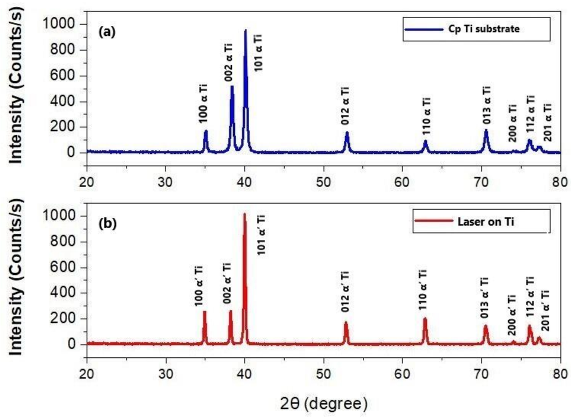

Figure 8. XRD of (a) Cp Ti and (b) after surface laser treatment shows the phase transformation from alpha to the martensite phase

3. 4. Microhardness Results

Vickers microhardness was also used to evaluate the tracks after laser remelting of Cp Ti at various laser scanning speeds. As the laser scanning speed increased the hardness increased as shown in Table 4. The laser-material interaction time is low at higher laser scanning speeds, and subsequently higher cooling rate and thermal gradient than the lower laser scanning speeds. Rapid solidification and cooling that occurred at high laser speed induced a higher microhardness value which agrees with reported data by Tavakoli et al. (21).

The effect of heat input and interaction time between the laser beam and Cp Ti can be observed in Figure 9. This reveals the gradients of microhardness values depending on heat input in the region of laser – CpTi interaction. The maximum microhardness can result from higher scanning speed and lower heat input. That means the heat transfer was higher than at high heat input and subsequently higher cooling rate.

In order to determine the corrosion rate of the Cp Ti after laser treatment, it must overlap the tracks on the surface. So, it's necessary to select the best suitable parameters of the laser remelting process to overlap. Track No. 3 with a scanning speed of 6 mm/s was selected to produce the overlapped samples. Due to the results obtained from tests previously as illustrated in this study. The appearance of the surface after laser treatment is shown in Figure 10, which also exhibits successful laser overlap over the whole Cp Ti surface. It can observe the distribution of pulses throughout the surface.

3. 5. Chemical Corrosion Results

Despite of excellent corrosion resistance of Ti, further improvement

TABLE 4. Revealed the microhardness results at each laser scanning speed using Vickers microhardness analysis

No. of Track	Laser Speed (mm/s)	Microhardness Value (Hv)
1	10	291.5
2	8	251
3	6	220.9
4	4	219.3

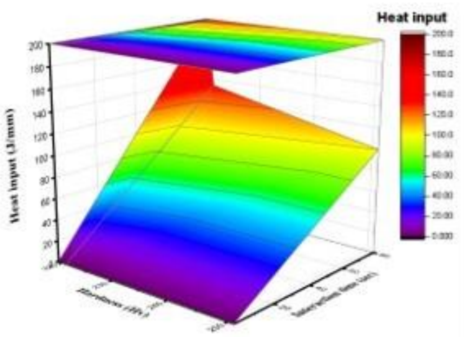

Figure 9. Indicates the relationship between microhardness, interaction time of the laser beam, and heat input of the different laser scanning speeds used in this investigated study

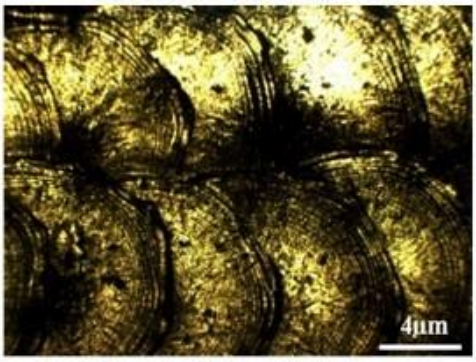

Figure 10. Surface appearance after the pulsed laser surface remelting at 6 mm/s scanning speed

is still required. In order to enlarge Ti application areas in severe environments. Laser surface remelting of Ti could be a promising tool to be approved in this area. The corrosion rate in millimeters per year (mm/y) for the as-received Cp Ti substrate and the substrate after laser treatment was evaluated by using an electrochemical system. The OCP value was increased from - 0.383 to - 0.362 volts after surface laser treatment of the Ti substrate. This pushed the corr. potential upward, indicating that the laser treatment increases substrate surface protection, as shown in Figure 11. Also, it can be observed from the curve after laser remelting, that the voltage decreases but returns and rises by virtue of the laser treatment that changes the properties of the surface layer that is subjected to interaction with the solution. When comparing the curve with the condition before laser treatment, it was found that the voltage decreases gradually and continuously.

Tafel plots in Figure 12 revealed that there are no pitting corrosion sites before and after the laser treatment (negative loop) during immersion of the laser-treated substrate in the salt solution. However, despite that, the laser treatment showed an additional improvement through the decrease in the value of the current density from $7.969*10^{-7}$ to $3.969*10^{-7}$ Amp which agree with

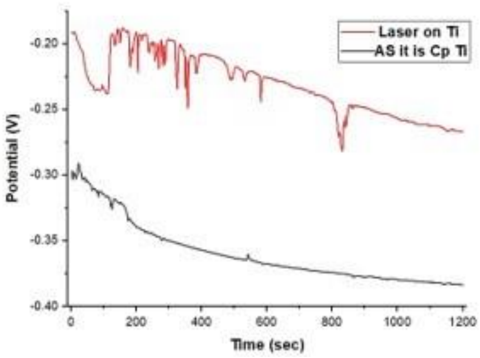

Figure 11. OCP curves for the Cp Ti before and after the laser treatment

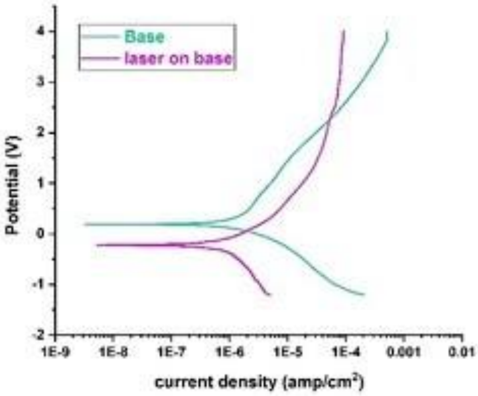

Figure 12. Cyclic polarization behavior for the base Cp Ti substrate and the Cp Ti substrate after laser treatment in 3.5% NaCl solution

reported data by Tavakoli et al. (21). Furthermore, there is a noble shift of the curve if compared with untreated Ti. The E. corr decreased (from -0.194 to -0.223 volt) after the protection of the Ti surface using laser treatment. Due to the martensitic phase transformation and rapid solidification resulting from laser surface remelting which lead to decreased corrosion rate (15). Table 5 gives the potentiodynamic corrosion results of samples before and after the surface treatment. These findings indicated that the probability of pitting prediction and propagation is very low.

TABLE 5. Chemical corrosion parameters and results

ITEM	E corr. (volt)	I corr. (Amp.)	Corr. Rate mm/y	OCP (volt)
Ti substrate	-0.194	7.969×10^{-7}	1.806×10^{-2}	-0.383
Laser on Ti substrate	-0.223	3.969×10^{-7}	8.995×10^{-3}	-0.362

4. CONCLUSION

The variation of microstructure, morphology, constituent phases, microhardness, and corrosion resistance of a laser-remelted Cp Ti with changing laser scanning speeds have been studied. The laser scanning speed was varied between 4 and 10 mm/s. The results revealed the obtaining of a completely different microstructure as a result of rapid cooling rates. As the scanning speed decreases, the surface roughness and average grain diameter decrease. Microhardness values increased with increasing the laser scanning speed. The maximum value of microhardness in this investigated study was 291.5 Hv. at a scanning speed of 10 mm/s. Due to the short interaction time between the substrate surface and laser beam and high cooling rate. Also, this study demonstrated the obvious improvement in corrosion resistance after laser remelting of the Ti surface. Laser surface remelting leads to a decrease in the corrosion rate from 1.806× 10^{-2} to 8.995× 10^{-3} mm/y and enlarges the materials application range in severe service environments.

5. REFERENCES

1. Poulon-Quintin A, Watanabe I, Watanabe E, Bertrand C. Microstructure and mechanical properties of surface treated cast titanium with Nd: YAG laser. Dental Materials. 2012;28(9):945-51. https://doi.org/10.1016/j.dental.2012.04.008
2. Syaripuddin S, Sopiyan, S., Aditya, S., Yudanto, S. D., and Susetyo, F. B. . Synthesis of Hard Layer by Titanium Addition During Welding Process and Quenched Directly. International Journal of Engineering, IJETransactions C: Aspects. 2023;36(3): 532–9. https://doi.org/10.5829/ije.2023.36.03c.13
3. Tekle Abegaz S. We are IntechOpen, the world's leading publisher of Open Access books Built by scientists, for scientists. 2021.
4. Abaei M, Rahimipour MR, Farvizi M, Eshraghi MJ. Microstructure and Corrosion Behavior of Al-Cu-Fe Quasi-crystalline Coated Ti-6Al-4V Alloy. International Journal of Engineering, Transactions A: Basics. 2023;36(10):1880-91. https://doi.org/10.5829/ije.2023.36.10a.13
5. Prando D, Brenna A, Diamanti MV, Beretta S, Bolzoni F, Ormellese M, et al. Corrosion of titanium: Part 1: Aggressive environments and main forms of degradation. Journal of applied biomaterials & functional materials. 2017;15(4):e291-e302. https://doi.org/10.5301/jabfm.5000387
6. Jaquez-Muñoz J, Gaona-Tiburcio C, Lira-Martinez A, Zambrano-Robledo P, Maldonado-Bandala E, Samaniego-Gamez O, et al. Susceptibility to pitting corrosion of Ti-CP2, Ti-6Al-2Sn-4Zr-2Mo, and Ti-6Al-4V alloys for aeronautical applications. Metals. 2021;11(7):1002. https://doi.org/10.3390/met11071002
7. Seo B, Park H-K, Park C-S, Park K. Role of Ta in improving corrosion resistance of titanium alloys under highly reducing condition. Journal of Materials Research and Technology. 2023;23:4955-64. https://doi.org/10.1016/j.jmrt.2023.02.158
8. Matthews A, Artley R, Holiday P. 2005 Revisited-the UK Surface Engineering Industry to 2010: An Update of the'UK Engineering Coatings Industry in 2005'Report: National Surface Engineering Centre, NASURF; 1998.
9. Merche D, Vandencasteele N, Reniers F. Atmospheric plasmas for thin film deposition: A critical review. Thin Solid Films. 2012;520(13):4219-36. https://doi.org/10.1016/j.tsf.2012.01.026
10. Duley WW. Laser processing and analysis of materials: Springer Science & Business Media; 2012.
11. Sasikumar Y, Indira K, Rajendran N. Surface modification methods for titanium and its alloys and their corrosion behavior in biological environment: a review. Journal of Bio-and Tribo-Corrosion. 2019;5:1-25. https://doi.org/10.1007/s40735-019-0229-5
12. Manna I, Majumdar JD, Chandra BR, Nayak S, Dahotre NB. Laser surface cladding of Fe–B–C, Fe–B–Si and Fe–BC–Si–Al–C on plain carbon steel. Surface and Coatings Technology. 2006;201(1-2):434-40. https://doi.org/10.1016/j.surfcoat.2005.11.138
13. Bi G, Chen S, Jiang J, Li Y, Chen T, Chen X-B, et al. Effects of Laser Surface Remelting on Microstructure and Corrosion Properties of Mg-12Dy-1.1 Ni Alloy. Journal of Materials Engineering and Performance. 2023;32(6):2587-97. https://doi.org/10.1007/s11665-022-06933-y
14. Merino RI, Laguna-Bercero MA, Lahoz R, Larrea Á, Oliete PB, Orera A, et al. Laser processing of ceramic materials for electrochemical and high temperature energy applications. boletín de la sociedad española de cerámica y vidrio. 2022;61:S19-S39. https://doi.org/10.1016/j.bsecv.2021.09.007
15. Sun Z, Annergren I, Pan D, Mai T. Effect of laser surface remelting on the corrosion behavior of commercially pure titanium sheet. Materials Science and Engineering: A. 2003;345(1-2):293-300. https://doi.org/10.1016/S0921-5093(02)00477-X
16. Bahloula A, Sahourb M, Oumeddoura R, Pillonc G. Structural characterization and surface modification of titanium plates after Nd: YAG laser treatment. Portugaliae Electrochimica Acta. 2020;38(4):215-28. https://doi.org/10.4152/pea.202004215
17. B265-11 A, editor Standard Specification for Titanium and Titanium Alloy Strip, Sheet, and Plate2011: American Society for Testing Materials.
18. Lütjering G, Williams J, Gysler A. Microstructure and mechanical properties of titanium alloys. Microstructure And Properties Of Materials: (Volume 2)2000. p. 1-77.
19. Asalzadeh S, Yasserian K. The Effect of Various Annealing Cooling Rates on Electrical and Morphological Properties of TiO 2 Thin Films. Semiconductors. 2019;53:1603-7. https://doi.org/10.1134/S1063782619160036
20. Mahamood RM, Akinlabi ET, Akinlabi S. Laser power and scanning speed influence on the mechanical property of laser metal deposited titanium-alloy. Lasers in Manufacturing and Materials Processing. 2015;2:43-55. https://doi.org/10.1007/s40516-014-0003-y
21. Khosroshahi M, Tavakoli J, Mahmoodi M. Characterization of Nd: YAG laser radiation effects on Ti6Al4V physico-chemical properties: an in vivo study. International Journal of Engineering. 2007;20(1):1-11.

Persian Abstract

چکیده

تأثیر ذوب مجدد سطح لیزر با استفاده از سرعت‌های مختلف روبشی بر روی ریزساختار، زبری و سختی تیتانیوم خالص تجاری (درجه 2) در این تحقیق مورد بررسی قرار گرفت. از لیزر پالسی Nd:YAG با توان بالا استفاده شد. سرعت اسکن لیزر مورد استفاده در این مطالعه 4، 6، 8 و 10 میلی‌متر بر ثانیه و سایر پارامترهای لیزر (قدرت، فرکانس پالس، قطر پرتو) ثابت بودند. عملکرد خوردگی سطح لیزر دوباره ذوب شد و Cp تیتانیوم سپس با اندازه‌گیری‌های دینامیکی بالقوه در محلول NaCl 3.5% ارزیابی شد. نتایج نشان داد که به دلیل تبدیل بدون انتشار پس از درمان سطحی لیزر و تشکیل فاز مارتنزیت، تیمار پس از لیزر سطح به طور قابل توجهی با قبل از درمان متفاوت بود. نتایج با استفاده از میکروسکوپ نوری، FE-SEM، XRD، AFM و تجزیه و تحلیل میکروسختی نشان داده شد. مشخص شد که کمترین سرعت اسکن، 4 میلی‌متر بر ثانیه، به دلیل انرژی ورودی بالا و سرعت خنک‌کنندگی پایین، کمترین زبری و کمترین اندازه متوسط دانه (26.06 نانومتر) را دارد، در حالی که بالاترین سرعت اسکن (10 میلی‌متر بر ثانیه) است. بیشترین ریزسختی (291.5 Hv) را به دلیل زمان اندرکنش کوتاه بین سطح بستر و پرتو لیزر و سرعت خنک کنندگی بالاتر داشت. نتایج همچنین بهبود آشکار مقاومت حفره‌ای CpTi را در محیط‌های سخت در نتیجه تأثیر ذوب مجدد لیزر نشان داد.

IJE TRANSACTIONS A: Basics Vol. 37 No. 01, (January 2024) 187-200

International Journal of Engineering

Journal Homepage: www.ije.ir

Energy Efficiency with Internet of Things Based Fuzzy Inference System for Room Temperature and Humidity Regulation

F. Furizal[a], S. Sunardi*[b], A. Yudhana[b], R. Umar[a]

[a] *Department of Informatics, Universitas Ahmad Dahlan, Indonesia*
[b] *Department of Electrical Engineering, Universitas Ahmad Dahlan, Indonesia*

P A P E R I N F O

Paper history:
Received 06 August 2023
Received in revised form 11 September 2023
Accepted 12 September 2023

Keywords:
Control System
Fuzzy Control
Energy Efficiency
Saving Consumption
Comfortable Environment

A B S T R A C T

Energy consumption is a crucial aspect in the effort to optimize the utilization of resources and reduce energy wastage. Focusing on energy efficiency can result in operational cost savings, a reduction in greenhouse gas emissions, and support for environmental sustainability for future generations. Therefore, it is important to consider energy efficiency in daily life, especially in the use of electricity for electronic devices. This research aims to compare the energy efficiency of two different approaches to Air Conditioner (AC) usage: the manual method and the fuzzy logic method. The manual method involves eight tests with direct power measurements over a 30-minute period at various AC temperature settings, namely 18°C, 20°C, 23°C, 24°C, 25°C, 26°C, 27°C, and 30°C. On the other hand, the fuzzy logic method involves six tests allowing for dynamic temperature adjustments based on room conditions. The research findings indicate that the fuzzy logic method achieves lower average power consumption, except at 30°C, where the manual method is slightly more efficient (a difference of 140,745 watts). This difference is primarily attributed to the "cooling and fan" mode used at lower temperatures in the manual method, resulting in higher power consumption. Furthermore, this research reveals the potential of the fuzzy logic in optimizing AC power usage based on real-time conditions, achieving approximately a 41.96% energy savings. The primary contribution of this study is to provide practical insights into how the fuzzy logic method can significantly reduce AC energy consumption, support energy efficiency efforts, and contribute to environmental sustainability.

doi: *10.5829/ije.2024.37.01a.17*

1. INTRODUCTION

The Internet of Things (IoT) has become one of the most prominent technologies in the evolving digital era (1-5). IoT has transformed the way humans interact with devices and systems in their surroundings, ranging from smart homes to autonomous vehicles (6-8). IoT is often integrated with artificial intelligence (AI) (9). One area where IoT has made a significant contribution is in enhancing comfort and energy efficiency in the environment, especially in regulating room temperature and humidity (10-12). The regulation of room temperature and humidity is a crucial aspect of creating a comfortable and productive environment. Excessive heat or cold, as well as inappropriate humidity levels, can disrupt the comfort and health of room occupants. Moreover, inefficient regulation of temperature and humidity can lead to energy wastage, negatively impacting the environment, both directly and indirectly.

Currently, tools widely available in the market tend to favor manual settings, such as the implementation of the ON/OFF system. This manual method is inefficient in energy usage because it is unresponsive to minor temperature fluctuations, does not consider humidity, and results in significant energy wastage. The consequences include increased energy costs, excessive utilization of natural resources, inconvenience to room occupants, and an overall decrease in energy efficiency.

In an effort to effectively enhance the regulation of room temperature and humidity, Fuzzy Inference Systems (FIS) have emerged as efficient solutions (13-15). FIS is a regulatory method rooted in fuzzy logic, enabling machines to make decisions based on multiple influencing variables (16). In the context of regulating

*Corresponding Author Email: sunardi@mti.uad.ac.id (S. Sunardi)

Please cite this article as: Furizala F., Sunardi S., Yudhana A, Umar R. Energy Efficiency with Internet of Things Based Fuzzy Inference System for Room Temperature and Humidity Regulation. International Journal of Engineering, Transactions A: Basics, 2024;37(01):187-200.

room temperature and humidity, FIS empowers IoT devices to intelligently manage indoor temperature and humidity based on specified parameters. Therefore, in this study, researchers will investigate energy consumption when employing FIS and IoT to control room temperature and humidity using AC. Energy consumption plays a pivotal role in achieving resource efficiency (17-19).

This research aims to reduce unnecessary energy consumption, safeguard the environment, promote sustainability, enhance productivity, foster technological innovation, and improve quality of life. By developing more efficient solutions, this research yields benefits in the form of energy conservation, reduction in greenhouse gas emissions, enhanced operational efficiency, adoption of intelligent technologies, and the creation of a more comfortable and healthier environment. This objective directs the transition towards wiser, more sustainable, and more impactful energy utilization for individuals. This research represents a continuation of prior studies on temperature and humidity control systems utilizing FIS and IoT-based AC (20). However, this study specifically concentrates on devising an effective and efficient AC control system for regulating room temperature and humidity using Tsukamoto's FIS and IoT methods, without evaluating the efficiency of energy consumption, both in the short-term and long-term usage (20). Particularly, it addresses the utilization of long-term AC systems, which are categorized as inefficient (21-23).

Previously, Orhan Ekren and Serhan Küçüka had conducted research on fuzzy logic-based control algorithms for regulating compressor speed and Electronic Expansion Valve (EEV) opening percentages in chiller systems. This research aimed to enhance the efficiency of the chiller system by utilizing a Variable Speed Scroll Compressor (VSSC) and EEV. Fuzzy logic algorithms were employed to govern the compressor speed based on the chiller water output temperature, while the opening percentage of the EEV was controlled based on the refrigerant superheat value at the evaporator outlet. The study's findings revealed a performance improvement of 17% when compared to thermostatically controlled fixed-speed chiller systems, as well as superior control over water temperature achieved through the use of fuzzy-controlled VSSC (24).

Ahmed et al. (25) proposed a scheme utilizing fuzzy logic to control central air conditioning and maintain room temperature and humidity close to predefined targets. This aims to reduce electrical energy consumption and create comfort in various rooms of different sizes and conditions. The result is comfortable rooms with higher energy efficiency. Subsequently, Riyadh Waheed et al. (26) highlighted the role of fuzzy logic-based controllers in enhancing the efficiency of air conditioning, especially in classrooms. The research findings indicated that fuzzy logic-based controllers are superior in regulating room temperature and humidity compared to traditional controllers.

By the use of fuzzy logic controllers in air conditioning systems Francis et al. (27) have successfully reduced electricity consumption by adjusting the compressor speed and operating mode according to environmental conditions and user needs. This demonstrates significant potential for energy savings in air conditioning systems, particularly in urban areas, while considering various input parameters such as temperature, occupancy, time, and weather conditions. A review by Belman-Flores et al. (28) stated that the use of fuzzy logic controllers in refrigeration and air conditioning systems (RACs) has proven their ability to improve thermal efficiency compared to classical controllers like ON/OFF and PID. Computer simulations and experimental tests also showed that the use of fuzzy controllers can reduce energy consumption.

In another study, Nasution (29) evaluated vehicle AC systems using Fuzzy Logic Control (FLC) algorithms to continuously regulate compressor speed. Experiments were conducted with variations in set point temperature, internal heat load, and compressor speed. The results demonstrated that the utilization of FLC led to significant energy savings and improved indoor comfort when compared to conventional ON/OFF controls. This technique holds the potential to enhance the efficiency and overall performance of passenger vehicle AC systems. Furthermore, this research is corroborated by a study conducted by Khayyam et al. (30) who also discussed the development of intelligent energy management systems for optimizing the utilization of AC systems in vehicles. The system incorporates data from various information systems to make intelligent decisions, including predicting road power demand and employing intelligent control strategies. Simulations indicate that this system can achieve energy savings of up to 12% when compared to conventional systems and other energy management systems.

Additionally, the efficacy of Fuzzy logic in attaining energy efficiency is further supported by other studies, such as those conducted by Chu et al. (31). This study proposed the use of the Least Enthalpy Estimator (LEE) in the Fan Coil Unit (FCU) controller in Heating, Ventilating, and Air Conditioning (HVAC) systems to conserve energy and maintain thermal comfort levels. The LEE-based fuzzy FCU controller demonstrates the ability to accurately predict loads and adjust the FCU system's output based on temperature and relative humidity. Through experimentation, this controller successfully achieved the thermal comfort, energy efficiency, and reliability necessary in FCU control systems.

Regarding the efficiency of fuzzy logic, Saini et al. (32) also provided statements in their research supporting the efficiency achieved by fuzzy logic. Their study utilized fuzzy logic to control loads in a Solar Home System with the aim of efficiently managing energy usage. Test results indicated that the use of fuzzy logic could reduce power consumption for lighting and fans compared to control without fuzzy logic.

While previous research has attempted to apply FIS and IoT in various contexts, such as solar home systems, chiller systems, or vehicle air conditioning, there is still a gap in research that focuses on room temperature and humidity regulation using AC with a comprehensive assessment of energy consumption. Previous studies often did not compare energy consumption between manual systems and fuzzy-based systems to understand the potential energy savings that can be achieved.

Therefore, in this study, we specifically examine room temperature and humidity regulation using AC while evaluating energy consumption. This research makes a stronger contribution to developing more efficient solutions for sustainable environmental control through AC usage by attempting to compare energy consumption between manual and fuzzy-based systems to determine potential energy savings.

2. METHOD

The subsections outlined in this method section encompass three main aspects: the research stages, the application of fuzzy Tsukamoto, the specifications of the AC system used, and the methods employed for energy consumption analysis.

2. 1. Research Stages

This research builds upon prior studies that primarily focused on assessing the environmental impact of AC systems following the implementation of fuzzy logic. The research process encompassed several stages, including requirements analysis, tool and application design, tool and application development, fuzzy logic integration into the tools, and testing the tools' impact on room conditions. These stages were systematically evaluated to attain the research objectives.

The developed tools and applications were then utilized to collect energy consumption data within AC systems. Subsequently, this data underwent analysis to gain insights into the influence of fuzzy logic on energy efficiency and the potential savings it can offer. As a result, this study aims to provide comprehensive and detailed insights into the impact of fuzzy logic on energy efficiency within AC systems. An overview of the research stages is illustrated in Figure 1.

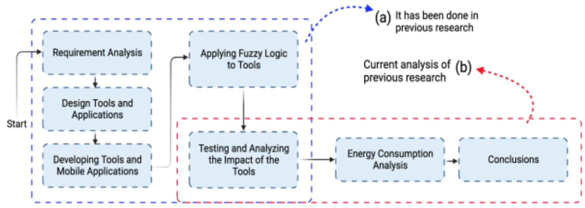

Figure 1. The research comprises two sets of stages: (a) stages that were previously conducted [20], and (b) the more advanced stages implemented in this study

2. 2. Fuzzy Tsukamoto

The Fuzzy Tsukamoto model is a fuzzy logic-based control approach developed in past decades (33, 34). This approach combines the principles of fuzzy logic with intuitively defined linguistic rules to control complex and ambiguous systems. Fuzzy Tsukamoto utilizes the concept of fuzzy membership to depict uncertainty in system inputs and outputs. This concept allows system variables to exhibit varying levels of membership in different categories. For instance, in room temperature control, variables like "*cold*" and "*hot*" can have membership levels or fuzzy sets such as "*slightly cold*", "*medium cold*", "*slightly hot*", and "*medium hot*" (35). These membership levels describe the degree to which an input or output value belongs to a particular category. Linguistic rules are employed in the Fuzzy Tsukamoto model to establish connections between system inputs and outputs. These rules comprise conditional statements that link input conditions with output actions. For instance, "*IF the room temperature is low, THEN the heating rate is increased*". These rules are formulated based on expert knowledge in the relevant domain and are represented in the form of fuzzy sets.

Essentially, Fuzzy Tsukamoto is one of three models within FIS. The other two models are Mamdani and Sugeno reported in literature (36-38). FIS serves as a mathematical framework or model employed for implementing fuzzy logic in decision-making or system control (39, 40). FIS encompasses several key components that collaborate to generate outputs based on fuzzy inputs. FIS can find applications in various domains involving decision-making, system control, and the processing of uncertain or ambiguous data. Within FIS, existing human knowledge or expertise is represented in the form of fuzzy rules and applied to generate outputs based on given input conditions. FIS enables systems to process fuzzy data by amalgamating human knowledge with mathematical techniques, leading to more adaptable and flexible decision-making.

The control process utilizing Fuzzy Tsukamoto comprises several stages. Initially, the system input is transformed into fuzzy sets using membership functions. This initial stage is referred to as the fuzzification stage (41-43). Subsequently, linguistic rules are employed to establish connections between the fuzzy sets of inputs and the desired output. The subsequent stage involves the inference process, during which linguistic rules are assessed to generate the appropriate level of output membership. Lastly, the results of the inference are converted into crisp values through defuzzification, thereby producing numerical output that can be utilized for system control.

2. 2. 1. Fuzzification Fuzzification is the process of converting crisp (non-fuzzy) variables into fuzzy variables by using membership functions (20, 44, 45). Fuzzification allows mathematical representation of uncertainties in the system using fuzzy sets (44-48). The crisp variables that will be used as system inputs are converted into fuzzy sets using the membership function. The membership function associates the crisp value with the membership level in the fuzzy set. Each fuzzy set consists of a set of possible values for the relevant crisp variable. The membership function in fuzzification describes the extent to which a crisp value belongs to a fuzzy set. Membership functions are usually represented in the form of curves, such as triangular curves (49), trapezoidal curves, or other curves corresponding to the characteristics of variables and their domains. This curve shows the membership levels of variables in a fuzzy set at various points of their value.

Fuzzification is an important step in the fuzzy logic-based control process, as it converts crisp data into fuzzy representations that fuzzy systems can use to make decisions and produce appropriate outputs (50, 51). In combination with fuzzy inference and defuzzification, fuzzification assists fuzzy systems in modeling and controlling complex systems by taking into account the uncertainty and ambiguity inherent in system inputs. The fuzzification process is written in Equation 1.

$$x = fuzzifier(x_0) \tag{1}$$

where x_0 is a firm value vector of an input variable, x is a fuzzy set vector defined as a variable, and fuzzifier is a fuzzification operator that converts a firm value to a fuzzy set (52).

2. 2. 2. Machine Inference At the inference system stage, fuzzy rules are used to draw conclusions based on fuzzy set theory and fuzzy rules in the form of IF-THEN statements (53). This IF-THEN statement can usually also consist of one or more antecedents (also called premises) located within the IF section with one or more consequent (also called conclusions) located within the THEN section. In general, a rule can have multiple premises associated with an AND statement (conjunction), an OR statement (disjunction), or a combination of the two. In this case, Zadeh identified three basic operators used in fuzzy rules, namely the AND, OR, and NOT operators (54, 55). The AND operator is used to retrieve the minimum element between the two fuzzy sets involved (56). In this context, the AND operator results in the lowest membership level of the corresponding fuzzy set (Equation 2). The OR operator, on the other hand, is used to find the maximum element between two fuzzy sets. Using the OR operator, the highest membership level of the associated fuzzy set is taken (Equation 3). The NOT operator is used to subtract the value of 1 with a negated fuzzy element. In other words, if a fuzzy set has a membership level of α, then using the NOT operator, the membership level becomes 1 – α (Equation 4) (57). In the context of this study, the AND operator is applied to each formed fuzzy rule. The use of this AND operator results in the lowest membership value of the fuzzy set involved in each of those rules. Mathematically, the AND operator can be described using Equation 2.

$$\mu K \cap L = \min(\mu K[x], \mu L[x]) \tag{2}$$

$$\mu K U L = \max(\mu K[x], \mu L[x]) \tag{3}$$

$$\mu K' = 1 - \mu K(x) \tag{4}$$

2. 2. 3. Defuzzification Defuzzification is a transformation that restates the output from a fuzzy domain into a crisp domain. Fuzzy output is obtained through the execution of some fuzzy membership functions. There are several methods that can be used in the defuzzification process, namely **(1)** *Weighted Average Method* (58-60), a method that calculates the average value by assigning a certain weight or weight to each element in the data set aimed at reflecting the relative importance or contribution of each element to the final result, **(2)** *Mean-Max Membership* (61-63), a method that combines several overlapping membership rules by taking the maximum value of each set membership at a point, then calculate the average of those maximum values, **(3)** *Centroid (Center of Gravity) Method* (64, 65), a method that calculates the center point (centroid) of a membership set using the weighted principle based on membership level. The membership value of each point on the set is multiplied by the position of that point, then added and divided by the total membership value, **(4)** *Height Method (Max-Membership Principle)* (66, 67), a method that takes the maximum value of the membership level in a membership set as a representation of the membership value of the entire set, **(5)** *Center of Sums* (68-70), a method that calculates the center of input values by adding input points and dividing them by the total number of inputs, **(6)** *First (or Last) of Maxima* (66, 71, 72), a method that selects the first (or last) point at which the membership level reaches the maximum value of a membership set as a representation of the overall membership value of that set, and **(7)** *Center of Largest Area* (73, 74), a method that calculates the center of the area of a membership set by taking the midpoint at the interval with the largest set area. The defuzzification method used in this study is the *Weighted Average* written in Equation 5.

$$x^* = \frac{\sum_{i=1}^{n} \mu c(\bar{x}_i).\bar{x}_i}{\sum_{i=1}^{n} \mu c(\bar{x}_i)} \quad (5)$$

where $\sum_{i=1}^{n}$ represents an algebraic sum with respect to the membership function of *n* fuzzy sets. This method has the limitation that it can only be used on fuzzy sets with symmetric membership functions (75).

2. 3. AC Specifications Used As explained in the introduction, this study focuses on the analysis of energy consumption on the use of AC as an air conditioner. AC performance will be analyzed and evaluated to understand the impact of its use on power consumption after fuzzy logic is enacted in regulating AC values. One important step in power consumption analysis is obtaining the associated AC specifications. To collect AC specifications, first of all, it is necessary to know the electrical power consumed by the air conditioner. This information can usually be found on the technical specifications of the AC or on the label attached to the AC unit itself. This electrical power is expressed in units of watt (W) and is an important indicator for understanding the extent to which AC consumes power while operating.

Another important specification to know is the AC efficiency factor (76-78). The efficiency factor describes the level of efficiency of an AC in producing cooling relative to the power consumed (76). The efficiency factor is usually expressed as a percentage and can affect power consumption significantly. Therefore, knowing the efficiency factor of AC allows for more accurate calculations in estimating AC power consumption at different temperatures.

Based on the Decree of the Minister of Defense of the Republic of Indonesia No. 782/VIII/2015, the power standard for AC is calculated based on Paarden Kracht (PK) where 1 PK is equivalent to 0.7355 kW (79). While the AC used is equivalent to ½ PK, so ½ PK x 0.7355 kW = 0.368 kW. Then, the magnitude of ½ PK is equal to ±5000 BTU/h (British Thermal Units per hour) (80, 81). In addition, based on the reference read (82), the calculation of energy consumption per year can be obtained by Equation 6.

$$\text{AE} = \frac{Q * t}{EER} \quad (6)$$

where *AE* stands for *"Annual Energy"* which refers to the total energy consumed or used by a system, device, or equipment in a one-year period. *Q* is the Capacity that represents the cooling capacity or cooling load of the air conditioner. This capacity is measured in units such as BTU/h, kilowatts (kW), or tons. Capacity describes the amount of heat that an AC can remove in a given period of time. While *t* (operating time) refers to the operating time of the air conditioner. This is the amount of time that AC is used or operating in units such as hours, minutes, or seconds. While Energy Efficiency Ratio (*EER*) is the ratio between the cooling capacity of AC and its input power. To calculate EER, you need to know the cooling capacity and AC input power in appropriate units, such as BTU/h and watts or kW. EER can be calculated using Equation 7 (83).

$$EER = \frac{\emptyset_{tci}}{P_t} \quad (7)$$

$$\emptyset_{tci} = \sum P_{ic} + (h_{w1} - h_{w2})W_r + \emptyset_{lp} + \emptyset_{li} \quad (8)$$

In Equation 7, $\emptyset_{tci}$ refers to the total cooling capacity required on the indoor side, while P_t describes the total power consumed by the equipment under test. While $\emptyset_{tci}$ obtained using Equation 8. The P_{ic} reflects the total power entering the indoor side test chamber, including lighting power, electrical power consumed by the equipment, and heat generated by compensation and humidification devices; h_{w1} is the specific enthalpy of water supplied to the indoor side test chamber, while h_{w2} describes the specific enthalpy of moisture condensed and exiting the chamber. P_{ic} is the condensation rate of water vapor in the room; $\emptyset_{lp}$ describes heat leakage that occurs through partitions that separate the inside of the room from the outside; $\emptyset_{li}$ described heat leaks occurring through the walls, floor, and ceiling of an indoor side test chamber (83).

By obtaining comprehensive AC specifications, including electrical power and efficiency factors, this study can continue a more detailed analysis of AC power consumption. The analysis will provide deeper insight into the extent to which the role of fuzzy logic in regulating AC values can affect the power consumption required to maintain room temperature at a certain level.

2. 4. Energy Consumption Analysis Method The test was carried out by turning on the AC for 30 minutes using the manual method and the fuzzy method. The calculation of electrical power is measured to obtain energy consumption. During the test, AC power was measured using a watt meter and recorded once every minute. One record per minute is assumed to represent the electrical power used in 1 minute, so to get the electrical power usage for 1 minute is calculated using Equation 9.

$$P_{minute} = P \ x \ 60s \quad (9)$$

In Equation 9, *P* is the electrical power used in 1 second. While P_{minute} is electrical power used in 1 minute. After getting the electrical power consumption per minute, the next calculated electrical power consumption during the test, which is ½ hour or 30 minutes. So, to obtain the total use of electrical power within 30 minutes obtained using Equation 10.

$$P_{\frac{1}{2}hour} = \frac{P_{minute} \ x \ 60 \ minutes}{2} \quad (10)$$

Or convert in 1 hour (60 minutes) using Equation 11.

$$P_{hour} = P_{minute}\ x\ 60\ minutes \tag{11}$$

If you want to convert it in kilowatt-hours (kWh), you can use Equation 12.

$$E_{(kWh)} = \frac{P_{hour}}{1600000} \tag{12}$$

Energy (E) in kWh is equal to power (P) in watts (W), multiplied by the time period t in hours, divided by 1000 as in Equation 13.

$$E_{(kWh)} = \frac{P_{(W)}\ x\ t_{hour}}{1000} \tag{13}$$

The watt meter used is as in Figure 2.

3. MAIN RESULTS

3. 1. Hypothesis The hypothesis of this study posits that the incorporation of fuzzy logic into room temperature and humidity regulation systems can lead to reduced resource consumption through several means. Firstly, fuzzy logic enables intelligent and adaptive control of temperature and humidity. Utilizing sensors to measure the current temperature and humidity, fuzzy inference systems can make informed decisions regarding whether to activate or deactivate heating or air conditioning devices. This prevents unnecessary energy usage when the temperature or humidity already falls within the desired range. Secondly, by employing linguistic variables and well-defined rules, fuzzy inference systems can finely tune temperature and humidity settings. For instance, if the room temperature is only slightly above the desired threshold, a fuzzy inference system can generate adjustments that proportionally reduce heating or air conditioning power. This mitigates excessive energy consumption associated with traditional ON/OFF methods.

Furthermore, fuzzy logic can take into account other factors influencing the comfort of room occupants. For example, if the external temperature is low but the humidity level is high, a fuzzy inference system can generate settings that slightly raise the temperature and lower the humidity to maintain comfort. By considering humidity, fuzzy inference systems contribute to optimizing overall energy utilization. Additionally, fuzzy logic enables the scheduling of energy usage based on observed usage patterns. For instance, if room temperature tends to increase during daylight hours, a fuzzy inference system can pre-condition the room by activating the heater or AC beforehand. This approach enhances energy efficiency and prevents excessive energy usage once the desired temperature is reached.

Figure 2. Watt Meter AC Digital Volt

3. 2. Discussion In this experiment, the air conditioner (AC) was operated for a duration of 30 minutes to assess its power consumption. The testing was conducted using two distinct methodologies: the manual approach and the fuzzy logic approach. The manual approach involved direct measurement and calculation of AC power consumption over the 30-minute period. Data for this method were manually recorded from wattage meter readings at 1-minute intervals, which were then used to compute the total AC power consumption. On the other hand, the fuzzy logic approach also recorded electrical power consumption through manual readings from the watt meter, similar to the manual method. However, the fuzzy method utilized a real-time fuzzy logic algorithm to regulate the AC's temperature.

The objective of these tests was to compare the energy consumption of each approach. The test results will yield valuable insights into managing AC power consumption, which can be leveraged for energy conservation and reducing operational costs.

3. 2. 1. Testing with Manual Method The manual method was assessed by measuring electrical power consumption at various AC temperature setpoints. A total of 8 tests were conducted, with each test performed at a distinct temperature setting: 18°C, 20°C, 23°C, 24°C, 25°C, 26°C, 27°C, and 30°C. Each test spanned 30 minutes to guarantee precise and uniform data collection. The testing procedure is illustrated in Figure 3.

Figure 3 displays the test conducted at an AC temperature setpoint of 25°C. The utilized modes in each test are "*Cooling mode*" and "*Fan mode*" both operating concurrently. In each test, data is meticulously recorded at 1-minute intervals based on the watt meter readings to

Figure 3. Manual Measurement Process of Electric Power at AC Temperature = 25°C

ensure comprehensive data collection. Variations in AC power consumption at various temperatures can be observed and analyzed. The fluctuations in electrical energy consumption, examined in all manual method tests, are summarized in Figure 4.

Figure 4 displays the results of testing the use of AC within a period of 30 minutes with two different modes, namely *"Cooling and fan mode"* and *"Fan only mode"*. In this test, the difference in energy consumption in the two modes is very clear. In *"Cooling and fan mode"*, the AC works to reach a set temperature setpoint, while running the fan for air circulation. This mode requires high power because the AC must cool the room by lowering the temperature to the desired setpoint and also maintain air circulation with the help of fans. The test results showed that the highest electrical power per second occurred at an AC temperature setpoint of 20°C, where power consumption reached 447.3 watts. This indicates that the lower the temperature to be achieved, the greater the power required by the AC in this mode. Meanwhile, in *"Fan only mode"*, the AC only functions as a fan without cooling the room. This mode results in much lower electrical power consumption compared to the *"Cooling and fan mode"* mode. The lowest electrical power occurs at an AC temperature setpoint of 30°C, where the power consumption per second is only 16.6 watts. This is because AC only uses power to run the fan without doing the cooling process, so the power requirement is lower. This test provides conclusions about the impact of using both modes on AC electrical energy consumption. The *"Cooling and fan mode"* mode is more suitable for achieving lower temperatures, but requires more power. On the other hand, the *"Fan only mode"* mode is suitable for situations where cooling is not required, and this helps in saving energy.

3. 2. 1. Testing with Fuzzy Logic Method

Testing with the fuzzy logic method requires several main components: fuzzy variables, fuzzy membership functions, and fuzzy rules. These components are used in three stages in Fuzzy Tsukamoto. Fuzzy variables consist of input and output variables. Input variables are used as input in the form of crisp values and are converted to fuzzy values in the fuzzification stage, while output variables are used in the defuzzification stage as the output of the fuzzy logic in the form of crisp values. The input variables used are room temperature and humidity, while the output variable is the AC temperature.

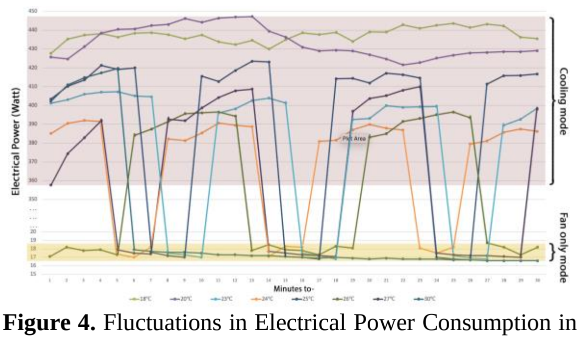

Figure 4. Fluctuations in Electrical Power Consumption in Each Test on the Manual Method

The selection of room temperature and humidity as input parameters in controlling AC temperature using fuzzy logic is based on physics and human comfort. Temperature affects human comfort and can impact AC efficiency, while humidity is also important because it can affect the feeling of warmth or cold. Proper control of both of these parameters can result in more efficient energy use and maintain indoor air quality.

To apply both of these parameters in fuzzy logic, they are divided into several fuzzy sets. The room temperature variable is divided into five fuzzy sets: Very Cold, Cold, Normal, Hot, and Very Hot. Meanwhile, the humidity variable is also divided into five fuzzy sets: Dry, Normal, Quite Wet, Wet, and Very Wet. On the output variable side, the AC temperature used has a range of 18-32°C, divided into three fuzzy sets: Cold, Normal, and Hot. The temperature curve is shown in Figure 5. The humidity curve is shown in Figure 6, and the AC temperature curve in Figure 7. As for the fuzzy rules with monotonic reasoning, there are a total of 25 rules corresponding to the two input variables, each having five fuzzy sets. The formed fuzzy rules are shown in Figure 8.

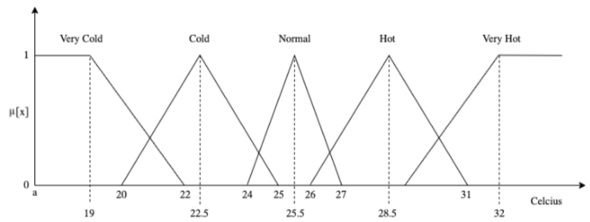

Figure 5. Room temperature membership function curve

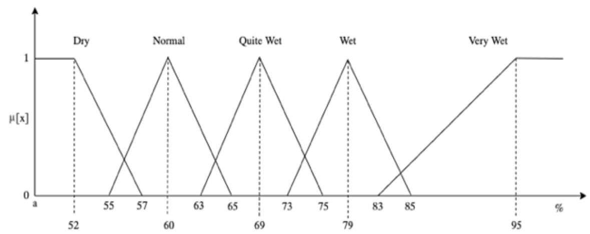

Figure 6. Room humidity membership function curve

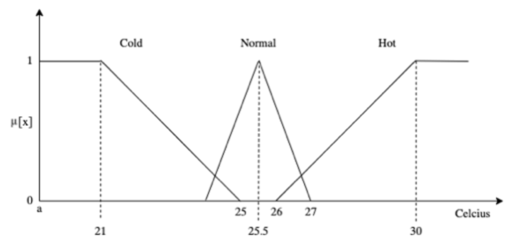

Figure 7. AC temperature membership function curve

AC Temp		Humidity				
		Dry	Normal	Quite Wet	Wet	Very Wet
Room Temp	Very Cold	Hot	Hot	Hot	Hot	Normal
	Cold	Hot	Hot	Hot	Normal	Normal
	Normal	Normal	Normal	Normal	Normal	Normal
	Hot	Normal	Normal	Cold	Cold	Cold
	Very Hot	Normal	Cold	Cold	Cold	Cold

Figure 8. Fuzzy rules

The membership function curves and fuzzy rules in Figures 5-8 are used to control room temperature, which will affect electrical power consumption. This fuzzy method was tested by measuring electrical power consumption on six tests. The temperature setpoint of the AC is not fixed and depends on the temperature and humidity conditions of the room during the test process. Similar to manual method testing, fuzzy method testing is also tested in a duration of 30 minutes in each test. This fuzzy method also presents 2 made air conditioners during the testing process, namely *"Cooling and fan mode"* and *"Fan only mode"*. The comparison of AC temperature setpoints to their electrical power consumption is listed in Figure 9.

Figure 9 shows the ratio of AC temperature setpoints to their electrical power consumption in all tests on fuzzy control methods. The value described by the graph of electrical power consumption is taken for 30 minutes at

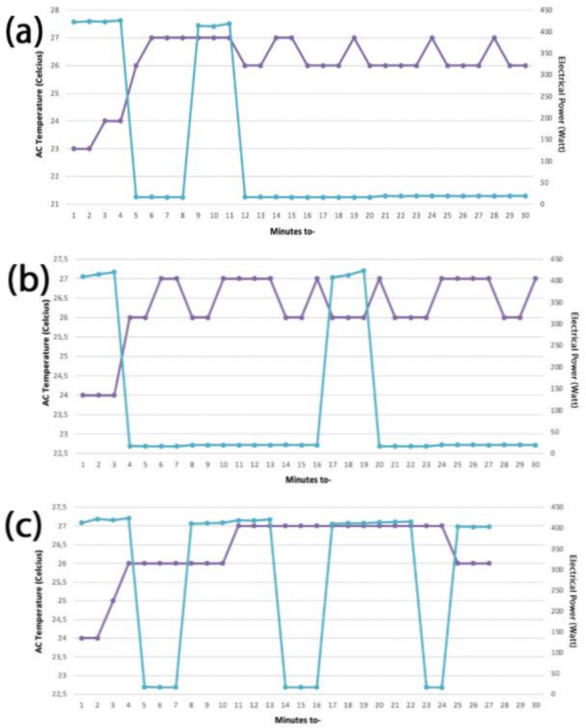

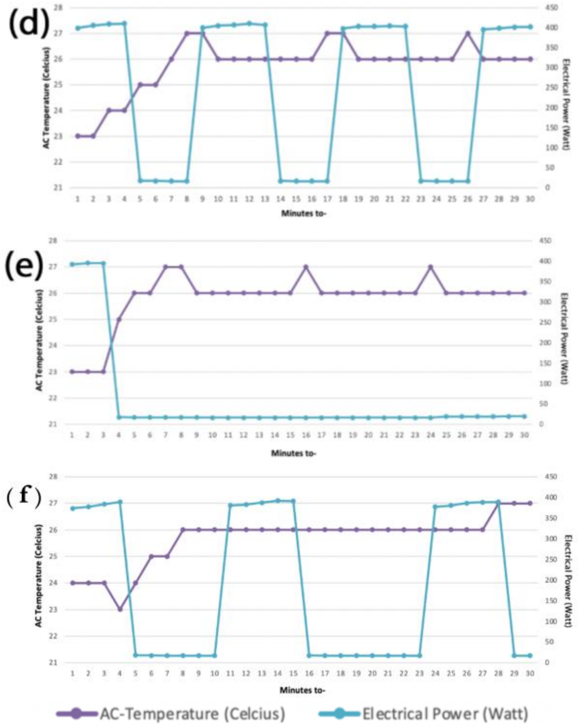

Figure 9. Comparison of AC Temperature Setpoint to Electric Power Consumption (Controlled Using Fuzzy Logic)

intervals of 1 minute. This means that the record is taken per minute for 30 minutes. During the testing process, the AC provided action in "cooling and fan" mode and "fan only" mode. A comparison of basic statistics in each mode can be seen in Figure 10.

In Figure 10, there are maximum power test results per second measured on six different tests. These results show that the highest value is reached at 425.6 watts, and this value is obtained when the AC operates in "cooling and fan" mode. The "cooling and fan" mode involves the AC in the process of cooling the room by running a fan for air circulation. Meanwhile, the lowest value in Figure 10 was recorded at 16.1 watts, and this value was obtained when the AC operated in "fan only" mode or only used a fan without cooling the process. In this mode, the AC does not require large power because its function is limited only to running the fan for air circulation without lowering the room temperature. To be able to evaluate each test, the total electrical power in each test using fuzzy control mode is shown in Figure 11.

The total electrical power consumption in Figure 11 is obtained by calculation using Equations 9 and 10. The highest electrical power consumption was obtained in the 3rd test with a consumption of 479347 watts or equivalent to 0.133 kWh (Equation 12). While the most efficient or lowest consumption was obtained in the 5th test with a total electrical power consumption of 98742

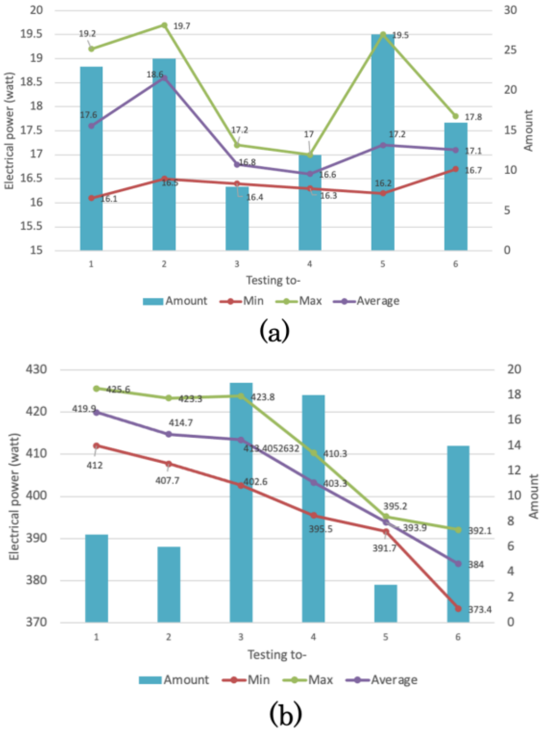

Figure 10. Comparison of maximum, average, and minimum electrical power in the test with fuzzy logic at (a). fan only mode; and (b). Cooling and fan mode”

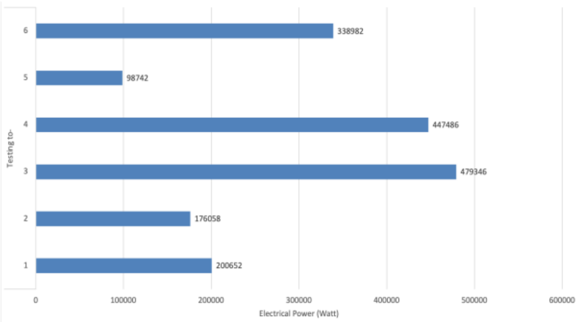

Figure 11. Total power consumption in each test with fuzzy logic control

watts or equivalent to 0.027 kWh. If averaged all electrical power consumption in all tests, then a value of 290211 watts or equivalent to 0.081 kWh is obtained. This value is categorized as more efficient when compared to manual methods that tend to consume a lot of electrical power. The results of the comparison between the total electric power consumption of the manual method with the average electric power consumption of the fuzzy method are listed in Figure 12.

Figure 12 shows that the average power consumption using the fuzzy method is lower than most tests on the manual method. Electric power consumption with the fuzzy method is only less efficient than using the

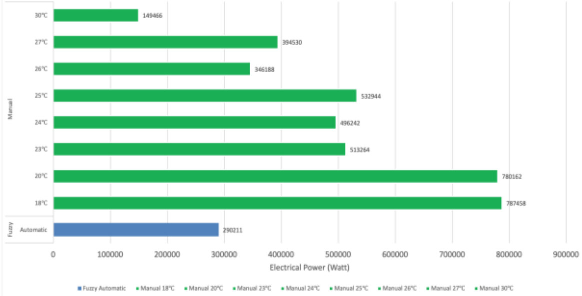

Figure 12. Comparison Between the Total Electric Power Consumption of the Manual Method with the Average Electric Power Consumption of the Fuzzy Method

manual method at the AC temperature setpoint = 30°C, which is with a difference of 140745 watts (0.039 kWh). While manual control at other AC temperature setpoints (18°C, 20°C, 23°C, 24°C, 25°C, 26°C, and 27°C) consumes much more electrical power when compared to the average power consumption in fuzzy control. The largest difference is in the manual control setpoint of 18°C and followed by the setpoint of 20°C. This is because at setpoints of 18°C and 20°C, the AC works in maximum conditions in *“Cooling and fan”* mode every second. This makes electrical power consumption also increase. Based on these results, it can also be concluded that electrical power consumption is also influenced by the amount of temperature that AC wants to produce. The smaller the desired temperature, the greater the power required by the AC, so this will make electrical energy consumption higher (84). To see the comparison of the difference in average electrical power consumption between these two methods (manual and fuzzy), it can be seen in Figure 13.

Figure 13 shows that the difference in average energy consumption is quite significant, reaching 209,820.75 watts (0.058 kWh). The average power consumption of the manual method is nearly twice that of the fuzzy method. Energy savings from the use of the fuzzy method amount to approximately 41.96%. A comparison with some previous studies is shown in Table 1.

Table 1 illustrates an interesting comparison across various studies regarding the use of fuzzy logic in controlling AC for energy savings. Different research outcomes show varying degrees of energy savings achievable through this approach. In 2018, a study by

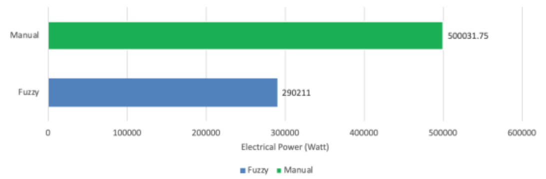

Figure 13. Comparison of the average total electrical power consumption of manual method and fuzzy method

TABLE 1. Comparison with some previous studies

Ref.	Method	Controlled device	Energy savings	Year
(85)	Fuzzy logic	Electronic devices, including the AC	40%	2018
(84)	Fuzzy logic	AC	33.55%	2019
(82)	Fuzzy logic	AC	25%	2020
(27)	Fuzzy logic	AC	62%	2022
(86)	Fuzzy logic	AC	16-25%	2023
This Research	Fuzzy logic	AC	41,96%	2023

Pratama and Sarno (85) on controlling electronic devices, including AC, with fuzzy logic successfully achieved 40% energy savings. Meanwhile, Berouine et al. (84) in 2019 and Shah et al. (82) in 2020 focused on AC control with fuzzy logic, achieving savings of approximately 33.55% and 25%, respectively. However, in 2022, a study by Francis et al. (27) achieved an impressive energy savings of 62% when controlling AC with fuzzy logic. Recent research in 2023 shows varying results, with energy savings ranging from 16% to 25% when controlling AC with fuzzy logic (86).

This study, conducted in 2023, achieved an energy savings of approximately 41.96% when controlling AC using fuzzy logic. A visual comparison of all the literature is shown in Figure 14.

When compared to several previous studies as outlined, this research demonstrates a commendable contribution, trailing behind only the study conducted by Francis et al. (27) with a difference of 20.04%. Nevertheless, these findings already indicate that the application of fuzzy logic in AC control can optimize electrical power usage intelligently by adapting operations to the actual needs of the room and environmental conditions. In the "cooling and fan" mode, the fuzzy method allows for the restriction of AC activity when the desired temperature has been achieved or considers room temperature fluctuations to reduce unnecessary power consumption. These results can also serve as a smart solution to reduce energy consumption across various contexts.

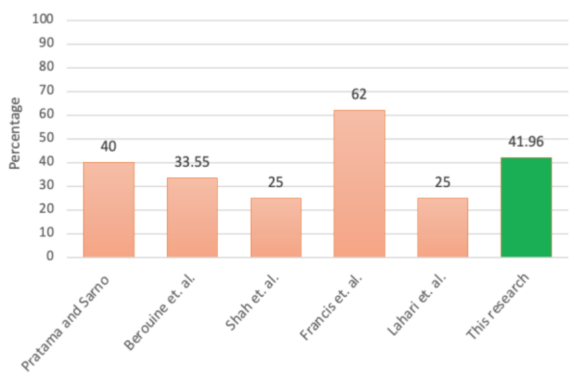

Figure 14. Comparison of Energy Savings with Previous Studies

4. CONCLUSIONS

The results of this study involved AC running for 30 minutes to observe power consumption by applying two different methods, namely the manual method and the fuzzy method. The manual method involves direct measurement and calculation of AC power used over a 30-minute period by manually recording data from watt meter readings at 1-minute intervals. Meanwhile, the fuzzy method also records electrical power consumption manually, but uses fuzzy logic algorithms to control the temperature of the AC in real-time. The test results show that the fuzzy method is more energy efficient than the manual method, except at a 30°C AC temperature setpoint. The difference is due to the *"Cooling and fan"* mode used at lower temperatures in the manual method, resulting in higher power consumption. Overall, the average test results of each method indicate that the fuzzy method has a lower average electrical power consumption compared to the manual method, with a significant difference. The use of the fuzzy method can achieve energy savings of approximately 41.96%. This demonstrates the potential of fuzzy methods in optimizing AC power usage in a smarter and adaptive manner based on room and environmental conditions.

5. ACKNOWLEDGMENTS

This work is supported by the Ministry of Education, Culture, Research, and Technology of the Republic of Indonesia based With Contract number: 181/E5/PG.02.00.PL/2023. The authors also gratefully acknowledge the helpful comments and suggestions of the reviewers, which have improved the presentation.

6. REFERENCES

1. Asman FF, Permata E, Fatkhurrokhman M. A prototype of smart lock based on internet of things (IoT) with ESP8266. Jurnal Ilmiah Teknik Elektro Komputer dan Informatika (JITEKI). 2019;5(2):101-11. 10.26555/jiteki.v5i2.15317
2. Riadi I, Syaefudin R. Monitoring and Control Food Temperature and Humidity using Internet of Things Based-on Microcontroller. Jurnal Ilmiah Teknik Elektro Komputer dan Informatika. 2021;7(1):108-17. 10.26555/jiteki.v7i1.20213
3. Tun SYY, Madanian S, Mirza F. Internet of things (IoT) applications for elderly care: a reflective review. Aging clinical and experimental research. 2021;33:855-67. 10.1007/S40520-020-01545-9/METRICS

4. Prasetia Y, Putrada AG, Rakhmatsyah A. Evaluation of IoT-based grow light automation on hydroponic plant growth. Jurnal Ilmiah Teknik Elektro Komputer dan Informatika. 2021;7(2):314-25. 10.26555/jiteki.v7i2.21424

5. Rajak AA. Emerging technological methods for effective farming by cloud computing and IoT. Emerging Science Journal. 2022;6(5):1017-31. 10.28991/ESJ-2022-06-05-07

6. Seuwou P, Banissi E, Ubakanma G. The future of mobility with connected and autonomous vehicles in smart cities. Digital twin technologies and smart cities. 2020:37-52. 10.1007/978-3-030-18732-3_3

7. Umair M, Cheema MA, Cheema O, Li H, Lu H. Impact of COVID-19 on IoT adoption in healthcare, smart homes, smart buildings, smart cities, transportation and industrial IoT. Sensors. 2021;21(11):3838. 10.3390/s21113838

8. Salis A. HighTech and Innovation. 10.28991/HIJ-2021-02-04-01

9. Tawsif K, Aziz NAA, Raja JE, Hossen J, Jesmeen M. A systematic review on emotion Recognition System using physiological signals: Data Acquisition and Methodology. Emerging Science Journal. 2022;6(5):1167-98. 10.28991/ESJ-2022-06-05-017

10. Zhuang D, Gan VJ, Tekler ZD, Chong A, Tian S, Shi X. Data-driven predictive control for smart HVAC system in IoT-integrated buildings with time-series forecasting and reinforcement learning. Applied Energy. 2023;338:120936. 10.1016/j.apenergy.2023.120936

11. Somefun TE, Abdulkareem A, Awosope CO, Akanji O. Smart home comfort and energy conservation using internet of things. TELKOMNIKA (Telecommunication Computing Electronics and Control). 2022;20(2):357-65. 10.12928/telkomnika.v20i2.18928

12. Cano-Suñén E, Martínez I, Fernández Á, Zalba B, Casas R. Internet of Things (IoT) in Buildings: A Learning Factory. Sustainability. 2023;15(16):12219. 10.3390/su151612219

13. Sridharan M. Application of Mamdani fuzzy inference system in predicting the thermal performance of solar distillation still. Journal of Ambient Intelligence and Humanized Computing. 2021;12(11):10305-19. 10.1007/s12652-020-02810-5

14. Ortega LC, Otero LD, Otero C. Fuzzy inference system framework to prioritize the deployment of resources in low visibility traffic conditions. IEEE Access. 2019;7:174368-79. 10.1109/ACCESS.2019.2956918

15. Martinez-Molina A, Alamaniotis M. Enhancing historic building performance with the use of fuzzy inference system to control the electric cooling system. Sustainability. 2020;12(14):5848. 10.3390/su12145848

16. D'Aniello G. Fuzzy logic for situation awareness: a systematic review. Journal of Ambient Intelligence and Humanized Computing. 2023;14(4):4419-38. 10.1007/s12652-023-04560-6

17. Mansouri N. An Efficient Task Scheduling Based on Seagull Optimization Algorithm for Heterogeneous Cloud Computing Platforms. International Journal of Engineering. 2022;35(2):433-50. 10.5829/IJE.2022.35.02B.20

18. AlizadehKharazi B, Alvanchi A, Taghaddos H. A novel building information modeling-based method for improving cost and energy performance of the building envelope. International Journal of Engineering, Transactions B: Applications,. 2020;33(11):2162-73. 10.5829/ije.2020.33.11b.06

19. Mahmoodabadi M, Dresscher D, Stramigioli S. A new mechanical design for legged robots to reduce energy consumption. International Journal of Engineering, Transactions C: Aspetcs. 2020;33(12):2530-7. 10.5829/ije.2020.33.12c.14

20. Furizal F, Sunardi S, Yudhana A. Temperature and humidity control system with air conditioner based on fuzzy logic and internet of things. Journal of Robotics and Control (JRC). 2023;4(3):308-22. 10.18196/jrc.v4i3.18327

21. Ebrahimpour B, Moazemi Goudarzi A, Kaviani A. Enhancing performance of an air conditioner by preheating and precooling of liquid desiccant and non-processed air. International Journal of Engineering, Transactions B: Applications,. 2022;35(2):425-32. 10.5829/IJE.2022.35.02B.19

22. Ebenezer SP, Pramanick A, Ramachandran K. Window air conditioner with orthodox refrigerants. International Journal of Engineering, Transactions B: Applications,. 2019;32(2):322-7. 10.5829/ije.2019.32.02b.18

23. Ravi P, Krishnaiah A, Azizuddin M. Design and Experimentation of Roll Bond Evaporator for Room Air Conditioner with R-22 as Refrigerant. International Journal of Engineering, Transactions A: Basics. 2017;30(4):558-66. 10.5829/idosi.ije.2017.30.04a.14

24. Ekren O, Küçüka S. Energy saving potential of chiller system with fuzzy logic control. International Journal of Energy Research. 2010;34(10):897-906. 10.1002/ER.1621

25. Ahmed SS, Majid MS, Novia H, Abd Rahman H. Fuzzy logic based energy saving technique for a central air conditioning system. Energy. 2007;32(7):1222-34. 10.1016/j.energy.2006.07.025

26. Waheed SR, Adnan MM, Suaib NM, Rahim MSM, editors. Fuzzy logic controller for classroom air conditioner. Journal of Physics: Conference Series; 2020: IOP Publishing. 10.1088/1742-6596/1484/1/012018

27. Francis M, Luqman R, Charles D, Audu A. Energy savings for air conditioning system using fuzzy logic controller design for Northeastern Nigeria. International Journal Applied Technology Research. 2022;3(2):91-105. 10.35313/ijatr.v3i2.95

28. Belman-Flores JM, Rodríguez-Valderrama DA, Ledesma S, García-Pabón JJ, Hernández D, Pardo-Cely DM. A review on applications of fuzzy logic control for refrigeration systems. Applied Sciences. 2022;12(3):1302. 10.3390/app12031302

29. Nasution H. Development of fuzzy logic control for vehicle air conditioning system. TELKOMNIKA (Telecommunication Computing Electronics and Control). 2008;6(2):73-82. 10.12928/telkomnika.v6i2.553

30. Khayyam H, Nahavandi S, Hu E, Kouzani A, Chonka A, Abawajy J, et al. Intelligent energy management control of vehicle air conditioning via look-ahead system. Applied thermal engineering. 2011;31(16):3147-60. 10.1016/J.APPLTHERMALENG.2011.05.023

31. Chu C-M, Jong T-L, Huang Y-W. Thermal comfort control on multi-room fan coil unit system using LEE-based fuzzy logic. Energy Conversion and Management. 2005;46(9-10):1579-93. 10.1016/j.enconman.2004.08.002

32. Makmur S, Muhammad RD, Muhammad A, Golda EP. Modeling and implementing a load management system for a solar home system based on Fuzzy Logic. SINERGI. 2023;27(2):261-70. 10.22441/sinergi.2023.2.014

33. Vashishtha S, Susan S. Fuzzy rule based unsupervised sentiment analysis from social media posts. Expert Systems with Applications. 2019;138:112834. 10.1016/j.eswa.2019.112834

34. Chauhan S, Shet JP, Beram SM, Jagota V, Dighriri M, Ahmad MW, et al. Rule Based Fuzzy Computing Approach on Self-Supervised Sentiment Polarity Classification with Word Sense Disambiguation in Machine Translation for Hindi Language. ACM Transactions on Asian and Low-Resource Language Information Processing. 2023;22(5):1-21. 10.1145/3574130

35. Al-Taie SAM, Khaleel BI. Palm Print Recognition Using Intelligent Techniques: A review. Jurnal Ilmiah Teknik Elektro Komputer dan Informatika. 2023;9(1):156-64. 10.26555/jiteki.v9i1.25777

36. Dore P, Chakkor S, El Oualkadi A, Baghouri M. Real-time intelligent system for wind turbine monitoring using fuzzy system. e-Prime-Advances in Electrical Engineering, Electronics and Energy. 2023;3:100096. 10.1016/j.prime.2022.100096
37. Borany A, Sadkhan SB, editors. Decision-making approach in Cognitive Radio using Tsukamoto and Mamdani FIS. 2021 1st Babylon International Conference on Information Technology and Science (BICITS); 2021: IEEE. 10.1109/BICITS51482.2021.9509910
38. Jasim MA, Atia TS. An IoT-Fuzzy-Based Jamming Detection and Recovery System in Wireless Video Surveillance System. International Journal of Computational Intelligence and Applications. 2023:2350004. 10.1142/S1469026823500049
39. Vatankhah Ghadim H, Tarafdar Hagh M, Ghassem Zadeh S. Fermat-curve based fuzzy inference system for the fuzzy logic controller performance optimization in load frequency control application. Fuzzy Optimization and Decision Making. 2023;22(4):555-86. 10.1007/s10700-022-09402-2
40. Rai S, Srinivas R, Magner J. Using fuzzy logic-based hybrid modeling to guide riparian best management practices selection in tributaries of the Minnesota River Basin. Journal of Hydrology. 2022;608:127628. 10.1016/j.jhydrol.2022.127628
41. Atletiko FJ, Rakhmawati NA, Ts HA. Determination of freight rates based on package dimension and distance of delivery using fuzzy logic system in Angkotin application. Procedia Computer Science. 2019;161:527-34. 10.1016/j.procs.2019.11.152
42. Nugraha E, Wibawa A, Hakim M, Kholifah U, Dini R, Irwanto M, editors. Implementation of fuzzy tsukamoto method in decision support system of journal acceptance. Journal of Physics: Conference Series; 2019: IOP Publishing. 10.1088/1742-6596/1280/2/022031
43. Omomule TG, Ajayi OO, Orogun AO. Fuzzy prediction and pattern analysis of poultry egg production. Computers and electronics in agriculture. 2020;171:105301. 10.1016/J.COMPAG.2020.105301
44. Sunardi S, Yudhana A, Furizal F. Optimasi Pengendalian Suhu dan Kelembapan Ruangan di Kota Yogyakarta Menggunakan Metode Fuzzy. JURIKOM (Jurnal Riset Komputer). 2022;9(6):1749-59. 10.30865/jurikom.v9i6.5060
45. Dini MZ, Rakhmatsyah A, Wardana AA. Detection of Oxygen Levels (SpO2) and Heart Rate Using a Pulse Oximeter for Classification of Hypoxemia Based on Fuzzy Logic. J Ilm Tek Elektro Komput dan Inform. 2022;8(1):17-26. 10.26555/jiteki.v8i1.22139
46. de Andrés-Sánchez J. A systematic review of the interactions of fuzzy set theory and option pricing. Expert Systems with Applications. 2023:119868. 10.1016/j.eswa.2023.119868
47. Obianyo JI, Okey OE, Alaneme GU. Assessment of cost overrun factors in construction projects in Nigeria using fuzzy logic. Innovative Infrastructure Solutions. 2022;7(5):304. 10.1007/s41062-022-00908-7
48. Sivaparthipan C, Anand M, Agarwal N, Dhingra M, Raja L, Victor A, et al. IoT-based patient stretcher movement simulation in smart hospital using type-2 fuzzy sets systems. Production Planning & Control. 2023:1-16. 10.1080/09537287.2023.2217419
49. Rinanto N, Marzuqi I, Khumaidi A, Sarena ST. Obstacle Avoidance using Fuzzy Logic Controller on Wheeled Soccer Robot. Jurnal Ilmiah Teknik Elektro Komputer dan Informatika. 2019;5(1):26-35. 10.26555/jiteki.v5i1.13298
50. Kambalimath S, Deka PC. A basic review of fuzzy logic applications in hydrology and water resources. Applied Water Science. 2020;10(8):1-14. 10.1007/s13201-020-01276-2
51. Ahmed TI, Bhola J, Shabaz M, Singla J, Rakhra M, More S, et al. Fuzzy logic-based systems for the diagnosis of chronic kidney disease. BioMed Research International. 2022;2022. 10.1155/2022/2653665
52. Yudhana A. Tsukamoto Fuzzy Inference System on Internet of Things-Based for Room Temperature and Humidity Control. IEEE Access. 2023;11:6209-27. 10.1109/ACCESS.2023.3236183
53. Umam F, Dafid A, Cahyani AD. Implementation of Fuzzy Logic Control Method on Chilli Cultivation Technology Based Smart Drip Irrigation System. Jurnal Ilmiah Teknik Elektro Komputer dan Informatika. 2023;9(1):132-41. 10.26555/jiteki.v9i1.25813
54. Yogachi E, Nasution V, Prakarsa G, editors. Design and Development of Fuzzy Logic Application Mamdani Method in Predicting The Number of Covid-19 Positive Cases in West Java. IOP Conference Series: Materials Science and Engineering; 2021: IOP Publishing. 10.1088/1757-899X/1115/1/012031
55. Singerman PG, O'Rourke SM, Narayanan RM, Rangaswamy M. Language-based cost functions: Another step toward a truly cognitive radar. IEEE Transactions on Aerospace and Electronic Systems. 2021;57(6):3827-43. 10.1109/TAES.2021.3082714
56. Janarthanan R, Balamurali R, Annapoorani A, Vimala V. Prediction of rainfall using fuzzy logic. Materials Today: Proceedings. 2021;37:959-63. 10.1016/j.matpr.2020.06.179
57. Król A, Sierpiński G. Application of a genetic algorithm with a fuzzy objective function for optimized siting of electric vehicle charging devices in urban road networks. IEEE Transactions on Intelligent Transportation Systems. 2021;23(7):8680-91. 10.1109/TITS.2021.3085103
58. Mitsuishi T, editor Study on Continuity of Defuzzification Using Density Moment Method. 2023 IEEE 13th Symposium on Computer Applications & Industrial Electronics (ISCAIE); 2023: IEEE. 10.1109/ISCAIE57739.2023.10165332
59. Hardi S, Triwiyono A, editors. Expert system for diagnosing osteoarthritis with fuzzy Tsukamoto method. Journal of Physics: Conference Series; 2020: IOP Publishing. 10.1088/1742-6596/1641/1/012107
60. Mert A, editor On the WABL Defuzzification method for intuitionistic fuzzy numbers. Intelligent and Fuzzy Techniques in Big Data Analytics and Decision Making: Proceedings of the INFUS 2019 Conference, Istanbul, Turkey, July 23-25, 2019; 2020: Springer. 10.1007/978-3-030-23756-1_7/COVER
61. Madani Y, Erritali M, Bengourram J, Sailhan F. A hybrid multilingual fuzzy-based approach to the sentiment analysis problem using SentiWordNet. International Journal of Uncertainty, Fuzziness and Knowledge-Based Systems. 2020;28(03):361-90. 10.1142/S0218488520500154
62. Upadhyay K, Dantu R, He Y, Salau A, Badruddoja S, editors. Make consumers happy by defuzzifying the service level agreements. 2021 Third IEEE International Conference on Trust, Privacy and Security in Intelligent Systems and Applications (TPS-ISA); 2021: IEEE. 10.1109/TPSISA52974.2021.00011
63. Sahunthala S, Geetha A, Parthiban L, editors. Computational Fuzzy Inference Logic For Effectively Analyzing Customer Survey. 2020 Fourth International Conference on I-SMAC (IoT in Social, Mobile, Analytics and Cloud)(I-SMAC); 2020: IEEE. 10.1109/I-SMAC49090.2020.9243516
64. Küçük M, Pakdamar F, İpekçi CA. Modeling a rheological cement mixture suitable for 3D printing technology with Fuzzy Logic. A| Z Itu Journal of the Faculty of Architecture. 2022;19(3):689-702. 10.5505/itujfa.2022.25993
65. Liang Z, Liu L, Ding H, Wang G, Feng B, Wang S, et al., editors. Intelligent Control Strategy of Wind Curtain Type Anti-drift Sprayer Based on LSSVM Wind Speed Prediction and Fuzzy Control. International Conference on Guidance, Navigation and Control; 2022: Springer. 10.1007/978-981-19-6613-2_673

66. Radhamani C, editor Crispification of temporal intuitionistic fuzzy sets. AIP Conference Proceedings; 2020: AIP Publishing. 10.1063/5.0026009/1026820

67. Khatri P, Gupta KK, Gupta RK. Raspberry Pi-based smart sensing platform for drinking-water quality monitoring system: A Python framework approach. Drinking Water Engineering and Science. 2019;12(1):31-7. 10.5194/DWES-12-31-2019

68. Jayade S, Ingole D, Ingole MD, Tohare A, editors. Cholera Disease Detection using Fuzzy Logic Technique. 2021 3rd International Conference on Electrical, Control and Instrumentation Engineering (ICECIE); 2021: IEEE. 10.1109/ICECIE52348.2021.9664703

69. Praharaj M, Mohan B. Modeling and analysis of mamdani two-term controllers using non-uniformly distributed multiple fuzzy sets and CoA/CoG defuzzification. IETE Technical Review. 2022;39(4):918-39. 10.1080/02564602.2021.1933628

70. Salgado-Plasencia E, Carrillo-Serrano RV, Toledano-Ayala M. Development of a DSP Microcontroller-Based Fuzzy Logic Controller for Heliostat Orientation Control. Applied Sciences. 2020;10(5):1598. 10.3390/app10051598

71. Plebankiewicz E, Wieczorek D. Adaptation of a cost overrun risk prediction model to the type of construction facility. Symmetry. 2020;12(10):1739. 10.3390/sym12101739

72. Mallick AK, Das A, editors. An analytical survey of defuzzification techniques. 2021 IEEE 4th International Conference on Computing, Power and Communication Technologies (GUCON); 2021: IEEE. 10.1109/GUCON50781.2021.9573993

73. Torra V, Garcia-Alfaro J, editors. Towards an adaptive defuzzification: using numerical Choquet integral. Modeling Decisions for Artificial Intelligence: 16th International Conference, MDAI 2019, Milan, Italy, September 4–6, 2019, Proceedings 16; 2019: Springer. 10.1007/978-3-030-26773-5_11

74. Yadav RS. Application of soft computing techniques to calculation of medicine dose during the treatment of patient: A fuzzy logic approach. Handbook of Computational Intelligence in Biomedical Engineering and Healthcare: Elsevier; 2021. p. 151-78.

75. Chakraverty S, Sahoo DM, Mahato NR. Concepts of soft computing. Springer, Singapore. 2019;1007:978-81. 10.1007/978-981-13-7430-2_7

76. Smith CN, Hittinger E. Using marginal emission factors to improve estimates of emission benefits from appliance efficiency upgrades. Energy Efficiency. 2019;12:585-600. 10.1007/s12053-018-9654-4

77. Ha PTH. A concept for energy-efficient high-rise buildings in Hanoi and a calculation method for building energy efficiency factor. Procedia engineering. 2016;142:154-60. 10.1016/j.proeng.2016.02.026

78. Sowa T, Vasconcelos M, Schnettler A, Metzger M, Hammer A, Reischboek M, et al. Method for the operation planning of virtual power plants considering forecasting errors of distributed energy resources. Electrical Engineering. 2016;98:347-54. 10.1007/s00202-016-0419-9

79. Ufie R, Tupamahu CS, Sarwuna SJ, Frans J. KAJI Performansi Refrigeran R-290, R-32, Dan R-410a Sebagai Alternatif Pengganti R-22. ALE Proceeding. 2021;4:133-9. 10.30598/ale.4.2021.133-139

80. Prianto E, Windarta J, Harianja B. The role of vegetation and landscape in the energy efficiency—of tropical building. Advanced Science Letters. 2017;23(3):2211-4. 10.1166/asl.2017.8671

81. Fitriana S. Analisis Menentukan Rekomendasi Penyejuk Udara Yang Tepat Menggunakan Metode Moora. EVOLUSI: Jurnal Sains dan Manajemen. 2019;7(1). 10.31294/evolusi.v7i1.5010

82. Shah ZA, Sindi HF, Ul-Haq A, Ali MA. Fuzzy logic-based direct load control scheme for air conditioning load to reduce energy consumption. IEEE Access. 2020;8:117413-27. 10.1109/ACCESS.2020.3005054

83. Andrade A, Restrepo A, Tibaquira JE. EER or Fcsp: A performance analysis of fixed and variable air conditioning at different cooling thermal conditions. Energy Reports. 2021;7:537-45. 10.1016/j.egyr.2020.12.041

84. Berouine A, Akssas E, Naitmalek Y, Lachhab F, Bakhouya M, Ouladsine R, et al., editors. A fuzzy logic-based approach for HVAC systems control. 2019 6th international conference on control, decision and information technologies (CoDIT); 2019: IEEE. 10.1109/CoDIT.2019.8820356

85. Pratama AC, Sarno R, editors. Android application for controlling air conditioner using fuzzy logic. 2018 6th International Conference on Information and Communication Technology (ICoICT); 2018: IEEE. 10.1109/ICoICT.2018.8528726

86. Ayyasamy S. Modified Smart Air Conditioner Using Fuzzy Logic. 2023. 10.21203/rs.3.rs-2785784/v1

Persian Abstract

چکیده

مصرف انرژی یک جنبه حیاتی در تلاش برای استفاده بهینه از منابع و کاهش اتلاف انرژی است. تمرکز بر بهره وری انرژی می تواند منجر به صرفه جویی در هزینه های عملیاتی، کاهش انتشار گازهای گلخانه ای و حمایت از پایداری زیست محیطی برای نسل های آینده شود. بنابراین، توجه به بهره وری انرژی در زندگی روزمره، به ویژه در استفاده از برق برای وسایل الکترونیکی مهم است. هدف این تحقیق مقایسه کارایی انرژی دو رویکرد مختلف برای استفاده از تهویه مطبوع (AC) است: روش دستی و روش منطق فازی. روش دستی شامل هشت آزمایش با اندازه‌گیری مستقیم توان در یک دوره ۳۰ دقیقه‌ای در تنظیمات مختلف دمای AC، یعنی ۱۸ درجه سانتی‌گراد، ۲۰ درجه سانتی‌گراد، ۲۳ درجه سانتی‌گراد، ٢٤ درجه سانتی‌گراد، ۲۵ درجه سانتی‌گراد، ٢٦ درجه سانتی‌گراد، ۲۷ درجه سانتی‌گراد است. و ۳۰ درجه سانتی گراد از سوی دیگر، روش منطق فازی شامل شش آزمایش است که امکان تنظیم دمای دینامیکی بر اساس شرایط اتاق را فراهم می کند. یافته‌های تحقیق نشان می‌دهد که روش منطق فازی به جز در دمای ۳۰ درجه سانتی‌گراد که روش دستی کمی کارآمدتر است (تفاوت ١٤٠٧٤٥ وات) به میانگین توان مصرفی کمتری دست می‌یابد. این تفاوت در درجه اول مربوط به حالت "خنک کننده و فن" است که در دماهای پایین تر در روش دستی استفاده می شود و در نتیجه مصرف برق بیشتر می شود. علاوه بر این، این تحقیق پتانسیل منطق فازی را در بهینه‌سازی مصرف برق AC بر اساس شرایط بلادرنگ نشان می‌دهد و تقریباً ٤١.٩٦ درصد صرفه‌جویی در مصرف انرژی را به دست می‌آورد. سهم اصلی این مطالعه ارائه بینش های عملی در مورد اینکه چگونه روش منطق فازی می تواند به طور قابل توجهی مصرف انرژی AC را کاهش دهد، از تلاش های بهره وری انرژی حمایت کند و به پایداری محیطی کمک کند.

IJE TRANSACTIONS A: Basics Vol. 37 No. 01, (January 2024) 201-212

International Journal of Engineering

Journal Homepage: www.ije.ir

A Comparative Analysis of Axial and Radial Forces in Windings of Amorphous Core Transformers

B. D. Thanh*[a], T. H. Le[a], V. D. Quoc[b]

[a] *Faculty of Engineering and Technology, Quy Nhon University, Quy Nhon, Viet Nam*
[b] *School of Electrical and Electronic Engineering, Hanoi University of Science and Technology, Viet Nam*

PAPER INFO

Paper history:
Received 22 August 2023
Received in revised form 18 September 2023
Accepted 19 September 2023

Keywords:
Amorphous Core Transformer
Short-circuit Current
Electromagnetic Force
Radial and Axial Forces
Leakage Flux

ABSTRACT

The aim of this study is to examine and analyze the axial and radial forces, electromagnetic forces (EMFs) acting on the low and high-voltage windings of an amorphous core transformer via the two different approaches: an analytic approach and a 3-D finite element method (FEM). Firstly, the analytic method is proposed to analyze the distribution of leakage magnetic field in the magnetic circuit and the forces acting on the transformer windings. The FEM embedded in the Ansys Maxwell tool is then proposed to compute and simulate the axial and radial forces under three different operating conditions: no-load, rated full-load, and short-circuit. The obtained results from two different methods such as the rated voltage, rated current, short-circuit current, axial and radial forces and EMFs in the low and high-voltage windings are finally compared to illustrate an agreement of methods. The validation of the methods is applied on a three-phase amorphous core transformer of 1600kVA-22/0.4kV.

***doi**: 10.5829/ije.2024.37.01a.18*

1. INTRODUCTION

The utilization of amorphous material in the magnetic circuits of distribution transformers has gained prominence since its development in 1970s. These transformers, known as amorphous transformers (ATs), have become prevalent in power systems due to their lower no-load losses compared to traditional transformers. This reduction in losses contributes to an overall decrease in the total losses of power systems. The extensive research has demonstrated that the ATs can achieve a significant reduction of 50-70% in no-load losses compared to transformers with silicon steel cores (1-5). Due to the special structure of the steel core and the coil with the rectangular shape of the ATs, the distribution of electric field and forces on the windings will be different on the same turn of the coil. Under the normal operating conditions, the electromagnetic forces (EMFs) acting on the windings are small due to the relatively small magnitude of the leakage flux. However, under the short-circuit condition, the electromagnetic forces (EMFs) generated as a result of the interaction between the leakage flux and the short-circuit current are very large, this can lead to translation, destruction, or even explosion of the windings (6-10).

In practices, among various types of transformer faults, winding faults account for approximately 33% of the total occurrences. These faults typically arise from short-circuits between turns within the high voltage (HV) or low voltage (LV) windings, between different layers of windings, between HV and LV windings, or even between phases within the same winding. In such cases, the resulting EMFs or mechanical forces (MFs) can cause bending or destruction of the transformer windings (11-16). The EMF can be further categorized into two distinct components: axial force (Fx) and radial force (Fy). The Fx generated by the interaction between the current in the winding and the axial magnetic field (By) is perpendicular to the winding axis. On the other hand, the Fy produced from the interaction between the current in the winding and the horizontal magnetic field (Bx), is parallel to the winding axis (17-22).

*Corresponding Author Email: doanthanhbao@qnu.edu.vn
(B. D. Thanh)

Please cite this article as: Thanh BD, Le TH, Quoc VD. A Comparative Analysis of Axial and Radial Forces in Windings of Amorphous Core Transformers. International Journal of Engineering, Transactions A: Basics, 2024;37(01):201-212.

Wang et al. (7) provided a detailed description of the design and operation of a three-phase AT with a capacity of 630 kVA-10.5/0.4 kV. The study focused on acquiring the fundamental characteristics of the AT through standard short-circuit and no-load tests. The utilization of amorphous alloy as the iron core material in the AT offers several advantages, including reduced losses and excellent magnetization characteristics. Consequently, amorphous alloys have found widespread application in small-capacity distribution power transformers.

Zhong et al. (8) used a finite element method (FEM) to compute the stress and strain of the end covers and the winding clamps of the AT of 800 kVA/10 kV. Based on that, the shell-form transformer demonstrated the superior capability to withstand short-circuits, and historical evidence has primarily relied on the use of silicon steel iron core materials. Kumbhar and Kulkarni (23) analyzed the EMFs acting on the windings of split-winding transformers by using a nonlinear-transient field-circuit coupled finite element model. In this study, a three-phase split-winding transformer of 70MVA-220/3.6/6.9kV was simulated and examined via the FEM under both preset and postset short-circuit test conditions. Mouhamad et al. (24) conducted the short-circuit withstand tests of Metglas 2605SA1-based amorphous transformers, rated 240 to 630kVA. In this paper, the authors focused on calculating the short-circuit current and the electrodynamic forces experienced by the transformer windings. However, their work did not explicitly address the distribution of the leakage magnetic field or the axial and radial forces within the transformers. Bal et al. (25) used the FEM embedded in ANSYS Maxwell simulation program to analyze the electromagnetic transients and compute the losses, voltages, currents and magnetic fluxes of a three-phase oil-type distribution transformer with a capacity of 25kVA. Li et al. (26) presented the distribution of EMF in a three-phase power transformer of a 50MVA/110 kV under short-circuit conditions via the FEM. Jin et al. (27) explored the stress distribution characteristics of a composite wire-paper winding structure when subjected to radial electromagnetic forces. A copper-paper layered ring was employed as the experimental setup. The study involved calculating both the hoop stress distribution and the radial stress distribution within the winding structure. The FEM was then used to verify the obtained results. Zhai et al. (28) established a three-dimensional model of the transformer to investigate the electrodynamic force and deformation of transformer windings under short-circuit conditions. The distribution transformers have received limited attention in previous studies, with few investigations conducted on this specific type of transformer. Furthermore, the existing literature lacks a comprehensive model for calculating Fx and Fy in distribution transformers. However, in literature review (29-32), the FEM is employed to analyze and compute various parameters such as leakage magnetic field, leakage reactance, and electromagnetic forces in both the HV and LV windings of the transformer during short-circuit tests. In these studies, a mathematical model was proposed to calculate the current and transient electromagnetic force. The leakage magnetic field density and average electromagnetic force were provided based on FEM simulation results. These obtained results using FEM are then compared with those of the analytic method.

The EMFs can be calculated by using different methods. The analytic method can provide a comprehensive and faster solution. Unfortunately, these methods may not be applied in models with nonlinear materials, complex geometric structures, and/or boundary conditions. Therefore, the FEM method based on Ansys Maxwell 3D software in the time domain is applied to solve the problem with complex shapes, multi-physics environment, and the EMFs calculation in each part or each position of the windings. Thanh et al. (33) used 2D FEM to analyze and calculate the magnetic field for a 160kVA indefinite shape MBA. In this paper, the model is considered in a short-circuit mode with maximum current, without considering the 3D model under various operating conditions such as no-load, rated load, and three-phase short-circuit conditions on the low-voltage side.

In general, as mentioned above, the FEM to analyze and calculate the distribution of magnetic fields, fringing and leakage impedances and electromagnetic forces acting on the HV and LV windings of the MBA in short-circuit conditions. They also provided formulas to calculate the overcurrent and electromagnetic force during short-circuit conditions. The results obtained include 2D FEM images of the magnetic field density and average electromagnetic forces, which are then compared with classical analytical methods. Furthermore, there are very few research works on the magnetic field and electromagnetic force of the armorphous steel-core MBA. No research has comprehensively analyzed and evaluated various operating conditions of the armorphous MBA using 3D FEM models, progressing from analytical models to full 3D FEM models. Using a 3D FEM model approaches a nearly real representation of the MBA, allowing for the analysis of multi-physics phenomena, including mechanical, electrical, and thermal effects. This approach helps accurately to determine the winding strength in various short-circuit condition, which can be challenging to achieve through analytical methods and experiments.

Based on the development from published paper by Thanh et al. (33), in this context, the magnetic vector potential. Formulations (A) is first presented to define the distribution of leakage magnetic field in the magnetic circuit and the distribution of EMFs in the transformer windings. Then, the FEM is developed based on Ansys Maxwell 3D in the time domain to simulate electromagnetic parameters of a three-phase TA of 1600kVA, 22/0.4 kV under several operating conditions, such as no-load, rated full-load and short-circuit. The obtained results from the FEM are verified and compared with the analytic model in terms of accuracy. In addition, the EMFs acting on the HV and LV windings will be also determined in the case of a three-phase short-circuit of the LV winding. This research is conducted based on the following assumptions: (1) the neglect of eddy current effects in the windings; (2) the assumption of uniform current density in the windings; (3) the consideration of a symmetric model for analysis.

2. SHORT-CIRCUIT ELECTROMAGNETIC FORCE ANALYSIS

2. 1. Short-circuit Current

The short-circuit current flowing in the windings has the potential to cause damage to the transformer windings. This transient short-circuit current comprises two different components, namely (8, 29, 34):

$$\begin{aligned} i_{SC} &= i_{hos} + i_{dos} \\ &= I_n\sqrt{2}.\sin\left(\omega t - \phi - \varphi_n\right) + I_n\sqrt{2}.\sin(\phi + \varphi_n).e^{-\frac{R_n}{X_n}\omega t} \end{aligned} \tag{1}$$

where:
- i_{hos} is the harmonic oscillation,
- i_{dos} is the damped oscillation,
- $I_n = \frac{U_{rated}}{Z_n}$ is the root mean square (SMS) of short-circuit current (A),
- $\varphi_n = \mathrm{arctg}\frac{X_n}{R_n}$ is the phase angle (rad),
- U_{rated} is the rated voltage
- Z_n is the short-circuit impedance (Ω),
- X_n and R_n are respectively short-circuit resistance and reactance (Ω),
- t is the time (s),
- ϕ is the angle depending on the short-circuit time (rad),
- ω is the angular frequency (rad/s).

2. 2. Analytic Model for Computation of the Leakage Magnetic Fields and EMFs in Transformer Windings

Based on Maxwell's equations, the separate equation for the stationary electromagnetic field (∂/∂t = 0) in the transformer windings associated with the current density J, the Laplace-Poisson's equation for A(x,y,z) can be obtained as follows (22, 26, 28, 33):

$$\nabla^2\mathbf{A}(x,y,z) = \begin{cases} -\mu\mathbf{J} & \text{in the windings} \\ 0 & \text{others} \end{cases} \tag{2}$$

In three-dimensional Descartes coordinates, Equation 2 can be written as:

$$\frac{\partial^2\mathbf{A}(x,y,z)}{\partial x^2} + \frac{\partial^2\mathbf{A}(x,y,z)}{\partial y^2} + \frac{\partial^2\mathbf{A}(x,y,z)}{\partial z^2} = -\mu\,\mathbf{J} \tag{3}$$

where A(x,y,z) is the magnetic vector potential, μ is the relative permeability (H/m) and J is the electric current density in the windings (A/m^2).

In Figure 1, the magnetic field is perpendicular to the plane (∂A/∂z = 0). Hence, Equation 3 can be represented as:

$$\frac{\partial^2\mathbf{A}(x,y)}{\partial x^2} + \frac{\partial^2\mathbf{A}(x,y)}{\partial y^2} = -\mu\mathbf{J} \tag{4}$$

where the **J** can be computed via the electric current density in the HV winding ($\mathbf{J}_1$) and LV winding ($\mathbf{J}_2$), that is:

$$\mathbf{J}_1 = \frac{W_1 i_1}{a_1 b_1};\ \mathbf{J}_2 = \frac{W_2 i_2}{a_2 b_2} \tag{5}$$

where a_1b_1 and a_2b_2 are the cross-sections of the HV and LV windings, respectively. The quantities i_1 and i_2 are the electric currents in HV and LV windings, respectively.
The magnetic vector potential **A** (x,y) in Equation 4 can be analysed in the form of a harmonic series:

$$\mathbf{A}\left(x,y\right) = \sum_j\sum_k A_{j,k}\cos(m_j x).\cos(n_k y) \tag{6}$$

where $A_{j,k}$ is the constant of integration calculation. The terms of m and n are the phase angles.

The components of a magnetic field in the x- and y-axis at the boundaries of the magnetic window are

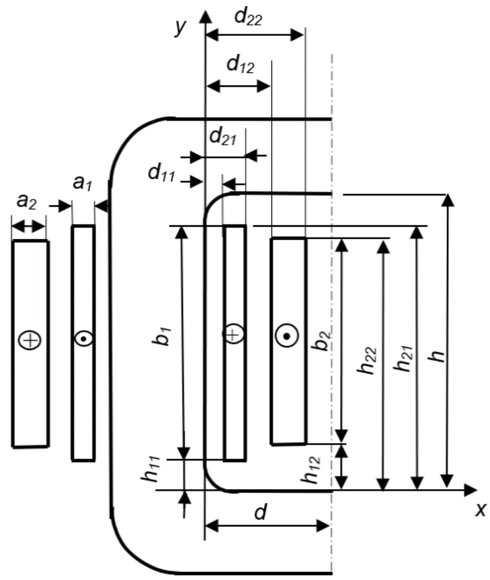

Figure 1. Typical dimensions of windings and the magnetic circuit

considered as a zero (i.e., $B_x = 0$ and $B_y = 0$). The boundary conditions (BCs) are defined as:

$$\sin(m_j d) = 0 \rightarrow m_j = (j-1)\frac{\pi}{d} \tag{7}$$

$$\sin(n_k h) = 0 \rightarrow n_k = (k-1)\frac{\pi}{h} \tag{8}$$

where j and k are the integers.
For j = k = 1 and $m_1 = n_1 = 0$, the harmonic sequence is a constant. The constant of integration $A_{j,k}$ can be generally illustrated as:

$$A_{j,k} = \frac{4\,\mu_0}{d.h}\frac{1}{m_j n_k (m_j^2 + n_k^2)} \times \left[\begin{array}{l} J_1\left(\sin m_j d_2^1 - \sin m_j d_1^1\right)\left(\sin n_k h_2^1 - \sin n_k h_1^1\right) \\ +J_2\left(\sin m_j d_2^2 - \sin m_j d_1^2\right) x\ (\sin n_k h_2^2 - \sin n_k h_1^2) \end{array} \right] \tag{9}$$

The magnetic flux density (**B**) can be given as $\mathbf{B} = \nabla \times \mathbf{A}$, the components of **B** in the x- and y- axis at the boundaries of the magnetic window are expressed as:

$$\begin{cases} B_x = \dfrac{\partial \mathbf{A}(x,y)}{\partial y} \\ B_y = -\dfrac{\partial \mathbf{A}(x,y)}{\partial x} \end{cases} \tag{10}$$

2. 3. The Axial and Radial Forces in the Windings

As presented, the EMFs acting on the transformer windings are the interaction between the transient currents and the leakage magnetic field within the winding regions. For that, the EMF can be split into two components, i.e., the F_x and F_y as shown in Figure 2. The observed trends of these forces are as follows:

- They exert compression forces, leading to a reduction in the radius of the inner coil.
- They exert tension forces, resulting in an increase in the radius of the outer coil.
- They exert compression forces, causing a decrease in the height of both coils.

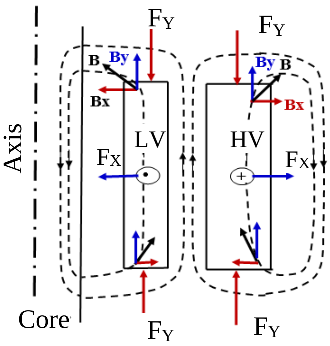

Figure 2. Components of magnetic induction field Fx and Fy in the transformer windings

⁎ *The components of EMF in the LV winding, per unit length of the winding*:
The radial force ($F_{X\text{-}LV}$) in the x-axis is defined as:

$$F_{X\_LV} = \int_{d_1^1}^{d_2^1}\int_{h_1^1}^{h_2^1} J_1 B_y \,dx\,dy = -J_1 \int_{d_1^1}^{d_2^1}\int_{h_1^1}^{h_2^1} \frac{\partial \mathbf{A}(x,y)}{\partial x}\,dx\,dy \tag{11}$$

In the same way, the radial force ($F_{y\text{-}LV}$) in the y-axis is defined as:

$$F_{Y\_LV} = \int_{d_1^1}^{d_2^1}\int_{h_1^1}^{h_2^1} J_1 B_x \,dx\,dy = J_1 \int_{d_1^1}^{d_2^1}\int_{h_1^1}^{h_2^1} \frac{\partial \mathbf{A}(x,y)}{\partial y}\,dx\,dy \tag{12}$$

⁎ *The components of EMF in the HV winding, per unit length of the winding*:
The radial force ($F_{X\text{-}HV}$) in the x-axis is defined as:

$$F_{X\_HV} = \int_{d_1^2}^{d_2^2}\int_{h_1^2}^{h_2^2} J_2 B_y \,dx\,dy = -J_2 \int_{d_1^2}^{d_2^2}\int_{h_1^2}^{h_2^2} \frac{\partial \mathbf{A}(x,y)}{\partial x}\,dx\,dy \tag{13}$$

In the similar way, the radial force ($F_{y\text{-}HV}$) in the y-axis is defined as:

$$F_{Y\_HV} = \int_{d_1^2}^{d_2^2}\int_{h_1^2}^{h_2^2} J_2 B_x \,dx\,dy = -J_2 \int_{d_1^2}^{d_2^2}\int_{h_1^2}^{h_2^2} \frac{\partial \mathbf{A}(x,y)}{\partial y}\,dx\,dy \tag{14}$$

3. ANALYTICAL TEST

The practical test problem is a three-phase amorphous core transformer of 1600kVA-22/0.4kV produced by the Sanaky transformer manufacturing factory as depicted in Figure 3. The parameters are given in Table 1. The cross-section of the core is the rectangular with the magnetic tape width b = 170 mm, thickness 2b = 340 mm; circuit window height H_{cs} = 550 mm, and distance between two cylinder centers Mo = 435 mm.

The short-circuit currents in the HV and LV windings are illustrated in Figures 4 and 5, respectively. The maximum short-circuit currents in the HV and LV windings are shown in Table 2.

Figure 3. Model of a three-phase 1600kVA-22/0.4kV

TABLE 1. Basic parameters of a three-phase amorphous core transformer

No.	Parameter	Value
1	No. of phases	3
2	Frequency [Hz]	50
3	Capacity [kVA]	1600
4	Wiring connections	Δ/Y-11
5	Hv/LV [kV]	22/0.4
6	Turns of HV/LV windings	1001/10
7	Phase current in HV/LV windings [A]	24.24/2309.4
8	Short-circuit current in HV/LV windings [A]	542.28/51664.43

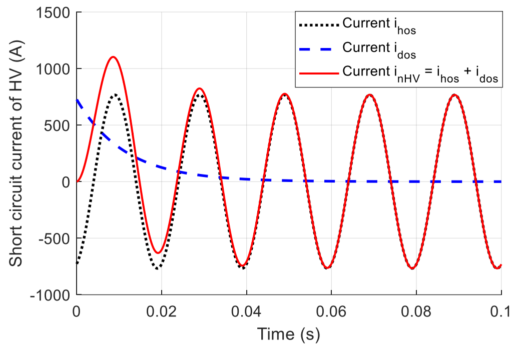

Figure 4. Distribution of the short-circuit current in the HV winding

TABLE 2. Maximum short-circuit currents in the HV and LV windings

Parameter	LV winding	HV winding
Maximum short-circuit current (A)	111090	1102.8

Based on Equation 5, the electric current densities in the LV and HV windings can be respectively calculated as:

$$J_1 = J_{nLV} = \frac{W_{LV} i_{nLVmax}}{a_1 b_1} = \frac{10\times 111090}{23\times 520}\times 10^6 = 92.88\times 10^6 (A/m^2) \tag{15}$$

$$J_2 = J_{nHV} = \frac{W_{HV} i_{nHVmax}}{a_2 b_2} = \frac{1001\times 1102,8}{37\times 520}\times 10^6 = 57.38\times 10^6 (A/m^2) \tag{16}$$

By using the MATLAB software, the magnetic vector potential **A** is demonstrated in Figure 6.

From Equations 11 to 14, the F_x and F_y in the LV winding are pointed out in Figures 7 and 8, respectively.

In Figure 7, it can be seen that the LV winding along the y-axis (height of winding) is pushed inwards by the F_x. The distribution of this force gradually diminishes towards the two ends of the winding. The maximum value of the radial force occurs at the middle of the winding, reaching a peak value of F_{xmax} = 24.94.10^7 N/m^2.

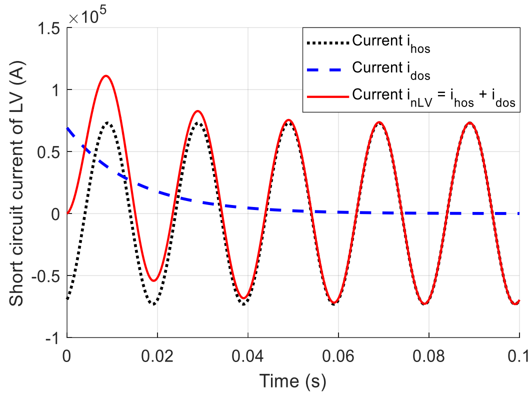

Figure 5. Distribution of the short-circuit current in the LV winding

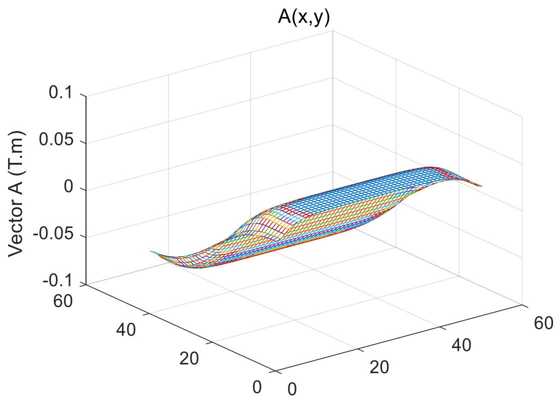

Figure 6. Distribution of magnetic vector potential

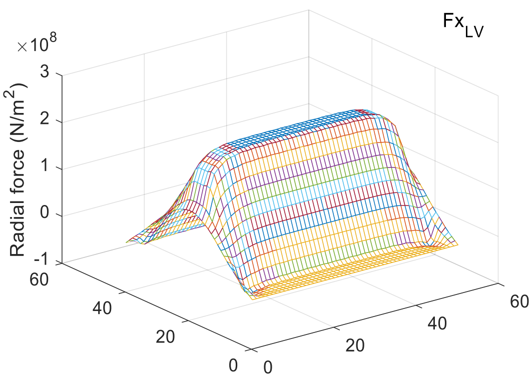

Figure 7. Radial force (F_x) in the LV winding

Figure 8 illustrates that the distribution of F_y is predominantly concentrated at the two ends of the winding, with a maximum value of F_{ymax} = ± 1.862×10^7N/m^2. In contrast, the F_y becomes zero at the midpoint of the winding.

The distribution of F_x along the y-axis (height of winding) of the HV winding is presented in Figure 9. It shows that the LV winidng is pushed far away. The distribution of this force gradually decreases to the two ends of the winding. The maximum value of radial force is at the middle of the winding with F_{xmax} = -15.44×10^7N/m^2. In the same way, the distribution of F_y is given in Figure 10. It can be seen that this force concentrates at the two ends of the winding with the maximum value of F_{ymax} = ± 3.31×10^7N/m^2. It becomes zero in the middle of the winding. The maximum EMFs acting on the HV and LV windings are represented in Table 3.

4. NUMERICAL TEST

An analytic test was given in the previous Section, in this section, the FEM is applied to verify the results from the analytic model. Keep the same prameters of the amorphous core transformer of 1600kVA – 22/0.4kV given already in Figure 1 and Table 1. The steel code of 2605HB1M has the magnetic induction field B = 1.63T. The amorphous core is pointed out in Figure 11. The geometry of the steel core generated in Ansys Maxwell 3D given in Figure 12. To minimize the calculation time, half of the cross-section in 3D is utilized due to the model inherent symmetry. In addition, the insulation material and support structure are neglected in this model (31).

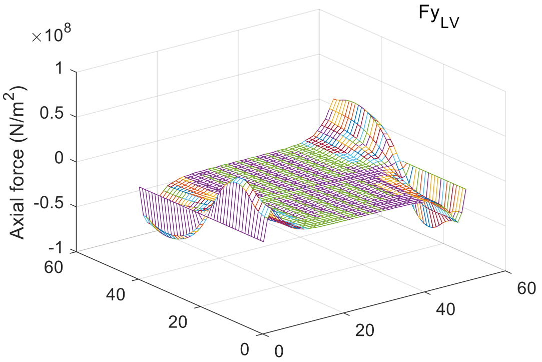

Figure 8. Axial force (F_y) in the LV winding

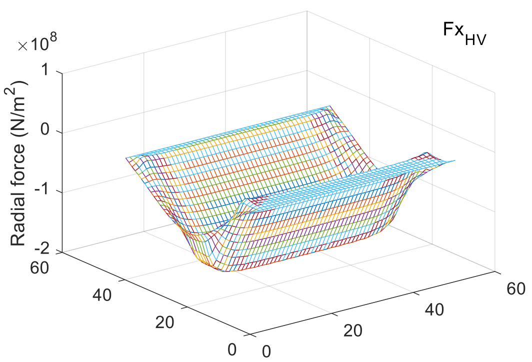

Figure 9. Radial force (F_x) in the HV winding

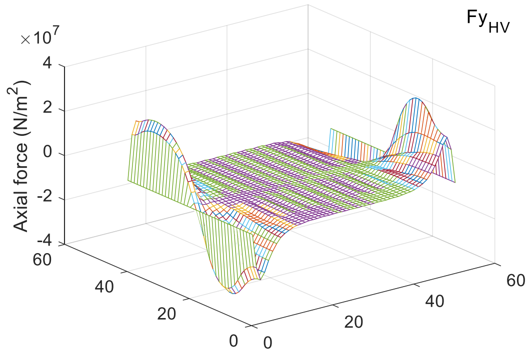

Figure 10. Axial force (F_y) in the HV winding

TABLE 3. Maximum EMFs acting on the HV and LV windings

Maximum force (10^7) (N/m^2)	LV winding	HV winding
F_{xmax}	24.94	-15.44
F_{ymax}	± 5.35	± 3.31

The algorithm for calculation of the F_x and F_y using Ansys Maxwell 3D in different operating conditions is proposed in Figure 13.

The simulation test includes three different operating conditions: no-load, rated full-load, and short-circuit. The time intervals for each condition are as follows:

- Firstly, the no-load condition is simulated from 0 to 50 ms
- Secondly, the rated full-load condition is simulated from 50 to 100ms

Figure 11. Steel core of the three-phase amorphous core transformer

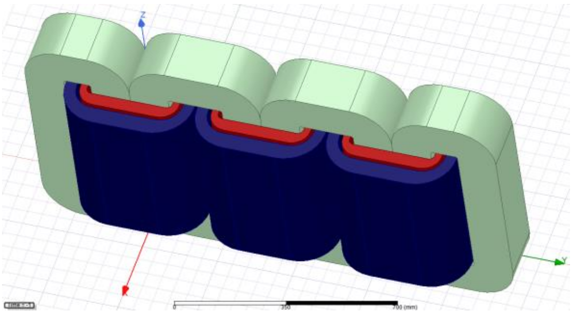

Figure 12. Geometry of the steel core generated in Ansys Maxwell 3D

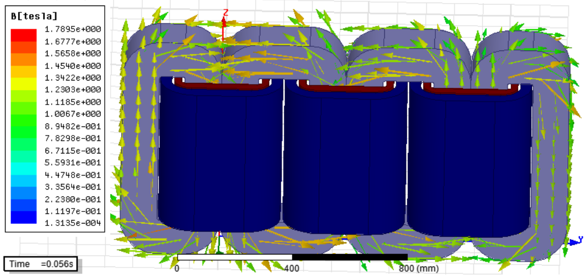

Figure 14. Distribution of magnetic flux density (B) at t = 56ms

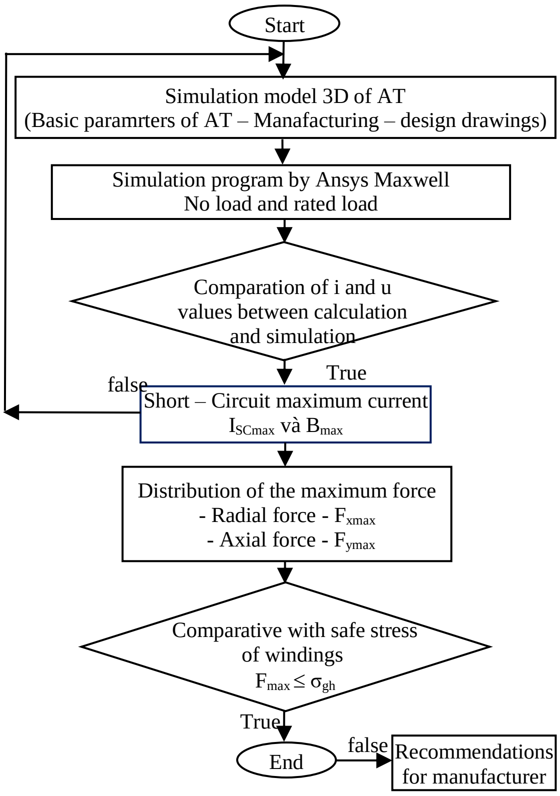

Figure 13. Algorithm for computation of Fx and Fy using Ansys Maxwell 3D

- Finally, the short-circuit condition is simulated from 150 ms to 300ms.

Figure 14 illustrates the distribution of B in the steel core of at a specific time t = 56ms.

The investigation focuses on the value and direction of the magnetic field in the magnetic circuit under both no-load and rated full-load conditions. In this analysis, the maximum magnetic flux density achieved is B_{max} = 1.78T. Subsequently, the study examines the voltages and currents in the windings of the AT, as follows.

4. 1. Under the Rated Full-load Condition The three-phase rated voltage in HV and LV windings are shown in Figures 15 and 16, respectively. According to Figure 15, the simulated value of the rated voltage in the HV winding is 311320V (with a calculated value of 31112.7V. Similarly, as illustrated in Figure 16, the simulated value of the rated voltage in the LV winding is 310.7V (with a calculated value of 326.6V). The maximum error between the simulated and calculated values is 4.9%.

The three-phase rated currents in the HV and LV windings is presented in Figures 17 and 18. In Figure 17, the simulated value of the rated current in the HV winding is 33.22A (compared to a calculated value of 34.28A), whereas the simulated value of the rated current in LV winding is 3274.14A (compared to a calculated value of 3265.99A in Figure 18. The maximum error

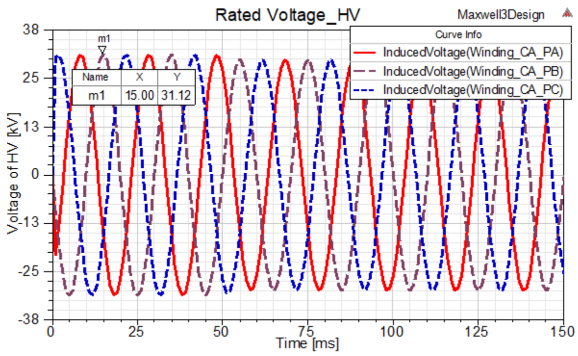

Figure 15. Three-phase rated voltage in the HV winding

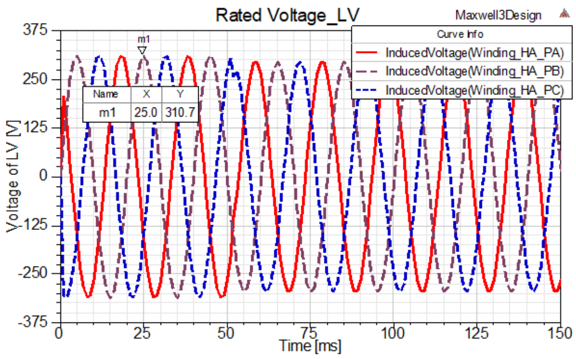

Figure 16. Three- phase fated voltages in the LV winding

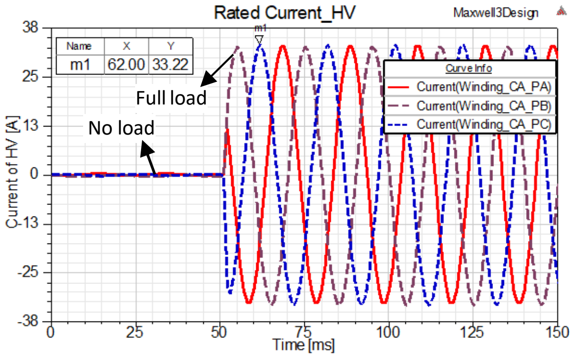

Figure 17. Three- phase rated currents in the HV winding

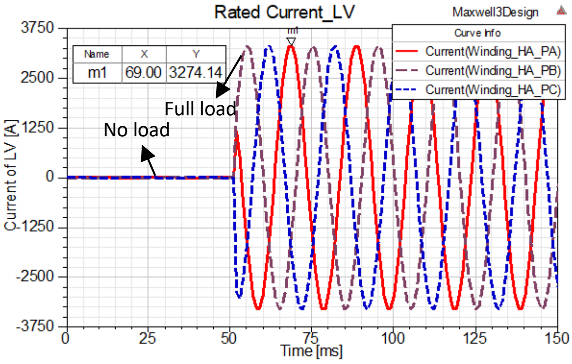

Figure 18. Three- phase rated currents in the LV winding

between the simulated and calculated values is 3.1%. The values obtained for voltages and currents using the simulation method align closely with the values derived from the analytic method under both no-load and rated full-load conditions.

4. 2. Under the Short-circuit Condition

**) Short-circuit current*

The short-circuit test of the LV winding is performed in a three-phase configuration, controlled by switch S as shown in Figure 19. The short-circuit test is initiated at t = 150ms. At this specific time, the voltage in phase B becomes zero, while the short-circuit current in phase B reaches its maximum value. The simulation is then conducted up to 300ms, with an incremental time step of $\Delta t = 0.1$ms

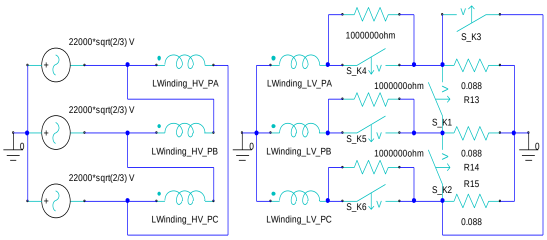

Figure 19. Diagram of control circuit

**) Distributions of leakage magnetic field and electromagnetic forces*

The problem is considered in the time domain, allowing for the analysis of the magnetic induction distribution within the magnetic circuit and windings at various operating times of the AT. Specifically, during the short-circuit period, the currents, magnetic field, and electromagnetic forces in the windings are examined at the time when the short-circuit current reaches its maximum value. Figure 20 illustrates the simulated magnetic induction at t = 159ms during the short-circuit condition.

At t = 159ms, which corresponds to the maximum short-circuit current in phase B, the leakage magnetic field within the winding intensifies to B = 2.6T, while the magnetic induction within the magnetic circuit decreases. A significant portion of the distributed leakage magnetic field is concentrated in the region between the HV and LV windings. Figures 21 and 22 showcase the short-circuit currents within the HV and LV windings, respectively.

As depicted in Figure 21, at t = 159ms, the short-circuit current in the HV winding of phase B reaches its maximum value, with I_{CA_max} = 1109.4A. This value is 33 times greater than the rated phase current. Similarly, Figure 22 demonstrates that at t = 159 ms, the short-circuit current in the LV winding of phase B attains its maximum value, with I_{HA_max} = 111076A. This value is

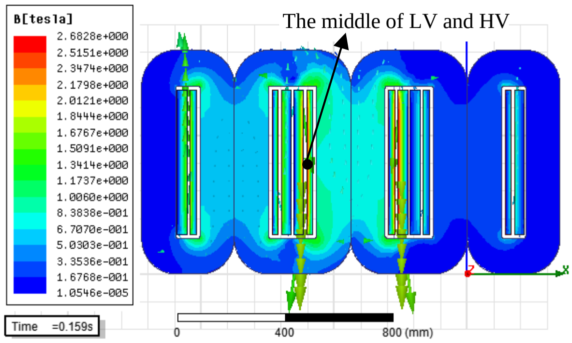

Figure 20. Magnetic induction at the time of t = 159ms

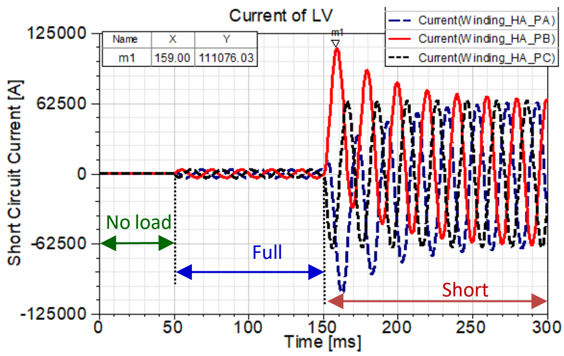

Figure 21. Short-circuit currents in the HV winding

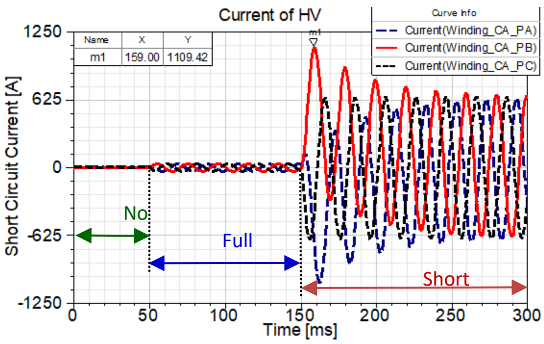

Figure 22. Short-circuit currents in the LV winding

TABLE 4. Comparion of the currents and voltages between the analytic method and FEM

Condition	Winding	Analytic method	FEM	Error %
Ratedphase voltage (V)	HV	31112.7	31120	0.02
	LV	326.6	310.7	4.9
Rated phase current (A)	HV	34.28	33.22	3.1
	LV	3265.99	3274.14	0.2
Short-circuit impulse current (A)	HV	1102.8	1109.4	0.6
	LV	111090	111076	0.01

34 times greater than the rated phase current. Table 4 presents a comparison of the currents and voltages in the HV and LV windings obtained through both the analytic method and the simulation method.

Based on the comparison results presented in Table 4, there are differences between the values obtained using the two methods. It should be noted that these disparities arise because the insulation material and support structure of the AT were disregarded in the model used for this analysis.

4. 3. EMFs Acting on the HV and LV Windings

The FEM embeded in Ansys Maxwell tool is proposed to analyze both the direction and magnitude of the magnetic field vector surrounding the winding space, as well as the maximum current density during short-circuit conditions. This enables the determination of the distributions of EMFs acting on the HV and LV windings.

At the cross-section of transformer in the Oxy plane, the EMFs can be divided into two components, i.e., $F_x = B_y.\ J_z$ and $F_y = B_x.\ J_z$.

The distributions of F_x and F_y in the LV winding at the time t = 159 ms are shown in Figure 23 and Figure 24.

As depicted in Figure 23, the F_x reaches its maximum value at the midpoint of the winding, with $F_{xmax\_LV} = 24.10\times10^7 N/m^2$ for the LV winding. Similarly, in Figure 24, the F_y attains its maximum values at the two ends of the winding, with $F_{ymax\_LV} = \pm 5.46\times10^7 N/m^2$ for the LV winding.

Similarly, the distributions of F_x and F_y in the HV winding at the time t = 159ms are pointed out in Figures 25 and 26.

In Figure 25, the F_x gets the maximum value at the middle of the winding with $F_{xmax\_HV} = -15.76\times10^7 N/m^2$, whereas the F_y gets the maximum values at the two ends of the winding $F_{ymax\_LV} = \pm 3.39\times10^7 N/m^2$ in Figure 26. The maximum values of F_x and F_y and in the HV and LV windings between two methods are given in Table 5.

The maximum total F_x is concentrated at the center between the outer boundary of the LV winding and the

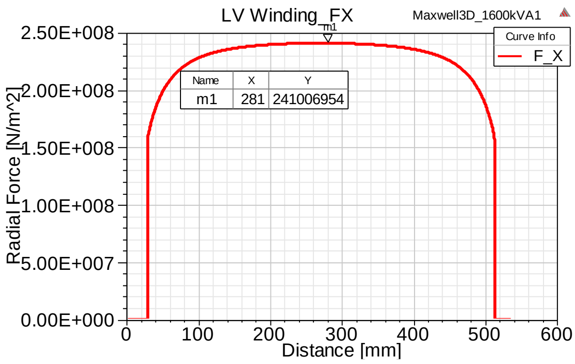

Figure 23. Distribution of F_x in the LV winding

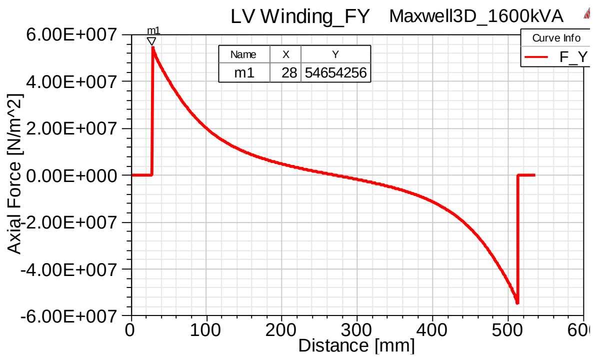

Figure 24. Distribution of F_y in the LV winding

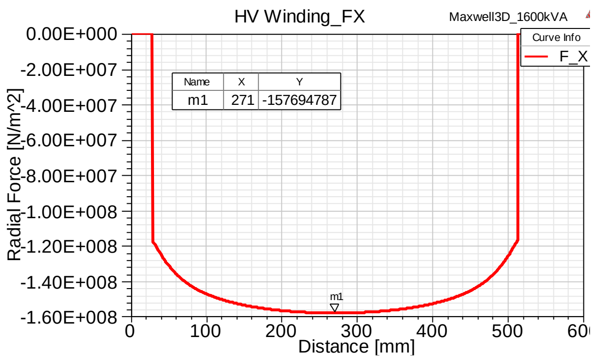

Figure 25. Distribution of F_x in the HV winding

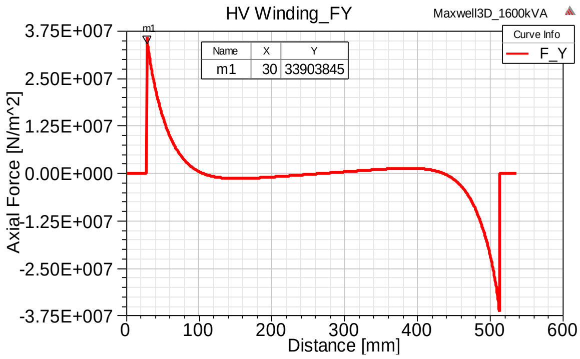

Figure 26. Distribution of the F_y in the LV winding

TABLE 5. Comparative results of the maximum values of F_x and F_y between two different methods

Winding	$F_{max}\times10^7$ (N/m^2)	Analytic method	FEM 3D	Error (%)
LV	F_{xLVmax}	24.94	24.10	3.37
	F_{yLVmax}	± 5.35	± 5.46	2.05
HV	F_{xHVmax}	– 15.44	– 15.76	2.07
	F_{yHVmax}	± 3.31	± 3.39	2.41

inner boundary of the HV winding. This force exerts a pulling effect on the winding. The maximum force, as presented in Table 5, is F_{xmax} = 24.94×10^{7}N/m^2. If the winding is considered as a solid object, the allowable stress for copper is typically within the range of $\sigma_{safe\ stress}$ = (5÷10)×10^{7}N/m^2 (15). Consequently, when a short circuit occurs with the maximum current, the maximum stress on the winding exceeds the permissible limit.

5. CONCLUSIONS

In this study, a mathematical model based on Maxwell's equations is introduced, enabling the derivation of Laplace-Poisson's equation for the magnetic vector potential formulation. Using this equation, the F_x and F_y acting on the windings of the AT of 1600kVA - 22/0.4kV have been successfully calculated. Additionally, the FEM, employing Ansys Maxwell 3D software based on Transient magnetic, is utilized to compute and simulate magnetic flux density and forces under three operating conditions: no-load, rated full-load. After that, it was confirmed that the FEM 3D simulation model was accurate, and researched the short circuit on the LV winding to find maximum the short circuit current; maximum radial and axial electromagnetic force. The obtained values of currents and voltages during rated full-load and short-circuit conditions are compared. The comparison results show that the mathematical modeling and 3D FEM completely coincide. This force may exceed the allowable limit for the winding, thereby risking its destruction, breakage, or displacement during a short circuit. Use the 3D FEM model to research and calculate and simulate the working modes of the transformer and the short circuit and destructive fault modes that experimental methods cannot do.

For future research, it is suggested to further employ the FEM based on Ansys Maxwell 3D software to investigate the distributions of EMFs at various positions in the windings. The simulation of the AT to determine the maximum force in the windings is crucial for the design, manufacturing, testing, and operation of energy-saving amorphous transformers.

6. ACKNOWLEDGEMENTS

This work was supported by the project B2022-DQN-03 sponsored by the Ministry of Education and Training, Vietnam.

7. REFERENCES

1. Steinmetz T, Cranganu-Cretu B, Smajic J, editors. Investigations of no-load and load losses in amorphous core dry-type transformers. The XIX International Conference on Electrical Machines-ICEM 2010; 2010: IEEE. 10.1109/ICELMACH.2010.5608162
2. Bahmani MA. Core loss calculation in amorphous high frequency high-power transformers with different topologies. 2011.
3. Roginskaya L, Yalalova Z, Gorbunov A, Rakhmanova J, editors. Features of amorphous steel magnetic cores for transformers operating at mains frequency. 2020 International Conference on Electrotechnical Complexes and Systems (ICOECS); 2020: IEEE. 10.1109/ICOECS50468.2020.9278451
4. Nazmunnahar M, Simizu S, Ohodnicki P, Bhattacharya S, McHenry M. Finite-element analysis modeling of high-frequency single-phase transformers enabled by metal amorphous nanocomposites and calculation of leakage inductance for different winding topologies. IEEE Transactions on Magnetics. 2019;55(7):1-11. 10.1109/TMAG.2019.2904007
5. Li D, Zhang L, Li G, Lu Z, Zhou S. Reducing the core loss of amorphous cores for distribution transformers. Progress in natural science: Materials international. 2012;22(3):244-9. https://doi.org/10.1016/j.pnsc.2012.04.005
6. Zakrzewski K, Tomczuk B, Koteras D. Amorphous modular transformers and their 3D magnetic fields calculation with FEM. COMPEL-The international journal for computation and mathematics in electrical and electronic engineering. 2009;28(3):583-92. 10.1108/03321640910950034
7. Wang Y, Zhao X, Han J, Li H, Guan Y, Bao Q, et al. Development of a 630 kVA three-phase HTS transformer with amorphous alloy cores. IEEE transactions on applied superconductivity. 2007;17(2):2051-4. 10.1109/TASC.2007.898162
8. Zhong H, Niu W, Lin T, Han D, Zhang G, editors. The analysis of short-circuit withstanding ability for a 800KVA/10KV shell-form power transformer with amorphous alloy cores. 2012 China International Conference on Electricity Distribution; 2012: IEEE. 10.1109/CICED.2012.6508689
9. Bkhaitawi A, Abdoos AA, Ebadi A. Presenting an Adaptive Restraint Method to Improve Performance of Ground Differential Protection of Power Transformer. International Journal of

Engineering, Transactions A: Basic. 2022;35(11):2213-9. 10.5829/ije.2022.35.11b.16

10. Ebadi A, Hosseini S, Abdoos A. A New Simple Method to Avoid Maloperation of Transformer Restricted Earth Fault Relay during External Fault Events. International Journal of Engineering, Transactions C: Aspects. 2021;34(9):2070-6. 10.5829/IJE.2021.34.09C.04
11. Sharifian M, Esmaeilzadeh R, Farrokhifar M, Faiz J, Ghadimi M, Ahrabian G. Computation of a single-phase shell-type transformer windings forces caused by inrush and short-circuit currents. Journal of Computer Science. 2008;4(1):51-8. 10.3844/jcssp.2008.51.58
12. Luo M, Dujic D, Allmeling J, editors. Leakage flux modelling of multi-winding transformer using permeance magnetic circuit. 2016 IEEE Applied Power Electronics Conference and Exposition (APEC); 2016: Ieee. 10.1109/APEC.2016.7468009
13. Hsieh M-F, Hsu C-H, Fu C-M, Huang Y-M. Design of transformer with high-permeability ferromagnetic core and strengthened windings for short-circuit condition. IEEE Transactions on Magnetics. 2015;51(11):1-4. 10.1109/TMAG.2015.2457956
14. Ahn H-M, Oh Y-H, Kim J-K, Song J-S, Hahn S-C. Experimental verification and finite element analysis of short-circuit electromagnetic force for dry-type transformer. IEEE Transactions on Magnetics. 2012;48(2):819-22. 10.1109/TMAG.2011.2174212
15. Dekler M. Transformer_Engineering_-_Design_and_Practice-Chapter 6: Short Circuit Stresses and Strength. no year. 2000.
16. Ahn H-M, Lee B-J, Kim C-J, Shin H-k, Hahn S-C, editors. Finite element modeling of power transformer for short-circuit electromagnetic force analysis. 2012 15th International Conference on Electrical Machines and Systems (ICEMS); 2012: IEEE.
17. Zhang H, Yang B, Xu W, Wang S, Wang G, Huangfu Y, et al. Dynamic deformation analysis of power transformer windings in short-circuit fault by FEM. IEEE Transactions on Applied Superconductivity. 2013;24(3):1-4. 10.1109/TASC.2013.2285335
18. Ahmad A, Javed I, Nazar W, Mukhtar MA. Short circuit stress analysis using FEM in power transformer on HV winding displaced vertically & horizontally. Alexandria engineering journal. 2018;57(1):147-57. 10.1016/j.aej.2016.10.006
19. Dawood K, Komurgoz G, editors. Investigating effect of Electromagnetic Force on Sandwich Winding Transformer using Finite Element Analysis. 2021 28th International Workshop on Electric Drives: Improving Reliability of Electric Drives (IWED); 2021: IEEE. 10.1109/IWED52055.2021.9376371
20. Kothavade JU, Kundu P, editors. Investigation Of Electromagnetic Forces In Converter Transformer. 2021 IEEE 2nd International Conference on Smart Technologies for Power, Energy and Control (STPEC); 2021: IEEE. 10.1109/STPEC52385.2021.9718676
21. Zhao Y, Chen W, Jin M, Wen T, Xue J, Zhang Q, et al. Short-circuit electromagnetic force distribution characteristics in transformer winding transposition structures. IEEE Transactions on Magnetics. 2020;56(12):1-8. 10.1109/TMAG.2020.3028832
22. Štafl M. Electrodynamics of electrical machines. (No Title). 1967.
23. Kumbhar GB, Kulkarni S. Analysis of short-circuit performance of split-winding transformer using coupled field-circuit approach. IEEE Transactions on power delivery. 2007;22(2):936-43. 10.1109/TPWRD.2007.893442
24. Mouhamad M, Elleau C, Mazaleyrat F, Guillaume C, Jarry B. Short-circuit withstand tests of metglas 2605SA1-based amorphous distribution transformers. IEEE transactions on magnetics. 2011;47(10):4489-92. 10.1109/TMAG.2011.2155632
25. Bal S, Demirdelen T, Tümay M, editors. Three-phase distribution transformer modeling and electromagnetic transient analysis using ANSYS Maxwell. 2019 3rd International Symposium on Multidisciplinary Studies and Innovative Technologies (ISMSIT); 2019: IEEE. 10.1109/ISMSIT.2019.8932953
26. Li Y, Xu Q, Lu Y. Electromagnetic force analysis of a power transformer under the short-circuit condition. IEEE Transactions on Applied Superconductivity. 2021;31(8):1-3. 10.1109/TASC.2021.3107799
27. Jin M, Zhao Y, Wen T, Chen W, Zhang Q, Zhu T, et al., editors. Stress Distribution Characteristics of Composite Wire-Paper Winding Structure under the Radial Electromagnetic Force. 2021 IEEE Electrical Insulation Conference (EIC); 2021: IEEE. 10.1109/EIC49891.2021.9612347
28. Zhai Y, Zhu R, Li Q, Wang X, Gu Y, Li S, editors. Simulation Research on Electrodynamic Force and Deformation of Transformer Windings under Short-circuit Condition. 2022 IEEE International Conference on High Voltage Engineering and Applications (ICHVE); 2022: IEEE. 10.1109/ICHVE53725.2022.9961358
29. Feyzi MR, Sabahi M, editors. Finite element analyses of short circuit forces in power transformers with asymmetric conditions. 2008 IEEE international symposium on industrial electronics; 2008: IEEE. 10.1109/ISIE.2008.4677272
30. Zhao Y, Wen T, Li Y, Ni H, Zhang Q, Chen W, editors. A FEM-based simulation of electromagnetic forces on transformer windings under short-circuit. 2018 IEEE International Power Modulator and High Voltage Conference (IPMHVC); 2018: IEEE. 10.1109/IPMHVC.2018.8936726
31. Dawood K, Komurgoz G, Isik F, editors. Computation of the Axial and Radial forces in the Windings of the Power Transformer. 2019 4th International Conference on Power Electronics and their Applications (ICPEA); 2019: IEEE. 10.1109/ICPEA1.2019.8911132
32. Jin M, Wen T, Chen W, Zhao Y, Wu J, Wu X, et al., editors. Influence of Frequency Components of Short-Circuit Electromagnetic Force on Vibration Characteristics of Power Transformer Windings. 2022 IEEE International Conference on High Voltage Engineering and Applications (ICHVE); 2022: IEEE. 10.1109/ICHVE53725.2022.9961671
33. Thanh BD, Tung DD, Le T-H. Computation of electromagnetic forces in the windings of amorphous core transformers. Archives of Electrical Engineering. 2023:521-39--39. 10.24425/aee.2023.145423
34. Yahiou A, Mellah H, Bayadi A. Inrush Current Reduction by a Point-on-wave Energization Strategy and Sequential Phase Shifting in Three-Phase Transformer. International Journal of Engineering, Transactions C: Aspects. 2022;35(12):2321-8. 10.5829/IJE.2022.35.12C.07

Persian Abstract

چکیده

هدف از این مطالعه بررسی و تجزیه و تحلیل نیروهای محوری و شعاعی، نیروهای الکترومغناطیسی (EMF) است که بر روی سیم‌پیچ‌های ولتاژ پایین و ولتاژ بالا یک ترانسفورماتور هسته آمورف از طریق دو رویکرد مختلف: یک رویکرد تحلیلی و یک روش محدود سه بعدی تأثیر می‌گذارند. روش عنصر (FEM). در مرحله اول، روش تحلیلی برای تجزیه و تحلیل توزیع میدان مغناطیسی نشتی در مدار مغناطیسی و نیروهای وارد بر سیم پیچ ترانسفورماتور پیشنهاد شده است. سپس FEM تعبیه‌شده در ابزار Ansys Maxwell برای محاسبه و شبیه‌سازی نیروهای محوری و شعاعی تحت سه شرایط عملیاتی مختلف پیشنهاد می‌شود: بدون بار، بار کامل نامی و اتصال کوتاه. نتایج به‌دست‌آمده از دو روش مختلف مانند ولتاژ نامی، جریان نامی، جریان اتصال کوتاه، نیروهای محوری و شعاعی و EMF در سیم‌پیچ‌های ولتاژ پایین و بالا در نهایت برای نشان دادن توافق روش‌ها با یکدیگر مقایسه می‌شوند. اعتبار سنجی روش ها بر روی یک ترانسفورماتور هسته آمورف سه فاز kVA-22/0.4kV۱۶۰۰ اعمال می شود.

AIMS AND SCOPE

The objective of the International Journal of Engineering is to provide a forum for communication of information among the world's scientific and technological community and Iranian scientists and engineers. This journal intends to be of interest and utility to researchers and practitioners in the academic, industrial and governmental sectors. All original research contributions of significant value focused on basics, applications and aspects areas of engineering discipline are welcome.

This journal is published in three quarterly transactions: Transactions A (Basics) deal with the engineering fundamentals, Transactions B (Applications) are concerned with the application of the engineering knowledge in the daily life of the human being and Transactions C (Aspects) - starting from January 2012 - emphasize on the main engineering aspects whose elaboration can yield knowledge and expertise that can equally serve all branches of engineering discipline.

This journal will publish authoritative papers on theoretical and experimental researches and advanced applications embodying the results of extensive field, plant, laboratory or theoretical investigation or new interpretations of existing problems. It may also feature - when appropriate - research notes, technical notes, state-of-the-art survey type papers, short communications, letters to the editor, meeting schedules and conference announcements. The language of publication is English. Each paper should contain an abstract both in English and in Persian. However, for the authors who are not familiar with Persian, the publisher will prepare the latter. The abstracts should not exceed 250 words.

All manuscripts will be peer-reviewed by qualified reviewers. The material should be presented clearly and concisely:

- *Full papers* must be based on completed original works of significant novelty. The papers are not strictly limited in length. However, lengthy contributions may be delayed due to limited space. It is advised to keep papers limited to 7500 words.
- *Research* notes are considered as short items that include theoretical or experimental results of immediate current interest.
- *Technical notes* are also considered as short items of enough technical acceptability with more rapid publication appeal. The length of a research or technical note is recommended not to exceed 2500 words or 4 journal pages (including figures and tables).

Review papers are only considered from highly qualified well-known authors generally assigned by the editorial board or editor in chief. Short communications and letters to the editor should contain a text of about 1000 words and whatever figures and tables that may be required to support the text. They include discussion of full papers and short items and should contribute to the original article by providing confirmation or additional interpretation. Discussion of papers will be referred to author(s) for reply and will concurrently be published with reply of author(s).

INSTRUCTIONS FOR AUTHORS

Submission of a manuscript represents that it has neither been published nor submitted for publication elsewhere and is result of research carried out by author(s). Presentation in a conference and appearance in a symposium proceeding is not considered prior publication.

Authors are required to include a list describing all the symbols and abbreviations in the paper. Use of the international system of measurement units is mandatory.

- On-line submission of manuscripts results in faster publication process and is recommended. Instructions are given in the IJE web sites: www.ije.ir-www.ijeir.info
- Hardcopy submissions must include MS Word and jpg files.
- Manuscripts should be typewritten on one side of A4 paper, double-spaced, with adequate margins.
- References should be numbered in brackets and appear in sequence through the text. List of references should be given at the end of the paper.
- Figure captions are to be indicated under the illustrations. They should sufficiently explain the figures.
- Illustrations should appear in their appropriate places in the text.
- Tables and diagrams should be submitted in a form suitable for reproduction.
- Photographs should be of high quality saved as jpg files.
- Tables, Illustrations, Figures and Diagrams will be normally printed in single column width (8cm). Exceptionally large ones may be printed across two columns (17cm).

PAGE CHARGES AND REPRINTS

The papers are strictly limited in length, maximum 8 journal pages (including figures and tables). For the additional to 8 journal pages, there will be page charges. It is advised to keep papers limited to 3500 words.

Page Charges for Papers More Than 8 Pages (Including Abstract)	
For International Author ***	**$55 / per page**
For Local Author	**100,000 Toman / per page**

AUTHOR CHECKLIST

- Author(s), bio-data including affiliation(s) and mail and e-mail addresses).
- Manuscript including abstracts, key words, illustrations, tables, figures with figure captions and list of references.
- MS Word files of the paper.

International **J**ournal of **E**ngineering, P.O. Box 13145-1659, Tehran, I.R. Iran
Materials and Energy Research Center, 5 Ahuramazda St., Alvand Ave., Argentina Sq., Tehran, Islamic Republic of Iran
www.merc.ac.ir - www.emerc.ac.ir